Dissertation zur Erlangung des Doktorgrades

der Fakultät für Chemie und Pharmazie

der Ludwig-Maximilians-Universität München

Nanostructured Current Collectors for Electrochemical Applications Based on Transparent Conducting Oxides

Kristina Peters

aus

Schachtinsk, Kasachstan

2017

ACKNOWLEDGEMENTS

First of all I want to express the deepest gratitude to my supervisor Prof. Dr. Dina Fattakhova-Rohlfing for her continuous support at all stages of my Master and PhD studies. I want to thank her for being available, whenever I needed help, but giving me enough freedom to work independently on challenging and exciting topics, which helped me to become an independent and better researcher. I greatly appreciate her openness in our discussions, the creative ideas, her positivity and enthusiasm, and finally her ability to motivate me throughout my whole doctoral research. Furthermore I am very thankful for the possibility to work on so many interesting collaboration projects and to attend scientific events all over the world. Deepest thanks particularly for Dina's contribution in manuscript preparation, paper submission process and for reviewing this thesis.

I am also very grateful to Prof. Dr. Thomas Bein, for being my second supervisor and for his advice and guidance throughout my whole PhD time. The fruitful discussions during our group and subgroup meetings always provided helpful tips and inspired me to consider things from another perspective. I also want to appreciate Thomas for providing optimum working conditions, especially making the latest, high-end analytical instruments available in our group that significantly contributed to the success of my PhD projects.

I greatly acknowledge CENS, the GDCh and the Lautrach Stiftung for covering the costs for some of my conferences travels. Furthermore, I want to thank the Römer foundation for awarding me the 'Römer'-award for my master thesis and the European Materials Research Society for awarding me the Graduate Student Award in recognition of an outstanding paper contribution to the 2017 E-MRS Spring Meeting.

Also very special thanks to all cooperation partners from different institutions and different countries, who were closely involved in my PhD projects and performed key experiments for many successful publications. Especially I want to thank Dr. Morgan Stefik from the University of South Carolina for the successful work on various projects. My special thanks also to Prof. Dr. Müller-Buschbaum for involving me in the projects on dye-sensitized solar cells, Prof. Dr. Leister for the cooperation on photosystems, Prof. Dr. Lisdat for the successful collaboration on bioelectrocatalysis on 3D TCO electrodes and Prof. Dr. Schmuki for the

ABSTRACT

Transparent conducting oxides (TCOs) are an important class of materials combining transparency in the visible region with a high electronic conductivity. The reseach on TCOs has been historically focused on the development of planar thin films, which are widely used as transparent electrodes in various display technologies, smart windows or solar cells. However, motivated by the needs of emerging applications, there is also a growing interest in non-planar TCO morphologies. For example, TCO nanoparticles attract significant interest for low-temperature wet chemical deposition of conducting coatings, as conductive additives in composite materials or as electrode materials in lithium ion batteries. Three-dimensional nanostructured TCO layers gain increasing importance as a novel type of electrodes for photoelectrochemical and optoelectronic devices due to the combination of a high surface area with a large conducting interface and optical transparency. Templated self-assembly approaches are very suitable for the fabrication of such porous TCO scaffolds giving access to pore sizes ranging from small mesopores to large macropores. The pore morphology can be easily adjusted by the choice of template, enabling the design of materials with a porous structure optimized for the desired applications. An approach pursued in this thesis is the use of pre-formed crystalline TCO nanoparticles as building blocks, as they allow the formation of a crystalline scaffold at mild conditions and enable a better control over the morphology and conductivity as compared to conventionally used sol-gel precursors. This approach requires the development of suitable nanoparticles, which have to be dispersible and compatible with the template. The objective of this thesis is therefore the development of new synthetic strategies towards highly dispersible TCO nanoparticles and their assembly to high surface area TCO electrodes with a defined pore structure.

Chapter 1 introduces important classes of TCOs and gives an overview of their basic optoelectronic properties. The second part covers the different synthesis strategies towards nanostructured TCO morphologies, particularly zero-dimensional nanoparticles and three-dimensional high surface area nanomaterials. The last part will give a short review of selected applications of nanostructured TCOs. Chapter 2 discusses the basic principles of the analytical methods employed to characterize structure, morphology and transport properties of the nanomaterials.

Chapter 3 describes a new solvothermal synthesis of nanosized tin oxide and antimony-doped tin oxide (ATO) nanoparticles using *tert*-butanol as a solvent. The ATO nanoparticles resulting from this reaction are ultrasmall, crystalline and highly dispersible in polar solvents. The electrical conductivity of the nanoparticles significantly increases upon substitutional doping with antimony, reaching the highest ever reported value for as-synthesized small ATO nanoparticles ($6.8 \times 10^{-2}\ \mathrm{S\ cm^{-1}}$). To evaluate the conductivity mechanism and to assess different contributions to the total conductivity, terahertz spectroscopy was performed (Chapter 6). The measurements revealed that the conductivity increase upon doping is caused by the transition from hopping in the undoped samples to band-like conduction in the doped samples. Furthermore it could be shown that the dc conductivity of the pressed pellets is limited mainly by grain boundaries rather than by the bulk nanoparticle conductivity.

The electrical conductivity, crystallinity, small size, and high dispersibility in polar solvents render the obtained ATO nanoparticles promising building blocks for the fabrication of more complex conducting architectures using different templates. Chapter 3 and 4 cover different routes towards 3D high surface area ATO films. In Chapter 3 macroporous ATO films with large pores of 300 nm were fabricated using poly(methyl methacrylate) (PMMA) templates either via a simple one-step co-assembly procedure or via a two-step liquid infiltration method. The resulting macroporous ATO electrodes feature a high optical transparency and a large periodically ordered conducting interface. In Chapter 4 3D porous ATO films are discussed, which were made using the novel amphiphilic PEO-*b*-PHA polymer. By tuning the solution processing conditions, ATO electrodes with pore sizes ranging from 10 nm mesopores to 80 nm macropores can be produced. Particularly notable is the access to uniform macroporous films with a nominal pore size of around 80 nm that is difficult to obtain by other techniques. The increase in surface area fully translates into an increase in accessible conducting interface, which is demonstrated by the adsorption of small molybdenum polyoxometalate anions. Furthermore the importance of the pore dimensions of a 3D ATO host structure on the photoelectrochemical performance of Photosystem I (PSI) based biophotovoltaics is shown.

Another 3D-TCO system studied in this work is tin doped indium oxide (ITO). It is prepared by a direct co-assembly of ultra-small indium tin hydroxide (nano-ITOH) nanoparticles and PMMA latex beads, which is described in Chapter 5. The nano-ITOH particles transform into cubic ITO at 400 °C, resulting in macroporous ITO films with a reasonable high electric conductivity and an open interconnected pore structure. The open porous scaffolds were shown to be suitable conducting platforms for immobilization of bulky redox species or for

the deposition of functional electroactive layers. Electrochemically accessible surface coverage of cytochrome c and hemoglobin redox proteins immobilized on a macroporous ITO electrode is by about one order of magnitude higher than on a flat one.

Chapters 7-10 show the applications of macroporous ATO and ITO electrodes as versatile current collectors. In Chapter 7 n-type semiconducting spinel zinc ferrite ($ZnFe_2O_4$) is prepared by atomic layer deposition and used as a photoabsorber material for light-driven water-splitting. The photocurrent can be increased up to five times by using nanostructured ATO scaffolds underneath the absorber layer. Chapters 8-10 shows the applicability of macroporous ITO electrodes for enhanced bioelectrocatalysis of immobilized biological redox enzymes. Different enzymes (pyrroloquinoline quinone-dependent glucose dehydrogenase, Chapter 8; fructose dehydrogenase, Chapter 9; xanthine dehydrogenase, Chapter 10) entrapped in a conductive, conjugated polymer on macroporous ITO result in a significantly increased bioelectrocatalytic signal compared to that of flat ITO electrodes.

The last part of this thesis (Chapter 11) describes the development of a new high capacity anode material for lithium ion batteries based on ATO/graphene composites. The nanocomposites were fabricated *in-situ* using the solvothermal *tert*-butanol route. The use of extremely small conversion-type ATO nanoparticles anchored on the conducting graphene surface increases the lithium insertion rate and minimizes the destructive effect of significant volume changes accompanied with the conversion and alloying/dealloying processes. These features result in a record high capacity of $577\,\mathrm{mAh\,g^{-1}}$ at a rate of 60C, meaning full charging and discharging within one minute.

This thesis shows the great potential of various nanoparticle based TCO morphologies for energy conversion devices. The small size of the conducting TCO nanoparticles is beneficial for the use as building blocks towards new high surface electrodes. The possibility to tune the porous structure of the current collectors by using different templates and processing conditions opens new perspectives for tailoring the TCO morphology to meet the demands of different applications. Furthermore, novel nanocomposites of ATO nanoparticles with graphene demonstrate ultrafast electrochemical lithium insertion with a high specific capacity, making them promising anodes for lithium-ion batteries.

TABLE OF CONTENTS

1.INTRODUCTION

1.1. TRANSPARENT CURRENT COLLECTORS: REQUEST FOR NEW MORPHOLOGIES

Transparent conductor (TC) materials, including transparent conducting oxides (TCOs), play a critical role in many optoelectronic devices due to a unique combination of electronic conductivity and transparency in the visible range. Their ability to conduct electric charges while allowing light transmission makes these metal oxide films ideal transparent current collectors for numerous optoelectronic devices such as flat-panel monitors, photovoltaic devices, organic light emitting diodes (OLEDs), smart windows and photoelectrochemical cells (see Figure 1.1). For most of these applications, TCO films are prepared by physical methods in the form of thin dense films reaching low resistivities of up to 10^{-4} $\Omega\,cm^{-1}$ and high transparencies above 90%.[1]
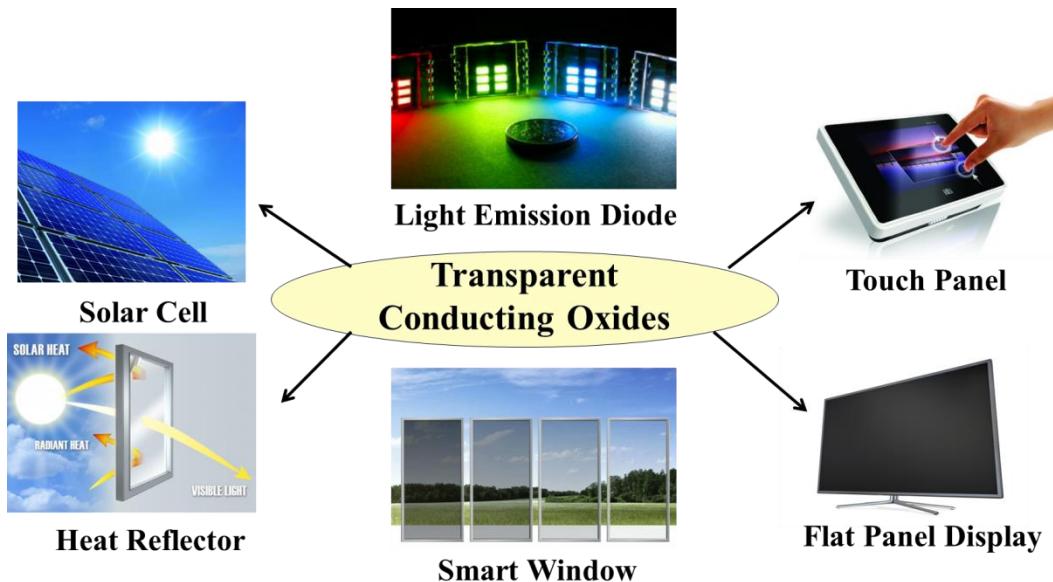
Figure 1.1   Applications of TCOs.

Motivated by new applications, extensive research was carried out in the past decade towards the development of novel type of nanostructured TCO electrodes. Particularly, three-dimensional (3D) porous TCO platforms with interconnected pores are very attractive as

electrode layers for optoelectrochemical and optoelectronic devices. Generally, 3D-electrode architectures exhibit a large interfacial surface area, which allows for a high loading of active material while maintaining short charge transport distances and a high transparency throughout the whole film thickness. This results in a larger number of electrons that can be collected from a smaller geometric electrode area, leading directly to an increased efficiency of optoelectronic devices. The research on the development of different 3D-electrode morphologies is very intense; the prevailing number of the reported systems is however based on either conventional non-transparent conductors like metal or carbon based materials, or optically transparent but low-conducting wide band-gap metal oxides.[1-4] Metallic or carbonaceous conductors are however only transparent in the form of very thin layers. When thick transparent porous electrode layers are needed, which is the case for many electrochemical applications based on surface-immobilized species, the metals or carbon compounds cannot be used because of strong absorbance. On the other hand, wide-band compounds are transparent, but show too high resistance as thick layers. Therefore, the use of transparent conducting oxides for the 3D electrode fabrication is a powerful strategy to overcome these limitations. The high surface area TCO electrodes were shown to improve the performance of many devices including electrochromics,[5] electrochemical sensors,[6-13] gas sensors,[14-16] catalysts,[11-13,17-20] batteries,[21] photovoltaics[22-29] and photoelectrodes.[30-36]

High surface area TCOs also offer a valuable alternative to typically used carbon supports for electrocatalysts. They provide a large physical surface for fine dispersion of precious metal nanocatalysts, which is necessary to reduce the amount of noble metal. An important prerequisite for the success of these devices is the stability of the electrode material towards oxidation at high potentials, whereas transparency is usually not required. Even at harsh conditions TCOs (especially SnO_2-based TCOs) exhibit a higher chemical stability compared to carbon supports, which significantly decreases the performance and operation lifetime of the catalysts.[18-20,37]

The limited number of available high surface area TCO electrodes is primarily due to synthetic challenges, which arise from the combination of demanding properties such as electrical conductivity, optical transparency as well as a defined and accessible interior pore structure. The following chapter will provide an overview of the basic material properties of TCOs used in this thesis and aims to give some theoretical background knowledge for understanding the coexistence of transparency and conductivity.

1.1.1.   TRANSPARENT CONDUCTING OXIDES (TCOS)

1.1.1.1.   MATERIAL OVERVIEW

TCOs have evolved since Badeker first observed in 1907 that an evaporated film of metallic cadmium become transparent after exposure to air (causing oxidation), while maintaining its conductive properties.[1,38] Historically these materials were dominated by a small set of binary materials including SnO_2, ZnO, In_2O_3 (Figure 1.2).[1,38] Up to date this field has expanded to a large variety of ternary TCOs or further materials of increased compositional complexity, including not only oxides.[1,4]
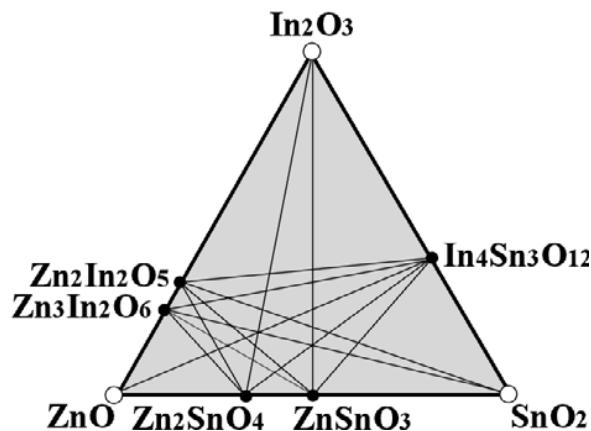
Figure 1.2   Conventional TCO semiconductors.[39]

Due to the rapid growing market for new optoelectronic devices, like touch screens and wearable electronic devices, much effort has been made to find alternatives for traditional metal oxide based TCOs.[1,2] The challenge is to find a material that can combine high electrical conductivity with optical transparency, while simultaneously being low-cost, scalable, and in some cases compatible with flexible substrates.[1] With the discovery of amorphous indium zinc oxide and amorphous indium gallium zinc oxide a strong push in the community towards amorphous TCO took place in the 2000's.[1] Amorphous TCO materials can have comparable electrical and optical properties to traditional crystalline TCOs with the additional fabrication benefits of homogenous films with very smooth surfaces at low temperatures. These features are favorable for plastic substrates and flexible electronic applications.[1,4]

Beyond classical oxide based materials, in the past years more and more non-oxide based TC materials were discovered. Possible non-oxide candidates can be divided into three categories: (1) carbon based materials, such as carbon nanotubes (CNTs) and graphenes, (2) metallic nanoparticles (NPs) and nanowires (NWs), and (3) conductive polymers, such as PEDOT:PSS.[1-4] The robustness and flexibility, as well as the simple, room temperature processing of these systems make them ideal for the application in flexible electronics. Among the transparent conductive coatings (TCCs), currently silver metal CNT- and NW-based TCCs are probably the most advanced. It is expected that graphene will play a more significant role once suitable wet deposition methods are developed. Furthermore, the combination of several types of methods and materials could be an approach to achieve efficient hybrid TCCs with superior properties.[1,2] At the end, there may not be a 'Holy Grail' transparent conducting material, as each material has its own unique advantages and physical properties for niche applications.[1]

1.1.1.2.   INDIUM TIN OXIDE (ITO)

Tin doped indium oxide, typically called indium tin oxide or ITO, is the most important TCO used in the past 60 years and also nowadays with a market share of more than 97% of all transparent conductive coatings.[2] It is the benchmark TCO as it offers the highest available transmissivity for visible light (over 90%) combined with the highest electrical conductivity (10^4 S cm^{-1}).[4] It crystallizes in the bixbyite crystal structure (see Figure 1.3) with a cubic Ia3 space-group symmetry and a unit cell containing 40 atoms. The indium atoms are sixfold coordinated by oxygen forming a close packed lattice.[4,40]
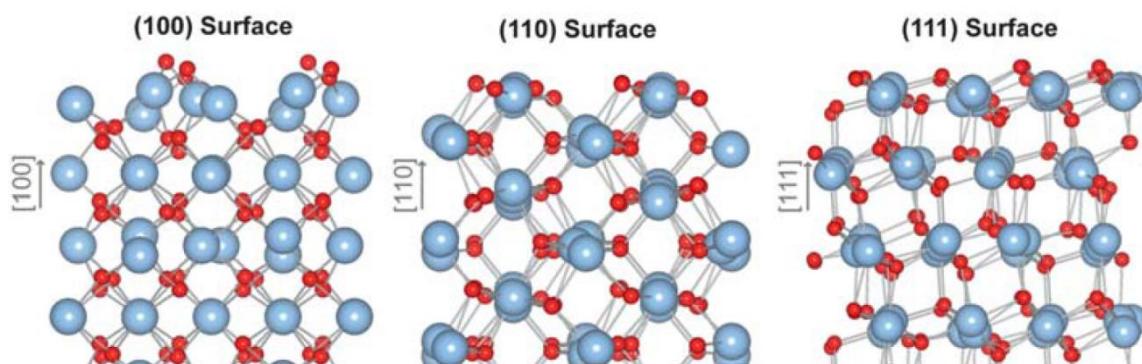
Figure 1.3   Crystal structure of In$_2$O$_3$ (bixbyite) in different orientations. The blue and the red balls represent indium and oxygen atoms, respectively.[41]

Indium oxide is a n-type semiconductor due to its ability to form oxygen vacancies with a band gap of 2.9 eV[4,42]. The conductivity of In_2O_3 strongly depends on the oxygen partial pressure and ranges from 10^{-4} to 10^3 S cm^{-1} for its undoped form.[42] The resistance can be further reduced by substituting In^{3+} by Sn^{4+} ions. The small atomic radii difference between In^{3+} (ionic radius 0.62 Å)[4] and Sn^{4+} (ionic radius 0.69 Å)[4] allows for the incorporation of Sn atoms into the bixbyite crystal structure without significant distortion of its crystalline lattice. This process generates one extra electron leading to the formation of donor bands with s-like symmetry, which overlap with the conduction band of In_2O_3.[43] However, the change in conductivity is not linearly dependent on the Sn content, which can be explained by a decreased electron mobility due to enhanced scattering effects from impurity ions at higher doping concentrations. Upon Sn doping also compensating effects can occur, like the incorporation of oxygen interstitials, which trap Sn donor electrons. The oxygen interstitials are very unstable and can be removed by reducing treatment to release the free carriers. Likewise, an oxidizing annealing can insert oxygen interstitials and trap the carriers.[42-45]

Despite its high performance, indium based TCO materials have a major drawback, namely the low abundance of indium. According to the United States Geological Survey (2007)[46] the worldwide indium reserves are estimated to be only 6000 tons. Although approximately 80% – 90% of the indium can be recycled, it is widely believed that, due to the growing demand of ITO, indium shortage may occur in the very near future.[2,46] Other disadvantages are high production costs, a low chemical stability and brittleness of ITO films, which prevents its utilization for the fabrication of flexible, stretchable, and bendable devices. Consequently, search for alternative TCO films comparable to, or even better than ITO is underway.[2,39]

1.1.1.3. ANTIMONY DOPED TIN OXIDE (ATO)

Beside ITO, tin dioxide (SnO_2, stannic oxide) is one of the most extensively studied transparent conducting materials due to its high availability, low price and higher thermal and chemical stability.[47] In nature it occurs as the mineral cassiterite. It crystallizes in the rutile-type structure with a tetragonal $P4_2/mnm$ space-group symmetry, in which each tin atom is surrounded by six oxygen atoms in an octahedral array, and each oxygen atom is surrounded by three tin atoms in a planar array (Figure 1.4). Beside SnO_2, another known tin oxide is the so called stannous oxide (SnO). SnO has the less common litharge structure, which is very unstable and converts to a mixture of SnO_2 and metallic Sn at elevated temperatures.[48]
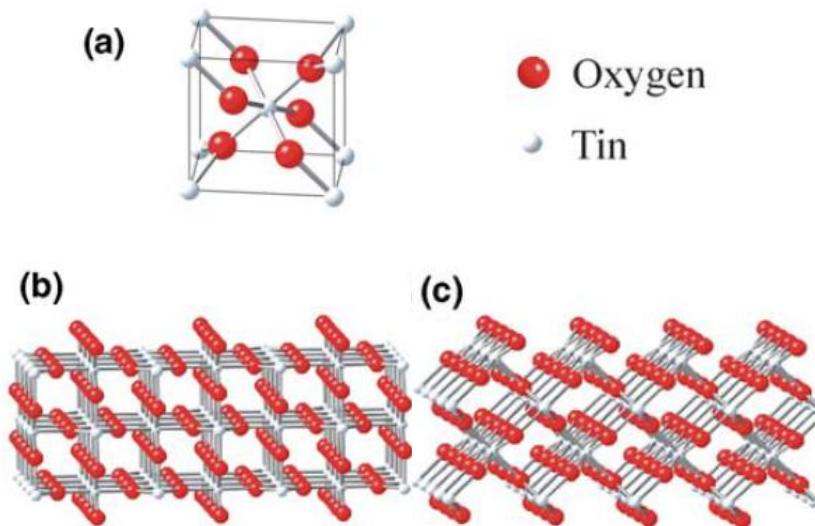
Figure 1.4   (a) Unit cell of SnO_2 (cassiterite) and (b+c) the crystal structure in different orientations. The white and the red balls represent tin and oxygen atoms, respectively.[49]

SnO_2 is a wide-gap semiconductor and in its stoichiometric form a good insulator. Non-stoichiometry, in particular oxygen deficiency, turns the insulator into a conductor. The formation energy of such oxygen vacancies as well as tin interstitials is very low, which explains the often observed conductivity of pure SnO_2.[48,49] The conductivity can be increased either by adjusting the oxygen partial pressure in order to increase the oxygen deficiency in the crystal structure, or by extrinsic dopants. Fluorine (F^-) and antimony (Sb^{5+}) are the most common used anion and cation donor dopants substituting O^{2-} and Sn^{4+} sites, respectively.[4] Fluorine doped tin oxide (FTO) is the dominant TCO in SnO_2-based binary systems. In comparison to ITO, FTO is less expensive and shows better thermal and chemical stability, but its conductivity as well as transmittance is lower. Beside ITO it is the second widely used

TCO material, mainly in solar cells due to its better stability in hydrogen-containing environment and at high temperatures required for device fabrication.[47]

Another chemically robust alternative to ITO is antimony-doped tin oxide (ATO). The antimony ions occupy Sn sites in the rutile structure. But as Sb occurs multivalent it can be incorporated in different oxidation states. The substitution of Sn^{4+} (r = 0.69 Å)[4] by Sb^{5+} (r = 0.60 Å)[4] leads to the formation of a donor center, which is located close to the conduction band of SnO_2 and results in additional charge carrier generation, whereas the replacement by Sb^{3+} (r = 0.76 Å)[4] creates an acceptor site inside the band gap and results in the creation of acceptor states. If both sites are present, compensating effects might occur.[4,49] Similar to ITO, the change in conductivity is not linearly dependent on the Sb content. At very low dopant levels, Sb is primarily incorporated by substitution of Sn atoms into the crystal lattice. With increasing doping concentration, the incorporated Sb ions are more likely to occupy interstitial sites which can result in the formation of Sb_2O_3, Sb_2O_5 or other antimony oxide enriched nanophases.[50] Furthermore, various groups have demonstrated that at lower doping levels Sb^{5+} is the dominant component, while at higher doping concentration the Sb^{3+} content increases, which is counterproductive for charge carrier generation.[4,49-51] In general, lower doping concentrations are favorable, as higher doping levels lead to a decreased electron mobility due to enhanced scattering effects from impurity ions.[4,49] Another drawback of antimony doping in high concentrations is a slight blue coloration of white SnO_2. The decreased transmission of longer wavelengths is due to a lowering of the plasma frequency, which is a direct consequence of the increased charge carrier concentration.[52-56] Consequently, there is a trade-off between conductivity and transparency in the infra-red (IR) region.[48,53]

1.1.2.   TCOS: THEORETICAL BACKGROUND

For engineering a transparent conductor, a semiconductor has to be chosen with a band gap large enough to exhibit only very little absorption in the visible range (> 3 eV). As electrical conductivity and optical transparency are the key properties of TCOs, understanding of the basic electronic characteristics of this class of materials is required. The electrical conductivity (σ) is defined as a product of the carrier concentration (N), the carrier charge (e) and the mobility (μ):[4]

$$\sigma = N \cdot e \cdot \mu \qquad \text{Equation 1.1}$$

The mobility can be described as the ease in which charge carriers can move through the material. It is defined in terms of the average scattering time (τ) and the carrier effective mass (m^*) as:[1]

$$\mu = \frac{e \cdot \tau}{m^*} \qquad \text{Equation 1.2}$$

In order to increase the mobility either the scattering time must be increased or the effective mass decreased. The latter is an intrinsic property, which requires the development of new materials. The former is influenced by any factors inhibiting the movement of carriers through a material (decreases τ) and is therefore directly related to the TC morphology and quality. Resistivity arises from scattering due to impurities, point defects, structural defects (vacancies, dislocations, stacking faults) and grain boundaries. Phase separation and porosity also result in further scattering. The former is of particular concern in solution processing and can be overcome using controlled reaction conditions. However scattering in porous materials (primary on grain boundaries) is inevitable and is the main reason for a lower conductivity in porous compared to dense packed materials.[1,4] However, this only applies for crystalline materials. In 1996 Honoso *et al.*[57] discovered amorphous materials as a new class of TCOs, where conduction is achieved through overlapping large s-orbitals resulting in a small effective mass of the electron. The s-orbitals are spherical and thus non-directional, so that the bonding directionality is not required for an effective electron transport.[1,4,57] Typical examples are amorphous indium zinc oxide and amorphous indium gallium zinc oxide. Practically all amorphous TCOs exhibit a large mobility and include at least In^{3+} or Sn^{4+} as post transition metal oxide cations.[1,4]

Electronic carriers can be generated both intrinsically and extrinsically, either by introducing defects such as interstitials and vacancies or by introducing doping atoms of different valence states in a host lattice. Intrinsic defects can be produced entropically driven at temperatures above 0 K. Each defect (vacancy or interstitial) is balanced by free charge carriers to maintain charge neutrality. Additional deposition or annealing in a reduced oxygen partial pressure environment (e.g. N_2 or forming gas) can increase the number of oxygen vacancies and thus the conductivity. However, the nonstoichiometric oxygen content in undoped TCOs is difficult to control and is therefore less used in practical applications. Defects are more commonly induced extrinsically by doping with substitutional atoms of different valence states. Doping introduces allowed energy states within the band gap of a semiconductor that corresponds to the dopant type. Depending on weather electrons or holes are the majority carrier, TCOs can be classified as n-type or p-type, respectively. For the n-type doped metal oxides extrinsic dopant-induced charges (electrons) form an energy level just below the bottom edge of the conduction band (CB). This donor level is very close to the CB, so that essentially all electrons are excited into the CB at room temperature. For the p-type doped metal oxides impurity dopants result in the formation of an energy level located above the edge of the valence band (VB). These acceptor levels are usually far enough above the VB so that only a small fraction of these can produce holes in the VB at room temperature. These two most common band structure types are shown schematically in Figure 1.5.[1,4,49,58]
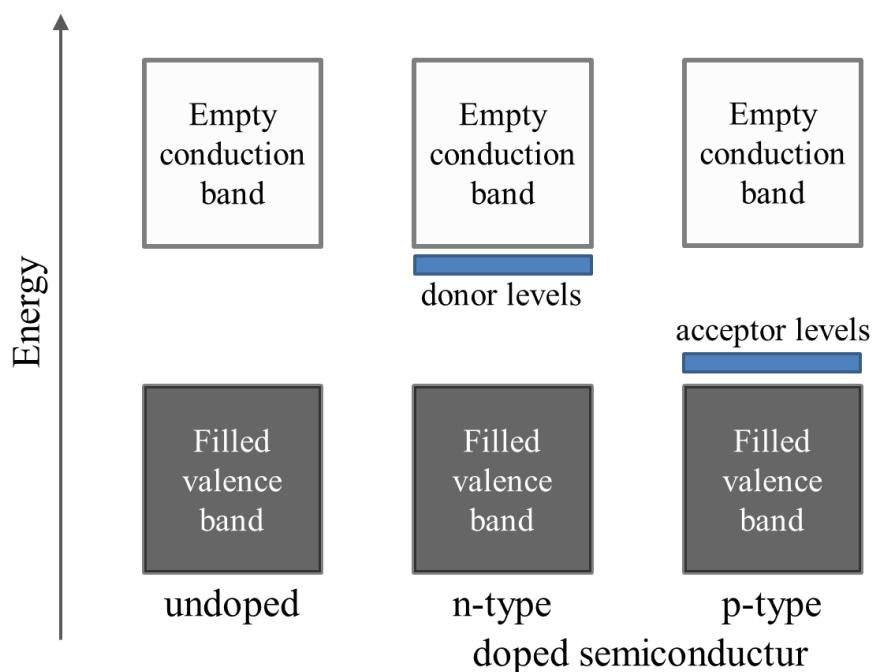
Figure 1.5   Schematic diagram showing the typical band structures for undoped as well as n- and p-type doped semiconductor.

With the addition of various donor dopants, the energy needed to excite an electron from the VB to the CB increases due to the filling of conduction band with free electron carriers (E_2 in Figure 1.6). This effect, also known as the Burstein-Moss effect[46,59,60], is responsible for band-gap widening at increased carrier concentrations and consequently for the blue-shift of the UV absorption edge, which will be further discussed below.[4,46,47] An opposite effect responsible for a smearing of the band gap (E_1 in Figure 1.6) is the electron-impurity scattering. In this case the doping concentration is so high that the donor band overlaps with the conduction band and electrons behave like free electrons.[4,46,60,61]
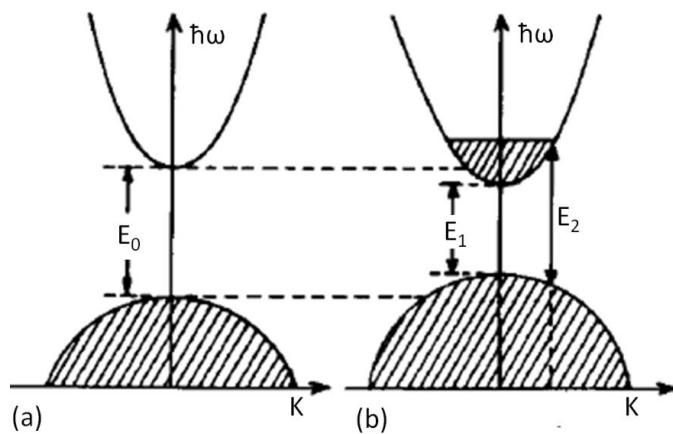
Figure 1.6   Band gap changes by donor doping. E_0 is the intrinsic band gap, E_1 is the decreased band gap due to electron impurity scattering, E_2 is the increased band gap due to the Burstein-Moss effect.[60]

Typical doping atoms are Sb^{5+} and F^- for SnO_2 (the resulting materials are called ATO and FTO, respectively), Sn^{4+} for In_2O_3 (ITO) and Al^{3+} for ZnO (AZO). Occupation of X^n sides by Y^{n+1} atoms results in the generation of free electrons (n-type doping), which increases the charge carrier concentration and consequently the conductivity. The majority of the TCOs are n-type electron conductors due to their ability to form oxygen vacancies[4] and due to a high dispersion of the density of states near the conduction band minimum,[4,58] which is indicative for a low conduction electron mass or, in other words, a high electron mobility. P-type hole conducting TCOs are difficult to obtain. The reason for that is that O-2p orbitals, which form hole-transport pathways, are strongly localized in most metal oxides and their energy levels are deeper than the valence orbitals of the metal atoms. This results in a large effective mass of the holes and therefore in the low mobility, making them unable to migrate easily within the material. Up to date there are only few reports on p-type TCO materials like for example $CuAlO_2$[4], $SrCu_2O_2$[4], $LaCuOS$[4], $BaCuSF$[4], NiO[1], $NiCo_2O_4$[1] and $CuCr_2O_2$:Mg[1].

Besides the electronic structure of the metal oxide and the dopant, the lattice stability of the host metal oxide should be considered for the successful doping. According to the Hume-Rothery rule, the size difference of the atomic radii between the host and the dopant atoms should be less than 15%.[4] Discrepancies between the host and the dopant atom radii result in a decrease of lattice stability and can generate unfavorable compensation of the dopant by intrinsic effects. Cation- or anion-vacancies will pin free charge carriers and weaken the doping in n- or p-type doped TCOs, respectively.
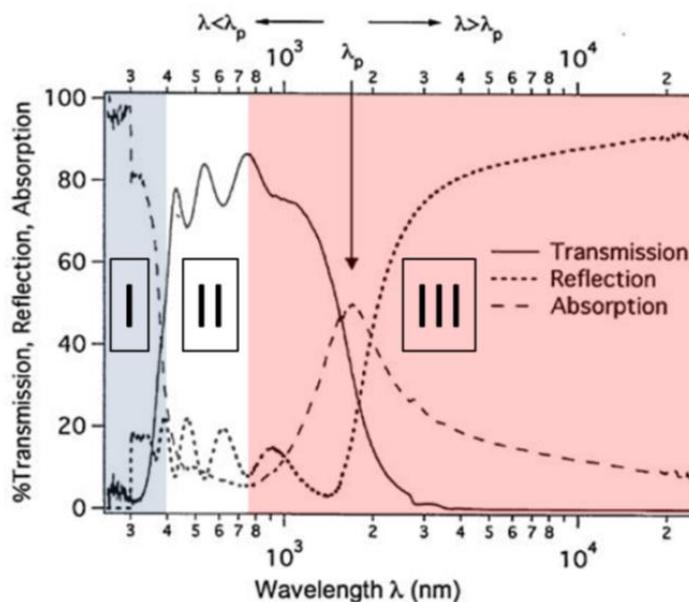
Figure 1.7   Transmission, reflection, and absorption spectra of a typical TCO.[1]

As already mentioned at the beginning of this section, the optical properties of a material are intimately related to its electronic properties. The transmission, reflection, and absorption spectra of a typical TCO are shown in Figure 1.7. There are three characteristic regions in the spectra. First, a TCO is transparent in the visible region (region II in Figure 1.7) of the spectrum (400 – 750 nm or $h\nu = 3.1–1.7$ eV), which is achieved using semiconductors with a large band gap (> 3 eV). At shorter wavelengths (< 350 nm or >3.5 eV, corresponding to region I in Figure 1.7) a drop in the transmission and an increase in the absorption can be observed, which is due to the fundamental band gap excitations from the valence to the conduction band. In the third region (III), at longer wavelengths (>1500 nm) a decrease in transmission and increase in reflection is observed. The gradual long wavelength decrease is due to collective oscillations of conduction band electrons known as plasmons. When the frequency of the incident photons matches the frequency of the collective electron oscillation in a material, light at this so called plasma wavelength (λ_p) is absorbed. When $\lambda > \lambda_p$ the

wavefunction decays and no radiation can propagate, resulting in reflection. The carrier concentration is inversely related to the plasma wavelength ($\lambda_p \propto 1/\sqrt{N}$), which creates a fundamental trade-off between conductivity and the long wavelength transparency.[1,4,49] In other words, a continually growing doping concentration increases the number of charge carriers and thus the conductivity, but decreases the optical transmission and makes the optical window narrower. Hence, one key factor in the development of good transparent conductors is the introduction of high-mobility carriers, so a high electrical conductivity can be achieved with a small number of carriers.[1,4,49]

1.2. NANOSTRUCTURED TCOS

In general, nanostructured materials can be divided into four classes based on the dimensions of their structural elements (Figure 1.8): zero-dimensional (0D; nanoclusters, nanoparticles), one-dimensional (1D; nanowires, rods, nanotubes), two-dimensional (2D; layers and sheets) and three-dimensional nanomaterials (3D). The 3D-structures are assemblies of 0D, 1D and 2D structural elements, which are in close contact with each other and form interfaces.[62-64] The following chapter will provide an overview of the various experimental strategies currently used to fabricate the zero-dimensional TCO nanoparticles as well as three-dimensional high surface area TCO nanomaterials.
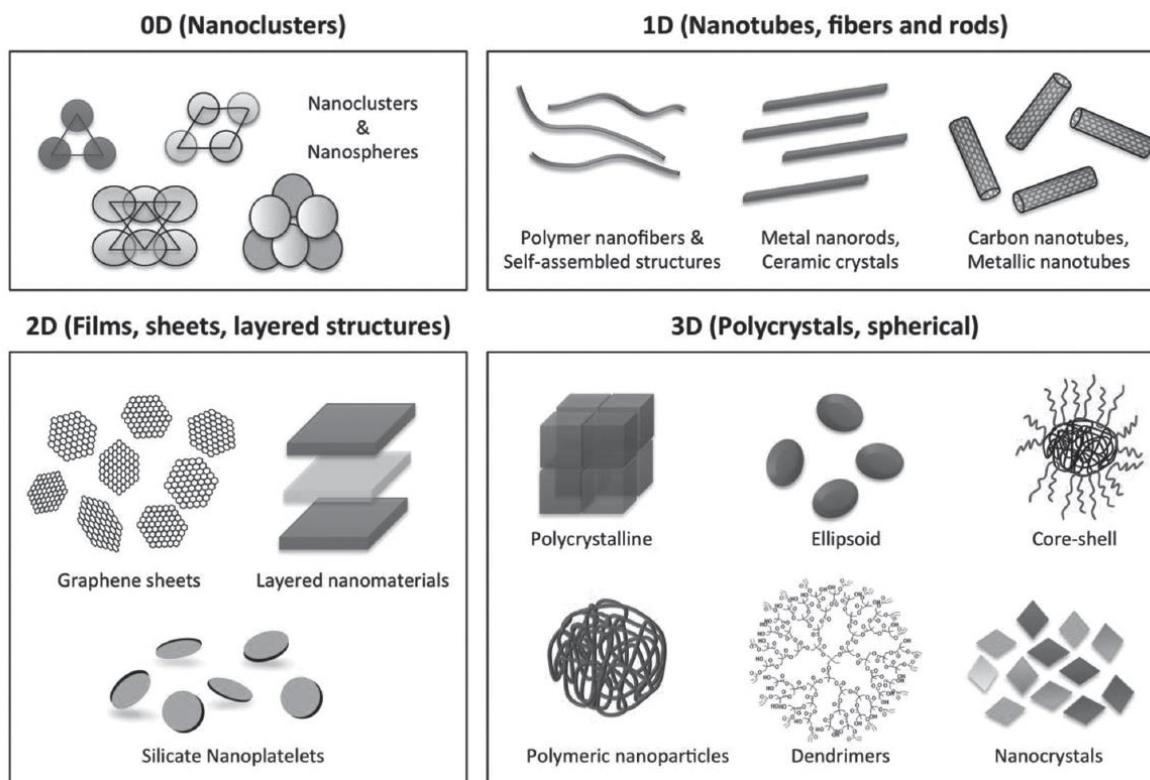
Figure 1.8   Illustrated are the various dimensions (0D, 1D, 2D, 3D) and corresponding materials available for implementation within nanocomposite designs.[63]

1.2.1.   TCO NANOPARTICLES

Due to the practical importance of TCO nanoparticles, for example for the fabrication of composite materials or as building blocks for the assembly of more complex 3D-conducting architectures, numerous strategies to their synthesis have been proposed aiming to achieve high electrical conductivity, crystallinity, narrow particle size distribution and good dispersibility. In general, nanoparticles can be fabricated using either 'top-down' or 'bottom-up' approaches.[62,65] The former uses physical methods such as milling or lithography for downscaling bulk materials, while the latter one refers to the build-up of nanostructures from molecular precursors. 'Top-down' is the most common large scale approach enabling fabrication of nanoparticles from practically available materials. Its major disadvantages however are the low control over the particle shape, a broad particle size distribution and usually a rather large particles size. The 'bottom-up' approach offers better possibilities to obtain smaller nanoparticles, a more homogeneous chemical composition and also a more narrow particle size distribution.[62,65] Many different synthesis techniques, especially gas-phase and liquid-phase syntheses, give access to nanomaterials with a wide range of compositions, well-defined and uniform crystallite sizes, extraordinary crystallite shapes and complex assembly properties.[4] The liquid-phase routes often provide more flexibility with regard to the controlled variation of structural, compositional and morphological features of the nanoparticles.

Aqueous and non-aqueous sol-gel syntheses were shown by several groups to be particularly suitable for the fabrication of TCO nanoparticles.[21,55,56,66-80] Sol-gel processes can be defined as the conversion of a precursor solution into an inorganic solid via inorganic polymerization reactions induced by the solvent.[65] Regardless of the approach, higher synthesis temperatures are typically required to solubilize precursors, induce polymerization, and/or convert amorphous nanoparticles to the crystalline form. Different possible steps in the sol-gel formation of different morphologies are schematically shown in Figure 1.9. The first step is a formation of a stable solution (I) of the metal precursor in a solvent, followed by condensation reactions (II) leading to the formation of an oxide- or alcohol-bridged network with increasing viscosity (the gel). Further condensation (III) results in an even more interconnected, rigid and porous inorganic network enclosing liquid phase. The gel can be dried under ambient or supercritical conditions (IV), resulting in xerogels or aerogels, respectively. Supercritical drying allows the liquid to be slowly dried off without causing the solid matrix in the gel to

collapse from capillary action, as would happen with conventional evaporation (xerogels). The last step (V) is a heating step to remove surface bound organic groups as well as to induce crystallization and densification.[65]
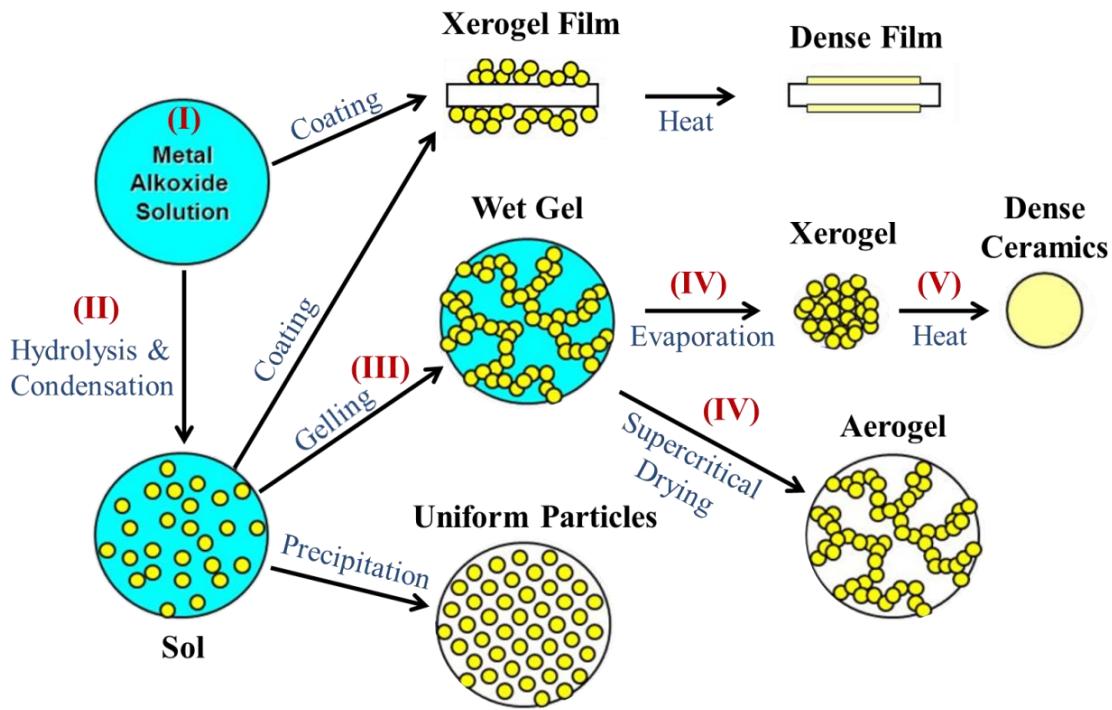
Figure 1.9   Various steps in the sol-gel process to control the morphology of the products.

Nanoparticles of different TCO materials such as indium tin oxide (ITO) and antimony doped tin oxide (ATO) have been synthesized by various methods including co-precipitation,[55,81-85] hydrothermal,[56,69-71,86] solvothermal,[55,72-80] sol-gel,[21,66] microwave assisted synthesis,[67,68] thermal decomposition,[87,88] hot injection,[89] combustion[90,91] and DC arc plasma jet synthesis.[54] One of the simplest methods is the hydrothermal sol-gel process, which is based on the hydrolysis and condensation of molecular precursors. The rate of this type of reactions is generally fast, which often results in a loss of morphological and also structural control over the final oxide material due to limited kinetic control of the reaction. Furthermore, the synthesis of substituted and mixed oxide nanocrystals can pose difficulties due to different reactivities and different decomposition temperatures of multiple metal oxide precursors.[65,92] One of efficient possibilities to overcome these limitations is the use of less reactive organic solvents instead of water, which generally slows down the reaction rates and offers a higher control over the particle size, morphology and crystallinity. The non-aqueous sol-gel synthesis routes primarily rely on the use of high boiling point solvents at solution temperatures over

200 °C. Typical solvents are for example hydrocarbons (octadecene[79,87,89]), diols (ethylene glycol,[76,93] diethylene glycol,[77] triethylene glycol), long chain alcohols (octanol,[78] oleyl alcohol[75,92]), aromatic alcohols (toluene,[55] benzyl alcohol[55,74]) or ionic liquids (one of reported examples is $[N(CH_3)(C_4H_9)_3][N(SO_2CF_3)_2]$[67]). Addition of suitable surfactants provides means to mediate the nanoparticle's growth and to prevent their agglomeration in solution. In general, surfactants cap the surface of the nanoparticles, which allows for an excellent control over the crystal size, a narrow particle size distribution, a good control over the crystal shape and a high degree of redispersibility.[65,79,92] Typical surfactants are organic ligands like long-chain acids (n-octanoic acid,[89] oleic acid,[87] hexanoic acid[70]), long-chain amines (oleylamine,[73,87,88] octadecylamine[79] tetramethylammonium hydroxide,[76] tetrabutylammonium hydroxide,[94] triethanolamine[84]) or poly-vinylpyrrolidone (PVP).[84,95] For example, Kanie *et al.*[76] have demonstrated the beneficial effect of quaternary ammonium hydroxide in the solvothermal synthesis of ITO nanoparticles in ethylene glycol, resulting in a narrowed size distribution and smaller particle size. Ito *et al.*[75] developed a lower-temperature esterification reaction pathway for the synthesis of monodispersed ITO nanocrystals using oleyl alcohol as a solvent and oleic acid as a ligand and control reagent.
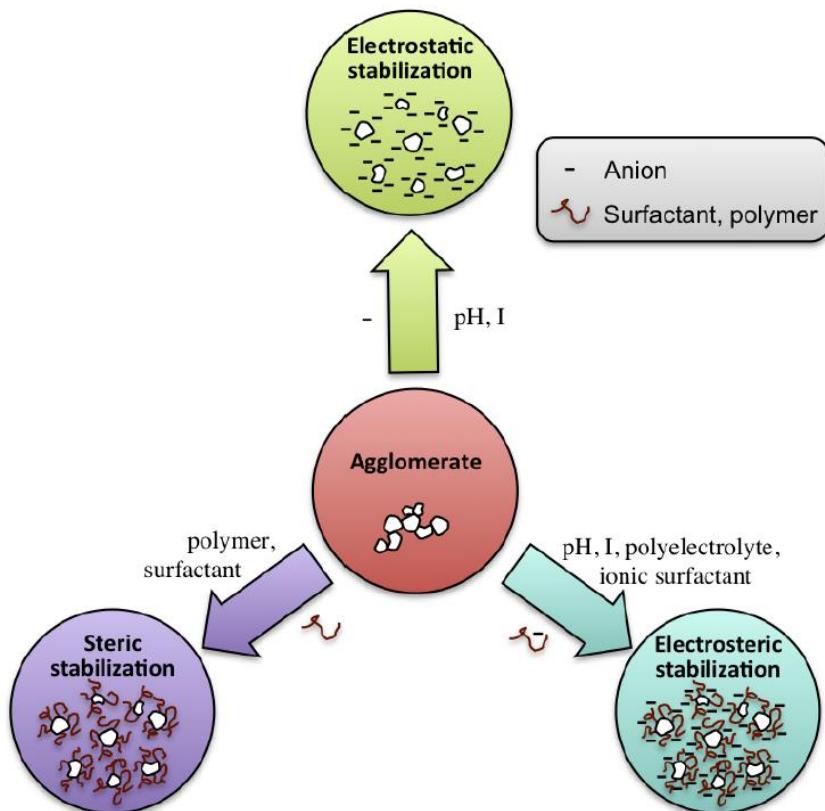
Figure 1.10   Schematic illustration of the main mechanisms for stabilization of nanoparticle dispersions, assuming positively charged surfaces.[96]

Dispersibility in suitable solvents is one of the key target properties of TCO nanoparticles, as it is of great interest for wet chemical deposition and printing of conducting crystalline coatings. This leads to expected benefits such as decreased processing costs, the possibility of coating temperature-sensitive substrates or surface patterning.[97] For a stable colloidal dispersion of metal oxide nanoparticles, repulsive forces among particles should be strong enough to avoid irreversible aggregation due to van der Waals attraction forces. Electrostatic, steric and electrosteric models (see Figure 1.10) have been proposed to describe and explain the particle-particle interactions and hence the tendency of nanoparticles to agglomerate.[96,98,99] Electrostatic stabilization is based on the formation of an electric double layer around the nanoparticle surface that is similarly charged for identical particles, resulting in a strong interparticle repulsion. In the case of steric stabilization, molecules adsorbed or bound to the particle surface create a protecting layer around the nanoparticles, which prevents particles from coming close enough to agglomerate due to attractive van der Waals forces. Finally, electrosteric stabilization is achieved by means of charged molecules and represents a combination of the aforementioned stabilization techniques.[96,99]
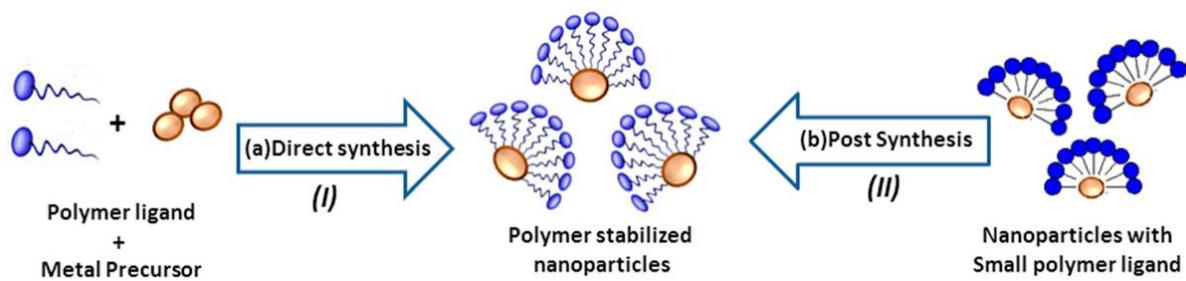
Figure 1.11 Schematic illustration of the fabrication of polymer stabilized nanoparticles (NPs): (a) in a direct (in-situ) synthesis and (b) in a post synthesis capping by a ligand exchange method.[100]

The majority of reported strategies to obtain dispersible TCO nanoparticles rely on the steric or electrosteric stabilization using coordinating ligands. The surfactants or polymers can be grafted either during the chemical synthesis of nanocrystals (*in-situ*) or through post-synthetic surface functionalization (see Figure 1.11).[96] The adsorbed surfactants or polymers have segments or chains that form an adlayer on the nanoparticle surfaces protecting them from agglomeration. As already discussed above, surfactants are commonly used as additives in solvothermal and hydrothermal reactions enabling to control the nanocrystal size, composition and morphology. Appropriate capping ligands to produce dispersible TCO nanoparticles *in-situ* are for example heteroatom-functionalized long-chain hydrocarbons like

alkylamines[73,87,88] and alkyl acids.[70,87] An alternative approach is the post-synthetic stabilization by ligand exchange with peptizing agents[94,97] or surfactants like alkylamines,[98] 3-methacryloxypropyltrimethoxysilane,[101] titanate coupling agents (isopropyl tri(N-ethylenediamino)ethyl titanate),[102] sodium polyacrylate,[103] poly-vinyl alcohol[103] or poly-PVP.[84,97] It should be however taken into account that the presence of bulky organic ligands on the particle surface is often detrimental for the conductivity of particle assemblies.

An alternative to steric or electrosteric stabilization is the electrostatic stabilization. The charging of metal oxide surfaces is primarily related to the protonation/dissociation of surface hydroxyl groups in water or other solvents and depends on the solution pH value:

$$M-OH_2^+ \quad \overset{H_3O^+}{\Longleftrightarrow} \quad M-OH \quad \overset{OH^-}{\Longleftrightarrow} \quad M-O^-$$

The pH value at which the net surface charge is neutral is called the isoelectric point (IEP). Addition of an acid or base, which shifts the pH sufficiently far away from the IEP, generally helps to disperse the primary particles and to stabilize the suspension. So far, only few types of electrically conducting monodisperse TCO nanoparticles dispersible without any stabilizing agents have been obtained. Practically all of them are formed in solution and are presumably stabilized by small solvent molecules or their reaction products adsorbed on the particle surface. The reported systems include ITO nanoparticles obtained in a polyol process[68,76,77,104] and ATO nanoparticles prepared in benzyl alcohol,[55] which are dispersible in ethylene glycol or alcohols without additional stabilization. However, due to the high boiling points of polyol and benzyl alcohol residues on the particles surface, they can be only removed at high temperatures resulting in particle growth and agglomeration. An alternative to the use of high boiling point solvents was reported by the group of Dina Fattakhova-Rohlfing[105-111], who introduced *tert*-butanol as new reaction medium for the solvothermal synthesis of various metal oxide nanoparticles. In this thesis *tert*-butanol was used for the fabrication of highly dispersible ATO nanoparticles (see Chapter 3 for further details).[105-111] It is assumed that the *tert*-butoxide groups offer sufficient steric control to hinder the particle growth and aggregation during the synthesis in the absence of any surfactants. The nanoparticles obtained in this way can be easily dispersed in various solvents by the addition of small amounts of acid (electrosteric stabilization). Due to the low boiling point of the non-aromatic *tert*-butanol (83 °C), *tert*-butoxide residues can be removed easily from the particle surface resulting in an enhanced purity of the final products.

Another approach to achieve charge-stabilized colloids was reported by Milliron *et al.*[112,113] and is depicted in Figure 1.12. They developed a post-synthetic general strategy to remove insulating bulky ligands from the surface of nanoparticles to produce soluble, charge-stabilized metal oxide colloids like ITO and TiO_2 using trialkyl oxonium salts ('Meerwein's salt').[113]
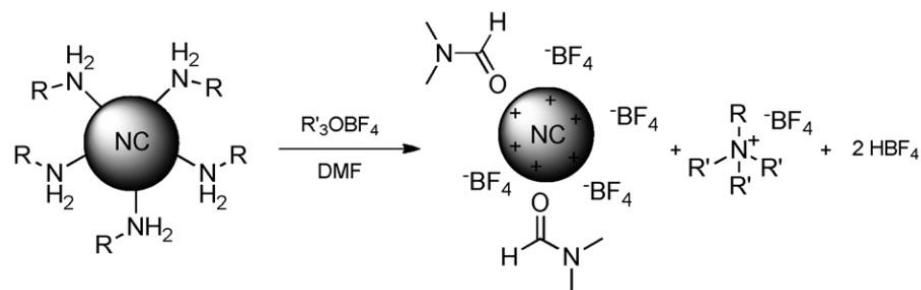
Figure 1.12 Reactive ligand stripping of amine-passivated nanocrystals with trialkyloxonium salts (NC = doped In_2O_3, Ag, FePt etc.).[112]

1.2.2.   3D-NANOSTRUCTURED TCOS: FABRICATION TECHNIQUES

Historically the research on TCO films has been focused on creating dense, highly transparent and conducting planar films for commercial applications in electronics, thermal glass coatings and other areas in which structured, light scattering films such as porous high surface area electrodes would be undesirable. However, in the past decade significant progress has been made in producing TCO electrodes with different types of porous structures and pore dimensions due to new applications and demands, which will be discussed in Chapter 1.3.[11-13,23,30,31,114] In general, such materials can be characterized by their porosity, especially their pore size distribution and pore shape. According to IUPAC nomenclature, porous materials can be classified into three categories depending on their pore size diameter, such as micropores with diameters less than 2 nm, mesopores with diameters in the range of 2-50 nm and macropores with diameters larger than 50 nm (Figure 1.13 a).[115] The pores may also be classified according to their shape: 0D-pore shape (closed, spherical), 1D-pore shape (channels, slit-like, cylindrical), 2D-pore shape (sheets, lamellar) and 3D-pore shape (cubic, ellipsoidal, more complex shapes).[64] The pores can be interconnected or closed and distributed randomly or periodically, depending on the synthesis route (Figure 1.13 b).
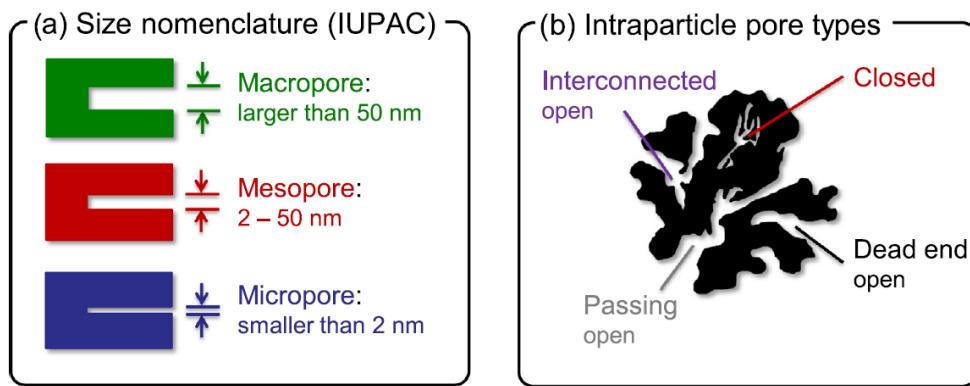
Figure 1.13   Pore nomenclature according to IUPAC (a) and classification of different pores types (b).[116]

Nanostructured TCOs can be obtained using various chemical and physical methods, which can be generally classified as template-free and template approaches. The following chapter will give an overview of the basic ways to fabricate three-dimensional ATO and ITO films.

1.2.2.1. SOLUTION BASED TEMPLATE-FREE TECHNIQUES

TCO films can be deposited from coating solutions on any wettable substrates by various deposition techniques such as spin-coating, dip-coating, drop-casting, doctor blading, different spraying techniques and various other methods, which are summarized in Figure **1.14**. Solution based methods offer advantages of scalability, high yield, and cost-effectiveness, enabling the manufacturing of a large variety of different morphologies.[117] The coating solutions with tunable viscosity (from fluid dispersions to pastes) can be prepared from crystalline powders or dispersed crystalline nanoparticles, as well as molecular precursor or oligomers using sol-gel transformations.[93,109,113,118-120]

Chemical Bath   Spin-coating   Dip-coating   Doctor Blade   Metering Rod

Slot-casting   Spray-coating   Screen Printing   Inkjet Printing   Aerosol Jet
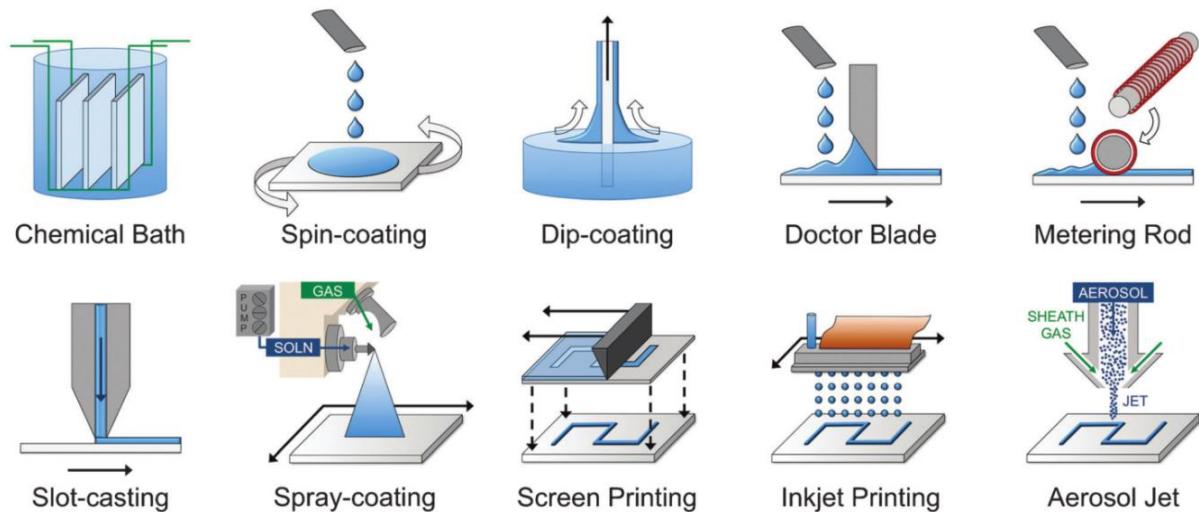
Figure 1.14 Overview of different solution deposition methods.[1]

One of the simplest approaches toward porous TCOs is the deposition of TCO powders or nanoparticles. By using already crystalline particles, the high temperatures required for TCO crystallization can be avoided. Therefore, the film processing can be performed at mild temperatures, making the particle deposition approach compatible with processing conditions for the fabrication of flexible, stretchable, and bendable devices.[35,93,109,113,118-122] The porosity of the obtained films is largely determined by the properties of the particles used for the assembly and by their packing, which results in a generally disordered textural porosity. This enables manufacturing of a large variety of different porous TCO films by selecting suitable particles as building blocks. Various groups[97,123-127] fabricated porous ITO coatings from redispersed nanoparticles reaching high conductivities of up to 140 S cm^{-1}, which were

reported by Ito *et al.*[125] for spin-coated thin films. Lili *et al.*[72] reported the fabrication of nanoparticle based porous ATO films via spin-coating featuring decreasing BET surface areas from 103 m^2 g^{-1} to 56 m^2 g^{-1} with increasing particle sizes (6.9–12.1 nm) and size-independent conductivities in the range of 6 S cm^{-1} and 20 S cm^{-1}. Goebber *et al.*[124] used spin- and dip-coating for the deposition of ATO and ITO dispersions featuring conductivities of 58 S cm^{-1} for ATO and 294 S cm^{-1} for ITO (after annealing in nitrogen). The porosity was not further characterized. Forman *et al.*[114] used spray deposition of nanoparticles, which is a simple and low-cost technique for large-scale film deposition, to achieve macroporous high surface area ITO electrodes with sheet resistances of 19 Ω sq^{-1}.

Alternatively, porous TCOs can be formed by the sol-gel approach. It is based on the conversion of a precursor solution into an inorganic solid via inorganic polymerization reactions induced by the solvent.[65] Compared to the nanoparticle based route, the sol-gel method is beneficial regarding the ease of deposition and a high smoothness of the resulting films. Although sol-gel chemistry is rather complex compared to the assembly of preformed nanoparticles, it is more versatile in terms of the final structure. The porous morphology (pore size, shape and crystallinity) can be varied by changing the sol-gel synthesis conditions before coating as well as post synthetic treatments (aging, drying and calcination). Das *et al.*[128] and Korösi *et al.*[129] developed new sol-gel methods towards nanostructured ITO electrodes with conductivities of up to 0.15 S cm^{-1};[128] the porosity of the films was however not investigated in detail. Duta *et al.*[130] have reported that porous ITO electrodes with comparable properties (such as resistance, transmission and band gap energy) can be obtained using either sol-gel approach or sputtering.

The template-free synthesis techniques (sol-gel and nanoparticle based) described above enable the facile and straightforward fabrication of porous films with a large variety of morphologies. The textural porosity of the films obtained using simple solution based techniques is usually irregular featuring a broad pore size distribution and irregular pore shapes. Additional challenges arise from the amorphous nature of the deposited sol-gel films/powders, which contain large amounts of organic substances such as residual ligands, non-evaporated solvents or additives. Annealing at elevated temperatures is the most conventional method to convert the gel into the oxide and achieve sufficient crystallinity and conductivity of the TCO. However, evaporation and crystallization during the thermal treatment lead to significant volume changes and shrinkage, which often results in a collapse of the porous networks. The final pore structure strongly depends on the calcination temperature and time, as high temperatures lead to a rapid growth of crystalline domains and

result in strong morphology changes.[35,93,109,113,118-122]

The techniques enabling the fabrication of highly porous material by avoiding pore collapse are the supercritical fluid extraction or freeze-drying approaches. Using supercritical drying the porous networks is formed by extracting the liquid component of the gel with CO_2 to obtain aerogels. This method allows the liquid to be slowly dried off without causing the solid matrix to collapse from capillary action, as would happen with conventional evaporation (xerogels).[131] Freeze-drying is based on freezing of a material, so that the frozen solvent acts as a template. Subsequent freeze-drying under vacuum allows the frozen solvent in the material to sublimate directly from the solid phase to the gas phase without a collapse of the solid scaffolds.[131]

Ozouf *et al.*[37] studied the porosity and conductivity of sol-gel prepared ATO aerogels and xerogels. They have shown that the aerogels prepared under supercritical conditions have a higher BET surface area (56 $m^2 g^{-1}$) as compared to xerogels (32 $m^2 g^{-1}$), but the conductivity of xerogels (1 S cm^{-1}) is roughly one orders of magnitude higher than that of aerogels (0.1 S cm^{-1}).[37] Pablo *et al.*[132] discussed the influence of calcination on the conductivity and porosity of the sol-gel prepared ATO aerogels. The highest conductivity (0.033 S cm^{-1}) was obtained after calcination at 800 °C, but the high temperatures result in a significant decrease in surface area (29.8 $m^2 g^{-1}$).[132] Baghi *et al.*[133] could show for sol-gel prepared ITO that variation of the Sn content results in a drastic changed morphology and particle size of the resulting materials with a maximum conductivity of 1 S cm^{-1}. The mesostructure of the porous films however collapsed from 231 $m^2 g^{-1}$ to 39 $m^2 g^{-1}$ upon calcination.[133] Rechberger *et al.*[134,135] reported the fabrication of nanoparticle-based ATO aerogels. The porous networks feature a reasonable high electrical conductivity (0.22 S cm^{-1}), while maintaining a high surface area (90-150 $m^2 g^{-1}$). An example for freeze-drying (also known as ice-templating) was shown by Li *et al.*[66] for the fabrication of porous ATO featuring an exceptional high conductivity (800 S cm^{-1}), although no further characterization of the porous structure was given.

1.2.2.2.   SOLUTION BASED TEMPLATED TECHNIQUES

The template-free approaches described above enable the facile fabrication of porous TCO materials. However, the porosity obtained by these methods is usually irregular, featuring either a broad distribution of pore sizes or pore shapes, or a random orientation of uniform pores. Much better control over the porosity and texture is achieved in templated approaches by using objects with a well-defined shape and 3D organization to guide the evolution of structure and morphology.[64] The templated approaches involve self-assembly methods, in which the periodically ordered template is formed *in-situ* (soft templating), as well as nanocasting or hard templating methods.[117] Soft-templating using surfactant-templated self-assembly of amphiphilic surfactants or block-copolymers is one of the most common ways to fabricate mesoporous TCO materials with a high control over size, shape and arrangement of pores. It is based on surfactant molecules that are composed of hydrophobic and hydrophilic parts and form supramolecular liquid-crystalline assemblies above a certain concentration, the so-called critical micelle concentrations (CMC), and act as the porosity templates.[64,131,136,137] The self-assembly is schematically depicted in Figure 1.15.
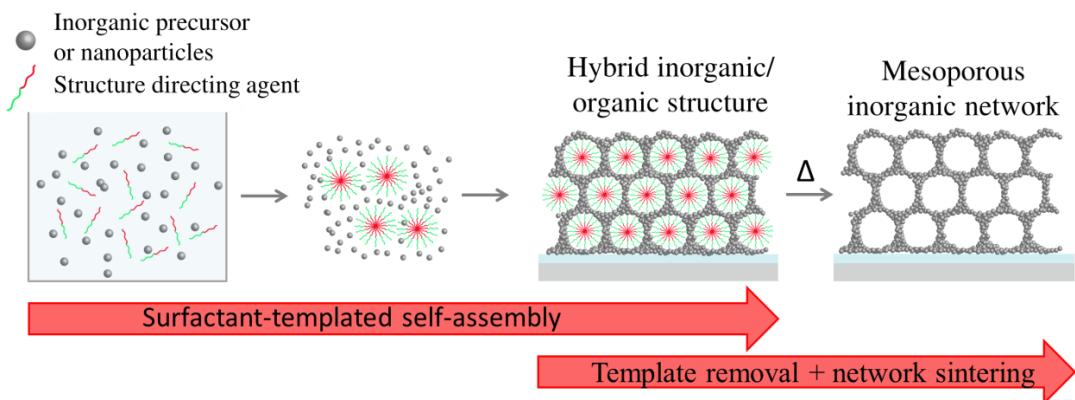
Figure 1.15   Scheme presenting the most representative steps of the surfactant-templated self-assembly.

A variation of the surfactant-templated self-assembly is the evaporation induced self-assembly (EISA) with a surfactant concentration below the critical micelle concentration. The micelle formation and their self-assembly into a periodic structure is triggered by evaporation of the solvent, which results in an increase of the surfactant concentration.[137] The advantage of this process is that the viscosity of the initial solutions is low, which enables solution based deposition of thin homogeneous films using deposition techniques such as dip-, spin- and

meniscus-coating. Another advantage of the EISA is the versatility, as the final pore shape can be changed by the solution processing conditions (e.g. from lamellar to cubic).[137]

Depending on the nature of structure directing agent (SDA), different kinds of morphologies such as porous spheres, fibers as well as more complex hierarchical porous morphologies can be prepared. The coating solutions are composed of a suitable surfactant and TCO precursors/TCO nanoparticles in a volatile solvent (typically alcohols, water-alcohol mixtures, or THF). The main prerequisite for a successful self-assembly is the compatibility of the precursors/nanoparticles with the surfactant without agglomeration or flocculation.[35,93,109,113,118-122,138] Porous TCOs can be fabricated as powders or films using different coating techniques, which are summarized in Figure 1.14. Depending on the deposition technique, the film thickness can be varied from a few nanometers to several micrometers.

The application of the liquid crystal templating and EISA approaches for the fabrication of mesoporous TCO films is restricted by the selection of a suitable solvent to disperse the SDAs as well as the inorganic component (molecular precursors/nanoparticles) without aggregation and phase separation of the two components. An additional criterion is to meet the conditions at which the SDAs assemble into supramolecular liquid-crystalline assemblies.[139] Adverse contributing factors for a successful assembly are a poor affinity between the sol–gel precursors and the organic template-directing mesophase. The first EISA fabrication of mesoporous SnO_2 was reported by Ulagappan et al.[140] by using an anionic surfactant (sodium dioctylsulfosuccinate) and a sol-gel precursor. However, the attempts to remove the surfactant and to crystallize the pore walls by calcination or extraction with solvents resulted in a collapse of the porous structure.[140,141] The difficulties arise from the amorphous nature of the as-prepared sols, which require solidification or crystallization of the framework and the removal of the surfactant. The sols typically contain large amounts of organics including surfactants and residual solvents, whose removal results in significant volume changes and shrinkage. Crystallization and the hardly controllable crystal growth during the thermal treatment further contribute to a partial or complete collapse of the porous networks. First SnO_2 based mesoporous networks, which are stable after template removal, were reported by Severin et al.[142] and Chen et al.[143] using tetradecylamine (TDA) and cetyltrimethyl-ammonium bromide (CTAB) as surfactant. The reasons for the successful template removal resulted from smaller particle size of the resulting crystalline domains and a higher thermal stability of the sol-surfactant reaction mixtures.

The synthesis of doped versions and mixed oxide nanocrystals is more challenging due to the different reactivities, hydrolysis conditions and different decomposition temperatures of multiple metal oxide precursors, and as a consequence a higher probability of side phase formation.[65,92,144] Emons *et al.*[145] were the first to synthesize mesoporous ITO powders from sol-gel-precursors (indium acetate and tin isopropoxide) using cetyltrimethylammonium bromide (CTAB) as a surfactant, however the resulting powders exhibited only a very low conductivity ($1 \cdot 10^{-3}$ S cm^{-1}). Pohl *et al*[146] fabricated periodic doped mesoporous ITO films using CTAB as surfactant, but the conductivity of the films was not investigated. Fattakhova-Rohlfing *et al.*[147] prepared mesoporous ITO films using 'KLE' type (poly(ethylene-co-butylene)-b-poly(ethylene oxides) and indium acetylacetonate to slow down the crystallization of indium oxide, resulting in a well-organized mesostructured and a reasonable high conductivity (50 S cm^{-1}). Hou *et al.*[144] described fabrication of highly ordered mesoporous ATO films using the Pluronic block copolymer F127 and sol-gel conditions reaching conductivities up to 10 S cm^{-1}.

Using different types of amphiphilic polymers, TCO layers with different types of mesoporous structures can be obtained.[93,120,144,147-156] Typical organic SDAs are commercially available surfactants like Pluronic[93,120,144,157-159] (with the general formula $PEO_xPPO_yPEO_x$, where PEO is poly(ethylene oxide) and PPO is poly(propylene oxide)), CTAB (cetyltrimethylammoniumbromid),[143,145,146,160] TDA (neutral surfactant tetradecylamine),[17,161] Brij (nonionic surfactants, poly-(oxyethylene) alkyl ethers)[162] and PVP (polyvinylpyrrolidon)).[163] However, the pore size of the TCO layers produced in this way is rather small, being typically in the range from 2 to 10 nm. Larger pores up to 30 nm for ATO[152] and 45 nm for ITO[148] were obtained using polymers with either a high effective interaction parameter or high molar mass such as KLE[147,150,164] (PEO-PHB type, a hydrogenated poly(butadiene-*b*-ethylene oxide), PIB-*b*-PEO type (polyisobutyleneblock-poly(ethylene oxide)),[148,151] PI-*b*-PEO (poly(isoprene-block-ethylene oxide),[139] PDMA-*b*-PS (poly(N,N-dimethylacrylamide)-b- polystyrene)[113] and sulfonated HmSEBmS (hydrogenated poly (alpha-methylstyrene)-b-poly (ethylene/butylene)-b-poly (alpha-methyl-styrene)[152,153]). Larger macroporous in the range of 50 to 100 nm are difficult to achieve by most reported self-assembly techniques due to a poor solubility of high molecular weight surfactants, yet the large pores are requested in many applications that are for example based on the transport of large biological moieties. Our group was able to obtain the fabrication of porous ATO films with very large pores up to 80 nm using a novel poly(ethylene oxide-*b*-hexyl acrylate) (PEO-*b*-PHA) block copolymer as a porosity template.[165] The high molar mass of the polymer and

tunable solution processing conditions enable the fabrication of ATO electrodes with adjustable nominal pore sizes from 10 nm mesopores to 80 nm macropores (see Chapter 4).[165]

Although surfactant templating is a simple and straightforward method enabling fabrication of highly ordered porous TCO films with tunable pore size, it reaches its limits when pores larger than 50-80 nm are required. In this case the use of hard templates like spherical beads of silica, polystyrene (PS) and poly(methyl methacrylate) (PMMA) can be the method of choice. The general strategy involves preparing composites of the beads and the precursor material followed by the removal of the beads to obtain the inverse porous 3D structures. The pore diameter can be easily controlled by selecting the suitable bead size (typically in a range from 0.2 to 2 μm). There are three common ways to obtain periodic macroporous structures using hard templates, which are schematically shown in Figure 1.16.
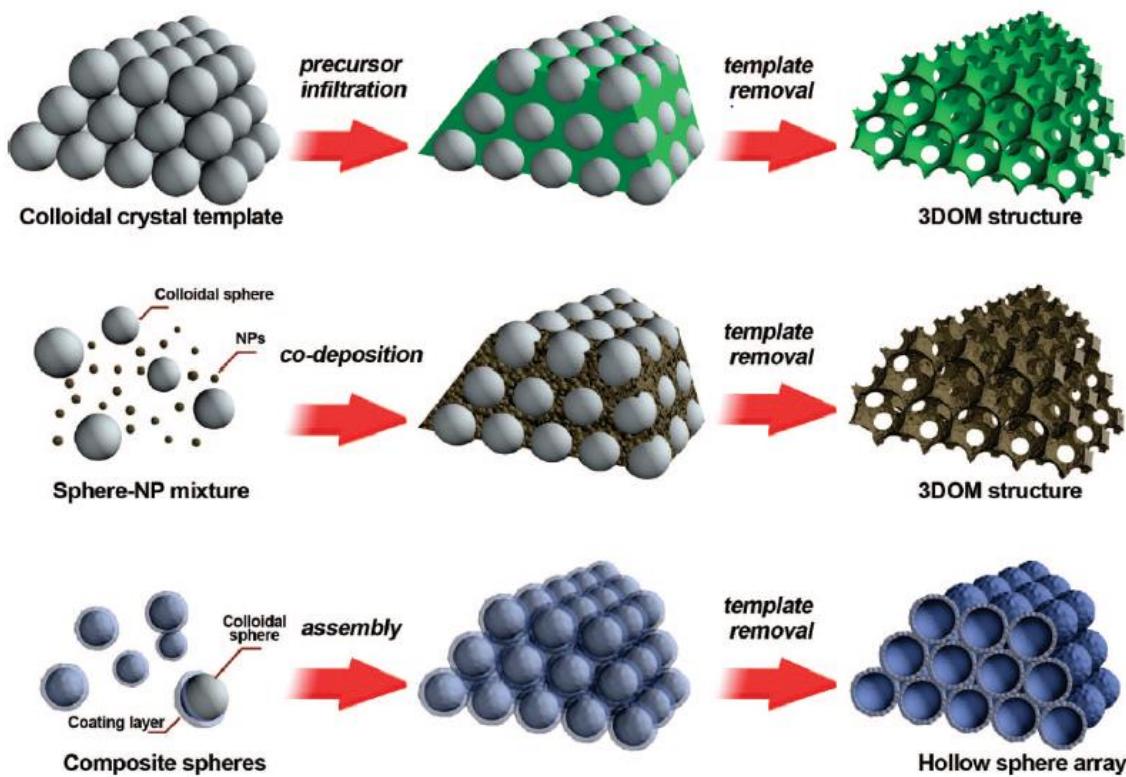
Figure 1.16   Three common methods for preparing periodic macroporous structures via hard templating (colloidal templating). Top: A preformed colloidal crystal template is infiltrated with precursor material which is processed to form the 3D open structure after removal of the template. Middle: Uniform templating spheres and nanoparticles (NPs) are co-deposited to form a 3D open structure after template removal. Bottom: Core-shell structures are assembled into periodic arrays, forming close-packed hollow shells.[166]

The most common approach is the liquid infiltration of a preformed colloidal crystal template (CCT), which is illustrated in Figure 1.16 (top). The structural replication is achieved by filling voids between the spheres in the colloidal crystal template with a precursor solution (which can include molecular precursors, sols or nanoparticle dispersion), which solidifies inside the template. Removal of the template results in the macroporous inverse opal structure. Inorganic templates such as silica beads can be removed by etching with hydrofluoric acid or strong base, while organic templates such as PS and PMMA are typically removed by thermal decomposition or dissolution in appropriate solvents.

Although the infiltration of opal templates is the most frequently used strategy, the fabrication of large-area crack-free macroporous films in this way is far from straightforward. A critical step is the liquid infiltration of the CCT array, as an excessive infiltration results in the formation of a dense overlayer, while an insufficient infiltration results in brittle structures with a low mechanical stability.[118,166] Alternatively, a so-called co-deposition method shown in Figure 1.16 (middle) can be used. In this approach the periodic composite is deposited in one step from a solution containing TCO precursor (dispersed nanoparticles or sols) and the template beads. The co-deposition method offers several advantages over the CCT method such as a better control over the precursor-to-template ratio, simplicity and shorter fabrication times. Furthermore, the morphology of the resulting scaffold such as the wall thickness and the size of the interconnecting windows can be controlled more precisely by varying the mass ratios of the nanoparticles/precursors and the beads. However, the general applicability of this approach is limited by the availability of dispersible nanoparticles or precursor species compatible with the polymer bead dispersions.[167] Finally, the macroporous materials can also be obtained by deposition of core-shell beads that are subsequently assembled into periodic arrays forming close-packed hollow shells (Figure 1.16 bottom). The availability of core-shell particles is however limited. Furthermore, the obtained structure contain as a rule encapsulated isolated pores limiting accessibility of the pore interior.[166]

Periodic TCO electrodes with inverse opal structure have been prepared by several groups using colloidal crystal templating.[23,118,168,169] Ozin et al.[35,118] fabricated periodic macroporous ATO films by liquid infiltration of preformed silica CCTs with sol-gel precursors, nanoparticles as well as a mixture of sol-gel precursors and nanoparticles. Xu et al.[170,171] and Zhang et al.[168] developed a method towards sol-gel based macroporous FTO and ITO films by infiltration of highly ordered PS and PMMA CCTs, respectively. In addition to wet chemical methods, also atomic layer deposition (ALD) can be used for the infiltration of CCTs.[23,33] Tétreault et al.[23] reported the successful fabrication of disordered polystyrene-based

macroporous AZO and SnO_2 films ($\approx 2.0\,\mu m$) by alternating pulses of organometallic precursors and a hydrolytic polycondensation agent. Riha *et al.*[33] has obtained inverse opal frameworks of indium tin oxide (ITO) with tunable pore sizes and pore wall thicknesses via ALD deposition of ITO on the close packed silica bead template. Compared to the CCT method, there are only few reports using the co-deposition method due to the limited availability of compatible nanoparticles/precursors and templates. Mersch *et al.*[172] reported the fabrication of macroporous ITO electrodes using the self-assembly of commercially available ITO nanoparticles and PS beads in a methanol/water mixture. Our group has developed a way to produce macroporous ATO and ITO electrodes using self-assembly of PMMA beads and preformed ATO or indium tin hydroxide (ITOH) nanoparticles, respectively, which will be discussed in Chapter 3 and Chapter 5.[119,169] Core-shell structured FTO electrodes were obtained by Xu *et al.*[171,173] by assembly of hollow close-packed FTO nanobeads.

A template based strategy to produce nanocolumnar TCO nanowires was reported by Wang *et al.*[27]. The ITO nanowire arrays were obtained by electrophoretic deposition of an ITO solution inside the channels of a polycarbonate membrane resting on an ITO-glass substrate. Besides latex beads, also biological objects can serve as hard templates for fabricating porous TCOs. The porous structure is achieved by direct replication of natural materials (by infiltration) or by biomimetic strategies, where extracted biotemplates like cellulose fibers undergo an assembly process. Typical bio-templates are for example celluloses (extracted from wood or cotton),[122,174-176] pollen grains[177] or eggshell membranes.[178] However, most of these reported porous morphologies were made of undoped, insulating In_2O_3 and SnO_2. Doped versions were reported by Aoki *et al.*[176] and Hu *et al.*[179], who fabricated free-standing, nanotubular ITO sheets by infiltrating cellulose filter paper using sol–gel precursors and conductive paper by infiltration of nanocellulose fibers with ITO or other conductive materials, respectively.

In general, the conductivity of porous electrodes is a serious issue due to increased grain boundary scattering and lower charge carrier mobility.[4,130,180] While dense TCO films with low porosity can reach high conductivities of up to $10^5\,S\,cm^{-1}$, the conductivity of porous TCO films fabricated by sol-gel or nanoparticle-based approaches is much lower with values between 10^2 to $10^3\,S\,cm^{-1}$.[4,119] To overcome this issues, a 'brick and mortar' approach, initially developed by Szeifert *et al.*[181] for mesoporous titania, can be applied. This approach is based on the fusion of preformed nanocrystals (bricks) through molecular precursors (mortar), which acts as a chemical glue. The method is schematically depicted in Figure 1.17 for the formation of porous ATO morphologies. Arsenault *et al.*[118] and Forman *et al.*[114] have

used this approach to fabricate ATO and ITO films. They have demonstrated that the conductivity of porous films build up from crystalline nanoparticles could be significantly increased by infiltration with a sol. The increased conductivity is due to reduced charge scattering at grain boundary contacts between the nanoparticles, which is the main scattering mechanism in nanocrystalline materials.[180]
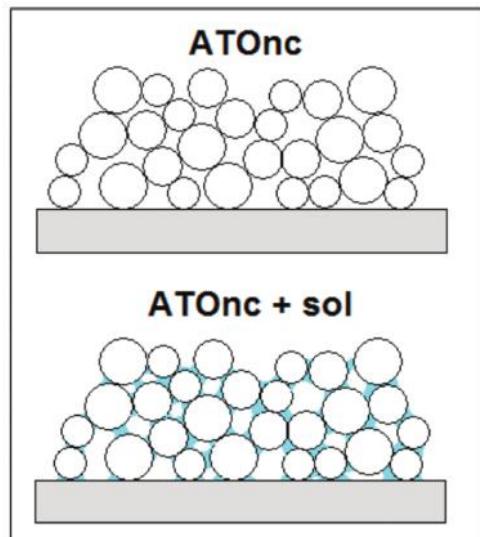
Figure 1.17 "Brick and mortar" approach[181]: crystalline ATO nanoparticles "bricks" are infiltrated with an ATO sol "mortar" (blue) resulting in lower porosity, higher conductivity, and better mechanical stability.[118]

1.2.2.3. GAS PHASE METHODS

Physical methods like CVD (chemical vapor deposition) or PVD (physical vapor deposition) are traditionally used for the fabrication of TCO materials providing crystalline coatings of a very high quality. Although being mostly used for producing thin dense films, these techniques can also be modified to fabricate nanostructured TCO coatings. Thus, high surface area electrodes composed of ATO[182,183] and ITO[184-187] nanowires can be grown using the vapor–liquid–solid method (VLS) in chemical vapour deposition. VLS is a powerful tool for the growth of one-dimensional structures like nanowires and nanorods. The growth of a crystal from atoms in a gas phase on a solid substrate is catalyzed by a metal catalyst, which is in a liquid state during the VLS deposition. The catalytic liquid significantly increases the adsorption of vapor to the nucleated seeds and therefore promotes the crystal growth in one direction.

Another template free approach is the glancing angle deposition (GLAD) technique, which was successful applied by Brett *et al.*[188-190] and Leem *et al.*[191] to produce nanocolumnar ITO electrode morphologies. It is a single step physical vapor deposition technique (PVD) that can be used to produce various porous thin film morphologies like straight pores, posts, zigzag, and helical structures. GLAD is an extension to oblique angle deposition where the substrate position is manipulated during film deposition. The basic principle is shown in Figure 1.18. An alternative concept to produce porous ATO nanofibers from colloidal ATO nanoparticle dispersions was reported by Ostermann *et al.*[24] using an electrostatic fiber fabrication technique called electrospinning.
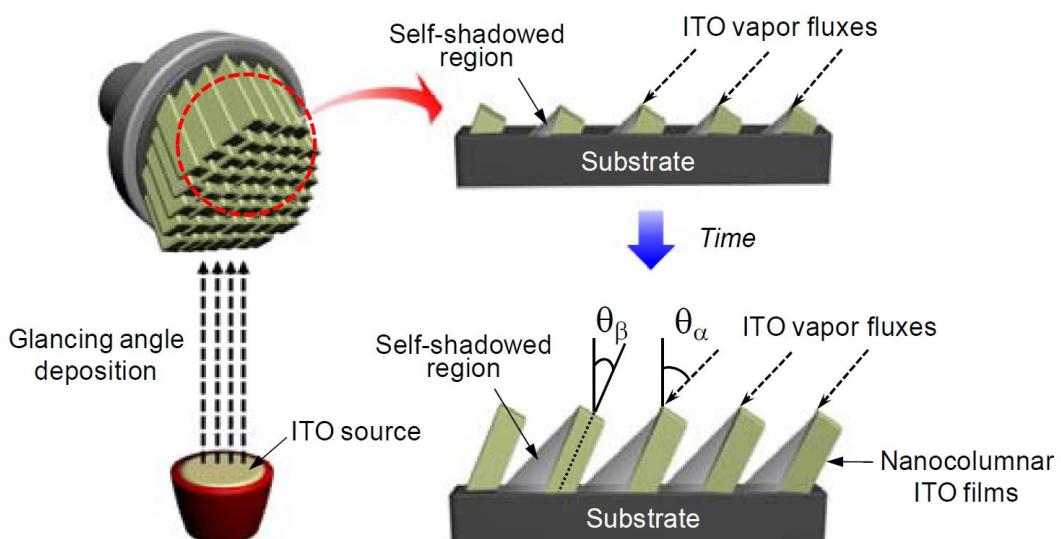
Figure 1.18 Schematic illustration for depositing ITO films using the GLAD method. GLAD ITO films can be deposited at different incident flux angles of θ_α. Although ITO vapor fluxes arrive at the substrate with an incident flux angle θ_α, the film is deposited with an inclined column angle (θ_β) during the deposition process, which is caused by the shadowing effect and results in the growth of porous columnar micro- or nanostructures. A helical column can be obtained by holding the deposition angle constant while rotating the substrate at a constant speed.[191]

1.3. APPLICATIONS OF TCOS

1.3.1.   HIGH SURFACE AREA TCO ELECTRODES

The following chapter will point out recent advances in the field of nanostructured TCO electrodes and their resulting advantages in device applications. In general, 3D porous TCO platforms with interconnected pores became very attractive as electrode layers for optoelectrochemical and optoelectronic applications due to the fact that both charge and current are linearly scaling with an increasing interface area. The optimum pore size and the type of porosity are dictated by the needs of individual application. Although microporous systems possess the highest internal surface area, the small pore size limits their application as a host matrix for applications requiring the incorporation of bulky species or mass transport. Therefore, the research focuses on the development of meso- and macroporous systems.[30,31,34,114,192] Such high surface area electrodes were shown to improve the performance of many devices including electrochromics[5], electrochemical sensors [6-13], gas sensors[14-16], catalysts[11-13,17-20], batteries[21] (see Chapter 1.3.3), photovoltaics[22-29] and photoelectrodes[30-36].
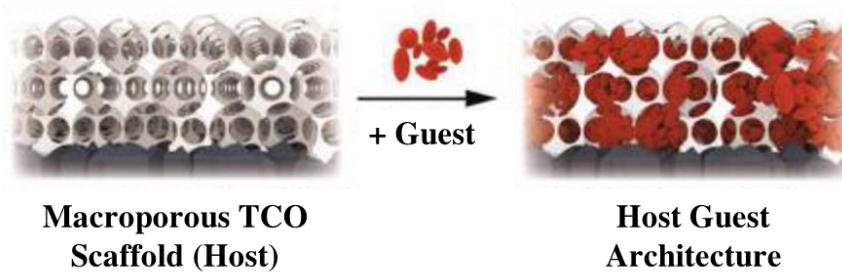
Figure 1.19   Schematic representation of host-guest architectures.[30]

Porous TCOs attract increasing attention also as extended transparent current collectors for photoelectrodes, for example in solar-driven photoelectrochemical (PEC) water splitting devices.[30-36] The photon to current conversion efficiency of photoelectrodes is defined by the efficiencies of light harvesting and charge collection processes, which are strongly affected by the thickness and the microstructure of the electrodes. Thin layer electrodes have as a rule the higher charge collection efficiency due to a matching charge collection depth, but an insufficient light harvesting efficiency. The trade-off between the photo- and charge collection can be often overcome by depositing thin absorber layer onto a transparent high-

surface-area electron collector in a so called host−guest architecture (see Figure 1.19). Such architectures provide a long optical pathway for substantially harvesting of the incident photon flux, a considerable higher specific surface area for absorber loading and a shortened electron transport route for effective charge collection. For this kind of applications large, interconnected pore systems are beneficial, as it allows mass transport of liquid or gas phase species throughout the structure resulting in enhanced device efficiency.[30,32,33] Moir *et al.*[35] and Riha *et al.*[33] deposited hematite on preformed macroporous ATO scaffolds using sol-gel or ALD, respectively, resulting in an up to seven fold enhanced photocurrent. Kondofersky *et al.*[30] and Xu *et al.*[32] extended the host-guest approach to the use of tin- and titanium-doped hematite on macroporous ATO to boost the PEC performance. In the present thesis (see Chapter 7) zinc ferrite ($ZnFe_2O_4$)/macroporous ATO host-guest architectures are used as photoabsorber material for light-driven water-splitting reaching five times higher photocurrents compared to flat films.[31] Wang *et al.*[36] reported on a more than doubled hydrogen evolution efficiency of CuO nanosheets on macroporous ATO electrodes compared to flat films. High surface area ATO powders have also emerged as promising candidate for applications as support material for catalysts. It provides a physical surface for fine dispersion of catalyst metal nanoparticles (Ir, Pt. Pd, Au, Ru), which is necessary for reducing the amount of precious metal. Strasser *et al.*[17-20] have demonstrated the stabilizing role of mesoporous high surface area ATO powders for several catalyst systems including Ir nanodendrites[19], $IrNiO_x$ core-shell particles[18] and IrO_x nanoparticles[20]. Especially its high corrosion and oxidation stability at high potentials as well as in a wide range of pH values makes ATO a valuable alternative to commonly used carbon black as support material.

Besides energy applications, porous TCOs are suitable platforms for biosensors. An electrochemical biosensor is an analytical device that contains an immobilized sensitive biomaterial (mainly an enzyme, but also antibody, antigen, organelles, DNA, whole cells or tissues) in a close contact with an electrode that is likely to convert a biological event into a quantitatively measurable electrical signal.[193] These systems rely on a fast interfacial redox reaction with the immobilized enzyme, a high stability of the immobilized enzyme as well as on a high sensitivity and selectivity. The pore sizes of the electrodes should be large enough to incorporate the biological units and bind them without deterioration of their biological functionality. The possibility to control the porosity of electrodes and the chemical surrounding inside the pores by chemical modification of the pore interior enables to increase the biomolecule stability. One of the simplest approaches for the incorporation of electro-active guests is adsorption on the surface of the porous framework by electrostatic

interactions. Schaming *et al.*[6] reported on the immobilization of oppositely charged hemeproteins cytochrome *c* and neuroglobin proteins within mesoporous ITO electrodes by changing the pH conditions. Kwan *et al.*[7] demonstrated that two different redox proteins, cytochrome *c* and the blue copper protein azurin, could be adsorbed in mesoporous ATO films with retention of their electron transfer functionality. Frasca *et al.*[8] have shown the successful immobilization and bioelectrocatalysis of *human* sulfite oxidase (*h*SO) in the nanostructured ATO thin film electrodes. Simmons *et al.*[9] demonstrated the size-specific incorporation of intact DNA nanocages into the pores of a mesoporous ATO for applications such as photovoltaics, sensors, and solar fuel cells. Covalent immobilization of the biomolecules is in many cases desirable as it substantially enhances the leaching stability. This has been demonstrated by Müller *et al.*[10] who compared the electrochemical performance of covalently attached and adsorbed cytochrome *c* on mesoporous ATO electrodes. They have shown that covalent bonding significantly enhances the binding stability and makes it much less susceptible to the influence of the environment, especially of the ionic strength of the electrolyte.[10] An elegant alternative strategy to improve the binding of biological units to an electrode is the entrapment in a conductive, conjugated polymer. In this thesis in Chapter 8-10, this concept is demonstrated for the immobilization of various enzymes including fructose dehydrogenase[11], pyrroloquinoline quinone-dependent glucose dehydrogenase[12] and xanthine dehydrogenase[13] to conducting high surface area ITO electrodes.

1.3.2. PSI BASED PHOTOVOLTAICS

In times of global warming and an increasing energy demand the interest in alternative energy sources significantly arose in the past decades. Especially solar energy is by far the most important renewable energy source on our planet. It is harnessed most efficiently by the photosynthesis representing the major energy-conversion process taking place on earth. The light driven oxygenic photosynthesis converts carbon dioxide and water into carbohydrates and oxygen, provides us with food and fossil fuels and finally affects our climate.[194,195] The centerpieces of this process are the photoactive reaction centers photosystem I (PSI) and photosystem II (PSII), which catalyze the reduction of ferredoxin and oxidation of water, respectively. While the early events of this reaction, namely the light-induced charge separation, occurs with an unsurpassed efficiency of 100%, the subsequent reactions in biological cells leads to a considerable decrease of the efficiency.[195] Recent advantages in biochemistry and nanotechnology provided tools to isolate the photosynthetic complexes and integrate them into a new class of bioelectrochemical devices. This enables the profitable use of the remarkable light induced charge separation efficiency at the earliest stage.[195-198] Another advantage of the use of PSI in such devices is its high availability, low cost production[198] (10 cents per cm^2 of active electrode area) and its stability up to 280 days[199,200] in wet electrochemical cells.

PSI uses a system of oriented chlorophylls to harness energy from incident photons by transferring them to a special pair of chlorophyll *a* molecules that build up the P_{700} reaction center. The charge separation occurs at the P_{700} reaction center, which is thereby oxidized to an electron deficient state P_{700}^+ resulting in a strong change in its redox potential from +0.43 V (P_{700}) to −1.3 V (P_{700}^*) (vs. NHE).[195,201] The electron is released in an electron transfer chain made up of several cofactors (A_0, A_1, F_x, F_A, F_B) that exhibit decreasing redox potentials (see Figure 1.20).[198,201] Each absorbed photon generates a charge separated state, P_{700}^+/F_B^-, achieving a quantum efficiency of nearly 100%. In natural photosynthesis electrons are shuttled away from F_B^- to ferredoxin, while P_{700}^+ captures an electron from reduced plastocyanin.[198,202] In bio-inspired artificial systems the photosynthetic complexes have to be coupled to conductive supports using various approaches that will be discussed in detail in the following section.
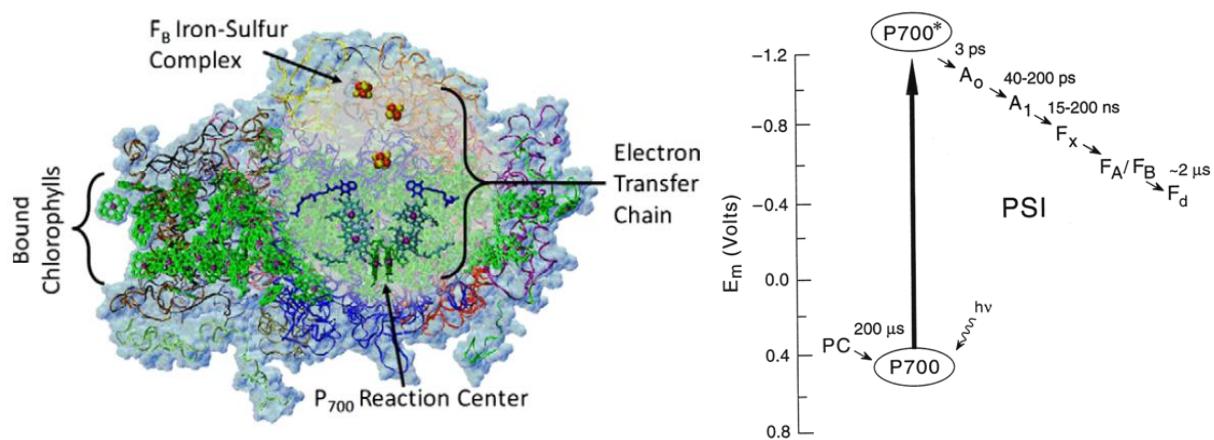
Figure 1.20   Left: Structure of plant PSI showing bounded chlorophylls, the P_{700} reaction center, the electron transfer chain and the final electron acceptor F_B.[198] Right: Scheme of the electron transfer chain.[203]

An important factor for the performance of bio-photovoltaic devices is the choice of the electrode material. It must be chosen carefully to match the redox potentials of the terminal cofactors (plastocyanin or ferredoxin sides). The most straightforward electron transfer pathway of immobilized PSI is the direct electron transfer from the active side to the electrode surface. A critical concern in the development of such bioelectrochemical devices is the orientation of the immobilized PSI protein complex on the electrode surface, as reduction and oxidation of the redox partners occur on opposite sides of the complex. Consequently the electron transfer pathway from the P_{700} reaction center to the F_B sites is sterically predefined.[201,204] The PSI can be integrated into devices isotopically, either with the P_{700} or F_B side proximal to the electrode, or anisotropically in some random, non-specific orientations.[204] A PSI-dependent net photocurrent is only detectable if the rates of either the donor reduction or acceptor oxidation at the electrode surface differ at least slightly from each other. However, in large protein complexes the active sides are usually embedded in the interior of the proteins, so that the direct electron transfer between the protein and the electrode is very unlikely. Freely diffusing redox mediators offer the easiest way to overcome the poor electronic coupling and establish an electron transfer between PSI and a suitable electrode surface. Appropriate mediators are for example freely diffusing redox active molecules with a redox potential lying between the redox potentials of the terminal P_{700} and F_B centers and the applied potential of the electrode. The most common used mediators are 2,6-dichlorophenolindophenol (DCPIP) in combination with sodium ascorbate as electron donor.[195,197,198] Other possible soluble electron donors (see Figure 1.21) are cytochrome c_6,

$[Fe(CN)_6]^{4-}$, $Os(bpy)_2Cl_2$ or Z813 Co(II)/Co(III) as well as ferredoxin, $[Fe(CN)_6]^{3-}$ or methyl viologen (1,10-dimethyl-4,40-bipyridinium) as electron acceptors.[199]
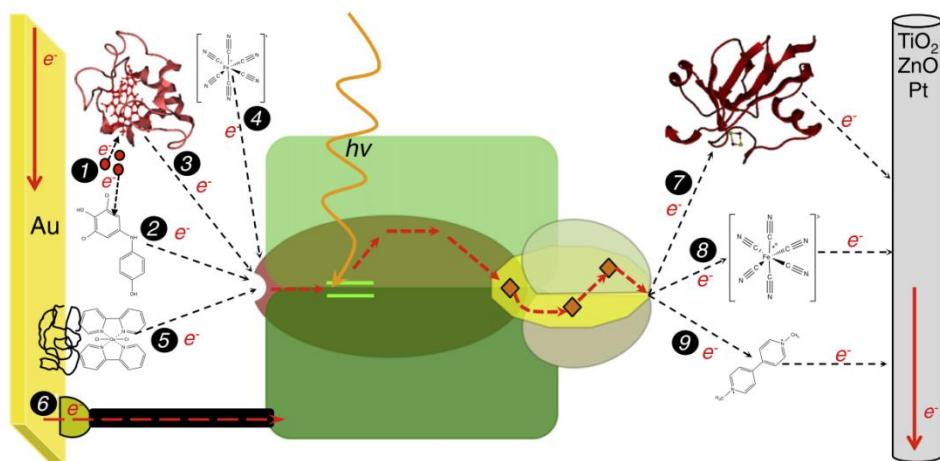
Figure 1.21 Biohybrid schemes integrating PSI with various electron transfer mediators. Soluble mediators (2) DCPIP, (3) cytochrome c_6, (4) $[Fe(CN)_6]^{4-}$, or (5) $Os(bpy)_2Cl_2$ can be reduced by Au electrode or (1) sodium ascorbate, allowing the electron transfer to (6) immobilized PSI. PSI can also be directly reduced by immobilization wire (6) (NTA–Ni–His$_6$–PSI). Soluble acceptors (7) ferredoxin, (8) $[Fe(CN)_6]^{3-}$, or methyl viologen can be used to transfer electrons from the FB Fe–S center of PSI to TiO_2, ZnO, or Pt electrode.[199]

In the last years, several strategies were developed to enhance the performance of PSI based photovoltaics. The covalent or electrostatic immobilization is the easiest way to wire PSI to an appropriate surface. To achieve a proper orientation of PSI, Faulkner *et al.*[204] used self-assembled monolayers bearing $-NH_2$ or $-COOH$ terminal groups for electrostatic binding as well as N-hydroxysuccinimide or terephthaldialdehyde modified surfaces for covalent binding of PSI yielding photocurrent densities of 100 nA cm^{-2}. Other groups used molecular wires like surface bound naphthoquinone-derivate,[205] a viologen derivate (NQC15EV)[195] or cytochrome *c*.[206] Another approach is the manipulation of the PSI itself to either enhance the photochemical activity and stability,[194,207] both in solution and in the dry state, or their binding affinity to the electrode.[208] Matsumoto *et al.*[207] have demonstrated that polycations like poly-L-lysine and poly-L-arginine significantly enhance the photochemical activity of PSI. Furthermore, poly-L-lysine stabilizes PSI in the dry state resulting in 84% activity recovery. Simmerman *et al.*[208] were able to enhance the surface selectivity of PSI via the use of especially designed ZnO and TiO_2 binding peptides (ZOBiPs/TOBiPs). Another approach to increase the absolute photocurrent of biophotovoltaics is the combination of PSI with a photoactive semiconductor like TiO_2[194,208-211] or hematite (α-Fe_2O_3).[212] Using nanostructured TiO_2 Mershin *et al.*[194] could obtain photocurrent densities up to 362 μA cm^{-2}.

To overcome the limitations of 2D arrangements and to generate higher photocurrents per geometrical electrode area, various strategies have been explored, which can be divided mainly into three groups: multilayer architectures,[212-215] 3D polymer gels[196,216-221] and 3D electrode surfaces.[165,194,197,206,211,222] Multilayer adsorption is one of the simplest ways to achieve a high loading by direct adsorption of the photoactive guest molecules to an electrode. Problematic about this approach is the anisotropical orientation of PSI multilayers, which results in limited current densities due to long electron transfer pathways accompanied by high recombination rates.[212-215] A more effective strategy is the entrapment of the PSI complex within a conductive redox polymer network, which acts both as three-dimensional immobilization matrix and as electron donor or acceptor. Yehezkeli et al.[223] were the first to report on bis-aniline-crosslinked PSI/Platinum nanoparticle composites using electropolymerization. Badura et al.[201] and Gizzie et al.[209,216] showed the successful integration of PSI into osmium-modified redox polymer hydrogels and polyaniline, respectively. The photocurrent could be enhanced up to 5.7 μAcm^{-2} using polyaniline films, which is a 200-fold increase over traditional PSI multilayer films of comparable thickness (185 nm), and up to 29 μAcm^{-2} using osmium-modified redox polymers.

Another approach that was explored also in this thesis is the use of nanostructured three-dimensional networks to increase the enzyme loading.[165,194,197,211,222] The highly structured electrode scaffold increases the PSI-electrode interface and reduces the average charge transfer distance. Especially high surface area TCO electrodes have shown to be very advantageous, as they allow effective light absorption through the whole film thickness and provide good electric communication between the biological entity and the electrode.[165,172,206,224-226] While many groups reported on wiring PSII on high surface area TCO electrodes,[172,224,225,227] there are only two reports on PSI modified porous TCOs.[165,206] Stieger et al.[206] have shown that the photocurrent linearly follows the thickness of PSI functionalized macroporous ITO electrodes reaching current densities of up to 150 $\mu A\ cm^{-2}$ for 40 μm thick electrodes without indications of limitation.

It can be envisioned that the combination of a redox polymer matrix with a high surface area TCO electrode would combine the best aspects of two advanced enzyme immobilization strategies resulting in a record performance. This could be already shown by Sokol et al.[227] for PSII wired on hierarchical indium tin oxide electrodes using Os complex-modified redox polymers.[227]

1.3.3. APPLICATION OF ATO AS ANODE MATERIAL IN LITHIUM ION BATTERIES

Lithium ion batteries (LIB) play a significant role in our daily life for powering portable devices like cellular phones, laptops and digital electronics and for the electro mobility sector.[228-231] Record-high oil prices have pushed consumers towards fuel-efficient electrical or hybrid vehicles to escape their dependence on petroleum and to address climate change. However, there is an ever increasing need for new rechargeable Li-ion batteries with significantly higher energy and power densities and faster charging rates in order to meet the growing demands for portable consumer devices with advanced functionalities and long-range electric vehicles.[228,232]

A typical LIB is composed of a graphite negative electrode (reductant, anode) and a transition-metal oxide based positive electrode (oxidant, cathode), which are electronically isolated from each other by a thin film separator and an electrolyte, as depicted in Figure **1.22**.[232-235] During discharge (see Figure 1.22 top), lithium ions diffuse from a lithiated anode into a delithiated cathode with concomitant oxidation and reduction of the two electrodes, respectively. The reverse process occurs during charge (see Figure 1.22 bottom).[235] Depending on the reversibility of those reactions, batteries can be non-rechargeable or rechargeable, which are also termed primary and secondary batteries, respectively.[233] The state of the art rechargeable LIBs are fabricated in the discharged state (see Figure 1.22 bottom).[234] The electrolyte is typically an ion conductive but electronically insulating medium that conducts Li ions between the anode and the cathode, but forces the electronic component to traverse an external circuit. It has to be stable in the potential window, in which the battery is operated to avoid reduction or oxidation of the electrolyte.[230,234] It is typically a solution of hexa-fluorophosphate ($LiPF_6$) or lithium perchlorate ($LiClO_4$) dissolved in an organic carbonate solvent mixture like ethylene carbonate (EC), propylene carbonates (PC), dimethyl carbonate (DMC), and diethyl carbonate (DEC).[230] The separator separates the electrodes spatially from each other preventing electrical short-circuits and allows only for Li ion diffusion. The electrodes themselves are complex systems composed of a metal current collector, the active compound, additives that increase the electrical conductivity (typically various types of carbon) and additives enhancing adhesion, mechanical strength and ease of processing (usually polymeric binders, such as polyvinylidene fluoride).
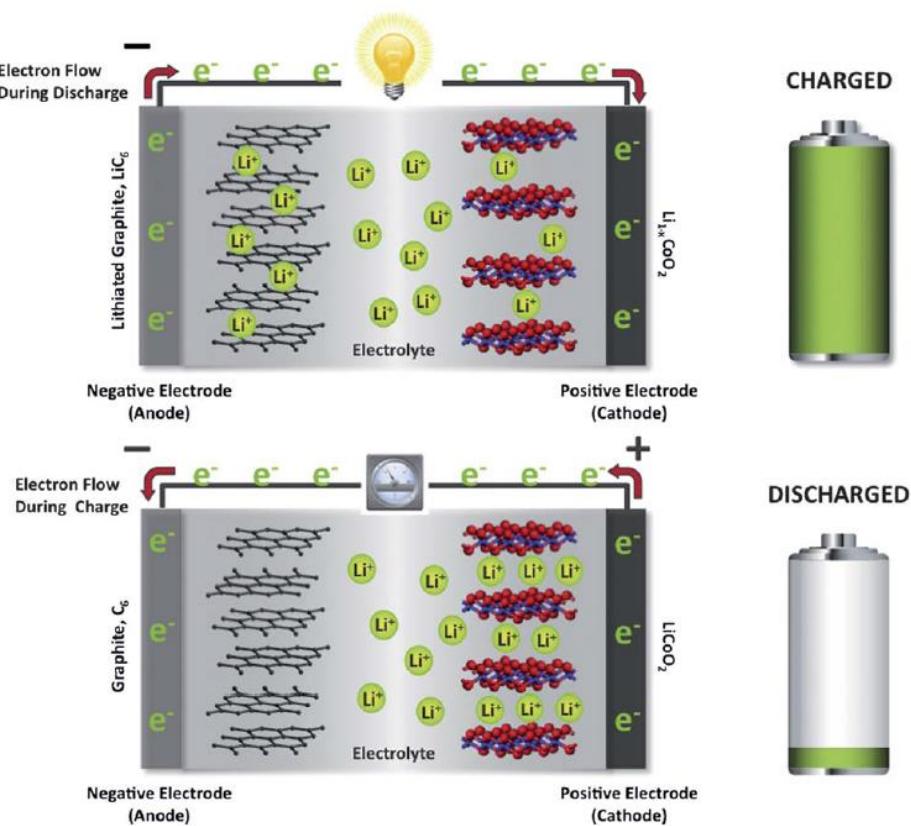
Figure 1.22   A schematic illustration of the working principles of a $Li_xC_6/Li_{1-x}CoO_2$ lithium-ion cell. During discharge (top), lithium ions diffuse from a lithiated graphite (Li_xC_6) structure (the anode) into a delithiated $Li_{1-x}CoO_2$ structure (the cathode). The reverse process occurs during charge (bottom).[235]

Batteries are characterized by several key figures such as the cell voltage (E_{cell})/open-circuit voltage, the theoretical capacity (C), Coulombic efficiency, the charge/discharge rate (C-rate), cycle life, the energy and output power (*P*).

Depending on the combination of electrode materials a potential difference of the electrochemical cell can be measured. The potential difference is also known as the open circuit voltage (V_{OC}) or as the electromotive force (emf). It is measured in V (= J C^{-1}) and is defined as:[236]

$$E_{cell} = E_{cathode} - E_{anode}$$ Equation 1.3

The maximum theoretical potential difference is fundamentally related to the theoretical maximum energy (maximum work, ΔG in J mol^{-1}) according to the equation:[236]

$$\Delta G = -nFE_{cell}$$ Equation 1.4

where n is the number of electrons involved in the reaction and F is the Faraday constant (96485 C mol^{-1}). A reaction takes place spontaneously if ΔG is negative. The more negative ΔG is, the more energy the battery can store.

The theoretical capacity (C) of a LIB anode or cathode material depends in the number of lithium ions that are involved in the lithiation and delithiation process upon full charging and discharging and is therefore a specific property of a material. The capacity can be given per unit weight (Ah g^{-1}) or volume (Ah L^{-1}). The theoretical capacity per unit weight (Ah g^{-1}) can be calculated using the following formula:

$$\text{Theoretical capacity [Ah g}^{-1}] = \frac{F\ [\text{A s mol}^{-1}] \cdot n_{Li}}{M\ [\text{g mol}^{-1}] \cdot 3600\ [\text{s h}^{-1}]} \qquad \text{Equation 1.5}$$

where F is the Faraday's constant (96485 C mol^{-1}), n_{Li} is the number of lithium ions per formula unit and M is the molecular mass of the electrode material. However in practice the obtained capacity is often lower. The real capacity (Q) can be determined by multiplying the measured current (in A) with the time (in hours, h) needed for a complete discharge or charge of the battery cell:[234]

$$Q\ [\text{Ah}] = I[\text{A}] \cdot t[\text{h}] \qquad \text{Equation 1.6}$$

The rate of charge flow, which is a current, is often expressed as C-rate in a battery research, where C stands for the maximum (theoretical) capacity of a battery. The C-rate is calculated as the time in hours (Δt) required for a full discharge/charge of a battery with a capacity C. A C-rate of 1C means that the discharge current will discharge the entire battery in 1 hour. For a battery with a capacity of 1 Ah, this equals a discharge current of 1 A. A rate of 10C corresponds to a full charging or discharging of the battery within 6 minutes (1/10 hours) and therefore a discharging or charging current of 10 A. Repetitive charging/discharging of a battery (cycling) typically results in an irreversible capacity loss due to different reasons such as the irreversible chemical transformation of the materials of the electrodes, chemical reactions on the electrode-electrolyte interfaces, or loss of mechanical stability due to significant volume changes of cell components during charge/discharge. The capacity fading per cycle is given by the Coulombic efficiency:[234]

$$\text{Coulombic efficiency [\%]} = 100 \cdot \frac{Q_{discharge}}{Q_{charge}} \qquad \text{Equation 1.7}$$

The cycle life of a battery is defined as the number of cycles until the capacity fades to 80% of its initial reversible value.[234]

Another figure of merit of a rechargeable cell is the amount of electrical energy stored in a battery. It can be defined either per unit mass (specific energy, Wh kg^{-1}) or per unit volume (energy density, Wh L^{-1}) (in battery research also commonly referred as gravimetric and volumetric energy density, respectively). The specific energy (Wh kg^{-1}) can be calculated by multiplying the theoretical capacity by the cell voltage according to the following equation:[232]

$$\text{Specific Energy [Wh kg}^{-1}] = \text{Theoretical Capacity [Ah g}^{-1}] \cdot \text{E}_{\text{cell}} \text{ [V]} \cdot 1000 \text{ [g kg}^{-1}] =$$

$$= \frac{F \left[\text{A s mol}^{-1}\right] \cdot n_{Li} \cdot E_{cell} \text{ [V]} \cdot 1000 \left[\text{g kg}^{-1}\right]}{M \left[\text{g mol}^{-1}\right] \cdot 3600 \left[\text{s h}^{-1}\right]} \qquad \text{Equation 1.8}$$

The output power (P) can also be defined either per unit mass (specific power, W kg^{-1}) or per unit volume (power density, W L^{-1}) and is defined as the energy at a given charge or discharge current (per unit mass or volume): [234]

$$\text{P [W kg}^{-1}] = \frac{E_{cell} \text{ [V]} \cdot I \text{ [A]} \cdot}{m \text{ [kg]}} \qquad \text{Equation 1.9}$$

The state-of-the-art cathode materials are layered $LiCoO_2$, $LiNiO_2$, $LiCo_{1-x}Ni_xO_2$, $LiNi_{1-y-z}Mn_yCo_zO_2$, olivine-type $LiFePO_4$ and spinel-type $LiMn_2O_4$, while graphite and lithium titanate ($Li_4Ti_5O_{12}$) are the most used anode materials.[228,233] However, these materials cannot meet the demands for batteries with significantly higher energy and power densities for new portable devices with advanced functionalities or long-range electric automobiles. The increase of the energy of LIBs can be achieved either by increasing the potential difference between the electrodes (for examples using high voltage cathodes) or by developing high capacity electrode materials, which can store more than just one mol Li per mol of transition metal oxide (see equation 1.5).

As a part of this research, the thesis has focused on the development of new high capacity anode materials. The following section will give an overview of the anode materials for LIBs.[233]

Depending on their lithium insertion reaction mechanism anode materials can be divided into three groups (see Figure 1.23): (1) intercalation/de-intercalation materials, (2) alloy/de-alloy materials and (3) conversion materials.[228,233] Typical intercalation/de-intercalation (also called insertion) materials are TiO_2, $Li_4Ti_5O_{12}$ and carbon based materials like porous carbon, carbon nanotubes and graphene. The Li$^+$ ions are incorporated in the crystal structure (into vacancies or in the carbon interlayer space) of the material without causing significant structural changes. The structural stability and relatively low volume changes (particular for $Li_4Ti_5O_{12}$,

a so called "zero strain material") are responsible for the very good cycle life. The main drawback of insertion materials is however their relatively low capacity limited by the available vacancies for Li ions.[228,233]
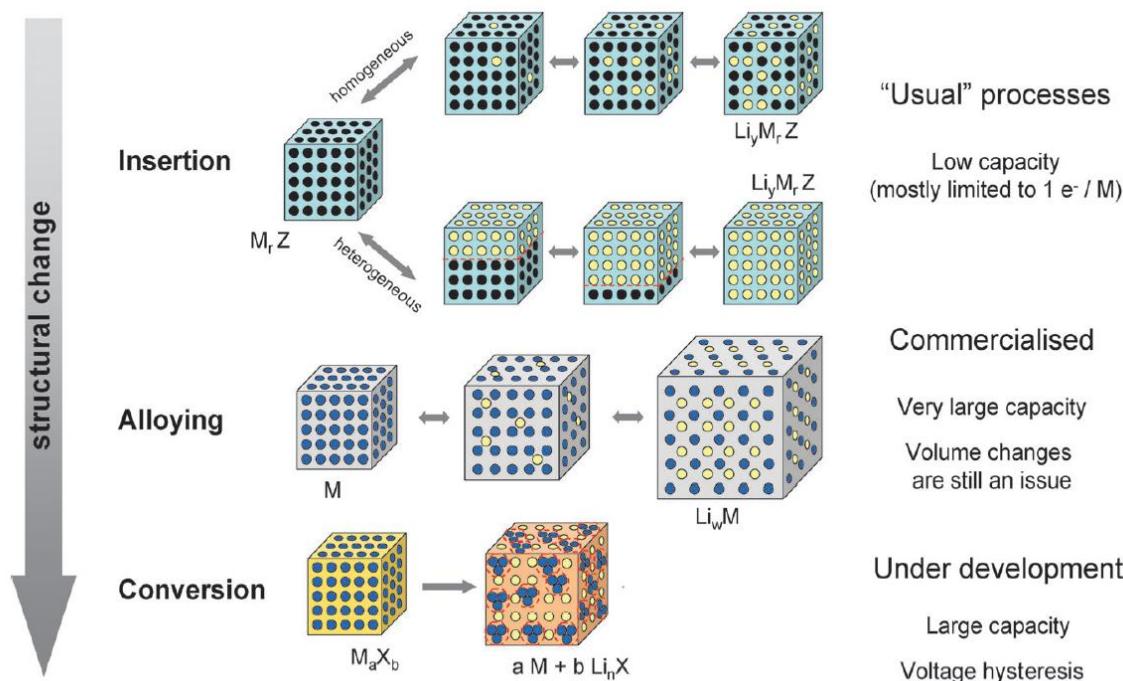
Figure 1.23 Schematic representation of the different reaction mechanisms observed in electrode materials for lithium ion batteries. Black circles: voids in the crystal structure, blue circles: metal, yellow circles: lithium.[233]

Another group of anode materials are so called alloy/de-alloy materials such as Si, Ge, Sn, Al, and Bi. The lithium insertion takes place by adding Li^+ to the reactant phase forming Li_xM alloys, which is associated with significant structural changes in the crystal structure. In contrast to intercalation/de-intercalation materials the lithium insertion is not limited to one Li^+ per transition metal atom reaching a significantly higher specific capacity and energy. However, serious issues associated with the huge volume changes result in a strong capacity fading and a poor cycling stability.[228,233]

Conversion materials have the general formula M_xN_y, where M = transition metal like Mn, Ni, Fe, Co, Cu, Mo, Cr, Ru etc. and N = O, S, F, P, N. As follows from the name, these reactions involve the full conversion of the transition metal from oxidized (cation) to its metallic state ($M_xN_y + z\,Li^+ + z\,e^- \rightarrow 4\,Li_zN_y + x\,M$). Such transformations often accommodate more than one Li atom per transition metal atom, resulting in very high capacities and energy densities. However, due to the significant chemical reorganization

accompanying intercalation/de-intercalation process, conversion materials show a large potential hysteresis, poor capacity retention and therefore a short cycle life.[228,233]

Among these three material classes alloying and conversion materials are very promising for future high capacity anodes, as the lithium insertion is not limited to one Li^+ per transition metal atom reaching a significantly higher specific capacity and energy compared to conventional graphite and LTO anodes. Especially tin oxide (SnO_2) based materials are very promising as they demonstrate both alloying and conversion mechanisms and therefore exhibit a quite high theoretical capacity. Furthermore SnO_2 is a very environmentally friendly, low cost and high abundant material.[228,237-239] In the past few years antimony-doped tin oxide (ATO) became a valuable alternative to SnO_2 due to its outstanding transport properties, like its higher electron and Li-ion conductivity compared to SnO_2.[55,169,237,240,241] The electrochemical reactions upon lithium insertion proceed in two steps: (1) a conversion reaction, where $Sn_{0.90}Sb_{0.10}O_2$ (ATO) is reduced to Sn and Sb and (2) a Sn-lithium alloying/dealloying reaction.

$$Sn_{0.90}Sb_{0.10}O_2 \text{ (ATO)} + 4\ Li^+ + 4e^- \leftrightarrow 0.90\ Sn + 0.10\ Sb + 2\ Li_2O \tag{1}$$

$$0.90\ Sn + 0.10\ Sb + 4.26\ Li^+ + 4.33e^- \leftrightarrow 0.90\ Li_{4.4}Sn + 0.10\ Li_3Sb \tag{2}$$
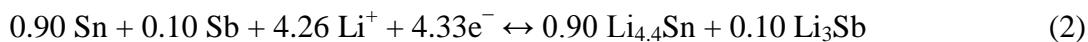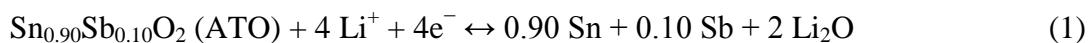
The overall electrochemical process involves 8.4 Li^+ ions or 8.26 Li^+ ions for one SnO_2 or ATO ($Sb_{10}Sn_{90}O_2$) formula unit corresponding to a theoretical capacity of 1494 mAh g^{-1} and 1466 mAh g^{-1} (see equation 1.5). However, in practice the capacity is often lower due to the irreversibility of the first step reaching only 783 mAhg^{-1}.[228,238,242-244] So far the highest theoretical capacities (> 1400 mAh g^{-1}) were achieved for nanoparticle assemblies with particle sizes below 10 nm.[245-247] For larger particles of 50-150 nm[248] and 200 nm[249] in size only maximum capacities below 800 mAhg^{-1} could be obtained, suggesting that in macrosized materials only Sn-lithium alloying/dealloying reactions take place.[248,249] Therefore, reducing the size of the active material from the conventional bulk state to the nanoscale seems to be a powerful tool to improve the capacity. This is most likely due to decreased activation energy of the electrochemical conversion reaction in nanosized materials compared to bulk materials, which results in reversible or at least partial reversible conversion process.[228,238,242-244] Furthermore, the higher surface to volume ratio of nanoparticles increases the contact area with the electrolyte and promotes faster diffusion of Li^+ ions within the material so that a higher charging rate can be achieved.[228,238]

Another serious issue of ATO/SnO_2 based LIBs is the poor cycling performance, which results from large volume changes of up to 358% during the charge and discharge reactions

leading to a mechanical disintegration of the anode and loss of electrical connectivity between the active materials. Therefore, much attention has been paid to improve the cycling stability and to reduce the irreversible capacity caused by volume changes. One way to overcome this problem is the use of porous nanostructures like mesoporous or hollow ATO/SnO_2 structures. The high porosity is capable of balancing the huge volume changes during the lithium insertion/extraction.[21,250,251] As already mentioned above, the higher surface area of porous active material also provides an increased surface area for electrolyte diffusion favoring high rate capability.

Another effective strategy to improve the cycling stability of tin-based materials is the incorporation of ATO/SnO_2 into a suitable matrix. Carbonaceous materials are promising matrices as they not only buffer the volume changes but also significantly improve the electrical conductivity of the composites, while being low cost, highly abundant and non-toxic. Until now, various types of carbonaceous materials including meso- and macroporous carbons,[239] carbon nanotubes (CNT),[252,253] carbon hollow particles[254] and graphene[121,237,245-249,255-279] have been tested in SnO_2 composites. Especially graphene based nanocomposites have gained extensive attention due to the outstanding properties of graphene nanosheets (GNS), such as a high theoretical capacity (744 mAh g^{-1}), excellent conductivity, large surface area, high mechanical flexibility and chemical stability.[238] Compared to graphite the capacity is approximately doubled, corresponding to a stoichiometry of Li_2C_6. Graphene however also suffers from capacity fading, which is caused by agglomeration and re-stacking upon drying. The combination of nanoparticles and graphene in form of nanocomposites is an effective strategy to use the full potential of both materials due to the synergetic effects of size and interfacial interactions preventing each other from restacking and agglomeration.[238] The porous structure of ATO- or SnO_2-graphene nanocomposite provides buffering space against the volume changes of ATO/SnO_2 nanoparticles during lithium insertion/extraction leading to an enhanced cycle performance, which is schematically depicted in Figure 1.24. Furthermore, an extended conductive network of graphene provides a good electronic contact with the nanoparticles, favoring efficient charge collection and a high rate capability.[246]
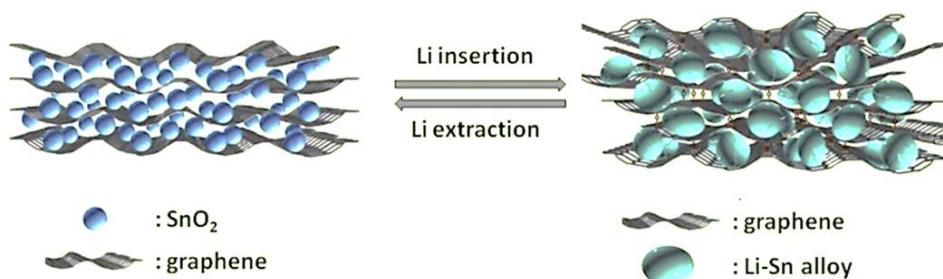
Figure 1.24 Schematic diagram depicting the buffering of volume changes by graphene on SnO_2 composites during Li insertion/extraction. Image adapted from Ref.[280].

There are different routes to obtain nanocomposites including hydro-/solvothermal *in-situ* syntheses of the nanoparticles on GNS,[245-247,249,255-274] self-assembly of preformed nanoparticles and GNS sheets,[237,248,275,276] mechanochemical ball milling,[277] electrostatic spray deposition (ESD)[278,279] and atomic layer deposition (ALD).[121] However, a quantitative comparison of the studies is difficult due to the lack of standard measurement procedures including identical scan rates for charging/discharging and comparable loadings in the LIB research community.

Most of the reported tin-based nanocomposites are based on undoped SnO_2, yet ATO is a valuable alternative due to its higher electron and Li-ion conductivity compared to SnO_2.[55,169,237,240,241] Wang *et al.*[164] reported the mesoporous ATO nanopowders for LIB, which show a high initial capacity of 1286 mAh g^{-1} but a strong capacity fading to 637 mAh g^{-1} after 100 cycles at 0.2 C. Zhao *et al.*[237] fabricated ATO/graphene hybrid structures for LIBs via the self-assembly of preformed nanoparticles and graphene oxide (GO) using a tetraethylenepentamine linker. The nanocomposite exhibits a high initial specific capacity of 1233 mAh g^{-1} at a current density of 100 mAh g^{-1} and a reasonable good cycling stability (887 mAh g^{-1} after 140 cycles) compared to unsupported nanoparticles ($\approx$200 mAh g^{-1} after 140 cycles). ATO/multiwall carbon nanotube nanocomposites were reported by Cevher *et al.*[252,253] and Guler *et al.*[281] by using a radio frequency magnetron sputtering process. They could also demonstrate the stabilizing effect of the CNTs on the cycling performance of the electrode reaching 597 mAh g^{-1} and 60 mAh g^{-1} after 100 cycles at 1C for the CNT-supported and unsupported ATO.[252,253] An *et al.*[282] recently reported a novel architecture of ATO nanoparticles sandwiched between a carbon nanofiber and a carbon skin for LIBs using electrospinning and hydrothermal methods. Also in this case unsupported ATO nanoparticles revealed much lower capacity retention after 100 cycles compared to carbon supported electrodes (97 mAh g^{-1} vs. 705 mAh g^{-1} at a current density of 100 mA g^{-1}).

Beside this few reports on ATO based LIBs, the prevailing number of groups deal with undoped SnO_2-based hybrid structures. Some of the developed materials even reach the theoretical capacity (> 1300 mAh g^{-1}) and exhibit a high cycling stability.[245-247] Liu *et al.*[245] prepared SnO_2/graphene nanostructures for using a simple one-step microwave-assisted hydrothermal method and reaching a remarkable capacity of 1359 mAh g^{-1} after 100 cycles at a current density of 100 mA g^{-1}. Liu *et al.*[247] fabricated mesoporous SnO_2/graphene nanocomposites using a scalable step wise approach, where Sn was converted into pure SnO_2 due to Kirkendall effect. The resulting composites feature a high reversible capacity of 1384 mAh g^{-1} after 50th cycles at 100 mA g^{-1}, corresponding to 98% of the first charge capacity.

The high capacities could be however obtained only at very low current densities (100 mA g^{-1}) corresponding to full charging or discharging in around 13 hours. At higher charging/discharging rates the capacity decreases rapidly. So far only few groups investigated the performance of SnO_2-based anodes at high current densities. Li *et al.*[257] prepared SnO_2 nanoparticles anchored on vertically aligned graphene, which maintain a specific capacity of 145 mAh g^{-1} at a current density of 20 A g^{-1} and exhibit an excellent cycling stability (210 mAh g^{-1}) over 5000 cycles at 6 A g^{-1}. Zhou *et al.*[283] reported on an even higher reversible capacity of 417 mAh g^{-1} for SnO_2/N-doped graphene composites at a current density of 20 A g^{-1}. Chen *et al.*[284] prepared SnO_2/graphene composites via a surfactant assisted hydrothermal route, which delivered a specific capacity 550 mAh g^{-1} at a current density of 10 A g^{-1}. The performance among ATO based electrodes is even worse. Zhao *et al.*[237] and An *et al.*[282] reached only capacities of 483 mAh g^{-1} and 411 mAh g^{-1} at current densities of 5 Ah g^{-1}and 2 A g^{-1}, respectively.

A SnO_2-based anode material combining all demands, in particular a high specific capacity, high cycling stability and high insertion/extraction rates has not been reported yet. Our group was able to obtain *in-situ* synthesized ATO/graphene nanocomposites using a novel microwave-assisted solvothermal route in *tert*-butanol (Chapter 11). The nanocomposites show promising features like a high capacity, good cycling stability and in particular the high rate capability. The outstanding lithium storage performance mainly results from the synergetic effect of the ultrasmall ATO nanoparticles and conductive graphene, which not only enhances the conductivity of the whole electrode but also provide a buffering matrix for the expansion of ATO during charging and discharging.

1.4. REFERENCES

(1)   Pasquarelli, R. M.; Ginley, D. S.; O'Hayre, R. *Chem. Soc. Rev.* **2011**, *40*, 5406.

(2)   Layani, M.; Kamyshny, A.; Magdassi, S. *Nanoscale* **2014**, *6*, 5581.

(3)   Yan, H.; Okuzaki, H. *Macromol. Symp.* **2010**, *296*, 286.

(4)   Ginley, D. S.; Hosono, H.; Paine, D. C. In *Handbook of Transparent Conductors*; Springer: New York, 2010.

(5)   Kim, H.; Park, Y.; Choi, D.; Ahn, S.-H.; Lee, C. S. *Appl. Surf. Sci.* **2016**, *377*, 370.

(6)   Schaming, D.; Renault, C.; Tucker, R. T.; Lau-Truong, S.; Aubard, J.; Brett, M. J.; Balland, V.; Limoges, B. *Langmuir* **2012**, *28*, 14065.

(7)   Kwan, P.; Schmitt, D.; Volosin, A. M.; McIntosh, C. L.; Seo, D. K.; Jones, A. K. *Chem. Commun.* **2011**, *47*, 12367.

(8)   Frasca, S.; Molero Milan, A.; Guiet, A.; Goebel, C.; Pérez-Caballero, F.; Stiba, K.; Leimkühler, S.; Fischer, A.; Wollenberger, U. *Electrochim. Acta* **2013**, *110*, 172.

(9)   Simmons, C. R.; Schmitt, D.; Wei, X.; Han, D.; Volosin, A. M.; Ladd, D. M.; Seo, D. K.; Liu, Y.; Yan, H. *ACS Nano* **2011**, *5*, 6060.

(10)   Müller, V.; Rathousky, J.; Fattakhova-Rohlfing, D. *Electrochim. Acta* **2014**, *116*, 1.

(11)   Sarauli, D.; Wettstein, C.; Peters, K.; Schulz, B.; Fattakhova-Rohlfing, D.; Lisdat, F. *ACS Catal.* **2015**, *5*, 2081.

(12)   Sarauli, D.; Peters, K.; Xu, C.; Schulz, B.; Fattakhova-Rohlfing, D.; Lisdat, F. *ACS Appl. Mater. Interfaces* **2014**, *6*, 17887.

(13)   Sarauli, D.; Borowski, A.; Peters, K.; Schulz, B.; Fattakhova-Rohlfing, D.; Leimkühler, S.; Lisdat, F. *ACS Catal.* **2016**, *6*, 7152.

(14)   Khun Khun, K.; Mahajan, A.; Bedi, R. K. *Chem. Phys. Lett.* **2010**, *492*, 119.

(15)   Wang, Y.; Mu, Q.; Wang, G.; Zhou, Z. *Sens. Actuators, B* **2010**, *145*, 847.

(16)   Ji, X.; Lu, W.; Ma, H. *Crystengcomm* **2012**, *14*, 7145.

(17)   Oh, H.-S.; Nong, H. N.; Strasser, P. *Adv. Funct. Mater.* **2015**, *25*, 1074.

(18)   Nong, H. N.; Oh, H. S.; Reier, T.; Willinger, E.; Willinger, M. G.; Petkov, V.; Teschner, D.; Strasser, P. *Angew. Chem. Int. Ed.* **2015**, *54*, 2975.

(19)   Oh, H.-S.; Nong, H. N.; Reier, T.; Gliech, M.; Strasser, P. *Chem. Sci.* **2015**, *6*, 3321.

(20)   Oh, H. S.; Nong, H. N.; Reier, T.; Bergmann, A.; Gliech, M.; Ferreira de Araujo, J.; Willinger, E.; Schlogl, R.; Teschner, D.; Strasser, P. *J. Am. Chem. Soc.* **2016**, *138*, 12552.

(21)   Wang, Y.; Djerdj, I.; Smarsly, B.; Antonietti, M. *Chem. Mater.* **2009**, *21*, 3202.

(22)   Yang, Z.; Gao, S.; Li, T.; Liu, F. Q.; Ren, Y.; Xu, T. *ACS Appl. Mater. Interfaces* **2012**, *4*, 4419.

(23)   Tétreault, N.; Arsenault, É.; Heiniger, L.-P.; Soheilnia, N.; Brillet, J.; Moehl, T.; Zakeeruddin, S.; Ozin, G. A.; Grätzel, M. *Nano Lett.* **2011**, *11*, 4579.

(24) Ostermann, R.; Zieba, R.; Rudolph, M.; Schlettwein, D.; Smarsly, B. M. *Chem. Commun.* **2011**, *47*, 12119.

(25) Li, L.; Xu, C.; Zhao, Y.; Ziegler, K. J. *Sol. Energy* **2016**, *132*, 214.

(26) Xia, X.; Wu, W.; Ma, J.; Liu, T.; Fei, D.; Liu, X.; Gao, C. *RSC Adv.* **2015**, *5*, 15772.

(27) Wang, H. W.; Ting, C. F.; Hung, M. K.; Chiou, C. H.; Liu, Y. L.; Liu, Z.; Ratinac, K. R.; Ringer, S. P. *Nanotechnology* **2009**, *20*, 055601.

(28) Dunkel, C.; von Graberg, T.; Smarsly, B.; Oekermann, T.; Wark, M. *Materials* **2014**, *7*, 3291.

(29) Lee, B.; Guo, P.; Li, S. Q.; Buchholz, D. B.; Chang, R. P. *ACS Appl. Mater. Interfaces* **2014**, *6*, 17713.

(30) Kondofersky, I.; Dunn, H. K.; Muller, A.; Mandlmeier, B.; Feckl, J. M.; Fattakhova-Rohlfing, D.; Scheu, C.; Peter, L. M.; Bein, T. *ACS Appl. Mater. Interfaces* **2015**, *7*, 4623.

(31) Hufnagel, A. G.; Peters, K.; Müller, A.; Scheu, C.; Fattakhova-Rohlfing, D.; Bein, T. *Adv. Funct. Mater.* **2016**, *26*, 4435.

(32) Xu, Y. F.; Rao, H. S.; Chen, B. X.; Lin, Y.; Chen, H. Y.; Kuang, D. B.; Su, C. Y. *Adv. Sci.* **2015**, *2*, 1500049.

(33) Riha, S. C.; Vermeer, M. J.; Pellin, M. J.; Hupp, J. T.; Martinson, A. B. *ACS Appl. Mater. Interfaces* **2013**, *5*, 360.

(34) Stefik, M.; Cornuz, M.; Mathews, N.; Hisatomi, T.; Mhaisalkar, S.; Gratzel, M. *Nano Lett.* **2012**, *12*, 5431.

(35) Moir, J.; Soheilnia, N.; O'Brien, P.; Jelle, A.; Grozea, C. M.; Faulkner, D.; Helander, M. G.; Ozin, G. A. *ACS Nano* **2013**, *7*, 4261.

(36) Wang, X. D.; Xu, Y. F.; Chen, B. X.; Zhou, N.; Chen, H. Y.; Kuang, D. B.; Su, C. Y. *ChemSusChem* **2016**, *9*, 3012.

(37) Ozouf, G.; Beauger, C. *J. Mater. Sci.* **2016**, *51*, 5305.

(38) Badeker, K. *Ann. Phys.* **1907**, *22*, 749.

(39) Minami, T. *Semicond. Sci. Technol.* **2005**, *20*, 35.

(40) Granqvist, C. G.; Hultaker, A. *Thin Solid Films* **2002**, *411*, 1.

(41) Walsh, A.; Catlow, C. R. A. *J. Mater. Chem.* **2010**, *20*, 10438.

(42) Hoel, C. A.; Mason, T. O.; Gaillard, J.-F. o.; Poeppelmeier, K. R. *Chem. Mater.* **2010**, *22*, 3569.

(43) Lany, S.; Zunger, A. *Phys. Rev. Lett.* **2007**, *98*, 045501.

(44) Frank, G.; Köstlin, H. *Appl. Phys. A* **1982**, *27*, 197.

(45) Bel Hadj Tahar, R.; Ban, T.; Ohya, Y.; Takahashi, Y. *J. Appl. Phys.* **1998**, *83*, 2631.

(46) Granqvist, C. G. *Sol. Energy Mater. Sol. Cells* **2007**, *91*, 1529.

(47) Liu, H.; Avrutin, V.; Izyumskaya, N.; Özgür, Ü.; Morkoç, H. *Superlattices Microstruct.* **2010**, *48*, 458.

(48) Kilic, C.; Zunger, A. *Phys. Rev. Lett.* **2002**, *88*, 095501.

(49) Batzill, M.; Diebold, U. *Prog. Surf. Sci.* **2005**, *79*, 47.

(50)   Koebel, M. M.; Nadargi, D. Y.; Jimenez-Cadena, G.; Romanyuk, Y. E. *ACS Appl. Mater. Interfaces* **2012**, *4*, 2464−2473.

(51)   Terrier, C.; Chatelon, J. P.; Roger, J. A. *Thin Solid Films* **1997**, *295*, 95.

(52)   Ginley, D. S.; Bright, C. *MRS Bull.* **2000**, *25*, 15.

(53)   Nütz, T.; zum Felde, U.; Haase, M. *J. Chem. Phys.* **1999**, *110*, 12142.

(54)   Jung, D.-W.; Park, D.-W. *Appl. Surf. Sci.* **2009**, *255*, 5409.

(55)   Müller, V.; Rasp, M.; Štefanić, G.; Ba, J.; Günther, S.; Rathousky, J.; Niederberger, M.; Fattakhova-Rohlfing, D. *Chem. Mater.* **2009** *21*, 5229.

(56)   Bai, F.; He, Y.; He, P.; Tang, Y.; Jia, Z. *Mater. Lett.* **2006**, *60*, 3126.

(57)   Hosono, H.; Yasukawa, M.; Kawazoe, H. *J. Non-cryst. Solids* **1996**, *203*, 334.

(58)   Baumanis, C.; Bloh, J. Z.; Dillert, R.; Bahnemann, D. W. *J. Biol. Chem.* **2007**, *282*, 24437.

(59)   Burstein, E. *Phys. Rev.* **1954**, *104*, 632.

(60)   Gupta, L.; Mansingh, A.; Srivastava, P. K. *Thin Solid Films* **1989**, *176*, 33.

(61)   Walsh, A.; Da Silva, J. L. F.; Wei, S.-H.-. *Phys. Rev. B* **2008**, *78*, 075211.

(62)   Cao, G.; Wang, Y. *Nanostructures & Nanomaterials: Synthesis, Properties, and Applications*; World Wcientific Publishing: London, 2011; Vol. 2.

(63)   Carrow, J. K.; Gaharwar, A. K. *Macromol. Chem. Phys.* **2015**, *216*, 248.

(64)   Fattakhova-Rohlfing, D.; Zaleska, A.; Bein, T. *Chem. Rev.* **2014**, *114*, 9487.

(65)   Niederberger, M.; Pinna, N. *Metal Oxide Nanoparticles in Organic Solvents*; Springer-Verlag: London, 2009.

(66)   Li, S. L.; Zhu, P. L.; Zhao, T.; Sun, R. *J. Sol-Gel Sci. Technol.* **2014**, *70*, 366.

(67)   Bühler, G.; Thölmann, D.; Feldmann, C. *Adv. Mater.* **2007**, *19*, 2224.

(68)   Hammarberg, E.; Prodi-Schwab, A.; Feldmann, C. *J. Colloid Interface Sci.* **2009**, *334*, 29.

(69)   Zhang, J.; Gao, L. *Mater. Chem. Phys.* **2004**, *87*, 10.

(70)   Lu, J.; Minami, K.; Takami, S.; Shibata, M.; Kaneko, Y.; Adschiri, T. *ACS Appl. Mater. Interfaces* **2012**, *4*, 351.

(71)   Burunkaya, E.; Kiraz, N.; Kesmez, Ö.; Erdem Çamurlu, H.; Asiltürk, M.; Arpaç, E. *J. Sol-Gel Sci. Technol.* **2010**, *55*, 171.

(72)   Lili, L.; Liming, M.; Xuechen, D. *Mater. Res. Bull.* **2006**, *41*, 541.

(73)   Kanehara, M.; Koike, H.; Yoshinaga, T.; Teranishi, T. *J. Am. Chem. Soc.* **2009**, *131*, 17736.

(74)   Ba, J.; Fattakhova Rohlfing, D.; Feldhoff, A.; Brezesinski, T.; Djerdj, I.; Wark, M.; Niederberger, M. *Chem. Mater.* **2006**, *18*, 2848.

(75)   Ito, D.; Yokoyama, S.; Zaikova, T.; Masuko, K.; Hutchison, J. E. *ACS Nano* **2014**, *8*, 64.

(76)   Kanie, K.; Sasaki, T.; Nakaya, M.; Muramatsu, A. *Chem. Lett.* **2013**, *42*, 738.

(77)   Hammarberg, E.; Prodi-Schwab, A.; Feldmann, C. *Thin Solid Films* **2008**, *516*, 7437.

(78)   Cuya Huaman, J. L.; Tanoue, K.; Miyamura, H.; Matsumoto, T.; Jeyadevan, B. *New J. Chem.* **2014**, *38*, 3421.

(79)   Gilstrap Jr, R. A.; Summers, C. J. *Thin Solid Films* **2009**, *518*, 1136.

(80)   Lu, Z.; Zhou, J.; Wang, A.; Wang, N.; Yang, X. *J. Mater. Chem.* **2011**, *21*, 4161.

(81)   Dusastre, V.; Williams, D. E. *J. Phys. Chem. B* **1998**, *102*, 6732.

(82)   Koivula, R.; Harjula, R.; Lehto, J. *Microporous Mesoporous Mater.* **2002**, *55*, 231.

(83)   Krishnakumar, T.; Jayaprakash, R.; Pinna, N.; Phani, A. R.; Passacantando, M.; Santucci, S. *J. Phys. Chem. Solids* **2009**, *70*, 993.

(84)   Pan, R.; Qiang, S.; Liew, K.; Zhao, Y.; Wang, R.; Zhu, J. *Powder Technol.* **2009**, *189*, 126.

(85)   Kim, K. Y.; Park, S. B. *Mater. Chem. Phys.* **2004**, *86*, 210.

(86)   Nütz, T.; zum Felde, U.; Haase, M. *J. Chem. Phys.* **1999**, *110*, 12142.

(87)   Lee, J.; Lee, S.; Li, G.; Petruska, M. A.; Paine, D. C.; Sun, S. *J. Am. Chem. Soc.* **2012**, *134*, 13410.

(88)   Thu, T. V.; Maenosono, S. *J. Appl. Phys.* **2010**, *107*, 014308.

(89)   Jin, Y.; Yi, Q.; Ren, Y.; Wang, X.; Ye, Z. *Nanoscale Res. Lett.* **2013**, *8*, 153.

(90)   Zheng, M.; Wang, B. *Transactions of Nonferrous Metals Society of China* **2009**, *19*, 404.

(91)   Zhang, J.; Gao, L. *Materials Letters* **2004**, *58*, 2730.

(92)   Ito, D.; Yokoyama, S.; Zaikova, T.; Masuko, K.; Hutchison, J. E. *ACS Nano* **2014**, *8*, 64.

(93)   Liu, Y.; Stefanic, G.; Rathousky, J.; Hayden, O.; Bein, T.; Fattakhova-Rohlfing, D. *Chem. Sci.* **2012**, *3*, 2367.

(94)   Lee, J.; Petruska, M. A.; Sun, S. *J. Phys. Chem. C* **2014**, *118*, 12017.

(95)   Hong, S.-J.; Cha, S.-J.; Lee, J.-Y.; Kim, Y.-S. *Electron. Mater. Lett.* **2017**, *13*, 37.

(96)   Faure, B.; Salazar-Alvarez, G.; Ahniyaz, A.; Villaluenga, I.; Berriozabal, G.; De Miguel, Y. R.; Bergstrom, L. *Sci. Technol. Adv. Mater.* **2013**, *14*, 023001.

(97)   Wolf, N.; Rydzek, M.; Gerstenlauer, D.; Arduini-Schuster, M.; Manara, J. *Thin Solid Films* **2013**, *532*, 60.

(98)   Grote, C.; Chiad, K. J.; Vollmer, D.; Garnweitner, G. *Chem. Commun.* **2012**, *48*, 1464.

(99)   Segets, D.; Marczak, R.; Schäfer, S.; Paula, C.; Gnichwitz, J.-F.; Hirsch, A.; Peukert, W. *ACS Nano* **2011**, *5*, 4658.

(100)   Razzaque, S.; Hussain, S.; Hussain, I.; Tan, B. *Polymers* **2016**, *8*, 156.

(101)   Posthumus, W.; Laven, J.; de With, G.; van der Linde, R. *J. Colloid Interface Sci.* **2006**, *304*, 394.

(102)   Cho, Y.-S.; Kim, H.-M.; Hong, J.-J.; Yi, G.-R.; Jang, S. H.; Yang, S.-M. *Colloids Surf., A* **2009**, *336*, 88.

(103)   Tan, Q.; Yu, G.; Liao, Y.; Hu, B.; Zhang, X. *Colloid. Polym. Sci.* **2014**, *292*, 3233.

(104)   Liu, Y. J.; Stefanic, G.; Rathousky, J.; Hayden, O.; Bein, T.; Fattakhova-Rohlfing, D. *Chem. Sci.* **2012**, *3*, 2367.

(105) Fominykh, K.; Feckl, J. M.; Sicklinger, J.; Döblinger, M.; Böcklein, S.; Ziegler, J.; Peter, L.; Rathousky, J.; Scheidt, E.-W.; Bein, T.; Fattakhova-Rohlfing, D. *Adv. Funct. Mater.* **2014**, *24*, 3123.

(106) Fominykh, K.; Chernev, P.; Zaharieva, I.; Sicklinger, J.; Stefanic, G.; Döblinger, M.; Müller, A.; Pokharel, A.; Böcklein, S.; Scheu, C.; Bein, T.; Fattakhova-Rohlfing, D. *ACS Nano* **2015**, *9*, 5180.

(107) Fominykh, K.; Tok, G. C.; Zeller, P.; Hajiyani, H.; Miller, T.; Döblinger, M.; Pentcheva, R.; Bein, T.; Fattakhova-Rohlfing, D. *Adv. Funct. Mater.* **2017**, 27, 1605121.

(108) Szeifert, J. M.; Feckl, J. M.; Fattakhova-Rohlfing, D.; Liu, Y.; Kalousek, V.; Rathousky, J.; Bein, T. *J. Am. Chem. Soc.* **2010**, *132*, 12605.

(109) Liu, Y.; Szeifert, J. M.; Feckl, J. M.; Mandlmeier, B.; Rathousky, J.; Hayden, O.; Fattakhova-Rohlfing, D.; Bein, T. *ACS Nano* **2010**, *4*, 5373.

(110) Feckl, J. M.; Fominykh, K.; Döblinger, M.; Fattakhova-Rohlfing, D.; Bein, T. *Angew. Chem. Int. Ed.* **2012**, *51*, 7459.

(111) Feckl, J. M.; Dunn, H. K.; Zehetmaier, P. M.; Müller, A.; Pendlebury, S. R.; Zeller, P.; Fominykh, K.; Kondofersky, I.; Döblinger, M.; Durrant, J. R.; Scheu, C.; Peter, L.; Fattakhova-Rohlfing, D.; Bein, T. *Adv. Mater. Interfaces* **2015**, *2*, 1500358.

(112) Rosen, E. L.; Buonsanti, R.; Llordes, A.; Sawvel, A. M.; Milliron, D. J.; Helms, B. A. *Angew. Chem. Int. Ed.* **2012**, *51*, 684.

(113) Buonsanti, R.; Pick, T. E.; Krins, N.; Richardson, T. J.; Helms, B. A.; Milliron, D. J. *Nano Lett.* **2012**, *12*, 3872.

(114) Forman, A. J.; Chen, Z.; Chakthranont, P.; Jaramillo, T. F. *Chem. Mater.* **2014**, *26*, 958.

(115) Terasaki, N.; Yamamoto, N.; Hiraga, T.; Yamanoi, Y.; Yonezawa, T.; Nishihara, H.; Ohmori, T.; Sakai, M.; Fujii, M.; Tohri, A.; Iwai, M.; Inoue, Y.; Yoneyama, S.; Minakata, M.; Enami, I. *Angew. Chem., Int. Ed.,* **2009**, *48*, 1585.

(116) Porada, S.; Zhao, R.; van der Wal, A.; Presser, V.; Biesheuvel, P. M. *Prog. Mater Sci.* **2013**, *58*, 1388.

(117) Shehzad, K.; Xu, Y.; Gao, C.; Duan, X. *Chem. Soc. Rev.* **2016**, *45*, 5541.

(118) Arsenault, E., N. Soheilnia, and G.A. Ozin, *ACS Nano* **2011**, *5*, 2984.

(119) Liu, Y.; Peters, K.; Mandlmeier, B.; Müller, A.; Fominykh, K.; Rathousky, J.; Scheu, C.; Fattakhova-Rohlfing, D. *Electrochim. Acta* **2014**, *140*, 108.

(120) Müller, V.; Rasp, M.; Rathousky, J.; Schutz, B.; Niederberger, M.; Fattakhova-Rohlfing, D. *Small* **2010**, *6*, 633.

(121) Li, X.; Meng, X.; Liu, J.; Geng, D.; Zhang, Y.; Banis, M. N.; Li, Y.; Yang, J.; Li, R.; Sun, X.; Cai, M.; Verbrugge, M. W. *Adv. Funct. Mater.* **2012**, *22*, 1647.

(122) Shchukin, D. G.; Caruso, R. A. *Adv. Funct. Mater.* **2003**, *13*, 789.

(123) Lu, H.-C.; Mao, J.-W.; Chiang, Y.-C. *Surf. Coat. Technol.* **2013**, *231*, 526.

(124) Goebbert, C.; Nonninger, R.; Aegerter, M. A.; Schmidt, H. *Thin Solid Films* **1999**, *351* 79.

(125) Ito, D.; Masuko, K.; Weintraub, B. A.; McKenzie, L. C.; Hutchison, J. E. *J. Nanopart. Res.* **2012**, *14*, 1.

(126) Luo, L.; Bozyigit, D.; Wood, V.; Niederberger, M. *Chem. Mater.* **2013**, *25*, 4901.

(127) Puetz, J.; Al-Dahoudi, N.; Aegerter, M. A. *Adv. Eng. Mater.* **2004**, *6*, 733.

(128) Das, N.; Biswas, P. K. *J. Mater. Sci.* **2012**, *47*, 289.

(129) Kőrösi, L.; Scarpellini, A.; Petrik, P.; Papp, S.; Dékány, I. *Appl. Surf. Sci.* **2014**, *320*, 725.

(130) Duta, M.; Anastasescu, M.; Calderon-Moreno, J. M.; Predoana, L.; Preda, S.; Nicolescu, M.; Stroescu, H.; Bratan, V.; Dascalu, I.; Aperathitis, E.; Modreanu, M.; Zaharescu, M.; Gartner, M. *J. Mater. Sci. - Mater. Electron.* **2016**, *27*, 4913.

(131) Yang, X. Y.; Chen, L. H.; Li, Y.; Rooke, J. C.; Sanchez, C.; Su, B. L. *Chem. Soc. Rev.* **2017**, *46*, 481.

(132) Pablo, J.; Baena, C.; Agrios, A. G. *ACS. Appl. Mater. Interfaces* **2014**, *6*, 19127.

(133) Baghi, R.; Zhang, K.; Wang, S.; Hope-Weeks, L. J. *Microporous Mesoporous Mater.* **2016**, *doi:10.1016/j.micromeso.2016.10.045*.

(134) Rechberger, F.; Ilari, G.; Niederberger, M. *Chem. Commun.* **2014**, *50*, 13138.

(135) Rechberger, F.; Städler, R.; Tervoort, E.; Niederberger, M. *J. Sol-Gel Sci. Technol.* **2016**, *80*, 660.

(136) Smarsly, B.; Fattakhova-Rohlfing, D. In *Solution processing of inorganic materials* Mitzi, D. B., Ed.; John Wiley & Sons: Hoboken, New Jersey, 2009, p 283.

(137) Brinker, C. J.; Lu, Y.; Sellinger, A.; Fan, H. *Avd. Mater.* **1999**, *11*, 579.

(138) Müller, V.; Rasp, M.; Rathouský, J.; Schütz, B.; Niederberger, M.; Fattakhova-Rohlfing, D. *Small* **2010**, *6*, 633.

(139) Stefik, M.; Song, J.; Sai, H.; Guldin, S.; Boldrighini, P.; Orilall, M. C.; Steiner, U.; Gruner, S. M.; Wiesner, U. *J. Mater. Chem. A* **2015**, *3*, 11478.

(140) Ulagappan, N.; Rao, C. N. R. *Chem. Commun.* **1996**, 1685.

(141) Qi, L.; Ma, J.; M., C.; Zhao, Z. *Langmuir* **1998**, *14*, 2579.

(142) Severin, K. G.; Abdel-Fattah, T. M.; Pinnavaia, T. J. *Chem. Commun.* **1998**, 1471.

(143) Chen, F.; Liu, M. *Chem. Commun.* **1999**, 1829.

(144) Hou, K.; Puzzo, D.; Helander, M. G.; Lo, S. S.; Bonifacio, L. D.; Wang, W.; Lu, Z.-H.; Scholes, G. D.; Ozin, G. A. *Adv. Mater.* **2009**, *21*, 2492.

(145) Emons, T. T.; Li, J.; Nazar, L. F. *J. Am. Chem. Soc.* **2002**, *124*, 8516.

(146) Pohl, A.; Dunn, B. *Thin Solid Films* **2006**, *515*, 790.

(147) Fattakhova-Rohlfing, D.; Brezesinski, T.; Rathouský, J.; Feldhoff, A.; Oekermann, T.; Wark, M.; Smarsly, B. M. *Adv. Mater.* **2006**, *18*, 2980.

(148) Graberg, T. v.; Hartmann, P.; Rein, A.; Gross, S.; Seelandt, B.; Röger, C.; Zieba, R.; Traut, A.; Wark, M.; Janek, J.; Smarsly, B. M. *Sci. Technol. Adv. Mater.* **2011**, *12*, 025005.

(149) Wang, Y.; Brezesinski, T.; Antonietti, M.; Smarsly, B. *ACS Nano* **2009**, *3*, 1373.

(150) Brezesinski, T.; Fischer, A.; Iimura, K. i.; Sanchez, C.; Grosso, D.; Antonietti, M.; Smarsly, B. M. *Adv. Funct. Mater.* **2006**, *16*, 1433.

(151) Hamd, W.; Chavarot-Kerlidou, M.; Fize, J.; Muller, G.; Leyris, A.; Matheron, M.; Courtin, E.; Fontecave, M.; Sanchez, C.; Artero, V.; Laberty-Robert, C. *J. Mater. Chem. A* **2013**, *1*, 8217.

(152) Suzuki, N.; Kamachi, Y.; Chiang, Y. D.; Wu, K. C. W.; Ishihara, S.; Sato, K.; Fukata, N.; Matsuura, M.; Maekawa, K.; Tanabe, H.; Ariga, K.; Yamauchi, Y. *Crystengcomm* **2013**, *15*, 4404.

(153) Suzuki, N.; Imura, M.; Sato, K.; Fukata, N.; Matsuura, M.; Maekawa, K.; Yamauchi, Y. *Dalton Trans.* **2013**, *42*, 6366.

(154) Rauda, I. E.; Buonsanti, R.; Saldarriaga-Lopez, L. C.; Benjauthrit, K.; Schelhas, L. T.; Stefik, M.; Augustyn, V.; Ko, J.; Dunn, B.; Wiesner, U.; Milliron, D. J.; Tolbert, S. H. *ACS Nano* **2012**, *6*, 6386.

(155) Volosin, A. M.; Sharma, S.; Traverse, C.; Newman, N.; Seo, D. K. *J. Mater. Chem.* **2011**, *21*, 13232.

(156) Sharma, S.; Volosin, A. M.; Schmitt, D.; Seo, D. K. *J. Mater. Chem. A* **2013**, *1*, 699.

(157) Yuliarto, B.; Zhou, H.; Yamada, T.; Honma, I.; Asai, K. *Chem. Lett.* **2003**, *32*, 510.

(158) Urade, V. N.; Hillhouse, H. W. *J. Phys. Chem. B* **2005**, *109*, 10538.

(159) Pan, J. H.; Chai, S. Y.; Lee, C.; Park, S. E.; Lee, W. I. *J. Phys. Chem. C* **2007**, *111*, 5582.

(160) Zhang, X.; Wu, W.; Tian, T.; Man, Y.; Wang, J. *Mater. Res. Bull.* **2008**, *43*, 1016.

(161) Zhu, J.; Tay, B. Y.; Ma, J. *Mater. Lett.* **2006**, *60*, 1003.

(162) Miyata, H.; Itoh, M.; Watanabe, M.; Noma, T. *Chem. Mater.* **2003**, *15*, 1334.

(163) Li, Y.; Liu, J.; Liang, J.; Yu, X.; Li, D. *ACS Appl. Mater. Interfaces* **2015**, *7*, 6574.

(164) Wang, Y.; Brezesinski, T.; Antonietti, M.; Smarsly, B. *ACS Nano* **2009**, *3*, 1373.

(165) Peters, K.; Lokupitiya, H. N.; Sarauli, D.; Labs, M.; Pribil, M.; Rathouský, J.; Kuhn, A.; Leister, D.; Stefik, M.; Fattakhova-Rohlfing, D. *Adv. Funct. Mater.* **2016**, *26*, 6682.

(166) Stein, A.; Li, F.; Denny, N. R. *Chem. Mater.* **2008**, *20*, 649.

(167) Hatton, B. *Proc. Natl. Acad. Sci. U.S.A.* **2010**, *107*, 10354.

(168) Zhang, X. a.; Man, Y.; Wang, J.; Liu, C.; Wu, W. *Sci. China Ser. E: Technol. Sci.* **2006**, *49*, 537.

(169) Peters, K.; Zeller, P.; Stefanic, G.; Skoromets, V.; Němec, H.; Kužel, P.; Fattakhova-Rohlfing, D. *Chem. Mater.* **2015**, *27*, 1090.

(170) Yang, Z.; Gao, S.; Li, W.; Vlasko-Vlasov, V.; Welp, U.; Kwok, W. K.; Xu, T. *ACS Appl. Mater. Interfaces* **2011**, *3*, 1101.

(171) Liu, F. Q.; Wu, H.; Li, T.; Grabstanowicz, L. R.; Amine, K.; Xu, T. *Nanoscale* **2013**, *5*, 6422.

(172) Mersch, D.; Lee, C. Y.; Zhang, J. Z.; Brinkert, K.; Fontecilla-Camps, J. C.; Rutherford, A. W.; Reisner, E. *J. Am. Chem. Soc.* **2015**, *137*, 8541.

(173) Jiang, Q. L.; Liu, F. Q.; Li, T.; Xu, T. *J. Mater. Chem. C* **2014**, *2*, 618.

(174) Zhu, S.; Zhang, D.; Gu, J.; Xu, J.; Dong, J.; Li, J. *J. Nanopart. Res.* **2009**, *12*, 1389.

(175) Ivanova, A.; Fattakhova-Rohlfing, D.; Kayaalp, B. E.; Rathousky, J.; Bein, T. *J. Am. Chem. Soc.* **2014**, *136*, 5930.

(176) Aoki, Y.; Huang, J.; Kunitake, T. *J. Mater. Chem.* **2006**, *16*, 292.

(177) Song, F.; Su, H.; Han, J.; Lau, W. M.; Moon, W.-J.; Zhang, D. *J. Phys. Chem. C* **2012**, *116*, 10274.

(178) Dong, Q.; Su, H.; Zhang, D.; Zhu, N.; Guo, X. *Scr. Mater.* **2006**, *55*, 799.

(179) Hu, L.; Zheng, G.; Yao, J.; Liu, N.; Weil, B.; Eskilsson, M.; Karabulut, E.; Ruan, Z.; Fan, S.; Bloking, J. T.; McGehee, M. D.; Wågberg, L.; Cui, Y. *Energy Environ. Sci.* **2013**, *6*, 513.

(180) Shanti, E.; Banerjee, A.; Chopra, K. L. *Thin. Solid Films* **1982**, *88*, 93.

(181) Szeifert, J. M.; Fattakhova-Rohlfing, D.; Georgiadou, D.; Kalousek, V.; Rathouský, J.; Kuang, D.; Wenger, S.; Zakeeruddin, S. M.; Grätzel, M.; Bein, T. *Chem. Mater.* **2009**, *21*, 1260.

(182) Klamchuen, A.; Yanagida, T.; Kanai, M.; Nagashima, K.; Oka, K.; Kawai, T.; Suzuki, M.; Hidaka, Y.; Kai, S. *J. Cryst. Growth* **2010**, *312*, 3251.

(183) Klamchuen, A.; Yanagida, T.; Nagashima, K.; Seki, S.; Oka, K.; Taniguchi, M.; Kawai, T. *Appl. Phys. Lett.* **2009**, *95*, 053105.

(184) Yumoto, H.; Sako, T.; Gotoh, Y.; Nishiyama, K.; Kaneko, T. *J. Cryst. Growth* **1999**, *203* 136.

(185) Meng, G.; Yanagida, T.; Nagashima, K.; Yoshida, H.; Kanai, M.; Klamchuen, A.; Zhuge, F.; He, Y.; Rahong, S.; Fang, X.; Takeda, S.; Kawai, T. *J. Am. Chem. Soc.* **2013**, *135*, 7033.

(186) Maloney, F. S.; Wang, W. *Appl. Phys. Lett.* **2016**, *109*, 243104.

(187) Tan, S.-S.; Kee, Y.-Y.; Wong, H.-Y.; Tou, T.-Y. *Surf. Coat. Technol.* **2013**, *231*, 98.

(188) Krause, K. M.; Taschuk, M. T.; Harris, K. D.; Rider, D. A.; Wakefield, N. G.; Sit, J. C.; Buriak, J. M.; Thommes, M.; Brett, M. J. *Langmuir* **2010**, *26*, 4368.

(189) Beaudry, A. L.; LaForge, J. M.; Tucker, R. T.; Li, P.; Taschuk, M. T.; Brett, M. J. *Cryst. Growth Des.* **2013**, *13*, 212.

(190) Renault, C.; Andrieux, C. P.; Tucker, R. T.; Brett, M. J.; Balland, V.; Limoges, B. *J. Am. Chem. Soc.* **2012**, *134*, 6834.

(191) Leem, J. W.; Yu, J. S. *Opt. Express* **2011**, *19*, 258.

(192) Le Formal, F.; Grätzel, M.; Sivula, K. *Adv. Funct. Mater.* **2010**, *20*, 1099.

(193) Walcarius, A. *Chem. Soc. Rev.* **2013**, *42*, 4098.

(194) Mershin, A.; Matsumoto, K.; Kaiser, L.; Yu, D.; Vaughn, M.; Nazeeruddin, M. K.; Bruce, B. D.; Graetzel, M.; Zhang, S. *Sci. Rep.* **2012**, *2*, 234.

(195) Badura, A.; Kothe, T.; Schuhmann, W.; Rögner, M. *Energy Environ. Sci.* **2011**, *4*, 3263.

(196) Badura, A.; Guschin, D.; Kothe, T.; Kopczak, M. J.; Schuhmann, W.; Rögner, M. *Energy Environ. Sci.* **2011**, *4*, 2435.

(197) Ciesielski, P. N.; Scott, A. M.; Faulkner, C. J.; Berron, B. J.; Cliffel, D. E.; Jennings, G. K. *ACS Nano* **2008**, *2*, 2465.

(198) Ciesielski, P. N.; Hijazi, F. M.; Scott, A. M.; Faulkner, C. J.; Beard, L.; Emmett, K.; Rosenthal, S. J.; Cliffel, D.; Jennings, G. K. *Bioresour. Technol.* **2010**, *101*, 3047.

(199) Nguyen, K.; Bruce, B. D. *Biochim. Biophys. Acta* **2014**, *1837*, 1553.

(200) Ciesielski, P. N.; Hijazi, F. M.; Scott, A. M.; Faulkner, C. J.; Beard, L.; Emmett, K.; Rosenthal, S. J.; Cliffel, D.; Kane Jennings, G. *Bioresour. Technol.* **2010**, *101*, 3047.

(201) Badura, A.; Guschin, D.; Kothe, T.; Kopczak, M. J.; Schuhmann, W.; Rögner, M. *Energy Environ. Sci.* **2011**, *4*, 2435.

(202) L. Stryer, J. B., J. L. Tymoczko *Biochemistry*; W. H. Freeman and Company: England, 2012.

(203) www.life.illinois.edu/govindjee/paper/fig12.gif (retrieved 01.11.2013)

(204) Faulkner, C. J.; Lees, S.; Ciesielski, P. N.; Cliffel, D. E.; Jennings, G. K. *Langmuir* **2008**, *24*, 8409.

(205) Terasaki, N.; Yamamoto, N.; Tamada, K.; Hattori, M.; Hiraga, T.; Tohri, A.; Sato, I.; Iwai, M.; Iwai, M.; Taguchi, S.; Enami, I.; Inoue, Y.; Yamanoi, Y.; Yonezawa, T.; Mizuno, K.; Murata, M.; Nishihara, H.; Yoneyama, S.; Minakata, M.; Ohmori, T.; Sakai, M.; Fujii, M. *Biochim. Biophys. Acta* **2007**, *1767*, 653.

(206) Stieger, K. R.; Feifel, S. C.; Lokstein, H.; Hejazi, M.; Zouni, A.; Lisdat, F. *J. Mater. Chem. A* **2016**, *4*, 17009.

(207) Matsumoto, K.; Zhang, S.; Koutsopoulos, S. *Biomacromolecules* **2010**, *11*, 3152.

(208) Simmerman, R. F.; Zhu, T.; Baker, D. R.; Wang, L.; Mishra, S. R.; Lundgren, C. A.; Bruce, B. D. *Bioconjugate Chem.* **2015**, *26*, 2097.

(209) Gizzie, E. A.; Scott Niezgoda, J.; Robinson, M. T.; Harris, A. G.; Kane Jennings, G.; Rosenthal, S. J.; Cliffel, D. E. *Energy Environ. Sci.* **2015**, *8*, 3572.

(210) Shah, V. B.; Henson, W. R.; Chadha, T. S.; Lakin, G.; Liu, H.; Blankenship, R. E.; Biswas, P. *Langmuir* **2015**, *31*, 1675.

(211) Fu, L.; Shi, Y.; Tian, S.; Wu, Y.; van Ree, T.; Pan Stanford Publishing Pte. Ltd.: 2015, p 127.

(212) Ocakoglu, K.; Krupnik, T.; van den Bosch, B.; Harputlu, E.; Gullo, M. P.; Olmos, J. D. J.; Yildirimcan, S.; Gupta, R. K.; Yakuphanoglu, F.; Barbieri, A.; Reek, J. N. H.; Kargul, J. *Adv. Funct. Mater.* **2014**, *24*, 7467.

(213) Ciesielski, P. N.; Faulkner, C. J.; Irwin, M. T.; Gregory, J. M.; Tolk, N. H.; Cliffel, D. E.; Jennings, G. K. *Adv. Funct. Mater.* **2010**, *20*, 4048.

(214) LeBlanc, G.; Chen, G.; Gizzie, E. A.; Jennings, G. K.; Cliffel, D. E. *Adv. Mater.* **2012**, *24*, 5959.

(215) Kincaid, H. A.; Niedringhaus, T.; Ciobanu, M.; Cliffel, D. E.; Jennings, G. K. *Langmuir* **2006**, *22*, 8114.

(216) Gizzie, E. A.; LeBlanc, G.; Jennings, G. K.; Cliffel, D. E. *ACS Appl. Mater. Interfaces* **2015**, *7*, 9328.

(217) Zhao, F.; Conzuelo, F.; Hartmann, V.; Li, H.; Nowaczyk, M. M.; Plumere, N.; Rogner, M.; Schuhmann, W. *J. Phys. Chem. B* **2015**, *119*, 13726.

(218) Zhao, F.; Sliozberg, K.; Rogner, M.; Plumere, N.; Schuhmann, W. *J. Electrochem. Soc.* **2014**, *161*, 3035.

(219) Kothe, T.; Pöller, S.; Zhao, F.; Fortgang, P.; Rogner, M.; Schuhmann, W.; Plumere, N. *Chem. Eur. J.* **2014**, *20*, 11029.

(220) Hartmann, V.; Kothe, T.; Poller, S.; El-Mohsnawy, E.; Nowaczyk, M. M.; Plumere, N.; Schuhmann, W.; Rogner, M. *Phys. Chem. Chem. Phys.* **2014**, *16*, 11936.

(221) Baker, D. R.; Simmerman, R. F.; Sumner, J. J.; Bruce, B. D.; Lundgren, C. A. *Langmuir* **2014**, *30*, 13650.

(222) Terasaki, N.; Yamamoto, N.; Hiraga, T.; Sato, I.; Inoue, Y.; Yamada, S. *Thin Solid Films* **2006**, *499*, 153

(223) Yehezkeli, O.; Wilner, O. I.; Vered, R. T.; Roizman-Sade, D.; Nechushtai, R.; Willner, I. *J. Phys. Chem. B* **2010**, *114*, 14383.

(224) Kato, M.; Cardona, T.; Rutherford, A. W.; Reisner, E. *J. Am. Chem. Soc.* **2012**, *134*, 8332.

(225) Kato, M.; Zhang, J. Z.; Paul, N.; Reisner, E. *Chem. Soc. Rev.* **2014**, *43*, 6485.

(226) Kato, M.; Cardona, T.; Rutherford, A. W.; Reisner, E. *J. Am. Chem. Soc.* **2013**, *135*, 10610.

(227) Sokol, K. P.; Mersch, D.; Hartmann, V.; Zhang, J. Z.; Nowaczyk, M. M.; Rögner, M.; Ruff, A.; Schuhmann, W.; Plumeré, N.; Reisner, E. *Energy Environ. Sci.* **2016**, *9*, 3698.

(228) Goriparti, S.; Miele, E.; De Angelis, F.; Di Fabrizio, E.; Proietti Zaccaria, R.; Capiglia, C. *J. Power Sources* **2014**, *257*, 421.

(229) Pei, Z.; Li, Z.; Zheng, X. *J. Nanosci. Nanotechnol.* **2016**, *16*, 9028.

(230) Roy, P.; Srivastava, S. K. *J. Mater. Chem. A* **2015**, *3*, 2454.

(231) Tollefson, J. *Nature* **2008**, *456*, 436.

(232) Abraham, K. M. *J. Phys. Chem. Lett.* **2015**, *6*, 830.

(233) Palacin, M. R. *Chem. Soc. Rev.* **2009**, *38*, 2565.

(234) Goodenough, J. B.; Park, K. S. *J. Am. Chem. Soc.* **2013**, *135*, 1167.

(235) Thackeray, M. M.; Wolverton, C.; Isaacs, E. D. *Energy Environ. Sci.* **2012**, *5*, 7854.

(236) Bard, J. R.; Faulkner, L. R. *Electrochemical Methods - Fundaments and Applications*; John Wiley & Sons, 2001.

(237) Zhao, X.; Zhang, J.; Zhang, J.; Gong, C.; Gu, X.; Ma, Z.; Zhou, J.; Yu, L.; Zhang, Z. *J. Power Sources* **2015**, *294*, 223.

(238) Deng, Y.; Fang, C.; Chen, G. *J. Power Sources* **2016**, *304*, 81.

(239) Raju, V.; Wang, X.; Luo, W.; Ji, X. *Chemistry* **2014**, *20*, 7686.

(240) Kim, Y. S.; Kim, W. B.; Joo, Y. L. *J. Mater. Chem. A* **2014**, *2*, 8323.

(241) Santos-Pena, J.; Brousse, T.; Sanchez, L.; Morales, J.; Scheich, D. M. *J. Power Sources* **2001**, *97-98*, 232.

(242) Yin, L.; Chai, S.; Wang, F.; Huang, J.; Li, J.; Liu, C.; Kong, X. *Ceram. Int.* **2016**, *42*, 9433.

(243) Guo, Q.; Chen, S.; Qin, X. *Mater. Lett.* **2014**, *119*, 4.

(244) Grigorova, E.; Mandzhukova, T. S.; Khristov, M.; Yoncheva, M.; Stoyanova, R.; Zhecheva, E. *J. Mater. Sci.* **2011**, *46*, 7106.

(245) Liu, L.; An, M.; Yang, P.; Zhang, J. *Sci. Rep.* **2015**, *5*, 9055.

(246) Lian, P.; Zhu, X.; Liang, S.; Li, Z.; Yang, W.; Wang, H. *Electrochim. Acta* **2011**, *56*, 4532.

(247) Liu, X.; Zhong, X.; Yang, Z.; Pan, F.; Gu, L.; Yu, Y. *Electrochim. Acta* **2015**, *152*, 178.

(248) Liang, J.; Zhao, Y.; Guo, L.; Li, L. *ACS Appl. Mater. Interfaces* **2012**, *4*, 5742.

(249) Yang, Y.; Gao, Y.; Cheng, T.; Ma, D.; Liu, J.; Li, X. *RSC Adv.* **2016**, *6*, 67011.

(250) Kim, H.; Cho, J. *J. Mater. Chem.* **2008**, *18*, 771.

(251) Li, N.; Martin, C. R.; Scrosati, B. *Electrochem. Solid-State Lett.* **2000**, *3*, 316.

(252) Cevher, O.; Guler, M. O.; Tocoglu, U.; Akbulut, H. *Int. J. Energy Res.* **2014**, *38*, 499.

(253) Cevher, O.; Tocoglu, U.; Akbulut, H. *Int. J. Hydrogen Energy* **2014**, *39*, 21429.

(254) Liang, J.; Yu, X. Y.; Zhou, H.; Wu, H. B.; Ding, S.; Lou, X. W. *Angew. Chem. Int. Ed.* **2014**, *53*, 12803.

(255) Du, Z.; Yin, X.; Zhang, M.; Hao, Q.; Wang, Y.; Wang, T. *Mater. Lett.* **2010**, *64*, 2076.

(256) Guo, Q.; Chen, S.; Qin, X. *Mater. Lett.* **2014**, *119*, 4.

(257) Li, N.; Sonsg, H.; Cui, H.; Wang, C. *Electrochim. Acta* **2014**, *130*, 670.

(258) Reddy, M. J.; Ryu, S. H.; Shanmugharaj, A. M. *Nanoscale* **2016**, *8*, 471.

(259) Wang, X.; Zhou, X.; Yao, K.; Zhang, J.; Liu, Z. *Carbon* **2011**, *49*, 133.

(260) Wu, G.; Wu, M.; Wang, D.; Yin, L.; Ye, J.; Deng, S.; Zhu, Z.; Ye, W.; Li, Z. *Appl. Surf. Sci.* **2014**, *315*, 400.

(261) Xu, C.; Sun, J.; Gao, L. *J. Mater. Chem.* **2012**, *22*, 975.

(262) Yao, J.; Shen, X.; Wang, B.; Liu, H.; Wang, G. *Electrochem. Commun.* **2009**, *11*, 1849.

(263) Zhang, H.; Gao, L.; Yang, S. *RSC Adv.* **2015**, *5*, 43798.

(264) Zhang, M.; Lei, D.; Du, Z.; Yin, X.; Chen, L.; Li, Q.; Wang, Y.; Wang, T. *J. Mater. Chem.* **2011**, *21*, 1673.

(265) Zhang, M.; Sun, Z.; Zhang, T.; Sui, D.; Ma, Y.; Chen, Y. *Carbon* **2016**, *102*, 32.

(266) Zhang, Y.; Jiang, L.; Wang, C. *Phys. Chem. Chem. Phys.* **2015**, *17*, 20061.

(267) Zhao, B.; Zhang, G.; Song, J.; Jiang, Y.; Zhuang, H.; Liu, P.; Fang, T. *Electrochim. Acta* **2011**, *56*, 7340.

(268) Zhao, K.; Zhang, L.; Xia, R.; Dong, Y.; Xu, W.; Niu, C.; He, L.; Yan, M.; Qu, L.; Mai, L. *Small* **2016**, *12*, 588.

(269) Zhong, C.; Wang, J.; Chen, Z.; Liu, H. *J. Phys. Chem. C* **2011**, *115*, 25115.

(270) Zhou, D.; Song, W.-L.; Li, X.; Fan, L.-Z. *Electrochim. Acta* **2016**, *207*, 9.

(271) Zhou, X.; Liu, W.; Yu, X.; Liu, Y.; Fang, Y.; Klankowski, S.; Yang, Y.; Brown, J. E.; Li, J. *ACS Appl. Mater. Interfaces* **2014**, *6*, 7434.

(272) Zhu, C.; Zhu, S.; Zhang, K.; Hui, Z.; Pan, H.; Chen, Z.; Li, Y.; Zhang, D.; Wang, D. W. *Sci. Rep.* **2016**, *6*, 25829.

(273) Zhu, X.; Zhu, Y.; Murali, S.; Stoller, M. D.; Ruoff, R. S. *J. Power Sources* **2011**, *196*, 6473.

(274) Zhu, Y. G.; Wang, Y.; Xie, J.; Cao, G.-S.; Zhu, T.-J.; Zhao, X.; Yang, H. Y. *Electrochim. Acta* **2015**, *154*, 338.

(275) Gao, T.; Huang, K.; Qi, X.; Li, H.; Yang, L.; Zhong, J. *Ceram. Int.* **2014**, *40*, 6891.

(276) Tian, R.; Zhang, Y.; Chen, Z.; Duan, H.; Xu, B.; Guo, Y.; Kang, H.; Li, H.; Liu, H. *Sci. Rep.* **2016**, *6*, 19195.

(277) Ye, F.; Zhao, B.; Ran, R.; Shao, Z. *Chemistry* **2014**, *20*, 4055.

(278) Dhanabalan, A.; Li, X.; Agrawal, R.; Chen, C.; Wang, C. *Nanomaterials* **2013**, *3*, 606.

(279) Jiang, Y.; Yuan, T.; Sun, W.; Yan, M. *ACS Appl. Mater. Interfaces* **2012**, *4*, 6216.

(280) Hwang, Y.-H.; Bae, E. G.; Sohn, K.-S.; Shim, S.; Song, X.; Lah, M. S.; Pyo, M. *J. Power Sources* **2013**, *240*, 683.

(281) Guler, M. O.; Cevher, O.; Tocoglu, U.; Cetinkaya, T.; Akbulut, H. *Acta Phys. Pol. A* **2013**, *123*, 383.

(282) An, G. H.; Lee, D. Y.; Lee, Y. J.; Ahn, H. J. *ACS Appl. Mater. Interfaces* **2016**, *8*, 30264.

(283) Zhou, X.; Wan, L. J.; Guo, Y. G. *Adv. Mater.* **2013**, *25*, 2152.

(284) Chen, B.; Qian, H.; Xu, J.; Qin, L.; Wu, Q.-H.; Zheng, M.; Dong, Q. *J. Mater. Chem. A* **2014**, *2*, 9345.

2.CHARACTERIZATION

This chapter deals with the various analytical techniques that were used in this thesis to characterize nanomaterials. The phase composition, crystallinity, domain size and dispersibility of nanomaterials were determined by X-ray diffraction (XRD), dynamic light scattering (DLS), and Raman spectroscopy. Nitrogen and krypton physisorption, grazing-incident small-angle X-ray scattering (GISAXS), scanning electron microscopy (SEM) and transmission electron microscopy (TEM) were used to investigate the porous structure and the morphology of the nanomaterials. Thermal behaviour was studied using thermogravimetric analysis (TGA). The elemental composition of the nanomaterials was analysed by energy dispersive X-ray spectroscopy (EDX) and X-ray Photoelectron Spectroscopy (XPS). The electrical conductivity and transparency of the TCO nanomaterials was studied by Hall conductivity measurements in the Van der Pauw geometry and UV/Vis spectroscopy, respectively. For the electrochemical characterization of the materials cyclic voltammetry and galvanostatic measurements were performed.

2.1. X-RAY DIFFRACTION (XRD)

2.1.1. WIDE ANGLE X-RAY SCATTERING (WAXS)

X-ray diffraction (XRD) is an important and widely used analytical technique, which allows identification of the crystal structure and phase composition of solids as well as related factors including lattice constants, geometry and orientation of crystals. The method called wide angle X-ray scattering (WAXS) is carried out for angles $5° < 2\,\theta < 100°$. X-rays are a form of electromagnetic radiation having a wavelength between 0.01 and 10 nm. In a typical XRD setup the X-rays are created inside a high vacuum tube, when highly accelerated electrons from the anode collide with the cathode metal (such as Cu, Al, Mo, Mg) under a high voltage. The interaction between characteristic monochromatic X-rays and matter results in different secondary effects, for example, scattering, absorption and reflection. The process of XRD is based on the interaction of X-ray photons with the electron shell of atoms in a crystal. Scattering of X-ray waves occurs on the different crystallographic planes of the material which derive from the periodicity of the crystal namely its symmetry and occupation with atoms in the unit cell. These scattering waves from the atoms interfere in-phase or out-of-phase. The out-of-phase scattering waves cancel each other out (destructive interference), while the in-phase scattering waves result in enhanced amplitude of waves (constructive interference). This process is called diffraction, and is illustrated in Figure 2.1.[1-3]
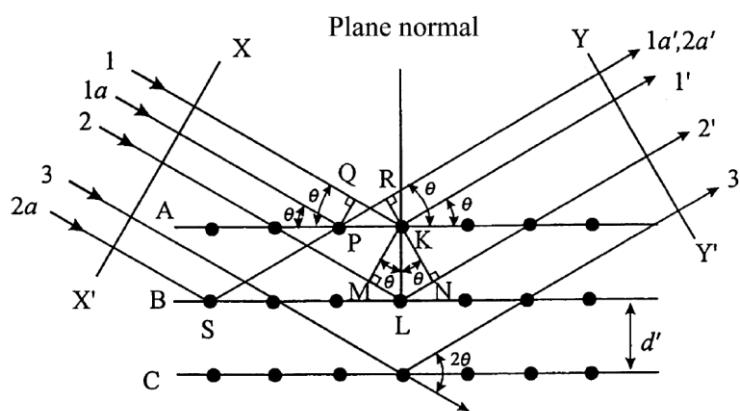
Figure 2.1   Schematic illustration of X-ray scattering by a crystal (Bragg condition).[2]

Constructive interference of the X-rays is given by fulfilling the Bragg's law:

$$n \lambda = 2 \, d' \, sin\theta$$
Equation 2.1

where n is the order of diffraction, d' is the interplanar spacing, λ is the X-ray wavelength (usually Cu K_α $\lambda = 1.540562$ Å) and θ is the incident angle.[2]

The intensity of the diffracted X-rays is measured as a function of the diffraction angle 2θ and the orientation of the sample. XRD is a nondestructive method and does not require a special preparation of a specimen. Besides information about the crystal structure also information about the crystal size can be obtained, as the peak broadening of the diffraction peaks depends on the domain size of the crystalline phase. The crystallite size can be estimated from the peak width using the Scherrer equation:[1]

$$D = \frac{k \, \lambda}{\beta \, cos\,\theta}$$
Equation 2.2

where D is the crystallite size, λ is the wavelength of the X-rays, β is the full width at half maximum (FWHM) of a diffraction peak, θ is the diffraction angle and k is the Scherrer constant.[1] Also the presence of size anisotropy, as well as its direction, can be detected from XRD pattern of nanoparticles by analysing the broadening of different individual lines using Scherrer equation.

Wide angle X-ray diffraction analysis was carried out in transmission mode using a STOE STADI P diffractometer with $CuK_{\alpha 1}$-radiation ($\lambda = 1.54060$ Å) and a Ge(111) single crystal monochromator equipped with a DECTRIS solid state strip detector MYTHEN 1K.

2.1.2. GRAZING-INCIDENT SMALL-ANGLE X-RAY SCATTERING (GISAXS)

GISAXS is a powerful tool in characterizing micro- and nanostructured thin films and surfaces. It provides averaged statistical significant information over all the illuminated sample area. It can also be used to show buried structures, which are located well below the surface and thus are inaccessible to local probe techniques such as AFM, and provides depth-dependent structural information using different incident angles.[4]

GISAXS involves a combination of three techniques: GID (grazing incidence diffraction), which uses a reflection geometry to perform surface and near surface sensitive scattering,

SAXS, which measures structures in a range of 3–50 nm in normal transmission mode, and diffuse scattering, which in reflection geometry probes morphologies of thin films and surfaces. It is a nondestructive method and does not require a special sample preparation (in situ characterization possible), yields excellent sampling statistics (averages over macroscopic regions to provide information on nanometer scale) and provides information on nano-structured surfaces in terms of object geometry, size distributions, and spatial correlations.[4]
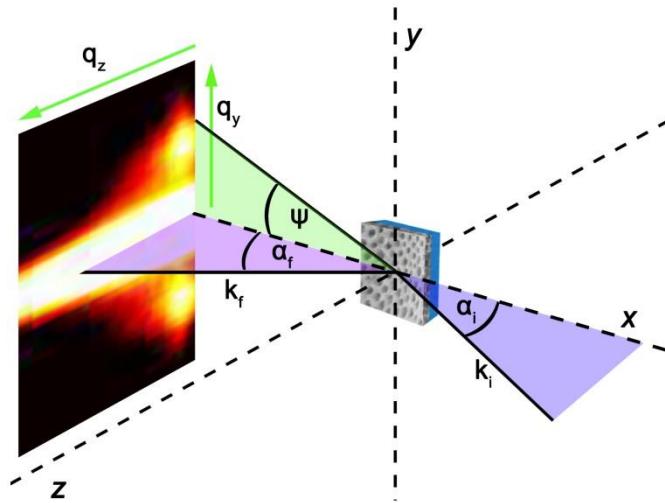
Figure 2.2   Scattering geometry used in GISAXS. The sample surface was tilted with respect to the incident beam by an incident angle α_i. The exit angle is denoted as α_f and the in-plane angle is Ψ.[5]

A typical GISAXS experiment for the investigation of macroporous films (see Chapter 4) is depicted in Figure 2.2. The incident beam strikes the sample under a small angle close to the critical angle of total external X-ray reflection. The sample surface defines the (x, y)-plane with the x-axis oriented along the X-ray beam direction and thus the y-axis being perpendicular to the scattering plane given through the incident angle α_i and the exit angle α_f. The intense reflected beam as well as the intense scattering in the incident plane is attenuated by a rod-shaped beam stop. The diffuse scattering from the sample is recorded with an area detector. The 2D images can be used to extract the in-plane scattered intensity as a function of q_y (at constant q_z).[4,5] GISAXS X-ray scattering experiments were performed by Hasala N. Lokupitiya and Dr. Morgan Stefik from the South Carolina SAXS Collaborative using a SAXSLab Ganesha. A Xenocs GeniX3D microfocus source was used with a Cu target to generate a monochromatic beam with a 0.154 nm wavelgth.

2.2. ELECTRON MICROSCOPY

Electron microscopy (EM) is a versatile tool to reveal the structure of studied materials. This technique has the possibility to show the internal microstructure of a solid by using transmission electron microscopy (TEM), the external surface morphology by using scanning electron microscopy (SEM) or the chemical composition of the sample by using energy dispersive X-ray spectroscopy (EDX).[1]

EM is based on electron bombardment of the sample, whereby the incident electrons can be absorbed, scattered and emitted by the sample. In Figure 2.3 the different interacting processes are summarized.
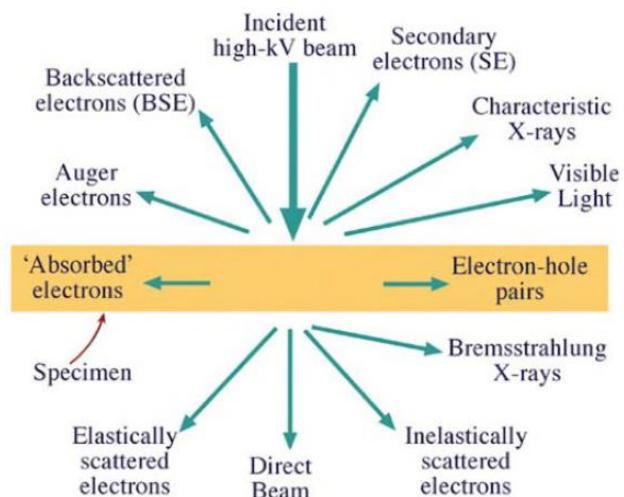
Figure 2.3 Signals generated from interactions between incident electrons and material. Most of them can be detected in different types of Electron microscopy.[6]

2.2.1. TRANSMISSION ELECTRON MICROSCOPY (TEM)

For TEM measurements, the electrons are accelerated by rather high voltages (80–400 keV) and focused by electromagnetic condenser lenses onto a thin specimen. The beam can be either focused to a small probe which is in the range of an atomic diameter or can be held parallel and illuminate a much larger area of a sample. After the interaction with the specimen only electrons that are transmitted and elastically scattered through the sample are used for imaging. For this purpose a fluorescent screen or a CCD camera is used. The image contrast results from inelastic or elastic scattering processes occurring during the transmission of the electrons through the sample. The contrast formation in TEM depends on the mode of operation. Image contrast at low resolution, the so-called amplitude contrast, can be obtained by excluding electrons scattered to certain angular ranges by means of the objective aperture. Bright Field images are obtained with the objective aperture centered on the transmitted beam excluding high scattering angles whereas dark field images are obtained by excluding the transmitted beam and low angle scattered electrons for the image formation. The resolution of TEM microscopes is significantly higher than that of light microscopes, which is a result of the small effective electron wavelengths (λ) due to the de Broglie relationship. The lateral spatial resolution of a TEM instrument increases with its operation voltage, so that currently used high-voltage TEMs obtain resolutions in the sub-nanometer region.[1,6]

The crystallographic structure of a sample can also be analyzed by high resolution transmission electron microscopy (HRTEM). This imaging mode allows the investigation of a specimen at the atomic scale. In contrast to conventional microscopy, in HRTEM only elastically scattered electrons are used for the image formation. In an optimized TEM the electron wave illuminating the specimen has a constant phase. Depending on the local projected structure a phase shift of the electron wave is obtained below the specimen. These local phase variations are converted to image contrast by the imaging system. Because of its high resolution this method is very important to study structural properties at the nanoscale.[1,6] By using a selected-area aperture and parallel illumination, it is possible to switch between imaging and diffraction mode. In the selected-area electron diffraction (SAED) mode the electron beam undergoes Bragg scattering resulting in a diffraction pattern in case of a crystalline sample, which can be used for the identification of the crystal structure of different parts of the sample on the micro and nanoscale.[6]

TEM measurements were carried out using a FEI Tecnai G2 20 S-TWIN, a Titan Themis 300 or a FEI Titan 80-300 operated at 200 kV or 300 kV. For TEM sample preparation the powders were grinded or dispersed in absolute ethanol, placed on a holey carbon coated copper grid and evaporated.

2.2.2.   SCANNING ELECTRON MICROSCOPY (SEM)

Scanning electron microscopy (SEM) is one of the most widely used techniques for the analysis and characterization of nanostructures and nanomaterials. The basic principle involves scanning of an incident electron beam line wise across the specimen surface with a certain frequency (raster scanning). The interaction of the incoming beam with the specimen generates a series of signals, which provides detailed information about the morphology and chemical composition. The beam can be accelerated by applying voltages from 0.1 to 30 kV. A high resolution image requires small beam diameters in the range of 1 to 10 nm which is focused by the objective lens onto the specimen surface. The impinging electrons penetrate and interact with the specimen and result in the emission of electrons and photons from the sample (Figure 2.4), which can be usually detected by an Everhart-Thornley detector. Three types of SEM detection and imaging modes are differentiated, the secondary electron images, backscattered electron images and elemental X-ray maps (Figure 2.4).
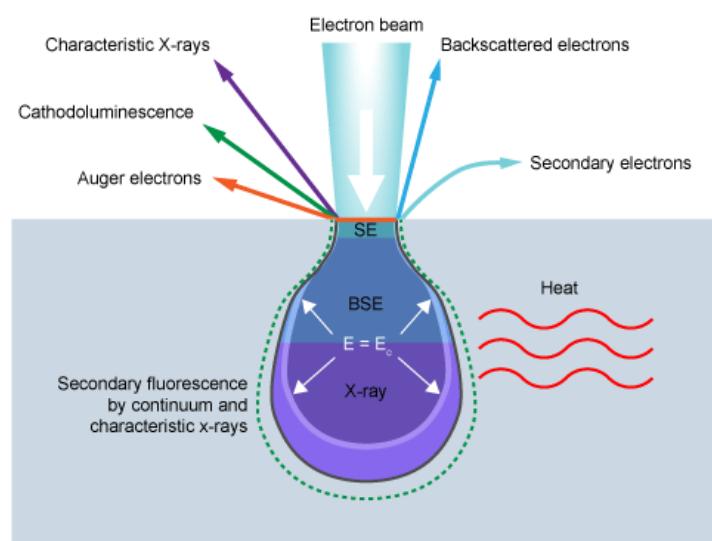
Figure 2.4   Schematic representation of the electron-specimen interaction volume in a SEM and the volume/depth from which the different signals originate.[7]

Secondary electrons (SE) (< 50 eV) are generated by inelastic scattering of high-energy primary electrons and are used for detailed images of the surface morphology, as they are only emitted from the specimens' surface. Backscattered electrons (BSE) are high-energy electrons that are elastically scattered by the atomic nucleus and possess the same energy as the incident primary electrons. Due to their higher energy they have a larger interaction volume. The probability of backscattering increases with the atomic number of the observed sample material so that the detection reveals a high contrast difference between different elements of the specimen. So the detection of SE and BSE gives complementary information about the topology and material composition. Besides electrons also characteristic X-rays are generated in the interaction volume, which can be used for a quantitative chemical analysis.[8,9]

The theoretical limit of the resolving power (R) of an SEM instrument is influenced by the wavelength of the electron beam and the numerical aperture of the system and is described by the following equation:[8,9]

$$R = \frac{\lambda}{2\,NA} \qquad\qquad \text{Equation 2.3}$$

Where λ is the electron wavelength and NA is the numerical aperture which describes the electron gathering ability of the objective or the electron providing ability of the condenser.[1]

SEM images were obtained with a JEOL JSM-6500F or a FEI Helios NanoLab G3 UC scanning electron microscope equipped with a field emission gun operated at 3–10 kV.

2.2.3. ENERGY DISPERSIVE X-RAY SPECTROSCOPY (EDX)

Energy dispersive X-ray spectroscopy (EDX) is a powerful analytical tool for elemental analysis. The technique is based on X-rays, which are generated by inelastic scattering of the electron beam and are emitted from a larger interaction volume. X-rays are generated when an electron from an inner shell is excited above the Fermi level by the primary electrons and outer shell electrons fill the inner shell vacancies. The energy difference of the electron of the outer donating shell and vacant inner shell thereby equals the X-ray photon energy corresponding to this transition. These X-rays energies and thus electron energy level differences are characteristic for an element and can be utilized for chemical composition analysis. The advantage of EDX compared to other elemental analysis techniques is the possibility to resolve the elemental distribution spatially, as the sample is analyzed point by point.[6,10,11]

EDX spectra are collected with EDX detectors, which can be installed both in TEM or SEM instruments. The active part of such a detector is a Si(Li) semiconductor. The incoming X-rays create electron-hole pairs in the semiconductor, which number is directly proportional to the energy of the incoming X-ray. [6,10,11]

EDX spectra were recorded with a JEOL JSM-6500F or a FEI Helios NanoLab G3 UC scanning electron microscope equipped with a field emission gun operated at 20 kV.

2.3. X-RAY PHOTOELECTRON SPECTROSCOPY (XPS)

X-ray photoelectron spectroscopy is a spectroscopic surface chemical analysis technique which permits both qualitative and quantitative determination of the elemental composition. Furthermore XPS can provide information about the chemical oxidation state of the investigated elements. This method is based on the photoelectric effect depicted in Figure **2.5**.[12]
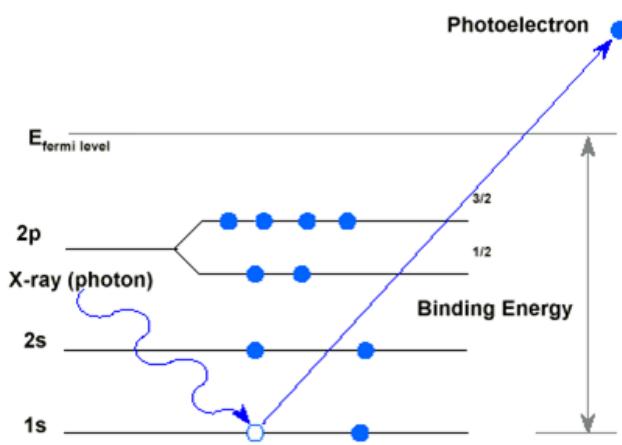
Figure 2.5   Generation of Photoelectrons under the X-ray irradiation.[13]

Under the irradiation with characteristic X-rays (such as Mg Kα or Al Kα), the core level electron bound to the atomic nucleus with the binding energy E_B absorbs the photon energy hv, where h is Planck's constant and v is the frequency of the incident photons. With the absorbed energy hv, a core level electron can be promoted from the inner shell of the atom to the vacuum level. Thus, a photoelectron with the kinetic energy E_k is generated. The relationship between incident X-ray photon energy hv, E_B and E_k can be written as in the following equation:[9,12]

$$E_k = hv - E_B - \Phi \qquad\qquad \text{Equation 2.4}$$

Here, Φ is the work function of the spectrometer. As hv is known from the applied characteristic X-ray source, the binding energy E_B can be obtained from measuring the kinetic energy E_k. Considering that the binding energy E_B is a characteristic value for each atom, the presence of peaks at different binding energies can be used to identify the elemental composition in the sample. However, for species with different valence states, the peak

positions show slight shifts relative to their neutral counterparts, according to their local chemical environment and formal oxidation state in the atom. These shifts are useful for distinguishing the oxidation states of atoms.[12]

In order to allow the collection and analysis of electrons escaping from the sample surface, the XPS technique requires ultra-high vacuum (UHV) conditions (below 10^{-7} Pa) to offer a suitable mean free path length of the electrons to reach the detector. Beside this, the sample surface should be cleaned to minimize any contamination, since the energies of emitted photoelectrons are much less than 1 keV with a very low mean free paths in the material due to strong electron matter interaction. The recorded photoelectron spectra can be fitted using Gaussian profiles, and the concentration of excited surface atoms is determined by measuring the integral intensity of the peaks after subtracting the background counts.[9,12]

X-ray photoelectron spectroscopy (XPS) measurements of the particles on a silicon substrate were performed by Dr. Patrick Zeller using a VSW TA10 X-ray source, providing non-monochromatic Al K_α radiation, and a VSW HA100 hemispherical analyser. The samples were cleaned by Ar^+ sputtering (VSW AS10 ion source) for 5 min at 1 keV.

2.4. DYNAMIC LIGHT SCATTERING (DLS)

Dynamic light scattering is a very common method to study the size and size distribution of nanoparticles in colloidal solutions. This technique is based on the scattering of light on colloidal particles due to Brownian motion in solution. The incident light is scattered in all directions resulting in constructive and deconstructive interference. Thus, the scattering intensity, which is traced by the detector, shows time-dependent fluctuations. The fluctuation rate of the scattering intensity is related to the mobility of the particles in the colloidal solution, and thus also to the particle size through an auto-correlation function. In other words, small particles diffuse very fast and result in fast fluctuation, while larger particles move slowly in the solution and thus cause slow fluctuations. Analyzing the fluctuation rate as a function of time gives insights into the particle size as well as its size distribution. The particle size can be calculated by using the Stokes-Einstein-Relation:[14]

$$d = \frac{kT}{3\pi\eta D} \qquad\qquad \text{Equation 2.5}$$

Where D is the diffusion coefficient, k is the Boltzmann constant, T is the Kelvin temperature, η is the solvent viscosity and d is the hydrodynamic radius of the particles.

For nanoparticles with a broad size distribution, laser light scattering from larger particles can be analyzed using the Mie theory, while scattering from small ones can be described by using Rayleigh scattering. The correlation between intensity fluctuation and particle size is summarized in the following equation:[14]

$$I = I_0 \frac{1+cos^2\theta}{2R^2}\left(\frac{2\pi}{\lambda}\right)^4 \left(\frac{n^2-1}{n^2+1}\right)^2 \left(\frac{d}{2}\right)^6 \qquad\qquad \text{Equation 2.6}$$

Where I and I_0 are the intensities of the scattered light and the incoming light, θ is the scattering angle, λ is the wavelength of the laser light, n is the refractive index of the nanoparticles, R is the distance to the nanoparticles and d is the hydrodynamic diameter.[9,14]

Dynamic light scattering (DLS) measurements were performed on a MALVERN Zetasizer-Nano instrument equipped with a 4 mW He-Ne laser ($\lambda = 633$ nm) and an avalanche photodiode detector.

2.5. SORPTION

Gas adsorption is a powerful technique in determining the surface area, the pore sizes and pore volume of porous structures regardless of their chemical composition and crystal structure. The analysis is based on monitoring the physisorption of gas molecules, typically nitrogen or krypton, on the surface of a porous sample at a constant temperature of 77 K in the case of nitrogen. Adsorption is usually described through isotherms, which reveal the amount of gas adsorbed or desorbed from a material as a function of the relative pressure. The relative pressure is defined as the p/p_0 ratio, where p is the equilibrium pressure and p_0 is the saturation vapor pressure. The quantity adsorbed is usually normalized by the mass of the adsorbent to allow comparison of different materials. When a gas is brought in contact with a porous media at a constant temperature, several mechanism of adsorption occur successively on the inner surface of the pores as the relative pressure is increased from zero to one. With increasing relative vapor pressure, first a monolayer is formed on the inner surface of the pores. As the relative pressure increases further, multilayer adsorption occurs followed by a pore filling through capillary condensation at higher relative pressures.[1,15]

The shape of the sorption isotherm varies depending on the type of adsorbent, the type of adsorbate and the intermolecular interactions between the gas and the surface. According to IUPAC classification, there are six main types of sorption isotherms as shown in Figure 2.6. Type I isotherms characterize microporous materials (< 2 nm). Type II and III describe the unrestricted multilayer adsorption on nonporous or macroporous (< 50 nm) materials with strong and weak adsorbate-adsorbent interactions, respectively. Type IV and V represent adsorption isotherms with a hysteresis with strong and weak adsorbate-adsorbent interactions, which is typical for mesoporous materials. Finally type VI shows the stepwise multilayer adsorption on a uniform non-porous surface. Point B in type II and IV designates the stage at which monolayer coverage is complete and multilayer adsorption begins.[1,15]
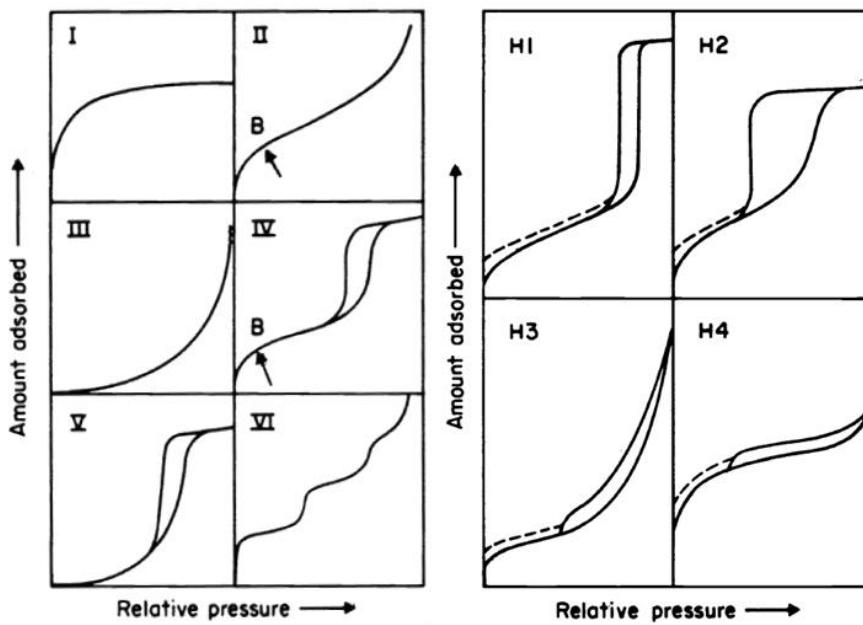
Figure 2.6   Types of physisorption isotherms (left) and types of hysteresis loops (right).[15]

The shape of the hysteresis loop, which is usually associated with capillary condensation in mesoporous structures, reveals information about the specific structure of the mesopores. The narrow, almost vertical parallel hysteresis loop of type H1 in Figure 2.6 is characteristic for materials with narrow pore size distributions, whereas the unsymmetrical loop of type H2 is typical for wide pore size and shape is not well-defined pore shapes. Type H3 and H4 are typical for aggregates of plate-like particles giving rise to slit-shaped pores or narrow slit-like pores, respectively.[1,15]

Nitrogen sorption measurements were performed on a Quantachrome Autosorb-1 instrument at the boiling point of liquid nitrogen (approximately 77 K). The specific surface area was determined with the Brunauer-Emmett-Teller (BET) method at $p/p_0 = 0.05-0.2$ using the ASiQwin software. The pore size distribution was calculated using the DFT/Monte Carlo method (ASiQwin software).

In addition to nitrogen, krypton sorption can be used to characterize the porosity of materials. Kr sorption is particularly useful for characterizing materials with a small total surface area, for example in thin meso- or macroporous films, due to the lower saturation vapour pressure of krypton compared to nitrogen. Using this method it is possible to determine surface areas down to a few cm^2. Krypton sorption isotherms on mesoporous and macroporous ATO films were performed and evaluated by Dr. Jiří Rathouský from the J. Heyrovský Institute of Physical Chemistry in Prague using a Micromeritics ASAP 2010 volumetric adsorption unit at

the boiling point of liquid nitrogen (77 K). The saturation pressure of solid krypton of $\approx$1.6 Torr and the occupied area of the krypton molecules in a complete monolayer of 0.21 nm^2 were used for the calculations (as provided by the Micromeritics software).

2.6. THERMOGRAVIMETRIC ANALYSIS (TGA)

Thermogravimetric analysis (TGA) is a powerful technique to characterize the thermal behavior of a sample. During the TGA experiment the sample is heated with a defined heat rate in a controlled atmosphere, while the resulting mass change of the substance is monitored as a function of temperature and time. Typically either a synthetic air mixture as oxidizing gas atmosphere or an inert gas like nitrogen is used. Depending on the atmosphere, reduction or oxidation events (phase transitions), decomposition or dehydration/solvent evaporation can occur causing a loss in weight. Additional to TGA, usually differential scanning calorimetry (DSC) analysis is performed. It is used to determine the enthalpy of those weight loss processes by measuring the energy needed for heating or cooling the sample in comparison to an inert reference. Therefrom endothermic processes, like evaporation or phase transformation can be distinguished from exothermic processes like combustion.[9,16]

In this thesis TGA/DSC was used to determine the amount of organic residues in the ATO/ITOH/TiO$_2$ nanoparticles, to monitor phase transformation of ITOH to ITO and to measure the amount of graphene in ATO/graphene nanocomposites by following the gradual decomposition of graphene oxide in air. The TGA/DLS measurements were performed on a NETZSCH STA 440 C TG/DSC (heating rate of 10 K min^{-1} in a stream of synthetic air of about 25 mL min^{-1}).

2.7. UV/VIS SPECTROSCOPY

Ultraviolet-visible (UV-VIS) spectroscopy is used to measure the absorbance of ultra violet $(10 - 400$ nm$)$[17] and visible light $(400 - 700$ nm$)$[17] by a sample. In general, electromagnetic radiation in the UV-Vis region interacts with matter and causes electronic transitions (excitation of electrons from the ground state to a high energy state). This technique can be used both quantitatively and qualitatively to determine the absorption properties of liquid and solid samples.

The UV-Vis spectrometer measures the intensity of light for each wavelength passing through both the reference cell (I_0) and the sample cell (I). The detected signal is the transmittance T $(T = I/I_0)$ in percent. The absorbance (A) of the sample is related to I and I_0 according to the following equation:[17,18]

$$A = -log_{10} \frac{I_0}{I}$$

Equation 2.7

The absorption can also be calculated by measuring films in transmission and reflection mode; it can be calculated using the following formula:[17,18]

$$A = 100 - R - T$$

Equation 2.8

where *A, R, T* is the amount of absorbed, reflected and transmitted light in percent.

UV-visible spectroscopy can also be used to measure the concentration of a sample, as the absorbance is proportional to the concentration of the substance in solution according to the Beer-Lambert Law. It can be expressed in form of the following equation:[18]

$$A = \varepsilon \cdot c \cdot l$$

Equation 2.9

where l is the optical path length, c is the concentration of solution and ε is the molar absorption coefficient.

In the present work UV-Vis spectroscopy was used to measure the transmittance of porous TCO electrodes. Additionally it was used to estimate the amount of photoactive Photosystem I protein complexes adsorbed on the surface of transparent macroporous ATO electrodes using their characteristic bands at wavelengths between $420 - 440$ and $670 - 680$ nm. The measurements were performed on a PerkinElmer Lambda 1050 spectrophotometer equipped with an integrating sphere.

2.8. RAMAN SPECTROSCOPY

Raman spectroscopy is a non-destructive, vibrational analytical technique based on inelastic scattering of monochromatic light, which is used to characterize and identify materials and its phase composition.
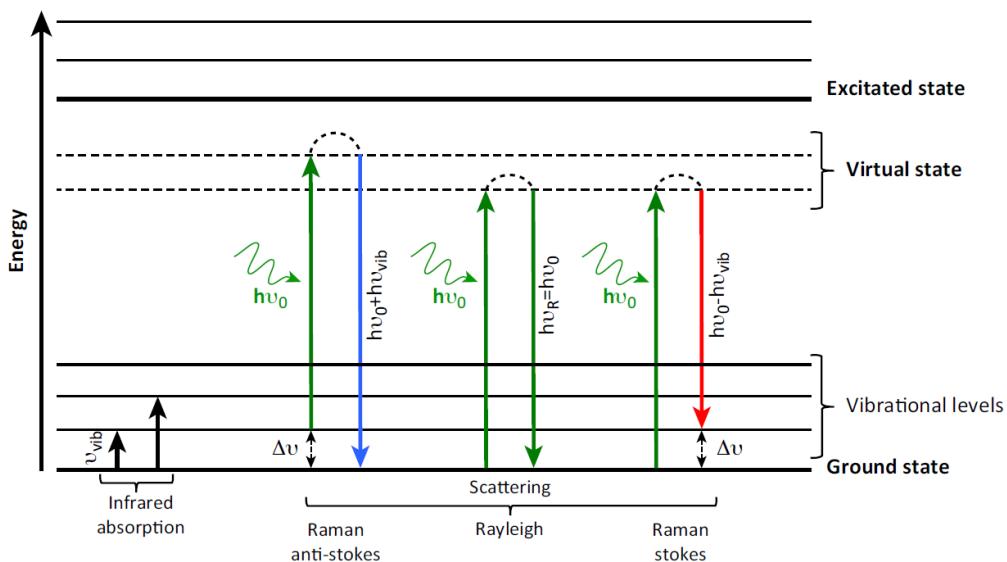
Figure 2.7   Diagram showing transitions occurring between energy levels during infrared absorption and Raman scattering phenomena.[19]

In a typical Raman spectroscopy experiment, a monochromatic incident laser beam is passed through the sample, interacts with these bonds and excites the molecule from the ground state into a higher energetic virtual level. The subsequent relaxation from the excited state leads to a simultaneous reemission of a photon from the front face of the sample, which is monitored. The detection geometry allows for the study of gases, pure liquids, solutions, suspensions and solids. Raman activity requires the fulfilment of the 'gross' selection rule that is the polarizability of the bonds has to change as the molecule vibrates.[1,20]

Vibrational and rotational energy levels can be explored by examining the frequencies present in the radiation scattered by molecules. About 1 in 10^7 of the incident photons collide with the molecules, give up some of their energy and emerge with a lower energy. These inelastic scattered photons constitute the lower-frequency Stokes radiation from the sample. Other incident photons may collect energy from the molecules and emerge as higher-frequency anti-Stokes radiation. The component of radiation elastically scattered without change of frequency is called Rayleigh radiation. In general Stokes lines have higher intensities in

comparison with Anti-Stokes lines due to the lower occupation of excited states at room temperatures. All excitation processes are illustrated in Figure 2.7.[20]

Raman spectroscopy was carried out using a LabRAM HR UV-Vis (Horiba Jobin Yvon) Raman Microscope (Olympus BX41) with a Symphony CCD detection system and a He-Ne laser (= 633 nm).

2.9. CONDUCTIVITY - HALL MEASUREMENTS

The Hall effect was discovered by Edwin Hall in 1879. Basically it describes the formation of a voltage across a sample transverse to an applied electric current and an external magnetic field perpendicular to the current. The basic physical principle underlying the Hall effect is the Lorentz force. When an electron moves along a direction perpendicular to an applied magnetic field, it experiences a force which acts normal to both, the direction of the magnetic field and the direction of the current, and moves in response to this force (see Figure 2.8). The "right hand rule" allows determining the direction of the force on a charge carrier based on its direction of motion and the direction of the applied magnetic field.[21]

Figure 2.8   Illustration of Hall effect.[21]

A Hall effect measurement system can be used to determine several material parameters, such as the Hall voltage (V_H), the carrier mobility (μ), carrier concentration (n), Hall coefficient (A_H), resistivity (R_H) and the conductivity type (n or p). With the addition of some other instruments, I-V characterization curves can be created with a similar test setup.

The resistivity can be determined using either a four-point probe or the van der Pauw measurement technique. In the van der Pauw method the bulk resistivity of the sample is

calculated from the sheet resistance. The sheet resistance R_S is calculated from a series of resistance measurements shown in Figure 2.9.
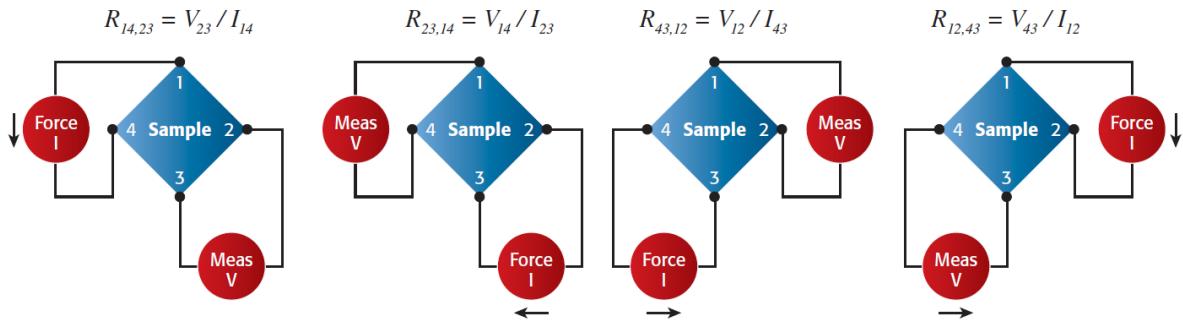
Figure 2.9   Resistance measurements based on the van der Pauw measurement technique.[21]

For van der Pauw resistivity measurements, the current is forced on adjacent nodes. Then the voltage is measured on adjacent nodes on the opposite side so everything that is being forced and measured is on neighbouring pins.

$$R_A = \frac{R_{21,34}+R_{12,43}+R_{43,12}+R_{34,21}}{4}$$ Equation 2.10

$$R_B = \frac{R_{32,41}+R_{23,14}+R_{14,23}+R_{41,32}}{4}$$

R_A and R_B are related to the sheet resistance R_S through the van der Pauw equation:

$$e^{\left(-\frac{\pi R_A}{R_S}\right)} + e^{\left(-\frac{\pi R_B}{R_S}\right)} = 1$$ Equation 2.11

The product of the sheet resistance (R_S) and sample thickness (d) gives the bulk electrical resistivity ρ.

$$\rho = R_S \cdot d$$ Equation 2.12

The charge carrier concentration n_c can be obtained from the Hall voltage V_H from the Hall effect measurement. The Hall voltage (V_H) is measured by forcing both a magnetic field perpendicular to the sample and a current through the sample. In the Hall effect resistivity measurement, the current is forced on the opposite nodes of the sample and then the voltage is also measured on the other opposite nodes. Two sets of measurements are performed; one with a magnetic field positive to the z direction and one with a magnetic field negative to the z direction (Figure 2.10).[21]

$$V_C = V_{24P} - V_{24N}$$
$$V_D = V_{42P} - V_{42N}$$

$$V_E = V_{13P} - V_{13N}$$
$$V_F = V_{31P} - V_{31N}$$
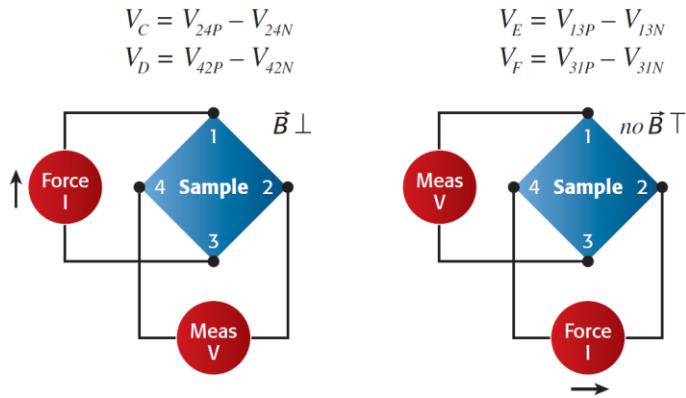
Figure 2.10   Hall voltage measurements on opposite nodes with both positive and negative polarity current and with the magnetic field both up and down.[21]

The voltages denoted as V_{24P} or V_{24N} are the measured voltages between node 2 and 4 applying positive or negative magnetic field, respectively. The resulting potential (V_H) is given by the following equation:[21]

$$V_H = \frac{V_C + V_D + V_E + V_F}{8} \qquad \text{Equation 2.13}$$

The magnitude of this Hall voltage is equal to $\frac{IB}{qnd}$ where I is the current flow, B is the magnetic field, d is the sample thickness and q (1.602 x 10^{-19} C) is the elementary charge. In some cases, it is convenient to use layer or sheet density ($n_s = n\,d$) instead of bulk density. Thus, by measuring the Hall voltage V_H and from the known values of I, B, and q, one can determine the sheet density n_s of charge carriers:[22]

$$n_s = \frac{IB}{qV_H} \qquad \text{Equation 2.14}$$

Since sheet resistance involves both sheet density and mobility, one can determine the Hall mobility (μ) from the equation:[22]

$$\mu = \frac{V_H}{R_S IB} = \frac{1}{qn_S R_S} \qquad \text{Equation 2.15}$$

Hall conductivity measurements were carried out on ECOPIA HMS 3000 apparatus in the Van der Pauw geometry using a magnetic field of 0.55 T. The measurements were performed on pellets (10 mm diameter), which were prepared by pressing finely grinded nanoparticles under a pressure of 10 tons/cm^2. Copper wire contacts for the dc conductivity measurements were connected to the pellet using a silver lacquer.

2.10.ELECTROCHEMICAL MEASUREMENTS

2.10.1. CYCLIC VOLTAMMETRY (CV)

Cyclic voltammetry is a powerful analytical tool to study the electrochemical behaviour of a material, in which the current is monitored as a function of the potential. The potential is changed linearly with a fixed scan rate in a specified voltage range (see Figure 2.11a). Thereby the current is measured resulting in a current-potential diagram also known as a voltammogram (VA) or cyclic voltammogram (CV) when the potential direction is reversed (see Figure 2.11b). CVs are typically measured in a three-electrode setup containing a working electrode, at which the reaction of interest is investigated, a reference electrode (an electrode having a constant defined potential such as Ag/AgCl/KCl or a normal hydrogen electrode (NHE)) and a counter electrode (typically an inert metal electrode such as Pt). The measurements are performed in an electrolyte, which is typically not stirred, so that mass transport to the electrode takes place via non-stationary diffusion. A typical CV curve for a reversible redox reaction is shown in Figure 2.11b.[20,23]
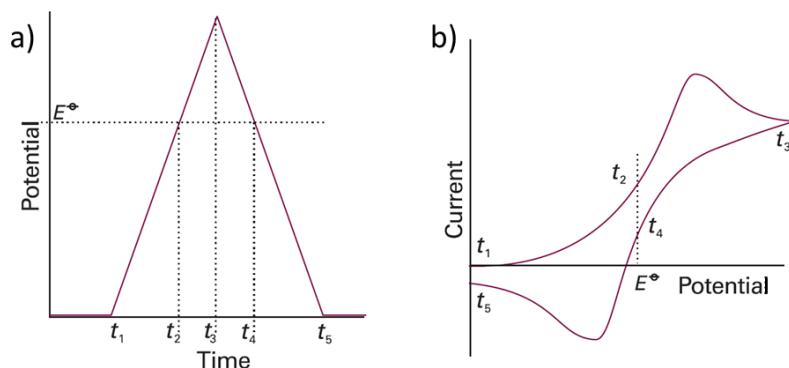
Figure 2.11   (a) The change of potential with time and (b) an example of the resulting current/potential curve in a cyclic voltammetry experiment.[20]

Cyclic voltammograms provide a lot information about the thermodynamics and kinetics of processes taking place at the electrode-electrolyte interface, the reversibity of redox processes, as well as the the amount of material involved in the reaction.

In general the processes on the electrode can be divided in faradaic and nonfaradaic processes. Faradaic processes comprise reactions in which charges are transferred across the metal-electrolyte interface resulting in a change of the oxidation state of reacting species. The

amount of chemical reaction caused by the flow of currents is proportional to the amount of electricity passed according to the Faraday's law. The processes resulting in charging of the electrode-electrolyte interface without the interfacial charge transfer are called nonfaradaic processes. An important example of such processes is charging of the electrical double layer (capacitive processes). In this case the electrode-solution interface behaves like a capacitor, with a charge q^M on the metal electrode and a reverse charge $-q^S$ in the electrolyte. The charge q^M represents an excess or deficiency of electrons in a very thin layer (< 10 Å) on the metal surface.[23] These charging can be used to estimate the electrochemically active surface area by measuring the nonfaradaic capacitive current associated with double-layer charging from the scan rate dependence (see Chapter 4).[5,23] The capacitance (C in farad, F) is defined as:[23]

$$C = \frac{q}{E}$$ Equation 2.16

where q is the charge stored on the capacitor (in coulombs, C) and E is the potential across the capacitor (in volts, V). The capacitance can also be obtained as the slope of the dependence of currents (I in C s^{-1}) versus the scan rate (in V s^{-1}) (Figure 2.12) at a potential where no Faradaic processes take place:

$$C = \frac{I}{scan\ rate}$$ Equation 2.17

Assuming a specific capacitance of 60 µF cm^{-2} for flat oxide electrodes[24-26] the corresponding surface area can be calculated by dividing the measured capacitance per surface area (in C cm^{-2}) by 60 µF cm^{-2} giving the so-called roughness factor (in cm^2 cm^{-2}), which is determined as the real surface area related to the geometric substrate area.
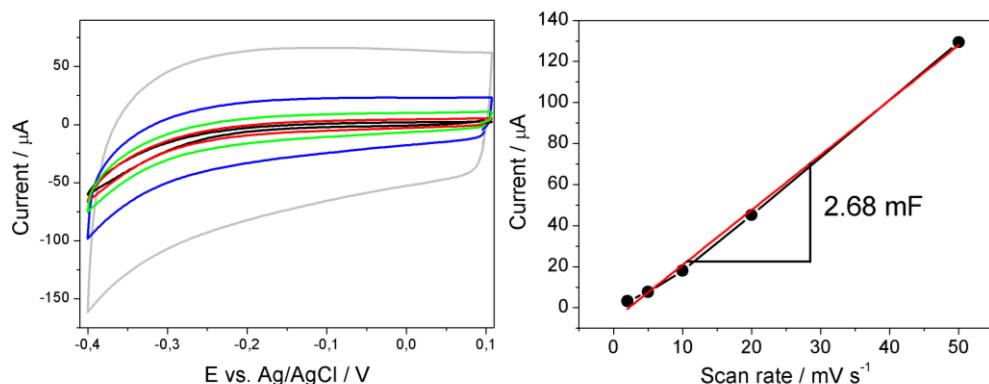
Figure 2.12   Left: Cyclic voltammograms recorded with different scan rates (grey line: 50 mV, blue line: 20 mV, green line: 10 mV, red line: 5 mV, black line: 2 mV). Right: Capacitive currents at -0.1 V vs. Ag/AgCl obtained at different scan rates. The determined slope is 2.68 mF, which equals 3.41 mF cm^{-2} (exposed area: 0.785 cm^2).

The faradaic processes can be used to calculate the amount of material involved in the reaction, as the peak area under the cathodic and anodic peaks corresponds to the amount of charges (electrons) transferred in the charge transfer process across the metal-solution interface. In this thesis this was used to calculate the amount of electroactive species (molybdenum polyoxometalate anion: $PMo_{12}O_{40}{}^{3}$) adsorbed on the surface of meso- and macroporous ATO films (see Chapter 4). The peak area directly correlates with the number of adsorbed polyoxometalate anions. The electrochemical loading (n in mol cm^{-2}) was calculated using the Faraday's law:[5]

$$n = \frac{Q}{z \cdot F \cdot A}$$ Equation 2.18

where Q is the total electric charge (in C), z is the number of electrons transferred per polyoxometalate anion ($z = 6$), F is the Faraday constant (96485 C mol^{-1}) and A the exposed area (in cm^2).[5]

CV is a versatile tool to characterize electrochemically active compounds in battery cells by identifying the characteristic reduction and oxidation potentials of the tested materials and also potential other phases (see Chapter 11). A negative scan direction corresponds to discharging of the battery, whereas a positive scan direction results in charging. The total gravimetric lithium insertion capacities can be determined by integrating the area under the CV curve upon charging or discharging and normalizing the obtained charge to the mass of the electrode. The cycling stability of an electrode can be obtained by repeated cycling (charging and discharging) of the electrode. A decrease in the peak height (and therefore in the total peak area) represents capacity fading.[20,23,27]

Another electrochemical measurement technique applied in this thesis is chronoamperometry. In this mode the current is monitored as a function of time, while applying a certain potential on the working electrode.[23] A special variation of this electrochemical technique is the photochronoamperometry, in which the current is monitored at a constant potential as a function of time under chopped light illumination (light on-off measurements). This mode was used to measure absolute photocurrent generation of PSI functionalized flat and porous films upon illumination with white light at a constant potential (see Chapter 4). The potential dependence of the measured current could be determined by recording CV curves (at a very slow scan rate) under chopped light illumination (see Chapter 4).

2.10.2. GALVANOSTATIC ANALYSIS

Galvanostatic experiments belong to the group of chronopotentiometric techniques. In a typical measurement a constant current is applied to the working electrode that causes oxidation/reduction of the observed material and results in a changed potential, which is monitored until a cut-off potential is reached. After a transition time τ the electrochemical insertion and extraction reactions can be inverted by applying the reverse current (Figure **2.13**). The capacity can be simply determined by normalizing the charge plotted on the x-axis to the time τ and the electrode mass. Depending on the amount of current applied compared to the active electrode mass, charging and discharging rates can be specified. The C-rate is often used to expressed the discharge/charge current normalize against the maximum capacity of a battery. It is therefore associated with the theoretical time (Δt) required for a full discharge/charge. Charging or discharging a battery in 1 hour to its full capacity is defined as 1 C. For a battery with a capacity of 1 Ah, this equals a discharge current of 1 A. A rate of 10C corresponds to a full charging or discharging of the battery within 6 minutes (1/10 hours) and therefore a discharging or charging current of 10 A. The cycling stability can be determined by repeated cycling experiments at different C-rates.[20,23]
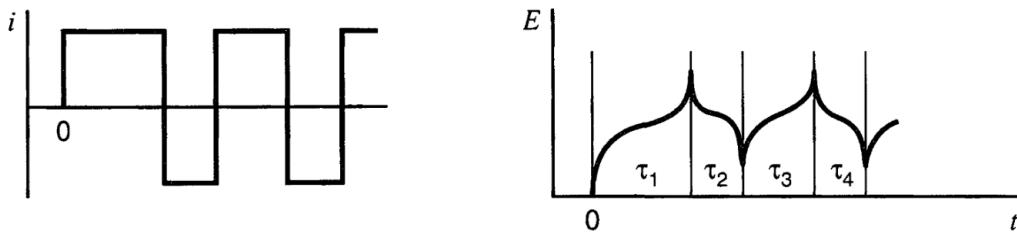
Figure 2.13   Applied current (left) and the resulting galvanostatic charge/discharge curve (right).[23]

Li-insertion experiments were carried out using an ECC-PAT-Core electrochemical test cell from EL-Cell GmbH, an AUTOLAB potentiostat/galvanostat PGSTAT302N with FRA32M module operating with a Nova 1.10.2 software. The set-up of the ECC-PAT-Core testing cell is schematically depicted in Figure 2.14.
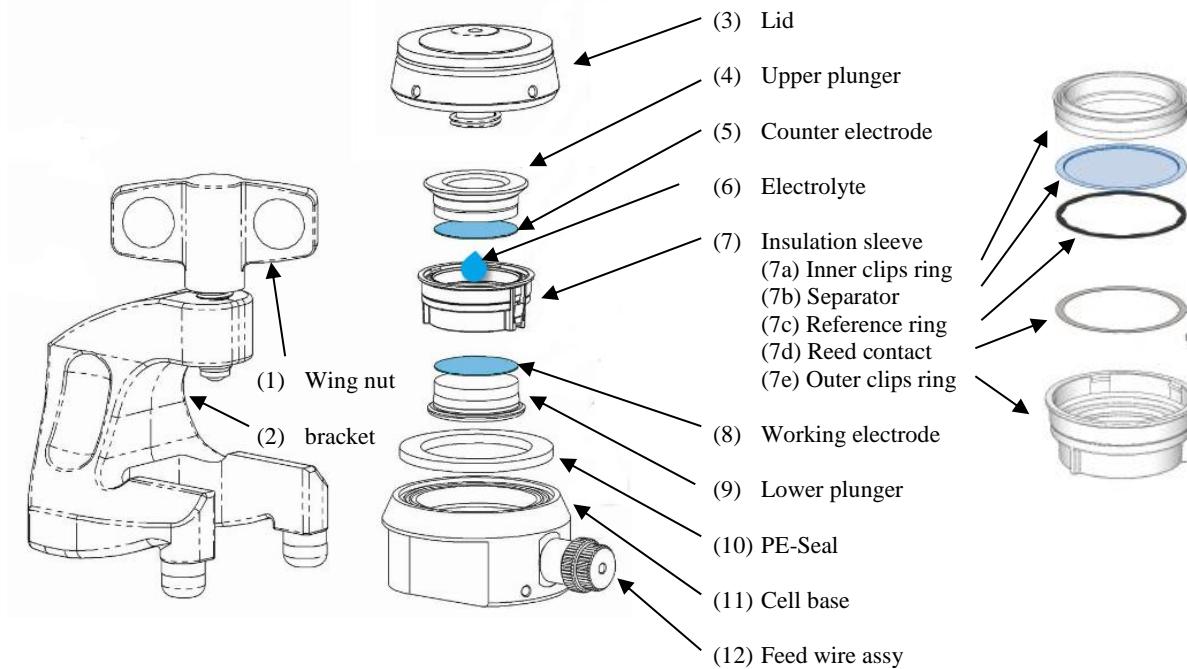
Figure 2.14 Scheme of an electrochemical testing cell and the insulation sleeve in particular.[28,29]

The main parts of the assembly are a copper foil coated with the nanocomposite material (8), a Li-counter electrode (5), a Li-reference ring (7c) and a separator (7b), which is slightly wetted with the battery electrolyte (6). The batteries were assembles starting from the working electrode. A copper foil pasted with the nanocomposite material is inserted to the insulation sleeve (7) with the active material facing towards the separator (7b), while the lower plunger (9) is placed upon the other side of the working electrode. The insulation sleeve (7) consists of a separator (7b), a Li-reference ring (7c) and a reed contact (7d), which are hold together by an outer (7e) and an inner clip ring (7a). The Li-counter electrode (5) was put on top of the separator, which was slightly wetted by the battery electrolyte. The assembly is closed with the upper plunger (4), and positioned in the cell base (11). For insulation a PE-seal is in between the lid (3) and the cell base (11). Finally the cell is pushed into the bracket (2) and hermetically sealed using a wing nut (1). The working electrode can be attached to the AUTOLAB setup *via* a socket in the cell base (11), the reference Li-ring (7c) through the feed wire assy (12) and the Li-counter electrode (5) along a socket in the lid (3).

2.11.REFERENCES

(1)   Cao, G.; Wang, Y. *Nanostructures & Nanomaterials: Synthesis, Properties, and Applications*; World Wcientific Publishing: London, 2011; Vol. 2.

(2)   Waseda, Y.; Matsubara, E.; Shinoda, K. *X-Ray Diffraction Crystallography - Introduction, Examples and Solved Problems*; Springer-Verlag Berlin Heidelberg, 2011.

(3)   Dinnebier, R. E.; Billinge, S. J. *Powder diffraction: theory and practice*; Royal society of chemistry, 2008.

(4)   Müller-Buschbaum, P. *Lect. Notes Phys.* **2009**, *776*, 61.

(5)   Peters, K.; Lokupitiya, H. N.; Sarauli, D.; Labs, M.; Pribil, M.; Rathouský, J.; Kuhn, A.; Leister, D.; Stefik, M.; Fattakhova-Rohlfing, D. *Adv. Funct. Mater.* **2016**, *26*, 6682.

(6)   Williams, D. B.; Carter, C. B. *Transmission Electron Microscopy: A Textbook for Materials Science*; Springer Science+Business Media, LLC, 2009.

(7)   http://www.ammrf.org.au/myscope/images/sem/volumes08.png (retrieved 17.11.2013).

(8)   Reimer, L. *Scanning Electron Microscopy - Physics of Image Formation and Microanalysis*; Springer Berlin Heidelberg, 1998.

(9)   Skoog, D. A.; Holler, F. J.; Crouch, S. R. *Principles of Instrumental Analysis*; Thomson, 2007.

(10)   Williams, D. B. C., C. B. *Transmission electron microscopy IV Spectrometry*; Plenum Press, 1996.

(11)   Williams, D. B. C., C. B. *Transmission electron microscopy III Spectrometry*; Plenum Press, 1996.

(12)   Qu, J.; Meyer, H. M. *X-Ray Photoelectron Spectroscopy (XPS)*; Springer US: Boston, MA, 2013.

(13)   https://fas.dsi.a-star.edu.sg/images/xps_10/Picture1.png (retrieved 17.11.2013).

(14)   Berne, B. J.; Pecora, R. *Dynamic Light Scattering: With Applications to Chemistry, Biology, and Physics*; Dover Publications, 2013.

(15)   Sing, K. S. W.; Everett, D. H.; Haul, R. A. W.; Moscou, L.; Pierotti, R. A.; Rouquerol, J.; Siemieniewska, T. *Pure Appl. Chem.,* **1985**, *57*, 603.

(16)   Coats, A. W.; Redfern, J. P. *Analyst* **1963**, *88*, 906.

(17)   Sahoo, U.; Seth, A. K.; Chawla, R. *Uv/ Visible Spectroscopy*; Lap Lambert Academic Publishing GmbH KG, 2012.

(18)   Clark, B. J.; Frost, T.; Russell, M. A. *UV Spectroscopy: Techniques, instrumentation and data handling*; Springer Netherlands, 1993.

(19)   Sule-Suso, J.; Forsyth, N. R.; Untereiner, V.; Sockalingum, G. D. *Trends Biotechnol.* **2014**, *32*, 254.

(20)   Atkins, P.; de Paula, J. *Physical Chemistry*; W. H. Freeman and Company: New York, 2006; Vol. 8. Edition.

(21)   http://www.google.de/url?sa=t&rct=j&q=&esrc=s&source=web&cd=11&ved=0CH0Q
FjAK&url=http%3A%2F%2Fwww.keithley.com%2Fdata%3Fasset%3D55773&ei=M
emIUqwQis7hBKbXgMgC&usg=AFQjCNEuUHjoay_hXm2nIFfOLfMBixMsOw
(retrieved 17.11.2013).

(22)   http://www2.warwick.ac.uk/fac/sci/physics/current/postgraduate/regs/mpags/ex5/t
echniques/electronic/hall-effect/ (retrieved 18.11.2013).

(23)   Bard, A. J.; Faulkner, L. R. *Electrochemical Methods: Fundamentals and
Applications*; Wiley, 2000.

(24)   McCrory, C. C.; Jung, S.; Peters, J. C.; Jaramillo, T. F. *J. Am. Chem. Soc.* **2013**, *135*,
16977.

(25)   Trasatti, S.; Petrii, O. A. *Pure Appl. Chem.* **1991**, *63*, 711.

(26)   Louie, M. W.; Bell, A. T. *J. Am. Chem. Soc.* **2013**, *135*, 12329.

(27)   Kissinger, P. T.; Heineman, W. R. *J. Chem. Educ.* **1983**, *60*, 702.

(28)   http://el-cell.com/wp-content/uploads/manuals/Manual_ECC-PAT-Core_Release_
2.0.pdf (retrieved 24.08.16).

(29)   http://el-cell.com/products/discover-the-pat-series (retrieved 24.08.16).

3. WATER-DISPERSIBLE SMALL MONODISPERSE ELECTRICALLY CONDUCTING ANTIMONY DOPED TIN OXIDE NANOPARTICLES

This chapter is based on the following publication:

Kristina Peters, Patrick Zeller, Goran Stefanic, Volodymyr Skoromets, Hynek Němec, Petr Kužel, Dina Fattakhova-Rohlfing
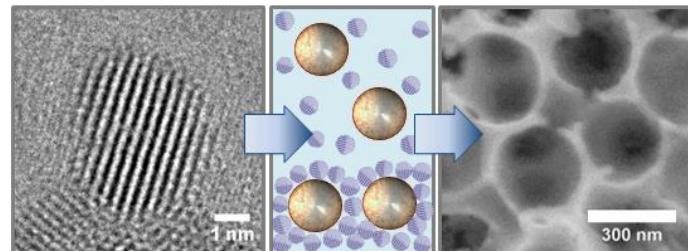
We describe fabrication of crystalline electrically conducting antimony-doped tin oxide (ATO) nanoparticles highly dispersible in polar solvents such as water and ethanol without any stabilizing agents. Non-agglomerated monodisperse ATO nanoparticles with different doping levels are obtained by a facile solvothermal reaction in *tert*-butanol, leading to the formation of monodisperse nanocrystals with a size of about 3 nm directly after synthesis. Electrical conductivity of ATO nanoparticles strongly increases due to the substitutional doping with antimony, reaching 6.8×10^{-2} S cm^{-1} for the as synthesized nanoparticles prepared with $3 - 5$ mol% Sb. This increase stems from transition from hopping in the undoped samples to band-like conduction in the doped samples as revealed by terahertz (THz) spectroscopy measurements describing transport on nanometer distances. The *dc* conductivity of the doped nanoparticles increases by about three orders of magnitude up to 62 S cm^{-1} after annealing in air at 500 °C. The electrical conductivity, crystallinity, small size and high dispersibility in polar solvents make the obtained ATO nanoparticles promising building blocks for the direct assembly of more complex conducting architectures using polymer

templates that could be damaged in organic solvents. We illustrate the benefits of the water-dispersible ATO nanoparticles by their assembly to periodic macroporous electrodes using poly(methyl methacrylate) (PMMA) beads as the porosity templates. Aqueous dispersion of ATO nanoparticles can be directly combined with PMMA beads that are easily removed by calcination, enabling a facile deposition of 3D-macroporous ATO electrodes featuring optical transparency and a large periodically ordered conducting interface.

3.1. INTRODUCTION

Transparent conducting oxides (TCOs) combine transparency in the visible range with high electrical conductivity, which makes them important materials for numerous optoelectronic and optoelectrochemical applications. TCOs are predominantly produced as thin dense layers, but the recent years are marked by a fast-growing interest in other types of TCO architectures motivated by the development of novel applications. Particularly, nanoparticles are one of intensively studied TCO morphologies. The colloidal dispersions of TCO nanoparticles are of significant interest for wet chemical deposition and printing of conducting crystalline coatings,[1-4] with expected benefits of decreased processing costs, the possibility of coating temperature-sensitive substrates or surface patterning. Furthermore, the TCO nanoparticles gain importance as building blocks for the assembly of porous electrode architectures.[5-10] Due to their practical relevance, nanoparticles of different TCO materials such as indium tin oxide (ITO), antimony doped tin oxide (ATO) and aluminium doped zinc oxide (AZO) are already available commercially.[11] Furthermore, TCO nanoparticles have been synthesized by various methods such as co-precipitation,[12-17] hydrothermal,[18-22] solvothermal,[17,23-31] sol-gel[32,33] and microwave assisted synthesis,[34,35] thermal decomposition,[36,37] hot injection,[38] combustion[39,40] and DC arc plasma jet synthesis.[41] Still, in spite of the numerous efforts, it is synthetically challenging to obtain TCO nanoparticles combining all the required properties such as sufficiently high electrical conductivity, crystallinity, desirable particle size, narrow particle size distribution and good dispersibility in suitable solvents. Particularly, it is the combination of the narrow particle size distribution with the high dispersibility which is difficult to address. Commercially available dispersions of the TCO nanoparticles feature agglomerated particles with a broad particle size distribution,[11] while the majority of the reported strategies to obtain dispersible TCO nanoparticles rely on their steric stabilization with bulky ligands or surfactants,[1,15,21,24,27,36,37,42-46] which is however often detrimental for the conductivity of the nanoparticle assemblies. So far, only a few types of electrically conducting monodisperse

TCO nanoparticles dispersible without any stabilizing agents have been obtained, practically all of them are formed in solution and are presumably stabilized by small solvent molecules or their reaction products adsorbed on the particle surface. The reported systems include ITO nanoparticles obtained in a polyol process, which are dispersible in ethylene glycol and alcohols without additional stabilization[27,28,35] and AZO nanoparticles prepared in a microwave-assisted synthesis route in benzyl alcohol.[3]

The only example of small dispersible antimony doped tin oxide (ATO) nanoparticles was reported by some of the authors using a solvothermal reaction in benzyl alcohol.[2,17] ATO is a chemically robust alternative to the ITO and AZO with a high corrosion stability both in strongly alkaline and strongly acidic solutions. The nanoparticles obtained by this route are about 3–4 nm in size and are perfectly dispersible in tetrahydrofuran (THF), however their dispersibility in polar solvents and especially in water is substantially worse. The high dispersibility in water and ethanol is however desirable for many applications, especially those involving polymer materials that can be damaged in the organic solvents.

Aiming at the fabrication of conducting ATO nanoparticles exhibiting high dispersibility in polar solvents such as water and ethanol we have explored *tert*-butanol as a novel nonaromatic reaction medium. In this publication we demonstrate that this approach leads to small monodisperse electrically conducting ATO nanoparticles dispersible in high concentrations in water, ethanol, isopropanol and acetone without any stabilizing agents.

We illustrate the benefits of the water-dispersible ATO nanoparticles by their assembly to periodic macroporous electrodes using poly(methyl methacrylate) (PMMA) beads as the porosity templates. Due to a very high surface area enabling incorporation of large amount of active materials, porous TCO scaffolds attract growing attention as advanced current collectors for bioelectrochemical, photoelectrochemical and optoelectronic devices.[5,6,8,9] Among available porous morphologies, TCO electrodes with an organized macroporous structure[5,47-49] offer ultimate benefits of uniformly large pores whose size and shape can be easily adjusted by the choice of porosity template, thus enabling engineering of materials with a custom designed porous structure optimized for the desired applications. Further advantages of macroporous TCO electrodes are open porosity enabling efficient mass transfer, and a periodic pore arrangement resulting in photonic crystal effects.[5] The use of crystalline nanoparticles often simplifies the nanostructure assembly procedure and brings additional advantages of a better control over the conductivity and crystallinity of the formed porous

scaffolds,[5] but the general applicability of this approach is restricted by the availability of suitable TCO nanoparticles.

In this work we demonstrate that the water-dispersible ATO nanoparticles are perfectly suitable for the facile fabrication of periodically nanostructured ATO electrodes using different approaches. Aqueous dispersion of ATO nanoparticles can be directly combined with poly(methyl methacrylate) (PMMA) beads that are easily removed by calcination, enabling a facile large-scale deposition of 3D-macroporous ATO electrodes featuring optical transparency and a periodically ordered conducting interface.

3.2. RESULTS AND DISCUSSION

3.2.1. SYNTHESIS OF ANTIMONY DOPED TIN OXIDE NANOPARTICLES

For the nanoparticle synthesis, tin(IV) and antimony(V) or antimony(III) compounds taken in different molar ratios were dissolved in a water-free *tert*-butanol and heated in hermetically sealed autoclaves at different temperatures. This reaction leads to formation of nanocrystalline particles as detected from the XRD patterns (Figure 3.1). The formation of crystalline phase requires a reaction temperature of at least 90 °C; no product formation was observed at lower temperatures. The particles size strongly depends on the synthesis temperature and the doping concentration. The increase in the reaction temperature leads to a practically linear increase in the crystallite size. For example particles prepared with 5% Sb at 100 °C have a very small size of around 2.8 nm as calculated from the line broadening of the 110 reflection in the XRD patterns, which increases to around 3.5 nm to reach ca. 4.3 nm for the particles synthesized at 125 °C and 150 °C, respectively. Besides the synthesis temperature, doping concentration has an influence on the crystallite size which is accompanied with the change in size anisotropy as will be discussed later. The particles with different Sb content are assigned further as ATO-X%, where X refers to the stoichiometric molar amount of Sb in the precursor solution. As we will show later, the real Sb content in the resulting nanoparticles is up to 60% higher than in the precursor solutions, so that the particles assigned as ATO-30% contain 50 mol% Sb.

XRD patterns of the particles synthesized at 100 °C from the reaction mixtures containing molar ratios of Sb and Sn from 0 mol% to 30 mol% agree with the reflections of pure SnO_2 (cassiterite structure, space group $P4_2/mnm$, JCPDS File Card No. 41-1445) without any

indication of a second phase like Sb_2O_3 or metallic tin (Figure 3.1a and Figure S3.1 in the Supplementary information). The increase in Sb content causes a small decrease of lattice parameters a and c of cassiterite lattice by up to 1% and 0.7%, respectively (Figure 3.1b and Table S3.1 in the Supplementary information), as well as a continuous decrease in unit cell volume (2.6%) after incorporation of up to 50 mol% of Sb (Figure S3.2 and Table S3.1 in the Supplementary information).
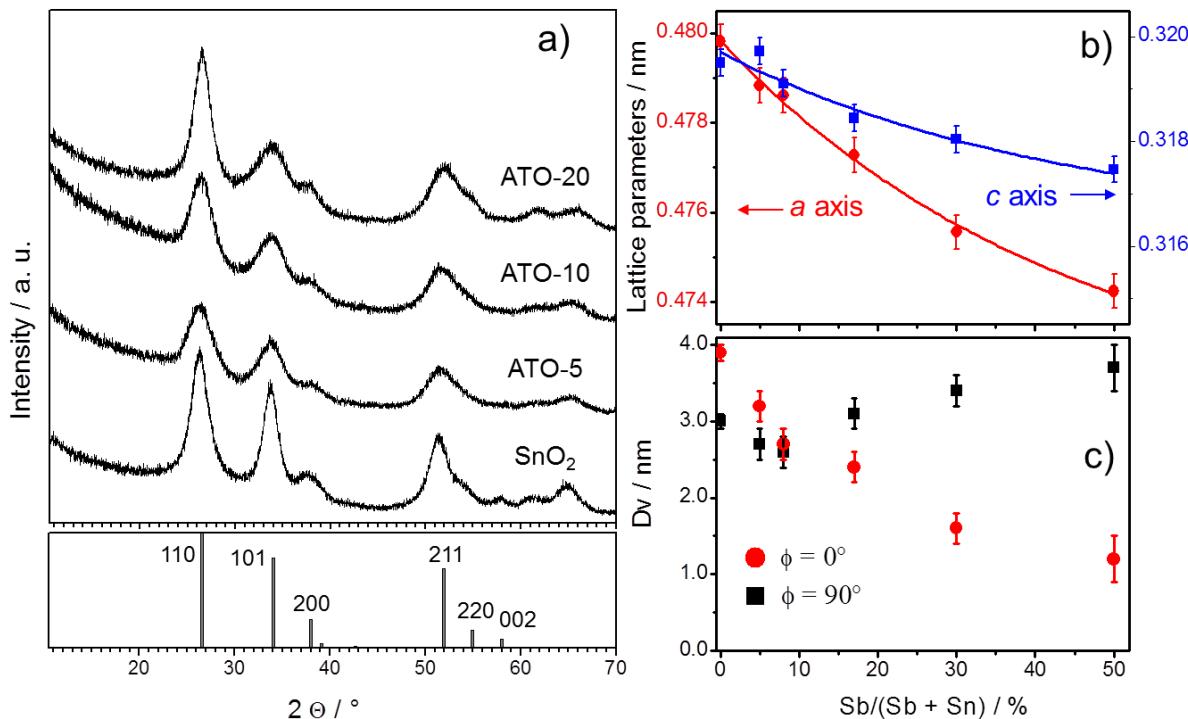
Figure 3.1 (a) XRD patterns of as-prepared ATO nanoparticles with varying antimony content. The particle assignment corresponds to the antimony content in the precursor solution. The bars in the bottom panel mark the position and the intensity of the diffraction lines of SnO_2 cassiterite (space group $P4_2/mnm$, JCPDS File Card No. 41-1445). Change of the (b) lattice parameters a (red) and c (blue) and (c) the volume-averaged domain size (D_V) in the directions parallel and perpendicular to the 001 axis of cassiterite-type lattice for the ATO nanoparticles containing different amounts of Sb, which is taken as the real Sb content determined from the XPS and ICP-OES measurements (average value).

In addition to the observed change in lattice parameters, change of the volume-averaged domain size D_V obtained by Le Bail refinement (Figure 3.1c and Table S3.2 in the Supplementary information) and the volume-averaged domain size (D_{hkl}) obtained by analysis of the broadening of individual lines using Scherrer equation (Figure S3.3 and Table S3.3 in the Supplementary information) point to the presence of size anisotropy for particles synthesized with different amounts of Sb. The direction of size anisotropy changes in dependence of the amount of incorporated antimony ions. Undoped SnO_2 particles are slightly

elongated in the direction of c axis. Incorporation of up to 8% Sb leads to a decrease of crystallite size for all directions. The particles containing 8% Sb are nearly spherical, as also confirmed by transmission electron microscopy (TEM) analysis (see below). Further increase in the Sb content results in a decrease of crystallite size in the c direction, but an increase of crystallite size in the perpendicular direction (a and b) (Figure 3.1c, Figure S3.3 and Table **S3.2** and Table S3.3 in the Supplementary information). The ATO nanoparticles prepared in *tert*-butanol demonstrate an unusually high uptake of Sb without any phase separation; the disappearance of the cassiterite type phase with formation of the metastable antimony(III) oxide type phase is observed first for the samples prepared with 40% of Sb in solution that contain more than 50 mol% Sb in the crystalline lattice according to the inductively coupled plasma optical emission spectrometry (ICP-OES) data (Figure S3.4 in the Supplementary information).

It is interesting to note that the change in the lattice parameters and size anisotropy for nanoparticles synthesized in *tert*-butanol are different to those observed by us for similar particles synthesized in benzyl alcohol.[17] For the latter, the lattice parameters change only in the b direction with an increasing antimony content, while the values of a and c remain unchanged. Another significant difference in the properties of ATO nanoparticles obtained via different solvothermal routes is their dispersibility. In contrast to ATO particles prepared in benzyl alcohol that are dispersible in sufficient concentrations only in tetrahydrofuran (THF),[20] the dried particles synthesized in *tert*-butanol are easily dispersible in high concentrations in polar solvents like ethanol and water. For the particles synthesized in the same conditions, the dispersibility is greatly influenced by the doping concentration. Undoped nanoparticles form aggregates with a hydrodynamic radius of ca. 16 nm in polar solvents like ethanol (Figure 3.2) after the addition of a few drops of concentrated hydrochloric acid. The introduction of up to 8% antimony into cassiterite structure significantly improves the dispersibility of the nanoparticles. The highest dispersibility is observed for the ATO-5% nanoparticles, which are perfectly dispersible in ethanol up to 30 wt% and isopropanol (30 wt%) without any peptizing agents (Figure 3.2) exhibiting a hydrodynamic radius of 4.6 nm. The obtained clear colloidal dispersions remain stable over several months. The dispersibility of the particles decreases rapidly with the increasing antimony content, so that stable colloidal dispersions can only be obtained by adding small amounts of hydrochloric acid (see Experimental part for the further details). The nanoparticles prepared with up to 5% Sb are dispersible in water (up to 10 wt%) but also in less polar solvents like acetone (15 wt%) (Figure 3.2).
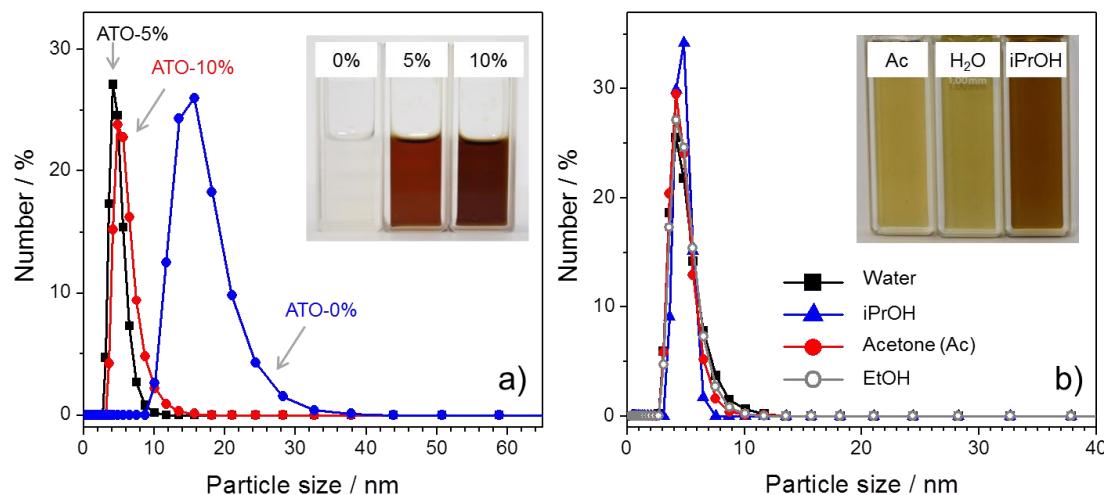
Figure 3.2 Dynamic light scattering (DLS) measurements of (a) colloidal dispersions of SnO_2, ATO-5% and ATO-10% nanoparticles in EtOH. The inset shows the corresponding images of colloidal dispersions with a nanoparticle concentration of 20 wt%; and (b) colloidal dispersions of ATO-5% nanoparticles in isopropanol, water, ethanol and acetone. The inset shows the images of the colloidal dispersions with a nanoparticle concentration of 15 wt% in acetone, 10 wt% in water and 30 wt% in isopropanol.

TEM images of ATO-5% (Figure 3.3) nanoparticles show non-agglomerated, well defined crystals with a narrow size distribution, whereas the undoped SnO_2 nanoparticles (Figure S3.5 in the Supplementary information) are slightly aggregated, in a good agreement with DLS measurements. The presence of well-developed lattice fringes reveals the crystalline structure of the particles, which is also confirmed by Fourier transformation of the HRTEM images of single nanoparticles. The lattice fringe distances (Figure 3.3b-d), the Fourier transformations of the HRTEM image (Figure 3.3e-g) and the selected area electron diffraction (SAED) pattern of the nanoparticles (Figure 3.3h) are in good agreement with the tetragonal cassiterite structure of ATO-5% deduced from the XRD patterns. The particles prepared with 5% Sb exhibit nearly spherical and uniform particle morphology with an average crystallite size of 3.10 nm±0.5 nm (calculated over 110 particles), which agrees well with the crystallite size obtained from the XRD data (2.8 nm). Notably, each single particle consists of only one crystalline domain without any internal grain boundaries, which clearly shows the single crystalline nature of each particle.
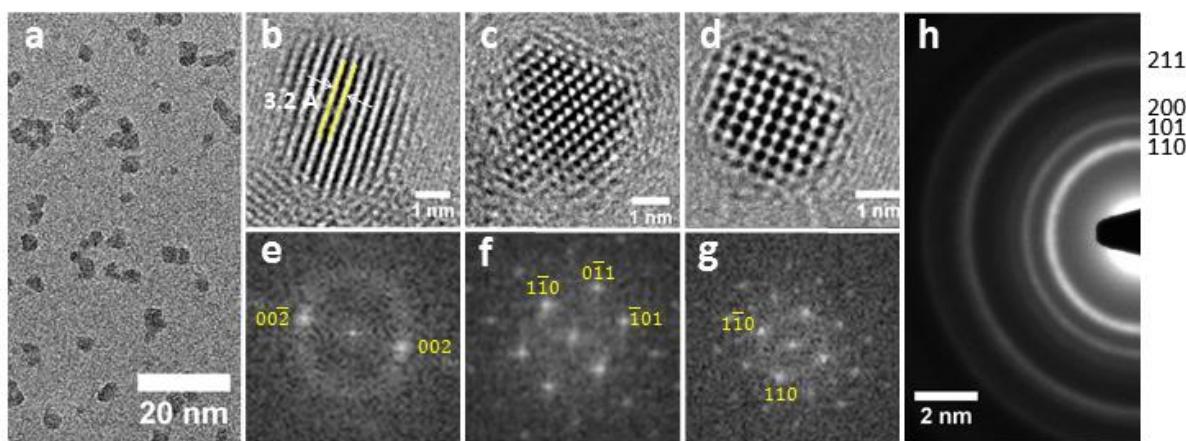
Figure 3.3 TEM images of ATO-5% nanoparticles: (a) overview of the nanoparticles dispersed on a TEM grid; (b)-(d) HRTEM images of single tetragonal nanoparticles aligned on [111] (c) and [001] (d) zone axis, (e)-(g) Fourier transformation of the HRTEM image of the corresponding ATO-5% nanoparticles pictured above; (h) SAED pattern of the nanoparticles. The corresponding d-values are 3.33 (110), 2.62 (101), 2.31 (200), 1.75 Å (211).

The Sb content in the obtained nanoparticles was analyzed by the ICP-OES and the X-ray photoelectron spectroscopy (XPS) methods. Surprisingly, the Sb content in the resulting nanoparticles was found to be up to 60% higher than that in the initial precursor mixture taken for the reaction (Table 3.1). The results of the ICP-OES measurements that provide an average Sb content in the whole sample, and the XPS measurements that deliver information only about the near-surface regions, are practically the same, excluding the formation of core-shell particles. Furthermore, the TEM images do not show any surface enrichment, second phase formation or any change in the crystalline structure on the particle surface. The results of several techniques point that the Sb is homogeneously distributed throughout the particles and that the Sb:Sn stoichiometry in the particles is different from that in the reacting solutions. A plausible explanation for the higher uptake of Sb is a kinetic control of the particle formation and growth, probably due the faster reaction rate of Sb compounds with *tert*-BuOH compared to the $SnCl_4$.
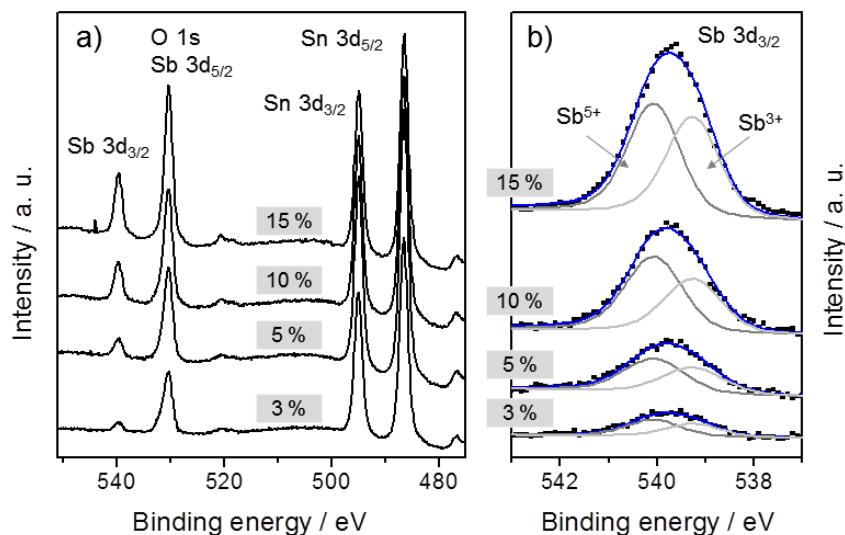
Figure 3.4   X-ray photoelectron spectra (XPS) of the as synthesized ATO nanoparticles prepared with different Sb content (indicated in labels next to the corresponding curves): (a) an overview and (b) the Sb $3d_{3/2}$ peak. The solid black squares in (b) correspond to the experimental spectra, the solid blue lines indicate the results of peak fits for Sb^{5+} (540.0 eV, dark gray line) and Sb^{3+} (539.2 eV, light gray line).

Table 3.1   Sb content in ATO nanoparticles determined using ICP-OES or XPS and the composition of the two valence states in Sb.

Sb content in the precursor solution [mol%]	Sb content in ATO nanoparticles [mol%]		Molar fractions of Sb^{3+} and Sb^{5+} atoms [mol%]	
	XPS	ICP-OES	Sb^{5+}	Sb^{3+}
3	5.1	5.5	55.6	44.4
5	7.7	8.7	56.4	43.6
10	16.2	19	58.2	41.8
15	24.3	26.4	52.7	47.3
20		30		
30		50.5		

Electrical conductivity of the ATO nanoparticles is generally influenced by the antimony content and its valence state in the tin oxide lattice. Antimony can be incorporated in two oxidation states, Sb^{5+} and Sb^{3+}. If both oxidation states coexist, compensating effects are observed, so that the conductivity is given by the Sb^{5+}/Sb^{3+} ratio.[50] For the nanoparticles with different Sb content, the Sb^{5+}/Sb^{3+} ratio was found to be practically the same for different doping concentrations according to the XPS measurements. It is different from the results obtained by other groups who often report the variation in the Sb^{5+}/Sb^{3+} ratio with the doping

concentration.[14,51] Independent of the doping concentration the Sb^{5+} species slightly dominate over the Sb^{3+} species, resulting in the preferential n-doping. Furthermore, the Sb^{5+}/Sb^{3+} ratio in the obtained nanoparticles does not depend on the oxidation state of the Sb compound in the initial reaction mixture, and is the same for the Sb(III) and the Sb(V) compounds.

Conductivity measurements were performed on pelletized ATO nanoparticles (Figure 3.5 and Table S3.4 in the Supplementary information). A conductivity of 2.8×10^{-3} S/cm was measured already for the undoped as prepared SnO_2 nanoparticles. This relatively high conductivity can be indicative for a high bulk defect concentration in the particles synthesized in *tert*-butanol due to formation of oxygen vacancies and tin interstitials. The introduction of up to 8% antimony in the cassiterite lattice leads to more than 20-fold increase in the conductivity, reaching 6.8×10^{-2} S/cm for the ATO-5% particles. The further increase in the Sb content leads to a slight decrease in the electrical conductivity. The observed effect can be attributed to experimentally determined lattice disorder resulting in a deteriorated charge carrier mobility.

The conductivity of 6.8×10^{-2} S/cm obtained for the particles synthesized in *tert*-butanol is the highest ever reported conductivity for non-annealed ATO nanoparticles of a few nm in size, which makes them very suitable for low temperature applications. To compare, Nütz *et. al.*[20] reported conductivities of around 1×10^{-6} S/cm for slightly larger ATO nanoparticles (4-9 nm) obtained by a hydrothermal reaction, while we have obtained conductivities of up to 1×10^{-4} S/cm for the ATO nanoparticles synthesized in benzyl alcohol.[17] The 680 times higher conductivity of the nanocrystals prepared in *tert*-butanol compared to those prepared in benzyl alcohol could be due to a better electrical contact between the nanoparticles in terms of a ligand-free surface. *Tert*-butanol residues can be removed under much milder conditions due to its lower boiling point (83 °C) compared to benzyl alcohol (205 °C).

Terahertz (THz) spectroscopy enables a non-contact probing of the local conductivity on the nanometer range. For this reason, it is a powerful technique for disentangling limitations of conductivity due to intrinsic properties of individual nanoparticles, and due to the connectivity and morphology of the nanoparticles within the pellets. The pellets made of as prepared undoped nanoparticles exhibit THz conductivity of about 0.7 S/cm (Table S3.4 in the Supplementary information). The significant (orders of magnitude) difference from the *dc* conductivity and limited dispersion in the THz spectral range indicate that hopping is the dominant charge transport mechanism; the *dc* conductivity is then limited by the longest hopping times in the system.

The doping with antimony leads to lower THz conductivity of the order of 0.1 S/cm for the as prepared ATO nanoparticles. However, it is important that the mechanism of conductivity changes from the hopping to band-like transport, which is the prerequisite for achieving efficient long-range transport, or equivalently, high *dc* conductivity. This is evidenced by the fact that the real part of THz conductivities increases significantly with frequency, which is a signature of band-like transport of charges (partially) confined in the nanoparticles.[52]

As expected, the conductivity of the nanoparticles strongly improves after annealing. The *dc* conductivity of the doped nanoparticles increases by about three orders of magnitude up to 62 S/cm after annealing in air at 500 °C. The maximum of conductivity for the calcined nanoparticles is observed for the particles containing 5 mol% Sb, which is slightly different from the as prepared nanoparticles where the particles containing 7 mol% Sb show the highest conductivity values (Figure 3.5 and Table S3.4 in the Supplementary information).

Surprisingly, both *dc* and THz conductivities of the undoped nanoparticles decrease after the calcination in air. Taken that a high defect concentration in the as prepared undoped SnO_2 is responsible for its hopping conductivity, it is reasonable to suggest that the healing of the defects upon calcination decreases the conductivity of the nanoparticles.
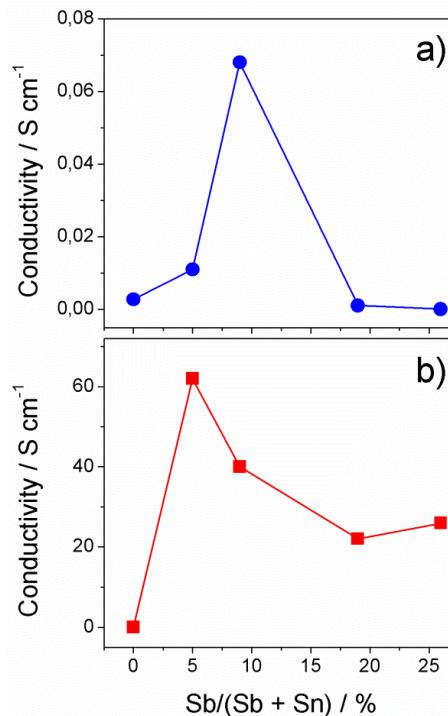
Figure 3.5   Conductivity of pellets pressed from ATO nanoparticles containing different Sb concentration: as prepared (a) and after calcination in air at 500 °C (b). The Sb level is taken as the real content determined by ICP-OES measurements.

3.2.2.   MACROPOROUS ELECTRODES ASSEMBLED FROM ATO NANOPARTICLES

Excellent dispersibility of ATO nanoparticles in water, ethanol and isopropanol makes them compatible with polymer materials that can be damaged in the organic solvents. This is especially beneficial for the assembly of complex electrically conducting scaffolds using polymer molds or polymer templates.

We demonstrate the suitability of ATO nanoparticle as building blocks for the assembly of complex morphologies by fabricating periodic macroporous electrodes. The macroporous electrodes are conventionally prepared via templated approaches using colloidal silica or polymer particles (latex beads) due to their ability to self-organize into periodic structures acting as templates for porosity.[5,47-49,53] Typical protocols involve either infiltration or coating of the pre-formed bead arrays with different TCO precursors (a two-step infiltration method), or a direct co-assembly of the TCO precursors and the latex beads (a one-step co-deposition method). Although various macroporous TCO electrodes have been already reported, there are still some issues to be addressed. The major problems are either an insufficient conductivity of the obtained scaffolds (as in case of sol-gel techniques[5]), or the elaborate fabrication procedure (as in case of atomic layer deposition, ALD[47,48,49]). Several groups, including some of the authors, have developed an alternative strategy to fabricate nanostructured TCO electrodes by using pre-formed crystalline nanoparticles for the nanostructure assembly.[5-10] The advantages offered by this route are the high electrical conductivity of the TCO scaffolds in combination with the facile fabrication procedure. The general applicability of this approach is however restricted by the availability of dispersible TCO nanoparticles and the compatibility of the particle dispersions with that of the template material. Because the conventional polymer beads such as PMMA or polystyrene are soluble in organic solvents typically used for the particle dispersions, the majority of the reported protocols is based on the chemically robust silica beads that are however difficult to remove. In this work we demonstrate that the water-dispersible ATO nanoparticles can be directly combined with the PMMA beads using different approaches, enabling a facile fabrication of macroporous conducting ATO electrodes.

For the fabrication of macroporous ATO layers via co-assembly procedure, a mixture of aqueous dispersions of PMMA beads and ATO nanoparticles was dip coated on various

substrates (Figure 3.6a) (see Experimental part for further details). An addition of hydroxypropyl cellulose (HPC) as a thickener helps to increase the thickness of the obtained layers and to obtain homogeneous coatings with good optical quality and a high mechanical stability. The thickness of the coatings can be changed from 0.7 μm to 2.5 μm by varying the viscosity of the coating solutions and the dip coating rate.

Beside the direct co-assembly of PMMA beads and ATO nanoparticles, the macroporous ATO layers can also be obtained by a liquid infiltration of inverse opals (Figure 3.6d). In the first step, the opal PMMA template is deposited by dip coating of colloidal PMMA dispersions on the glass or ITO substrates. The PMMA opal layers are infiltrated by dip coating of the films in 3 wt% aqueous dispersion of ATO nanoparticles in the second step. The very small particle size of as prepared ATO particles (2.8 nm) is beneficial for its infiltration into the voids of the inverse opal structure.
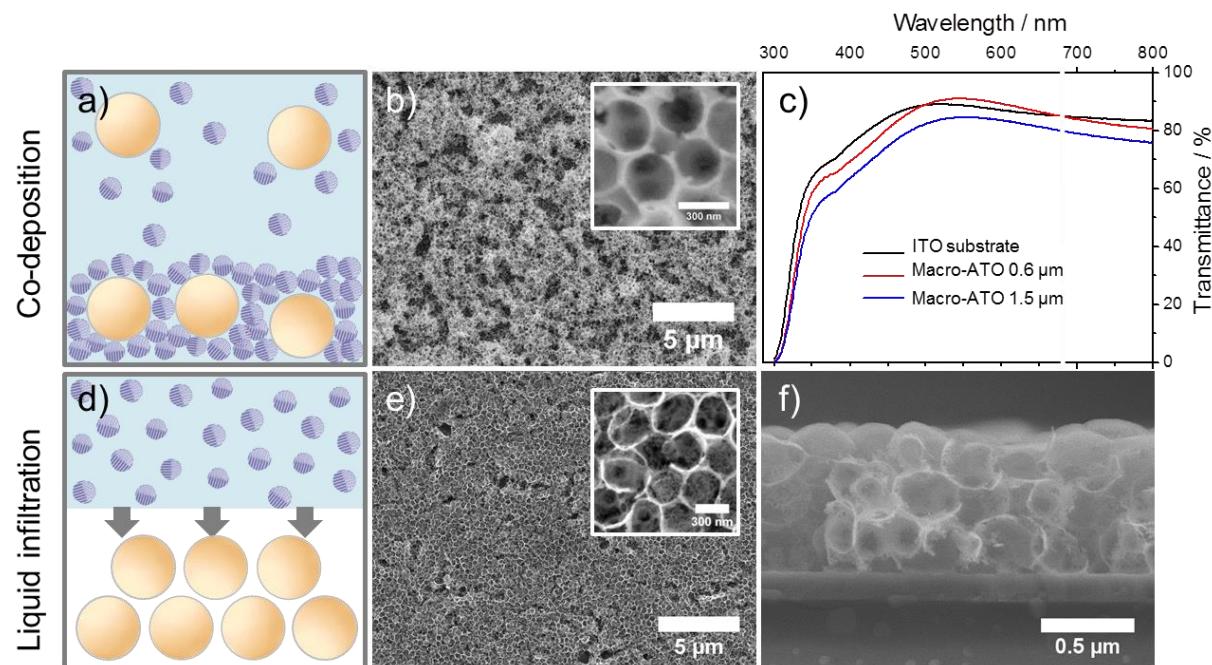
Figure 3.6 Scheme of the fabrication of macroporous ATO electrodes via co-deposition of ATO nanoparticles and PMMA beads (a) and liquid infiltration of inverse PMMA opals by ATO nanoparticles (d); top-view SEM images of films prepared by co-deposition (b) and liquid infiltration (e); (f) cross section SEM images of (e); (c) UV-vis transmittance of the planar ITO substrate: non-coated (black line) and coated with the macroporous ATO film with the thickness of 0.6 μm (red line) and 1.5 μm (blue line).

The layers prepared by both methods were annealed in air at 500 °C to remove the polymer template and to sinter the particles. Electron microscopy (SEM) images of the resulting macroporous films demonstrate that the films prepared by both deposition techniques provide homogeneous and crack-free coatings with a uniform macroporous structure (Figure 3.6). The

films are mechanically stable and have a good adhesion to the substrate. The films templated with 370 nm PMMA beads feature regular ellipsoidal pores with the size of ca. 300 nm x 200 nm after calcination at 500 °C due to the pore shrinkage caused by the particle sintering. The films obtained by liquid infiltration of inverse opals exhibit a higher degree of pore ordering and a more homogeneous and smooth surface compared to films obtained by the co-deposition of ATO nanoparticles and PMMA beads. The latter method however may be preferential for a facile large-scale fabrication of homogeneous and crack-free coatings due to its simplicity and shorter fabrication times. Figure 3.6c shows the optical transmission of the macroporous ATO films deposited on a commercial flat ITO coated glass substrate. The films of 600 nm and 1.5 μm have practically the same transmittance over 80% in the visible range as the parent ITO substrate.

3.3. CONCLUSIONS

Solvothermal reaction in *tert*-butanol enables a facile fabrication of small monocrystalline electrically conducting ATO nanoparticles of 3.1 nm±0.5 nm in size. The ATO nanoparticles resulting from this reaction feature a very high uptake of Sb into SnO_2 cassiterite lattice (more than 50 mol%) without any indication of phase separation or surface enrichment. This unusually high solubility limit can originate from the kinetic control of the ATO phase formation in a solvothermal process, as well as the effect of the nanoscale where the metastable and defect phases often show higher stability than in the bulk phase.

In spite of being just a few nanometers in size, the as prepared non-calcined ATO nanoparticles feature a reasonably high electrical conductivity of 6.8×10^{-2} S cm^{-1}, which is the highest ever reported value for the small ATO nanoparticles. THz measurements describing transport properties in the nanometer range reveal conductivities of up to 0.18 S cm^{-1} for the non-calcined ATO samples and, strikingly, prove a changed mechanism of conductivity inside the nanoparticles from a hopping mechanism in undoped SnO_2 to a band-like transport of charges in the doped ATO particles. The conductivity of the particles synthesized in *tert*-butanol is 680 times higher than that of comparably small particles synthesized in benzyl alcohol. The reason for the higher conductivity can be an improved contact resistance of the particles obtained in *tert*-butanol, as it can be much easier removed from the particle surface compared to benzyl alcohol. The higher conductivity can however also result from the higher defect concentration of the crystalline phases formed in the *tert*-BuOH synthesis, as could be suggested for the undoped SnO_2 nanoparticles.

An important feature of the ATO nanoparticles synthesized in *tert*-butanol is a good dispersibility without agglomeration in polar solvents such as water and ethanol without any stabilizing agents. We illustrate the benefits of the water-dispersible ATO nanoparticles by their assembly to periodic macroporous electrodes using PMMA beads as the porosity templates. Aqueous dispersion of ATO nanoparticles can be directly combined with PMMA beads that are easily removed by calcination, enabling a facile large-scale deposition of 3D-macroporous ATO electrodes featuring optical transparency and a large periodically organized interface. Besides the example shown above, the combination of electrical conductivity, crystallinity, small size and high dispersibility in polar solvents make the obtained ATO nanoparticles attractive material also for other types of applications. We envision the use of the water-dispersible ATO nanoparticles for coating of plastic substrates for flexible electronics, as a conductive additive for various composites, or for fabrication of more complex core-shell type heterojunction materials in solution.

3.4. EXPERIMENTAL SECTION

Materials. Antimony(V) chloride solution (1.0 M in methylene chloride), antimony(III) chloride, tin(IV) chloride solution (1.0 M in methylene chloride), *tert*-Butanol (99%) and hydroxypropyl cellulose (HPC) ($\geq$ 95%) were purchased from Sigma-Aldrich and used as received.

Synthesis. The antimony doped tin oxide (ATO) nanoparticles with different Sb contents were prepared by a solvothermal synthesis in *tert*-butanol, which served both as an oxide source and as a solvent. The particles with different Sb content are designated as ATO-X%, where X is the Sb/(Sb+Sn) molar ratio in percent. The choice of the tin and antimony sources is not decisive for the formation of crystalline nanoparticles. Any combination of the Sn and Sb compounds tested in this reaction, namely tin(IV) acetate, tin(IV) chloride, tin(IV) chloride pentahydrate, antimony(III) acetate and antimony(III) chloride leads to the formation of crystalline nanoparticles. In a typical synthesis procedure, an antimony source, usually antimony(V) chloride (1M $SbCl_5$ in CH_2Cl_2) or antimony(III) chloride, and tin (IV) chloride (1M $SnCl_4$ in CH_2Cl_2) were dissolved in *tert*-butanol and transferred into a Teflon- or glass-lined autoclave. The total molar amount of tin and antimony was kept constant equaling 4.78 mmol in a total volume of 14 ml of *tert*-butanol/dichloromethane (0.34 mol/L). For example, for the fabrication of particles designated as ATO-5%, 4.54 ml (4.54 mmol) $SnCl_4$ (1M in CH_2Cl_2) and 0.24 ml (0.24 mmol) $SbCl_5$ (1M in CH_2Cl_2) were dissolved in 9.22 ml of

tert-butanol and heated in hermetically sealed Teflon- or glass-lined autoclave at 100 °C for 20 hours. Light yellow to brownish suspensions were obtained after the solvothermal treatment. The ATO nanoparticles were flocculated by an addition of 14 mL dichloromethane, separated by centrifugation (47800 rcf for 15 min), washed twice in 14 mL acetone and centrifuged again at 47800 rcf for 15 min.

Macroporous ATO layers

Macroporous ATO were fabricated from the ATO nanoparticles (ATO-5%) and poly(methyl methacrylate) beads (PMMA) via a direct co-assembly as well as by the liquid infiltration of the colloidal crystal templates with nanoparticles. The PMMA beads with a diameter of 370 nm were synthesized according to the emulsion polymerization route described elsewhere.[54,55] In a typical procedure, bidistilled water (98.0 mL, Millipore Q grade) was degassed with nitrogen in a three-necked flask for 1 h, before sodium dodecylsulfate (5.6 mg) and methylmethacrylate (35.5 g) were added. The monomer mixture was stirred for 1 h at 90◦C in nitrogen atmosphere to obtain a homogenous emulsion. A solution of potassium peroxodisulfate (56 mg) in water (2 mL) was injected to initiate the polymerization. The solution turned white within 5 minutes, indicating the formation of polymer particles. The reaction was continued for2 h at 90 °C, before the flask was exposed to air and cooled with an ice bath. The colloidal solution was stirred overnight, filtered through glass wool and washed three times by centrifugation (50000 rcf; 30 minutes) and redispersion in water.

For the fabrication of macroporous films using the direct co-assembly, dry nanoparticles (ATO-5%) (60 mg) were dispersed in 375 ml ethanol containing small amounts of concentrated hydrochloric acid (2 drops). Separately, an aqueous colloidal PMMA suspension (15 wt%) was stirred for several hours and ultrasonicated for 30 min. The two dispersions were combined keeping an ATO/PMMA ratio of 1:5, which corresponds to 2 ml of 15 wt% PMMA beads to 375 ml of 16 wt% ATO-5% dispersion. This mass ratio provides the best structural uniformity. Higher ATO concentrations lead to formation of non-porous ATO domains, while lower ATO concentrations result in larger uncovered domains and additional in fragile scaffolds. Hydroxypropyl cellulose (HPC) (M_W ca. 100000) was added to the combined solution of ATO and PMMA and stirred overnight. The amount of cellulose was calculated as 10 wt% of the amount of PMMA beads, which corresponds to 1.3 wt% of HPC in the total volume. The homogeneous dispersion was dip coated on ITO substrates, dried at room temperature and calcined in air at 500 °C for 30 min (achieved with a ramp of 1 °C min^{-1}). The relative humidity and the temperature in the coating chamber were 35% and

20 °C, respectively. The film thickness of one layer could be tuned by varying the dip-coating rate and the viscosity of coating solutions. In general, thicker films were obtained at higher dip-coating rates or with more viscous solutions containing larger amounts of the HPC. The film thickness could be varied between 0.7 μm and 2 μm with the dip coating rate (0.5–1 mm s^{-1}), and between 0.7 μm and 2.5 μm with the cellulose concentration (1.3–2.6 wt% of HPC in the total volume at a dip coating rate of 0.5 mm s^{-1}). However the best film quality in terms of smoothness and surface coverage was obtained from solutions with low HPC concentrations (1-1.5%).

For the fabrication of macroporous ATO layers *via* the liquid infiltration method, an opal film was deposited by dip-coating (speed: 6.5 mm s^{-1}) of a 15 wt% PMMA dispersion on ITO substrates. The opal templates were annealed for 2 h at 80 °C in air to enhance the mechanical stability of the films. ATO-5% dispersion in water containing 3 wt% nanocrystals was used for infiltration of the opal films by dip-coating (speed: 6.5 mm s^{-1}). Finally the PMMA was removed by calcination at 500 °C (30 min, achieved by a ramp of 1 °C min^{-1}). The film thickness of one layer was 600 nm at a dip coating rate (PMMA deposition) of 6.5 mm s^{-1}.

Characterization.

Wide angle X-ray diffraction analysis was carried out in transmission mode using a STOE STADI P diffractometer with CuK$_\alpha$1-radiation (λ = 1.54060 Å) and a Ge(111) single crystal monochromator equipped with a DECTRIS solid state strip detector MYTHEN 1K. Powder XRD patterns of the samples were collected in a 2θ range from 5° to 70° with a step size of 1° and fixed counting time of 90 second per step. The size of the crystalline domains was calculated from the XRD patterns for the most intensive ATO signal (110 reflection) using the Scherrer equation. Due to the very steep background of the obtained XRD patterns fitting was performed after subtraction of the background using the program Match (for ATO-0%-ATO-20%) or GSAS (for ATO-30%), respectively. In the analysis only the first three lines were used (lines 110, 101 and 200), because the other lines significantly overlap. We made individual profile fitting using the program XFIT to show how the 2θ positions of lines 110 and 101 changed with the increase of Sb content (Figure 3.1). The precise lattice parameters were determined by using the Le Bail method56 of the whole XRD pattern with the program GSAS57 (graphical user interface EXPGUI58). The results of the Le Bail refinements were also used for the size strain analysis by following the procedure proposed in the Size/Strain Round Robin.[59] In the refinement we used a modified pseudo-Voigt function

defined by Thompson, Cox and Hastings,[60] which gave the following expression for the observed Gaussian and Lorentzian line widths:

$$\Gamma_G^2 = U\tan^2\theta + V\tan\theta + W + P/\cos^2\theta \qquad \text{Equation 3.1}$$

$$\Gamma_L = (X + Xe\cos\phi)/\cos\theta + (Y + Ye\cos\phi)\tan\theta + Z \qquad \text{Equation 3.2}$$

where Γ is the full width at half maximum (FWHM) of the line profile, and U, V, W, X, Y, Z, Xe and Ye are refinable parameters. The size and strain contribution to the line broadening can be given by the following equation:

$$\beta_S = \lambda/(D_V\cos\theta) \qquad \text{Equation 3.3}$$

$$\beta_D = e\,4\tan\theta \qquad \text{Equation 3.4}$$

where λ is the wavelength, D_v is the volume-averaged domain size and e represents the upper limits of micro-strain, while β_S and β_D represent the integral breadths of the Voigt function resulting from size and strain contributions, respectively. By comparing the equations 3.1 and (3.2) with the equations 3.3 and 3.4 it is easy to recognize that parameters X, Xe and P will relate to size broadening and Y, Ye and U to strain broadening. Therefore only those 6 profile parameters were refined in the Le Bail refinements of samples, while for all other profile parameters the values obtained for the refinement of the LaB_6 standard were taken. In order to obtain pure physically broadened profile parameters used in the calculation of the β_S and β_D values, the obtained values of the refined parameters U, X, Y, P for each sample were corrected by the corresponding values obtained from the standard (LaB_6). The most reliable data, obtained for pure cassiterite (sample ATO-0%) and sample ATO-20% show similar values for microstrain (~0.01), therefore this parameter was fixed at that value for all samples.

Dynamic light scattering measurements were performed on a MALVERN Zetasizer-Nano instrument equipped with a 4 mW He-Ne laser ($\lambda = 633$ nm) and an avalanche photodiode detector.

TEM measurements were carried out using a FEI Titan 80–300 equipped with a field emission gun operated at 300 kV. For the sample preparation a drop of a strongly diluted dispersion of a sample in ethanol was placed on a holey carbon coated copper grid and evaporated.

SEM images were obtained with a JEOL JSM-6500F scanning electron microscope equipped with a field emission gun operated at 5-10 kV. The films were prepared on ITO or FTO substrates and glued onto a brass sample holder with silver lacquer.

Thermogravimetric analysis of the samples was performed on a NETZSCH STA 440 C TG/DSC (heating rate of 10 K min^{-1} in a stream of synthetic air of about 25 mL min^{-1}).

X-ray photoelectron spectroscopy (XPS) measurements of the particles on a silicon substrate were performed using a VSW TA10 X-ray source, providing non-monochromatic Al Kα radiation, and a VSW HA100 hemispherical analyzer. The samples were cleaned by Ar^{+} sputtering (VSW AS10 ion source) for 5 min at 1 keV. The recorded elemental peaks were fitted with a Doniach-Sunjic function[61] convoluted with an Gaussian and linear background subtraction. As the O 1s and Sb 3d$_{5/2}$ peaks overlap, we used the Sb 3d$_{3/2}$ and the Sn 3d$_{3/2}$ peak (SnO$_2$ 3d$_{3/2}$ 495.0 eV) to derive the chemical composition from the ratio of the Sb 3d$_{3/2}$ peak area to the sum of the Sb 3d$_{3/2}$ and Sn 3d$_{3/2}$ peak areas from the measured integral intensity of the peaks. The composition of the valence states was evaluated by the Sb^{5+}/(Sb^{3+} + Sb^{5+}) ratio of the Sb 3d$_{3/2}$ peak following the method developed by Terrier et al.[51,62] Thereby the Sb 3d$_{3/2}$ peak was spitted into two components centered at 540.04 eV[14] for Sb^{5+} and 539.24 eV[14] for Sb^{3+}. This variation of the binding energy of the Sb 3d$_{3/2}$ peak is significant in XPS measurements and indicates clearly the presence of two oxidation states of antimony.

The UV-visible spectra of the samples were measured with a Perkin Elmer Lambda 1050 spectrophotometer equipped with an integrating sphere.

Conductivity measurements were carried out on ECOPIA HMS 3000 apparatus in the Van der Pauw geometry using a magnetic field of 0.55 T. The measurements were performed on pellets (10 mm diameter), which were prepared by pressing finely grinded nanoparticles under a pressure of 10 tons/cm^2. The contacts for the *dc* conductivity measurements were connected to the pellet using a silver lacquer.

The permittivity and conductivity at terahertz frequencies were measured in a non-contact way by time-domain terahertz transmission spectroscopy.[63] The useful bandwidth in our custom-made setup, based on a femtosecond laser oscillator, spans from 0.1 to 3 THz.[64] The measured conductivity spectra were analyzed using a recently proposed theoretical framework which combines a microscopic response of charges in nanoparticles and a model of depolarization fields in nanostructured samples (similarly as in previous publications);[65,66] a detailed description and analysis of the spectra will be provided elsewhere.

3.5. REFERENCES

(1)   Wolf, N.; Rydzek, M.; Gerstenlauer, D.; Arduini-Schuster, M.; Manara, J. *Thin Solid Films* **2013**, *532*, 60.

(2)   Luo, L.; Bozyigit, D.; Wood, V.; Niederberger, M. *Chem. Mater.* **2013**, *25*, 4901.

(3)   Luo, L.; Rossell, M. D.; Xie, D.; Erni, R.; Niederberger, M. *ACS Sustainable Chem. Eng.* **2013,** *1*, 152.

(4)   Goebbert, C.; Nonninger, R.; Aegerter, M. A.; Schmidt, H. *Thin Solid Films* **1999**, *351* 79.

(5)   Arsenault, E.; Soheilnia, N.; Ozin, G.A. *ACS Nano* **2011**, *5*, 2984.

(6)   Liu, Y.; Peters, K.; Mandlmeier, B.; Müller, A.; Fominykh, K.; Rathousky, J.; Scheu, C.; Fattakhova-Rohlfing, D. *Electrochim. Acta* **2014**, *140*, 108.

(7)   Liu, Y.; Stefanic, G.; Rathousky, J.; Hayden, O.; Bein, T.; Fattakhova-Rohlfing, D. *Chem. Sci.* **2012**, *3*, 2367.

(8)   Muller, V.; Rasp, M.; Rathousky, J.; Schutz, B.; Niederberger, M.; Fattakhova-Rohlfing, D. *Small* **2010**, *6*, 633.

(9)   Buonsanti, R.; Pick, T. E.; Krins, N.; Richardson, T. J.; Helms, B. A.; Milliron, D. J. *Nano lett.* **2012**, *12*, 3872.

(10)   Liu, Y.; Szeifert, J. M.; Feckl, J. M.; Mandlmeier, B.; Rathousky, J.; Hayden, O.; Fattakhova-Rohlfing, D.; Bein, T. *ACS Nano* **2010**, *4*, 5373.

(11)   Sigma-Aldrich: ITO (30 wt.% in isopropanol, <100 nm, Product No. 700460), AZO (2,5 wt.% in isopropanol, <50 nm, Product No. 793388); Alfa Aesar: ATO (13-22nm, https://www.alfa.com/en/cas/50926-11-9, Product No. 44930) and ITO (17-28nm, Product No. 44927); HuZheng: ATO solution/powder (6-20 nm)

(12)   Dusastre, V.; Williams, D. E. *J. Phys. Chem. B* **1998**, *102*, 6732.

(13)   Koivula, R.; Harjula, R.; Lehto, J. *Microporous Mesoporous Mater.* **2002**, *55*.

(14)   Krishnakumar, T.; Jayaprakash, R.; Pinna, N.; Phani, A. R.; Passacantando, M.; Santucci, S. *J. Phys. Chem. Solids* **2009**, *70*, 993.

(15)   Pan, R.; Qiang, S.; Liew, K.; Zhao, Y.; Wang, R.; Zhu, J. *Powder Technol.* **2009**, *189*, 126.

(16)   Kim, K. Y.; Park, S. B. *Mater. Chem. Phys.* **2004**, *86*, 210.

(17)   Müller, V.; Rasp, M.; Štefanić, G.; Ba, J.; Günther, S.; Rathousky, J.; Niederberger, M.; Fattakhova-Rohlfing, D. *Chem. Mater.* **2009** *21*, 5229.

(18)   Bai, F.; He, Y.; He, P.; Tang, Y.; Jia, Z. *Mater. Lett.* **2006**, *60*, 3126.

(19)   Zhang, J.; Gao, L. *Mater. Chem. Phys.* **2004**, *87*, 10.

(20)   Nutz, T.; zum Felde, U.; Haase, M. *J. Chem. Phys.* **1999**, *110*, 12142.

(21)   Lu, J.; Minami, K.; Takami, S.; Shibata, M.; Kaneko, Y.; Adschiri, T. *ACS Appl. Mater. Interfaces* **2012**, *4*, 351.

(22) Burunkaya, E.; Kiraz, N.; Kesmez, Ö.; Erdem Çamurlu, H.; Asiltürk, M.; Arpaç, E. *J. Sol-Gel Sci. Technol.* **2010**, *55*, 171.

(23) Lili, L.; Liming, M.; Xuechen, D. *Mater. Res. Bull.* **2006**, *41*, 541.

(24) Kanehara, M.; Koike, H.; Yoshinaga, T.; Teranishi, T. *J. Am. Chem. Soc.* **2009**, *131*, 17736.

(25) Ba, J.; Fattakhova Rohlfing, D.; Feldhoff, A.; Brezesinski, T.; Djerdj, I.; Wark, M.; Niederberger, M. *Chem. Mater.* **2006**, *18*, 2848.

(26) Ito, D.; Yokoyama, S.; Zaikova, T.; Masuko, K.; Hutchison, J. E. *ACS Nano* **2014**, *8*, 64.

(27) Kanie, K.; Sasaki, T.; Nakaya, M.; Muramatsu, A. *Chem. Lett.* **2013**, *42*, 738.

(28) Hammarberg, E.; Prodi-Schwab, A.; Feldmann, C. *Thin Solid Films* **2008**, *516*, 7437.

(29) Cuya Huaman, J. L.; Tanoue, K.; Miyamura, H.; Matsumoto, T.; Jeyadevan, B. *New J. Chem.* **2014**, *38*, 3421.

(30) Gilstrap Jr, R. A.; Summers, C. J. *Thin Solid Films* **2009**, *518*, 1136.

(31) Lu, Z.; Zhou, J.; Wang, A.; Wang, N.; Yang, X. *J. Mater. Chem.* **2011**, *21*, 4161.

(32) Li, S. L.; Zhu, P. L.; Zhao, T.; Sun, R. *J. Sol-Gel Sci. Technol.* **2014**, *70*, 366.

(33) Wang, Y.; Djerdj, I.; Smarsly, B.; Antonietti, M. *Chem. Mater.* **2009**, *21*, 3202.

(34) Bühler, G.; Thölmann, D.; Feldmann, C. *Adv. Mater.* **2007**, *19*, 2224.

(35) Hammarberg, E.; Prodi-Schwab, A.; Feldmann, C. *J. Colloid Interface Sci.* **2009**, *334*, 29.

(36) Lee, J.; Lee, S.; Li, G.; Petruska, M. A.; Paine, D. C.; Sun, S. *J. Am Chem. Soc.* **2012**, *134*, 13410.

(37) Thu, T. V.; Maenosono, S. *J. Appl. Phys.* **2010**, *107*.

(38) Jin, Y.; Yi, Q.; Ren, Y.; Wang, X.; Ye, Z. *Nanoscale Res. Lett.* **2013**, *8*, 153.

(39) Zheng, M.; Wang, B. *Trans. Nonferrous Met. Soc. China* **2009**, *19*, 404.

(40) Zhang, J.; Gao, L. *Mater. Lett.* **2004**, *58*, 2730.

(41) Jung, D.-W.; Park, D.-W. *Appl. Surf. Sci.* **2009**, *255*, 5409.

(42) Posthumus, W.; Laven, J.; de With, G.; van der Linde, R. *Colloids Surf. A* **2006**, *304*, 394.

(43) Cho, Y.-S.; Kim, H.-M.; Hong, J.-J.; Yi, G.-R.; Jang, S. H.; Yang, S.-M. *Colloids Surf. A* **2009**, *336*, 88.

(44) Lee, J.; Petruska, M. A.; Sun, S. *J. Phys. Chem. C* **2014**, *118*, 12017.

(45) Rosen, E. L.; Buonsanti, R.; Llordes, A.; Sawvel, A. M.; Milliron, D. J.; Helms, B. A. *Angew. Chem.* **2012**, *51*, 684.

(46) Grote, C.; Chiad, K. J.; Vollmer, D.; Garnweitner, G. *Chem. Commun.* **2012**, *48*, 1464.

(47) Tétreault, N.; Arsenault, É.; Heiniger, L.-P.; Soheilnia, N.; Brillet, J.; Moehl, T.; Zakeeruddin, S.; Ozin, G. A.; Grätzel, M. *Nano Lett.* **2011**, *11*, 4579.

(48) Riha, S. C.; Vermeer, M. J.; Pellin, M. J.; Hupp, J. T.; Martinson, A. B. *ACS Appl. Mater. Interfaces* **2013**, *5*, 360.

(49) Stefik, M.; Cornuz, M.; Mathews, N.; Hisatomi, T.; Mhaisalkar, S.; Gratzel, M. *Nano Lett.* **2012**, *12*, 5431.

(50) Ginley, D. S.; Hosono, H.; Paine, D. C. In *Handbook of Transparent Conductors*; Springer: New York, 2010.

(51) Terrier, C.; Chatelon, J. P.; Berjoan, R.; Roger, J. A. *Thin Solid Films* **1995**, *263*, 37.

(52) Němec, H.; Kužel, P.; Sundström, V. *Phys. Rev. B* **2009**, *79*, 5309

(53) Fattakhova-Rohlfing, D.; Zaleska, A.; Bein, T. *Chem. Rev.* **2014**, *114*, 9487.

(54) Mandlmeier, B.; Minar, N. K.; Feckl, J. M.; Fattakhova-Rohlfing, D.; Bein, T. *J. Mater. Chem. A* **2014**, *2*, 6504.

(55) Mandlmeier, B.; Szeifert, J. M.; Fattakhova-Rohlfing, D.; Amenitsch, H.; Bein, T. *J. Am Chem. Soc.* **2011**, *133*, 17274.

(56) Le Bail, A.; Duroy, H.; Fourquet, J. L. *Mater. Res. Bull.* **1988**, *23*, 447.

(57) Larson, A. C.; Von Dreele, R. B. *General Structure Analysis System GSAS, Los Alamos National Laboratory Report* **2001**.

(58) Toby, B. H. *J. Appl. Cryst.* **2001**, *34*, 210.

(59) Balzar, D.; Audebrand, N.; Daymond, M.; Fitch, A.; Hewat, A.; Langford, J. I.; Le Bail, A.; Louër, D.; Masson, O.; McCowan, C. N.; Popa, N. C.; Stephens, P. W.; Toby, B. H. *J. Appl. Cryst.* **2004**, *37*, 911.

(60) Thompson, P.; Cox, D. E.; Hastings, J. B. *J. Appl. Cryst.* **1987**, *20*.

(61) Doniach, S.; Sunjic, M. *J. Phys. C* **1970**, *3*, 285.

(62) Terrier, C.; Chatelon, J. P.; Roger, J. A. *Thin Solid Films* **1997**, *295*, 95.

(63) Grüner, G. *Millimeter and submillimeter wave spectroscopy of solids*; Springer-Verlag: Berlin and Heidelberg, Germany, 1998.

(64) Kužel, P.; Němec, H.; Kadlec, F.; Kadlec, C. *Opt. Exp.* **2010**, *18*.

(65) Zajac, V.; Němec, H.; Kadlec, C.; Kůsová, K.; Pelant, I.; Kužel, P. *New J. Phys.* **2014**, *16*, 093013.

(66) Němec, H.; Mics, Z. n.; Kempa, M.; Kužel, P.; Hayden, O.; Liu, Y.; Bein, T.; Fattakhova-Rohlfing, D. *J. Phys. Chem. C* **2011**, *115*, 6968.

3.6. SUPPORTING INFORMATION
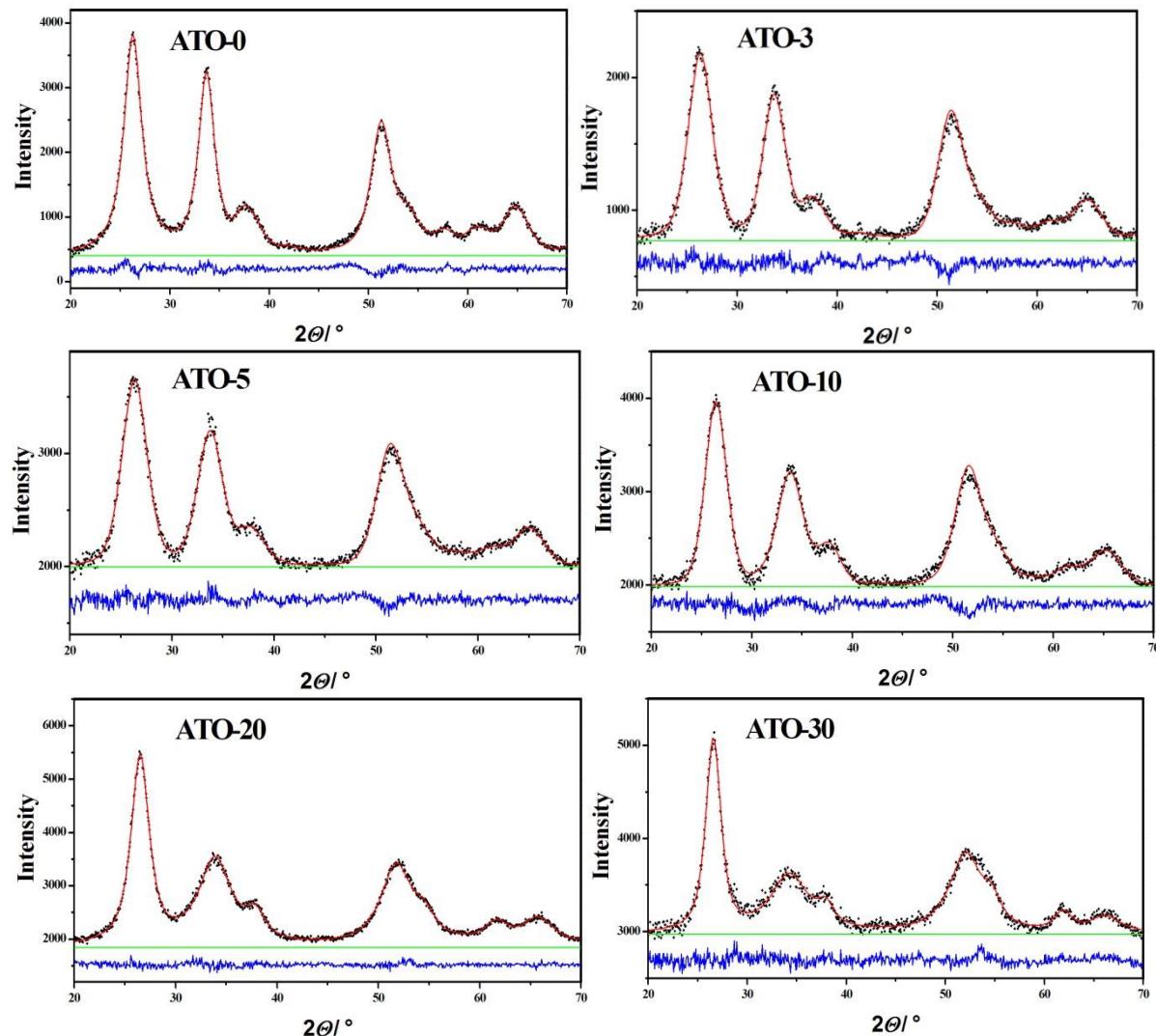
Figure S3.1 Diffraction patterns of the ATO samples prepared with up to 30 mol% of antimony in the precursor solution after background subtraction (program Match (for ATO-0%-ATO-20%) or GSAS (for ATO-30%) with graphical user interface EXPGUI).
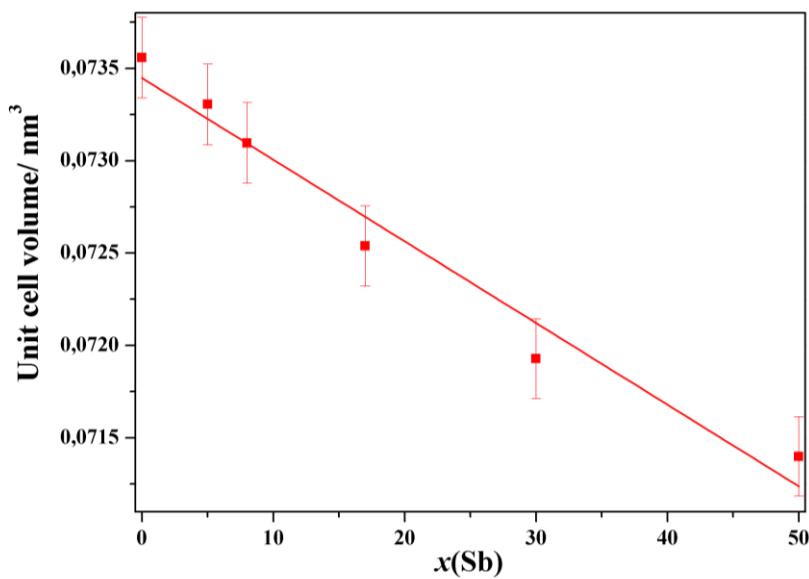
Figure S3.2 Change of the unit cell volume of cassiterite-type lattice (space group $P4_2/mnm$, JCPDS File Card No. 41-1445) of ATO nanoparticles containing different Sb concentrations. The Sb level x(Sb) is taken as the real content determined from the XPS and ICP-OES measurements (average value).

Table S3.1 Refined values of the lattice parameters and unit-cell volume of cassiterite-type ATO nanoparticles containing different Sb concentrations, estimated from the results of Le Bail refinements (GSAS program) of XRD patterns. The Sb level x(Sb) is taken as the real content determined from the XPS and ICP-OES measurements (average value).

Sample	x(Sb)	Lattice parameters		V / nm^3
		a / nm	c / nm	
ATO-0	0	4.798(2)	3.195(2)	73.6(2)
ATO-3	0.05	4.788(2)	3.197(2)	73.3(2)
ATO-5	0.08	4.786(2)	3.191(2)	73.1(2)
ATO-10	0.17	4.772(2)	3.184(2)	72.5(2)
ATO-20	0.30	4.755(2)	3.180(2)	71.9(2)
ATO-30	0.50	4.742(2)	3.175(3)	71.4(3)

Table S3.2 Refined values of the volume-averaged domain size (D_V) in the directions parallel and perpendicular to the axis 001 of ATO nanoparticles containing different Sb concentrations, estimated from the results of Le Bail refinements (GSAS program) of XRD patterns. The Sb level x(Sb) is taken as the real content determined from the XPS and ICP-OES measurements (average value).

Sample	x(Sb)	D_V ($\phi = 0°$)/ nm	D_V ($\phi = 0°$)/ nm
ATO-0	0	3.0(1)	3.9(1)
ATO-3	0.05	2.7(2)	3.2(2)
ATO-5	0.08	2.6(2)	2.7(2)
ATO-10	0.17	3.1(2)	2.4(2)
ATO-20	0.30	3.4(2)	1.6(2)
ATO-30	0.50	3.7(3)	1.2(3)
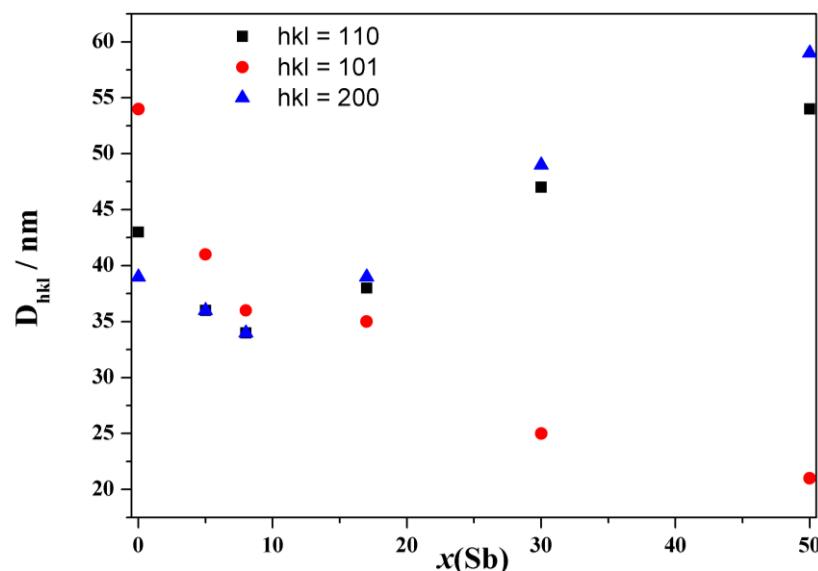
Figure S3.3 Change of the *v*olume-averaged domain size (D_{hkl}) in the directions perpendicular to planes 110, 101 and 200 estimated by using Scherrer equation of ATO nanoparticles containing different Sb concentrations. The Sb level x(Sb) is taken as the real content determined from the XPS and ICP-OES measurements (average value).

Table S3.3   Volume-averaged domain size (D_{hkl}) values in the directions perpendicular to planes 110, 101 and 200, as estimated by using Scherrer equation. The Sb level x(Sb) is taken as the real content determined from the XPS and ICP-OES measurements (average value).

Sample	x(Sb)	D_{110}/ nm	D_{101}/ nm	D_{200}/ nm
ATO-0	0	4.3	5.4	3.9
ATO-3	0.05	3.6	4.1	3.6
ATO-5	0.08	3.4	3.6	3.4
ATO-10	0.17	3.8	3.5	3.9
ATO-20	0.30	4.7	2.5	4.9
ATO-30	0.50	5.4	2.1	5.9
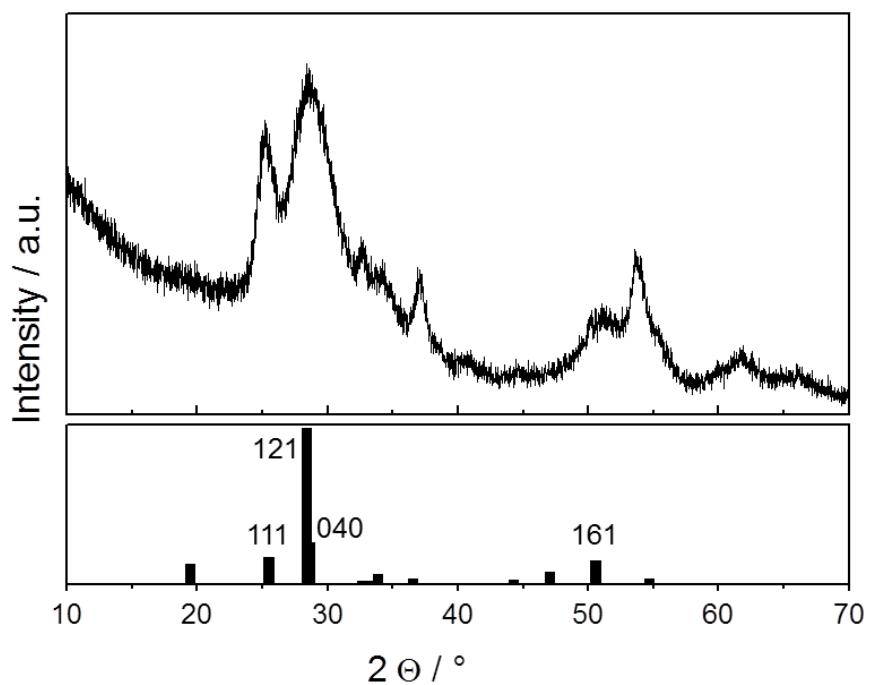
Figure S3.4   XRD pattern of as-prepared ATO-40% nanoparticles prepared with 40% in the precursor solution. The bars in the bottom panel mark the position and the intensity of the diffraction lines of Sb_2O_3 valentinite (space group *Pccn*, JCPDS File Card No. 01-071-0383).
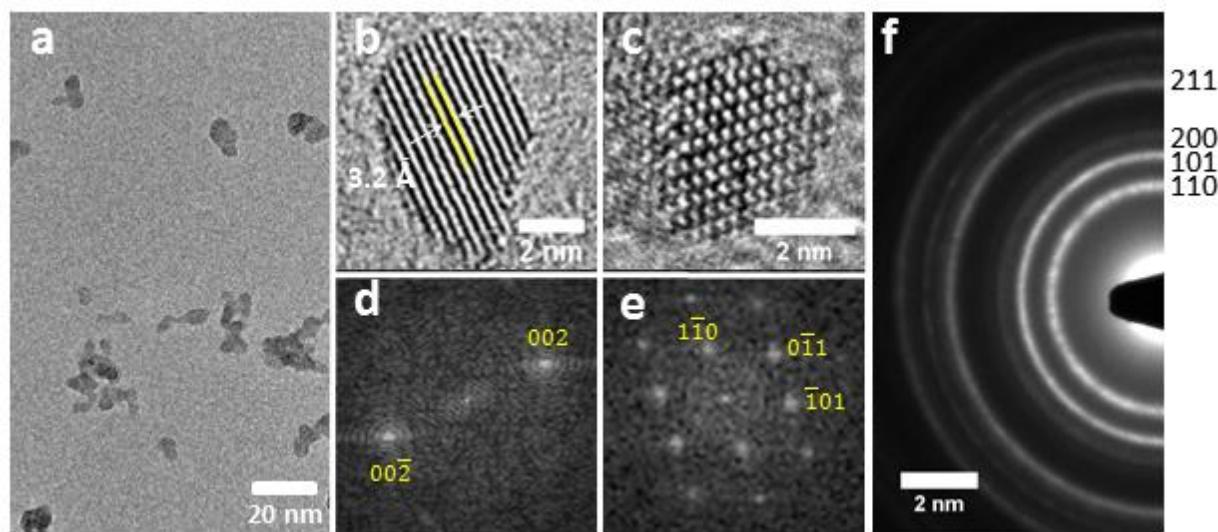
Figure S3.5 TEM images of undoped SnO_2 nanoparticles: (a) overview of the nanoparticles dispersed on a TEM grid; (b)+(c) HRTEM images of single tetragonal nanoparticles, (d)+(e) power spectrum obtained by Fourier transformation of the HRTEM images of the corresponding SnO_2 nanoparticles pictured above; (f) SAED pattern of the nanoparticles. The corresponding d-values are 3.33 (110), 2.62 (101), 2.31 (200), 1.75 Å (211).

Table S3.4 Conductivity of pellets pressed from ATO nanoparticles prepared with different antimony concentrations.

| Sample | Van der Pauw measurements | | THz conductivity at 0.2 THz of as prepared NPs [S/cm] |
	Conductivity of as prepared NPs [S/cm]	Conductivity of calcined NPs [S/cm]	
SnO_2	2.8×10^{-3}	3.6×10^{-4}	0.7
ATO-3%	1.1×10^{-2}	62	0.18
ATO-5%	6.8×10^{-2}	40	0.12
ATO-10%	1.1×10^{-3}	22	~0.14
ATO-20%	1.5×10^{-4}	26	

NANOSTRUCTURED ANTIMONY DOPED TIN OXIDE LAYERS WITH TUNABLE PORE
ARCHITECTURES AS VERSATILE TRANSPARENT CURRENT COLLECTORS FOR

117

4. NANOSTRUCTURED ANTIMONY DOPED TIN OXIDE LAYERS WITH TUNABLE PORE ARCHITECTURES AS VERSATILE TRANSPARENT CURRENT COLLECTORS FOR BIOPHOTOVOLTAICS

This chapter is based on the following publication:

Kristina Peters, Hasala N. Lokupitiya, David Sarauli, Mathias Labs, Mathias Pribil, Jiří Rathouský, Alexander Kuhn, Dario Leister, Morgan Stefik, Dina Fattakhova-Rohlfing
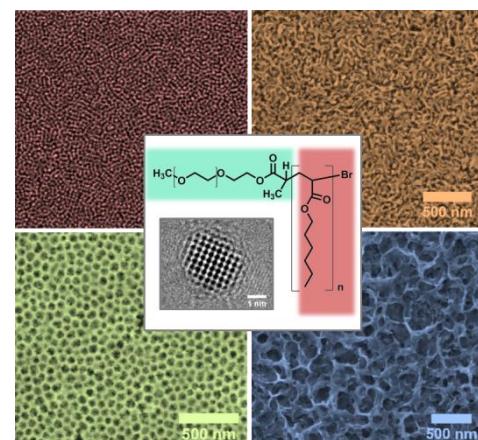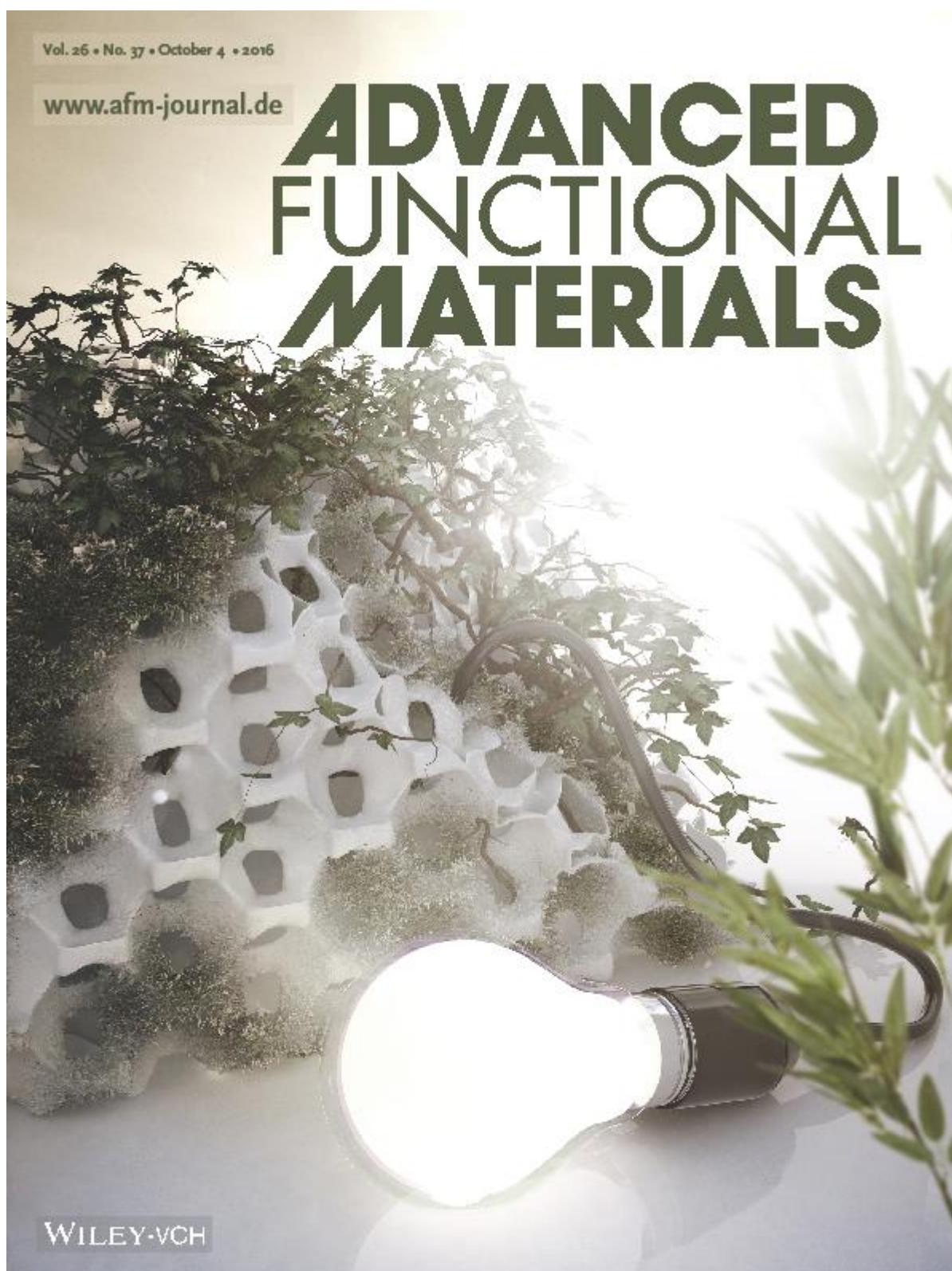
FRONT COVER

Image created by Christoph Hohmann (Nanosystems Initiative Munich, NIM) published as front cover in *Adv. Funct. Mater.* 37/2016 (used with permission from the publisher).

NANOSTRUCTURED ANTIMONY DOPED TIN OXIDE LAYERS WITH TUNABLE PORE
ARCHITECTURES AS VERSATILE TRANSPARENT CURRENT COLLECTORS FOR

119

Nanostructured transparent conducting oxide (TCO) layers gain increasing importance as high surface area electrodes enabling incorporation of functional redox species with high loading. We report the fabrication of porous TCO films, namely antimony-doped tin oxide (ATO), using the self-assembly of pre-formed ATO nanocrystals with poly(ethylene oxide-*b*-hexyl acrylate) (PEO-*b*-PHA) block copolymer. The high molar mass of the polymer and tunable solution processing conditions enable the fabrication of TCO electrodes with pore sizes ranging from mesopores to macropores. Particularly notable is access to uniform macroporous films with a nominal pore size of around 80 nm, which is difficult to obtain by other techniques. The combination of tunable porosity with a large conducting interface makes the obtained layers versatile current collectors with adjustable performance. While all the obtained electrodes incorporate a large amount of small redox molecules such as molybdenum polyoxometalate, only the electrodes with sufficiently large macropores are able to accommodate high amounts of bulky photoactive photosystem I (PSI) protein complexes. A rationally optimized morphology would provide a maximum surface area to enhance PSI loading while limiting the lower-limit of pore size to enable PSI uptake. With this strategy, we demonstrated a morphology with smaller pores than comparable colloidal template films (~150-400nm), and thus higher surface area while still enabling significant PSI uptake. A further advantage of smaller macropores is the concomitantly thinner walls that reduce undesired optical absorption by the TCO. The 11-fold enhancement of the current response of PSI modified macroporous ATO electrodes compared to PSI on planar indium tin oxide (ITO), makes this type of electrodes promising candidates for the development of biohybrid devices.

4.1. INTRODUCTION

The construction of optoelectronic and electrochemical devices based on biological units is a subject of intense research activity inspired by unprecedented high energy conversion efficiencies and evolution-optimized performance of many biological systems.[1,2] Some fascinating examples of biological energy conversion machinery include photosynthetic systems featuring an internal quantum yield close to unity.[3-10] By connecting such systems to electrodes one may obtain bioelectronic energy conversion devices such as solar cells, fuel cells and biosensors as was demonstrated by several groups.[6-8,11-13] One of the greatest challenges in the development of bioelectronic devices is integration of biological elements into an artificial environment of electronic circuits in a way that not only retains their

functionality, but also provides a communication with the electrode. This requires, on the one hand, efficient interfacing of biological and artificial systems and, on the other hand, high loading of biomolecules communicating with the electrode.

An established strategy to improve the charge collection efficiency in bioelectrochemical devices is optimization of morphology of current collectors, with the use of nanostructured electrode architectures instead of conventional planar electrodes.[7,14-20] Porous 3D-electrodes are particularly advantageous for applications involving immobilized species.[21-23] They enable high loading of functional guest molecules, their direct communication with the electrode and at the same time unrestricted mass transport of the species in electrolyte, providing a substantially more efficient electron transfer and consequently increased efficiency of the devices. Another attractive feature of the porous electrodes is the possibility to vary the surrounding of the biomolecules inside the pores by chemical modification of the pore surface. Furthermore, by tuning the pore size an additional means is provided to optimize the performance of the immobilized biomolecules.

Among existing electrode materials, nanostructured transparent conducting oxide (TCO) electrodes are of special importance as current collectors for transparent electronics. Being first introduced in 2006[24,25] porous 3D-TCO electrodes gained increasing popularity in various bioelectrochemical and optoelectrochemical applications.[26-34] In the past decade significant progress has been made in producing TCO electrodes with different types of porous structures and pore dimensions. J. M. Brett et al. have used glancing angle deposition (GLAD) to produce nanocolumnar TCO electrode morphologies.[35-37] Periodic TCO electrodes with inverse opal structure have been prepared by several groups using colloidal crystal templating.[38-41] These techniques enable the fabrication of highly periodic electrode architectures, but are restricted to relatively large pore dimensions from 100 nm – 2 μm. Much greater variability in pore morphology and pore dimensions can be achieved via soft templating with amphiphilic block copolymers in a so called evaporation-induced self-assembly (EISA) process.[42] Using different types of amphiphilic polymers, TCO layers with different types of mesoporous structures have been obtained.[24,27,32,43-52] The pore size of the TCO layers produced in this way is however rather small, being typically in the range from 2 to 10 nm. Larger mesopores up to 45 nm[43] were obtained using polymers with either a high effective interaction parameter or high molar mass such as KLE[24,44,45], PIB-*b*-PEO type[43,46], PI-*b*-PEO[53] and sulfonated HmSEBmS,[47,48] but fabrication of porous TCO electrodes with even larger pores becomes more challenging. Macroporous electrodes with 50 – 100 nm pores

NANOSTRUCTURED ANTIMONY DOPED TIN OXIDE LAYERS WITH TUNABLE PORE
ARCHITECTURES AS VERSATILE TRANSPARENT CURRENT COLLECTORS FOR

121

are difficult to achieve by most reported EISA techniques, yet they are crucial for applications requiring the transport of large biological moieties.

We report the fabrication of mesoporous to macroporous TCO films by the self-assembly of crystalline antimony-doped tin oxide (ATO) nanoparticles[40] with poly(ethylene oxide-*b*-hexyl acrylate) (PEO-*b*-PHA) block copolymer.[54] Changing the solution processing conditions enabled remarkably tunable TCO morphologies with adjustable nominal pore sizes from 10 nm mesopores to 80 nm macropores. Here the use of macroporous TCOs uniquely accommodated high amounts of bulky photoactive photosystem I (PSI) protein complexes resulting in an 11-fold enhancement of their photocurrents compared to the PSI on flat electrodes.

4.2. RESULTS AND DISCUSSION

The EISA fabrication of porous ATO films by PEO-*b*-PHA is illustrated in Scheme 4.1. In a typical procedure a colloidal solution containing ATO nanoparticles and PEO-*b*-PHA in different ratios was coated on various substrates using spin- or drop-casting techniques. The films were annealed in air at 500 °C to remove the template and to sinter the nanoparticles.
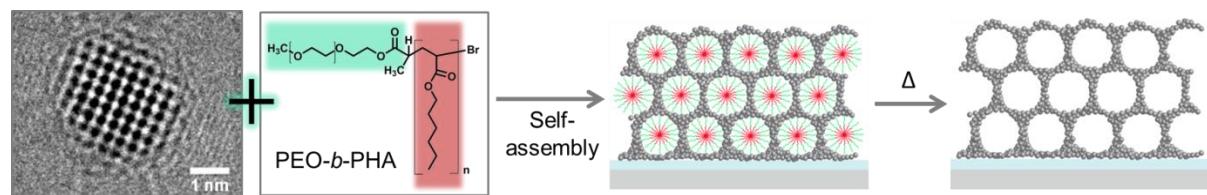
Scheme 4.1   Evaporation induced self-assembly of preformed ATO nanoparticles with PEO-b-PHA.

EISA with PEO-*b*-PHA was previously shown to be highly tunable with both the solution composition and processing conditions.[54] An essential choice in the self-assembly process is the selection of a suitable solvent to disperse the block copolymer. The Hildebrand solubility parameter (δ) provides a useful quantitative tool to predict solution behaviour based upon the strength of intermolecular interactions.[53,54] The PHA block of PEO-*b*-PHA is quite hydrophobic (δ = 16-17 $\sqrt{MPa}$) and is thus most soluble in typical organic solvents such as tetrahydrofuran (THF, δ = 19-20 $\sqrt{MPa}$). The addition of more polar co-solvents such as isopropyl alcohol (iPrOH) (δ = 23.8 $\sqrt{MPa}$) or ethanol (EtOH) (δ = 26.2 $\sqrt{MPa}$) linearly adjusts the δ value of the solvent mixture. Increasing the offset between the δ value of the solvent and that of the solvophobic block (PHA) increases the equilibrium micelle size and

provides a means to predictably tune the resulting micelle templates.[54] Here, the solubility parameters provide a means to estimate the interfacial surface tension that drives increasing micelle sizes as balanced against the entropic loss associated with polymer chain stretching. Here, we used a PEO-*b*-PHA with Mn 66,000 g/mol to enable a wide range of micelle sizes depending on the solution composition. An additional criterion for EISA is the dispersion of the inorganic component. Here we found that addition of EtOH greatly improves the film uniformity, presumably due to improved solvation of the ATO nanoparticles. Films prepared from dispersions containing THF only or iPrOH/THF mixtures exhibited uneven coverage of the substrate.

The ATO nanoparticles synthesized via the *tert*-butanol route[40] disperse without agglomeration in numerous solvents including THF, EtOH and iPrOH. Such highly soluble nanoparticles greatly ease the design of solution conditions for all components involved in EISA. The very small size of ATO particles of 2.8 nm is also beneficial for self-assembly with polymers since the resulting micelles pack most regularly when the nanocrystals are several times smaller than the resulting wall thickness: nanocrystals with sizes comparable to the wall-thickness can disrupt ordering.[55] The detailed characterization of the used ATO nanoparticles is presented in the supporting information (Figure S4.3 and Figure S4.4). An inorganic-to-organic ratio (I:O) between 1:2 and 1:1 provided the best structural uniformity. Higher nanoparticle concentrations (2:1) resulted in nonporous regions, while lower particle concentrations lead to disordered morphologies with very thin and brittle pore walls and large uncovered regions.

The use of PEO-*b*-PHA was reported by some of the authors previously[54] to enable persistent micelle templates (PMT), where the wall thickness was independently tunable with constant pore size by changing the relative fraction of the inorganic component.[54] Rather than using solution conditions for the kinetic entrapment of persistent micelles, we examined the role of micellization conditions on the resulting pore size. We found that the film morphology is very sensitive to the amount of ethanol and hydrochloric acid (HCl) in the coating solutions. This is reasonable considering that the solubility parameters for both ethanol and HCl are quite far from that of PHA. The addition of such polar co-solvents was used to tune the resulting micelle size. This systematically adjustable parameter enabled porous morphologies with both tunable size and tunable morphology. Depending on the solution solubility parameter (see Table 4.1 in the experimental section), several types of pore structures were obtained (top-view scanning electron microscopy (SEM) images in Figure 4.1). The ATO films prepared with low solubility parameters exhibited a mesoporous structure composed of inorganic

NANOSTRUCTURED ANTIMONY DOPED TIN OXIDE LAYERS WITH TUNABLE PORE
ARCHITECTURES AS VERSATILE TRANSPARENT CURRENT COLLECTORS FOR

123

spheres with a relatively small pore size of 10-20 nm (Figure 4.1a, "mesoATO"). A worm-like disordered morphology with elongated pores of average dimensions of 20×100 nm (Figure 4.1b) was observed upon addition of HCl leading to higher solution solubility parameter. Increasing the solution solubility parameter even further resulted in ordered macroporous films featuring large uniform spherical pores with a size of around 80 nm (see Figure 4.1c, "macroATO"). These very large macropore sizes for a material prepared with block copolymers in combination with the ordered porosity make the obtained films very attractive for the immobilization of bulky functional moieties. MacroATO enables unique benefits and will be characterized in more detail below. Further increasing the solution solubility parameter led to the formation of a foam-like disordered macropore structure with undefined pore shape and a broad distribution of pore size from 50 to 300 nm (Figure 4.1d).
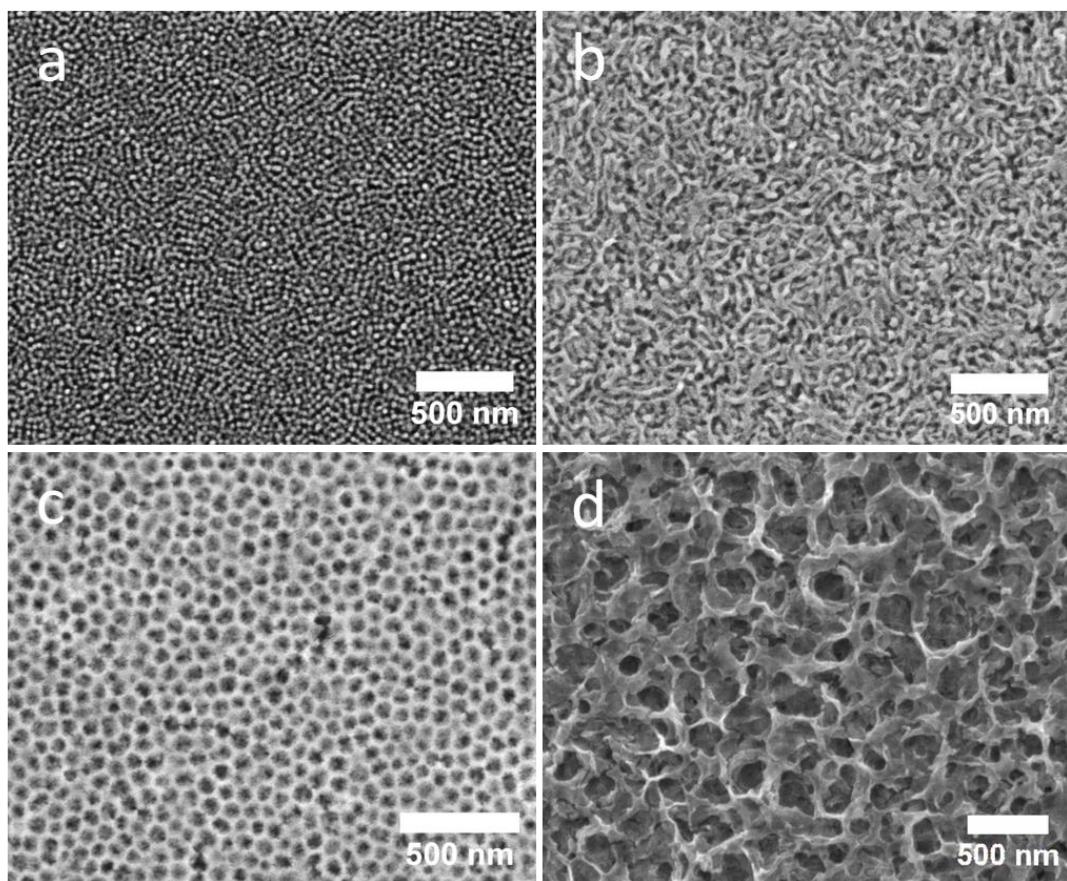
Figure 4.1   Top-view SEM images of PEO-b-PHA templated films prepared with different HCl concentrations on ITO. The precursor dispersion was prepared by adjusting the ATO/polymer ratio at 0.5 with 25 mg PEO-b-PHA in THF or THF/EtOH mixtures. (a) Mesoporous structure at HCl concentrations of 0.6% in the total volume of THF (mesoATO). (b) Worm-like mesoporous structure at lower HCl concentrations (1.3% in the total volume of EtOH/THF). (c) Ordered macroporous structure at HCl concentrations of 3.2% (in the total volume of EtOH/THF) (macroATO). (d) Disordered macroporous structure at higher HCl concentrations (4.8% in the total volume of EtOH/THF) (see Experimental part for fabrication details).

The observed sequence of morphologies and characteristic length scales may be rationalized in terms of the solubility parameters of the co-assembly solution. Starting from THF-rich solutions, the initial polymer micelles are able to transition to the classic behaviour of bulk block copolymers in the condensed state.[53] Slightly higher solubility parameters inhibit the transition to bulk-type behaviour and result in worm-like morphologies. Starting from yet higher solution solubility parameters enables the preservation of polymer micelles.

All the described coatings obtained from THF/EtOH mixtures are homogeneous and crack-free over several hundred micrometres (see lower magnification SEM images in Figure **S4.1**a, b in the supporting information) without delamination from the ITO substrate (Figure S4.2 in the supporting information) and high smoothness (see AFM images in the inset in Figure S4.1b in the supporting information). Thick films of over 1 μm show microcracks (Figure S4.1c, Supporting information) that however do not deteriorate their stability when applied as electrodes, which withstand different treatments (ultrasonication, long-time soaking in different electrolytes) without mechanical damage or peeling off the substrate. The thickness of the films is easily tunable from ca. 100 nm to almost 2 μm by changing the deposition technique and the amount of precursor solution. Thus, macroATO films of 0.5 μm, 1 μm and 1.8 μm thickness can be produced by drop casting 15 μl, 30 μl and 60 μl of the coating solution, respectively, on an area of 2.25 cm^2. Thin films (130 nm) can be prepared by spin coating the reaction mixture (see experimental section and Table 4.1 for further details). The SEM images of the film cross-sections demonstrate that the open porous scaffold is also formed in the direction perpendicular to the substrate with a very good adhesion to the substrate without delamination (Figure 4.2a and Figure S4.2 in the supporting information). The films show an excellent transparency as can be seen in the transmittance spectra in Figure S4.1d in the supporting information. The films of 60 nm and 1 μm thickness have practically the same transmittance of over 80-90% in the visible range as the parent ITO substrate.

An important prerequisite for the sufficient electrical conductivity of polycrystalline materials is a good connectivity between the crystalline domains, which is however often a problem in the porous scaffolds assembled from pre-formed crystalline nanoparticles.[38,56] Transmission electron microscopy (TEM) analysis of the macroATO films annealed in air at 500 °C reveals that although the PEO-*b*-PHA-templated scaffold is highly porous, the pore walls are dense, being composed of sintered, interconnected nanoparticles (Figure 4.2b and c). Selected area electron diffraction (SAED) pattern of the nanoparticles (Figure 4.2d) are in good agreement with the tetragonal cassiterite structure of ATO deduced from the X-ray diffraction (XRD) patterns (Figure S4.4 in the supporting information). The size of the crystalline domains of

NANOSTRUCTURED ANTIMONY DOPED TIN OXIDE LAYERS WITH TUNABLE PORE
ARCHITECTURES AS VERSATILE TRANSPARENT CURRENT COLLECTORS FOR

125

around 5 - 6 nm in the annealed scaffold is almost twice as big as the size of the parent nanoparticles taken for the structure assembly, pointing to particle sintering. The particle size determined from TEM analysis is in good agreement with that calculated from the line broadening of the 110 reflection of cassiterite structure in the XRD patterns (Figure S4.4 in the supporting information), which increases from 2.8 nm for the as-prepared to 4.8 nm for the calcined macroATO films. The sintering of the nanoparticles followed by the densification of the inorganic fraction explains the observed shrinkage of the pores after calcination, which is more pronounced in the direction perpendicular to the substrate resulting in an ellipsoidal pore shape (Figure 4.2a).
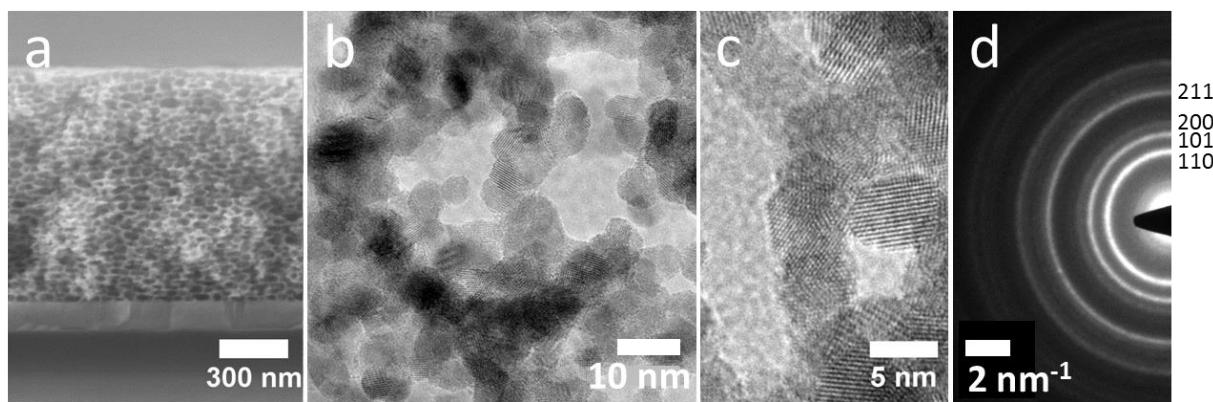
Figure 4.2   (a) Cross section SEM image of a macroATO film prepared by EISA of preformed ATO nanoparticles and PEO-*b*-PHA block copolymer. (b) and (c) TEM images of a single pore showing pore walls assembled from sintered nanoparticles. (d) Selected area electron diffraction (SAED) pattern of the macroATO film. The corresponding d-values are in a good agreement with the tetragonal cassiterite structure of ATO (3.33 (110), 2.62 (101), 2.31 (200), and 1.75 Å (211)).

Grazing-incident small-angle X-ray scattering (GISAXS) measurements were used to examine the morphology of macroATO films, both as-made and calcined. The 2D detector images shown in Figure 4.3a,b were used to extract in-plane scattered intensity as a function of q_y at constant q_z (see Figure S4.5 in the supporting information for coordinate system). The integration was performed over a 10 pixel wide stripe to improve the signal-to-noise ratio. The first scattering peak values for as-made and calcined films were obtained at 0.073 nm^{-1} and 0.074 nm^{-1}, respectively, which correspond to spacings of 86.1 nm and 84.6 nm (Figure **4.3**). The GISAXS patterns had only a few in-plane spots that elongated along q_z, which were attributed to the random packing of spheres.[54] The random packing of hard spheres can generate multiple peaks due to the radial distribution function. The observed scattering patterns are difficult to correlate to the specific physical dimensions of the system.[57] The

spacing values obtained from SAXS for both as-made and calcined films were consistent with the nominal feature sizes observed by SEM and HRTEM.
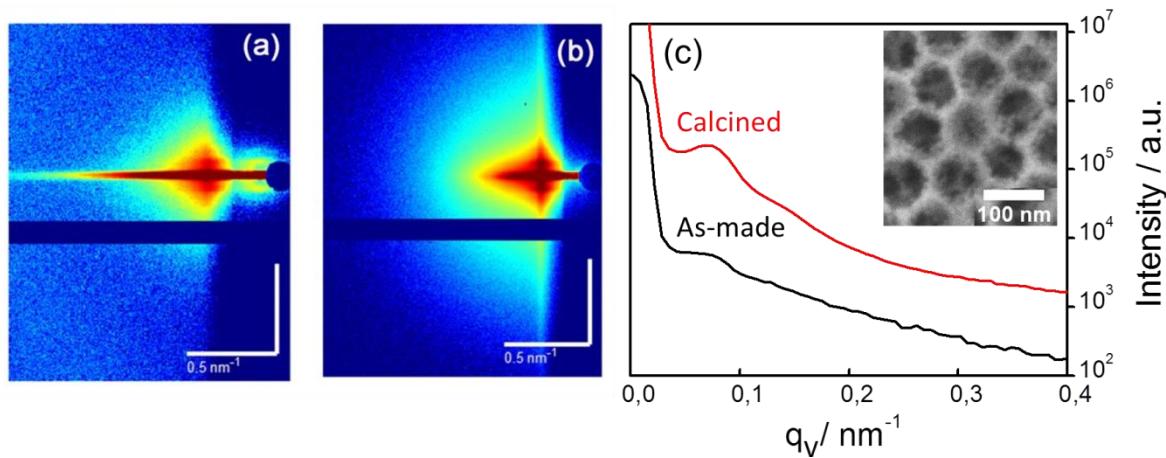
Figure 4.3   a+b) 2D GISAXS detector images of as-made (a) and calcined (b) films at an incidence angle of $\alpha_i = 0.25°$. c) The 2D images were used to extract in-plane scattered intensity as a function of q_y (at constant q_z). The first scattering peak values for as-made and calcined films correspond to spacings of 86.1 nm and 84.6 nm, respectively, which are in good agreement with the morphology obtained from SEM top view images (inset).

The porosity of the films and the total accessible surface area were studied using krypton sorption measurements. The adsorption isotherm does not reach a plateau at a relative pressure of 1 and keeps rising, which indicates the presence of pores wider than 10 nm (see Figure S4.6 in the supporting information).[58,59] The roughness factor, which is determined as the real surface area related to the geometric substrate area, was calculated to be 54 cm^2/cm^2 for a 1 μm thick macroATO, corresponding to a specific surface area related to the total film volume of 54 $m^2\,cm^{-3}$. For a 50 nm thin mesoATO film the specific surface area of the film related to the substrate area (roughness factor) and the film total volume equal 17 $cm^2\,cm^{-2}$ and 330 $m^2\,cm^{-3}$, respectively. The increase in surface area related to the total volume from 54 m^2/cm^3 for the macroATO to 330 $m^2\,cm^{-3}$ for the mesoATO is in line with the expected surface area increase for the smaller pore structure.

For the application as conducting electrodes it is important that the increase in the surface area due to the nanostructuring fully translates to the increase in electrochemically conducting interface. The electrochemically active surface area was estimated by measuring the non-Faradaic capacitive current associated with double-layer charging from the scan rate dependence of cyclic voltammograms (CVs). The differential capacitance is directly proportional to the electrode surface area; this effect applies however only to conducting materials and is commonly used for the assessment of surface area of conducting

NANOSTRUCTURED ANTIMONY DOPED TIN OXIDE LAYERS WITH TUNABLE PORE
ARCHITECTURES AS VERSATILE TRANSPARENT CURRENT COLLECTORS FOR

127

electrodes[60-62] (see experimental part and Figure S4.8 in the Supporting information for further details). The specific surface area (roughness factor) obtained from electrochemical measurements (57 $cm^2 cm^{-2}$ and 103 $cm^2 cm^{-2}$ for 1 µm and 1.8 um thick macroATO films, respectively) is in a perfect agreement with that obtained from the Kr sorption measurements (54 $cm^2 cm^{-2}$ and 97 $cm^2 cm^{-2}$ for 1 µm and 1.8 µm, respectively), which confirms that the porous ATO scaffold is electrically conducting.

Furthermore, the increase in conducting surface area was estimated via measuring the electrochemical response of redox species grafted to the electrode surface. For this purpose we used a well-known Keggin-Type molybdenum polyoxometalate anion $PMo_{12}O_{40}^{3-}$ (Mo-POM), since polyoxometalates are known to adsorb spontaneously on various electrode materials[63,64] including metal oxides such as ITO[65]. The Mo-POM has been immobilized on the porous ATO electrodes by incubation in a 5 mmol solution of the polyoxometalate in 0.1 M H_2SO_4 overnight. The amount of Mo-POM molecules adsorbed on the ATO surface can be calculated from cyclic voltammograms of the functionalized meso- and macroporous ATO electrodes (Figure 4.4 and Figure S4.7), which show a 6-electron reduction of $PMo_{12}O_{40}^{3-}$ to $H_6PMo_{12}O_{40}^{3-}$ well documented in the literature (the three distinct pairs of redox peaks detected for the POM monolayers on the planar electrodes merge into two broad pairs of peaks on the porous electrodes).[66,67] The molar loading of Mo-POM in meso ATO was found to be 6.8·10^{-9} mol cm^{-2} for the 50 nm thick film, which corresponds to a volumetric loading of 1.4·10^{-3} mol cm^{-3} when normalized to the film thickness (Figure 4.4). The macroATO films also demonstrate a high uptake of Mo-POM although with a lower loading as compared to the mesoATO films due to the lower specific surface area of the macroporous structure. It is important however that the loading is proportional to the film thickness, being 2.3·10^{-4} mol cm^{-3}, 3.2·10^{-4} mol cm^{-3} and 4·10^{-4} mol cm^{-3} for 0.5 µm, 1 µm and 1.8 µm thick macroATO films. This indicates that the electrochemically accessible surface area scales with the increasing electrode thickness as well.
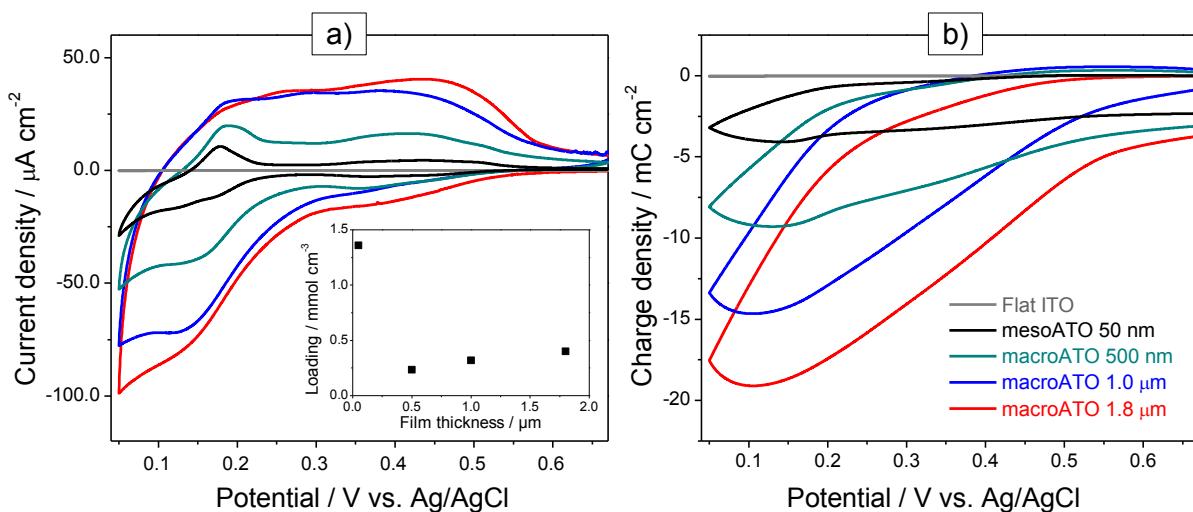
Figure 4.4   Cyclic voltammograms (left) and corresponding charge-potential curves (right) of Mo-POM adsorbed on macroATO films with varying thickness (0.5-1.8 µm) and on mesoATO (50 nm thick) in comparison to flat ITO (grey line). CVs were recorded in 0.1 M H_2SO_4 with a scan rate of 1 mV s^{-1}. The inset shows the Mo-POM loading normalized to the film volume as a function of the film thickness.

The possibility to control and tailor the accessible porosity, combined with the good electrical conductivity and optical transparency, makes the obtained ATO films an ideal material for hosting photo/electroactive biomolecules such as nanosized proteins and enzymes. This is of particular importance for the development of bioelectronic devices based on underlying electron transfer between the biomolecules and surfaces. In order to test the suitability of our meso/macroporous electrode architectures for these applications, the large photoactive photosystem I (PSI) protein complex has been chosen as a model system. Due to a practically unity quantum efficiency [7,12,68,69] and a unidirectional electron transport vector, PSI is intensively explored by various groups as an attractive energy conversion unit for fabrication of biophotovoltaic devices.[2,7,70] The major challenge in this context is achieving effective interfacial electrochemical responses of a sufficiently high loading of responsible bioentities, which can be partially addressed by the use of porous extended current collectors.

For the electrode fabrication we have used PSI isolated from Arabidopsis thaliana wild type (ecotype Columbia) plants[71,72] with a mean size of ca. 13 nm. The PSI complexes were assembled on the electrode surfaces using vacuum-assisted deposition of thick layers according to an already established procedure.[70] To explore the impact of pore size on the efficiency of PSI incorporation, the biomolecules were deposited on porous ATO electrodes

NANOSTRUCTURED ANTIMONY DOPED TIN OXIDE LAYERS WITH TUNABLE PORE
ARCHITECTURES AS VERSATILE TRANSPARENT CURRENT COLLECTORS FOR

129

with the same thickness of ca. 1.8 µm but the different pore size (mesoATO and macroATO, respectively), as well as on planar ITO electrodes.

According to UV-vis spectra, all electrodes contain the same amount of PSI directly after deposition. The mechanical stability of the vacuum-dried thick PSI layers is however very poor, and the larger part of the deposited PSI is washed away after incubating the electrodes in operational buffer solution or after prolonged electrochemical measurements. The UV-vis spectra of the washed electrodes exhibit no spectral characteristics of bound PSI for the planar ITO and mesoATO electrodes. However, for the macroATO electrodes characteristic bands at wavelengths between 420–440 nm and 670–680 nm consistent with the chlorophylls of bound PSI could be observed also after washing (Figure 4.5). The total loading of PSI in macroATO electrodes after washing was calculated to be 9.5 ± 1.8 pmol/cm^2 (see Experimental part for further details). Taking into account the real surface area (roughness factor) of the macroporous ATO electrodes of 97 cm^2/cm^2 determined by Kr sorption, we derive a PSI surface coverage of 0.10 ± 0.02 pmol/cm^2. Compared to published surface coverage values for a PSI monolayer (ca. 0.7 pmol/cm^2)[73], it is reasonable to conclude that less than a monolayer of PSI is adsorbed on the inner surface of the macroporous ATO electrodes.
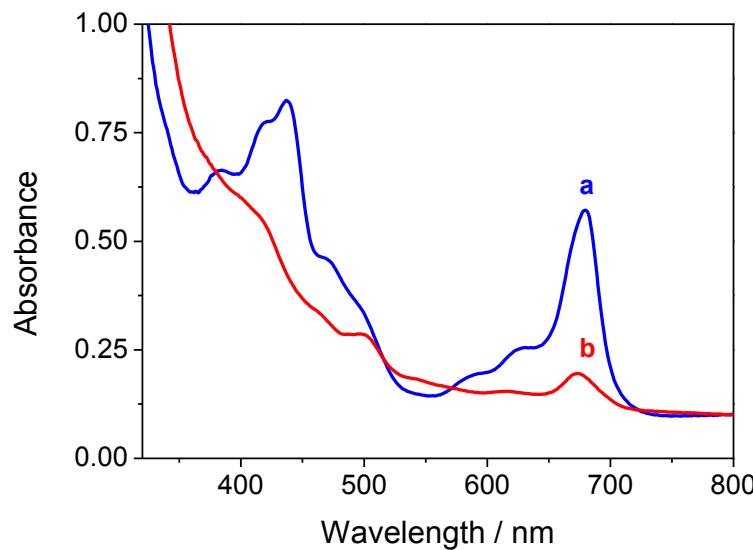
Figure 4.5   UV-visible absorption spectra of PSI films fabricated on macroATO: (a) after a vacuum-assisted drop casting; b) the same electrode after soaking in an operational buffer. Both spectra display features typical for PSI complexes.

The operational performance of the PSI-ITO, PSI-mesoATO and PSI-macroATO electrodes has been followed by photochronoamperometric and chopped light potentiodynamic measurements under illumination with white light and an intensity of 100 mW cm^{-2} (1 sun).

Illumination of PSI-loaded samples results in photoactivated charge separation at the internal P_{700} site, which drives an electron through the protein complex until it reaches the iron-sulfur cluster located on the stromal site of PSI. In contrast to small redox molecules like Mo-POM performing direct electrochemistry, in large protein complexes the active sites are embedded in the interior of the proteins, so that the direct electron transfer between the protein and the electrode is very unlikely.[74] Therefore, a 2,6-dichlorophenolindophenol (DCPIP/DCPIPH$_2$) / ascorbic acid mixture has been used as a commonly applied redox shuttle for the PSI based systems.[70,75-77] Control experiments reveal that both ITO and ATO scaffolds alone are not photoactive, so that the generated current upon illumination can only be attributed to bound PSI. The equilibrium potential at which no current was measured has been determined from the chopped light potentiodynamic measurements to be $+50 \pm \pm 20$ mV vs. Ag/AgCl for each electrode (see Figure 4.6a). It means that for potentials more positive and more negative than this value anodic and cathodic currents, respectively, have been measured under illumination.
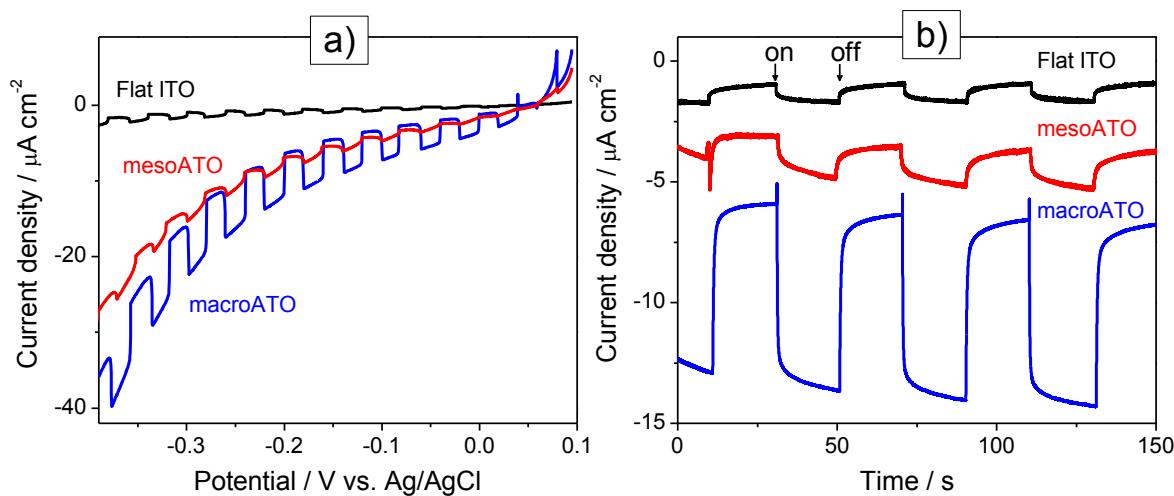
Figure 4.6   Photoelectrochemical measurements of PSI-modified macroATO electrode (blue line), mesoATO electrode (red line) and a flat ITO (black line) in DCPIP/ascorbic acid in 5 mmol phosphate buffer: (a) chopped light potentiodynamic measurements and (b) photochronoamperometry at -0.3 V vs. Ag/AgCl. The measurements were performed with a light intensity of 1 sun; exposed area of the electrodes is 0.196 cm^2.

Figure **4.6**b summarizes the performances of PSI-flat ITO, PSI-mesoATO and PSI-macroATO electrodes measured at E = -0.3 V vs. Ag/AgCl. Even if UV-vis measurements did not detect PSI bound on washed flat ITO and mesoATO electrodes due to a low loading, photocurrents with a density of ~0.7 μA cm^{-2} and 1.5 μA cm^{-2} could be measured for both electrodes upon illumination. These photocurrents can be clearly attributed to some amount of PSI bound to the electrodes. The 2-fold increased photocurrent of PSI on mesoporous ATO

NANOSTRUCTURED ANTIMONY DOPED TIN OXIDE LAYERS WITH TUNABLE PORE
ARCHITECTURES AS VERSATILE TRANSPARENT CURRENT COLLECTORS FOR

131

electrodes compared to flat ITO can be explained by its higher surface area resulting from the higher surface roughness of thick mesoATO electrodes. The PSI-macroATO electrodes show significantly enhanced photocurrent densities of ~7.7 $\mu A\,cm^{-2}$ compared to flat or mesoporous electrodes. The 11-fold increase in the photocurrent density of PSI on macroATO electrodes compared to that on flat ITO is a clear indication of the increased PSI loading due to the higher surface area of macroporous electrodes. It is remarkable that the mesoATO electrodes featuring the highest specific surface area and correspondingly the highest uptake of small molecules such as Mo-POM described above show practically no advantages when combined with the large bioentities. This fact clearly demonstrates the importance of pore size control in the design of hybrid electrode systems and makes macroATO electrodes with the pore size of ca. 80 nm a promising electrode morphology. Noteworthy in this respect is also a very high long-term stability of the PSI integrated into porous electrode scaffold. After 70 and 140 days at 4 °C in air the current density decreased only by 33% and 40%, respectively, of their initial photocurrent (see Figure S4.9 in the supporting information), which is a very good value for a non-optimized system without use of stabilizing peptide surfactants[7] or polymer films[78].

From the determined surface coverage we can now calculate the ensemble turnover of the enzyme within the macropores and ensure that appreciable activity of the enzyme is conserved. The turnover rate k_{cat} is defined as the maximum photocurrent (C/s), contributed only from PSI, divided by the quantity of PSI on the surface. Using the known surface coverage of PSI on the electrode and its photocurrent contribution, we have calculated the turnover rate to be 8.4 ± 0.5 electrons $s^{-1}\,PSI^{-1}$. In spite of the inefficient mediator system used in our study, this value is significantly higher than the turnover rate values determined for differently modified electrodes, reported to be in the range from 0.2–5 electrons $s^{-1}\,PSI^{-1}$.[78-81] Taking into account that the walls of macroporous ATO electrode are electrically conducting and that the PSI incorporated in the pores is in direct contact with the electrode surface, the mediator molecules travel much shorter distances to the electrode compared to multilayer or polymer electrodes with a similar thickness. Therefore, we can explain the higher value of k_{cat} by a large electrode–biomolecule contact area and shorter diffusion pathways for the electron transportation towards the electrode. Significantly higher values of k_{cat} of 335 ± 20 electrons $s^{-1}\,PSI^{-1}$ were reported only by Plumere[82] who applied a much more efficient redox hydrogel mediator for wiring the PSI to the electrode surface. It should be however noticed that the reasonably high photocurrents of 7.7 $\mu A\,cm^{-2}$ were obtained on macroATO electrodes for less than a monolayer of PSI adsorbed on the electrode without any optimization of the interfacial

electron transfer. It can be expected that even higher electron-transfer rates and absolute photocurrent values may be achieved by combining porous electrodes developed in our work with optimized mediator systems.

4.3. CONCLUSIONS

Self-assembly of preformed ATO nanoparticles with a high molar mass poly(ethylene oxide-*b*-hexyl acrylate) (PEO-*b*-PHA) block copolymer enables a facile fabrication of porous transparent conducting layers with a tunable morphology. The pore structure was shown to be extremely sensitive to the amount of HCl in the coating solution and to a less extent to the choice of solvent, so that porous structures with pore sizes ranging from small mesopores (10nm) to disordered macropores (50-300nm) could be obtained. Of special interest is a possibility to fabricate macroporous films featuring large uniform spherical pores with the size of around 80 nm, which is difficult to achieve by any of the literature techniques. The porous ATO electrodes feature a greatly increased specific surface area compared to the planar electrodes, which is defined by the pore size and the film thickness. For the application as conducting electrodes it is important that the increase in surface area due to the nanostructuring fully translates into an increase in accessible conducting interface. This was demonstrated by adsorption of the small molybdenum polyoxometalate anion $PMo_{12}O_{40}{}^{3-}$ that show a significant increase in electrochemical response proportional to the accessible surface area. Most importantly we show the suitability of our electrodes to host photoactive biomolecules exemplified by the adsorption of the large protein complex PSI. UV-vis spectroscopy and photoelectrochemical measurements indicated that PSI is incorporated into the ca. 80 nm pores of macroATO, but not into the smaller pores of mesoATO, resulting in an 11-fold enhancement of the photocurrent compared to PSI adsorbed on flat ITO. The increase in the photocurrent density for PSI immobilized on macroATO electrodes clearly demonstrates the importance of nanostructuring and the nanostructure dimensions for the photoelectrochemical performance of hybrid electrodes. Even though our system can still be further optimized (pore size, thickness, protein orientation, experimental conditions etc.), the revealed data successfully verify the integration of large PSI molecules into the nanostructured transparent conducting oxide without losing its activity and original optoelectronic properties. Therefore, we believe it to be a promising scaffold for the fabrication of biophotovoltaic devices.

NANOSTRUCTURED ANTIMONY DOPED TIN OXIDE LAYERS WITH TUNABLE PORE
ARCHITECTURES AS VERSATILE TRANSPARENT CURRENT COLLECTORS FOR

133

4.4. EXPERIMENTAL SECTION

Synthesis: Antimony doped tin oxide (ATO) nanoparticles with a Sb doping level of 5 at% were prepared by a solvothermal route in *tert*-butanol described elsewhere[40]. In brief, 4.54 mL (4.54 mmol) of tin(IV) chloride (1 M in CH_2Cl_2) and 0.24 mL (0.24 mmol) of antimony(V) chloride solution (1.0 M in CH_2Cl_2) were dissolved in 9.22 ml of *tert*-butanol (all from Aldrich) and heated in a hermetically sealed Teflon lined autoclave at 100 °C for 20 h. The nanoparticles were flocculated by an addition of 14 mL of dichloromethane, separated by centrifugation (47800 rcf for 10 min), washed twice in 14 mL of acetone and centrifuged again at 4780 rcf for 10 min.

PEO-*b*-PHA diblock copolymer was synthesized by using atom transfer radical polymerization and the method is described in detail elsewhere.[54] The molar mass of the PHA was determined as 46,000 g/mol by 1H NMR relative to the 20,000 g/mol PEO macroinitiator. The molar mass dispersity was obtained as 1.2 using the gel permeation chromatography (GPC).

Fabrication of mesoporous and macroporous ATO layers: Mesoporous (mesoATO) and macroporous ATO (macroATO) layers were fabricated from preformed ATO nanoparticles and a PEO-*b*-PHA block copolymer. For the fabrication of the macroATO electrodes, dry nanoparticles (12.5 mg) were dispersed in 125 µl of ethanol and 45 µL concentrated hydrochloric acid. Separately, the polymer (25 mg) was dissolved in 1.25 mL inhibitor-free THF (anhydrous, ≥99.9%, Aldrich) with stirring at 60 °C until the turbid white/yellow solution turned clear. The two dispersions were combined and stirred for 24 h. The homogeneous mixture was drop-cast (10-125 µl) onto 2.25 cm^2 ITO or Si wafer, dried at room temperature (20 °C) and calcined in air at 500 °C for 30 min (achieved with a ramp of 1.25 °C min^{-1}). Worm-like mesoporous and disordered macroporous morphologies were fabricated by varying the amount of HCl in the ethanolic nanoparticle dispersion. For worm-like structures (Figure 4.1b) 12.5 mg nanoparticles were dispersed in 125 µl EtOH and 18 µl of HCl, whereas for disordered macroporous structures (Figure 4.1d) 70 µl of HCl was added to 125 µl EtOH. Thin macroATO films were prepared as described above using a higher I:O of 1:1 (25 mg ATO dispersed in 125 µl of ethanol and 45 µL concentrated hydrochloric acid). The ATO/polymer dispersion was spin-coated (80 µl, 1000 rpm, 20 s) on ITO or Si substrates. The mesoporous ATO films were prepared by dispersing ATO nanoparticles (12.5 mg) in

375 µl of inhibitor-free THF and 10 µL concentrated hydrochloric acid. Separately the block copolymer was dissolved in inhibitor-free THF as described above and combined with the ATO dispersion. After 24 h the homogeneous dispersions were drop- or spin-coated and calcined similar to the macroATO layers described above. The film thickness can be varied between 500 nm and 1.8 µm by changing the amount of the drop casting solution from 15 to 60 µl. The films obtained by drop casting show a very good uniformity over the larger area except the edges, where the film is thicker and partially peels off the substrate. The edge area is however relatively small compared to the total film area. Thicker films up to 4 µm can be prepared by drop casting 150 µl coating solution either in one step or by a subsequent coating of 75 µl, but these films showed large cracks and a very inhomogeneous film thickness. Thinner films were obtained by spin coating (film thickness 130 nm, see Table 4.1). The synthesis quantities are summarized in Table 4.1.

Table 4.1   Synthesis quantities for the different ATO morphologies with varying solvents, HCl amounts and I:O ratios. The mixed solubility parameters were calculated for each of the processing solutions, which were used to rank the films in terms of the X interaction parameter between PHA and the solvent. Higher values lead to micelles of increasing size, while smaller values lead to bulk morphologies.

name	I:O	polymer solution		NP solution				mixed solubility parameter	X-ranking PHA-solvent	description
		polymer (mg)	THF (mL)	ATO	THF (mL)	EtOH (mL)	HCL (uL)			
mesoATO	0.5	25	1.25	12.5	0.375	0	10	18.7	1	micellar
worm	0.5	25	1.25	12.5	0	0.125	18	19.5	2	worm like
macroATO	0.5	25	1.25	12.5	0	0.125	45	20.0	3	inverse micelle
disordered ATO	0.5	25	1.25	12.5	0	0.125	70	20.3	4	inverse micelle
spin	1	25	1.25	25	0	0.125	45	20.0	3	inverse micelle

Isolation of Photosystem I complexes from Arabidopsis thaliana: Arabidopsis thaliana wild type (ecotype Columbia) plants were grown in soil in a growth chamber at 80-100 µmol m^{-2} s^{-1} with a 12 h photoperiod. Material from 5-6 week old plants was used for thylakoid isolation[72] and subsequent photosystem I complex preparation[71]. Leaves were homogenized in 400 mM sorbitol, 50 mM Tricine pH 7.5, 0.2 mM phenylmethylsulfonyl fluoride (all from Roth), 1 mM benzamidine, and 5 mM aminocaproic acid (both from Sigma) and filtered through a mesh (Miracloth, Merck). After centrifugation (8,000×g, 5 min), thylakoids were washed twice in 5 mM EDTA pH 7.8 (Sigma; each centrifugation at 23,500×g, 5 min) and resuspended in water. Thylakoids were solubilized at a chlorophyll concentration of 1 mg/mL[83] in 1% dodecyl-β-D-maltoside (Sigma) at 0°C for 10 min. After centrifugation (16,000×g, 5 min), the supernatant was separated at 270,000×g, 4°C for 21 hours in a

NANOSTRUCTURED ANTIMONY DOPED TIN OXIDE LAYERS WITH TUNABLE PORE
ARCHITECTURES AS VERSATILE TRANSPARENT CURRENT COLLECTORS FOR

135

continuous sucrose gradient (400 mM sucrose (Roth), 20 mM Tricine pH 7.5, 0.06% dodecyl-β-D-maltoside), frozen, and thawn overnight at 4°C. After collection of the photosystem I complex fraction, the chlorophyll content was determined.

Adsorption of electroactive guests: For immobilization of Keggin-Type molybdenum polyoxometalate anion $PMo_{12}O_{40}^{3-}$ (Mo-POM), the electrodes were immersed overnight in a 5 mM solution of phosphomolybdic acid hydrate (Aldrich) in 0.1 M H_2SO_4, washed in 0.1 M H_2SO_4 and dried in air at room temperature for 3 hours. For the electrochemical characterization, the electrodes were masked with a Teflon-coated glass fiber adhesive tape leaving an exposed area of 0.785 cm^2, and measured in 0.1 M H_2SO_4 using a typical three-electrode system with Ag/AgCl/3M KCl as reference electrode and a Pt wire as counter electrode. Cyclic voltammetry measurements (Mo-POM) were carried out with a scan rate of 1 mV s^{-1} and a step potential of 0.24 mV in a potential range between 0.05 and +0.7 V vs. Ag/AgCl/3M KCl. The electrochemical loading per cm^2 (*n*) was calculated using the Faraday's law: $n = (Q/z\,F\,A)$, where *Q* is the total electric charge (peak area), *z* is the number of electrons transferred per ion ($z = 6$), *F* is the Faraday constant (96485 C mol^{-1}) and *A* the exposed area (0.785 cm^2). The Mo-POM surface coverage on flat electrodes equals $4.95 \cdot 10^{-11}$ mol cm^{-2}, which is in the same range as reported by Kuhn et al.[63] (5-$10 \cdot 10^{-11}$ mol cm^{-2}) and by Fattakhova et al.[67] ($2 \cdot 10^{-11}$ mol cm^{-2}) for monolayer adsorption. Comparing POM functionalized macroATO with flat ITO films, we could observe a 410-fold, a 650-fold and a 850-fold increase for 0.5 μm, 1 μm and 1.8 μm thick films, respectively. This increase is higher than predicted for monolayer adsorption and suggests that we deal with multilayer adsorption. Normalized to the film thickness and the surface roughness (determined from sorption measurements) we could observe loadings of $4.3 \cdot 10^{-6}$ mol m^{-2}, $5.9 \cdot 10^{-6}$ mol m^{-2} and $7.4 \cdot 10^{-6}$ mol m^{-2} for 0.5 μm, 1 μm and 1.8 μm thick macroATO films and $4.1 \cdot 10^{-6}$ mol m^{-2} for a 50 nm mesoATO film. These normalized values are all in the same range showing the homogeneous multilayer adsorption inside the porous structure.

The conducting surface area was evaluated from the capacitive current measurements. The electrodes with exposed area of 0.785 cm^2 were cycled at scan rates ranging from 2 to 50 mV in (electrolyte, buffer) in a potential range between -0.05 and -0.2 V vs. Ag/AgCl/3M KCl, where no Faradaic processes take place. The capacitance was obtained as the slope of dependence of currents at -0.1 V vs. scan rate (see Figure S4.8 in the supporting information). Assuming a specific capacitance of 60 uF cm^{-2} for flat oxide electrodes[60-62], we obtained surface areas of 57 $cm^2\,cm^{-2}$ and 103 $cm^2\,cm^{-2}$ for 1 μm and 1.8 um thick macroATO electrodes.

PSI was immobilized on mesoATO and macroATO as well as on flat ITO electrodes by drop casting 10 μL of the buffered PSI solution (containing 4.9 μg/μL PSI) on a masked area of 0.196 cm^2. After impregnation overnight, the films were dried under vacuum and measured in an aqueous electrolyte composed of 5 mM sodium 2,6-dichloroindophenolate hydrate (Aldrich), 100 mM ascorbic acid (Acros), and 100 mM NaCl (Aldrich) in 5 mM pH 7 phosphate buffer (Acros) using a typical three-electrode system with Ag/AgCl/3M KCl as reference electrode and a Pt wire as counter electrode. Photochronoamperometric light on/off measurements were performed under illumination through the substrate side using an AM 1.5 solar simulator (Solar Light Model 16S) at 100 mW cm^{-2} (1 sun) (interval time of 0.01 s). Potentiodynamic light on/off measurements were performed with a scan rate of 1 mV s^{-1} in a potential range between −0.5 and +0.1 V vs. Ag/AgCl/3M KCl.

The incorporation of PSI into the porous structure was followed by UV-Vis spectroscopy (see Figure 4.5). The comparison of the spectra reveals that a certain amount of PSI is washed away after soaking in electrolyte, since the observed absorbance of the chlorophyll bands corresponding to incorporated PSI decreased ~5.25-fold. These results have been used to calculate the surface coverage for both electrodes. For the initial dried PSI electrodes a value of 49 ± 9 pmol cm^{-2} has been derived, whereas 9.5 ± 1.8 pmol cm^{-2} has been calculated for the electrodes soaked in buffer. Taking into account the above determined roughness factor related to real (geometrical) surface of 97 cm^2 cm^{-2}, we derive the real PSI coverage of 0.10 ± 0.02 pmol cm^{-2}.

Characterization methods: Wide angle X-ray diffraction analysis was carried out in transmission mode using a STOE STADI P diffractometer with CuK$_{\alpha1}$-radiation (λ = 1.54060 Å) and a Ge(111) single crystal monochromator equipped with a DECTRIS solid state strip detector MYTHEN 1K. Powder XRD patterns of the samples were collected in a 2θ range from 5° to 70° with a step size of 1° and a fixed counting time of 45 seconds per step. The size of the crystalline domains was calculated from the XRD patterns for the most intensive ATO signal (110 reflection) using the Scherrer equation.

GISAXS X-ray scattering experiments were performed using a SAXSLab Ganesha at the South Carolina SAXS Collaborative. A Xenocs GeniX3D microfocus source was used with a Cu target to generate a monochromatic beam with a 0.154 nm wavelength. The instrument was calibrated using a NIST reference material 640c and checked with a silver behenate reference with the first order scattering vector $q* = 1.076$ nm^{-1}, where $q = 4\pi\lambda^{-1}\sin\theta$ with a total scattering angle of 2θ. A Pilatus 300 K detector (Dectris) was used to collect the two-

NANOSTRUCTURED ANTIMONY DOPED TIN OXIDE LAYERS WITH TUNABLE PORE
ARCHITECTURES AS VERSATILE TRANSPARENT CURRENT COLLECTORS FOR

137

dimensional (2D) scattering patterns. Radial integration of 2D WAXS patterns reduced the data to 1D profiles using SAXS GUI software. GISAXS experiments were conducted with an incident angle near 0.25^o, and the samples were rotated relative to the incident beam as shown in Figure S4.6 in the Supporting information. The sample-to-detector distance of 1050 mm was used. The in-plane q_y data were processed using Matlab scripts and the following Equation 4.1[84] where, α_f is the in-plane scattering angle, the out-of-plane scattering angle Ψ and wavelength of monochromatic beam λ.

$$q_y = \frac{2\pi \cos \alpha_f \sin\Psi}{\lambda} \qquad \text{Equation 4.1}$$

Dynamic light scattering (DLS) measurements were performed on a MALVERN Zetasizer-Nano instrument equipped with a 4 mW He-Ne laser ($\lambda = 633$ nm) and an avalanche photodiode detector.

Krypton sorption isotherms were obtained at the boiling point of liquid nitrogen (77 K) using a Micromeritics ASAP 2010 volumetric adsorption unit. Three 1.5×1.5 cm^2 glass slides coated with porous ATO films were simultaneously measured. Prior to the adsorption experiments, the sample was outgassed in a tailor-made cell at 180 °C for 24 hours. The surface area was calculated using the BET equation, as an average from three independent experiments. The saturation pressure of solid krypton of ca. 1.6 Torr and the occupied area of the krypton molecules in a complete monolayer of 0.21 nm^2 were used for the calculations (as provided by the Micromeritics software).

SEM images were obtained with a JEOL JSM-6500F scanning electron microscope equipped with a field emission gun operated at 5 kV. The films were prepared on ITO substrates and glued onto a brass sample holder with silver lacquer.

Atomic force microscopy (AFM) images were recorded with a Nanoink NScriptor DPN system in tapping mode.

TEM measurements were carried out using a FEI Tecnai G2 20 S-TWIN equipped with a field emission gun operated at 200 kV. For the sample preparation, a macroporous ATO film was scratched from an ITO substrate, placed on a holey carbon coated copper grid and evaporated.

Absorbance and transmission spectra of the samples were measured with a Perkin Elmer Lambda 1050 spectrophotometer equipped with an integrating sphere.

Electrochemical measurements were performed on a µ-Autolab III potentiostat (Metrohm) at room temperature in a quartz cell using a typical three-electrode system with Mo-POM or PSI modified meso-ATO films on ITO as working electrode, Ag/AgCl/3M KCl as reference electrode and a Pt wire as a counter electrode.

4.5. REFERENCES

(1)   Kato, M.; Zhang, J. Z.; Paul, N.; Reisner, E. *Chem. Soc. Rev.* **2014**, *43*, 6485.

(2)   Kothe, T.; Plumere, N.; Badura, A.; Nowaczyk, M. M.; Guschin, D. A.; Rogner, M.; Schuhmann, W. *Angew. Chem. Int. Ed.* **2013**, *52*, 14233.

(3)   Amdursky, N.; Marchak, D.; Sepunaru, L.; Pecht, I.; Sheves, M.; Cahen, D. *Adv. Mater.* **2014**, *26*, 7142.

(4)   Kamran, M.; Delgado, J. D.; Friebe, V.; Aartsma, T. J.; Frese, R. N. *Biomacromolecules* **2014**, *15*, 2833.

(5)   Kothe, T.; Poller, S.; Zhao, F.; Fortgang, P.; Rogner, M.; Schuhmann, W.; Plumere, N. *Chem. Eur. J.* **2014**, *20*, 11029.

(6)   LeBlanc, G.; Chen, G.; Gizzie, E. A.; Jennings, G. K.; Cliffel, D. E. *Adv. Mater.* **2012**, *24*, 5959.

(7)   Mershin, A.; Matsumoto, K.; Kaiser, L.; Yu, D.; Vaughn, M.; Nazeeruddin, M. K.; Bruce, B. D.; Graetzel, M.; Zhang, S. *Sci. Rep.* **2012**, *2*, 234.

(8)   Zhao, F.; Conzuelo, F.; Hartmann, V.; Li, H.; Nowaczyk, M. M.; Plumere, N.; Rogner, M.; Schuhmann, W. *J. Phys. Chem. B* **2015**, *119*, 13726.

(9)   Lai, Y. H.; Kato, M.; Mersch, D.; Reisner, E. *Faraday Discuss.* **2015**, *176*, 199.

(10)   Nocera, D. G. *Acc. Chem. Res.* **2012** *45*, 767.

(11)   Ocakoglu, K.; Krupnik, T.; van den Bosch, B.; Harputlu, E.; Gullo, M. P.; Olmos, J. D. J.; Yildirimcan, S.; Gupta, R. K.; Yakuphanoglu, F.; Barbieri, A.; Reek, J. N. H.; Kargul, J. *Adv. Funct. Mater.* **2014**, *24*, 7467.

(12)   Yu, D.; Wang, M.; Zhu, G.; Ge, B.; Liu, S.; Huang, F. *Sci. Rep.* **2015**, *5*, 9375.

(13)   Kato, M.; Cardona, T.; Rutherford, A. W.; Reisner, E. *J. Am. Chem. Soc.* **2013**, *135*, 10610.

(14)   Liu, Y.; Peters, K.; Mandlmeier, B.; Müller, A.; Fominykh, K.; Rathousky, J.; Scheu, C.; Fattakhova-Rohlfing, D. *Electrochim. Acta* **2014**, *140*, 108.

(15)   Sarauli, D.; Peters, K.; Xu, C.; Schulz, B.; Fattakhova-Rohlfing, D.; Lisdat, F. *ACS Appl. Mater. Interfaces* **2014**, *6*, 17887.

(16)   Sarauli, D.; Wettstein, C.; Peters, K.; Schulz, B.; Fattakhova-Rohlfing, D.; Lisdat, F. *ACS Catal.* **2015**, *5*, 2081.

(17)   Mersch, D.; Lee, C. Y.; Zhang, J. Z.; Brinkert, K.; Fontecilla-Camps, J. C.; Rutherford, A. W.; Reisner, E. *J. Am. Chem. Soc.* **2015**, *137*, 8541.

(18) Moir, J.; Soheilnia, N.; O'Brien, P.; Jelle, A.; Grozea, C. M.; Faulkner, D.; Helander, M. G.; Ozin, G. A. *ACS Nano* **2013**, *7*, 4261.

(19) Luo, H.; Fang, Z.; Song, N.; Garvey, T.; Lopez, R.; Meyer, T. J. *ACS Appl. Mater. Interfaces* **2015**, *7*, 25121.

(20) Brongersma, M. L.; Cui, Y.; Fan, S. *Nat. Mater.* **2014**, *13*, 451.

(21) Walcarius, A.; Kuhn, A. *TrAC, Trends Anal. Chem.* **2008**, *27*, 593.

(22) Szamocki, R.; Reculusa, S.; Ravaine, S.; Bartlett, P. N.; Kuhn, A.; Hempelmann, R. *Angew. Chem. Int. Ed.* **2006**, *45*, 1317

(23) Heim, M.; Reculusa, S.; Ravaine, S.; Kuhn, A. *Adv. Funct. Mater.* **2012**, *22*, 538.

(24) Fattakhova-Rohlfing, D.; Brezesinski, T.; Rathouský, J.; Feldhoff, A.; Oekermann, T.; Wark, M.; Smarsly, B. M. *Adv. Mater.* **2006**, *18*, 2980.

(25) Pohl, A.; Dunn, B. *Thin Solid Films* **2006**, *515*, 790.

(26) Frasca, S.; Milan, A.; Guiet, A.; Goebel, C.; Pérez-Caballero, F.; Stiba, K.; Leimkühler, S.; Fischer, A.; Wollenberger, U. *Electrochim. Acta* **2013**, *110*, 172.

(27) Müller, V.; Rasp, M.; Rathousky, J.; Schutz, B.; Niederberger, M.; Fattakhova-Rohlfing, D. *Small* **2010**, *6*, 633.

(28) Müller, V.; Rathousky, J.; Fattakhova-Rohlfing, D. *Electrochim. Acta* **2014**, *116*, 1.

(29) Kwan, P.; Schmitt, D.; Volosin, A. M.; McIntosh, C. L.; Seo, D. K.; Jones, A. K. *Chem. Commun.* **2011**, *47*, 12367.

(30) Nong, H. N.; Oh, H. S.; Reier, T.; Willinger, E.; Willinger, M. G.; Petkov, V.; Teschner, D.; Strasser, P. *Angew. Chem. Int. Ed.* **2015**, *54*, 2975.

(31) Oh, H.-S.; Nong, H. N.; Strasser, P. *Adv. Funct. Mater.* **2015**, *25*, 1074.

(32) Liu, Y.; Stefanic, G.; Rathousky, J.; Hayden, O.; Bein, T.; Fattakhova-Rohlfing, D. *Chem. Sci.* **2012**, *3*, 2367.

(33) Walcarius, A. *Chem. Soc. Rev.* **2013**, *42*, 4098.

(34) Zhou, H.; Ge, J.; Zhang, M.; Yuan, S. *Res. Chem. Intermed.* **2016**, *42*, 1929.

(35) Renault, C.; Andrieux, C. P.; Tucker, R. T.; Brett, M. J.; Balland, V.; Limoges, B. *J. Am. Chem. Soc.* **2012**, *134*, 6834.

(36) Beaudry, A. L.; LaForge, J. M.; Tucker, R. T.; Li, P.; Taschuk, M. T.; Brett, M. J. *Cryst. Growth Des.* **2013**, *13*, 212.

(37) Krause, K. M.; Taschuk, M. T.; Harris, K. D.; Rider, D. A.; Wakefield, N. G.; Sit, J. C.; Buriak, J. M.; Thommes, M.; Brett, M. J. *Langmuir* **2010**, *26*, 4368.

(38) Arsenault, E., N. Soheilnia, and G.A. Ozin, *ACS Nano* **2011**, *5*, 2984.

(39) Zhang, X. a.; Man, Y.; Wang, J.; Liu, C.; Wu, W. *Sci. China Ser. E: Technol. Sci.* **2006**, *49*, 537.

(40) Peters, K.; Zeller, P.; Stefanic, G.; Skoromets, V.; Němec, H.; Kužel, P.; Fattakhova-Rohlfing, D. *Chem. Mater.* **2015**, *27*, 1090.

(41) Tétreault, N.; Arsenault, É.; Heiniger, L.-P.; Soheilnia, N.; Brillet, J.; Moehl, T.; Zakeeruddin, S.; Ozin, G. A.; Grätzel, M. *Nano Lett.* **2011**, *11*, 4579.

(42) Smarsly, B.; Fattakhova-Rohlfing, D. In *Solution processing of inorganic materials* Mitzi, D. B., Ed.; John Wiley & Sons: Hoboken, New Jersey, 2009, p 283.

(43) Graberg, T. v.; Hartmann, P.; Rein, A.; Gross, S.; Seelandt, B.; Röger, C.; Zieba, R.; Traut, A.; Wark, M.; Janek, J.; Smarsly, B. M. *Sci. Technol. Adv. Mater.* **2011**, *12*, 025005.

(44) Wang, Y.; Brezesinski, T.; Antonietti, M.; Smarsly, B. *ACS Nano* **2009**, *3*, 1373.

(45) Brezesinski, T.; Fischer, A.; Iimura, K. i.; Sanchez, C.; Grosso, D.; Antonietti, M.; Smarsly, B. M. *Adv. Funct. Mater.* **2006**, *16*, 1433.

(46) Hamd, W.; Chavarot-Kerlidou, M.; Fize, J.; Muller, G.; Leyris, A.; Matheron, M.; Courtin, E.; Fontecave, M.; Sanchez, C.; Artero, V.; Laberty-Robert, C. *J. Mater. Chem. A* **2013**, *1*, 8217.

(47) Suzuki, N.; Kamachi, Y.; Chiang, Y. D.; Wu, K. C. W.; Ishihara, S.; Sato, K.; Fukata, N.; Matsuura, M.; Maekawa, K.; Tanabe, H.; Ariga, K.; Yamauchi, Y. *Crystengcomm* **2013**, *15*, 4404.

(48) Suzuki, N.; Imura, M.; Sato, K.; Fukata, N.; Matsuura, M.; Maekawa, K.; Yamauchi, Y. *Dalton Trans.* **2013**, *42*, 6366.

(49) Hou, K.; Puzzo, D.; Helander, M. G.; Lo, S. S.; Bonifacio, L. D.; Wang, W.; Lu, Z.-H.; Scholes, G. D.; Ozin, G. A. *Adv. Mater.* **2009**, *21*, 2492.

(50) Rauda, I. E.; Buonsanti, R.; Saldarriaga-Lopez, L. C.; Benjauthrit, K.; Schelhas, L. T.; Stefik, M.; Augustyn, V.; Ko, J.; Dunn, B.; Wiesner, U.; Milliron, D. J.; Tolbert, S. H. *ACS Nano* **2012**, *6*, 6386.

(51) Volosin, A. M.; Sharma, S.; Traverse, C.; Newman, N.; Seo, D. K. *J. Mater. Chem.* **2011**, *21*, 13232.

(52) Sharma, S.; Volosin, A. M.; Schmitt, D.; Seo, D. K. *J. Mater. Chem. A* **2013**, *1*, 699.

(53) Stefik, M.; Song, J.; Sai, H.; Guldin, S.; Boldrighini, P.; Orilall, M. C.; Steiner, U.; Gruner, S. M.; Wiesner, U. *J. Mater. Chem. A* **2015**, *3*, 11478.

(54) Lokupitiya, H. N.; Jones, A.; Reid, B.; Guldin, S.; Stefik, M. *Chem. Mater.* **2016**, *28*, 1653.

(55) Ong, G. K.; Williams, T. E.; Singh, A.; Schaible, E.; Helms, B. A.; Milliron, D. J. *Nano Lett.* **2015**, *15*, 8240.

(56) Hartmann, P.; Lee, D.-K.; Smarsly, B. M.; Janek, J. *ACS Nano* **2010**, *4*, 3154.

(57) Wang, X. D., E. E.; Lodge, T. P. *Macromolecules* **2002**, *35*, 9687.

(58) Rathouský, J.; Kalousek, V.; Yarovyi, V.; Wark, M.; Jirkovský, J. *J. Photochem. Photobiol. A: Chem.* **2010**, *126*, 216.

(59) Rathouský, J.; Kalousek, V.; Kolář, M.; Jirkovský, J.; Barták, P. *Catal. Today* **2011**, *161*, 202.

(60) McCrory, C. C.; Jung, S.; Peters, J. C.; Jaramillo, T. F. *J. Am. Chem. Soc.* **2013**, *135*, 16977.

(61) Louie, M. W.; Bell, A. T. *J. Am. Chem. Soc.* **2013**, *135*, 12329.

(62) Trasatti, S.; Petrii, O. A. *Pure & Appl. Chem.* **1991**, *63*, 711.

(63) Kuhn, A.; Mano, N.; Vidal, C. *J. Electroanal. Chem.* **1999**, *462* 187.

(64) Klemperer, W. G.; Wall, C. G. *Chem. Rev.* **1998**, *98*, 297.

(65) Kuhn, A.; Anson, F. C. *Langmuir* **1996**, *12*, 5481.

NANOSTRUCTURED ANTIMONY DOPED TIN OXIDE LAYERS WITH TUNABLE PORE
ARCHITECTURES AS VERSATILE TRANSPARENT CURRENT COLLECTORS FOR

141

(66) Li, L.; Li, W.; Sun, C.; Li, L. *Electroanal.* **2002**, *14*, 368.

(67) Fattakhova Rohlfing, D.; Rathousky, J.; Rohlfing, Y.; Bartels, O.; Wark, M. *Langmuir* **2005**, *21*, 11320.

(68) Gordiichuk, P. I.; Wetzelaer, G. J.; Rimmerman, D.; Gruszka, A.; de Vries, J. W.; Saller, M.; Gautier, D. A.; Catarci, S.; Pesce, D.; Richter, S.; Blom, P. W.; Herrmann, A. *Adv. Mater.* **2014**, *26*, 4863.

(69) Terasaki, N.; Yamamoto, N.; Hiraga, T.; Sato, I.; Inoue, Y.; Yamada, S. *Thin Solid Films* **2006**, *499*, 153.

(70) Ciesielski, P. N.; Hijazi, F. M.; Scott, A. M.; Faulkner, C. J.; Beard, L.; Emmett, K.; Rosenthal, S. J.; Cliffel, D.; Jennings, G. K. *Bioresour. Technol.* **2010**, *101*, 3047.

(71) Jensen, P. E.; Gilpin, M.; Knoetzel, J.; Scheller, H. V. *J. Biol. Chem.* **2000**, *275*, 24701.

(72) Haldrup, A.; Naver, H.; Scheller, H. *The Plant Journal* **1999**, *17*, 689.

(73) Terasaki, N.; Yamamoto, N.; Tamada, K.; Hattori, M.; Hiraga, T.; Tohri, A.; Sato, I.; Iwai, M.; Iwai, M.; Taguchi, S.; Enami, I.; Inoue, Y.; Yamanoi, Y.; Yonezawa, T.; Mizuno, K.; Murata, M.; Nishihara, H.; Yoneyama, S.; Minakata, M.; Ohmori, T.; Sakai, M.; Fujii, M. *Biochim. Biophys. Acta* **2007**, *1767*, 653.

(74) Badura, A.; Kothe, T.; Schuhmann, W.; Rögner, M. *Energy Environ. Sci.* **2011**, *4*, 3263.

(75) Iyanagi, T.; Yamazaki, I.; Anan, K. F. *Biochim. Biophys. Acta* **1985**, *806*, 255.

(76) Izawa, S. *Acceptors and donors for chloroplast electron transport.*; Academic Press: New York, 1980.

(77) Vassiliev, I. R., Jung, Y.S., ; Mamedov, M. D.; Semenov, A. Y.; Golbeck, J. H. *Biophys. J.* **1997**, *72*, 301.

(78) Gizzie, E. A.; LeBlanc, G.; Jennings, G. K.; Cliffel, D. E. *ACS Appl. Mater. Interfaces* **2015**, *7*, 9328.

(79) Terasaki, N.; Yamamoto, N.; Hiraga, T.; Sato, I.; Inoue, Y.; Yamada, S. *Thin Solid Films* **2006**, *499*, 153

(80) Baker, D. R.; Simmerman, R. F.; Sumner, J. J.; Bruce, B. D.; Lundgren, C. A. *Langmuir* **2014**, *30*, 13650.

(81) Manocchi, A. K.; Baker, D. R.; Pendley, S. S.; Nguyen, K.; Hurley, M. M.; Bruce, B. D.; Sumner, J. J.; Lundgren, C. A. *Langmuir* **2013**, *29*, 2412.

(82) Zhao, F.; Sliozberg, K.; Rogner, M.; Plumere, N.; Schuhmann, W. *J. Electrochem. Soc.* **2014**, *161*, 3035.

(83) Porra, R. J.; Thompson, W. A.; Kriedemann, P. E. *Biochim. Biophys. Acta* **1989**, *975*, 384.

(84) Hexemer, A.; Müller-Buschbaum, P. *IUCrJ* **2015**, *2*, 106.

4.6. SUPPORTING INFORMATION
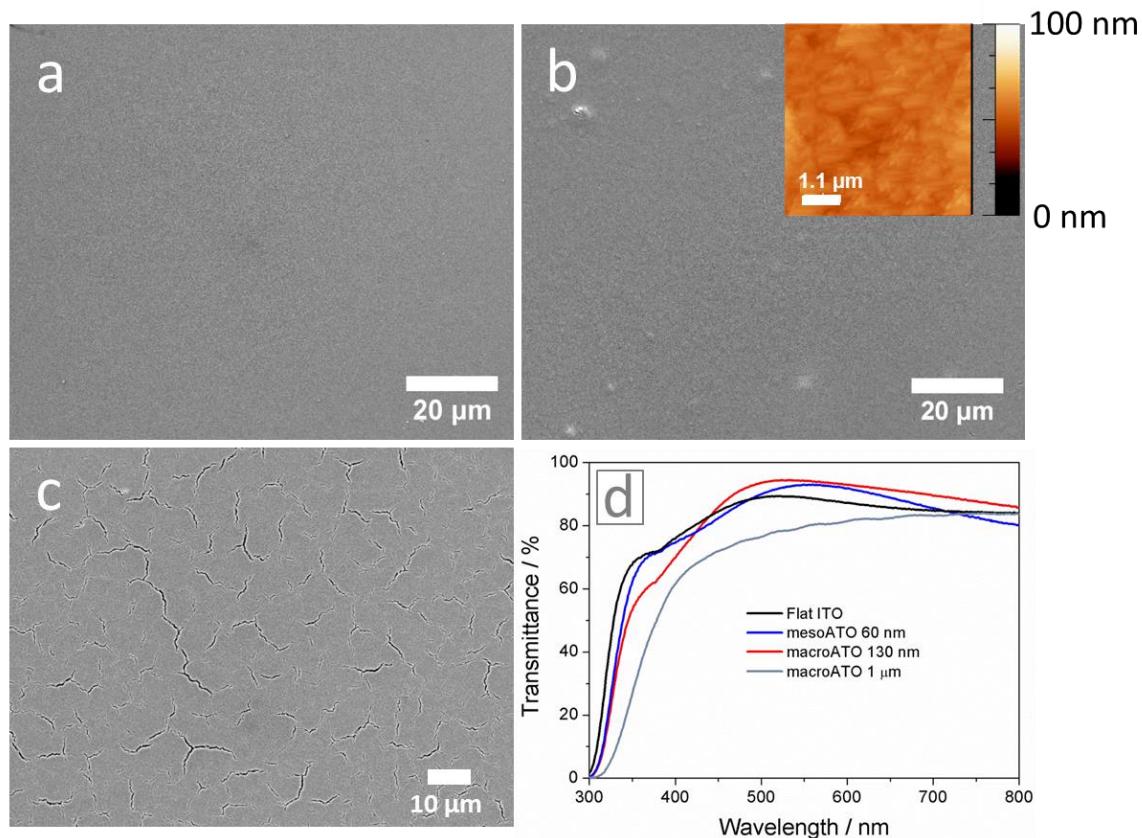
Figure S4.1   Low magnification SEM images of mesoATO (a) and macroATO (b+c). Thin (a) mesoATO (60nm) and (b) macroATO (130nm) showing homogeneous crack free coatings over several micrometers. The inset in (b) shows the corresponding AFM image of a thin macroATO electrode demonstrating a rather smooth film with a surface roughness of ca. 30 nm over an area of 5 μm^2. (c) A thick macroATO film (1 μm) showing microcracks. (d) UV-vis transmittance spectra of the planar ITO substrate: uncoated (black line), coated with a 60 nm mesoATO (blue line), a 130 nm (red line) and a 1 μm macroATO (grey line) film.

NANOSTRUCTURED ANTIMONY DOPED TIN OXIDE LAYERS WITH TUNABLE PORE
ARCHITECTURES AS VERSATILE TRANSPARENT CURRENT COLLECTORS FOR

143
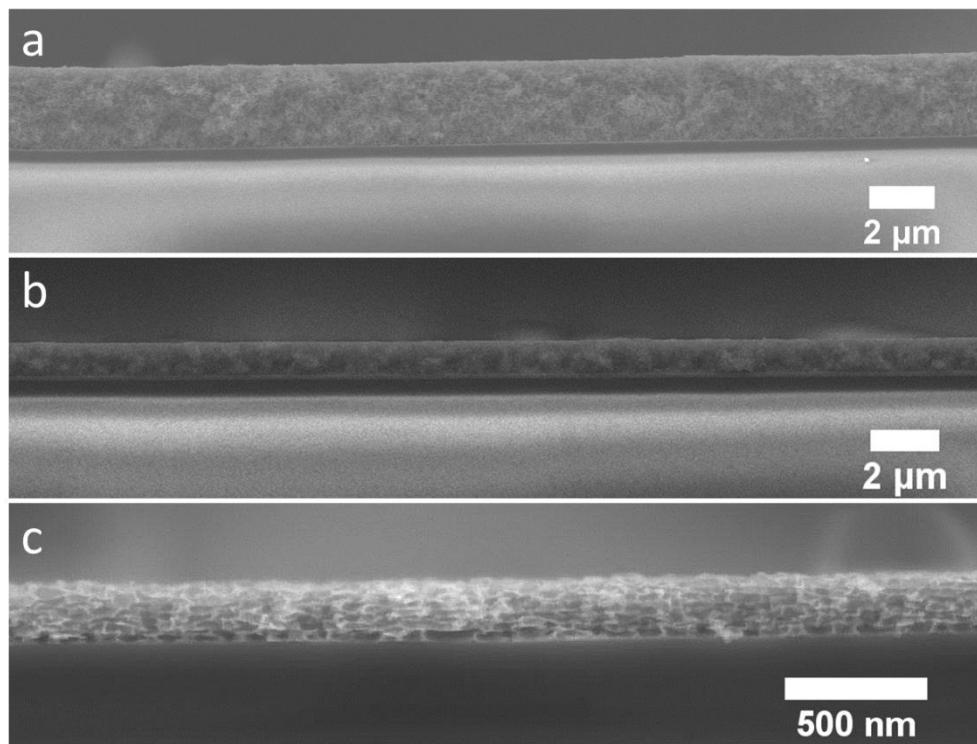
Figure S4.2   SEM cross-section images of a 2 µm (a), 1 µm (b) and a 300 nm (c) thick drop cast macroATO film. The films have a good adhesion to the substrate and are not delaminating.
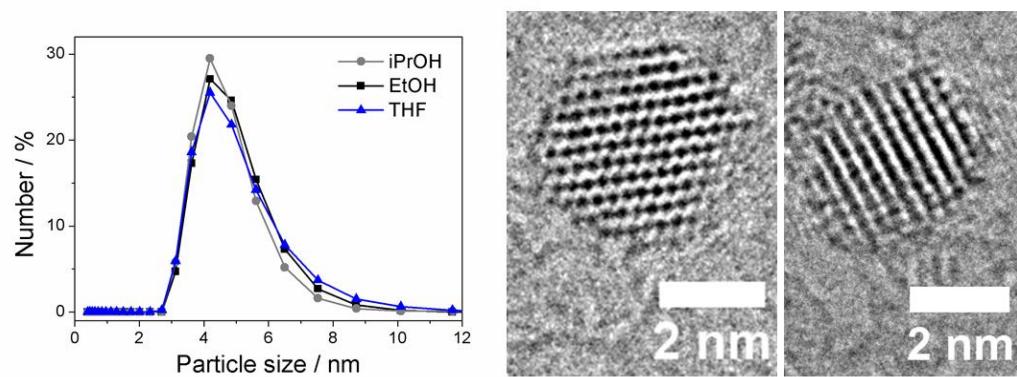
Figure S4.3   Left: Dynamic light scattering (DLS) measurements of colloidal dispersions of ATO nanoparticles with an antimony concentration of 5 at% in isopropyl alcohol (● grey line), EtOH (■ black line) and in THF(▲ blue line). Right: TEM images of ATO nanoparticles aligned on different zone axes.
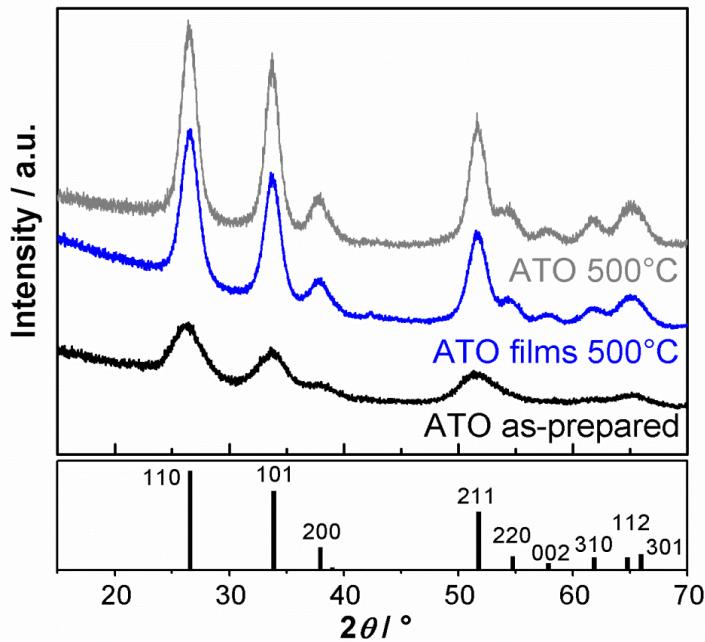
Figure S4.4 XRD patterns of as-prepared ATO-5% nanoparticles (black line), ATO-5% nanoparticles (grey line) and macroATO films assembled from nanoparticles after calcination at 500°C (blue line). The size of the nanoparticles was calculated from the line broadening of the 110 reflection, which increased from 2.8 nm for the as-prepared to 4.8 nm and 5.3 nm for the calcined films and nanoparticles, respectively. The bars in the bottom panel mark the position and the intensity of the diffraction lines of SnO_2 cassiterite (space group $P4_2/mnm$, JCPDS File Card No. 41-1445).
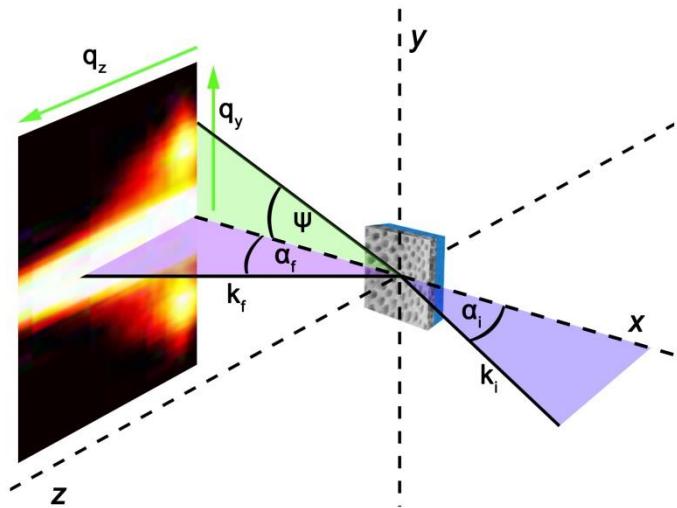
Figure S4.5 Sketch of the scattering geometry used in GISAXS. The sample surface was tilted with respect to the incident beam by an incident angle α_i. The exit angle is denoted as α_f and the in-plane angle is Ψ.

NANOSTRUCTURED ANTIMONY DOPED TIN OXIDE LAYERS WITH TUNABLE PORE
ARCHITECTURES AS VERSATILE TRANSPARENT CURRENT COLLECTORS FOR

145
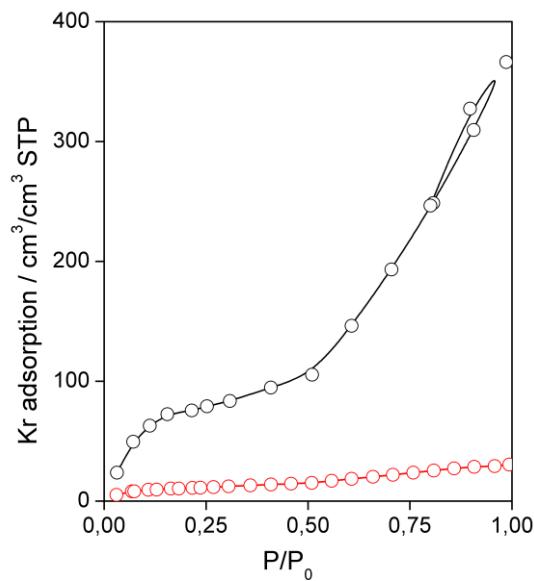
Figure S4.6 Adsorption isotherms of krypton at ca. 77 K on mesoATO (black) and macroATO (red). The adsorption is expressed per the total volume of the respective film.
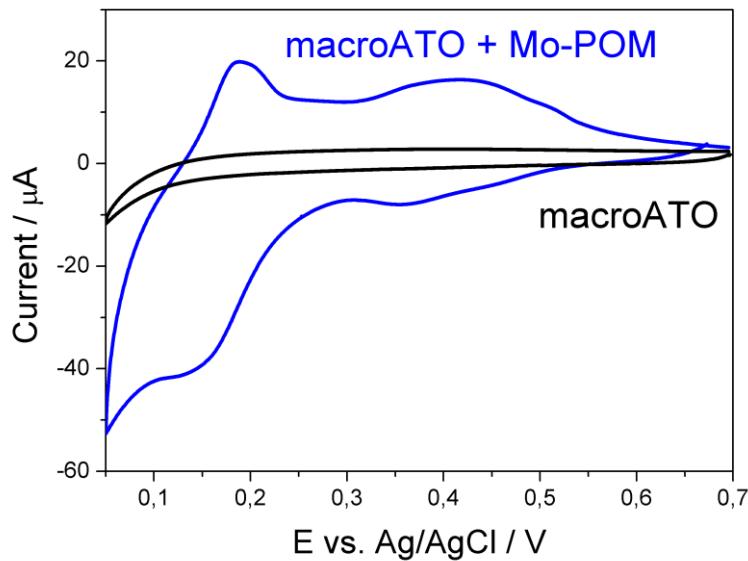
Figure S4.7 Cyclic voltammogram (CV) of bare (black curve) and Mo-POM functionalized (blue line) macroATO films with a thickness of 0.5 µm. CVs were recorded in 0.1 M H_2SO_4 with a scan rate of 1 mV s^{-1}.
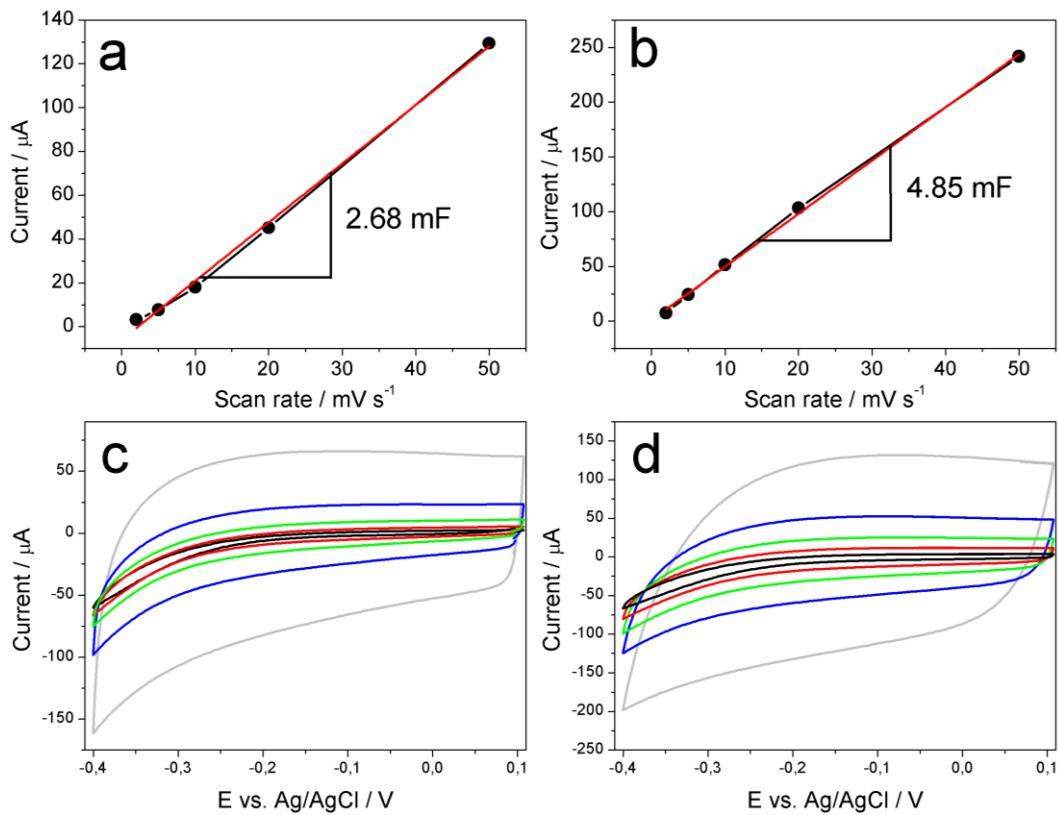
Figure S4.8 Electrochemical capacitance measured in 0.1 M NaCl vs. Ag/AgCl on a 1 µm (a+c) and a 1.8 µm (b+d) macroATO film. a+b) Capacitive currents at -0.1 V vs. Ag/AgCl obtained at different scan rates. The determined slope is 2.68 mF (a) and 4.85 mF (b), which equals 3.41 mF cm^{-2} (a) and 6.18 mF cm^{-2} (b). The corresponding cyclic voltammograms during the measurement with different scan rates are shown below (c+d) (grey line: 50 mV, blue line: 20 mV, green line: 10 mV, red line: 5 mV, black line: 2 mV). The surface area was calculated by dividing the measured capacitance by the assumed capacitance for flat oxide electrodes (60 µF) and equals 57 cm^2 cm^{-2} and 103 cm^2 cm^{-2} for 1 µm and 1.8 um thick macroATO electrodes.

NANOSTRUCTURED ANTIMONY DOPED TIN OXIDE LAYERS WITH TUNABLE PORE
ARCHITECTURES AS VERSATILE TRANSPARENT CURRENT COLLECTORS FOR

147
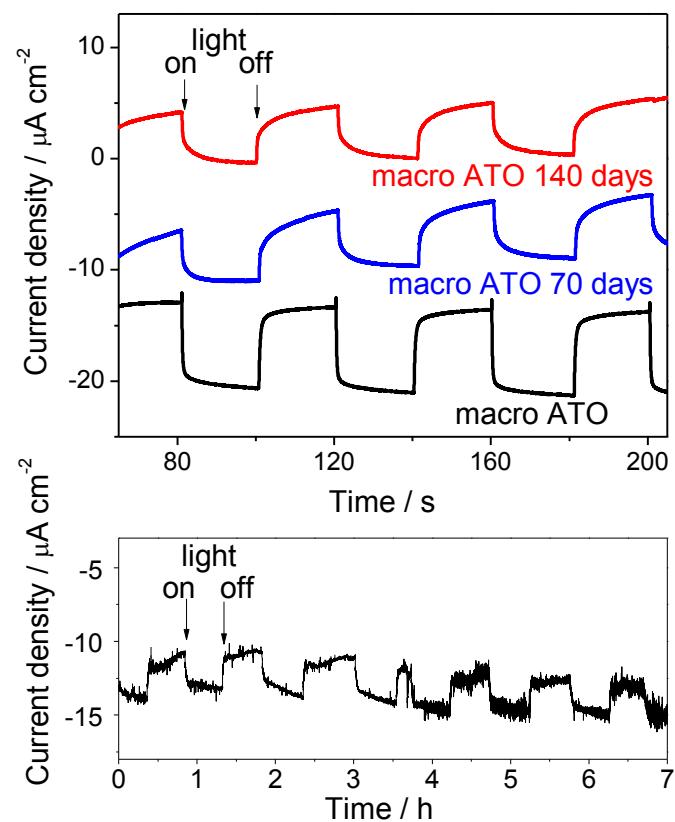
Figure S4.9 Photochronoamperometric stability measurements of a PSI modified macroATO electrodes with different thicknesses at -0.3 V vs. Ag/AgCl/3M KCl under chopped light illumination with a light intensity of 1 sun and an exposed area of 0.196 cm^2. Top: A PSI modified macroATO electrode (1.8 µm) freshly prepared (black line) and measured again after 70 (blue line) and 140 days (red line) stored at 4 °C. The PSI functionalized electrodes lost 33% and 40% of their initial photocurrent after 70 and 140 days, respectively.   Bottom: A PSI modified macroATO electrode (500 nm) measured at illumination times of 30 min. No decrease in photocurrent could be observed after 7 hours.

5. MACROPOROUS INDIUM TIN OXIDE ELECTRODE LAYERS AS CONDUCTING SUBSTRATES FOR IMMOBILIZATION OF BULKY ELECTROACTIVE GUESTS

This chapter is based on the following publication:

Yujing Liu*, Kristina Peters*, Benjamin Mandlmeier, Alexander Müller*, Ksenia Fominykh, Jiri Rathousky, Christina Scheu, Dina Fattakhova-Rohlfing

*Yujing Liu and Kristina Peters contributed equally

Macroporous indium tin oxide (ITO) electrodes with a defined uniform pore size were prepared via direct co-assembly of ultra-small indium tin hydroxide (nano-ITOH) nanoparticles and poly(methyl methacrylate) (PMMA) latex beads. The use of nano-ITOH nanoparticles enables a facile large-scale fabrication of homogeneous crack-free coatings with good adhesion to the substrate, good optical quality and tunable thickness, which easily transform at 400 °C into crystalline ITO with similar morphology. Macroporous ITO films exhibit reasonable high electric conductivity of $4.0 \pm 0.3 \, \text{S cm}^{-1}$ and open interconnected pores with a uniform size of ca. 300 nm, which makes them suitable conducting platforms for immobilization of bulky redox species or for deposition of functional electroactive layers. Deposition of functional semiconducting layers on the walls of the porous ITO scaffold was shown for titanium dioxide, which penetrates the ITO framework as shown by transmission electron microscopy (TEM) analysis of a cross-section. The obtained layers were used as conducting substrates for the immobilization of heme proteins cytochrome c and hemoglobin, which demonstrate a direct electron transfer to the macroporous ITO electrode. Surface

coverage of cytochrome c adsorbed on the macroporous ITO electrode is more than 12 times higher than on a planar one, reaching 400 pmol cm^{-2} for a film of ca. 360 nm in thickness. Hemoglobin adsorbed on the macroporous ITO electrodes also demonstrates a noticeably high surface coverage of ca. 160±20 pmol cm^{-2}, which is roughly 7–10 times higher than the theoretical value for monolayer coverage.

5.1. INTRODUCTION

The deposition of nanostructured electrode layers with a defined morphology is an important challenge in modern electrochemistry, as it enables the controlled design of complex electrochemical systems[1,2]. Transparent conducting oxides (TCOs) play a special role in electrochemistry, being used as transparent electrode layers for optoelectrochemical and electrochromic applications as well as spectroelectrochemistry. Dense flat layers of TCOs such as doped indium, tin or zinc oxides have been known and used for a long time, but only recently has the fabrication of conducting 3D-TCO networks been reported[3-12]. Such architectures are especially attractive as conducting hosts for immobilized species owing to their large interface area enabling high loading of functional redox guests, electrical conductivity of the framework providing direct communication with the incorporated species, and optical transparency allowing interactions with light.

Since the first publication in 2006[3], several porous TCO architectures have been developed, which include indium tin oxide[3,7,8,10,11] and doped tin oxide[4,6,9,12]. The major efforts have been aimed at the fabrication of mesoporous TCO materials about 10 nm in the pore size. Such morphologies feature a very high surface area enabling high loading of functional guests. However, the relatively small pore diameter precludes the incorporation of bulkier moieties, especially larger biological entities such as enzymes or protein complexes, which stimulated the quest for materials with larger pores, especially those in the macropore range (i.e., over 50 nm).

Macroporous films offer distinctive morphological features, such as an open porous architecture enabling efficient mass transfer, an interconnected framework beneficial for charge transport processes, and large pore sizes advantageous for the incorporation of bulky guest species or functional layers. They are usually made using latex beads as templates for the porosity. Typical protocols involve either infiltration of the voids of ordered bead arrays with different TCO precursors (the so-called infiltration method involving the bead assembly and their subsequent infiltration with suitable precursors), or a direct co-assembly of the TCO

precursors and the latex beads (the so-called co-deposition method)[13-18]. The latter method may offer a better control over the precursor-to-template ratios, simplicity and shorter fabrication times, provided the accompanying challenges, such as colloid stability, have been overcome.

Fabrication of the macroporous TCO layers with pores several tenths to several hundreds of nanometers in size has been reported by Ozin et al.[19,20] and Xu et al.[21,22], who fabricated periodic macroporous antimony doped tin oxide (ATO) films and fluorine doped tin oxide (FTO) films with inverse opal structures. In ref.[23] the disordered template of polystyrene spheres was infiltrated by atomic layer deposition by alternating pulses of organometallic precursors and hydrolytic polycondensation agent. Alternatively, macroporous nanobead FTO electrodes were obtained by the assembly of hollow FTO nanobeads[24]. Finally, disordered macroporous foams of undoped In_2O_3 and SnO_2 were prepared by the impregnation of cellulose membranes with pre-formed nanoparticles[14]. For the preparation of TCO films, where the suitable crystallinity is a major prerequisite for a successful performance, the use of pre-formed crystalline nanoparticles as building blocks was shown to be advantageous[4,7,14,20]. Classical sol-gel techniques, which provide basically amorphous material requiring a heat treatment to achieve sufficient crystallinity, do often not give sufficient control over the crystallinity. The particle-based procedures can overcome this limitation, but the success of this preparation route depends on the availability of suitable building blocks for the assembly of 3D-porous structures. The nanoparticles used for the assembly have to be completely dispersible in polar solvents compatible with the PMMA beads.

We describe the fabrication of transparent conducting indium tin oxide (ITO) electrodes with a uniform macroporous structure which is based on controlled co-assembly of ultra-small indium tin hydroxide (nano-ITOH) nanoparticles earlier developed in our group[7] and poly(methyl methacrylate) (PMMA) latex beads, leading to macroporous layers with the pores several hundreds of nanometers in size. The perfect dispersibility of nano-ITOH without any stabilizing agents, their preferential interaction with the hydrophilic part of templates leading to their self-assembly, and a facile transformation of the assembled hydroxides into crystalline ITO with similar morphology make them very attractive building blocks for the preparation of nanostructured ITO materials with controlled nano-morphologies. In this paper we demonstrate the use of nano-ITOH nanoparticles for the facile large-scale deposition of 3D-macroporous ITO electrodes featuring optical transparency and a large conducting interface.

5.2. RESULTS AND DISCUSSION

The fabrication of macroporous ITO films by a co-assembly approach is schematically illustrated in Figure 5.1. In a typical procedure, a mixture of aqueous dispersions of PMMA beads and indium tin hydroxide (nano-ITOH) nanoparticles is coated on various substrates using dip- or spin-coating techniques. A mass ratio of the amounts of polymer beads and of inorganic precursor was optimized to achieve a uniform porous morphology of the final films. A mass ratio of 3:1 w/w of PMMA beads and inorganic precursor (calculated as the mass of ITO formed after calcination), respectively, provides the best structure uniformity for all tested precursors types and different PMMA beads sizes. The higher concentration of the inorganic precursor results in formation of non-porous ITO domains, while larger fraction of the PMMA beads leads to thin ITO walls and consequently a fragile porous scaffold.
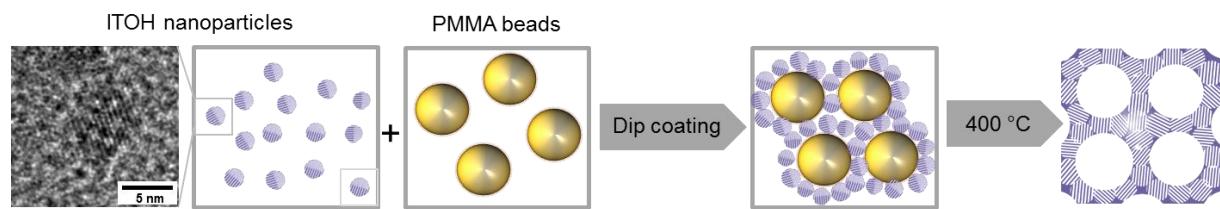
Figure 5.1   Scheme of the fabrication of macroporous ITO electrodes via co-assembly of ITOH nanoparticles and the PMMA colloidal template. High resolution TEM image of a single ITOH nanoparticle on a carbon-coated TEM grid is shown in inset.

Besides a suitable PMMA/nano-ITOH ratio, the fabrication of porous ITO films with good optical quality and high mechanical stability requires addition of hydroxypropyl cellulose (HPC) to the coating solution. The films prepared without the HPC exhibit insufficient coverage of the substrate with the formation of porous ITO islands and uncovered areas, high roughness, and rather low mechanical stability. The quality of the coating practically does not improve due to pretreatment of the substrate by, e.g., repetitive washing, plasma cleaning or adsorption of adhesive layers of polyelectrolytes. In contrast, the addition of HPC to the coating solution significantly improves adhesion of the ITO layers to the substrate, as well as the surface coverage, smoothness and mechanical stability of the macroporous ITO films. The positive effect of the hydroxypropyl cellulose on the morphology of the obtained electrodes can be attributed to several factors. The presence of HPC strongly increases colloidal stability of the mixed ITOH-PMMA dispersions that remain stable for several weeks, while mixtures without HPC precipitate after several hours. HPC apparently stabilizes both the ITOH and

PMMA colloids and presumably affects the interactions between nano-ITOH particles and PMMA template during co-assembly, promoting formation of uniform macroporous films. Additionally, HPC increases viscosity of the aqueous coating solutions, improves the wetting of the substrate and decreases the surface tension, resulting in the improved homogeneity, surface coverage and adhesion of the films. Similar effect of the HPC on the quality of the coating was also observed for titania films deposited from pre-formed crystalline nanoparticles[28].

Coating the HPC-containing solutions on different substrates provides smooth composite layers with a good adhesion to the substrate and a tunable thickness, which can be controlled by the variation of viscosity of coating solutions and the dip coating rate. In general, thicker films are obtained with more viscous solutions containing larger amounts of the HPC, however at HPC concentrations exceeding 2 wt% (corresponding to 20 wt% HPC per mass of the PMMA phase) the films quality deteriorates due to the increasing roughness. The best film quality in terms of smoothness and the surface coverage was obtained for the solutions with a total HPC concentration of 1 wt%. Using this approach, very thin films corresponding to almost a monolayer coating of the PMMA bead arrays can be deposited at slow dip coating rates. Thicker films of up to several micrometers in thickness can be obtained by increasing the dip-coating rate or, if even thicker films are required, by repeated coating. Cross section of a typical film consisting of three subsequently deposited layers is shown in Figure 5.3b.

The layers deposited from the mixed dispersions of PMMA beads and ITOH hydroxide nanoparticles have to be annealed in air at 400 °C to remove the polymer template and to form the porous ITO replica. The heating step is also important for the transformation of the nano-ITOH building blocks to the cubic ITO phase. The ITO films obtained after annealing at 400 °C are thinner than the deposited PMMA bead arrays, which is mainly due to densification of the pore walls during recrystallization of indium tin hydroxide to the indium tin oxide. This process is accompanied by the removal of water due to the condensation of hydroxide groups, leading to a decrease in the volume of the ITO component. In spite of the densification of the scaffold during thermal treatment, no crack formation was observed for the films up to 1 μm in thickness owing to the mechanical flexibility of the open porous framework able to accommodate the volume changes, and to the preferentially unilateral pore shrinkage in the direction perpendicular to the substrate. Even thicker films (up to 2.5 μm in thickness) are substantially homogeneous, with only few microcracks, which do not significantly affect the film transparency and its mechanical stability.

XRD patterns of the films assembled from indium tin hydroxide nanoparticles and PMMA beads demonstrate that the ca. 3 x 8 nm ITOH nanoparticles with the hexagonal crystalline structure (detailed information about the morphology and the structure of the ITOH nanoparticles is provided elsewhere[7]) are completely transformed to the cubic bixbyite ITO phase after calcination at 400 °C (Figure 5.2). The size of the ITO crystalline domains estimated from the line broadening in the XRD patterns using the Scherrer equation is 11 ± 2 nm. It is interesting to note that the presence of the PMMA template restricts the growth of the crystalline domains during calcination, while heating of nano-ITOH particles without addition of the PMMA results in formation of an ITO phase with crystalline domains sized 25 ± 2 nm and therefore double as large (Figure 5.2).
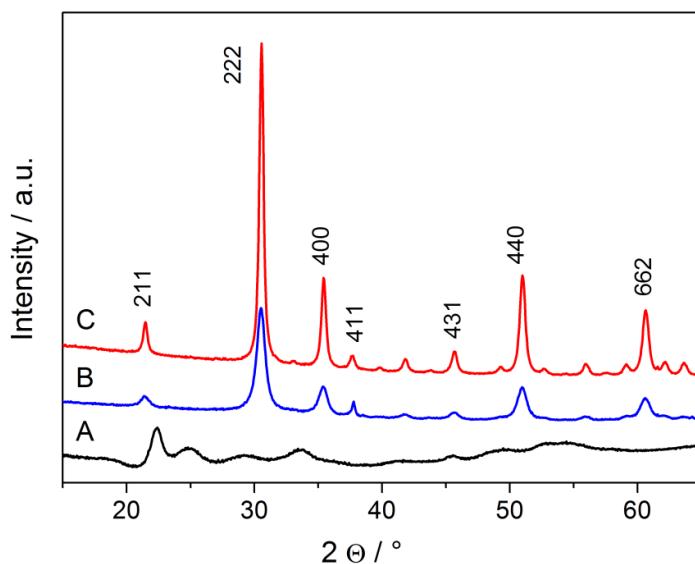
Figure 5.2   XRD pattern of nano-ITOH nanoparticles: as prepared (A, black line) and calcined at 400 °C in air in the presence of the PMMA template (B, blue line) and without the PMMA template (C, red line).

Morphology of the final macroporous ITO films was investigated by electron microscopy (SEM and TEM) and atomic force microscopy (AFM) (Figure 5.3). Top view SEM images of the calcined porous ITO films reveal homogeneous crack-free smooth coatings with a uniform pore structure (Figure 5.3a). After calcination, the average pore size of the film templated with 370 nm PMMA beads equals 300 nm, corresponding to ca. 20% shrinkage in the lateral direction (Figure 5.3b). Similar information is provided by the AFM images, which show relatively smooth porous morphology with uniform exposed pores (Figure 5.3c). The TEM images of the cross-sections demonstrate that the open porous scaffold is formed also in the direction perpendicular to the substrate and that the porous ITO layer has a very good adhesion to the substrate without delamination (Figure 5.4a). The shrinkage of the pores after

calcination is more pronounced in the direction perpendicular to the substrate, resulting in ellipsoidal pore shape.
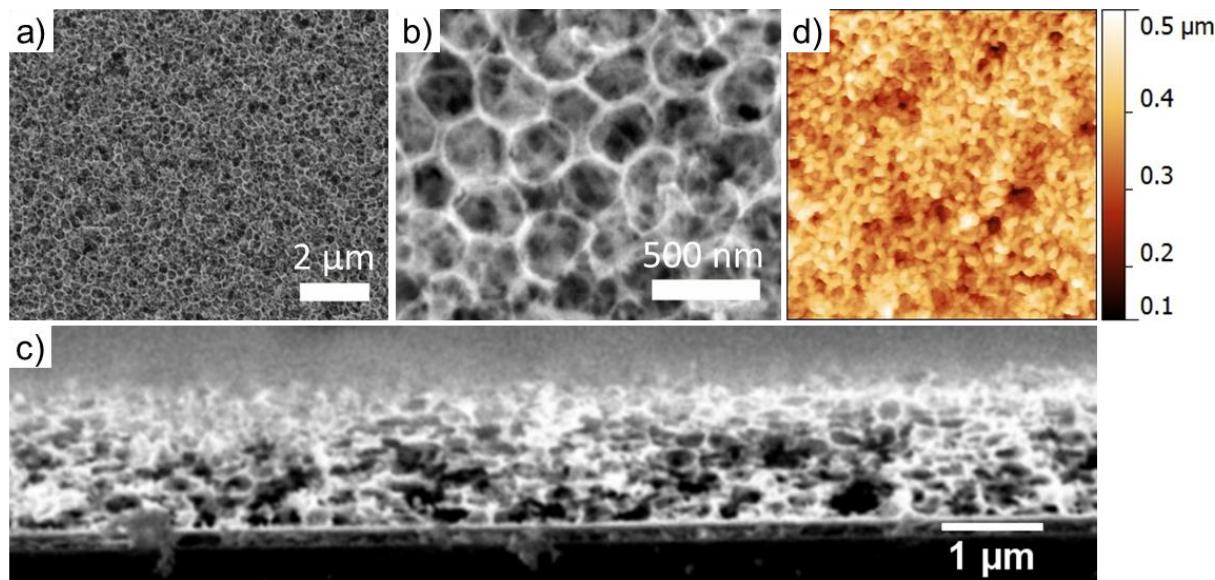
Figure 5.3 Top view (a, b) and cross-section (c) SEM images, and AFM image in the tapping mode (d) of the films assembled from nano-ITOH particles and PMMA spheres. The films were fabricated by a repeated dip coating (3 times) of HPC-containing dispersions of nano-ITOH and PMMA (see Experimental part for the experimental details) and calcined at 400 °C in air; the average thickness of the films obtained in this way is 1.3 μm.

Electrical conductivity of the macroporous ITO scaffold formed after calcination at 400 °C in air is not particularly high, being around 0.35 ± 0.30 S cm^{-1}. The conductivity of the porous scaffold is however substantially increased after the additional heat treatment in forming gas atmosphere at 400 °C reaching 4.0 ± 0.3 S cm^{-1}, which is comparable to the conductivity of mesoporous ITO electrodes assembled from hydroxide nanoparticles obtained by us previously[7]. The macroporous ITO films are transparent without haze. Figure 5.4 shows optical transmittance of the macroporous ITO films of 460 nm and 660 nm in thickness deposited on a commercial flat ITO film used as a substrate, which have practically the same transmittance over 85% in the visible range as the parent ITO substrate.
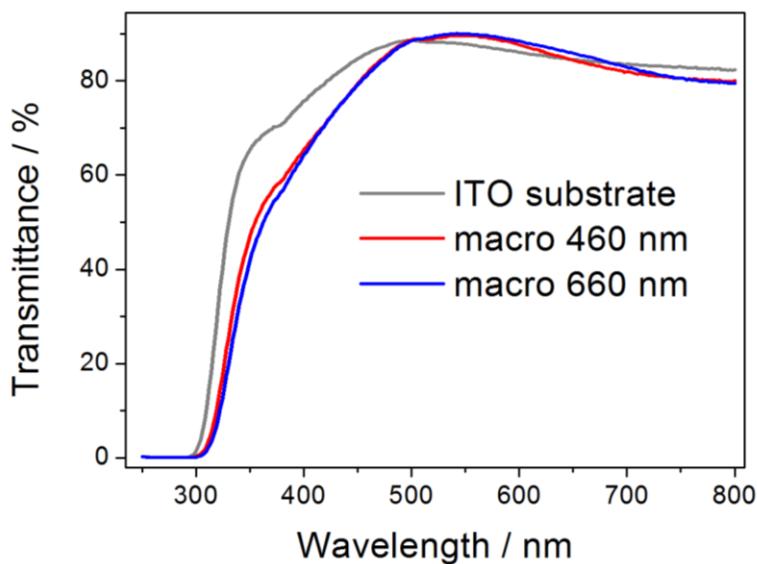
Figure 5.4 UVvis transmittance of the planar ITO substrate: non-coated (grey line) and coated with the macroporous ITO film with the thickness of 460 nm (red line) and 660 nm (blue line).

Advantages of the indium tin hydroxide nanoparticles as inorganic building blocks in the co-precipitation procedure become obvious when comparing the morphology of the films assembled in a similar way using sol-gel precursor obtained by hydrolysis of In and Sn salts, which is conventionally used for fabrication of ITO layers. The co-precipitation results in a highly accessible and uniform macroporous structure after calcination (Figure 5.5a), while the same procedure using sol-gel precursor leads to formation of a rough porous structure having an undefined wall morphology (Figure 5.5b). The few larger non-uniform pores might be due to the initial agglomeration of PMMA spheres.
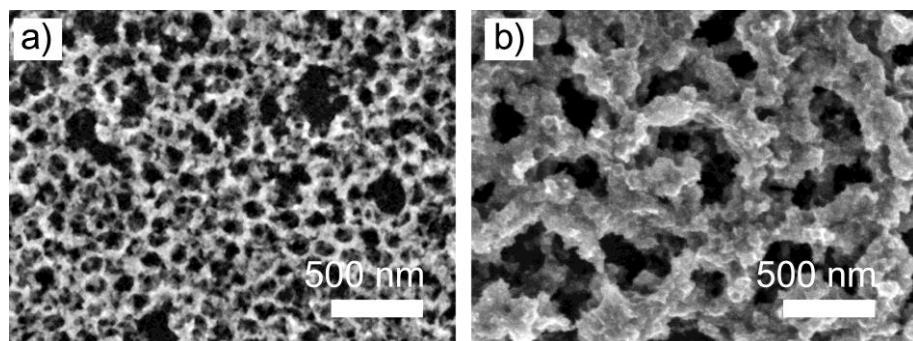
Figure 5.5 SEM top-view images of the ITO films obtained by a co-precipitation of PMMA beads (size 100 nm) with (a) nano-ITOH particles and (b) molecular $InCl_3$ and $SnCl_4$ precursors.

The films obtained by a direct co-deposition of ITOH nanoparticles and PMMA beads do not exhibit long range periodicity of the pore ordering observed for various macroporous materials templated with latex beads[29-32]. However, it is important that the films have a good adhesion to the substrate, a large and uniform pore size and open interconnected pores, which makes macroporous ITO layers suitable conducting platforms for the immobilization of bulky redox species or for deposition of functional electroactive layers. The idea of using transparent porous electrodes as conducting supports for deposition of thin absorber layers has been intensively discussed in the recent years, especially in relation to the development of novel photoelectrocatalytic systems[20] and photovoltaic cells[22,23]. We have tested the possibility of deposition of functional semiconducting layers on the walls of the porous ITO scaffold on the example of titanium dioxide, which is one of the commonly used semiconducting oxides for photo(electro)catalysis. For the deposition of titania layer, substrates with macroporous ITO films were dip coated in a prehydrolyzed sol gel solution of titania precursor followed by annealing at 400 °C in air. To investigate distribution of titania along the film depth with a high spatial resolution, cross sections were prepared and analyzed using TEM. In Figure 5.6, BF images of both uncoated and TiO_2 coated ITO networks on a polycrystalline ITO substrate are shown. The morphology of the coated films closely resembles that of non-coated ones along the film depth, without clogging the pores or formation of a titania crust on the top. The film thickness of the uncoated and TiO_2 coated films were 470±70 nm and 230±70 nm, respectively, with the standard deviations indicating a similar surface roughness. The nanoparticles are sintered together as shown in Figure 5.6, forming a truly macroporous structure as opposed to a conglomerate of nanostructured particles. To analyze the distribution of TiO_2 nanoparticles in the ITO network, EDX mapping was done in STEM mode as shown in Figure 5.6. It could be shown that the TiO_2 nanoparticles infiltrate the ITO network completely, making the macroporous ITO films promising conducting platforms for wet chemical deposition of semiconducting layers. It should however be noticed that the macroporous ITO scaffold is not chemically stable in the acidic solutions which easily etch away the thin ITO walls (as we have observed for the titania sol-gel solution containing concentrated HCl), which puts some limitations on the composition of the coating solutions.
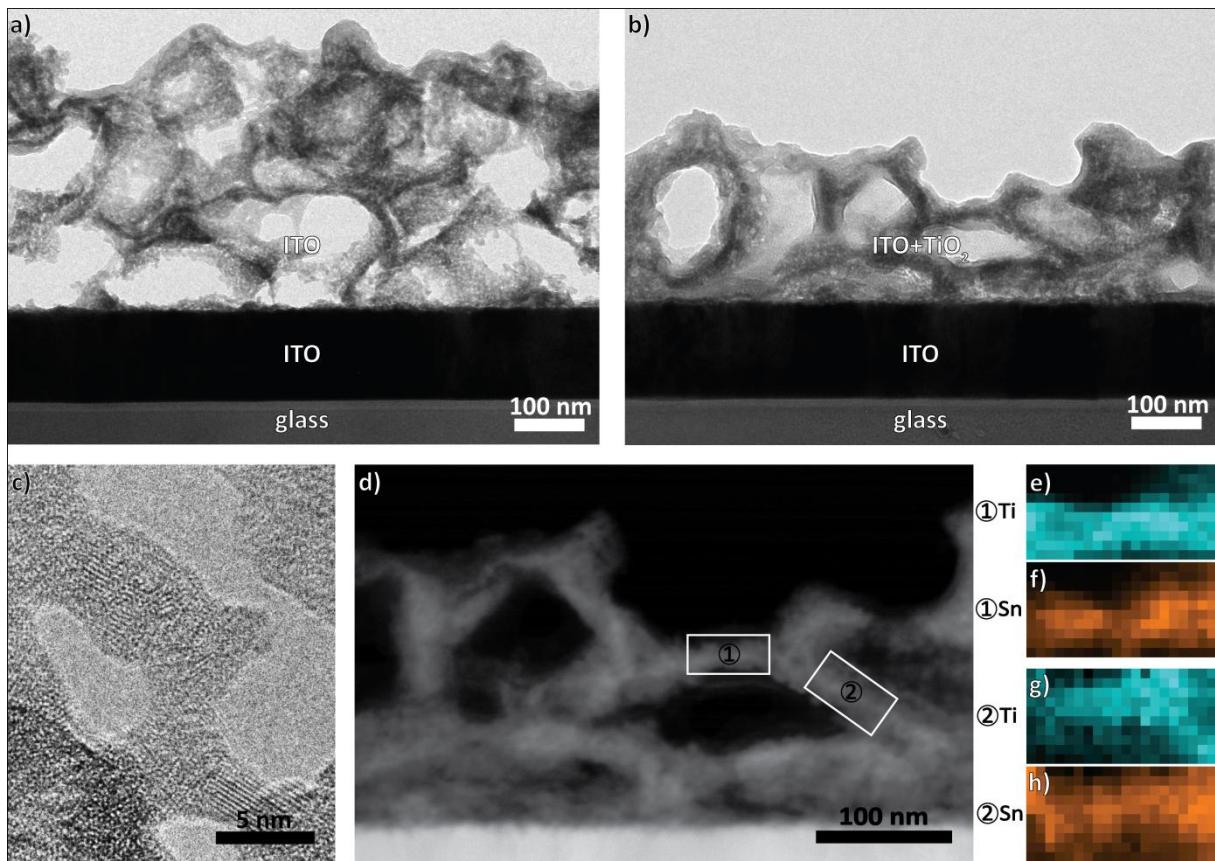
Figure 5.6   (a) Cross section of a macroporous ITO layer without titania coating. (b) Cross section of a macroporous ITO layer with titania coating: (c) HRTEM image of a thin part of a network; d) STEM image of a titania coated ITO framework; (e)-(h) titanium (cyan), indium and tin (orange) elemental mapping of the two regions marked in image (d)

Suitability of the macroporous ITO electrodes as conducting platforms for the immobilization of bulky redox moieties was investigated for common heme proteins capable of direct electron transfer to the electrode. As redox proteins we have selected cytochrome c with a size of ca. 2.6 x 3.2 nm[33], and hemoglobin with a size of ca. 5 x 6 nm[1]. The redox proteins were adsorbed on the ITO electrodes by immersing them into solution of the corresponding protein.
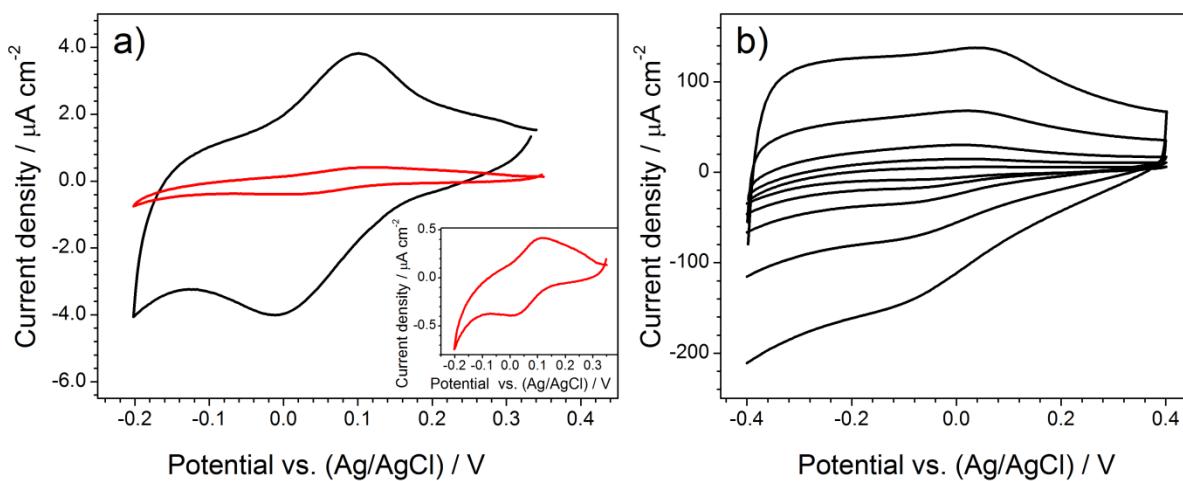
Figure 5.7   Cyclic voltammograms of (a) cytochrome c adsorbed on the macroporous ITO (black line) and flat ITO (red line, also shown in inset) electrodes at a scan rate 0.005 V/s. The measurements were performed in 0.05M phosphate buffer with pH 7.4; and (b) hemoglobin adsorbed on the macroporous ITO electrode. The voltammograms were taken at the scan rates 0.5 V/s, 0.2 V/s, 0.1 V/s and 0.05 V/s (from top to bottom). The measurements were performed in 0.05M phosphate buffer with pH 5.0.

The electrochemical activity of cytochrome c adsorbed on the macroporous ITO electrodes as well as on the planar ITO films used as the reference was investigated by cyclic voltammetry. For both types of electrodes a couple of well-defined redox peaks are observed, which are characteristic for the heme FeIII/FeII redox couple in cytochrome c molecules[34-36] (Figure **5.7**). The formal potential values are 0.066±0.004 V vs. Ag/AgCl sat (0.263±0.004 V vs. NHE) and 0.060±0.004 V vs. Ag/AgCl sat (0.267±0.004 V vs. NHE) for cytochrome c adsorbed on planar ITO and on macroporous ITO electrodes, respectively. The value of formal potential on both flat and nanostructured electrodes is close to the value of native cytochrome c in solution (0.296±0.005 V vs. NHE) reported by us[6] and by other authors[36-39], indicating that cytochrome c is incorporated into the pores of macroporous ITO without any denaturation.

The surface coverage obtained for the cytochrome c adsorbed after immersion for 3 days in 50 µM solution of cytochrome c is 30±5 pmol cm^{-2} for the planar ITO electrode, which is higher than the theoretical value of 20 pmol cm^{-2} for a compact monolayer of cytochrome c[40,41]. The adsorption of cytochrome c on both planar and porous ITO electrodes is weaker compared to that on an antimony doped tin oxide (ATO) electrode reported by us previously[6], for which formation of a very stable monolayer of protein showing behavior typical of surface-confined species was observed. In contrast, for cytochrome c adsorbed on the ITO electrode we assume formation of a loosely adsorbed multilayer leaching from the

electrode after repetitive cycling, and a combined surface and diffusion control of current due to diffusion of the desorbed protein to the electrode surface. This follows from a rather high surface coverage obtained even for the planar ITO electrode, in combination with a non-linear dependence of peak current on the scan rate, some asymmetry of the anodic and the cathodic peaks, and peak-to peak separation of 50 mV and 56 mV for the flat and the macroporous ITO, respectively, even at the slowest scan rate of 2 mV s^{-1}. The difference in binding of cytochrome c to the surface of ITO and ATO electrodes can be attributed mostly to the difference in their surface charge and corresponding strength of electrostatic interactions.

Although the properties of the adsorbed cytochrome c layers still have to be improved by optimization of the grafting procedure, important for this work is that the surface coverage of the cytochrome c immobilized in the similar way on the macroporous ITO electrode is more than 12 times higher than on the planar one, reaching 400 pmol cm^{-2} for the film of ca. 360 nm in thickness. The increase in the electrochemically accessible protein loading on the macroporous ITO electrode is in a good agreement with the surface roughness of the electrodes of this type (similar increase in the surface coverage was observed also for the macroporous Au electrode with the same size of pores[42]), making the macroporous ITO electrodes assembled from ITOH nanoparticles suitable platforms for immobilization of different redox moieties. This conclusion is also supported by data obtained by us for another heme protein, hemoglobin, adsorbed on the macroporous ITO layers. Hemoglobin, which has a nearly spherical shape with the diameter of ca. 5 x 6 nm, is bulkier than the cytochrome c, which restricts the choice of possible porous electrode architectures suitable for its immobilization. Hemoglobin adsorbed on the macroporous ITO electrodes demonstrates a couple of well-defined redox peaks at potential E0 = -0.027±0.005 V vs. Ag/AgCl sat (0.170±0.005 V vs. NHE) at pH 5.0 (Figure 5.7b), in a good agreement with the values reported in the literature[43]. Hemoglobin has a better adhesion to the surface of macroporous ITO electrodes compared to the cytochrome c described above, forming electrochemically stable layers showing practically no decrease in electrochemical response after prolonged cycling at different scan rates. Voltammograms of hemoglobin adsorbed on the macroporous ITO electrodes have a nearly symmetrical shape and close to linear dependence of the peak current on the scan rate typical for surface-immobilized species. Integration of anodic and cathodic peaks provides a noticeably high surface coverage of ca. 160±20 pmol cm^{-2}, which is ca. 7–10 times higher than the theoretical value for monolayer coverage (18.9 pmol cm^{-2})[42].

5.3. CONCLUSIONS

We have shown that the preformed nano-ITOH particles are very suitable building blocks for the assembly of macroporous ITO films by the co-deposition technique using PMMA beads as a template for porosity. In addition to the controlled size and the easy dispersibility, there is another very important feature of these nanoparticles, namely the ease of their conversion to the oxide form. The use of nano-ITOH nanoparticles enables a facile large-scale fabrication of homogeneous crack-free ITO coatings with a good adhesion to the substrate, good optical quality and tunable thickness. The integration of hydroxypropyl cellulose to modify the interaction between nano-ITOH with PMMA spheres obviously improves the quality of final films.

The films obtained by a direct co-deposition of nano-ITOH nanoparticles and PMMA beads exhibit an open interconnected macroporosity, which makes them suitable conducting platforms for immobilization of bulky redox species or for deposition of functional electroactive layers. The suitability of the macroporous ITO electrodes as conducting platforms for immobilization of bulky redox moieties was demonstrated for common heme proteins cytochrome c and hemoglobin. For both proteins adsorbed on the macroporous ITO electrodes a couple of well-defined redox peaks was observed characteristic for the heme FeIII/FeII redox couple in corresponding proteins. Surface coverage of both cytochrome c and hemoglobin immobilized on the macroporous ITO electrode is by about one order of magnitude higher than on a flat one. We envision that the obtained macroporous ITO layers can be used as transparent electrically conducting platforms for immobilization of even bulkier redox entities including enzymes and protein complexes, which can be beneficial for different optoelectrochemical, photoelectrochemical and electrochromic applications.

5.4. EXPERIMENTAL SECTION

Synthesis of macroporous ITO thin film electrodes.

Macroporous indium tin oxide (ITO) electrodes used in this work were prepared by a direct co-assembly of poly(methyl methacrylate) beads (PMMA) and indium tin hydroxide nanoparticles (nano-ITOH). PMMA beads with diameter of 370 nm and 100 nm were synthesized according to emulsion polymerization route described elsewhere[25,26]. In a typical procedure, bidistilled water (98.0 mL, Millipore Q grade) was degassed with nitrogen in a three-necked flask for 1 h, before sodium dodecylsulfate (5.6 mg) and methylmethacrylate (35.5 g) were added. The monomer mixture was stirred for 1 h at 90 °C in nitrogen atmosphere to obtain a homogenous emulsion. A solution of potassium peroxodisulfate (56 mg) in water (2 mL) was injected to initiate the polymerization. The solution turned white within 5 minutes, indicating the formation of polymer particles. The reaction was continued for 2 h at 90 °C, before the flask was exposed to air and cooled with an ice bath. The colloidal solution was stirred overnight, filtered through glass wool and washed three times by centrifugation (50000 rcf; 30 minutes) and redispersion in water. Indium tin nano-hydroxides were prepared by a procedure described elsewhere[7]. Briefly, 0.091 g of tin (IV) chloride (Aldrich) was added to a clear solution of 0.698 g of indium (III) chloride (ABCR) in 7 mL of ethylene glycol (Sigma-Aldrich, ≥99%, used without further drying); dissolution of all the salts is very exothermal and has to be performed at 0 °C in the ice bath under stirring. The molar ratio of tin and indium was 1 : 9 mol : mol. Separately, 0.420 g of sodium hydroxide (Aldrich, 97%) was dissolved in 7 mL of ethylene glycol at 0 °C. Both solutions were combined at 0 °C and stirred for another 15 minutes. The mixture was transferred into a Teflon or glas-lined autoclave, which was kept in a laboratory oven pre-heated at 205 °C for 24 hours. The autoclave after reaction was taken out the oven and cooled down in air. The formed product was separated by centrifugation (47800 rcf for 20 min). The precipitate was washed once in ca. 14 ml of bidistilled water (manual stirring) and centrifuged again at 47800 rcf for 20 min. The water should be decanted immediately after centrifugation to prevent dissolution of ITOH nanoparticles. The still wet pellet resulting from centrifugation was collected and stored in a closed vessel to prevent drying. The solid content of the collected material was determined for each new batch gravimetrically by weighing of a certain amount before and after evaporation of water. The average solid content in the washed nanoparticles after centrifugation was 40 + 10%.

For the fabrication of macroporous films, still wet nano-ITOH nanoparticles (300 mg) containing 100 mg dry inorganic content were dispersed in 0.75 mL water (Millipore Q grade), stirred at room temperature until the colloidal solution turned transparent or slightly opaque (this process can take up to 2 days), and ultrasonicated for 30 min. Separately, aqueous colloidal PMMA suspension (15 wt%) was stirred for 1 hour and ultrasonicated for 30 min. The amount of PMMA beads is calculated from the weight of the ITOH nanoparticles (dry content) as 3 weight parts of PMMA to 1 weight part of ITOH; in this example it corresponds to 2 ml of 15 wt% PMMA dispersion. Finally, hydroxypropyl cellulose (HPC) (MW ca. 100000, from Sigma-Aldrich) was added to a combined solution of PMMA and nano-ITOH, stirred together for 3-4 hours and ultrasonicated for 30 min. The amount of cellulose corresponds to 10 wt% of the PMMA beads; in this example it is 30 mg of HPC in a total volume of 3 ml, which corresponds to 1 wt% HPC. The homogeneous dispersion was dip coated on glass or planar ITO substrates, dried at room temperature and calcined in air at 400 °C (achieved with a ramp of 13 °C min^{-1}) for 30 min. The film thickness of one layer was around 400 nm after calcination. Thicker films of up to several micrometers in thickness can be obtained by repeated coating. For multiple coating, the films were heated after each dip coating step at 80 °C for 45 min and finally calcined according to the procedure described above. The best films quality was obtained for the solution containing 1 wt% HPC at the dip coating rate of 0.63 mm s^{-1}. The relative humidity and the temperature in the coating chamber were 35% and 20 °C, respectively. To improve the electrical conductivity of the ITO layers, they were additionally heated in forming gas (composed of 5% hydrogen and 95% nitrogen) at 400 °C (achieved with a ramp of 2 °C min^{-1}) for 30 min.

For the fabrication of films with the molecular precursors, 55 mg $InCl_3$ (0.249 mmol) and 9.7 mg $SnCl_4$ (0.036 mmol) were dissolved in 2 mL 15 wt% PMMA suspension, otherwise the film processing was similar to that described above.

Titania coating

The TiO2 layer was deposited on the macroporous ITO films by spin-coating the titania precursor solution and additional heat treatment. 60 mM $Ti(OEt)_4$ solution was prepared by dissolving 0.070 g $Ti(OEt)_4$ in 5 mL abs. EtOH. This solution was stirred for 1 hour, then heated at 60 °C in an oven for 40 min, filtered and spin coated (3000 rpm for 30 s) on a substrate covered with macroporous ITO film prepared as described above. The coated films were calcined in air at 450 °C (achieved with a ramp of 0.6° min) for 30 min.

Immobilization of cytochrome c and hemoglobin on macroporous ITO

Cytochrome c from bovine heart (MW ca. 13000, Fluka) and hemoglobin from bovine blood were adsorbed on the macroporous ITO films by immersion in a 50 μM aqueous protein solution at 4°C for 12 h and 24 h for cytochrome c and for hemoglobin, respectively. Prior electrochemical characterization, the films were rinsed with water, dried in N_2 and masked with an adhesive glass fiber tape leaving an exposed area of 0.24 cm^2. Planar ITO electrode (VisionTek Systems Ltd.) treated in a similar way was used as a reference.

Film characterization

Wide angle X-ray diffraction analysis (XRD) was carried out in reflection mode using a Bruker D8 Discover diffractometer with Ni-filtered CuK$_\alpha$-radiation ($\lambda = 1.5406$ Å) equipped with a Vantec-1 position-sensitive detector. Film thickness was measured by profilometry (Veeco Dektak 156).

Scanning electron microscopy was performed on a JEOL JSM-6500F scanning electron microscope equipped with a field emission gun, at 4 kV. Bright field (BF) and high resolution (HR) transmission electron microscopy (TEM) as well as scanning transmission electron microscopy in high-angle annular dark-field mode (HAADF-STEM) were performed using a field-emission FEI Titan 80-300 operated at 300 kV. The system is equipped with an EDAX energy-dispersive X-Ray spectroscopy (EDX) detector which was used in STEM mode to acquire EDX maps. Cross sections were prepared by epoxy glue embedding, grinding, dimple grinding and polishing with argon ions following a routine by Strecker *et al.*[27]. AFM images were recorded by a Nanoink DPN system in non-contact mode.

UV-vis transmittance spectra were measured with a U-3501 Spectrophotometer (Hitachi). Conductivity measurements on macroporous ITO films on glass substrate were carried out on ECOPIA HMS 3000 apparatus in the Van der Pauw geometry.

Electrochemical characterization

Cyclic voltammetry was performed using Autolab potentiostat/galvanostat PGSTAT302N with FRA32M module operating with Nova 1.9 software in a standard three electrode electrochemical cell using a Pt mesh as counter electrode, Ag/AgCl/sat. KCl as reference electrode (0.197 V vs. NHE), and macroporous ITO films coated on ITO glass as the working electrode. For the electrolyte (0.05 M phosphate buffer, pH 7.4), 0.25 g of potassium dihydrogen phosphate (KH_2PO_4) and 1.51 g of disodium hydrogen phosphate (Na_2HPO_4) were dissolved in 250 ml of distilled water. The buffer solution was adjusted to pH 5.0 by an

addition of phosphoric acid. Cyclic voltammograms were taken in a range of scan rates from 0.002 to 1 V s^{-1}. The charge during oxidation and reduction of redox proteins was evaluated by integration of the corresponding peaks in the respective voltammograms after subtraction of the background current, as approximated by a polynomial. Both cathodic and anodic branches of the voltammograms were used for the flat ITO as well as for the macroporous ITO electrodes, and an average charge value was taken for the calculation of surface coverage.

5.5. REFERENCES

(1)   Walcarius, A.; Minteer, S. D.; Wang, J.; Lin, Y. H.; Merkoci, A. *J. Mater. Chem. B* **2013**, *1*, 4878.

(2)   Li, Y.; Fu, Z. Y.; Su, B. L. *Adv. Funct. Mater.* **2012**, *22*, 4634.

(3)   Fattakhova-Rohfing, D.; Brezesinski, T.; Rathousky, J.; Feldhoff, A.; Oekermann, T.; Wark, M.; Smarsly, B. *Adv. Mater.* **2006**, *18*, 2980.

(4)   Müller, V.; Rasp, M.; Rathouský, J.; Schütz, B.; Niederberger, M.; Fattakhova-Rohlfing, D. *Small* **2010**, *6*, 633.

(5)   Müller, V.; Rasp, M.; Stefanic, G.; Ba, J.; Günther, S.; Rathousky, J.; Niederberger, M.; Fattakhova-Rohlfing, D. *Chem. Mater.* **2009**, *21*, 5229.

(6)   Müller, V.; Rathousky, J.; Fattakhova-Rohlfing, D. *Electrochim. Acta* **2014**, *116*, 1.

(7)   Liu, Y. J.; Stefanic, G.; Rathousky, J.; Hayden, O.; Bein, T.; Fattakhova-Rohlfing, D. *Chem. Sci.* **2012**, *3*, 2367.

(8)   Frasca, S.; von Graberg, T.; Feng, J.-J.; Thomas, A.; Smarsly, B. M.; Weidinger, I. M.; Scheller, F. W.; Hildebrandt, P.; Wollenberger, U. *ChemCatChem* **2010**, *2*, 839.

(9)   Hou, K.; Puzzo, D.; Helander, M. G.; Lo, S. S.; Bonifacio, L. D.; Wang, W. D.; Lu, Z. H.; Scholes, G. D.; Ozin, G. A. *Adv. Mater.* **2009**, *21*, 2492.

(10)   Schaming, D.; Renault, C.; Tucker, R. T.; Lau-Truong, S.; Aubard, J.; Brett, M. J.; Balland, V.; Limoges, B. *Langmuir* **2012**, *28*, 14065.

(11)   Volosin, A. M.; Sharma, S.; Traverse, C.; Newman, N.; Seo, D.-K. *J. Mater. Chem.* **2011**, *21*, 13232.

(12)   Wang, Y.; Brezesinski, T.; Antonietti, M.; Smarsly, B. *ACS Nano* **2009**, *3*, 1373.

(13)   Stein, A.; Wilson, B. E.; Rudisill, S. G. *Chem. Soc. Rev.* **2013**, *42*, 2763.

(14)   Shchukin, D. G.; Caruso, R. A. *Adv. Funct. Mater.* **2003**, *13*, 789.

(15)   Davis, S. A.; Breulmann, M.; Rhodes, K. H.; Zhang, B.; Mann, S. *Chem. Mater.* **2001**, *13*, 3218.

(16)   Gundiah, G.; Rao, C. N. R. *Solid State Sci.* **2000**, *2*, 877.

(17)   Nandiyanto, A. B. D.; Iskandar, F.; Okuyama, K. *Chem. Eng. J.* **2009**, *152*, 293.

(18)   Stein, A.; Li, F.; Denny, N. R. *Chem. Mater.* **2007**, *20*, 649.

(19) Arsenault, E.; Soheilnia, N.; Ozin, G. A. *ACS Nano* **2011**, *5*, 2984.

(20) Moir, J.; Soheilnia, N.; O'Brien, P.; Jelle, A.; Grozea, C. M.; Faulkner, D.; Helander, M. G.; Ozin, G. A. *ACS Nano* **2013**, *7*, 4261.

(21) Yang, Z.; Gao, S.; Li, W.; Vlasko-Vlasov, V.; Welp, U.; Kwok, W.-K.; Xu, T. *ACS Appl. Mater. Interfaces* **2011**, *3*, 1101.

(22) Yang, Z.; Gao, S.; Li, T.; Liu, F.-Q.; Ren, Y.; Xu, T. *ACS Appl. Mater. Interfaces* **2012**, *4*, 4419.

(23) Tétreault, N.; Arsenault, É.; Heiniger, L.-P.; Soheilnia, N.; Brillet, J.; Moehl, T.; Zakeeruddin, S.; Ozin, G. A.; Grätzel, M. *Nano Lett.* **2011**, *11*, 4579.

(24) Jiang, Q. L.; Liu, F. Q.; Li, T.; Xu, T. *J. Mater. Chem. C* **2014**, *2*, 618.

(25) Mandlmeier, B.; Szeifert, J. M.; Fattakhova-Rohlfing, D.; Amenitsch, H.; Bein, T. *J. Am. Chem. Soc.* **2011**, *133*, 17274.

(26) Mandlmeier, B.; Minar, N.; Feckl, J. M.; Fattakhova-Rohlfing, D.; Bein, T. *J. Mater. Chem. A* **2014**, *2*, 6504.

(27) Strecker, A.; Salzberger, U.; Mayer, J. *Prakt. Metallogr.* **1993**, *30*, 482.

(28) Feckl, J. M.; Haynes, A.; Bein, T.; Fattakhova-Rohlfing, D. *New J. Chem.* **2014**, *38*, 1996.

(29) Walcarius, A.; Kuhn, A. *Trac-Trends Anal. Chem.* **2008**, *27*, 593.

(30) Szamocki, R.; Reculusa, S.; Ravaine, S.; Bartlett, P. N.; Kuhn, A.; Hempelmann, R. *Angew. Chem. Int. Ed.* **2006**, *45*, 1317.

(31) Heim, M.; Reculusa, S.; Ravaine, S.; Kuhn, A. *Adv. Funct. Mater.* **2012**, *22*, 538.

(32) Velev, O. D.; Gupta, S. *Adv. Mater.* **2009**, *21*, 1897.

(33) Shang, W.; Nuffer, J. H.; Muñiz-Papandrea, V. A.; Colón, W.; Siegel, R. W.; Dordick, J. S. *Small* **2009**, *5*, 470.

(34) Zhao, J.; Zhu, W.; Liu, T.; Yang, J.; Li, G. *Anal. Bioanal. Chem.* **2010**, *397*, 695.

(35) Yin, Y.; Wu, P.; Lü, Y.; Du, P.; Shi, Y.; Cai, C. *J. Solid State Electrochem.* **2007**, *11*, 390.

(36) Eddowes, M. J.; Hill, H. A. O. *J. Amer. Chem. Soc.* **1979**, *101*, 4461.

(37) Liu, Y.-C.; Zhao, J.; Wu, W.-L.; Yang, Z.-S. *Electrochim. Acta* **2007**, *52*, 4848.

(38) Yeh, P.; Kuwana, T. *Chem. Lett.* **1977**, 1145.

(39) Eddowes, M. J.; Hill, H. A. O. *J. Chem. Soc. Chem. Comm.* **1977**, 771b.

(40) Guo, K.; Hu, Y.; Zhang, Y.; Liu, B.; Magner, E. *Langmuir* **2010**, *26*, 9076.

(41) Willit, J. L.; Bowden, E. F. *J. Phys. Chem.* **1990**, *94*, 8241.

(42) Wang, C. H.; Yang, C.; Song, Y. Y.; Gao, W.; Xia, X. H. *Adv. Funct. Mater.* **2005**, *15*, 1267.

(43) Tian, H.; Liang, F.; Jiao, J.; Hu, J. *J. Am. Chem. Soc.* **2013**, *160*, 125.

6. CONDUCTIVITY MECHANISMS IN Sb-DOPED SnO₂ NANOPARTICLE ASSEMBLIES: DC AND TERAHERTZ REGIME

Volodymyr Skoromets, Hynek Němec, Jaromír Kopeček, Petr Kužel, Kristina Peters, Dina Fattakhova-Rohlfing, Aliaksei Vetushka, Martin Müller, Kristina Ganzerová, Antonin Fejfar
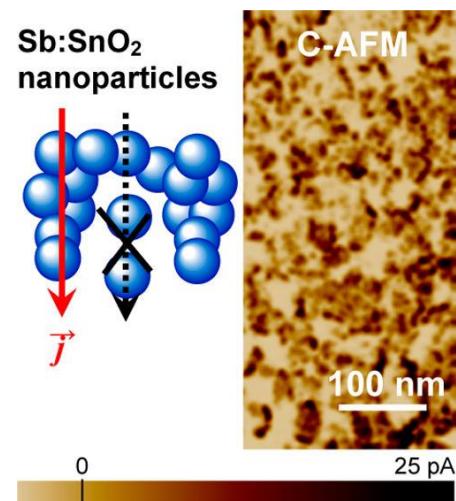
The joint project is a collaboration of different groups to investigate the conductivity and the conduction mechanism of SnO₂ and Sb-doped SnO₂ nanoparticles. The following experiments were performed by K. Peters: 1) fabrication of SnO₂ and Sb-doped SnO₂ nanoparticles with different doping concentrations; 2) preparation of pellets by pressing preformed nanoparticles with different doping concentrations and annealing them under varying conditions; 3) structural characterization (phase and particle size by XRD, porosity by sorption); 4) investigation of the bulk conductivity of the pellets using Hall measurements. C-AFM and THz conductivity measurements as well as their evaluation were done by Volodymyr Skoromets, Hynek Němec, Jaromír Kopeček, Petr Kužel, Aliaksei Vetushka, Martin Müller, Kristina Ganzerová and Antonin Fejfar.

Assemblies of undoped and antimony-doped tin oxide nanoparticles synthesized via a non-aqueous sol−gel procedure, pressed into pellets, and annealed under various conditions were investigated using time-domain terahertz spectroscopy, scanning electron microscopy, atomic force microscopy, and dc conductivity measurements. Combination of these methods made it possible to resolve the conductivity limitations imposed by intrinsic properties of the material and by the morphology of the samples. Percolation of the nanoparticles was confirmed in all samples. The undoped samples exhibit a weak hopping conductivity, whereas band-like conduction of charges partially confined in the nanoparticles dominates in the doped samples. The conductivity of nanoparticles and their connectivity can be greatly controlled during the sample preparation, namely by the calcination temperature and by the order of technological steps. A substantial increase of the conductivity inside nanoparticles and of the charge transport between them is achieved upon calcination at 500 °C.

6.1. INTRODUCTION

Nanostructuring has a strong impact on the performance of semiconducting materials in electronic and electrochemical applications. Interface-related processes acquire a greatly increasing role in nanoscale assemblies and, owing to the diminishing size of the bulk, the electron- and ion-transport properties dramatically change. Optimization of nanomaterials largely relies on the possibility of controlling their morphology and on the ability to resolve individual factors controlling their charge carrier transport properties. In particular, disentangling conductivity contributions related to the material intrinsic properties and to the morphology effects is an important task, which is, however, difficult to accomplish using conventional methods.

Terahertz (THz) spectroscopy[1] is a powerful method to investigate the charge transport in nanostructured materials[2]; this is because it enables non-contact probing of the material conductivity by freely propagating pulses of broadband electromagnetic radiation[3,4] and because the probing frequency is adequate for identifying charge-transport processes occurring on nanometer distances[5,6]. The THz conductivity spectra contain information on charge carrier scattering processes in the volume of nanoparticles, as well as on the carrier confinement due to interactions with nanoparticle boundaries[7,8].

In this paper, we describe the use of THz spectroscopy for elucidating charge-transport mechanisms in nanosized transparent conducting oxides (TCOs) composed of ultrasmall antimony-doped tin oxide (ATO) nanoparticles.[9] Transparent conducting oxides combining

optical transparency with electrical conductivity are important materials for a variety of optoelectronic and optoelectrochemical applications.[10] Nanoparticles are one of intensively studied TCO morphologies;[11,12,13,14,15,16,17] examples of their application span from wet chemical deposition of conducting coatings and patterned electrodes to assemblies of nanostructured electrodes for electrocatalytical and electroanalytical applications.[18,19,20,21,22,23]

The conductivity of the TCO materials composed of nanoparticles strongly depends on their intrinsic properties (or particle quality), which are greatly influenced by the method of fabrication, type and degree of doping, size, and defect chemistry. Besides the intrinsic conductivity of single nanoparticles, the dc conductivity of particle assemblies depends on all the processes that charges encounter in series during their long-distance motion[24,25,26]. These processes are mainly controlled by the sample morphology and by the quality of nanoparticle connections, and they become dominating with the decreasing particle size.

In order to reveal which transport mechanism is the limiting one for the dc conductivity in nanoparticle assemblies, it is essential to assess selectively and to characterize various conductivity contributions. Such information is encoded in the conductivity spectrum measured over a broad frequency range as explained in Figure 6.1. We investigate charge transport in nanoscale TCO samples composed of ATO nanoparticles prepared by a solvothermal reaction and pressed into pellets. To evaluate the influence of intrinsic particle properties on the conductivity, the particles prepared in the same way but with varying doping levels were studied. The effects of the morphology and, particularly, of the connectivity between nanoparticles were controlled by changing the thermal treatment conditions during the sample preparation. We developed and applied a theoretical framework linking the charge transport over various distances with measured terahertz conductivity spectra. These results are complemented with dc conductivity measurements and local probe microscopy techniques; this allows us to set up a microscopic picture of the conductivity on various length scales and explain the impact of various technological steps on the sample response. The approaches developed in this paper pave a way to understanding the richness of transport mechanisms in a variety of complex nanostructured materials.
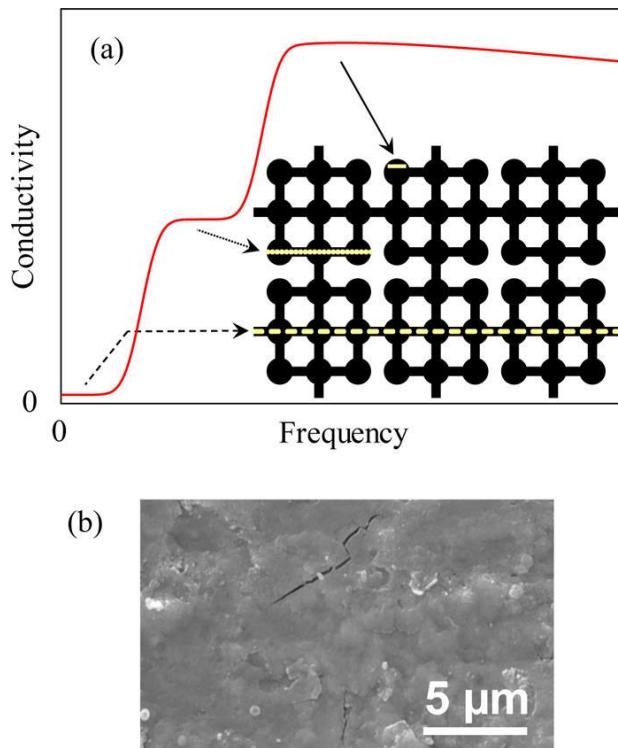
Figure 6.1   (a) Illustration of the conductivity spectrum in a structure containing conducting particles with various sizes (length scales). Only pathways crossing the entire sample (dashed line) contribute to the dc conductivity: in the scheme, the dc conductivity is very low as these pathways are rare and narrow. For higher frequencies, transport over shorter distances (such as the dotted line) starts to become effective and the conductivity increases (the middle plateau). If the frequency is increased further, even more confined charges contribute to the conductivity (e.g., charge motion within individual nanoparticles sketched by the solid line) and an additional increase is observed. Finally, the inertia of charges will start to limit the transport which implies a conductivity decrease at sufficiently high frequencies−this ensures that sum rules for optical conductivity are satisfied. (b) SEM image of cracks present in the investigated pellets made of ATO-10% nanoparticles. The cracks do not pose an obstacle for high-frequency conductivity, but they may significantly alter dc conductivity. Measurement of high-frequency response is thus practically insensitive to possible macroscopic defects in the material.

The paper is organized as follows: in section 6.2, we describe the samples and technological steps of their preparation; in section 6.3, we provide a brief theoretical introduction into the THz conductivity and describe models used for the data analysis. Finally, the experimental data are presented in section 6.4 and discussed in section 6.5.

6.2. RESULTS AND DISCUSSION

Antimony doped tin oxide (ATO) nanoparticles with different antimony-doping concentrations were prepared by a solvothermal synthesis in *tert*-butyl alcohol, which was described elsewhere[9].

In a typical synthesis procedure, different molar ratios of antimony chloride (1 M $SbCl_5$ in CH_2Cl_2, Aldrich) and tin chloride (1 M $SnCl_4$ in CH_2Cl_2, Aldrich) were dissolved in water-free tert-butyl alcohol and transferred into a Teflon- or glass-lined autoclave, which was kept in a laboratory oven preheated at 100 °C for 20 h. The total molar amount of tin and antimony was kept constant equaling 4.78 mmol in a total volume of 14 mL of tert-butyl alcohol/dichloromethane (0.34 mol/L). The particles with different Sb content are assigned as ATO-X% (with X = 0%, 3%, 5%, and 10%), where X refers to the stoichiometric molar amount of Sb in the precursor solution. The antimony content in the nanoparticles was found to be up to 60% higher than the molar amount of Sb in the initial precursor mixture taken for the reaction, which was shown by inductively coupled plasma optical emission spectroscopy (ICP-OES) and X-ray photoelectron spectroscopy (XPS). Therefore, the real Sb content was found to be 5%, 8% and 17% for ATO-3%, ATO-5% and ATO-10%, respectively. The ATO nanoparticles were flocculated by the addition of ca. 14 mL dichloromethane, separated by centrifugation (47800 rcf for 15 min), washed once in dichloromethane, twice in acetone and dried in air at 60 °C. The dried nanoparticles obtained in this way (as prepared) are crystalline corresponding to the cassiterite structure, with a mean particle size of 3 nm as described elsewhere. The particles dried in air at 60 °C contain ca. 15% organics as determined by thermal gravimetric (TGA) analysis. For fabrication of pellets for THz measurements the organic residues were removed by heating the nanoparticles for 200 °C in air. The thermal treatment practically does not change the crystallinity and crystal size of the nanoparticles as can be seen from the XRD patterns (Figure 6.2), but effectively removes organic residues. Additionally the dried nanoparticles were annealed in air at 500 °C. This heating step results in an increase in the size of crystalline domains and a possible particle sintering. The increase in particle size with temperature differs for the particles with different doping levels and is more significant for the undoped nanoparticles. Thus, the particle size changes from 4 to 14 nm for as prepared and calcined (500 °C) undoped nanoparticles, and from 3 to 5.5 nm for the ATO-5% nanoparticles.
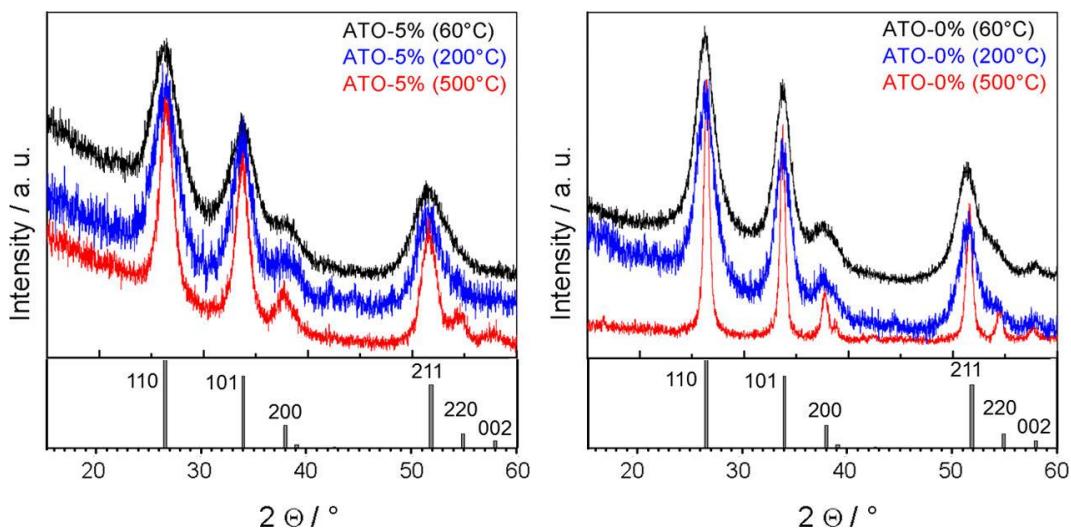
Figure 6.2 XRD patterns of ATO-5% (left) and ATO-0% (right) nanoparticles dried at 60 °C (black line) and calcined at 200 °C (blue line) or 500 °C (red line), respectively. The bars in the bottom panel mark the position and the intensity of the diffraction lines of SnO_2 cassiterite (space group $P4_2$/mnm, JCPDS File Card No. 41-1445). The particle size increased from 3 to 5.5 nm upon calcination at 500 °C for the ATO-5% nanoparticles (left) and from 4 to 14 nm for the undoped nanoparticles (right).

The conductivity measurements were performed on pelletized ATO nanoparticles, which were prepared by pressing finely ground nanoparticles under a pressure of 10 tons/cm^2 (960 MPa). The pellets obtained in this way are denoted as $\alpha C_{200}P$ and $\beta C_{500}P$ for the particles calcined at 200 or 500 °C, respectively. The samples denoted as $\gamma C_{200}PC_{500}$ underwent two calcination steps lasting 20 h each, one at 200 °C before pressing and a second at 500 °C after pressing. Finally, a set of samples $\delta C_{500}PC_{500}$ calcined at 500 °C both before and after pressing was prepared. Thus, we disposed of four series of samples denoted $\alpha-\delta$ with progressively enhanced annealing conditions as summarized in Table 6.1. The dc conductivity was measured using a two-point probe method with source measure unit Keithley 237. The contacts were made of colloidal gold and the shortest distance between the contact areas was considered for the evaluation of the conductivity. The conductivity was determined from the linear part of the I–V characteristics. The porosity spor of the pellets was determined by nitrogen sorption for all samples (Figure 6.3); it was within the 30–40% range.

Table 6.1   Preparation Conditions of the Investigated Samples.

Sample	Calcination of nanoparticles (before pressing)	Calcination of pellets (after pressing)
$\alpha C_{200}P$	20 hours at 200°C	—
$\beta C_{500}P$	20 hours at 500°C	—
$\gamma C_{200}PC_{500}$	20 hours at 200°C	20 hours at 500°C
$\delta C_{500}PC_{500}$	20 hours at 500°C	20 hours at 500°C

Complex THz transmission spectra of the pellets were measured in a custom-made setup[27] for time-domain THz spectroscopy[1] based on a femtosecond laser oscillator. The pellets were rather thin, and consequently, the time-domain signals coming from internal Fabry−Pérot reflections in the samples partially overlapped. For this reason, temporal windowing [28] of the individual internal reflections was not applied, and the transmission spectra were calculated from the Fourier transforms of long time-domain scans which include all these internal reflections. Spectra of the permittivity and conductivity were subsequently retrieved directly from these transmission spectra using an appropriate transmittance formula, e.g., eq 1 in ref 28.

All the samples were very fragile and could not withstand, e.g., mechanical polishing; for this reason, their optical quality was rather poor. The pellets were not plane parallel, and their thickness varied across the sample and could not be very precisely determined. We estimate that the accuracy of the thickness determination is of ∼15%; this introduces a similar systematic error in the real part of the refractive index.[29] Therefore, an error of ∼30% is expected in the real part of the permittivity (this corresponds to the uncertainty of 30% in the slope of the imaginary part of the conductivity). The presence of weak Fabry−Pérot-like interferences observed in some spectra is also related to these effects.
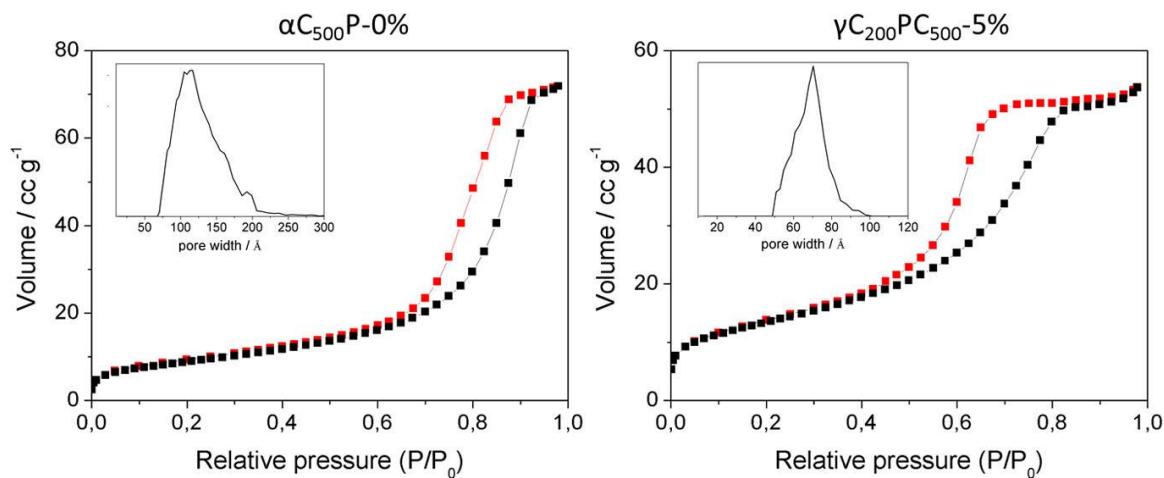
Figure 6.3   Nitrogen sorption isotherms of the pellets $\alpha C_{200}P$-0% (left) and $\gamma C_{200}PC_{500}$-5% (right). The inset shows the pore size distribution determined using density functional theory (DFT). The calculations are made for interactions of nitrogen with a model adsorbate surface (since these calculations are limited to only a few materials, we considered interactions with a silica surface which usually provides a reliable approximation for the majority of metal oxide surfaces). The calculations involved the nonlocal DFT equilibrium model for silica with cylindrical pores (116.8 Å for $\alpha C_{200}P$-0% and 70.3 Å for $\gamma C_{200}PC_{500}$-5%). The specific surface area was determined with the Brunauer−Emmett−Teller (BET) method at p/p0 = 0.05−0.2 and was 31.3 m^2/g and 47.3 m^2/g for $\alpha C_{200}P$-0% (left) and $\gamma C_{200}PC_{500}$-5% (right), respectively.

Another problem connected with the high sample fragility is the impossibility of using conductive atomic force microscopy (C-AFM) in contact mode due to relatively high interaction force between the AFM tip and the sample (typically 50−100 nN). To probe the electric properties of our samples we used C-AFM in PeakForce mode with a maximum interaction force (set point) of ∼1 nN. The samples were characterized by a Bruker Icon AFM using Cr/Pt coated silicon cantilevers BudgetSensors ElectriMulti75-G with a force constant of ∼3 N/m, and a resonant frequency of ∼75 kHz. The radius of a new tip was ∼25 nm.kHz.

6.3. THEORETICAL DESCRIPTION

In homogeneous systems, sample properties such as the permittivity or conductivity spectra directly represent the response function of polar excitations or charges in the material. However, the investigated pellets are inhomogeneous, which implies that the measured (effective) properties of samples differ from the response functions of charges in the nanocomponents. This difference finds its origin in the depolarization fields which build up in any composite material: the local electric field then differs from the applied one (represented here by the incident THz pulse) and we need to distinguish between the microscopic permittivity or conductivity (the "true" response functions to the local electric field) and the measured effective permittivity or conductivity (macroscopic response to the applied field).

Any in-depth analysis of the measured spectra in inhomogeneous systems must involve two steps.[30,31] In the first one, it is necessary to develop a model of the microscopic conductivity (response to the local THz electric field). In the second one, depolarization fields must be accounted for. Since the size of the investigated nanoparticles is much smaller than the probing wavelength, we can employ the effective medium approximation to transform the microscopic conductivity into the macroscopic one, which can be directly compared with (or fitted to) the measured data.

6.3.1. MODELS OF MICROSCOPIC RESPONSE

The complex permittivity spectrum ε of the SnO_2 nanoparticles can be decomposed into contributions due to the lattice vibrations ε_v and due to the conduction of charges $\Delta\varepsilon$

$$\varepsilon(f) = \varepsilon_v(f) + \Delta\varepsilon(f) \qquad \text{Equation 6.1}$$

where f is the frequency of probing radiation. The dominating part of the background lattice permittivity ε_v in the THz range is given by three lowest-frequency polar phonon modes

$$\varepsilon_v(f) = \left(\varepsilon_{dc} - \sum_{j=1}^{3} \frac{F_j}{f_j^2}\right) + \sum_{j=1}^{3} \frac{F_j}{f_j^2 - f^2 - i\Gamma f/2\pi} \qquad \text{Equation 6.2}$$

where the phonon frequencies f_j and oscillator strengths F_j were taken from Ref. 32; these modes lie high above our accessible spectral range ($f_j \geq 6$ THz). The first term at the right-

hand-side of equation 6.2 stands for the high-frequency permittivity ε_∞ due to excitations above the three considered phonons; for practical reasons explained below, we decided to introduce here explicitly the dc permittivity ε_{dc}, which was calculated as the mean value from the tensor components measured in ref. 33: $\varepsilon_{dc} = (2\varepsilon^\perp + \varepsilon^{||})/3 \approx 10.7$. The damping of phonons in the nanoparticles may be larger than in bulk due to extrinsic dielectric losses[34]. The damping in the fits describes background losses of our samples (not related to the conduction-band carriers) well below the phonon frequencies. For these reasons we adopted an approximation where the damping Γ is a fitting parameter common to all three modes.

Throughout this paper we use an equivalence between the complex permittivity and the complex conductivity $\varepsilon = i\sigma/(\omega\varepsilon_0)$ (where ε_0 is the permittivity of vacuum and $\omega = 2\pi f$ is angular frequency), i.e. each component of the permittivity can be equivalently expressed also in terms of the conductivity and vice versa. The description of sample properties in terms of the complex conductivity (instead of the complex permittivity) is especially advantageous for systems where the real conductivity does not vanish at low frequencies. Indeed, in such a case the imaginary part of the permittivity increases as $1/\omega$ upon lowering the frequency, which may lead to problems with fitting of the complex permittivity. We systematically denote the contribution of conduction band charges injected by doping of our samples by a symbol "Δ"; i.e.

$$\Delta\varepsilon(f) = \frac{i\Delta\sigma(f)}{\omega\varepsilon_0} \qquad \text{Equation 6.3}$$

which, following Equation 6.1, is added to the background lattice permittivity. The observed conduction mechanisms depend on the doping and on the preparation conditions of the nanoparticles and pellets. We need to discuss two types of transport mechanisms:

(1) Hopping conductivity can be understood as a superposition of relaxations with a very broad distribution of relaxation times[35]. Although hopping conductivity must saturate at high frequencies (and finally relax to zero to reflect the inertia of charge carriers and satisfy the sum rule), there are only few models which reflect at least the saturation behavior. As an approximation, we use here the random free-energy barrier mode[36]

$$\Delta\sigma_{hop}(f) = i\omega\sigma_\infty\tau_{max}\tau_{min}\left[1 + \frac{\ln\tau_{max} - \ln\tau_{min}}{\ln\frac{1-i\omega\tau_{min}}{1-i\omega\tau_{max}}}\right]\frac{\ln\tau_{max} - \ln\tau_{min}}{\tau_{max} - \tau_{min}} \qquad \text{Equation 6.4}$$

where the conductivity saturates at the value $\sigma\infty$ for frequencies higher than $1/\tau_{min}$ (see Figure 3 in ref 37). Here, the distribution of the relaxation times is delimited by τmin and

τmax, which are related to the shortest and longest hopping times, respectively. The parameter $1/\tau$min is of the order of the lowest phonon frequency, and the THz range may be pertinent for its determination. The longest hopping time is typically in the ms or μs range (far below THz spectral range), and it is the reason why the dc conductivity corresponding to hopping is very low in most materials.

(2) Bandlike conduction of free charges (electrons) in bulk materials is usually described by the Drude model. However, in the studied nanometer-sized particles the confinement effects are important. Although the Drude−Smith model[38] is frequently used to fit the data, it is a phenomenological model yielding only a limited insight into the properties of the material.[30] Here we calculate the response using Monte-Carlo method[39] which has a clear relation to microscopic properties such as nanoparticle size, mean carrier scattering time τs inside the nanoparticles, and efficiency of internanoparticle transport (probability that a charge scattered at a nanoparticle surface is transferred into the neighboring nanoparticle[7]). The calculations provide the charge mobility spectrum μband; the conductivity is subsequently calculated using

$$\Delta\sigma_{band}(f) = ne_0\mu_{band}(f) \qquad\qquad \text{Equation 6.5}$$

where n is the density of charge carriers contributing to the transport and e_0 is the electric charge of each carrier.

6.3.2.   EFFECTIVE MEDIUM APPROXIMATION

The effective response is inherently related to the morphology of the material and its behavior is particularly controlled by the degree of percolation of its conductive part.[7,31,40]. Recently, we have proposed a general model for an effective photoconductivity starting from the Bergman representation of effective medium theory. This model takes into account the existence of a percolated part of the sample and of its nonpercolated part described by a single dominant depolarization factor: [30,31]

$$\Delta\sigma_{\text{eff}} = V\Delta\sigma + \frac{B\Delta\sigma}{1 + iD\Delta\sigma/(\omega\varepsilon_0)}$$
<div align="right">Equation 6.6</div>

The percolated and nonpercolated contributions correspond to the first and second right-hand-side term of Equation 6.6, respectively. It has been shown[30] that this expression encompasses also frequently used effective medium models like the Maxwell-Garnett model, which describes rather simple sample morphologies where inclusions with permittivity ε_p are sparsely distributed in a percolated matrix with permittivity ε_m:

$$\sigma_{\text{eff}} = -i\omega\varepsilon_0\varepsilon_m \frac{\varepsilon_p(1 + Ks) + \varepsilon_m K(1 - s)}{\varepsilon_p(1 - s) + \varepsilon_m(K + s)}$$
<div align="right">Equation 6.7</div>

where s and K are the volume filling fraction and the shape factor of the inclusions, respectively. This model can be used in two ways:

(A) The sample is composed of nonconducting matrix with nonpercolated (sparse, well isolated) conducting inclusions (Figure 6.4 a; the parameter s corresponds to the volume fraction of ATO in our samples). To introduce the conductivity $\Delta\sigma$ of inclusions we substitute $\varepsilon p \rightarrow \varepsilon p + i\Delta\sigma/(\omega\varepsilon_0)$ into Equation 6.7. The change in the effective conductivity can be then transformed to the form of Equation 6.6 with V = 0 and with appropriate expressions for B and D as functions of the volume filling fraction and of the shape factor of the inclusions.[41]

(B) The sample is composed of a conducting percolated matrix, i.e., $\varepsilon m \rightarrow \varepsilon m + i\Delta\sigma/(\omega\varepsilon0)$ and of nonconducting isolated inclusions (in this case, s expresses the porosity of the samples). Strictly speaking, this model describes a conductor containing voids with well-defined shape (Figure 6.4 b). When the conductivity of the matrix is switched on, the effective permittivity of the composite changes again by $\Delta\sigma_{\text{eff}}$ which fulfills Equation 6.6. This time, however, the percolation strength V is non-zero:

$$V = K \frac{1-s}{K+s}.$$

Equation 6.8

In practice, such a topology closely resembles that of a percolated network of particles in contact with each other (Figure 6.4 c).
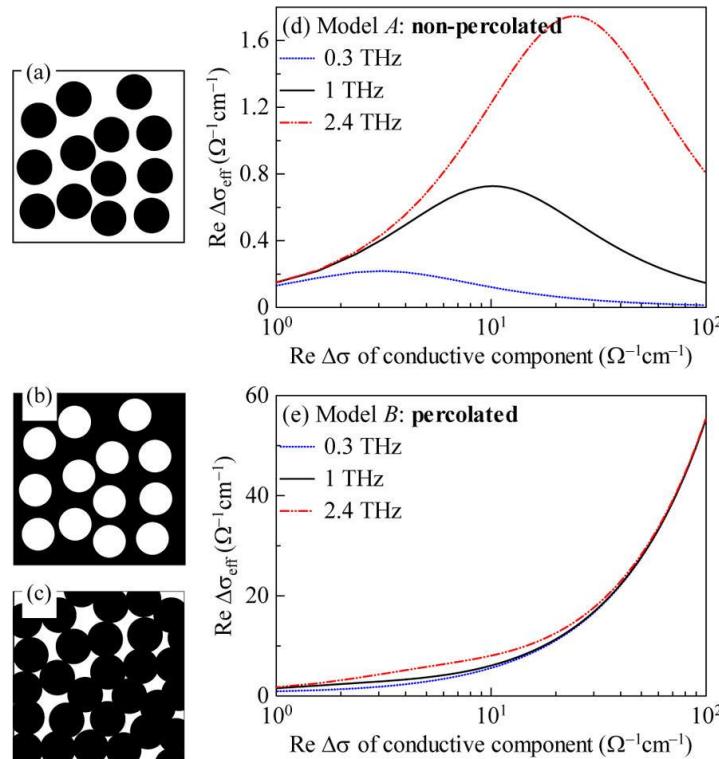
Figure 6.4   (a−c) Illustration of various morphologies (white = insulator, black = conductor). (a) Nonpercolated conducting particles. (b) Percolated conducting matrix containing nonconducting voids. (c) Topologically, the majority of real systems of percolated particles is equivalent to the percolated conducting matrix containing nonconducting voids as in (b). (d, e) Real part of the effective conductivity in the Maxwell−Garnett approximation as a function of the real conductivity contribution of the conductive component. Model A: conductive (nonpercolated) inclusions and insulating matrix. Model B: nonconductive inclusions and conductive (percolated) matrix. The calculations were performed for K = 2 and for the volume filling factor of the conductive component equal to 0.65.

The effective conductivity has a strikingly different behavior in these two cases as it is shown in Figure 6.4 d+e. In this figure, we assumed a real microscopic conductivity $\Delta\sigma$ in the conductive component of the sample and we calculated the real part of the total effective (macroscopic) conductivity σ_{eff} within the models (A) and (B). In order to obtain estimations quantitatively comparable to those expected for our samples, the following parameters were used in these calculations: for model (A), $\varepsilon_m = 1$, $\varepsilon_p = \varepsilon_{dc} + i\Delta\sigma/(\omega\varepsilon_0)$, $s = 1 - s_{por}$ and K = 2; and for model (B), $\varepsilon_p = 1$, $\varepsilon_m = \varepsilon_{dc} + i\Delta\sigma/(\omega\varepsilon_0)$, $s = s_{por}$ and K = 2 (the porosity $s_{por} = 35\%$ was taken from the sorption measurements).

We stress that for a percolated system the effective conductivity shows a monotonic behavior and can reach an arbitrarily high value upon an increase of $\Delta\sigma$ (see Figure 6.4 e). In contrast, the shape of the effective conductivity for a nonpercolated system is determined by the plasmonic resonance, [30,42] and its maximum value cannot exceed a well-defined limit as observed in Figure 6.4d: 2 Ω^{-1} cm^{-1} for frequencies below 2.5 THz (and for the above permittivities). A possibly different value of the shape factor K does not affect these conclusions: the effective conductivity is rather insensitive to its variations, particularly in case B.[31]

6.4. EXPERIMENTAL RESULTS

6.4.1. DOPED SAMPLES

The measured THz conductivity spectra of the doped samples are summarized in Figure 6.5 and Figure 6.6. The common characteristic of the spectra is an increase of the real part toward higher frequencies. In general, this is a signature of charge localization, either as a result of the charge confinement or as a manifestation of the depolarization fields. The lowest THz conductivity is observed in nanoparticles calcined at 200 °C before pressing ($\alpha C_{200}P$). Calcination at 500 °C before pressing ($\beta C_{500}P$) markedly improves the conductivity in the entire THz spectrum. An additional conductivity enhancement is achieved when the calcination at 500 °C takes place after pressing the samples ($\gamma C_{200}PC_{500}$); the samples undergoing this procedure become nearly opaque in the THz range and the THz conductivity can be quantitatively determined only in a very narrow frequency interval (Figure 6.6). Note also the strong negative imaginary part in all the spectra which is mainly due to the high value of the static dielectric constant ε_{dc}.
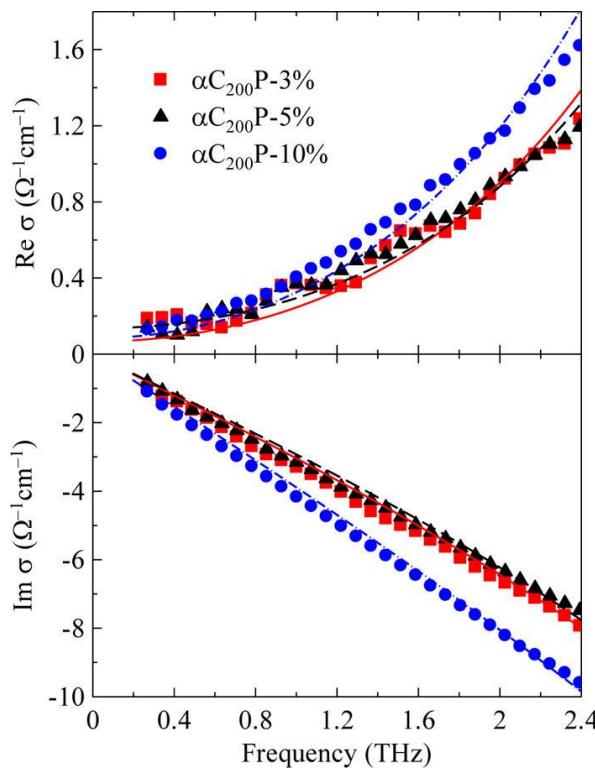
Figure 6.5 Conductivity spectra of pellets made of doped nanoparticles calcined at 200 °C before pressing (αC$_{200}$P). Symbols: measured spectra. Lines: fit assuming phonon response plus constant conductivity in the THz range.

The samples βC$_{500}$P and γC$_{200}$PC$_{500}$ exhibit effective conductivities clearly exceeding the level of ~2 Ω^{-1}cm^{-1}. Following the effective medium description developed in the previous section and illustrated in Figure 6.4, we can safely conclude that for doped samples of series β and γ we deal with a percolated network of nanoparticles, since only this system can be compatible with such high conductivities.

For the αC$_{200}$P samples, the observed effective conductivities just attain the upper limits achievable in nonpercolated systems; however, this can occur only if the microscopic conductivity of nanoparticles is close to 25 Ω^{-1} cm^{-1}. Below, we show our measurements on the undoped samples; these results suggest that in all series of the samples (α, β, and γ) we deal with an at least partly percolated network of nanoparticles. It is then reasonable to assume that the conductivity in all our samples (including αC$_{200}$P) arises predominantly from the percolated parts. The presence of percolation pathways is also supported by the measurements of local current using conductive AFM (C-AFM, Figure 6.7): there are substantial areas (dark color scale in the Figure) where an electrical current flows through the entire thickness of the pellets. It should be also noted that many places on the surface exhibit

substantially lower conductivity: this indicates that certain limited areas in the pellets are electrically isolated from the rest.
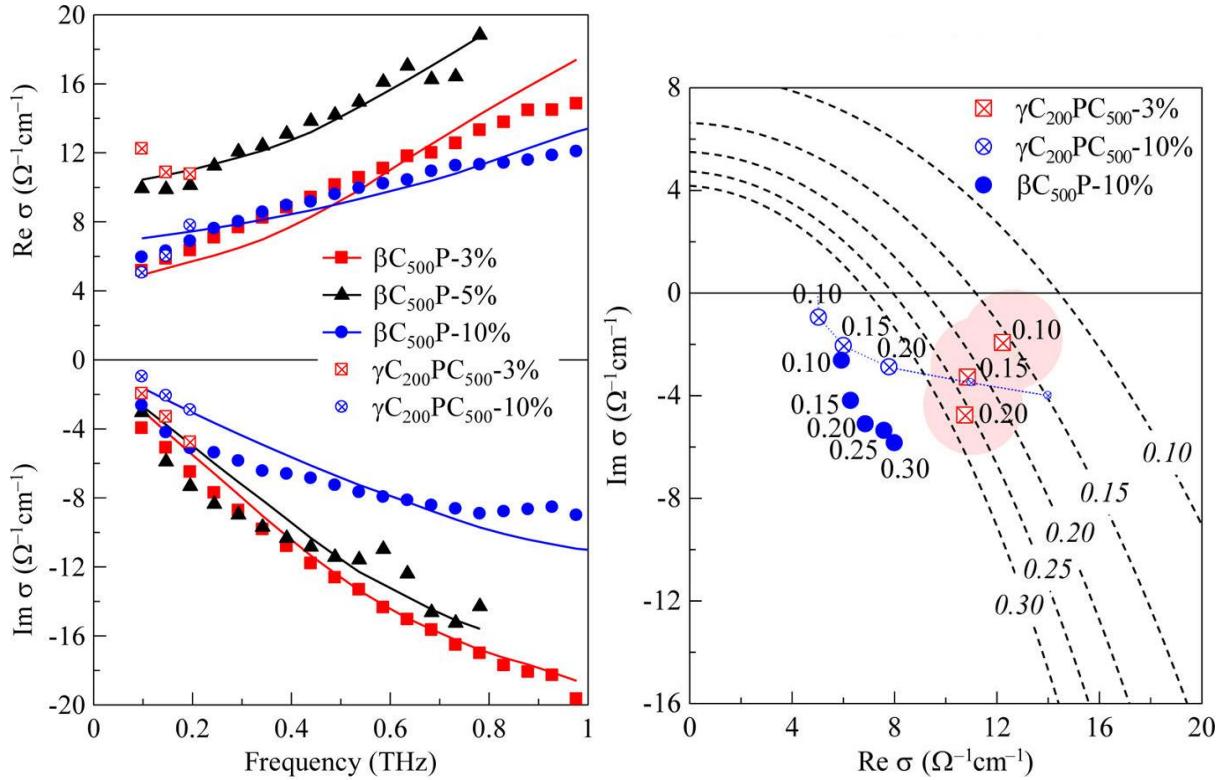
Figure 6.6   Left: Conductivity spectra of the doped samples calcined at 500 °C before ($\beta C_{500}P$) or after pressing ($\gamma C_{200}PC_{500}$). Symbols: measured spectra. Lines: fits of the $\beta C_{500}P$ samples. Right: Analysis of the measurement sensitivity. The dashed lines indicate conductivities leading to a transmission amplitude of 1% in our samples; this is the sensitivity level of our setup at the lowest frequencies; values above or to the right of these curves cannot be detected (the sensitivity level is frequency-dependent; the frequencies in THz are indicated by numbers in italics). The regular font numbers in the vicinity of symbols show the corresponding frequency in THz. The sample $\gamma C_{200}PC_{500}$-10% is transparent enough only for frequencies up to 0.20 THz; for higher frequencies, the real part of the conductivity increases so that the transmission amplitude drops below 1% and the signal cannot be reliably resolved (the behavior of the conductivity is illustrated by small points and dotted lines). The conductivity of $\gamma C_{200}PC_{500}$-3% reaches the very detection limit; we can only deduce an order-of-magnitude estimate of the low-frequency conductivity (the shaded areas illustrate the errors of the measured conductivities).
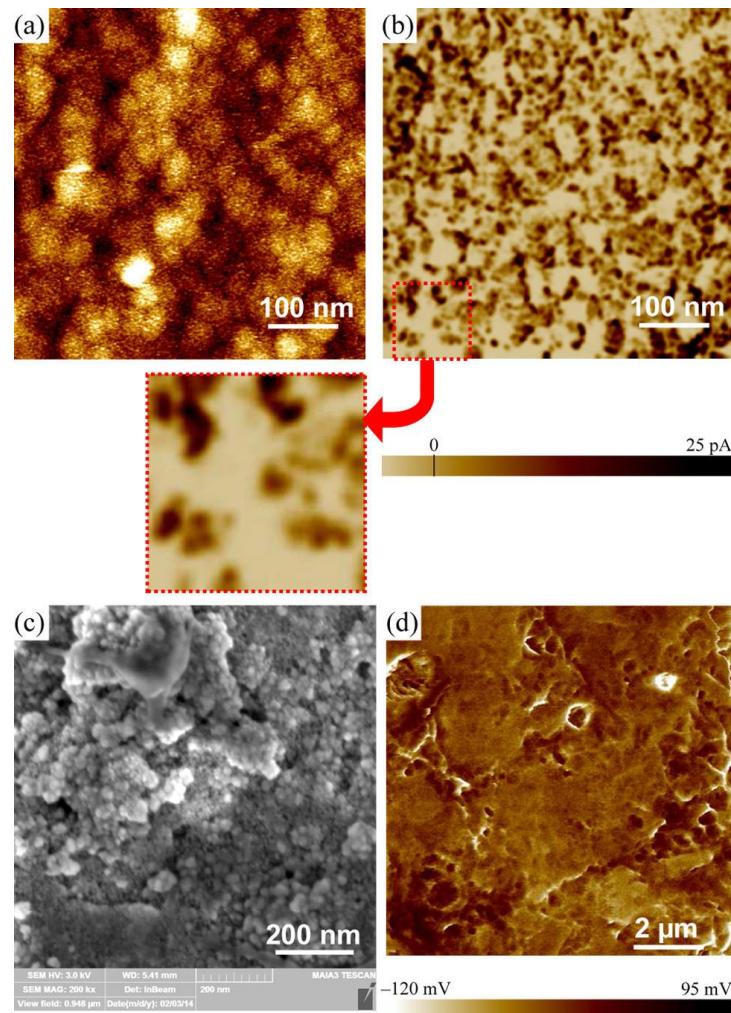
Figure 6.7 Topography of the $\alpha C_{200}PC_{500}$-10% sample. (a) Height map measured using AFM is quite noisy because of the sample fragility. Since the image is convoluted with the profile of the AFM tip, single nanoparticles cannot be resolved, and we only see their aggregates. (b) Local current map measured by PeakForce C-AFM (and processed by low-pass filter) in the same area of the sample (the bias of the tip was −0.5 V); due to the difference in conductivity it is possible to resolve single nanoparticles with the size of ∼6 nm. (c) SEM image of the surface of the $\gamma C_{200}PC_{500}$-10% sample; it shows the porous morphology of the pellets composed of larger clusters of several tens of nm in size. (d) Electric potential at the surface measured by Kelvin probe force microscopy.

6.4.2. UNDOPED SAMPLES

For undoped samples, the conductivity due to charge carriers is low and the dielectric contribution largely dominates; it is then more useful to think in terms of the permittivity instead of the conductivity. The measured spectra of undoped samples are shown in Figure **6.8**. Regardless of the calcination procedure, the lattice vibrations strongly influence the total response: their contribution is at least comparable to (or even higher than) that of the charge carrier conductivity. This statement can be inferred from an almost flat real part and a small imaginary part of the permittivity which does not exhibit any $1/\omega$ tail at low frequencies characteristic for a nonvanishing dc conductivity. To estimate the degree of percolation in these samples we calculated the effective permittivity using the Maxwell–Garnett models A and B described previously. In these particular calculations, we took into account a purely dielectric response of nanocrystals due to phonons defined by (2). The real parts of the measured permittivity spectra lie between the effective permittivity values calculated using the two models (see Figure 6.8). We can therefore assume that percolation pathways in the nanoparticle network do exist.
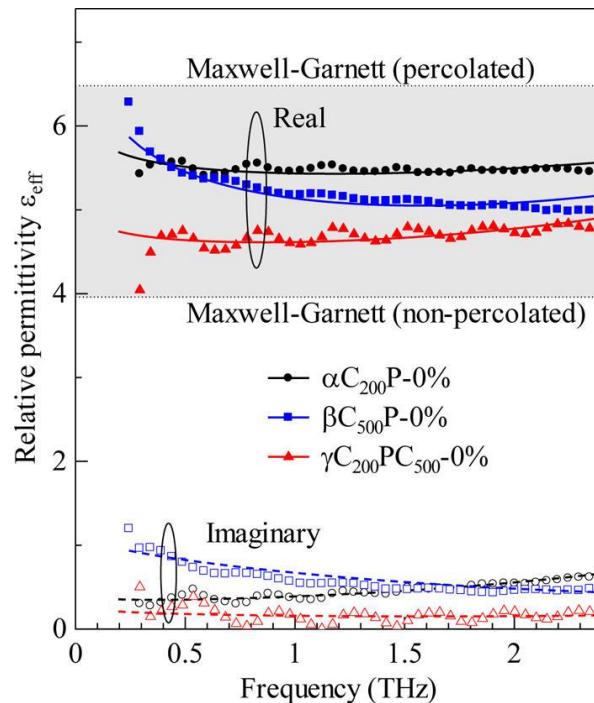
Figure 6.8   Spectra of the permittivity of undoped samples. Symbols: measured data. Lines: fits by the model described in the text. The horizontal dotted lines delimit the ranges into which the real part of the effective permittivity should fall for a nonpercolated (bottom part) and fully percolated (top part) network of nanoparticles within the Maxwell−Garnett approximation.

On the one hand, it is probable that a certain amount of nanoparticles remain nonpercolated. The same argument applies also for $\alpha C_{200}P$-doped samples; this is as well supported by C-AFM measurements on the $\alpha C_{200}P$-doped samples where insulating areas were observed on the surface of the pellets. On the other hand, the microscopic conductivity $\Delta\sigma$ is very low both in undoped samples and in $\alpha C_{200}P$ doped samples. It has been previously shown, cf. eq 13 and the related discussion in ref 7, that for such a low $\Delta\sigma$ the effective conductivity is not sensitive to the percolation degree. In other words, for low $\Delta\sigma$ the contributions of percolated and nonpercolated components are the same.

6.5. DISCUSSION

6.5.1. FIT MODELS

We fitted the experimental data by the expression based on model (B):

$$\sigma_{\mathrm{eff}} = \left(-i\omega\varepsilon_0\varepsilon_v + \Delta\sigma\right)\frac{\varepsilon_p\left(1+Ks\right)+\left(\varepsilon_v + i\Delta\sigma/(\omega\varepsilon_0)\right)K\left(1-s\right)}{\varepsilon_p\left(1-s\right)+\left(\varepsilon_v + i\Delta\sigma/(\omega\varepsilon_0)\right)\left(K+s\right)} \qquad \text{Equation 6.9}$$

where the shape factor $K = 2$, the pore-filling fraction $s_{\mathrm{por}} = s$ can be considered as a free parameter but it should lie within the range 0.3–0.4 (which was experimentally determined for our samples), and $\varepsilon_p = 1$ (air voids). The background lattice permittivity ε_v possesses a single free parameter Γ for each sample series (α, β, and γ); however, the values of this parameter are determined from the spectra of undoped samples where the phonon modes constitute a significant contribution. These values are then used for fitting the spectra of doped samples, and Γ is not considered as a free parameter anymore.

The conductivity $\Delta\sigma$ is given by a proper microscopic conductivity model. (i) For doped samples $\Delta\sigma$ is given by Equation 6.5, and it is calculated using Monte Carlo simulations. The free parameters of the fits are the probability of charge transport among nanoparticles p_F, the nanoparticle size d, and the carrier density n. The value of the "bulk" scattering time inside nanoparticles τ_s is not important as the scattering at the nanoparticle boundaries largely dominates. Note that we are able to obtain quantitative fits only for series β. (ii) For undoped samples, the experimental results were fitted by the hopping model (Equation 6.4), and the free fitting parameters are high-frequency conductivity (σ_∞), phonon damping Γ, and

maximum hopping rate $1/\tau_{min}$ (the minimum hopping rate $1/\tau_{max}$ is very low and does not affect the THz spectra).

Table 6.2   Conductivities of the doped samples.

Sample	$\dfrac{\sigma_{dc}}{\Omega^{-1}cm^{-1}}$	$\dfrac{\sigma_{eff}\ (0.2\ THz)}{\Omega^{-1}cm^{-1}}$	$\dfrac{p_F}{\%}$	$\dfrac{n}{cm^{-3}}$
$\alpha C_{200}P$-3%	$(0.8 \div 4)\times 10^{-3}$	0.18		
$\alpha C_{200}P$-5%	1.6×10^{-3}	0.12		
$\alpha C_{200}P$-10%	$(0.3 \div 1.1)\times 10^{-3}$	0.14		
$\beta C_{500}P$-3%	0.33	6	5	3.7×10^{18}
$\beta C_{500}P$-5%	0.60	10	11	4.3×10^{18}
$\beta C_{500}P$-10%	0.68	7	14	2.5×10^{18}
$\gamma C_{200}PC_{500}$-3%	0.5	11		
$\gamma C_{200}PC_{500}$-5%	1.5			
$\gamma C_{200}PC_{500}$-10%	1.0	8		
$\delta C_{500}PC_{500}$-3%	62			
$\delta C_{500}PC_{500}$-5%	40			
$\delta C_{500}PC_{500}$-10%	22			

6.5.2.   DOPED SAMPLES

The increase in the real part of the THz conductivity of $\alpha C_{200}P$ nanoparticles (Figure 6.5) is strongly mixed with the response of the phonon modes; it is not then possible to conclude unambiguously on the shape of the conductivity spectrum, and therefore, one cannot assess the properties of the short-range charge transport in these samples. However, a weak conduction contribution can be clearly distinguished near 0.2 THz where the phonon response tends to vanish. The results are summarized in Table 6.2: the sub-THz conductivity values are almost 2 orders of magnitude higher than the measured dc conductivity ($\sim 10^{-3}\ \Omega^{-1}cm^{-1}$). This clearly indicates the presence of energy barriers strongly suppressing charge transport between nanoparticles. Both, the THz and dc conductivities are substantially improved upon calcination at 500 °C either before or after pressing the pellets (samples $\beta C_{500}P$ and $\gamma C_{200}P_{500}$ in Figure 6.6 and Table 6.2); the THz conduction response now dominates in the spectra, and the phonon contribution is much less prominent. We observe a significant enhancement of the

effective conductivity close to our lower spectral limit (∼0.2 THz). This demonstrates that the resistance at the interface between nanoparticles is significantly lowered compared to that observed in the pellets annealed at lower temperature (200 °C). The dc conductivity is about 1 order of magnitude lower than σ_{eff} at 0.2 THz; this indicates that energy barriers suppressing the long-range charge transport are still present. It is interesting to note that the dc conductivities do not vary substantially with doping and remain much lower than the THz ones (Figure 6.9); this corroborates the conclusion that the dc conductivity is controlled mainly by interfaces rather than by the conductivity inside the nanoparticles. Elimination of the barriers is thus one of the important technological targets for the optimization of the dc conductivity of these materials. Indeed, a further important enhancement of the dc conductivity was achieved in the $\delta C_{500}PC_{500}$ samples;[9] no THz measurements could be performed on these samples as their high conductivity value makes them completely opaque to the THz radiation.
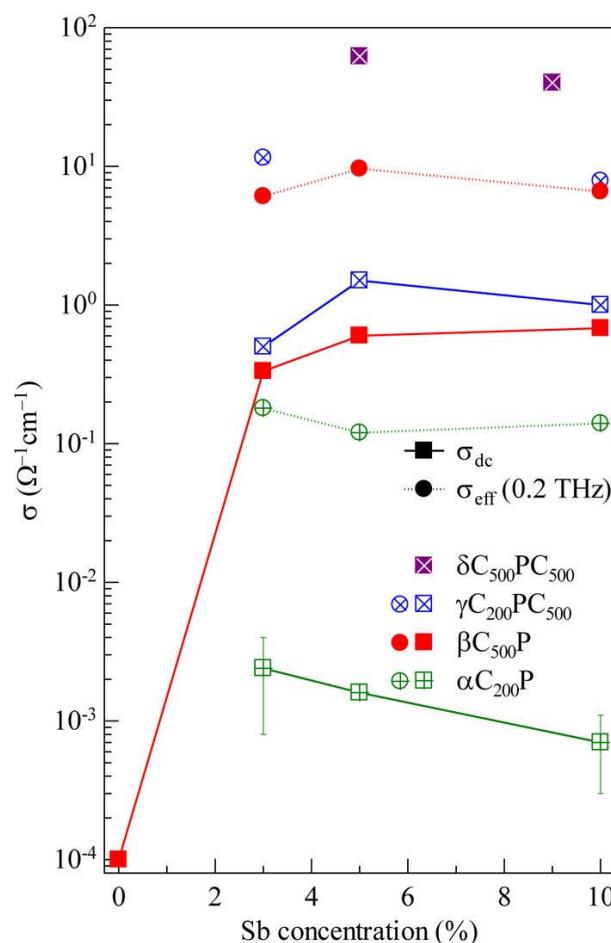
Figure 6.9   Summary of various conductivities in the doped samples.

For the $\beta C_{500}P$ samples, we can examine the shape of the conductivity spectra. All of them can be described using the Monte Carlo calculations providing that the size of the nanoparticles is about 26 nm and that there is a nonzero probability p_F of the internanoparticle charge transport (Table 6.2; an electron-scattering time of 66 fs was used in simulations issuing from the mobility value reported in ref 43). The nanoparticle size is considerably larger than that observed by SEM or from X-ray diffraction pattern (5−7 nm, Figure 6.7c). However, a broad distribution of nanoparticle sizes in these samples can be expected. It has been pointed out in ref. 41 that the THz conductivity signal originating in nanoparticles with a particular size scales with their total volume rather than with their number. In addition, as a rule, the mobility in larger nanoparticles is higher than in smaller nanoparticles. Consequently, even a small amount of larger nanoparticles can significantly contribute to the conductivity of sample and dominate in the THz spectrum. Furthermore, in some nanoparticle clusters (as observed in Figure 6.7c) interfaces with low concentration of defects may appear which do not act as barriers for the charge transport. Such a behavior was reported, e.g., in CdS nanocrystals prepared by chemical bath deposition.[44]

We observe that increasing the doping level has a positive influence on the connectivity of nanoparticles as indicated by the increasing probability p_F of internanoparticle charge transport in samples of series β. However, this probability remains rather low, which suggests that the contact resistance between nanoparticles can still be technologically improved (series γ and δ). Note that the charge density in nanoparticles decreases for the highest doping concentration−this indicates that the lattice is able to accommodate only a limited amount of dopants. Calcination at 500 °C after pressing (series γ) somewhat enhances the dc conductivity, which means that some of the nonconducting interfaces are converted into the conducting interfaces during the annealing. However, it is not possible to get further information on charge transport in samples $\gamma C_{200}PC_{500}$ as they were not transparent above 0.2 THz (Figure 6.6).

6.5.3. UNDOPED SAMPLES

There is clear evidence (real and imaginary parts of the permittivity increasing toward lower frequencies) of the conduction in sample $\beta C_{500}P$-0% (blue squares in Figure 6.8). The spectral shape corresponds to the hopping conductivity described by eq 4 with $\tau_{min} = 84$ fs. In the two other samples ($\alpha C_{200}P$-0% and $\gamma C_{200}PC_{500}$-0%), there is only a weak vertical offset in the imaginary part of the permittivity, which qualitatively indicates a nonvanishing THz conductivity also in these two materials. The hopping mechanism in the undoped samples also correlates with the very low value of the measured dc conductivity: the dc transport is limited by the longest hopping times which are not effective in the THz spectral region (Table 6.3). In this view, it makes sense that the saturated hopping conductivity σ_∞ (representing the intrinsic properties of SnO$_2$ nanoparticles) varies only moderately among samples prepared using various calcination procedures, whereas there are orders of magnitude differences in the dc conductivity (reflecting both the longest hopping times and the connectivity between nanoparticles). We suggest that there are impurities or imperfections which are responsible for the hopping conduction.

Table 6.3 Conductivities of undoped samples.

Sample	σ_{dc} ($\Omega^{-1}cm^{-1}$)	σ_∞ ($\Omega^{-1}cm^{-1}$)
$\alpha C_{200}P$-0%	3×10^{-8}	0.7
$\beta C_{500}P$-0%	1×10^{-4}	2.2
$\gamma C_{200}PC_{500}$-0%	1×10^{-7}	0.4

6.6. CONCLUSIONS

Charge transport in nanostructured materials is a complex process involving a number of steps on various length and time scales, reflecting the intrinsic properties of nanoparticles as well as morphological effects. The developed analysis of terahertz conductivity spectra offers the possibility to disentangle and characterize these properties in complex semiconductor nanostructures.

For the investigated pellets made of undoped and Sb-doped SnO_2 nanoparticles, we assessed the connectivity and the intrinsic conductivity mechanisms of nanoparticles for a variety of annealing conditions and obtained a global picture of charge transport in these assemblies (Figure 6.10). We found that the nanoparticles form a network with a high degree of dielectric percolation. Conductivity of undoped nanoparticles is governed by hopping mechanism. Doping introduces a bandlike conduction inside the nanoparticles. Calcination of doped samples at low temperatures (200 °C) leads to a poor intrananoparticle conductivity and to a very limited inter-nanoparticle charge transport. Calcination at elevated temperatures (500 °C) enhances the conductivity inside the nanoparticles and improves the conductivity of the contact area between nanoparticles, but the interface resistance remains rather high and constitutes a parameter which can still be considerably improved. Calcination at low temperature before pressing and at high temperature after pressing leads to a somewhat enhanced level of conductivity of the nanoparticles as well as of the dc conductivity. The best conductivity is achieved for samples calcined at 500 °C both before and after pressing: the conductivity of the nanoparticles remains high whereas barriers limiting charge transport between the nanoparticles are largely eliminated.
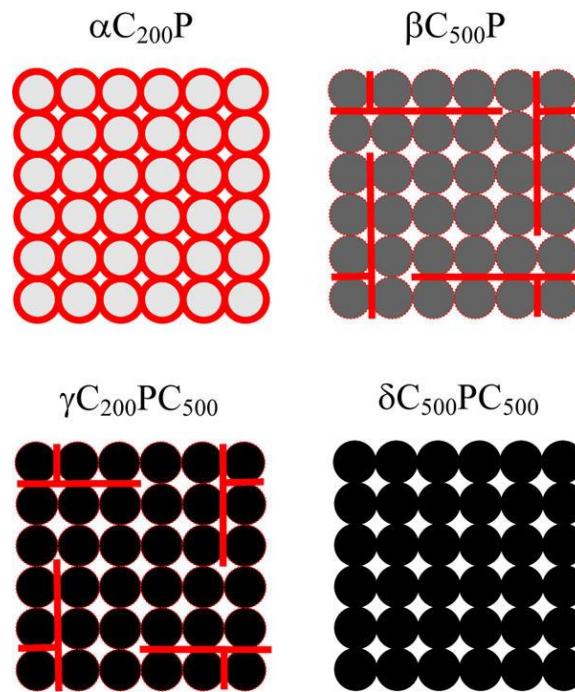
Figure 6.10 Schematic illustration of the morphology of pellets made of doped nanoparticles with different calcination conditions (the gray scale indicates the level of the intrananoparticle conductivity, the thickness of the red lines represents the interface resistance). The conductivity of $\alpha C_{200}P$ nanoparticles is rather low, and the dc transport is significantly suppressed by high interface resistance between individual nanoparticles. The conductivity of nanoparticles is substantially improved after annealing at 500 °C before pressing ($\beta C_{500}P$), but the interface resistance still remains the parameter considerably limiting long-distance transport. The dc conductivity is further limited by dead interfaces between larger aggregates of nanoparticles [in reality, the active/dead interface ratio is much smaller as compared to the illustration−this stems from the high ratio of $\sigma_{eff}(0.2\ THz)/\sigma_{dc}$]. Calcination after pressing ($\gamma C_{200}PC_{500}$) leads to a somewhat enhanced level of the intrananoparticle conductivity as well as of the dc conductivity of the pellets. The best conductivity is achieved for samples calcined at 500 °C both before and after pressing: the conductivity of nanoparticles remains high, whereas barriers limiting charge transport between nanoparticles are largely eliminated.

6.7. REFERENCES

(1)   Grüner, G. *Millimeter and submillimeter wave spectroscopy of solids*, Springer-Verlag, Berlin, Heidelberg, **1998**.

(2)   Ulbricht, R.; Hendry, E.; Shan, J.; Heinz, T. F.; Bonn, M. Carrier *Rev. Mod. Phys.* **2011**, *83*, 543.

(3)   Jeon, T.-I.; Grischkowsky, D. *Phys. Rev. Lett.* **1997**, *78*, 1106.

(4)   Schmuttenmaer, C. A. *Chem. Rev.* **2004**, *104*, 1759.

(5)   Lloyd-Hughes, J.; Jeon, T.-I. *Int. J. Infrared Millimeter Waves* **2012**, *33*, 871.

(6)   Němec, H.; Rochford, J.; Taratula, O.; Galoppini, E.; Kužel, P.; Polívka, T.; Yartsev, A.; Sundström, V. *Phys. Rev. Lett.* **2010**, *104*, 197401.

(7)   Němec, H.; Kužel, P.; Sundström, V. *J. Photochem. Photobiol. A* **2010**, *215*, 123.

(8)   Ponseca, Jr., C. S.; Němec, H.; Wallentin, J.; Anttu, N; Beech, J. P.; Iqbal, A.; Borgström, M.; Pistol, M.-E.; Samuelson, L.; Yartsev, A. *Phys. Rev. B* **2014**, *90*, 085405.

(9)   Peters, K.; Zeller, P.; Štefanić, G.; Skoromets, V.; Němec, H.; Kužel, P.; Fattakhova-Rohlfing, D. *Chem. Mater.* **2015**, *27*, 1090.

(10) Ginley, D. S.; Hosono, H.; Paine, D. C. In *Handbook of Transparent Conductors; Springer*, New York, **2010**.

(11) Liu, Y.; Szeifert, J. M.; Feckl, J. M.; Mandlmeier, B.; Rathouský, J.; Hayden, O.; Fattakhova-Rohlfing, D.; Bein, T. *ACS Nano* **2010**, *4*, 5373.

(12) Liu, Y.; Štefanić, G.; Rathouský, J.; Hayden, O.; Bein, T.; Fattakhova-Rohlfing, D. *Chem. Sci.* **2012**, *3*, 2367.

(13) Müller, V.; Rasp, M.; Štefanić, G.; Ba, J.; Günther, S.; Rathouský, J.; Niederberger, M.; Fattakhova-Rohlfing, D. *Chem. Mater.* **2009**, *21*, 5229.

(14) Ba, J.; Fattakhova-Rohlfing, D.; Feldhoff, A.; Brezesinski, T.; Djerdj, I.; Wark, M.; Niederberger, M. *Chem. Mater.* **2006**, *18*, 2848.

(15) Ito, D.; Yokoyama, S.; Zaikova, T.; Masuko, K.; Hutchison, J. E. *ACS Nano* **2014**, *8*, 64.

(16) Lee, J.; Lee, S.; Li, G.; Petruska, M. A.; Paine, D. C.; Sun, S. *J. Am. Chem. Soc.* **2012**, *134*, 13410.

(17) Hammarberg, E.; Prodi-Schwab, A.; Feldmann, C. *J. Colloid Interface Sci.* **2009**, *334*, 29.

(18) Williams, V. O.; DeMarco, E. J.; Katz, M. J.; Libera, J. A.; Riha, S. C.; Kim, D. W.; Avila, J. R.; Martinson, A. B. F.; Elam, J. W.; Pellin, M. J.; Farha, O. K.; Hupp, J. T. *ACS Appl. Mater. Interfaces* **2014**, *6*, 12290.

(19) Lai, S. C. S.; Dudin, P. V.; Macpherson, J. V.; Unwin, P. R. *J. Am. Chem. Soc.* **2011**, *133*, 10744.

(20) Sarauli, D.; Wettstein, C.; Peters, K.; Schulz, B.; Fattakhova-Rohlfing, D.; Lisdat, F. *ACS Catal.* **2015**, *5*, 2081.

(21) Sarauli, D.; Peters, K.; Xu, C.; Schulz, B.; Fattakhova-Rohlfing, D.; Lisdat, F. *ACS Appl. Mater. Interfaces* **2014**, *6*, 17887.

(22) Müller, V.; Rasp, M.; Rathouský, J.; Schutz, B.; Niederberger, M.; Fattakhova-Rohlfing, D. *Small* **2010**, *6*, 633.

(23) Liu, Y.; Peters, K.; Mandlmeier, B.; Müller, A.; Fominykh, K.; Rathouský, J.; Scheu, C.; Fattakhova-Rohlfing, D. *Electrochim. Acta* **2014**, *140*, 108.

(24) Laquai, F.; Wegner, G.; Bässler, H. *Phil. Trans. R. Soc. Lond. A* **2007**, *365*, 1473.

(25) Vukmirović, N.; Ponseca, C. S.; Němec, H.; Yartsev, A.; Sundström, V. *J. Phys. Chem. C* **2012**, *116*, 19665.

(26) Nelson, J.; Chandler, R. E. *Coord. Chem. Rev.* **2004**, *248*, 1181.

(27) Kužel, P.; Němec, H.; Kadlec, F.; Kadlec, C. *Opt. Exp.* **2010**, *18*, 15338.

(28) Duvillaret, L.; Garet, F.; Coutaz, J.-L. *IEEE J. Sel. Topics Quantum Electron.* **1996**, *2*, 739.

(29) Duvillaret, L.; Garet, F.; Coutaz, J.-L. *Appl. Opt.* **1999**, *38*, 409.

(30) Kužel, P.; Němec, H. *J. Phys. D: Appl. Phys.* **2014**, *47*, 374005.

(31) Němec, H.; Zajac, V.; Rychetský, I.; Fattakhova-Rohlfing, D; Mandlmeier, B.; Bein, T; Mics, Z.; Kužel, P. *IEEE T. THz. Science Technol.* **2013**, *3*, 302.

(32) Borges, P. D.; Scolfaro, L. M. R.; Alves, H. W. L. ; da Silva Jr., E. F. *Theor. Chem. Acc.* **2010**, *126*, 39.

(33) van Daal, H. J. *J. Appl. Phys.* **1968**, *39*, 4467.

(34) Petzelt, J.; Kamba, S. *Mater. Chem. Phys.* **2003**, *79*, 175.

(35) Elliott, S. R. *Adv. Phys.* **1987**, *36*, 135.

(36) Dyre, J. C. *J. Appl. Phys.* **1988**, *64*, 2456.

(37) Němec, H.; Mics, Z.; Kempa, M.; Kužel, P.; Hayden, O.; Liu, Y.; Bein, T.; Fattakhova-Rohlfing, D. *J. Phys. Chem. C* **2011**, *115*, 6968.

(38) Smith, N. V. *Phys. Rev. B* **2001**, *64*, 155106.

(39) Němec, H.; Kužel, P.; Sundström, V. *Phys. Rev. B* **2009**, *79*, 115309.

(40) Jensen, S.A.; Tielrooij, K.-J.; Hendry, E.; Bonn, M.; Rychetský, I.; Němec, H. *J. Phys. Chem. C* **2014**, *118*, 1191.

(41) Zajac, V.; Němec, H.; Kadlec, C.; Kůsová, K.; Pelant, I.; Kužel, P. *New J. Phys* **2014**, *16*, 093013.

(42) Nienhuys, H.-K.; Sundström, V. *Appl. Phys. Lett.* **2005**, *87*, 012101.

(43) Fonstad, C. G.; Rediker, R. H. *J. Appl. Phys.* **1971**, *42*, 2911.

(44) Mics, Z.; Němec, H.; Rychetský, I.; Kužel, P.; Formánek, P.; Malý, P.; Němec, P. *Phys. Rev. B* **2011**, *83*, 155326.

7. ZINC FERRITE PHOTOANODE NANOMORPHOLOGIES WITH FAVORABLE KINETICS FOR WATER-SPLITTING

This chapter is based on the following publication:
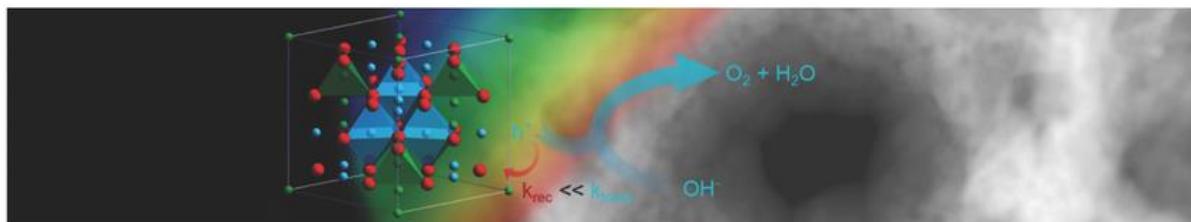
Alexander G. Hufnagel, Kristina Peters, Alexander Müller, Christina Scheu,
Dina Fattakhova-Rohlfing, Thomas Bein

The joint project is a collaboration of different groups to investigate spinel type zinc ferrite ($ZnFe_2O_4$) as a photoabsorber material for light-driven water-splitting. A. G. Hufnagel developed the atomic layer deposition process for the fabrication of zinc ferrite and performed the electrochemical characterization experiments. K. Peters fabricated macroporous ATO electrodes, which served as transparent conducting support for the zinc ferrite absorber layer, and measured SEM of the assemblies. A. Müller characterized the host-guest architectures by TEM.

FRONT COVER
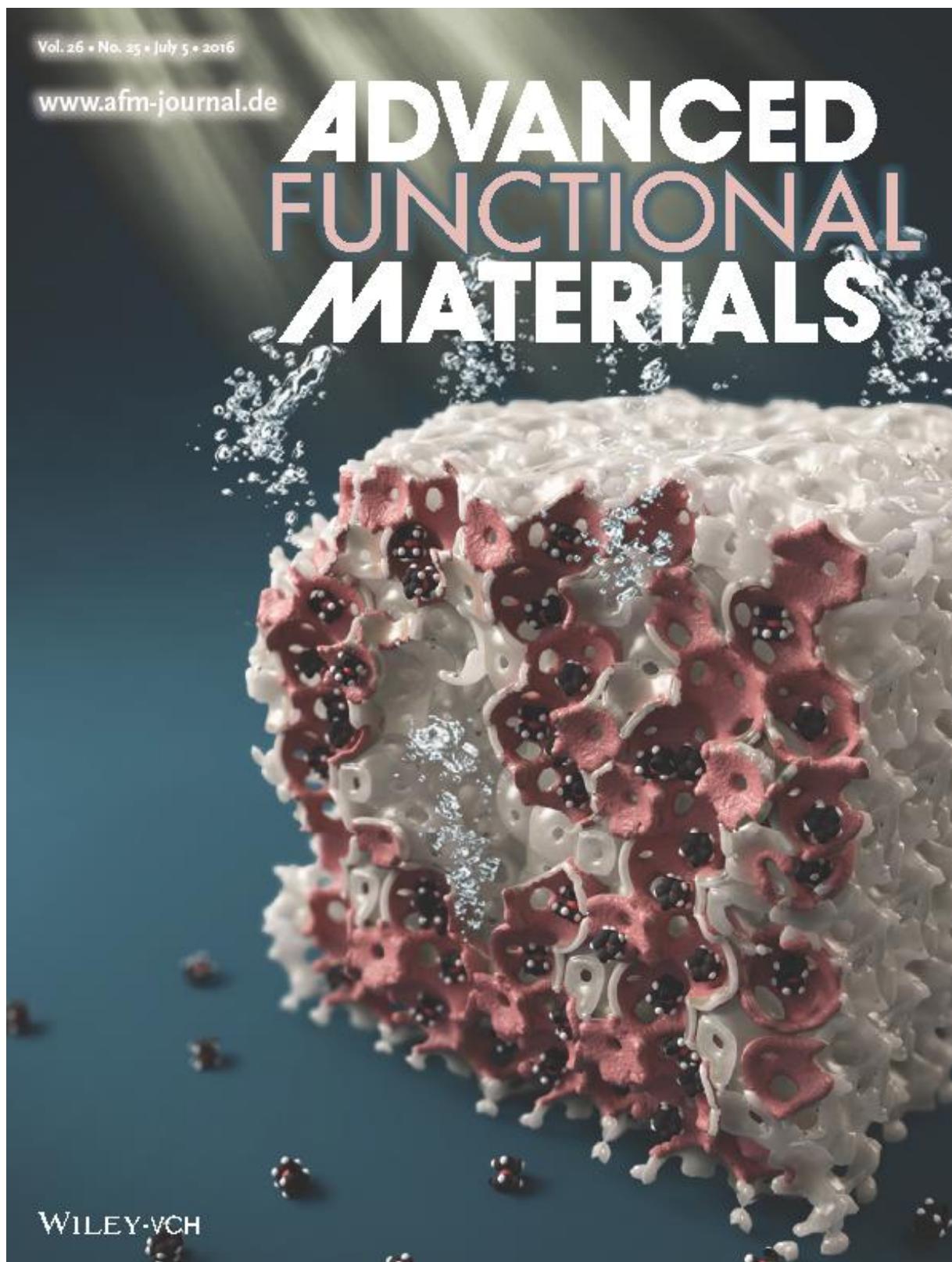
Image created by Christoph Hohmann (Nanosystems Initiative Munich, NIM) published as front cover in Adv. Funct. Mater. 25/2016 (used with permission from the publisher).

The n-type semiconducting spinel zinc ferrite ($ZnFe_2O_4$) is used as a photoabsorber material for light-driven water-splitting. It is prepared for the first time by atomic layer deposition. Using the resulting well-defined thin films as a model system, the performance of $ZnFe_2O_4$ in photoelectrochemical water oxidation is characterized. Compared to benchmark α-Fe_2O_3 (hematite) films, $ZnFe_2O_4$ thin films achieve a lower photocurrent at the reversible potential. However, the oxidation onset potential of $ZnFe_2O_4$ is 200 mV more cathodic, allowing the water-splitting reaction to proceed at a lower external bias and resulting in a maximum applied-bias power efficiency (ABPE) similar to that of Fe_2O_3. The kinetics of the water oxidation reaction are examined by intensity-modulated photocurrent spectroscopy. The data indicate a considerably higher charge transfer efficiency of $ZnFe_2O_4$ at potentials between 0.8 and 1.3 V versus the reversible hydrogen electrode, attributable to significantly slower surface charge recombination. Finally, nanostructured $ZnFe_2O_4$ photoanodes employing a macroporous antimony-doped tin oxide current collector reach a five times higher photocurrent than the flat films. The maximum ABPE of these host–guest photoanodes is similarly increased.

7.1. INTRODUCTION

The photooxidation of water at semiconducting oxide electrodes is a promising way of sustainably producing hydrogen for use as a high-energy fuel or as a precursor in large-scale chemical processes. Its discovery by Boddy in 1968 initiated an ongoing extensive search for materials fulfilling the conditions for largescale application.[1–3] These are stability, abundance, efficient light harvesting in the visible spectrum, favorable band alignment, fast interfacial water oxidation kinetics, and nontoxicity. Numerous semiconducting oxides which partially fulfill these conditions have been investigated to date, including α- Fe_2O_3 (hematite), $BiVO_4$ and others. [2,4,5] The search for alternative materials has recently spawned interest in the spinel ferrite phases formed by ternary oxide compounds of iron and divalent metal oxides.[6–9] Zinc ferrite ($ZnFe_2O_4$) is an n-type semiconductor such as hematite. It has been used in heterojunction devices together with TiO_2, Fe_2O_3 and $CaFe_2O_4$.[10–15] Studies investigating water photooxidation on neat $ZnFe_2O_4$ have so far been less numerous. The photoelectrochemistry of samples prepared by high temperature solid state reactions was investigated by de Haart and Blasse.[16] Tahir and Wijayantha obtained highly structured $ZnFe_2O_4$ films by aerosol-assisted chemical vapor deposition (AACVD) and determined their performance in water photooxidation, while Kim and co-workers converted ZnO-coated β-

INTRODUCTION

FeOOH nanorods to zinc ferrite by thermal and microwave annealing and examined the influence of oxygen vacancies.[17–20] The maximum photocurrents reached were about 350 and 320 $\mu A\ cm^{-2}$, respectively, at the reversible potential (1.23 V vs. reversible hydrogen electrode (RHE)). These studies have examined the material in complex morphologies, which were formed spontaneously by solution-based and gas phase deposition methods. While inexpensive, these methods allow only limited control over the composition and nanostructure of the resulting films, which makes an assessment of the intrinsic performance of the material and optimization by tuning the morphology difficult. Atomic layer deposition (ALD) can be used to prepare well-defined single component films as well as junction devices on smooth and structured substrates, on which the intrinsic factors influencing photoelectrochemical performance can be studied. ALD is a unique and versatile technique for the preparation of oxide thin film photoelectrodes. It can be used to deposit uniform, conformal thin films on both flat and highly structured substrates. Particularly oxides with a thin space charge layer and short charge carrier diffusion lengths, such as hematite, benefit from such a thin film architecture.[21–24] Gao et al. first employed ALD in the preparation of a phase-pure ternary oxide ($CuWO_4$) by ALD for use as a photoanode.[25] To improve light harvesting while keeping the film thickness low, so-called host–guest electrodes, in which a thin absorber layer is applied to a structured conductive substrate, have been developed.[26–29] In this study, we prepare $ZnFe_2O_4$ by ALD for the first time. The resulting well-defined thin films serve as a model system, allowing an assessment of the intrinsic water photooxidation performance of zinc ferrite and comparison to ALD Fe_2O_3 films as an extensively studied benchmark. We derive the semiconductor characteristics by optical absorbance spectroscopy and Mott–Schottky analysis. Intensity-modulated photocurrent spectroscopy (IMPS) reveals favorable surface hole transfer kinetics in zinc ferrite. While the photocurrents are lower than those of hematite films, the photocurrent onset potential of $ZnFe_2O_4$ is about 200 mV more cathodic, enabling water splitting at a lower bias potential. This results in a comparable applied-bias power efficiency (ABPE) for both films. Finally, we use the ALD process to prepare nanostructured host–guest $ZnFe_2O_4$ electrodes by conformally coating macroporous ATO substrates. This increases the photocurrent by a factor of 5 at the reversible potential.

7.2. RESULTS AND DISCUSSION

7.2.1.   MODEL Fe_2O_3 AND $ZnFe_2O_4$ THIN FILMS

Sequential or alternating growth of different metal oxides by atomic layer deposition results in nanolaminate stacks. By annealing at the appropriate temperature, these can be used to prepare both solid solution mixed oxides and stochiometrically well-defined ternary and higher oxide films. The ALD cycle ratio can be used to adjust the stochiometry of the resulting oxide material over a wide range. To obtain stoichiometric $ZnFe_2O_4$, the required ZnO: Fe_2O_3 cycle ratio was calculated to be approximately 1:9 (see Supporting Information). Accordingly, nanolaminates were deposited on fluorine-doped tin oxide (FTO) substrates with 810 cycles of Fe_2O_3 and 90 cycles of ZnO. Samples with Fe_2O_3 on top of ZnO and ZnO on top of Fe_2O_3 were prepared. In addition to the stacked oxides, neat zinc oxide and hematite films were made using only one of the components. An overview of all samples is given in Table 7.1 and Figure 7.1a. The measured thickness of the oxide layers in all samples is close to the expected values. Hematite deposition on ZnO results in a slightly thicker film than on FTO, which may be caused by faster nucleation on this substrate.

Table 7.1   Cycle sequences and thicknesses, determined by ellipsometry, of the nanolaminate samples.

Sample	ALD cycles	Thickness [nm]
FTO/Fe_2O_3	810	18.0
FTO/ZnO	90	8.6
FTO/ZnO/Fe_2O_3	90 + 810	8.0 + 20.7
FTO/Fe_2O_3/ZnO	810 + 90	19.5 + 8.3

Figure 7.1b shows X-ray diffraction (XRD) patterns of the flat films after calcination at 600 °C, recorded at grazing incidence. In all patterns, reflections of the cassiterite structure of FTO (*) dominate. The single oxide samples show reflections of hexagonal ZnO and hematite, respectively. In the pattern of FTO/ZnO/ Fe_2O_3, α-Fe_2O_3 is evident, together with small amounts of $ZnFe_2O_4$. Only in FTO/Fe_2O_3/ZnO was the zinc ferrite phase quantitatively

formed by sequential deposition and calcination. The absence of any reflections attributable to Fe_2O_3 or ZnO in this pattern shows that the chosen cycle ratio resulted in the deposition of both oxides with the stochiometry required to form $ZnFe_2O_4$. An alternating nanolaminate was also created, consisting of 90 repetitions of 9 cycles of Fe_2O_3 and one cycle of ZnO. However, this contained no $ZnFe_2O_4$ phase as-deposited or after calcination. We attribute this to delayed nucleation of the hematite layer on top of ZnO. Previous studies have shown a significantly reduced growth rate for Fe_2O_3 during the first 20 to 40 cycles.[30,31] This means that in an alternating nanolaminate deposition mode, the Fe_2O_3 is constantly forced to renucleate on the ZnO interlayers and does not achieve its regular growth rate.
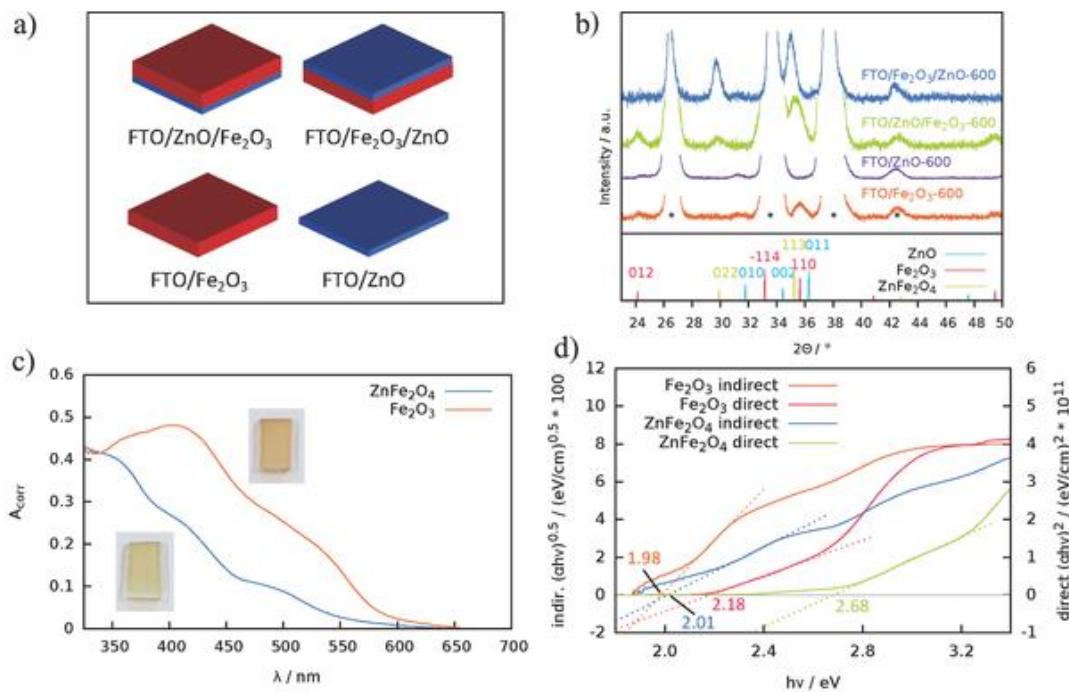
Figure 7.1   a) Schematic representation and nomenclature of the deposited nanolaminate samples. b) GIXRD patterns of the calcined thin film samples on FTO. c) Reflections of the cassiterite structure of FTO are marked by an asterisk (*) and have been truncated for clarity. Reflectance-corrected absorbance spectra with photographs (c) and Tauc plots (d) of the calcined Fe_2O_3 and $ZnFe_2O_4$ samples.

From these findings we conclude that conformal $ZnFe_2O_4$ thin films can be successfully prepared by ALD of ZnO on top of Fe_2O_3 followed by heat treatment. On the other hand, deposition in reverse order does not achieve the same result. It is possible that at higher calcination temperatures the spinel phase would also be formed quantitatively from the deposition sequence used for $FTO/ZnO/Fe_2O_3$, but this was not investigated due to the limited thermal stability of the FTO/glass substrates. We tentatively attribute the difference in reactivity to the formation mechanism of $ZnFe_2O_4$ at low temperatures reported by Feltz and

Martin.[32] It requires a mobile ZnO phase on the surface of Fe_2O_3 as well as partial oxygen loss and reoxidation. Zn^{2+} ions diffuse into the bulk of the iron oxide to form the spinel phase. By ALD of ZnO on Fe_2O_3 we form this arrangement, whereas the reversed order of deposition results in a ZnO layer confined between FTO and Fe_2O_3. We hypothesize that in this case the surface mobility of the Zn^{2+} ions and oxygen exchange with the atmosphere are impeded, preventing the formation of $ZnFe_2O_4$ at the low calcination temperature used.

In the following discussion, FTO/ Fe_2O_3 and FTO/ Fe_2O_3/ZnO thin films calcined at 600 °C will be referred to as Fe_2O_3 (or hematite) and $ZnFe_2O_4$ (or zinc ferrite), respectively. The UV/vis absorbance spectra of the hematite and zinc ferrite thin films are shown in Figure 7.1c. The Fe_2O_3 sample has an absorption onset at 590 nm as well as the absorption bands at 366, 407, and 521 nm previously reported for ALD hematite thin films.[22,23] Zinc ferrite shows absorption bands at 350, 410, and 490 nm that are weaker than those of the hematite film. The direct and indirect optical gaps of Fe_2O_3 and $ZnFe_2O_4$ were determined from Tauc plots, shown in Figure 7.1d. In all cases a distinct linear region can be observed. The indirect and direct band gap energies are 1.98 and 2.18 eV for Fe_2O_3 and 2.01 and 2.68 eV for $ZnFe_2O_4$, respectively. The indirect gaps, therefore, are very similar, but the direct gap of $ZnFe_2O_4$ is 0.5 eV larger than that of hematite. Since the absorption coefficients of indirect transitions are generally much lower than those of direct transitions, the optical absorption in thin films is dominated by the direct gap. This explains the much lower absorption of zinc ferrite in the green wavelength region between its direct and indirect band gap. As a result, the light harvesting efficiency of zinc ferrite films falls short of that of comparable hematite films. Taking the corrected absorbance into account, the theoretical maximum photocurrent density J_{abs} that the examined electrodes could achieve if each photon they absorbed was converted into one electron contributing to the photocurrent (i.e., assuming an absorbed-photon-to-current efficiency of 100% over the entire spectral range) was calculated (see Supporting Information). The resulting values of J_{abs} are 5.47 mA cm^{-2} for Fe_2O_3 and 2.75 mA cm^{-2} for $ZnFe_2O_4$. Thus, it is evident that the light harvesting efficiency of $ZnFe_2O_4$ has to be improved to be competitive with hematite.

The cyclic voltammograms recorded under illumination through the substrate are shown in Figure 7.2a. Fe_2O_3 shows the highest photocurrent density, reaching 240 µA cm^{-2} at the reversible potential, which is indicated by a vertical gray line in the graph. The water oxidation onset potential is 1.1 V. By comparison, the $ZnFe_2O_4$ sample reaches a current density of only 50 µA cm^{-2} at the reversible potential. On the other hand, the onset potential of 0.9 V versus RHE is more cathodic by 200 mV than that of Fe_2O_3, showing that a lower

external bias requirement is a clear advantage of $ZnFe_2O_4$ over Fe_2O_3. Despite the lower light harvesting efficiency, zinc ferrite produces a higher photocurrent density than hematite in the potential range between 0.9 and 1.13 V versus RHE. IPCE curves at the reversible potential with 0.1 sun bias illumination are shown in Figure 7.2b. The low photocurrent of flat $ZnFe_2O_4$ is a result of its low absorbance and conversion cutoff at 500 nm. Fe_2O_3 has a higher absorbance and its conversion range extends up to 590 nm, which is advantageous due to the higher flux of solar photons at the longer wavelengths.
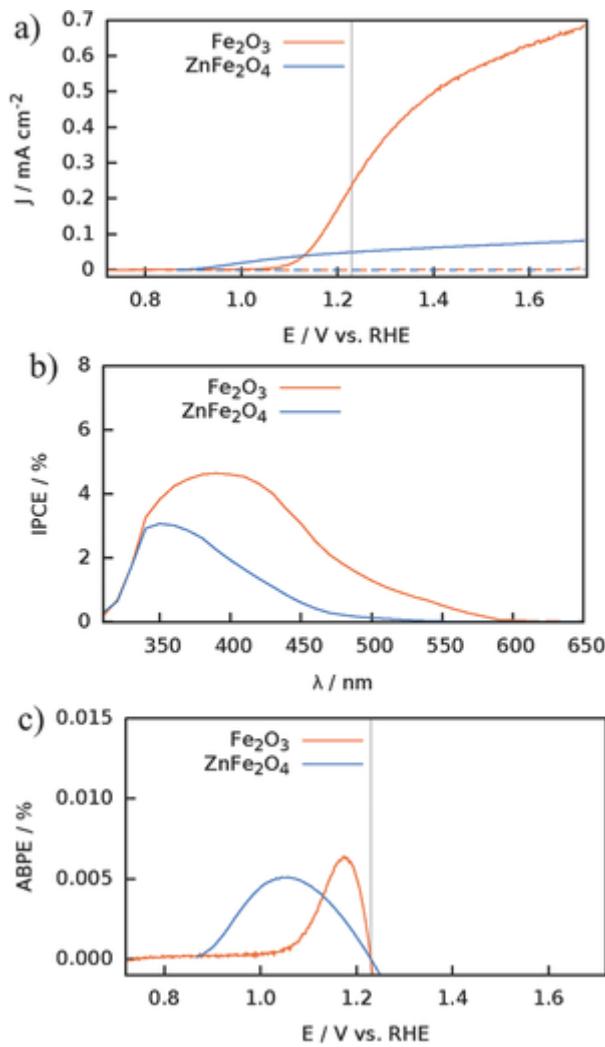
Figure 7.2   a) J–V curves of the calcined Fe_2O_3 and $ZnFe_2O_4$ thin films recorded under illumination through the substrate at 1 sun. Solid and dashed lines represent light and dark currents, respectively. The vertical grey line indicates the reversible oxygen evolution potential (1.23 V vs RHE). b) IPCE spectra recorded at 0.1 sun bias illumination. c) ABPE curves calculated from J–V curves.

The applied-bias power efficiency, ABPE, combines photocurrent J_{photo} and bias potential E into an overall photopower and relates them to the total irradiated solar power $P_{irradiated}$

(100 mW cm^{-2} at 1 sun) as described by Equation 7.1, thus giving an overall representation of a material's performance.[2,33]

$$\text{ABPE} = \frac{J_{\text{photo}}(1.23\ \text{V}-\text{E})}{P_{\text{irradiated}}}$$

Equation 7.1

Figure 7.2c shows ABPE curves of the two films. The maximum values of Fe_2O_3 and $ZnFe_2O_4$ are nearly identical, even though the latter reaches its peak at a lower potential. Thus, the power gain from the photoactive semiconductor can be similar for both electrodes. Zinc ferrite would be the material of choice in cases where only a low external bias voltage is available, for example in tandem cells with a PV cell or photocathode. Numerous methods for improving the performance of ALD hematite photoanodes have been developed in recent years, including interlayers on the substrate, dopants, catalysts, and surface state passivation.[3,23,27,34–37] While these can yield hematite electrodes with a lower onset potential than the ones shown in this study, we chose to compare $ZnFe_2O_4$ and Fe_2O_3 films without any such improvements and examine only the intrinsic performance of both materials.

The semiconductor characteristics of hematite and zinc ferrite thin film electrodes were probed by impedance spectroscopy to determine the donor density and flatband potential. The equivalent circuit used to fit the data is shown in Figure 7.3b. It is composed of the cell series resistance R_s and two RC elements attributed to the space charge layer (C_{SC}, R_{SC}) in the semiconductor and the Helmholtz layer (C_{H}, R_{CT}) at the electrolyte interface. The fitted values for the space charge capacitance C_{SC} (Figure S7.1d, Supporting Information) were used to characterize the materials by Mott–Schottky analysis (cf. Supporting Information), using ε_{T} values 32 and 100 for Fe_2O_3 and $ZnFe_2O_4$, respectively.[17,22,38] The plots are shown in Figure 7.3a. Both $ZnFe_2O_4$ and Fe_2O_3 show a linear region with a positive slope, which is typical of n-type semiconductors. However, the donor density N_d and the flatband potential E_{fb} differ significantly. E_{fb} is 0.64 V versus RHE for $ZnFe_2O_4$ and 0.75 V versus RHE for Fe_2O_3, which is in good agreement with earlier reports.[16,23,39] In n-type semiconductors, the conduction band (CB) edge commonly lies 0.1 to 0.2 V above E_{fb}, thus the latter can be used as a lower limit approximation of the CB.[38] Assuming a similar distance of E_{fb} from the CB, the CB of both oxides is more positive than the H_2O/H_2 redox couple, which precludes unbiased water-splitting. However, the difference is smaller in the case of $ZnFe_2O_4$, which can therefore intrinsically achieve water photooxidation at lower external bias voltages than hematite. The actual photocurrent onset potentials (cf. Figure 7.2a) are 0.9 and 1.1 V, respectively, confirming this observation. The donor density also differs by more than an order of magnitude, with hematite exhibiting a value of $7 \cdot 10^{18}$ cm^{-3} and zinc ferrite reaching

$2 \cdot 10^{17}\,\mathrm{cm^{-3}}$. From these values, the width of the space charge layer W_{SC} can be estimated (cf. Supporting Information) resulting in space charge layer widths of only 16 nm for hematite and 146 nm for zinc ferrite at 1.23 V versus RHE. The value of W_{SC} implies that in $ZnFe_2O_4$ photogenerated holes can potentially be extracted to the surface from much deeper in the layer than in Fe_2O_3. This effect could possibly balance the impact of the large direct band gap, which implies a long absorption depth for photons with energies between the direct and indirect band gaps. However, in our experiment an approximately 70 nm thick layer of $ZnFe_2O_4$ on FTO performed worse in terms of onset potential and maximum photocurrent than the 28 nm layer used throughout this study (Figure S7.4, Supporting Information). Since 70 nm is only half the calculated thickness of the space charge layer for this material, there must be a different reason for the reduced performance, possibly, such as in hematite, a short diffusion length of photogenerated holes in the bulk. This demonstrates that a thicker compact layer is not a viable architecture for better $ZnFe_2O_4$ electrodes.
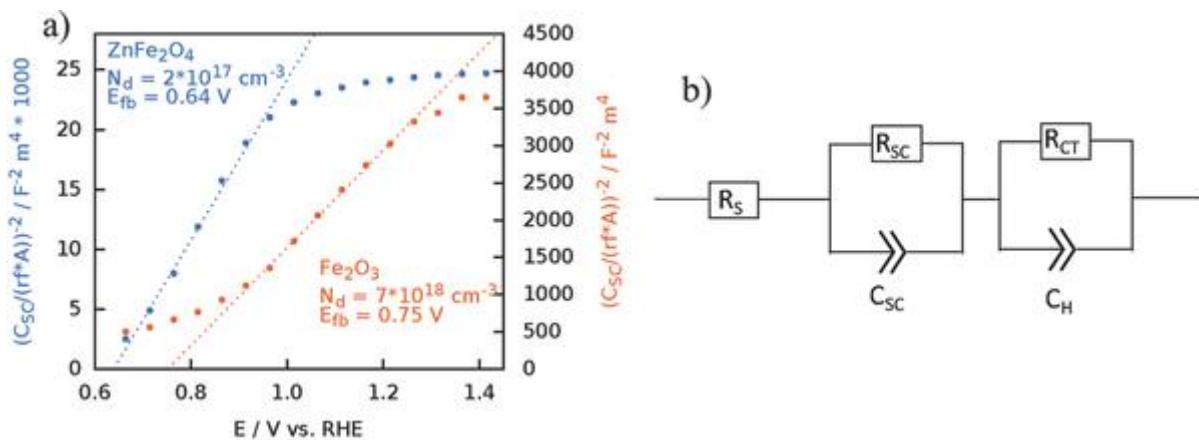
Figure 7.3   a) Mott–Schottky plots of $ZnFe_2O_4$ and Fe_2O_3 electrodes derived from impedance spectroscopy carried out in the dark. Note the different vertical scales. b) Equivalent circuit used to fit impedance data.

To investigate the kinetics of photoelectrochemical water oxidation at the $ZnFe_2O_4$ and Fe_2O_3 films, we recorded photocurrent transients under chopped illumination. The transient photocurrent density at 1.16 V versus RHE is shown in Figure 7.4a. Fe_2O_3 has transient behavior typical for hematite film electrodes.[40,41] The charge transfer efficiency η_{trans} can be calculated from the instantaneous J_{inst} and steady state J_{SS} photocurrents according to Equation 7.2, which also shows its relation to the rate constants for charge transfer k_{trans} and surface electron/hole recombination k_{rec}. By contrast, the photocurrent density behavior of $ZnFe_2O_4$ shows no switch-on or switch-off transients and resembles the square wave shape of the illumination intensity. Figure S7.2 of the Supporting Information shows how η_{trans} depends

on the operating potential. For both Fe_2O_3 and $ZnFe_2O_4$ films the transfer efficiency is zero at low potentials, and then starts to increase around the photocurrent onset potential. At high potentials, the transfer efficiency approaches unity for both materials. The advantage of $ZnFe_2O_4$ over Fe_2O_3 becomes apparent at potentials between 0.8 and 1.4 V, where the transfer efficiency of the former is greater. This shows that $ZnFe_2O_4$ requires a lower potential than hematite to make hole injection into the OH^-/O_2 redox couple in the electrolyte faster than electron/hole recombination at the surface.
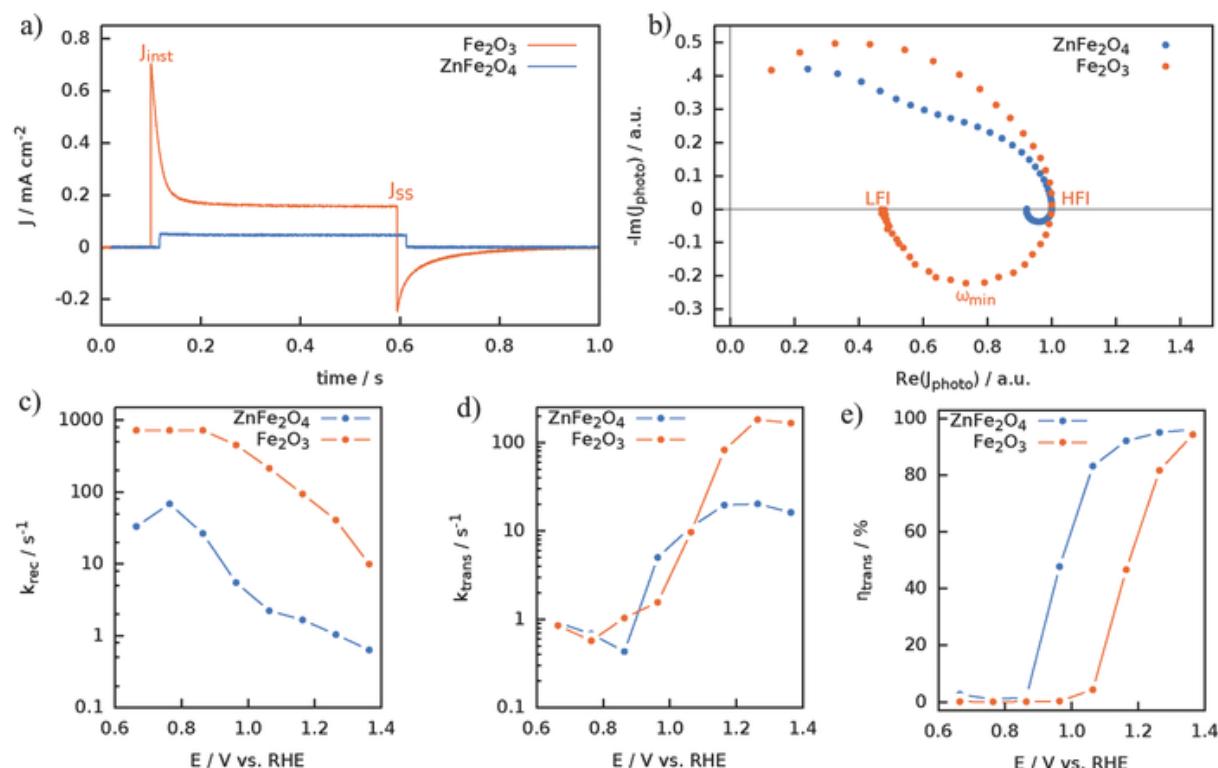
Figure 7.4   Photocurrent transients of Fe_2O_3 and $ZnFe_2O_4$ recorded at 1.16 V versus RHE under chopped illumination. a) The data of $ZnFe_2O_4$ have been shifted by 20 ms for clarity. b) Normalized IMPS spectra at 1.16 V versus RHE of Fe_2O_3 and $ZnFe_2O_4$. c) Surface recombination rate constant, d) charge transfer rate constant, and e) charge transfer efficiency extracted from IMPS spectra recorded at different potentials.

While the rate constants are not readily determined from transient data, they can be directly calculated from IMPS spectra.[42,43] In this perturbation method the complex photocurrent response to a small sinusoidal variation of the illumination intensity is recorded at various frequencies. The resulting Nyquist plots are characterized by a negative semicircle representing the charge transfer process, from which the kinetic parameters can be extracted by a phenomenological evaluation. Its low and high frequency intercepts LFI and HFI correspond to the instantaneous and steady state current densities of chopped illumination experiments (Equation 7.2)

$$\eta_{\text{trans}} = \frac{J_{\text{SS}}}{J_{\text{inst}}} = \frac{k_{\text{trans}}}{k_{\text{trans}}+k_{\text{rec}}} = \frac{\text{LFI}}{\text{HFI}} \qquad \text{Equation 7.2}$$

The time constant of the process is $\omega_{\text{min}} = k_{\text{trans}} + k_{\text{rec}}$ and can be derived from the perturbation frequency at the minimum of the semicircle. Figure 7.4b shows normalized IMPS spectra of Fe_2O_3 and $ZnFe_2O_4$ flat films recorded at 1.16 V versus RHE. The negative semicircle is much smaller for $ZnFe_2O_4$ compared to Fe_2O_3, indicating that a larger fraction of the holes reaching the semiconductor surface is transferred to the electrolyte. Figure 7.4c,d shows the rate constants of charge transfer and surface recombination for both materials. Recombination at the $ZnFe_2O_4$ surface is slower than at the Fe_2O_3 surface over the entire potential range by up to two orders of magnitude. Also, while Fe_2O_3 shows faster charge transfer at potentials exceeding 1.1 V, below this potential both materials are approximately equal. In consequence, $ZnFe_2O_4$ has an advantage in terms of η_{trans} between 0.9 and 1.3 V (Figure 7.4e). At sufficiently high potentials (>1.0 V for $ZnFe_2O_4$ and >1.3 V for Fe_2O_3) k_{trans} exceeds k_{rec} in both materials, leading to transfer efficiencies approaching unity, similar to the trend observed in the transient experiments. The superior behavior of $ZnFe_2O_4$ is, however, not attributable to faster interfacial charge transfer but rather to the much slower rate of surface recombination, which constitutes the main competing pathway by which photogenerated holes that have reached the surface are lost. This can be a considerable advantage of zinc ferrite over hematite as k_{trans} can typically be increased readily by applying a surface oxygen evolution catalyst, while it is more difficult to reduce k_{rec}, which is an intrinsic material property.

Our experiments on flat model systems highlight the intrinsic differences between $ZnFe_2O_4$ and Fe_2O_3. The lower flatband potential and low rate of surface recombination of zinc ferrite result in a more cathodic water photooxidation onset potential. On the other hand, its photocurrent is limited by the low optical absorption, which is a result of the large direct band gap. In consequence, the power harvesting capability of both thin film materials is similar.

7.2.2. HOST-GUEST ZnFe$_2$O$_4$ ELECTRODES

One way to further improve zinc ferrite photoanodes is by increasing the light harvesting efficiency. Since in our experiments, thicker ZnFe$_2$O$_4$ layers resulted in a lower photocurrent, we opted instead to employ a so-called host–guest architecture. We grew thin films of zinc ferrite on a highly structured macroporous scaffold of transparent, conductive antimony-doped tin oxide (ATO). These scaffolds are current collectors with high surface area and a pervading, connected pore system allowing electrolyte access throughout the layer. These were conformally coated by ALD with a zinc ferrite precursor laminate and calcined to obtain a conformal polycrystalline layer of ZnFe$_2$O$_4$. To achieve uniform films inside the tortuous pore structure, stop-flow deposition was used. Due to the different characteristics of this ALD process, the cycle ratio and layer thickness were adjusted (cf. Supporting Information). 360 cycles of hematite ALD followed by 31 cycles of ZnO ALD resulted in layer thicknesses of 13.8 nm for Fe$_2$O$_3$ and 3.2 nm for ZnO on Si witness substrates. The macroporous scaffold with a calcined ZnFe$_2$O$_4$ absorber layer will be referred to as m-ZnFe$_2$O$_4$.

The morphology of the host–guest architecture was analysed by scanning electron microscopy (SEM, Figure 7.5). The macroporous layer is approximately 4.5 μm thick and has spherical pores approximately 300 nm in diameter. It consists of an ordered ATO matrix, enclosing a network of interconnected pores. Images of the uncoated scaffold are shown in Figure 7.5b and Figure S7.5 of the Supporting Information. The ZnFe$_2$O$_4$ coats the scaffold throughout its whole thickness (Figure 7.5a).
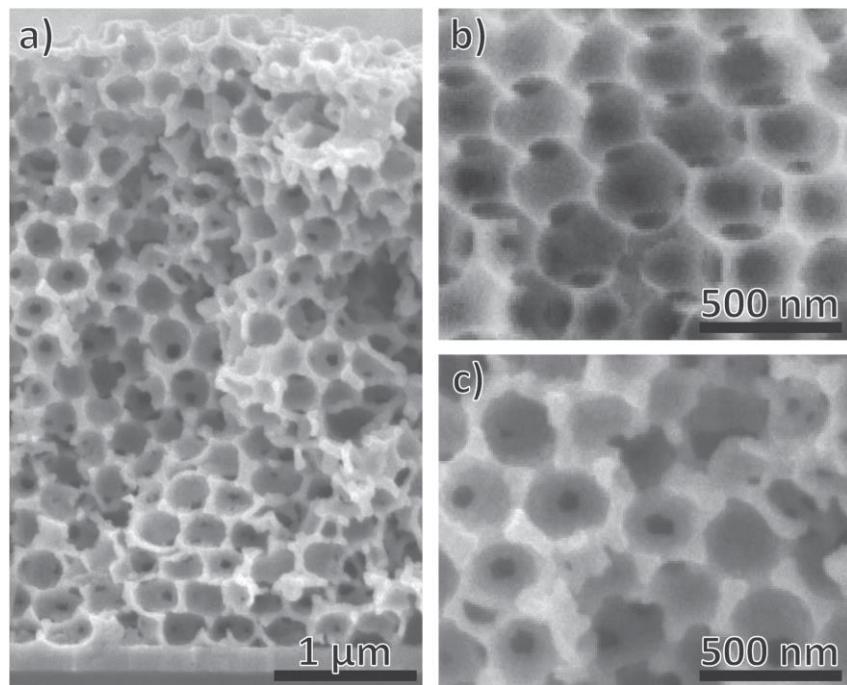
Figure 7.5   Overview SEM image of m-ZnFe$_2$O$_4$. a) The ITO substrate is visible at the bottom of the image. b) Close-up SEM images of an uncoated and c) a ZnFe$_2$O$_4$-coated ATO scaffold.

A more detailed structural and crystallographic analysis is afforded by transmission electron microscopy (TEM). In Figure 7.6a, the ZnFe$_2$O$_4$ can easily be identified by a strong contrast in the HAADF-STEM image and by EDX, which yields an average Fe/Zn-ratio of 1.9 ± 0.3, closely matching the desired stochiometry. Interplanar spacings in HRTEM images of the ferrite layer and reflections in electron diffraction patterns (Figure 7.6b,c) match the crystal structure of zinc ferrite, further confirming the successful synthesis and precluding contaminant phases such as Fe$_2$O$_3$ or ZnO. The ZnFe$_2$O$_4$ layer has a thickness of 42 ± 21 nm (Figure 7.5b, and Figure S7.6, Supporting Information). The large deviation from the thickness of 17 nm observed on Si witness substrates can be explained by the formation of small particles instead of a continuous layer, which introduces voids into the ZnFe$_2$O$_4$ layer and decreases the density. These particles are 12 ± 3 nm in diameter and monocrystalline Figure S7.6c, Supporting Information).
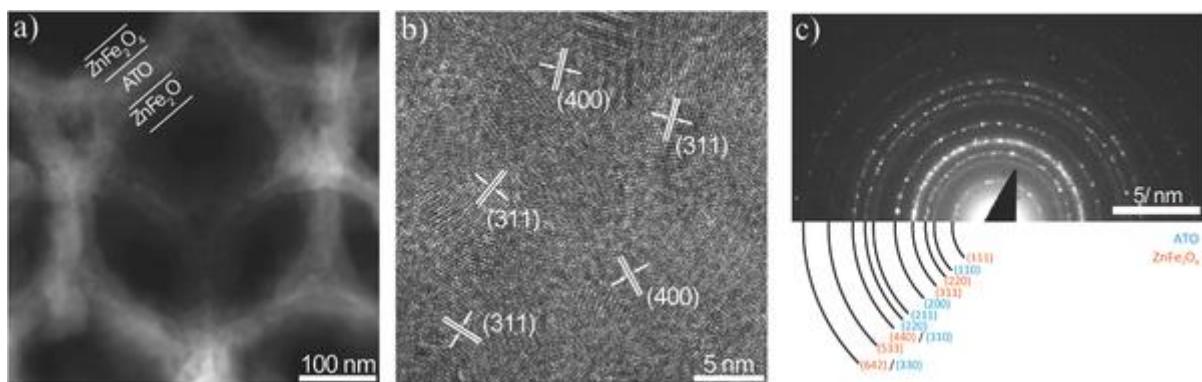
Figure 7.6 a) HAADF-STEM image of a single pore of m-$ZnFe_2O_4$, with the scaffold and coating layers distinguishable by Z-contrast. b) HRTEM image of the $ZnFe_2O_4$ layer, showing several crystalline domains. c) Electron diffraction pattern of m-$ZnFe_2O_4$.

Figure 7.7a shows the optical absorbance of the macropouros ATO substrate and the m-$ZnFe_2O_4$ electrode. Since a correction for reflectance as for the flat films was not possible (cf. Supporting Information), some of the attenuation will be caused by reflectance and scattering and the data should be regarded as upper limits of the absorbance. The substrate is transparent for $\lambda > 450$ nm and absorbs only small fractions of the visible spectrum. By contrast, m-$ZnFe_2O_4$ can absorb light very effectively up to 570 nm. This represents a marked improvement in light harvesting efficiency over the unstructured zinc ferrite film, which is a result of the longer pathway of light through the absorber material. The difference can also be seen in photographs of both samples (Figure 7.1c and Figure 7.7a). The color of m-$ZnFe_2O_4$ is distinctively darker. $J - V$ curves of the flat films and of m-$ZnFe_2O_4$ are compared in Figure **7.7**b. The macroporous sample shows a remarkable, more than fivefold increase in photocurrent over the nonstructured zinc ferrite film, resulting in a photocurrent of 260 µA cm^{-2} at the reversible potential. At the same time, the onset potential remains the same at 0.9 V. This indicates that the improvement is a result of the superior light harvesting efficiency and that the photoactive material is still the zinc ferrite film. A similar improvement is seen in the IPCE. This is increased by the scaffold by a factor of 4 to 5, resulting in an efficiency comparable to Fe_2O_3 flat films at longer wavelengths and significantly higher efficiency below 450 nm. The structured $ZnFe_2O_4$ electrode achieves its peak ABPE at the same potential as the flat zinc ferrite film, though its value is more than four times higher (Figure **7.7**d). By comparison, the nanostructured $ZnFe_2O_4$ films with the highest photocurrent density of 350 µA cm^{-2} at the reversible potential, reported by Tahir and Wijayantha, had an onset potential of 1.15 V.[17,19] While the ABPE was not calculated in this report, our m-$ZnFe_2O_4$ photoanode reaches its peak ABPE even below this potential. Thus, while our system does not

deliver record photocurrent at the reversible potential, the photocurrent at lower potentials, where an actual energy gain occurs, matches or exceeds that of other reported $ZnFe_2O_4$ electrodes.
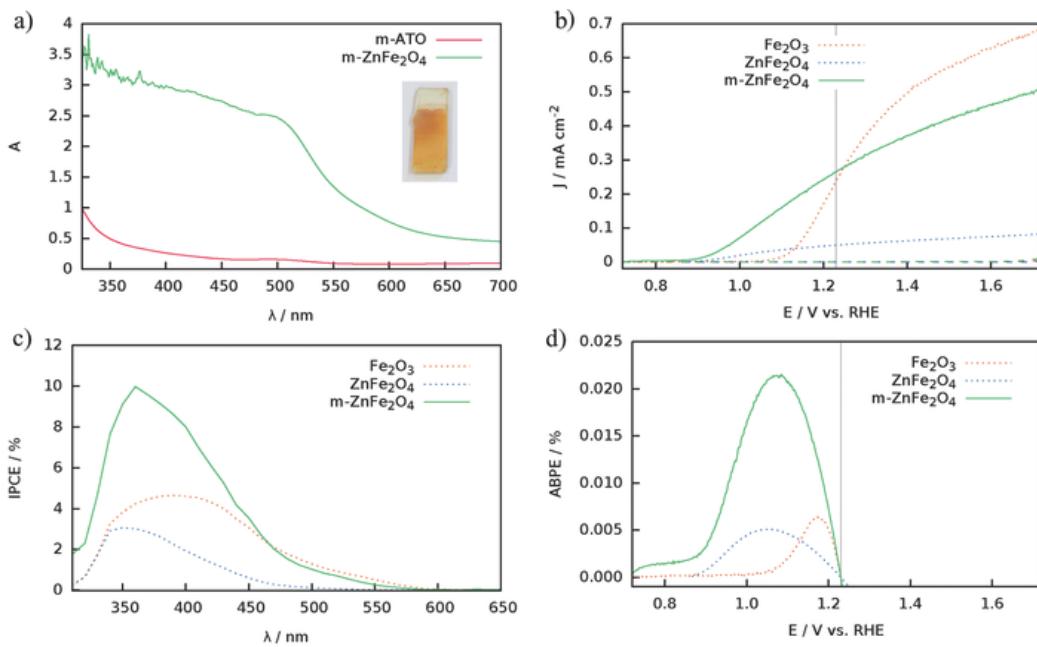
Figure 7.7   a) Absorbance of the macroporous ATO substrate and calcined m-$ZnFe_2O_4$ sample, b) *J–V* curves, c) IPCE spectrum, and d) ABPE curve of calcined m-$ZnFe_2O_4$ compared to flat films of $ZnFe_2O_4$ and Fe_2O_3 on FTO. Dotted lines indicate the dark currents.

Figure S7.3 of the Supporting Information shows chronoamperometric data of m-$ZnFe_2O_4$ recorded at the reversible potential in the dark for 15 min, followed by 1 sun illumination for a further 3 h. The initial decay of the photocurrent after illumination starts can be explained by capacitive charging of the semiconductor surface and by the formation of oxygen bubbles inside the pore structure, which partially impede electrolyte access. No similar decay is observed for flat $ZnFe_2O_4$ films. The data show that the m-$ZnFe_2O_4$ electrodes are stable and do not deteriorate when operated for several hours.

We attribute the immensely beneficial effect of the scaffold on zinc ferrite thin film photoanodes to two factors. First, the light harvesting efficiency is increased drastically without compromising electron conduction to the back FTO layer. Previous studies have also shown this for hematite, but we assume that due to the larger difference between the direct and indirect band gap, $ZnFe_2O_4$ can benefit more from this effect, as the absorption of the more numerous intermediate wavelength photons is substantially increased.[27,28] Second, highly structured hematite electrodes tend to suffer from increased recombination losses mediated by surface states.[44] In this study we have shown that the rate of surface

recombination in zinc ferrite is significantly lower, which may indicate a lower density of such recombination centers. For structured electrodes of either material, surface recombination is expected to scale linearly with the surface area. We therefore conclude that the lower rate of surface recombination has a beneficial effect on flat and structured $ZnFe_2O_4$ electrodes alike. While a similar host–guest electrode using pure hematite as the photoabsorber was not prepared, Riha et al. have reported a photocurrent density of about 250 µA cm^{-2} at the reversible potential for a comparable ALD hematite-coated inverse opal photoanode without the use of an OER catalyst.[27] A study made on sol-gel derived hematite on an ATO scaffold showed 400 µA cm^{-2}.[29] While this study has focused on the light harvesting and surface kinetic properties of $ZnFe_2O_4$ as compared to Fe_2O_3, further work is required to elucidate how the bulk properties such as carrier diffusion lengths and exciton separation impact the photocurrent and how modifications to the synthesis (e.g., doping) can benefit the photoabsorbers.

7.3. CONCLUSIONS

We have demonstrated the preparation of conformal $ZnFe_2O_4$ thin films by sequential atomic layer deposition of Fe_2O_3 and ZnO followed by thermal annealing. The material is stable during photoelectrochemical water oxidation in alkaline media. We showed that zinc ferrite has several advantages as a photoanode material compared to hematite: Its lower intrinsic donor density indicates a thicker space charge layer, which means that the zone where a driving force for exciton separation exists extends deeper into the semiconductor. Also, the rate of surface recombination is up to two orders of magnitude lower than that of Fe_2O_3. Most remarkably, the photocurrent onset potential is more cathodic by 200 mV, resulting in increased solar power conversion efficiency. Finally, we demonstrated how the low light-harvesting efficiency, resulting from the large direct band gap of $ZnFe_2O_4$, can be overcome by extending the light path in the absorber material. Coating a macroporous ATO scaffold with a thin zinc ferrite absorber layer led to a fivefold increase in photocurrent compared to flat films. We expect that the performance of zinc ferrite itself can be further improved. Our kinetic studies have shown that an improvement of k_{trans} at potentials below 1 V, which might be achieved by using a surface catalyst, should result in significantly increased photocurrents at even lower bias. Also, we expect that the intrinsic properties of zinc ferrite can be improved by doping. The spinel structure should be able to accommodate substitutional cationic dopants in either the tetrahedral (Zn^{2+}) or the octahedral (Fe^{3+}) positions as well as anionic doping of

the oxide lattice.[45,46] Further work may reveal a doping strategy to tune the band gap and offer a way of increasing the light harvesting efficiency complementary to our nanostructuring approach. These properties make zinc ferrite an attractive photoabsorber material meriting closer attention than it has received to date.

7.4. EXPERIMENTAL SECTION

A more detailed description of all methods used is given in the Supporting Information. Macroporous ATO electrodes were fabricated from preformed ATO nanoparticles, an ATO sol and poly(methyl methacrylate) (PMMA) beads via a liquid infiltration method described in previous reports.[47–49] In brief, monodisperse PMMA spheres were used for the self-assembly of opal film templates on ITO substrates. These were sequentially infiltrated with a dispersion of ATO nanoparticles and an ATO sol precursor by dip-coating. Finally, the PMMA spheres were removed by calcination at 500 °C in air, resulting in a macroporous, inverse opal ATO scaffold.

Atomic layer deposition of thin films was carried out in a Picosun R-200 reactor at 250 °C and approximately 6 hPa. Fe_2O_3 films were grown by alternately pulsing ferrocene and ozone into the reactor, separated by purges with nitrogen. For zinc oxide deposition, diethyl zinc (DEZ) and water were used as precursors. The conformality of coatings on porous substrates was improved by a stop-flow deposition protocol (cf. Supporting Information). After deposition, the electrodes were calcined in air at 600 °C for 30 min.

Layer thicknesses were determined by ellipsometry (J. A. Woollam M-2000 VASE) on Si(100) substrates. XRD patterns were recorded at grazing incidence on a Bruker D8 Discover diffractometer using a Ni-filtered Cu source. Absorbance and reflectance spectra were measured on a Perkin-Elmer Lambda 1050 UV/vis/NIR spectrophotometer. For the flat film samples, the reflectance-corrected absorbance was calculated as described in the Supporting Information. The morphology of the macroporous samples was studied using a JEOL JSM-6500F field emission SEM. TEM imaging was carried out using a FEI Titan Themis.

$J – V$ curves under simulated solar irradiation were measured using a µAutolab III potentiostat (Metrohm) with a Pt-mesh counter electrode and an Ag/AgCl reference electrode. The electrolyte was 0.1M NaOH. The light source was a Xe lamp AM 1.5 solar simulator (Solar Light Co. Model 16S) delivering 100 mW cm^{-2} (1 sun). The potential was scanned at a rate of 20 mV s^{-1}. Incident photon-to-current efficiency (IPCE) curves were recorded at 0.1 sun with

additional light from a 150 W Xe lamp passed through a monochromator (Horiba MicroHR) and an optical chopper. Chronoamperometry was performed at 1.23 V versus RHE. Photocurrent transients and IMPS spectra were recorded using a PGSTAT302N potentiostat (Metrohm) using an LED light source ($\lambda = 455$ nm). IMPS was performed in the frequency range between 100 mHz and 10 kHz. Impedance spectra were measured in the dark with frequencies ranging from 100 mHz to 100 kHz. The data were fitted using the electrochemical impedance spectroscopy (EIS) spectrum analyzer software.[50]

7.5. REFERENCES

(1)   Boddy, P. J. *J. Electrochem. Soc.* **1968**, *115*, 199.

(2)   Krol, R. van de; Liang, Y.; Schoonman, J. *J. Mater. Chem.* **2008**, *18*, 2311.

(3)   Zandi, O.; Hamann, T. W. *Phys. Chem. Chem. Phys.* **2015**, *17*, 22485.

(4)   Woodhouse, M.; Parkinson, B. A. *Chem. Soc. Rev.* **2009**, *38*, 197.

(5)   Castelli, I. E.; Hüser, F.; Pandey, M.; Li, H.; Thygesen, K. S.; Seger, B.; Jain, A.; Persson, K. A.; Ceder, G.; Jacobsen, K. W. *Adv. Energy Mater.* **2015**, *5,* 1400915.

(6)   Dillert, R.; Taffa, D. H.; Wark, M.; Bredow, T.; Bahnemann, D. W. *APL Mater.* **2015**, *3,* 104001.

(7)   Lin, Y.; Xu, Y.; Mayer, M. T.; Simpson, Z. I.; McMahon, G.; Zhou, S.; Wang, D. *J. Am. Chem. Soc.* **2012**, *134,* 5508.

(8)   Hou, Y.; Zuo, F.; Dagg, A.; Feng, P. *Angew. Chem. Int. Ed.* **2013**, *52*, 1248.

(9)   Ahmed, M. G.; Kandiel, T. A.; Ahmed, A. Y.; Kretschmer, I.; Rashwan, F.; Bahnemann, D. *J. Phys. Chem. C* **2015**, *119,* 5864.

(10)   Hou, Y.; Li, X.-Y.; Zhao, Q.-D.; Quan, X.; Chen, G.-H. *Adv. Funct. Mater.* **2010**, *20,* 2165.

(11)   McDonald, K. J.; Choi, K.-S. *Chem. Mater.* **2011,** *23,* 4863.

(12)   Miao, C.; Ji, S.; Xu, G.; Liu, G.; Zhang, L.; Ye, C. *ACS Appl. Mater. Interfaces* **2012**, *4,* 4428.

(13)   Cao, J.; Xing, J.; Zhang, Y.; Tong, H.; Bi, Y.; Kako, T.; Takeguchi, M.; Ye, J. *Langmuir* **2013**, *29,* 3116.

(14)   Guo, Y.; Fu, Y.; Liu, Y.; Shen, S. *RSC Adv.* **2014**, *4,* 36967.

(15)   Liu, Q.; Cao, F.; Wu, F.; Tian, W.; Li, L. *RSC Adv.* **2015**, *5,* 79440.

(16)   Haart, L. G. J. de; Blasse, G. *J. Electrochem. Soc.* **1985**, *132,* 2933.

(17)   Tahir, A. A.; Wijayantha, K. G. U. *J. Photochem. Photobiol. A* **2010**, *216,* 119.

(18)   Kim, J. H.; Jang, Y. J.; Kim, J. H.; Jang, J.-W.; Choi, S. H.; Lee, J. S. *Nanoscale* **2015**, *7,* 19144.

(19)   Tahir, A. A.; Burch, H. A.; Wijayantha, K. G. U.; Pollet, B. G. *Int. J. Hydrogen Energy* **2013**, *38,* 4315.

(20)   Kim, J. H.; Jang, J.-W.; Kim, J. Y.; Choi, S. H.; Magesh, G.; Lee, J.; Lee, J. S. *Adv. Energy Mater.* **2015**, *5,* 1401933.

(21)   Klahr, B. M.; Hamann, T. W. *J. Phys. Chem. C* **2011**, *115,* 8393.

(22)   Klahr, B. M.; Martinson, A. B. F.; Hamann, T. W. *Langmuir* **2011**, *27,* 461.

(23)   Zandi, O.; Klahr, B. M.; Hamann, T. W. *Energy Environ. Sci.* **2013**, *6,* 634.

(24)   Kim, D. W.; Riha, S. C.; DeMarco, E. J.; Martinson, A. B. F.; Farha, O. K.; Hupp, J. T. *ACS Nano* **2014**, *8,* 12199.

(25)   Gao, Y.; Zandi, O.; Hamann, T. W. *J. Mater. Chem. A* **2015**, *4,* 2826.

(26)   Stefik, M.; Cornuz, M.; Mathews, N.; Hisatomi, T.; Mhaisalkar, S.; Grätzel, M. *Nano Lett.* **2012**, *12,* 5431.

(27) Riha, S. C.; Klahr, B. M.; Tyo, E. C.; Seifert, S.; Vajda, S.; Pellin, M. J.; Hamann, T. W.; Martinson, A. B. F. *ACS Nano* **2013**, *7,* 2396.

(28) Riha, S. C.; DeVries Vermeer, M. J.; Pellin, M. J.; Hupp, J. T.; Martinson, A. B. F. *ACS Appl. Mater. Interfaces* **2013**, *5,* 360.

(29) Kondofersky, I.; Dunn, H. K.; Müller, A.; Mandlmeier, B.; Feckl, J. M.; Fattakhova-Rohlfing, D.; Scheu, C.; Peter, L. M.; Bein, T. *ACS Appl. Mater. Interfaces* **2015**, *7,* 4623.

(30) Ramachandran, R. K.; Dendooven, J.; Detavernier, C. *J. Mater. Chem. A* **2014**, *2,* 10662.

(31) Martinson, A. B. F.; DeVries, M. J.; Libera, J. A.; Christensen, S. T.; Hupp, J. T.; Pellin, M. J.; Elam, J. W. *J. Phys. Chem. C* **2011**, *115,* 4333.

(32) Feltz, A.; Martin, A. *Z. Anorg. Allg. Chem.* **1986**, *540,* 26.

(33) Peter, L. M. *Electroanalysis* **2015**, *27,* 864.

(34) Steier, L.; Herraiz-Cardona, I.; Gimenez, S.; Fabregat-Santiago, F.; Bisquert, J.; Tilley, S. D.; Grätzel, M. *Adv. Funct. Mater.* **2014**, *24,* 7681.

(35) Zandi, O.; Beardslee, J. A.; Hamann, T. *J. Phys. Chem. C* **2014**, *118,* 16494.

(36) Tallarida, M.; Das, C.; Cibrev, D.; Kukli, K.; Tamm, A.; Ritala, M.; Lana-Villarreal, T.; Gómez, R.; Leskelä, M.; Schmeisser, D. *J. Phys. Chem. Lett.* **2014**, *5,* 3582.

(37) Young, K. M. H.; Hamann, T. W. *Chem. Commun.* **2014**, *50,* 8727.

(38) Morrison, S. R. *Electrochemistry at Semiconductor and Oxidized Metal Electrodes,* Plenum Press, New York, NY, USA **1980.**

(39) Klahr, B.; Gimenez, S.; Zandi, O.; Fabregat-Santiago, F.; Hamann, T. *ACS Appl. Mater. Interfaces* **2015**, *7,* 7653.

(40) Peter, L. *J. Solid State Electrochem.* **2013**, *17,* 315.

(41) Dunn, H. K.; Feckl, J. M.; Müller, A.; Fattakhova-Rohlfing, D.; Morehead, S. G.; Roos, J.; Peter, L. M.; Scheu, C.; Bein, T. *Phys. Chem. Chem. Phys.* **2014**, *16,* 24610.

(42) Ponomarev, E. A.; Peter, L. M. *J. Electroanal. Chem.* **1995**, *396,* 219.

(43) Peter, L. M.; Wijayantha, K. G. U.; Tahir, A. A. *Faraday Discuss.* **2012**, *155,* 309.

(44) Le Formal, F.; Tétreault, N.; Cornuz, M.; Moehl, T.; Grätzel, M.; Sivula, K. *Chem. Sci.* **2011**, *2,* 737.

(45) Pal, M.; Brahma, P.; Chakravorty, D. *J. Magn. Magn. Mater.* **1996**, *152,* 370.

(46) Kahn, M. L.; Zhang, Z. J. *Appl. Phys. Lett.* **2001**, *78,* 3651.

(47) Mandlmeier, B.; Minar, N. K.; Feckl, J. M.; Fattakhova-Rohlfing, D.; Bein, T. *J. Mater. Chem. A* **2014**, *2,* 6504.

(48) Mandlmeier, B.; Szeifert, J. M.; Fattakhova-Rohlfing, D.; Amenitsch, H.; Bein, T. *J. Am. Chem. Soc.* **2011**, *133,* 17274.

(49) Peters, K.; Zeller, P.; Stefanic, G.; Skoromets, V.; Nêmec, H.; Kužel, P.; Fattakhova-Rohlfing, D. *Chem. Mater.* **2015**, *27,* 1090.

(50) Bondarenko, A. S.; Ragoisha, G. A. in *Progress in Chemometrics Research* (Ed.: A. L. Pomerantsev), Nova Science Publishers, New York, NY, USA **2005**, p. 89.

7.6. SUPPORTING INFORMATION

1.   Synthesis and Characterization Methods

FTO-coated glass substrates (Pilkington, 7 $\Omega\,cm^{-1}$) were cleaned before use by sequential sonication in Extran® (Merck) solution, ultrapure water and isopropanol for 15 min each and dried in a nitrogen stream. ITO glass substrates (Visiontek, 12 $\Omega\,cm^{-1}$) were prepared by sonication in Extran® solution, ethanol and acetone for 15 min each and dried in a nitrogen stream. Ferrocene (Aldrich, 98%) was purified by sublimation. All other chemicals were used as received.

1.1. Preparation of Macroporous ATO Scaffolds

Macroporous antimony-doped tin oxide (ATO) electrodes were fabricated from preformed ATO nanoparticles, an ATO sol and poly(methyl methacrylate) (PMMA) beads via the liquid infiltration method. The PMMA beads with a diameter of 340 nm were synthesized according to the emulsion polymerization route previously reported by Mandlmeier *et al.*[1,2] The inverse opal films were grown by the evaporation-induced self-assembly of the PMMA spheres (in 0.066%wt dispersion) at 60°C over 3 days on ITO or FTO substrates. ATO nanocrystals and an ATO sol were used for infiltration of the opal film. ATO nanoparticles with a dopant concentration of 5% were prepared by a solvothermal route in *tert*-butanol described in a previous report by Peters *et al.*[3] The nanoparticles were dispersed in isopropyl alcohol by adding a few drops of concentrated hydrochloric acid to give a 3%wt dispersion. The dispersion was used to infiltrate the opal films by dip-coating (speed: 0.63 mm s^{-1}). In a second step, the films were dip-coated in an ATO sol, which was prepared by adding ethanol (4 cm^3) dropwise to SnCl$_4$ (1.14 g, 4.4 mmol) and SbCl$_3$ (0.068 g, 0.3 mmol). Finally, the PMMA beads were removed by calcination at 500°C (30 min, rate 1°C min^{-1}).

1.2. Atomic Layer Deposition of Oxide Films

Atomic layer deposition of thin films was carried out in a Picosun R-200 reactor at 250 °C and approximately 6 hPa. The carrier and purging gas was N$_2$ (Air Liquide, 99.999%). For hematite deposition, ferrocene was used as the iron precursor and kept in a stainless steel cylinder at 90°C during depositions. The oxidant was ozone generated by an ozone generator (INUSA AC2025) fed with 1%vol. N$_2$ in O$_2$ (Air Liquide, 99.9995%). The pulse and purge

times were 1 s and 6 s for ferrocene and 6 s and 8 s for ozone at gas flow rates of 100 sccm (standard cubic centimeters per minute). The resulting growth rate was approximately 0.022 nm cycle^{-1}. For zinc oxide deposition, the metal and oxide precursors were diethyl zinc (Strem, 95%) and water (MilliQ, 18.2 MΩ cm) respectively. Both were contained in stainless steel cylinders and held at 20°C during depositions. The pulse and purge times were 0.1 s and 6 s for DEZ and 0.1 s and 8 s for water at gas flow rates of 100 sccm. This resulted in a growth rate of 0.09 nm cycle^{-1}, which is in agreement with earlier reports.[4] A formation of metallic Zn, as reported by Libera *et al.* for very long diethyl zinc exposures at 200°C and above in porous substrates, was not observed in XRD.[5]

To coat macroporous substrates, a stop-flow deposition protocol was used to improve penetration of the precursors into the structure. The precursor line flow was reduced to 40 sccm for 1.5 s, after which the chamber evacuation was interrupted. After another 1.3 s, the precursor pulse was initiated (1.5 s for ferrocene). Standard carrier gas flow and evacuation resumed 15.8 s after the cycle started. The total purge time was 15 s. Ozone, diethyl zinc and water pulses were modified similarly. After deposition, the electrodes were calcined in air at 600 °C with a heating rate of 3.2°C min^{-1} and 30 min holding time.

1.3. Material Characterization

Layer thicknesses were determined by ellipsometry (J. A. Woollam M-2000 VASE) on polished Si(100) witness substrates, placed in the ALD reactor next to the FTO substrates during depositions. The data were fitted using a stack model comprising the silicon substrate, a 2 nm native SiO_2 layer and one or two Cauchy material layers representing the deposited oxide films. X-ray diffraction (XRD) patterns were recorded at grazing incidence ($\Theta = 0.7°$) on a Bruker D8 Discover diffractometer with a Ni-filtered Cu source ($\lambda(Cu_{k\alpha1}) = 0.15406$ nm) operating at 40 kV and 30 mA. Theoretical reference XRD patterns for Fe_2O_3, ZnO and $ZnFe_2O_4$ were calculated using crystal structure data taken from the Inorganic Crystal Structure Database (ICSD).[6-8] Absorbance and reflectance spectra were measured on a Perkin-Elmer Lambda 1050 UV/Vis/NIR spectrophotometer with an integrating sphere. For the flat film samples, the reflectance-corrected absorbance was calculated according to Equation 7.3, which was modified to use the decadic logarithm for better comparability from the original derivation by Klahr and Hamann[9]

$$A_{corr} = -log_{10}\left(\frac{\frac{T_{samp}(\lambda)}{T_{subst}(\lambda)}}{1-\frac{R_{samp}(\lambda)-R_{subst}(\lambda)}{T_{subs}(\lambda)^2}}\right) \qquad \text{Equation 7.3}$$

T_{subst}, T_{samp}, R_{subst} and R_{samp} represent the transmittance and reflectance of the substrate and the sample (i.e. substrate with coating), respectively. This correction is not applicable to the macroporous samples as the derivation assumes a single absorber layer on a single transparent support layer. Therefore, the uncorrected absorbance is given for the macroporous substrate and the m-ZnFe2O4 sample. The morphology of the macroporous samples was studied using a JEOL JSM-6500F field emission scanning electron microscope (SEM) operating at an acceleration voltage of 5 kV. Images were acquired using a secondary electron detector. Additional morphological, crystallographic and compositional analysis was carried out using a FEI Titan Themis transmission electron microscope (TEM) at an acceleration voltage of 300 kV. Bright field (BF) images, high resolution TEM (HRTEM) images and diffraction patterns were acquired with a Ceta 16M camera, scanning TEM (STEM) images with a high-angle annular dark-field (HAADF) detector. The composition was analyzed by four Bruker Super-X 500 energy-dispersive X-ray (EDX) detectors. Samples were prepared by scraping material of the electrode film and depositing it on a holey carbon grid.

1.4. Photoelectrochemical Characterization

J-V-curves under simulated solar irradiation were measured using a µAutolab III potentiostat (Metrohm) in a three-electrode setup with the oxide film as the working electrode, a Pt-mesh counter electrode and an Ag/AgCl reference electrode. The electrolyte was 0.1 M NaOH contained in a 20 cm^3 quartz cell. The conversion between potential scales is given by Equation 7.4, where E_{RHE} and $E_{Ag/AgCl}$ represent the working electrode potential on the RHE and reference electrode scales, respectively.

$$E_{RHE} = 0.197 \text{ V} + 0.059 \text{ V} \cdot pH + E_{Ag/AgCl} \qquad \text{Equation 7.4}$$

The electrodes were masked with PTFE adhesive tape to limit the exposed film area to 0.159 cm^2 and illuminated through the substrate. The light source was a Xe lamp AM 1.5 solar simulator (Solar Light Co. Model 16S) delivering 100 mW cm^{-2} as verified by a certified Fraunhofer ISE silicon reference cell equipped with a KG5 filter. The potential was scanned between -0.25 and 0.75 V vs. Ag/AgCl at a rate of 20 mV s^{-1}. Incident photon-to-current efficiency (IPCE) curves were recorded using the same setup with the solar light intensity

reduced to 10% and additional monochromatic light from a 150 W Xe lamp passed through a monochromator (Horiba MicroHR) and an optical chopper operating at 0.2 Hz. The potential was fixed at 1.23 V vs. RHE (0.266 V vs. Ag/AgCl). The IPCE was calibrated against a certified Hamamatsu S1337 photodiode. For stability measurements, a larger quartz cell (40 cm^3) was used. Chronoamperometry was performed at 1.23 V vs. RHE for up to 3 h in constantly stirred electrolyte. Photocurrent transients and IMPS spectra were recorded using a similar electrochemical setup. A PGSTAT302N potentiostat (Metrohm) was used and the light source was a LED (λ = 455 nm) driven by a voltage-controlled constant current supply. The base photon flux was set to 10^{17} s^{-1} cm^{-2} using the same Hamamatsu photodiode. Photocurrent transients were recorded at potentials between -0.3 and 0.8 V vs. Ag/AgCl with a chopping frequency of 1 Hz. IMPS spectra were recorded between -0.3 and 0.5 V vs. Ag/AgCl in the frequency range between 100 mHz and 10 kHz with a perturbation amplitude of 10%. Impedance spectra were measured in the dark between -0.3 and 0.5 V vs. Ag/AgCl with frequencies ranging from 100 mHz to 100 kHz and a perturbation amplitude of 10 mV. The data were fitted using the EIS spectrum analyzer software.[10]

2. Calculation of ALD Cycle ratio for $ZnFe_2O_4$

Assuming that an ALD film material grows as a void-free and crystalline film, which is the case for both Fe_2O_3 and ZnO at 250°C, the deposited molar loading of material per cycle, L, can be calculated from the crystallographic data according Equation 7.5, where Z is the number of formula units per unit cell, V is the unit cell volume, N_A is Avogadro's constant and GPC the growth rate, i.e. the increase in layer thickness per cycle. The values of these quantities are shown in Table S7.1. To form $ZnFe_2O_4$ a molar ratio of $ZnO:Fe_2O_3$ of 1:1 must be maintained. This is achieved by choosing the cycle ratio of Fe_2O_3 and ZnO according to Equation 7.6, where n_c represents the number of ALD cycles of the respective oxide. Thus, while the exact composition cannot be matched as no fractional ALD cycles can be performed, a ratio of 9 cycles Fe_2O_3 per cycle of ZnO gives the closest possible approximation.

$$L = \frac{Z}{V \cdot N_A} \cdot GPC \qquad \text{Equation 7.5}$$

$$\frac{n_c(Fe_2O_3)}{n_c(ZnO)} = \frac{1}{1} \cdot \frac{L(ZnO)}{L(Fe_2O_3)} = 8.66 \qquad \text{Equation 7.6}$$

Table S7.1   Crytallographic data and calculated molar loading per cycle.[6,7]

Quantity	Fe_2O_3	ZnO
Z	6	2
V / [Å^3]	301.9	47.56
L / [mol cm^{-2} cycle^{-1}]	7.26 10^{-11}	6.28 10^{-10}

3. Calculation of Theoretical Photocurrents from Absorbance Spectra

The theoretical maximum photocurrent density J_{abs} that the examined electrodes could achieve if each photon they absorbed was converted into one electron contributing to the photocurrent (i.e. assuming an absorbed-photon-to-current-efficiency of 100% over the entire spectral range) was calculated according Equation 7.7, in which q represents the electron charge, λ the wavelength, $A_{corr}(\lambda)$ the spectral absorbance and $\Phi_{AM1:5G}(\lambda)$ is the photon flux given by the AM1.5G standard. While this gives the electrode-specific maximum photocurrent, the material-specific theoretical maximum photocurrent, J_{theo} can be obtained by assuming $A_{corr} = \infty$ (i.e. quantitative light absorption). For hematite with a band gap of 2.1 eV, this is 12.6 mA cm^{-2}.

$$J_{abs} = q \cdot \int_{\lambda_{min}}^{\lambda_{cutoff}} 1 - 10^{-A_{corr}(\lambda)} \cdot \Phi_{AM1.5G}(\lambda) \, d\lambda \qquad \text{Equation 7.7}$$

4. Mott-Schottky Analysis on Thin Film Samples

Equation7.8$\left(\frac{C_{SC}}{rf \cdot A}\right)^{-2} = \frac{2}{q \cdot \epsilon_0 \cdot \epsilon_r \cdot N_d}\left(E - E_{fb} - \frac{k \cdot T}{q}\right)$ Equation 7.8 was

used for Mott-Schottky analysis, where C_{SC} is the space charge capacitance, N_d denotes the donor density, A the geometrical electrode area, rf the roughness factor (1.25 for the thin films, estimated from TEM cross-sections), E_{fb} the flatband potential, E the applied potential, k is Boltzmann's constant, T the absolute temperature, q the electron charge, ϵ_0 the permittivity of free space and ϵ_r the relative permittivity of the material (32 for Fe_2O_3 [11] and 100 for $ZnFe_2O_4$[12])[13].

$$\left(\frac{C_{SC}}{rf \cdot A}\right)^{-2} = \frac{2}{q \cdot \epsilon_0 \cdot \epsilon_r \cdot N_d}\left(E - E_{fb} - \frac{k \cdot T}{q}\right) \qquad \text{Equation 7.8}$$

Equation 7.9 allows an estimation of the space charge layer width.[13]

$$W_{SC} = \sqrt{\frac{2 \cdot (E - E_{fb}) \cdot \epsilon_0 \cdot \epsilon_r}{q \cdot N_d}}$$

Equation 7.9

Here, E denotes the applied potential, E_{fb} is the flatband potential, ϵ_0 is the permittivity of free space and ϵ_r the relative permittivity of the film material. The resulting values for W_{SC} are 16 nm for hematite and 146 nm for zinc ferrite using an E of 1.23 V vs. RHE.
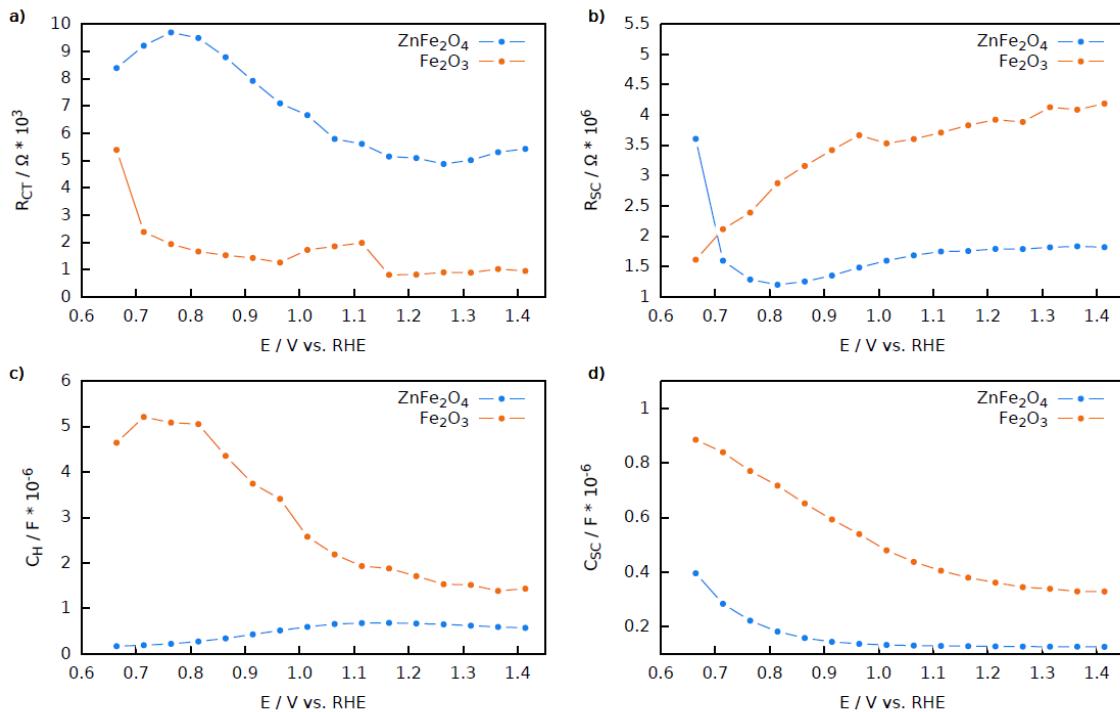
Figure S7.1 Fit results of PEIS measurements carried out in the dark on Fe₂O₃ and ZnFe₂O₄ flat films: a) Charge transfer resistance, b) space charge layer resistance, c) Helmholtz capacitance and (d) space charge layer capacitance.

5. Photocurrent Transient Analysis

The spiky photocurrent transients exhibited by hematite photoanodes can be explained by the movement of charge carriers within the semiconductor layer. When the light is switched on, an instantaneous positive current spike, J_{inst}, is registered, which decays into a steady state, J_{ss}. When the light is switched on, an instantaneous negative transient occurs, which decays to zero at potentials below the dark current onset. The switch-on transient can be attributed to the charging up of the space charge capacitance by a flux of photogenerated holes to the semiconductor surface, while the switch-on transient is caused by electrons recombining with the holes still present at the surface after illumination ends.[14,15]
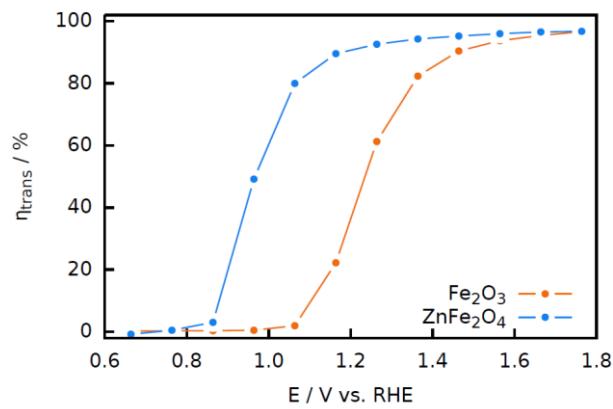
Figure S7.2 Charge transfer efficiency η_{trans} calculated from photocurrent transients at different potentials.

6. Characterization of m-ZnFe$_2$O$_4$
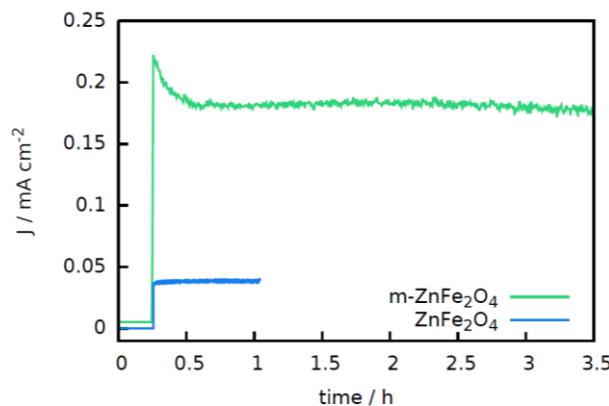
Figure S7.3   Photocurrent stability measurement at 1.23 V vs. RHE in the dark for 15 min followed by 1 sun illumination of a flat ZnFe₂O4 and a m-ZnFe₂O₄ electrode.
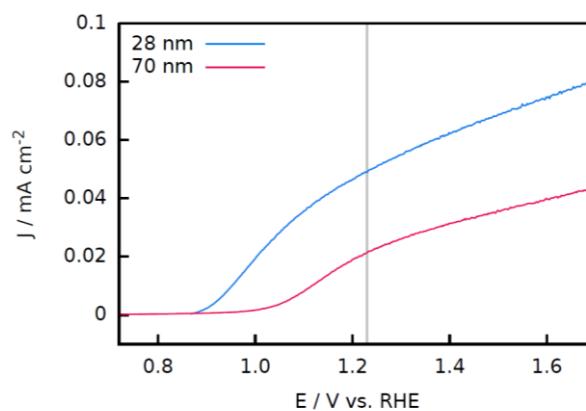
Figure S7.4   J-V curves of 28 nm and ca. 70 nm ZnFe$_2$O$_4$ films on FTO recorded under 1 sun illumination through the substrate.
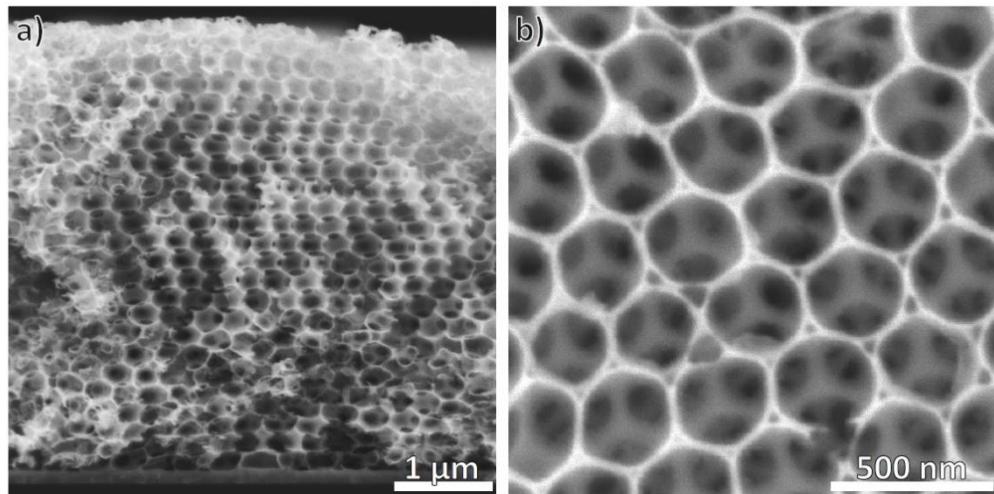
Figure S7.5   Cross-sectional (a) and top-view (b) SEM images of the macroporous ATO scaffold.
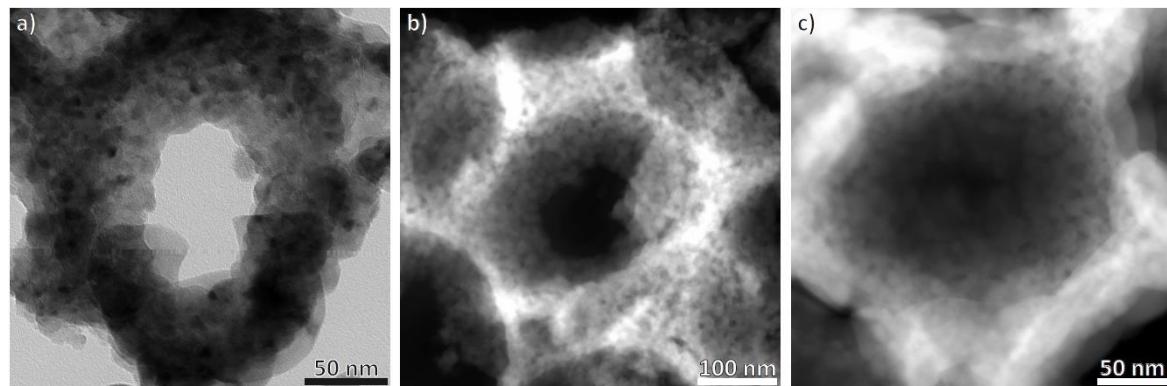
Figure S7.6   BF (a) and ADF STEM images (b,c) of several pores of m-ZnFe$_2$O$_4$.

7. References

(1)   Mandlmeier, B.; Szeifert, J. M.; Fattakhova-Rohlfing, D.; Amenitsch, H.; Bein, T. *J. Am. Chem. Soc.* **2011**, *133*, 17274.

(2)   Mandlmeier, B.; Minar, N. K.; Feckl, J. M.; Fattakhova-Rohlfing, D.; Bein, T. *J. Mater.Chem. A* **2014**, *2*, 6504.

(3)   Peters, K.; Zeller, P.; Stefanic, G.; Skoromets, V.; Nêmec, H.; Kužel, P.; Fattakhova-Rohlfing, D. *Chem. Mater.* **2015**, *27,* 1090.

(4)   Lujala, V.; Skarp, J.; Tammenmaa, M.; Suntola, T. *Appl. Surf. Sci.* **1994**, *82*, 34.

(5)   Libera, J. A.; Elam, J. W.; Pellin, M. J. *Thin Solid Films* **2008**, *516*, 6158.

(6)   Pailhé, N.; Wattiaux, A.; Gaudon, M.; Demourgues, A. *J. Solid State Chem.* **2008**, *181*, 2697.

(7)   Pola-Albores, F.; Antúnez-Flores, W.; Amézaga-Madrid, P.; Ríos-Valdovinos, E.; Valenzuela-Zapata, M.; Paraguay-Delgado, F.; Miki-Yoshida, M. *J. Cryst. Growth* **2012**, *351*, 77.

(8)   Rahimi, M.; Kameli, P.; Ranjbar, M.; Hajihashemi, H.; Salamati, H. *J. Mater. Sci.* **2012**, *48*, 2969.

(9)   Klahr, B. M.; Hamann, T. W. *J. Phys. Chem. C* **2011**, *115*, 8393.

(10)   Bondarenko, A. S.; Ragoisha G. A. in *Progress in Chemometrics Research* (Ed.: A. L. Pomerantsev), Nova Science Publishers, New York, **2005**, p. 89.

(11)   Klahr, B. M.; Martinson, A. B. F.; Hamann, T. W. *Langmuir* **2011**, *27*, 461.

(12)   Tahir, A. A.; Wijayantha, K. G. U. *J. Photochem. Photobiol. A* **2010**, *216*, 119.

(13)   Morrison, S. R. *Electrochemistry at semiconductor and oxidized metal electrodes*, Plenum Press, New York, **1980**.

(14)   Peter, L. M.; Wijayantha, K. G. U.; Tahir, A. A. *Faraday Discuss.* **2012**, *155*, 309.

(15)   Peter, L. *J. Solid State Electrochem.* **2013**, *17*, 315.

8. 3D-ELECTRODE ARCHITECTURES FOR ENHANCED DIRECT BIOELECTROCATALYSIS OF PYRROLOQUINOLINE QUINONE-DEPENDENT GLUCOSE DEHYDROGENASE

This chapter is based on the following publication:

David Sarauli, Kristina Peters, Chenggang Xu, Burkhard Schulz, Dina Fattakhova-Rohlfing, Fred Lisdat
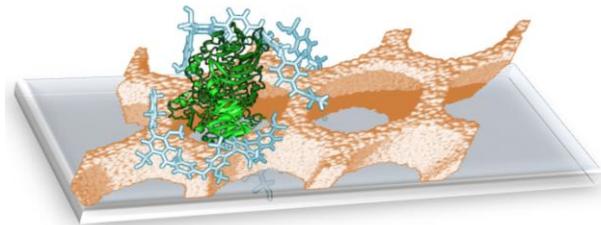
The joint project is a collaboration of different groups involving development of a complex electrode architecture for efficient direct bioelectrocatalysis. Dr. D. Sarauli, C. Xu and B. Schulz designed the bioelectrodes, which consist of a redox enzyme entrapped in a conductive polymer. Dr. D. Sarauli performed the bioelectrocatalytic measurements. K.Peters fabricated macroporous ITO electrodes to be used as a 3D conducting host scaffold, performed conductivity measurements to characterize conductivity of the scaffolds and measured SEM of the as-prepared and functionalized ITO electrodes.

We report on the fabrication of a complex electrode architecture for efficient direct bioelectrocatalysis. In the developed procedure, the redox enzyme pyrroloquinoline quinone-dependent glucose dehydrogenase entrapped in a sulfonated polyaniline [poly(2-methoxyaniline-5-sulfonic acid)-*co*-aniline] was immobilized on macroporous indium tin oxide (macroITO) electrodes. The use of the 3D conducting scaffold with a large surface area in combination with the conductive polymer enables immobilization of large amounts of enzyme and its efficient communication with the electrode, leading to enhanced direct bioelectrocatalysis. In the presence of glucose, the fabricated bioelectrodes show an exceptionally high direct bioelectrocatalytical response without any additional mediator. The catalytic current is increased more than 200-fold compared to planar ITO electrodes. Together with a high long-term stability (the current response is maintained for >90% of the initial value even after 2 weeks of storage), the transparent 3D macroITO structure with a conductive polymer represents a valuable basis for the construction of highly efficient bioelectronics units, which are useful as indicators for processes liberating glucose and allowing optical and electrochemical transduction.

8.1. INTRODUCTION

The fabrication of electronic devices based on biological units is a very attractive and an intensively explored concept because it offers a possibility of benefitting from extremely high efficiencies and selectivities of biological systems optimized by nature. Successful examples of such technologies include enzyme-based bioelectrochemical devices such as biosensors, biofuel cells and bioelectronics devices, which were already fabricated for a number of biomolecules.[1-7] A key for the electrochemical device functionality is an electronic communication between the electrode and an enzyme, which requires proper design of the electrode architectures. The composition and morphology of the electrode layers are particularly important; equally essential how the bioentities are bound to the electrodes without any deterioration of their biological functionality.[8-11]

Primarily highly conductive materials such as modified graphite or metals have been utilized as electrodes for the binding of redox biomolecules. However, these surfaces often produce an unwanted orientation of immobilized bioentities. Moreover, the nontransparent electrodes are not suitable for photoelectrochemical applications requiring interaction with light, as well as for fundamental spectroelectrochemical studies. In this context, transparent conducting oxides (TCOs), such as tin-doped indium oxide (ITO)[12-16] or other doped tin oxides[17-21] have emerged as intensively used electrodes for bioelectrochemical applications. Beside the

common planar geometries, TCO electrodes with controlled porous architectures have received a growing attention as alternative electrode materials for enzyme immobilization.[22-28] The interest in 3D-porous electrodes is caused by their large surface area and an accessible conducting interface enabling incorporation of large amounts of active species and their direct communication with the electrode.

Porous TCO electrodes have been successfully applied for the immobilization of various redox moieties. The reported examples include electrochemiluminescent dyes demonstrating more than 2 orders of magnitude higher electroluminescence intensity on porous electrodes compared to the planar ones.[29] Furthermore, redox proteins such as cytochrome *c* (cyt *c*),[24, 28, 30-32] ferredoxin,[33] hemoglobin[26] and azurin[31] were successfully incorporated into porous TCO electrodes with a very high loading related to the specific surface area of the porous electrode. So far, however, the advantages offered by porous TCO electrodes could be demonstrated only for relatively small biological species. Bulkier biological entities, such as the majority of the practically relevant enzymes, or more complex systems based on polymer-embedded enzymes, were practically not investigated, and a few reported systems did not show the expected increase in electrochemical activity[19,34] The major reasons for that are either the small pore size of the used TCO electrodes, making them inaccessible for the large species, or the poor communication between the incorporated enzyme and the electrode.

In this report, we demonstrate the clearly enhanced direct bioelectrocatalysis of the redox enzyme pyrroloquinoline quinone-dependent glucose dehydrogenase (PQQ-GDH) fixed by a sulfonated polyaniline copolymer (PMSA1) on macroporous ITO electrodes. This enzyme is insensitive to the oxygen level in the sample and exhibits high catalytic activity at physiological pH; hence, it represents an interesting bioentity for the engineering of biocatalytic glucose sensors.[7, 35-37] Moreover, biocatalytic electrodes made of carbon nanotube materials modified with PQQ-GDH have already been applied in biofuel cells effectively operating in physiological media.[38-41] Recently, we demonstrated the ability of sulfonated polyaniline copolymer containing 2-methoxyaniline-5-sulfonic acid and aniline monomers not only to react directly with PQQ-GDH,[42] but also to serve as a matrix without inhibiting the catalytic activity of the entrapped enzyme on gold and planar ITO electrodes.[43] In this study we introduce a new system by exploiting the polymer/enzyme interaction and combining both compounds with the highly porous 3D structure of macroporous ITO electrodes while ensuring a high enzyme activity and an efficient bioelectrocatalysis in the presence of glucose.

8.2. RESULTS AND DISCUSSION

8.2.1. FABRICATION AND CHARACTERIZATION OF MACRO ITO AND MACRO ITO/(PMSA1:PQQ-GDH) ELECTRODES

The principle of the used electrodes is depicted in Scheme 8.1. Because the accessibility of the electrode surface in 3D structures can limit the bioelectrochemical performance, we intended to use a porous ITO scaffold with sufficiently large pore size to allow the efficient transport of polymer and enzyme during the preparation but also to not limit the transport of the enzyme substrate into the 3D electrode during operation. For this purpose, we have composed our electrodes by the deposition of macroITO layers on top of commercial flat ITO substrates. The thickness of the porous ITO layer is about 1.2 μm after calcination. Scanning electron microscopy (SEM) and transmission electron microscopy (TEM) of these coatings reveal their homogeneous and crack-free morphology with a uniform pore structure composed of ca. 300 nm interconnected spherical pores (Figure 8.1a). The electrical conductivity of the porous ITO scaffold is 4.0 ± 0.3 S cm^{-1} after annealing in a forming-gas atmosphere at 400 °C.[26]
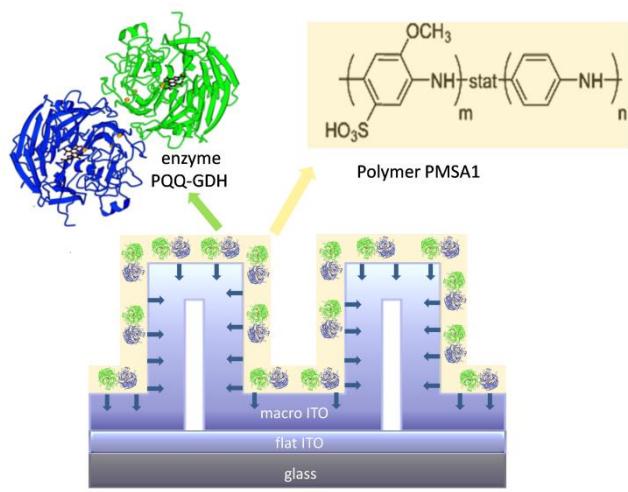
Scheme 8.1   The principle of the used electrode architecture.
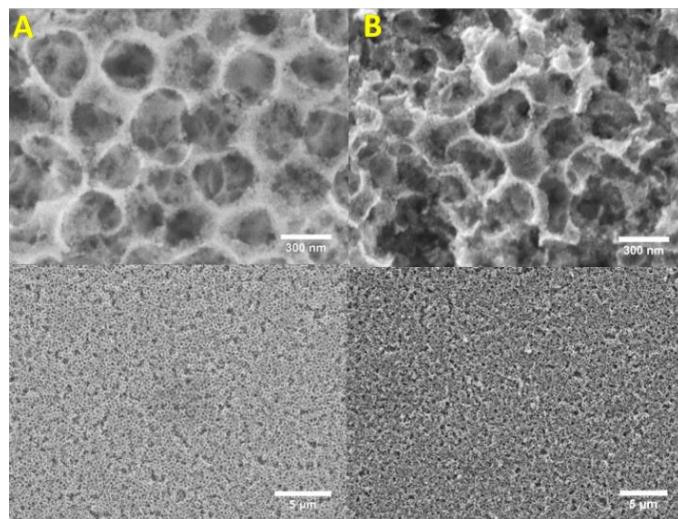
Figure 8.1   Top view SEM images of a) blank macroITO and b) macroITO/(PMSA1:PQQ-GDH) films.

The sulfonated polyaniline copolymer PMSA1 has been already shown to react efficiently with PQQ-GDH.[42] Because of its good biocompatibility, it can also serve as a matrix, in which PQQ-GDH can be entrapped without loss of the catalytic activity. Both arguments are used here as starting points for the study of this system on macroITO electrodes (Scheme 8.1). Figure 8.1b demonstrates the morphology of macroITO electrodes after the polymer and enzyme are allowed to deposit within the structure. It can be seen that the porosity and homogeneity are not damaged upon polymer and enzyme functionalization of the films even under current flow through the system. As a further confirmation, cyclic voltammetry of the polymer/enzyme-coated electrodes has been performed. It can be seen that the blank macroITO electrode does not show any redox transformation (Figure 8.2a, curve 1). After immobilization of PMSA1 alone (Figure 8.2a, curve 2), two clear redox couples are observed. A small peak at $E_{f1} = +0.08 \pm 0.02$ V and a more pronounced one at $E_{f2} = +0.25 \pm 0.05$ V vs. Ag/AgCl are consistent with leucoemeraldine to emeraldine and emeraldine to pernigraniline redox transitions, respectively, and are typical for sulfonated polyanilines.[44-47]
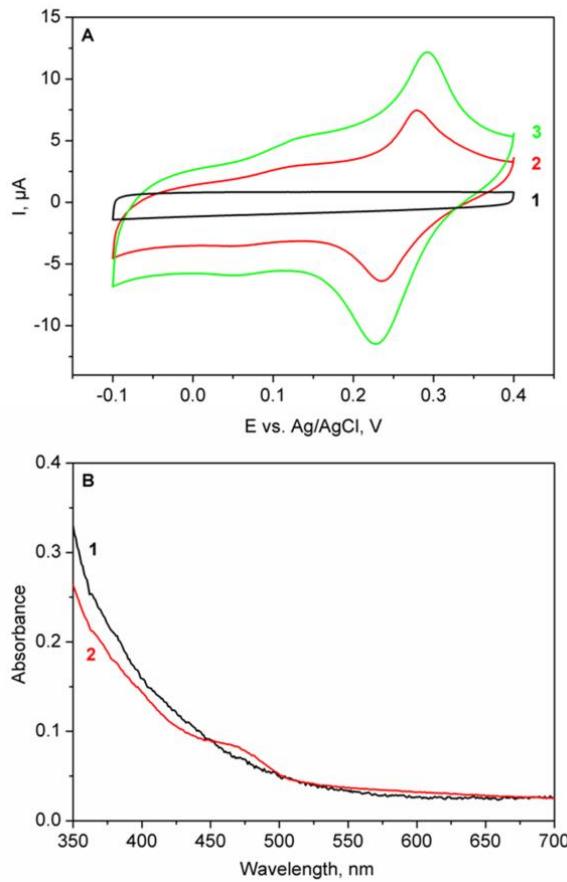
Figure 8.2 a) CV for the (1) blank macroITO, (2) macroITO/PMSA1, and (3) macroITO/(PMSA1;PQQ-GDH) electrodes; b) UV-Vis spectra of (1) blank macroITO and (2) macroITO/(PMSA1;PQQ-GDH) electrodes. Measurements are taken in 20 mM MES + 5 mM CaCl₂ buffer at pH 6.

The voltammetric behavior of the PMSA1 on the macroITO electrode is very similar to that observed on the planar ITO;[43] however, the amount of the immobilized PMSA1 is much higher on the macroporous ITO electrode compared to the flat one (see Materials and Methods).

The incorporation of the polymer can be clearly observed in the UV-vis spectra, which show a strong band at 469 nm assigned to a low-wavelength polaron band of the polyaniline emeraldine salt (ES) state[42,46]. The incorporation of the PQQ-GDH enzyme does not change the voltammetric behavior of the polymer matrix much. The entrapped PQQ-GDH enzyme does not show a direct electrochemical signal in the absence of the glucose substrate; however, its presence leads to a change in the charging properties resulting from the interaction of PQQGDH with the polymeric chains (Figure 8.2a, curves 2 and 3). Therefore, we assume that the polymer and PQQ-GDH can penetrate the porous electrode and the enzyme is immobilized by means of the polymer. It should be pointed out that the electrodes

are considered to be fully loaded with adsorbed material after 2 h of incubation in a polymer/enzyme solution because no additional increase in the current density occurs upon an increase of the incubation times to 1 or 2 days.

UV−vis spectra of the blank macroITO and macroITO/(PMSA1:PQQ-GDH) electrodes are summarized in Figure 8.2b. The appearance of the strong band at 469 nm assigned to a low-wavelength polaron band of the polyaniline ES state[42,46] indicates the immobilized polymer/enzyme network on macroITO. The concentration of the enzyme is not sufficient to have impact on the polymer spectra. Further spectroscopic features from the polymer are difficult to resolve because the macroITO electrodes show a basic absorbance in the range below 450 nm (Figure 8.2b, curve 1).
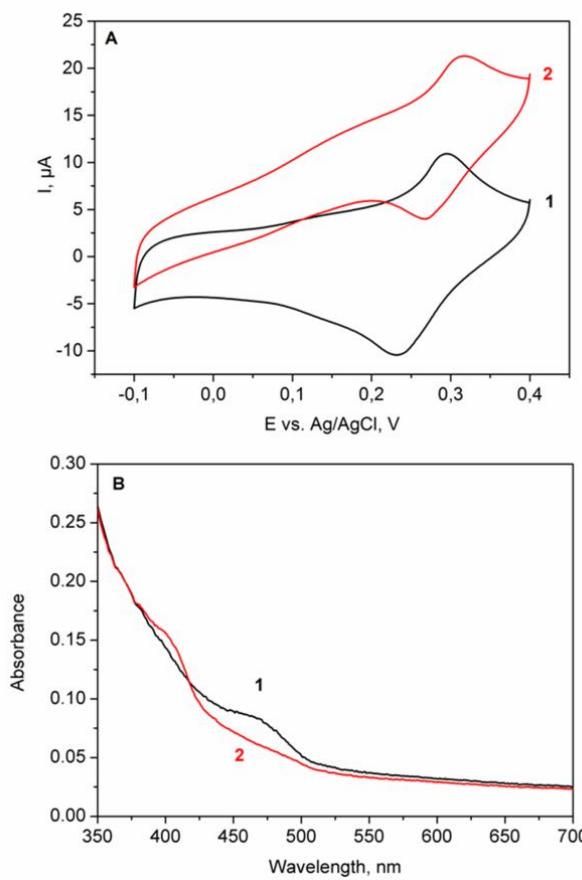
Figure 8.3   (a) CV and (b) UV-Vis of the macroITO/(PMSA1:PQQ-GDH) electrodes in the absence (1) and in the presence (2) of glucose. Measurements are taken in a 20 mM MES + 5 mM CaCl$_2$ buffer at pH 6.

8.2.2. BIOELECTROCHEMICAL OXIDATION OF GLUCOSE AT MACRO ITO/(PMSA1:PQQ-GDH) ELECTRODES

Upon the addition of the glucose substrate to the buffer solution, the macroITO/(PMSA1:PQQ-GDH) electrode shows a significant bioelectrocatalytic current, giving proof of the presence of the electroactive enzyme in the film (Figure 8.3a). Control experiments without enzyme show no glucose conversion in this potential range. The catalytic current starts from a potential of about E = −0.1 V vs. Ag/AgCl and reaches a change of $\Delta I =$ 13 ± 3 μA at E = +0.35 V, n = 3 (curve 2). Bioelectrocatalysis demonstrates efficient electron exchange between the redox center of the entrapped enzyme and the accessible porous conductive electrode surface, indicating that the polymer environment inside the macroITO pores ensures the catalytic activity of PQQ-GDH and allows efficient electron withdrawal from the reduced enzyme.

When we compare the catalytic current density of the macroporous PQQ-GDH electrode developed here with those of electrodes that have been constructed in a similar manner on flat ITO ($\Delta I = 57$ nA), a significant improvement of the bioelectrocatalytic properties of the system can be demonstrated. The catalytic currents for the same glucose concentration are increased by more than 2 orders of magnitude (~228-fold) by using macroITO electrodes. When one compares this enhancement with the electroactive area increase from flat ITO to porous macroITO – concluded from analysis of the voltammetric charging current in a pure buffer solution (see Materials and Methods), which gives about a 40-fold increase – it is obvious that not only the high surface within the macroITO structure but also the high polymer amount in combination with entrapment of the enzyme contribute to the drastically enhanced bioelectrocatalytic current. This is a clear achievement of the presented electrode, compared to other bioelectrocatalytic systems.[34]
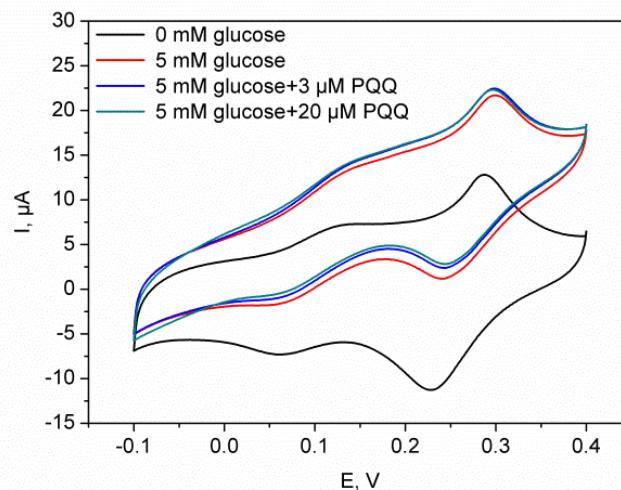
Figure 8.4 CV of macroITO/(PMSA1:PQQ-GDH) electrode in solutions containing glucose and increasing amounts of free PQQ. Measurements are performed in a 20 mM MES + 5 mM CaCl$_2$ buffer at pH 6 and scan rate of 5 mV/s.

In order to demonstrate application of the nanoporous system as an optical transducer, macroITO/(PMSA1:PQQGDH) electrodes have been measured by UV−vis in the presence and in the absence of substrate. Figure 8.3b demonstrates the spectral changes of the mixed polymer/enzyme film on macroITO in the absence (curve 1) and in the presence (curve 2) of 5 mM glucose. According to the known redox-state-dependent spectral characteristics of PMSA1,[42,43,46] it can be seen that reduction of the polymer upon the addition of glucose occurs with the appearance of a characteristic band at 408 nm. Despite absorbance of macroITO itself in this wavelength range, the polymer change can be clearly verified and supports our electrochemical data, demonstrating that electron transfer between the entrapped PQQ-GDH and the surrounding polymer in the macroporous electrodes can be followed also by optical means.

The start potential for glucose oxidation of the enzyme electrode macroITO/(PMSA1:PQQ-GDH) is located near the redox potential of the enzyme. However, the question arises as to whether the electrons are transferred directly to the electrode surface or small amounts of free PQQ are acting as mediators,[48, 49] because PQQ might be present in the polymer film or in the porous electrode as a result of partial denaturation of the holoenzyme during immobilization. To clarify this question, the macroITO/(PMSA1:PQQ-GDH) electrodes have been examined in the presence of 5 mM glucose with increasing concentration of free PQQ in solution. Figure 8.4 demonstrates that even an amount of 20 µM PQQ, which is 4 times higher than the

concentration of the enzyme during the entrapment process, does not cause any significant enhancement of the bioelectrocatalytic response. These measurements, together with the reconstitution procedure of the enzyme in which an excess of free PQQ with respect to the enzyme concentration is avoided, discard a hypothesis on the potential mediation of electron transfer by some denatured enzyme with liberated PQQ.

At this point, it is necessary to add some comments on the nature of electron transfer in the established polymer/enzyme electrode system. As one can see from Figure 8.4, the polymer is redox-active on the macroporous electrode. However, according to the formal potential of polymer conversions and the starting potential of bioelectrocatalysis, we conclude that its oxidation is not necessary to collect electrons from the reduced enzyme. This indicates that no mediation by the polymer takes place. Consequently, the conducting properties of sulfonated polyaniline have been exploited in this concept to drive electron transfer from the enzyme PQQ-GDH to the polymer-modified electrode. The polymer acts as an immobilization matrix, holding and wiring the enzyme within the pores of macroITO electrodes.

8.2.3. ANALYTICAL PERFORMANCE OF THE MACRO ITO/(PMSA1:PQQ-GDH) ELECTRODES.

Figure 8.5a shows the calibration curve obtained for macroITO/(PMSA1:PQQ-GDH) electrodes (n = 3). The oxidation current was determined as a function of the glucose concentration at E = +0.35 V vs. Ag/AgCl. The current follows the glucose concentration in the range from 0.025 to 2 mM and reaches saturation at 5−10 mM. An apparent Km value of 0.33 mM glucose has been calculated, which is considerably smaller than the intrinsic Km of soluble GDH in solution (~45 mM);[50-53] nevertheless, it fits into the range of apparent K_m (0.1 − 5mM) on some modified electrodes.[54-58] This shows that, besides enzyme kinetics, electron transfer, together with the accessibility of the enzyme's active center toward the substrate, are important factors for the behavior of the whole system. It has to be explicitly noted here that glucose detection can be performed at much lower potential because bioelectrocatalysis already starts at −0.1 V vs. Ag/AgCl. This is advantageous in complex media, in which other redox-active substances are present.
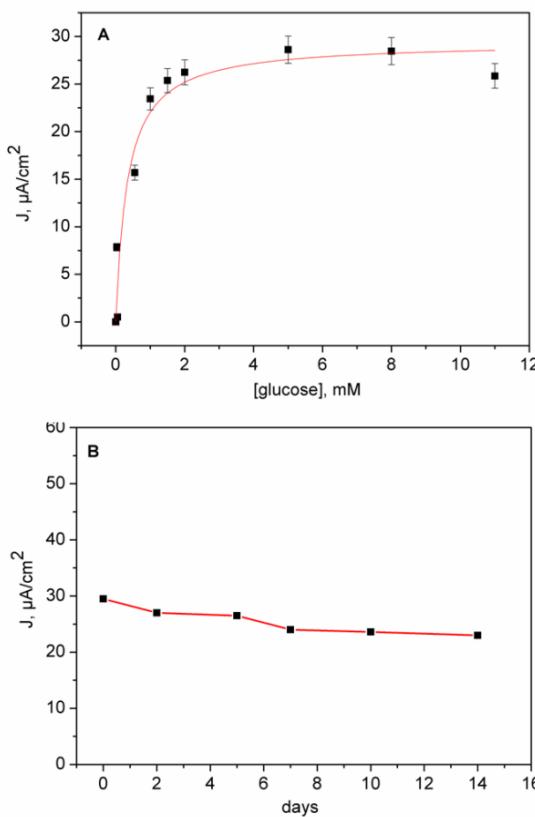
Figure 8.5   (a) Change in catalytic current density of the macroITO/(PMSA1:PQQ-GDH) electrode as a function of glucose concentration. Bioelectrocatalytic signals were registered from the respective cyclic voltammograms at E = +0.35V (surface area used for the calculation = 0.032 cm^2). (b) Stability of macroITO/(PMSA1:PQQ-GDH) at [glucose] = 5 mM. Measurements were performed in 20 mM MES + 5 mM CaCl$_2$ buffer at pH 6 and scan rate 5 mV s^{-1}.

Because long-term stability is an exceptionally important parameter for evaluation of the performance of a detection system, we have traced the stability of our macroITO/(PMSA1:PQQ-GDH) electrodes by testing their activity in a glucose solution, after the electrodes were kept at 4 °C in 20 mM MES + 5 mM CaCl$_2$, pH 6, when not in use. Figure **8.5**b shows that the catalytic current response maintained over 90% of the initial value after 12 days. This is significant progress compared to other kinds of PQQ-GDH immobilization procedures, resulting in substantial activity loss already during the first week, and demonstrates that the entrapment of PQQGDH in the sulfonated polyaniline films within the macroporous electrodes leads to an improved retainment of activity. Additionally, it has to be mentioned here that no intermittent treatment of the electrodes with PQQ has been performed, demonstrating that the environment in the 3D structure is well adapted to the enzyme. The high stability makes this type of architecture promising for consideration as a candidate for the construction of enzyme-based biosensors.

8.3. CONCLUSIONS

In summary, we have demonstrated an efficient platform for the entrapment of PQQ-GDH by fabricating a polymer/enzyme network inside the pores of macroITO. MacroITO has been shown to represent a suitable 3D electrode matrix for the incorporation of sulfonated polyaniline and PQQ-GDH, taking advantage of a pore size that does not limit immobilization of large amounts of enzyme in an active form. The amount of bound polymer within the macroporous electrodes is high enough to observe electrochemical signals and spectroscopic signatures. The large inner surface area of the material is well accessible for enzyme and substrate because a tremendously enhanced bioelectrocatalytic response in comparison with those of flat Au and ITO electrodes is observed. Bioelectrocatalysis starts near the potential of the enzyme redox center; i.e., no large overpotential is needed to drive the reaction. In particular, the mild fabrication process and the active role of the polymer film in closing the enzymatic cycle (i.e., withdrawing electrons from the reduced biomolecule) lead to a system with high stability because efficient bioelectrocatalysis can be detected even after more than 12 days in permanent electrolyte contact. We envision that the combination of the 3D porous electrode structure with a conductive polymer and an enzyme can be used for the development of many bioanalytical devices that combine optical and electrochemical detection for application in health care or environmental monitoring.

8.4. EXPERIMENTAL SECTION

Chemicals

MES [2-(N-morpholino)ethanesulfonic acid] buffer was purchased from Sigma-Aldrich (Taufkirchen, Germany), and dehydrated calcium chloride and anhydrous D-glucose were obtained from Fluka Analytics (Taufkirchen, Germany). They were used without further purification. Poly(2-methoxyaniline-5-sulfonic acid)-co-aniline polymer (PMSA1; Scheme 8.1) was synthesized as reported before[42, 59] sGDH (Acinetobacter calcoaceticus) was a kind gift from Roche Diagnostics GmbH. The enzyme was recombinantly expressed in Escherichia coli. PQQ was purchased from Wako Pure Chemical Industries. 18 MΩ Millipore water (Eschborn, Germany) was used for all types of measurements.

Preparation of nanostructured macroITO films

Porous indium tin oxide electrodes used in this work were prepared by a direct co-assembly of poly(methyl methacrylate) beads (PMMA) and indium tin hydroxide nanoparticles (nano-ITOH) as described before.[26] In brief, PMMA beads with diameter of 370nm were synthesized according to emulsion polymerization route.[60, 61] Indium tin nano-hydroxides were prepared by a solvothermal procedure.[27] In a typical synthesis of nano-ITOH, tin (IV) chloridepentahydrate (Aldrich) (0.122g, 0.35mmol) was added to a clear solution of indium (III) chloride (0.698g, 3.16mmol) (Aldrich) in 7mL of ethylene glycol (Aldrich, ≥99%, used without further drying). The molar ratio of tin and indium was 1:9 (mol:mol). Separately, 0.420g of sodium hydroxide (Aldrich, 97%) was dissolved in 7mL of ethylene glycol. Both solutions were combined at 0 °C, stirred for another 15 minutes and transferred into a glas-lined autoclave, which was kept in a laboratory oven pre-heated at 205 °C for 24 hours. The formed product was separated by centrifugation (47800 rcf for 20min), washed once in ca. 14 ml of bidistilled water (manual stirring) and centrifuged again at 47800 rcf for 20min. The water should be decanted immediately after centrifugation to prevent dissolution of ITOH nanoparticles.

For the fabrication of macroporous films, still wet nano-ITOH nanoparticles (300 mg) containing 100 mg of dry inorganic content were dispersed in 0.75 mL water (Millipore Q grade), stirred at room temperature until the colloidal solution turned transparent or slightly opaque and ultrasonicated for 30 min. Separately, aqueous colloidal PMMA suspension (15 wt%) was stirred for 1 hour and ultrasonicated for 30 min. The amount of PMMA beads was

calculated from the weight of the ITOH nanoparticles (dry content) as 3 weight parts of PMMA to 1 weight part of ITOH; in this example it corresponds to 2 ml of 15 wt% PMMA dispersion. Finally, hydroxypropyl cellulose (HPC) (MW ca. 100000, from Sigma-Aldrich) was added to a combined solution of PMMA and nano-ITOH, stirred together for 3-4 hours and ultrasonicated for 30 min. The amount of cellulose corresponds to 10 wt% of the PMMA beads; in this example it is 30 mg of HPC in a total volume of 3 ml, which corresponds to 1 wt% HPC. The ho-mogeneous dispersion was dip coated three times on planar ITO substrates at a dip coating rate of 0.63 mm s^{-1}with a drying step at 80 °C for 45 min after each coating. The relative humidity and the temperature in the coating chamber were 35% and 20 °C, respectively. The films were finally calcined in air at 400 °C (achieved with a ramp of 13 °C min^{-1}) for 30 min. To improve the electrical conductivity of the ITO layers, they were additionally heated in forming gas (composed of 5% hydrogen and 95% nitrogen) at 400 °C (achieved with a ramp of 2 °C min^{-1}) for 30 min.

Preparation of the enzyme solution

sGDH was dissolved in 5 mM MES buffer in the presence of 1 mM CaCl$_2$, and the pH was adjusted to 5. apoGDH was reconstituted by a PQQ/GDH ratio of 1 according to Olsthoorn and Duine.[62] For this purpose, sGDH and PQQ were incubated together for 1 h at room temperature in the dark. Aliquots were stored at -20 °C. Prior to each measurement, the specific activity of the reconstituted enzyme was determined to be 2200 ± 30 U mg^{-1} by using 2,6-dichlorophenol indophenol (DCIP) as an electron acceptor.

Construction of polymer/enzyme films

For the preparation of polymer/enzyme films, the previously cleaned rectangular ITO coated glass slides with surface resistivity 15–25 Ω cm^{-1} (obtained from Sigma-Aldrich, Taufkirchen, Germany) and nanostructured ITO were initially incubated in buffer solutions of the PMSA1–PQQ-GDH mixture (1.5 mg ml^{-1} PMSA1, 5 mM PQQ-GDH; 20 mM MES + 5 mM CaCl$_2$, pH 6) in darkness for 2 hours. Afterwards, the (PMSA1:PQQ-GDH) electrode was dipped into the same buffer without enzyme and polymer to wash away the unbound material.

Instruments and characterization methods

Film characterization by scanning electron microscopy was performed on a JEOL JSM-6500F scanning electron microscope equipped with a field emission gun, at10 kV. Bright field (BF) and high resolution (HR) transmission electron microscopy (TEM) as well as scanning transmission electron microscopy in high-angle annular dark-field mode (HAADF-STEM) were carried out using a field-emission FEI Titan 80-300 operated at 300kV.

Electrochemical measurements were performed at room temperaturein a homemade 1ml cell using an Ag/AgCl/1MKCl reference (Biometra, Germany) and a platinum wire counter electrode. Cyclic voltammetric experiments were carried out with a μAutolab Type II device (Metrohm, the Netherlands). The scan rate was set to 5 mV s^{-1}. The potential range was chosen as between -0.4 and +0.4 V vs. Ag/AgCl. Data analysis was performed using GPES software (General Purpose for Electrochemical System, Eco Chemie, Utrecht, the Netherlands). UV–Vis measurements were carried out using an Evolution 300 spectrophotometer (Thermo Fischer Scientific, Germany). The amount of immobilized polymer was compared by integration of voltammetric peaks measured on both flat ITO+polymer[43] and macroITO+polymer electrodes under the same experimental conditions (20mM MES + 5mM CaCl$_2$, pH 6, scan rate – 5mV/s). The electroactive area increase of the macroITO with respect to flat ITO was estimated by comparing the charging current of both electrodes at 0V vs. Ag/AgCl.

8.5. REFERENCES

(1)   Cracknell, J. A.; Vincent, K. A.; Armstrong, F. A. *Chem. Rev.* **2008,** *108*, 2439-2461.

(2)   Leger, C.; Bertrand, P. *Chem. Rev.* **2008,** *108*, 2379.

(3)   Lisdat, F.; Dronov, R.; Mohwald, H.; Scheller, F. W.; Kurth, D. G. *Chem. Commun.* **2009**, 274.

(4)   Ludwig, R.; Ortiz, R.; Schulz, C.; Harreither, W.; Sygmund, C.; Gorton, L. *Anal. Bioanal. Chem.* **2013,** *405*, 3637.

(5)   Noll, T.; Noll, G. *Chem. Soc. Rev.* **2011,** *40*, 3564.

(6)   Shleev, S.; Tkac, J.; Christenson, A.; Ruzgas, T.; Yaropolov, A. I.; Whittaker, J. W.; Gorton, L. *Biosens. Bioelectron.* **2005,** *20*, 2517.

(7)   Tkac, J.; Svitel, J.; Vostiar, I.; Navratil, M.; Gemeiner, P. *Bioelectrochemistry* **2009,** *76*, 53.

(8)   Hanefeld, U.; Gardossi, L.; Magner, E. *Chem. Soc. Rev.* **2009,** *38*, 453.

(9)   Rodrigues, R. C.; Ortiz, C.; Berenguer-Murcia, A.; Torres, R.; Fernandez-Lafuente, R. *Chem. Soc. Rev.* **2013,** *42*, 6290.

(10) Secundo, F. *Chem. Soc. Rev.* **2013,** *42*, 6250.

(11) Sheldon, R. A.; van Pelt, S. *Chem. Soc. Rev.* **2013,** *42*, 6223.

(12) Cherry, R. J.; Bjornsen, A. J.; Zapien, D. C. *Langmuir* **1998,** *14*, 1971.

(13) Dhand, C.; Das, M.; Sumana, G.; Srivastava, A. K.; Pandey, M. K.; Kim, C. G.; Datta, M.; Malhotra, B. D. *Nanoscale* **2010,** *2*, 747.

(14) El Kasmi, A.; Leopold, M. C.; Galligan, R.; Robertson, R. T.; Saavedra, S. S.; El Kacemi, K.; Bowden, E. F. *Electrochem. Commun.* **2002,** *4*, 177.

(15) Fang, A. P.; Ng, H. T.; Li, S. F. Y. *Biosens. Bioelectron.* **2003,** *19*, 43.

(16) Yagati, A. K.; Lee, T.; Min, J.; Choi, J. W. *Biosens. Bioelectron.* **2013,** *47*, 385.

(17) Cantale, V.; Simeone, F. C.; Gambari, R.; Rampi, M. A. *Sens. Actuators, B* **2011,** *152*, 206.

(18) Lamberti, F.; Agnoli, S.; Brigo, L.; Granozzi, G.; Giomo, M.; Elvassore, N. *ACS Appl. Mater. Interfaces* **2013,** *5*, 12887.

(19) Lavanya, N.; Radhakrishnan, S.; Sekar, C. *Biosens. Bioelectron.* **2012,** *36*, 41.

(20) Saha, S.; Tomar, M.; Gupta, V. *J. Appl. Phys.* **2012,** *111*, 5, 55.

(21) Wang, P.; Li, S. Q.; Kan, J. Q. *Sens. Actuators, B* **2009,** *137*, 662.

(22) Aksu, Y.; Frasca, S.; Wollenberger, U.; Driess, M.; Thomas, A. *Chem. Mater.* **2012,** *23*, 1798.

(23) Buonsanti, R.; Pick, T. E.; Krins, N.; Richardson, T. J.; Helms, B. A.; Milliron, D. J. *Nano Lett.* **2012,** *12*, 3872.

(24) Frasca, S.; von Graberg, T.; Feng, J. J.; Thomas, A.; Smarsly, B. M.; Weidinger, I. M.; Scheller, F. W.; Hildebrandt, P.; Wollenberger, U., *ChemCatChem* **2010,** *2*, 839.

(25) Hamd, W.; Chavarot-Kerlidou, M.; Fize, J.; Muller, G.; Leyris, A.; Matheron, M.; Courtin, E.; Fontecave, M.; Sanchez, C.; Artero, V.; Laberty-Robert, C., *J. Mater. Chem. A* **2013,** *1*, 8217.

(26) Liu, Y.; Peters, K.; Mandlmeier, B.; Müller, A.; Fominykh, K.; Rathousky, J.; Scheu, C.; Fattakhova-Rohlfing, D. *Electrochim. Acta* **2014**, *140*, 108.

(27) Liu, Y. J.; Stefanic, G.; Rathousky, J.; Hayden, O.; Bein, T.; Fattakhova-Rohlfing, D. *Chem. Sci.* **2012,** *3*, 2367.

(28) Schaming, D.; Renault, C.; Tucker, R. T.; Lau-Truong, S.; Aubard, J.; Brett, M. J.; Balland, V.; Limoges, B. *Langmuir* **2012,** *28*, 14065.

(29) Hou, K.; Puzzo, D.; Helander, M. G.; Lo, S. S.; Bonifacio, L. D.; Wang, W.; Lu, Z.-H.; Scholes, G. D.; Ozin, G. A. *Adv. Mater.* **2009,** *21*, 2492.

(30) Frasca, S.; Richter, C.; von Graberg, T.; Smarsly, B. M.; Wollenberger, U. *Eng. Life Sci.* **2011,** *11*, 554.

(31) Kwan, P.; Schmitt, D.; Volosin, A. M.; McIntosh, C. L.; Seo, D. K.; Jones, A. K. *Chem. Commun.* **2011,** *47*, 12367.

(32) Muller, V.; Rathousky, J.; Fattakhova-Rohlfing, D. *Electrochim. Acta* **2014,** *116*, 1.

(33) Reipa, V.; Mayhew, M. P.; Vilker, V. L. *Proc. Natl. Acad. Sci. U. S. A.* **1997,** *94*, 13554.

(34) Frasca, S.; Milan, A. M.; Guiet, A.; Goebel, C.; Perez-Caballero, F.; Stiba, K.; Leimkuhler, S.; Fischer, A.; Wollenberger, U. *Electrochim. Acta* **2013,** *110*, 172.

(35) Leech, D.; Kavanagh, P.; Schuhmann, W. *Electrochim. Acta* **2012,** *84*, 223.

(36) Rubenwolf, S.; Kerzenmacher, S.; Zengerle, R.; von Stetten, F. *Appl. Microbiol. Biotechnol.* **2011,** *89*, 1315.

(37) Zayats, M.; Willner, B.; Willner, I. *Electroanalysis* **2008,** *20*, 583.

(38) Katz, E.; MacVittie, K. *Energy Environ. Sci.* **2013,** *6*, 2791.

(39) Southcott, M.; MacVittie, K.; Halamek, J.; Halamkova, L.; Jemison, W. D.; Lobel, R.; Katz, E. *Phys. Chem. Chem. Phys.* **2013,** *15*, 6278.

(40) Scherbahn, V.; Putze, M. T.; Dietzel, B.; Heinlein, T.; Schneider, J. J.; Lisdat, F. *Biosens. Bioelectron.* **2014,** *61*, 631.

(41) Strack, G.; Nichols, R.; Atanassov, P.; Luckarift, H. R.; Johnson, G. R. *Meth. Mol. Biol. (Clifton, NJ, U.S.)* **2013,** *1051*, 217.

(42) Sarauli, D.; Xu, C. G.; Dietzel, B.; Schulz, B.; Lisdat, F. *Acta Biomater.* **2013,** *9*, 8290.

(43) Sarauli, D.; Xu, C.; Dietzel, B.; Schulz, B.; Lisdat, F. *J.Mater. Chem. B* **2014,** *2*, 3196.

(44) Dennany, L.; Innis, P. C.; McGovern, S. T.; Wallace, G. G.; Forster, R. J. *Phys. Chem. Chem. Phys.* **2011,** *13*, 3303.

(45) Masdarolomoor, F.; Innis, P. C.; Wallace, G. G. *Electrochim. Acta* **2008,** *53*, 4146.

(46) Pornputtkul, Y.; Strounina, E. V.; Kane-Maguire, L. A. P.; Wallace, G. G. *Macromolecules* **2010,** *43*, 9982.

(47) Sanchis, C.; Ghanem, M. A.; Salavagione, H. J.; Morallon, E.; Bartlett, P. N. *Bioelectrochemistry* **2011,** *80*, 105.

(48) Jin, W.; Wollenberger, U.; Scheller, F. W. *Biol. Chem.* **1998,** *379*, 1207.

(49) Karyakin, A. A. *Bioelectrochemistry* **2012,** *88*, 70.

(50) Dokter, P.; Frank, J.; Duine, J. A. *Biochem. J.* **1986,** *239*, 163.

(51) Durand, F.; Stines-Chaumeil, C.; Flexer, V.; Andre, I.; Mano, N. *Biochem. Biophys. Res. Commun.* **2010,** *402*, 750.

(52) Flexer, V.; Durand, F.; Tsujimura, S.; Mano, N. *Anal. Chem.* **2011,** *83*, 5721.

(53) Matsushita, K.; Shinagawa, E.; Adachi, O.; Ameyama, M. *Biochemistry* **1989,** *28*, 6276.

(54) Flexer, V.; Mano, N. *Anal. Chem.* **2014,** *86*, 2465.

(55) Gobel, G.; Schubart, I. W.; Scherbahn, V.; Lisdat, F. *Electrochem. Commun.* **2011,** *13*, 1240.

(56) Ivnitski, D.; Atanassov, P.; Apblett, C. *Electroanalysis* **2007,** *19*, 1562.

(57) Malinauskas, A.; Kuzmarskyte, J.; Meskys, R.; Ramanavicius, A. *Sens. Actuators, B* **2004,** *100*, 387.

(58) Strack, G.; Babanova, S.; Farrington, K. E.; Luckarift, H. R.; Atanassov, P.; Johnson, G. R. *J. Electrochem. Soc.* **2013,** *160*, G3178.

(59) Sarauli, D.; Xu, C. G.; Dietzel, B.; Stiba, K.; Leimkuhler, S.; Schulz, B.; Lisdat, F. *Soft Matter* **2012,** *8*, 3848.

(60) Mandlmeier, B.; Minar, N. K.; Feckl, J. M.; Fattakhova-Rohlfing, D.; Bein, T. *J. Mater. Chem. A* **2014,** *2*, 6504.

(61) Mandlmeier, B.; Szeifert, J. M.; Fattakhova-Rohlfing, D.; Amenitsch, H.; Bein, T. *J. Am. Chem. Soc.* **2011,** *133*, 17274.

(62) Olsthoorn, A. J. J.; Duine, J. A. *Arch. Biochem. Biophys.* **1996,** *336*, 42.

9. INTERACTION OF FRUCTOSE DEHYDROGENASE WITH A SULFONATED POLYANILINE: APPLICATION FOR ENHANCED BIOELECTROCATALYSIS

This chapter is based on the following publication:
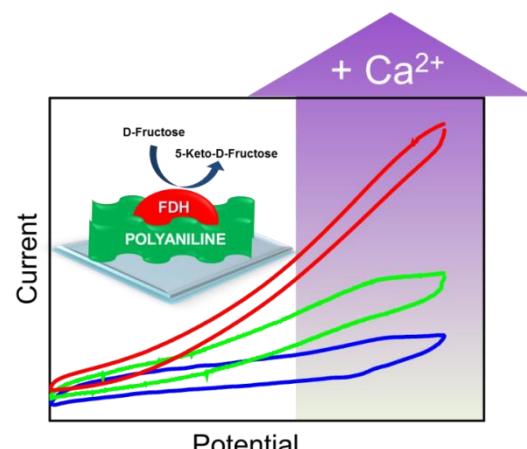
The joint project is a collaboration of different groups involving development of complex electrode architecture for efficient direct bioelectrocatalysis. Dr. D. Sarauli, C. Wettstein and B. Schulz designed the bioelectrodes, which consist of fructose dehydrogenase (FDH) entrapped in a conductive sulfonated polyaniline PMSA1. Dr. D. Sarauli performed the bioelectrocatalytic measurements and studied the enhanced catalytic activity of the bioelectrodes in the presence of Ca^{2+} ions. K.Peters fabricated macroporous ITO electrodes to be used as a 3D conducting host scaffold, performed conductivity measurements to characterize their conductivity and measured SEM to study the morphology.

We report on efficient bioelectrocatalysis of the redox enzyme fructose dehydrogenase (FDH) upon its interaction with the sulfonated polyaniline PMSA1 (poly(2-methoxyaniline-5-sulfonic acid)-co-aniline). This interaction has been monitored in solution and on the surface of planar and macroporous indium tin oxide (ITO) electrodes by UV−vis and cyclic voltammetric measurements. Moreover, an enhancement of the catalytic activity for fructose conversion induced by a structural change of sulfonated polyaniline PMSA1 caused by the presence of Ca^{2+} ions is observed. An entrapment of the Ca^{2+}-bound polymer and enzyme inside the pores of macroporous ITO electrodes leads to a significantly increased (~35-fold) bioelectrocatalytic signal in comparison to that of a flat ITO and allows the fabrication of highly efficient electrodes with good stability.

9.1. INTRODUCTION

Fabrication of electronic devices based on biomolecules such as proteins, enzymes, antibodies, or DNA fragments has attracted continuing attention due to the unprecedentedly high efficiencies and selectivities of biological systems. One of the major challenges for the commercial development of bioelectronic devices such as biosensors and biofuel cells is the implementation of biomolecules into electronic circuits, ensuring the complete retention of their biological properties.[1-8] Contacting biomolecules with electrode surfaces modified with conductive, conjugated polymers has become widely used for the construction of sensing units with electrochemical or optical readout. Even though the concept of direct polymer/biomolecule wiring is not new, only a limited number of functional systems, including the enzymes alcohol dehydrogenase, laccase, and pyrroloquinoline quinone dependent glucose dehydrogenase (PQQ-GDH), entrapped into polypyrrole, thiophene, or polyaniline have been demonstrated.[9-13]

The redox enzyme D-fructose dehydrogenase (FDH; EC 1.1.99.11) from *Gluconobacter Japonicus (*formerly *Gluconobacter Industrius)*[14] catalyzes the oxidation of D-fructose to produce 5-keto-D-fructose. Due to its strict substrate specificity to D-fructose,[15] it is widely used for the development of biosensors and biofuel cells.[16-18] FDH is a heterotrimeric membrane-bound enzyme with a molecular mass of ca. 140 kDa, consisting of subunits I (67kDa), II (51 kDa), and III (20 kDa). The enzyme is a flavoprotein-cytochrome *c* complex, since subunits I and II contain covalently bound flavin adenine dinucleotide (FAD) and heme C as prosthetic groups, respectively.[19] FDH allows a direct electron transfer (DET)-type

bioelectrocatalysis,[20,21] which strongly depends on the electrode material. However, until now no report on contacting FDH with the help of conducting polymers capable of enhancing its bioelectrochemical activity has been known.

We demonstrate here a FDH-based tunable bioelectrocatalytic system by entrapping the enzyme into a sulfonate polyaniline matrix on transparent electrode surfaces. Sulfonated polyanilines have already been established as materials suitable for the construction of different sensing electrodes as e.g. for detection of DNA hybridization[22,23] or low-molecular-weight compounds such as oxalate and organophosphate.[24,25] This is mainly due to their high conductivity in comparison to nonsubstituted polyanilines together with other advantages such as improved solubility and redox activity over a wide pH range.[26-31] Moreover, sulfonated polyanilines have been used in our group as building blocks for the design of novel multilayer architectures with cytochrome *c* only,[32,33] and cytochrome *c* with xanthine oxidase,[34] bilirubin oxidase,[35,36] and sulfite oxidase.[37]

It has also been demonstrated that the sulfonated polyaniline copolymer PMSA1, containing a 2-methoxyaniline-5-sulfonic acid (MAS) monomer, is not only able to react directly with PQQ-GDH,[38] but can also serve as an immobilization matrix without inhibiting the catalytic activity of the entrapped enzyme on gold,[11] planar ITO,[11] and macroporous ITO electrodes.[10] The polymer acts here as a conducting environment helping to close the enzymatic cycle by withdrawing electrons from the substrate-reduced enzyme.

In this study the interaction between the sulfonated polyaniline PMSA1 and FDH has been initially monitored in solution. The unprecedented enhancement of the catalytic reaction has been demonstrated upon addition of Ca^{2+} ions to the polymer/enzyme solution in the presence of the substrate fructose. Exploiting this interaction, a new, tuneable, and shuttle-free biohybrid system on electrodes has been constructed. For this purpose the enzyme has been entrapped into polymer films on indium tin oxide (ITO) and on the 3D structure of macroporous indium tin oxide (macroITO) electrode surfaces. The influence of Ca^{2+} ions on the polymer and the efficiency of the electron transfer with free and immobilized FDH is discussed.

9.2. RESULTS AND DISCUSSION

9.2.1. POLYMER ENZYME REACTION IN SOLUTION

Scheme 9.1 demonstrates the construction principle of our polymer/enzyme electrode. One prerequisite for the successful development of a functional and stable polymer/enzyme electrode system is an efficient electron transfer between the enzyme and the chosen polymer. Therefore, the interaction between PMSA1 and FDH has been first monitored in solution. For this purpose UV−vis spectroscopy measurements at different pH values (pH range 4.0−6.5) have been performed. The pH range has been chosen according to optimum pH values reported in the literature for the enzyme.[19,39,40]
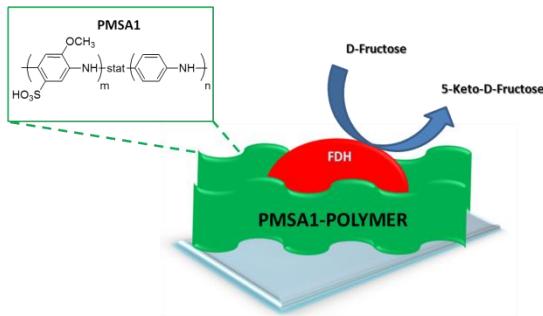
Scheme 9.1   Schematic illustration of the polymer based enzyme electrode architecture.

At these pH values PMSA1 polymer exists in its emeraldine salt (ES) oxidation state after synthesis.[38] Figure 9.1 illustrates the spectral changes occurring after addition of the substrate fructose to a solution containing a mixture of PMSA1 and FDH at pH 5.5. Two characteristic bands at 325 and 469 nm (curve 1) can be assigned to $\pi-\pi^*$ transitions and to a low-wavelength polaron band, respectively. They are characteristic of the ES state.[38] Upon addition of fructose strong bands at 330 and 393 nm appear, whereas the low-wavelength polaron band slightly shifts to 463 nm with decreased intensity. It seems that the electronic structure of PMSA1 is changed due to partial polymer reduction upon the enzymatic conversion of fructose, demonstrating the ability of PMSA1 to act as a reaction partner for FDH.
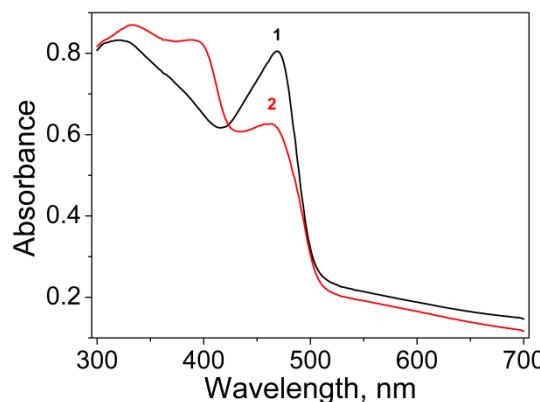
Figure 9.1   UV-vis spectra of PMSA1 with FDH in the absence (1) and in the presence (2) of the substrate fructose. Experimental conditions: [PMSA1] = 40 µg/mL, [FDH] = 18 µg/mL, [fructose] = 100 mM in 10 mM MES buffer at pH 5.5, t = 25 °C.

In order to gain an insight into the nature of the polymer−enzyme interaction, the overall charge on both reacting species has to be taken into account. Since the isoelectric points of both sulfonated polyaniline and FDH are determined to be pI <5.0,[41] it is evident that at pH >5.0 both species are negatively charged in solution, so that an electrostatic repulsion between the polymer and the FDH can be expected. Therefore, we have tested whether the interaction between the polymer and the enzyme can be tuned by changing the charge of PMSA1. One approach would be the use of Ca^{2+} ions, since it has been reported that they can coordinate to SO_3^- groups on aniline rings in emeraldine salt polyanilines, partially screening the electrostatic repulsions between SO_3^- negative charges along the chains.[42,43] Moreover, recently we have reported about the ability of Ca^{2+} ions to support the electrostatic interaction of two sulfonated polyanilines to form multilayer structures.[11] Therefore, the spectroscopic properties of PMSA1 in the presence of different Ca^{2+} amounts are the first to be clarified. Figure 9.2a demonstrates the overall change in UV−vis absorbance of polymer PMSA1 upon addition of increasing Ca^{2+} concentrations. A clear decrease of absorbance at 469 nm together with the appearance of a distinct band at 393 nm and a small increase in absorbance at wavelength >600 nm ([Ca^{2+}] >200 mM) can be followed. These results confirm that there is a strong interaction between calcium ions and the polymer chains, showing saturation at higher calcium concentrations (Figure 9.2b).
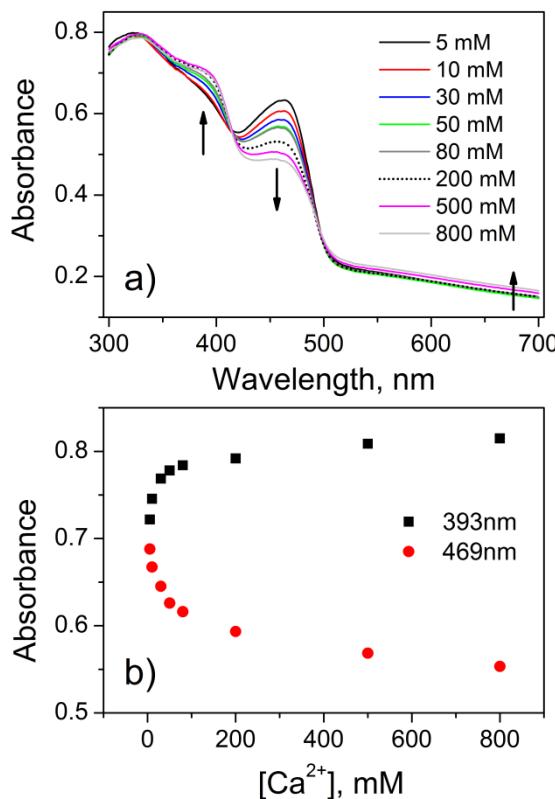
Figure 9.2   (a) Overall absorbance change of PMSA1 upon addition of different Ca^{2+} concentrations (from 5 to 800 mM). (b) Change in absorbance at 393 and 469 nm. Experimental conditions: [PMSA1] = 40 µg/mL in 10 mM MES buffer at pH 5.5.

To analyze the polymer changes, one should take into account that the self-doped polyanilines are known for their switching among completely oxidized (pernigraniline), halfoxidized (emeraldine), and completely reduced (leucoemeraldine) redox states.[43-45] The oxidation state strongly influences the conductivity and reactivity of polyanilines, whereas the highest conductivity can be ensured in the emeraldine state (ES).[46,47] Furthermore, interactions between different metal cations with sulfonate moieties of polyanilines have been reported by several groups.[43,48-50] On the basis of their spectroscopic observations two polymer conformations have been supposed, even though no structural confirmations have been provided. [43,48-50] According to these findings, we hypothesize that the spectroscopic features in Figure 9.2b are due to the change in different PMSA1 conformations (usually referred to as "extended coil" and "compact coil"), in line with existing arguments in the literature.[43,48-50]

The question that arises in this respect is whether the change in the polymer can affect its interaction with the enzyme FDH. For this purpose the same experimental conditions as in our starting measurements (Figure 9.1) have been kept, except of the addition of $[Ca^{2+}]$ = 20 mM to the solution of PMSA1, enzyme, and substrate. This calcium concentration corresponds to

the end of the linear range of Ca^{2+}-dependent absorbance changes of PMSA1 as depicted in Figure 9.2b. The addition of 20 mM of Ca^{2+} to the polymer/enzyme/fructose solution drastically changes the absorption spectrum (Figure 9.3a, curve 3). However, this spectrum cannot be unambiguously attributed to the completely reduced form of PMSA1.[38,43] It may rather represent a superimposed spectrum resulting from two different effects depicted in Figure 9.1 and Figure 9.2a. In order to get a more detailed insight into whether the presence of calcium ions changes the interaction with the enzyme, we have carried out cyclic voltammetry measurements under the same experimental conditions.
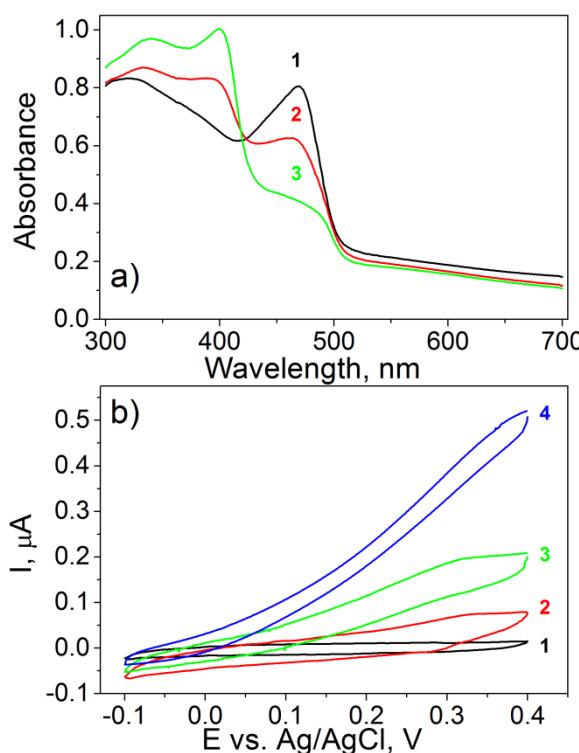
Figure 9.3 (a) UV−vis spectra of PMSA1 with FDH in the absence (1) and in the presence of fructose (2) together with the added Ca^{2+} (3). (b) CV of blank ITO electrode (1) and ITO electrode immersed in solution of PMSA1 + FDH without addition (2) and after addition (3) of fructose. Curve 4 corresponds to system 3 after addition of 20 mM Ca^{2+}. Experimental conditions: [PMSA1] = 40 μg/mL, [FDH] = 18 μg/mL, [Ca^{2+}] = 20 mM, [fructose] = 100 mM in 10 mM MES buffer at pH 5.5, t = 25 °C, scan rate 5 mV/s.

Cyclic voltammetric measurements (Figure 9.3b) have been performed on ITO electrodes with the polymer and enzyme in solution. The electrochemical response of the mixed solution of PMSA1 and FDH (curve 2) without fructose results in the appearance of a weak redox couple with a formal potential of +0.25 ± 0.05 V vs. Ag/AgCl as reported before.[10,43,51-53] After addition of fructose an oxidative bioelectrocatalytic current is observed starting slightly below 0 V vs. Ag/AgCl, indicating an electron flow toward the ITO surface. It reaches a value

of $\Delta I = 150$ nA at E = +0.35 V vs. Ag/AgCl. Furthermore, the addition of 20 mM Ca^{2+} results in a significant (3-fold) enhancement of the bioelectrocatalytic current ($\Delta I = 450$ nA at E = +0.35 vs. Ag/AgCl). These results clearly support the idea of an enhanced catalytic activity in the presence of Ca^{2+}, as indicated by the photometric measurements. However, it is not clear whether this fact originates from the improved interaction of the enzyme and the polymer or from an enhanced enzymatic conversion of fructose. Consequently, we have investigated this in more detail.

Since the electrochemical experiments clearly verify that the polymer can accept electrons from the enzyme, UV−vis was used to follow the reaction. Figure 9.4a summarizes pH dependent initial rates of the polymer reduction in the presence and in the absence of 20 mM Ca^{2+}, demonstrating a significant (2.5-fold) increase in the reaction rate in comparison to the Ca^{2+}-free conditions. However, in order to attribute the enhanced polymer reduction to the calcium-supported interaction between the polymer and the FDH, the activity of the enzyme in dependence on the Ca^{2+} concentrations needs to be studied in the absence of the polymer. We have performed the measurements of the enzyme activity according to the established assay (see the Experimental Section) in the presence of increasing Ca^{2+} concentrations (see Figure 9.4a). Clearly visible is an increase in enzymatic activity of FDH in the presence of Ca^{2+}. However, this increase is much smaller than that observed for the FDH−polymer reaction, being only about 1.45-fold of the activity in Ca^{2+}-free buffer. This means that the increase in reaction efficiency exemplified in Figure 9.4a and from the electrochemical measurements (Figure 9.3b), which show a 2.5-fold enhancement, can be mainly attributed to the improved interaction of the enzyme with the Ca^{2+}-bound polymer.
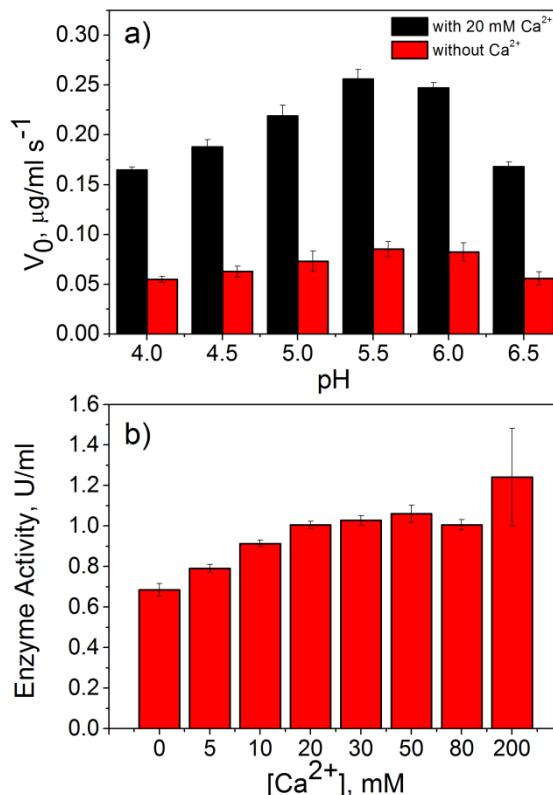
Figure 9.4 (a) pH-dependent initial rate V_0 of polymer reduction in the presence of FDH, fructose, and Ca^{2+} (measured by UV-vis). The reduction was measured at 408 nm. The rate was calculated from the time-dependent absorbance change according to the Lambert-Beer equation using the extinction coefficients of oxidized and reduced polymers. (b) Determination of the enzyme activity according to Ameyama[19] with increasing Ca^{2+} concentrations at pH 5.5. Experimental conditions: [polymer] = 40 µg/mL, [FDH] = 18 µg/mL, [fructose] = 100 mM in 10 mM MES buffer.

9.2.2. APPLICATION OF PMSA1 – FDH REACTION FOR THE CONSTRUCTION OF ENZYME ELECTRODES

In the next step of the study we have investigated whether it is possible to build efficient enzyme electrodes using the PMSA1 polymer and FDH, exploiting hereby the enhanced interaction in the presence of Ca^{2+} ions. For this purpose the approach of enzyme entrapment has been chosen in order to ensure a good stability of the system. First, planar ITO electrodes have been modified with a PMSA1 film and entrapped FDH.

The electrode modification has been performed by adsorption from polymer/enzyme solutions in the absence and in the presence of Ca^{2+} ions. Cyclic voltammograms of the

ITO/(PMSA1:FDH) electrode incubated in a Ca^{2+}-free buffer solution (Figure 9.5a, curve 1) without fructose are similar to those observed in solution, with one weak redox couple at E = +0.25 ± 0.05 V vs. Ag/AgCl attributed to the PMSA1 conversion. After addition of fructose (curve 2) bioelectrocatalytic currents are observed, giving proof of the presence of the electroactive enzyme in the film. The catalytic current starts at E = 0 V vs. Ag/AgCl, reaching the value of ΔI = 15 nA at E = +0.35 V vs. Ag/AgCl. After addition of 20 mM Ca^{2+} (curve 3) a clearly enhanced bioelectrocatalytic current with ΔI = 35 nA at E = +0.35 V vs. Ag/AgCl appears. This is in agreement with measurements in solution (Figure 9.3b); however, the catalytic current intensities are significantly smaller.
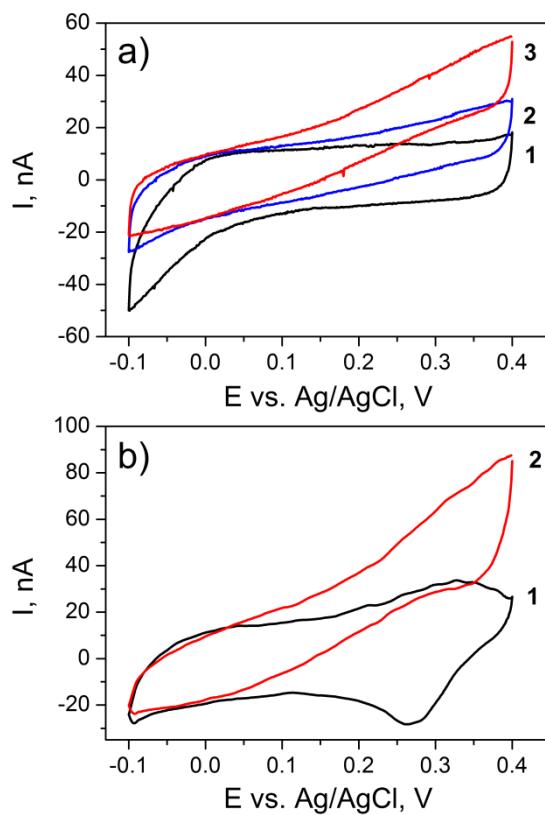
Figure 9.5   CVs of (a) ITO/(PMSA1:FDH) immobilized in Ca^{2+}-free solution (1), after addition of fructose (2), and after consequent addition of 20 mM of Ca^{2+} (3) and (b) ITO/(PMSA1:FDH) immobilized in the presence of Ca^{2+} (1) and in the presence of fructose (2). Experimental conditions: [fructose] = 100 mM in 10 mM MES buffer with or without 20 mM $CaCl_2$ at pH 5.5, t = 25 °C, scan rate 5 mV/s.

Cyclic voltammograms of the ITO/(PMSA1:FDH) electrode prepared in the presence of 20 mM of Ca^{2+} in MES buffer solution (Figure 9.5b, curve 2) demonstrate a higher bioelectrocatalytic response after addition of fructose, since the value of ΔI = 48 nA at E = +0.35 V vs. Ag/AgCl can be reached. This fact can be easily explained by a long incubation

time (2 h), during which time Ca^{2+} ions are expected to bind to the SO^{3-} groups on PMSA1, and thus the enzyme is coimmobilized with the Ca^{2+}-bound polymer for better interaction. Therefore, we are able to see the enhancement of the polymer-enzyme reaction also on ITO electrodes. It has to be emphasized here that in this case efficient bioelectrocatalysis has been observed by measuring the electrodes in buffer solution containing no free Ca^{2+} ions. Moreover, the starting potential of the bioelectrocatalytic fructose conversion is in agreement with the enzyme conversion on various electrode surfaces reported by Kano.[20,21]

Efficient bioelectrocatalysis has also been observed with PQQ-GDH immobilized on different surfaces with sulfonated polyanilines.[10,38,54-56] This was shown to proceed via a direct electron transfer pathway, even though interpretations of the reaction mechanism in the literature are controversial.[57] In order to evaluate whether a surface layer works as a mediator, one has to consider the formal potentials of the redox conversions of different components of the system. The sulfonated polyanilines are redox active, although the peaks in the immobilized state are sometimes rather weak. When a bioelectrocatalytic current would be observed at potentials corresponding to the redox potential of the polymer, indicating that the oxidation process of the polymer triggers the bioelectrocatalysis, mediation can be concluded. However, when the bioelectrocatalysis is observed at much lower potentials, a direct electron transfer mechanism is valid, exploiting the conducting properties of the polymer. For PQQ-GDH at polymer-modified electrodes the catalytic current starts at about -0.1 V vs. Ag/AgCl – far below the redox peaks of the polymer (+0.05 and +0.2 V vs. Ag/AgCl).[38] The starting potential of the electrocatalytic currents on the FDH-polymer electrode is also rather low (≈ 0 V vs. Ag/AgCl), also suggesting a direct electron transfer pathway for this system. The rather similar starting potentials for different enzymes may be attributed in the first row to the conductivity of sulfonated polyanilines. Consequently, also reports on the polymer-supported bioelectrocatalysis of PQQ-dependent alcohol dehydrogenase and PQQ-dependent aldehyde dehydrogenase need to be reconsidered, since redox activity is found at potentials of about +0.2 mV vs. Ag/AgCl, but catalysis already starts at potentials of about +0.05 mV vs. Ag/AgCl.[57] It should also be noted here that the addition of Ca^{2+} cations generally increases the bioelectrocatalytic activity of PQQ-containing enzymes,[58] but FDH is a FAD-containing enzyme, which was independently studied in the present report.[58]

In order to enhance the efficiency of the bioelectrocatalysis of FDH, 3D macroporous ITO electrode structures have been used. These materials have attracted great interest in recent years, since they can accommodate a largely increased amount of catalyst, resulting in enhanced signal generation. We have used a macroporous ITO electrode with a thickness of

the porous ITO layer of about 1.2 µm and a pore size of 300 nm (Figure 9.6b,c), allowing a good access of polymer and enzyme to the inner surface during the immobilization and substrate molecules during operation. The macroporous ITO electrodes are incubated with a PMSA1/FDH mixture containing a medium concentration ratio of 1.5 mg mL^{-1} PMSA1/18 µg/mL FDH (see the Experimental Section). This concentration has been selected on the basis of the variation of the polymer/enzyme ratio, which demonstrates that there is only a limited concentration range in which bioelectrocatalysis occurs. At polymer concentrations higher than 1.5 mg mL^{-1} rather small catalytic currents can be detected. SEM micrographs after immobilization of the polymer/enzyme system have shown that the 3D structure was not affected by the treatment with the polymer-enzyme mixture.

Figure 9.6a shows cyclic voltammograms in Ca^{2+}-free buffer solution of a macroITO/(PMSA1:FDH) electrode prepared in the presence of Ca^{2+} ions, which are recorded in the absence (1) and in the presence (2) of fructose. A redox couple at E = +0.25 ± 0.05 V vs. Ag/AgCl attributed to the PMSA1 conversion is clearly observed. Upon addition of fructose to the buffer solution, the macroITO/(PMSA1:FDH) electrode exhibits an efficient bioelectrocatalytic current. The catalytic current starts from a potential of about E = 0 V vs. Ag/AgCl and reaches at +0.35 V a value of ΔI = 1.6 ± 0.2 µA, with n = 3 (Figure 9.6a, curve 2). In addition, for this electrode architecture we can state that the oxidation process at +0.25 V vs. Ag/AgCl is not necessary to collect the electrons from the enzyme. The bioelectrocatalysis demonstrates the efficient electron exchange between a redox center of the entrapped enzyme and the accessible porous conductive electrode surface, indicating that the polymer environment inside the macroITO pores ensures the catalytic activity of FDH and allows efficient electron withdrawal from the reduced enzyme. However, at this point it cannot be stated which redox center is involved in the reaction with the polymer electrode. Since redox potentials of heme c moieties of FDH have been recently reported to be 10 ± 4, 60 ± 8, and 150 ± 4 mV vs. Ag/AgCl,[21] the heme involvement is highly probable, but interaction with the FAD subunit cannot be excluded.
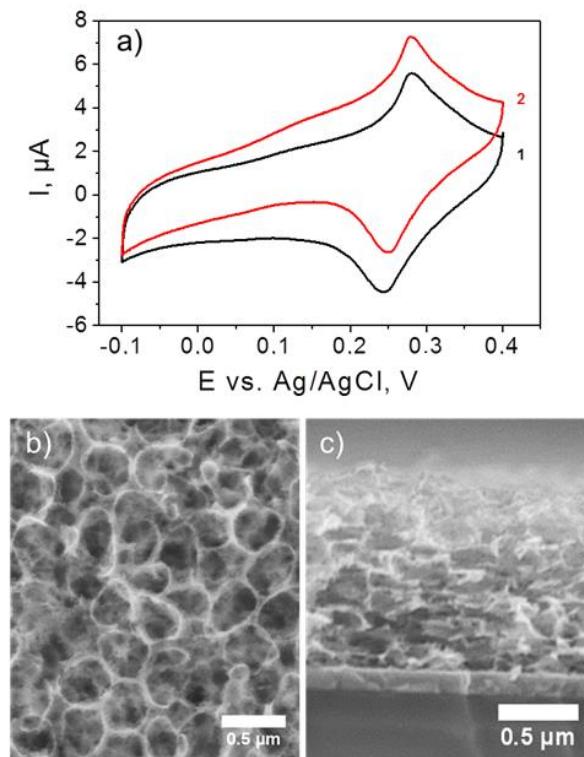
Figure 9.6 (a) CVs of macroITO/(PMSA1:FDH) immobilized in the presence of Ca^{2+} (1) and in the presence of fructose (2). Experimental conditions: [fructose] = 100 mM in 10 mM MES buffer with 20 mM $CaCl_2$ at pH 5.5, t = 25 °C, scan rate 5 mV/s. (b) Top view and (c) cross-section SEM images of the 3D macroporous ITO electrodes.

On comparison of the catalytic currents of the macroporous FDH electrodes with those on planar ITO (Figure 9.5b), a significant improvement of the bioelectrocatalytic properties of the system can be demonstrated, since a 35-fold increase in the catalytic current is achieved. This value is in good agreement with the almost 40 times higher electroactive area of the porous macroITO in comparison to that of the flat ITO, as determined from the analysis of the voltammetric charging current of both electrodes in a pure buffer solution (measured at a scan rate of 50 mV/s). Because long-term stability is an important parameter for evaluation of the performance of a detection system, we have traced the stability of our macroITO/(PMSA1:FDH) electrodes by testing their activity in a fructose solution, after the electrodes have been kept at 4 °C in 10 mM MES + 20 mM $CaCl_2$, pH 5.5, when not in use. The catalytic current response maintains over 50% of the initial value after 4 days, demonstrating that the entrapment of FDH in the sulfonated polyaniline films within the macroporous electrodes leads to a good retention of activity. Thus, our biohybrid system developed by making use of a sulfonated polyaniline and its interaction with FDH and combination with macroporous 3D structures is a promising candidate to be used for biosensorial purposes.

9.3. CONCLUSIONS

We have demonstrated that an interaction between the sulfonated polyaniline PMSA1 and the redox enzyme FDH occurs in solution and on the electrodes, enabling the fabrication of efficient FDH-based bioelectrocatalytic systems. Moreover, an unprecedented enhancement of the catalytic activity of the redox enzyme FDH has been found – induced by the coordination of Ca^{2+} ions to sulfonic acid groups on the aniline ring of PMSA1.

Further developments have been performed by coimmobilization of FDH and the polymer on flat and macroporous ITO structures. This has allowed the construction of efficient enzyme electrodes with a good stability. The magnitude of FDH bioelectrocatalysis can already be tuned during the immobilization process by exploiting the calcium-polymer interaction and 3D electrode structures. The direct bioelectrocatalysis in combination with a tunable efficiency and a high stability make this type of architecture a promising system for the construction of enzyme-based biosensors.

9.4. EXPERIMENTAL SECTION

Chemicals. MES (2-(N-morpholino)ethanesulfonic acid) buffer was purchased from Sigma-Aldrich (Taufkirchen, Germany), dehydrated calcium chloride, sodium dodecyl sulfate (SDS), iron(III) sulfate, and D-fructose were obtained from Fluka Analytics (Taufkirchen, Germany), and 85% phosphoric acid was provided by Merck (Darmstadt, Germany). They were used without further purification. Poly(2-methoxyaniline-5-sulfonic acid)-co-aniline polymer (PMSA1; Scheme 9.1) was synthesized as reported before.[38,59] Millipore water (18 MΩ) was used for all types of measurements.

Enzyme Solution. FDH from Gluconobacter japonicus was provided by Sigma-Aldrich as a lyophilized powder containing additional salts and agents for stabilization. According to the provider, the purchased sample of 4.5 mg of FDH contained 5.1% protein. Therefore, a 0.5 mg of protein/mL stock solution was prepared after dissolving the lyophilizate in 0.5 mL of McIlvaine buffer (pH 4.5). The enzyme solution was used without further purification. Its specific activity – 1186 U/mg of protein – was determined prior to the use as described by the

provider: the principle of the activity test is based on ferricyanide reduction by FDH in the presence of fructose.[19] The reaction is stopped by the addition of a solution containing phosphoric acid, SDS, and iron(III) sulfate. SDS denatures the enzyme and thus disables further reduction of ferricyanide. Iron(III) sulfate reacts with the reaction product (ferrocyanide) to Prussian blue, which is detected spectrophotometrically at 660 nm at room temperature.

Measurements in Solution. UV–Vis Spectroscopy. At first, PMSA1 and FDH were mixed successively in MES buffer (10 mM, pH 4.0–6.5). After mixing and addition of a constant amount of the substrate fructose, UV–vis spectra were collected in the absence and in the presence of 20 mM $CaCl_2$. Since the reduction of polymers is accompanied by the appearance of a strong absorbance band at 408 nm, the absorbance increase in time was followed at this wavelength. Afterward, the Lambert–Beer equation was used for the calculation of the corresponding reaction rates. The following concentrations were used: [PMSA1] = 40 μg/mL, [FDH] = 18 μg/mL, [fructose] = 100 mM (unless noted otherwise).

Cyclic Voltammetry. Previously cleaned rectangular ITO coated glass slides with surface resistivity 15–25 Ω sq^{-1} (obtained from Sigma-Aldrich, Taufkirchen, Germany) were used as working electrodes. PMSA1 polymer, FDH, and fructose were mixed successively in 10 mM

MES buffer in the absence and in the presence of 20 mM $CaCl_2$; afterward, cyclic voltammetry was applied to follow the reaction. The following concentrations were used: [PMSA1] = 40 μg/mL, [FDH] = 18 μg mL^{-1}, [fructose] = 100 mM (unless noted otherwise).

Construction of Polymer/Enzyme Films. For the preparation of polymer/enzyme films, the previously cleaned rectangular ITO coated glass slides and macroporous ITO (prepared by a direct coassembly of poly(methyl methacrylate) beads (PMMA) and indium tin hydroxide nanoparticles (nano-ITOH) with subsequent calcination as described before[10,60]) were initially incubated in buffer solutions of the PMSA1–FDH mixture (1.5 mg mL^{-1} PMSA1, 18 μg/mL FDH; 10 mM MES with or without 20 mM $CaCl_2$, pH 5.5) for 2 h. Afterward, the PMSA1/FDH electrode was dipped into the same buffer without enzyme and polymer to wash away the unbound material.

Instruments. Electrochemical measurements were performed at room temperature in a homemade 1 mL cell using an Ag/AgCl/1 M KCl reference (Biometra, Germany) and a platinum-wire counter electrode. Cyclic voltammetric experiments were carried out with a μAutolab Type II device (Metrohm, The Netherlands). The scan rate was set to 5 mV s^{-1}. The potential range was chosen as between -0.4 and +0.4 V vs. Ag/AgCl. Data analysis was performed using GPES software (General Purpose for Electrochemical System, Eco Chemie, Utrecht, The Netherlands). UV-vis measurements were carried out using an Evolution 300 spectrophotometer (Thermo Fischer Scientific, Germany).

9.5. REFERENCES

(1)   Ates, M. *Mater. Sci. Eng. C-Mater. Biol. Appl.* **2013**, *33*, 1853.

(2)   Fabiano, S.; Tran-Minh, C.; Piro, B.; Dang, L. A.; Pham, M. C.; Vittori, O. *Mater. Sci. Eng. C-Biomimetic Supramol. Syst.* **2002**, *21*, 61.

(3)   Jha, S. K.; Kanungo, M.; Nath, A.; D'Souza, S. F. *Biosens. Bioelectron.* **2009**, *24*, 2637.

(4)   Nemzer, L. R.; Schwartz, A.; Epstein, A. J. *Macromolecules* **2010**, *43*, 4324.

(5)   Cosnier, S. *Biosens. Bioelectron.* **1999**, *14*, 443.

(6)   Farace, G.; Vadgama, R. *Bioanalytical application of impedance analysis: Transducing in polymer-based biosensors and probes for living tissues*, 2004; Vol. 2.

(7)   Katz, E.; Minko, S.; Halamek, J.; MacVittie, K.; Yancey, K. *Anal. Bioanal. Chem.* **2013**, *405*, 3659.

(8)   Walcarius, A.; Kuhn, A. *Trac-Trends Anal. Chem.* **2008**, *27*, 593.

(9)   Ramanavicius, A.; Habermuller, K.; Csoregi, E.; Laurinavicius, V.; Schuhmann, W. *Anal. Chem.* **1999**, *71*, 3581.

(10)   Sarauli, D.; Peters, K.; Xu, C.; Schulz, B.; Fattakhova-Rohlfing, D.; Lisdat, F. *ACS Appl. Mater. Interfaces* **2014**, *6*, 17887.

(11)   Sarauli, D.; Xu, C. G.; Dietzel, B.; Schulz, B.; Lisdat, F. *J. Mat. Chem. B* **2014**, *2*, 3196.

(12)   Schuhmann, W.; Zimmermann, H.; Habermuller, K. V.; Laurinavicius, V. *Faraday Discuss.* **2000**, *116*, 245.

(13)   Wang, X. J.; Sjoberg-Eerola, P.; Immonen, K.; Bobacka, J.; Bergelin, M. *J. Power Sources* **2011**, *196*, 4957.

(14)   Kawai, S.; Goda-Tsutsumi, M.; Yakushi, T.; Kano, K.; Matsushita, K. *Appl. Environ. Microbiol.* **2013**, *79*, 1654.

(15)   Nakashima, K.; Takei, H.; Adachi, O.; Shinagawa, E.; Ameyama, M. *Clin. Chim. Acta* **1985**, *151*, 307.

(16)   Cracknell, J. A.; Vincent, K. A.; Armstrong, F. A. *Chem. Rev.* **2008**, *108*, 2439.

(17)   Gupta, A.; Singh, V. K.; Qazi, G. N.; Kumar, A. *J. Mol. Microbiol. Biotechnol.* **2001**, *3*, 445.

(18)   Tkac, J.; Svitel, J.; Vostiar, I.; Navratil, M.; Gemeiner, P. *Bioelectrochemistry* **2009**, *76*, 53.

(19)   Ameyama, M.; Shinagawa, E.; Matsushita, K.; Adachi, O. *J. Bacteriol.* **1981**, *145*, 814.

(20)   Kamitaka, Y.; Tsujimura, S.; Setoyama, N.; Kajino, T.; Kano, K. *Phys. Chem. Chem. Phys.* **2007**, *9*, 1793.

(21)   Kawai, S.; Yakushi, T.; Matsushita, K.; Kitazumi, Y.; Shirai, O.; Kano, K. *Electrochem. Commun.* **2014**, *38*, 28.

(22)   Hu, Y. W.; Yang, T.; Li, Q. H.; Guan, Q.; Jiao, K. *Analyst* **2013**, *138*, 1067.

(23) Wang, X. X.; Yang, T.; Li, X. A.; Jiao, K. *Biosens. Bioelectron.* **2011**, *26*, 2953.

(24) Fiorito, P. A.; de Torresi, S. I. C. *Talanta* **2004**, *62*, 649.

(25) Karyakin, A. A.; Bobrova, O. A.; Luckachova, L. V.; Karyakina, E. E. *Sens. Actuator B-Chem.* **1996**, *33*, 34.

(26) Doan, T. C. D.; Ramaneti, R.; Baggerman, J.; van der Bent, J. F.; Marcelis, A. T. M.; Tong, H. D.; van Rijn, C. J. M. *Sens. Actuator B-Chem.* **2012**, *168*, 123.

(27) Jaymand, M. *Prog. Polym. Sci.* **2013**, *38*, 1287.

(28) Jiang, Y.; Epstein, A. J. *J. Am. Chem. Soc.* **1990**, *112*, 2800.

(29) Liao, Y. Z.; Strong, V.; Chian, W.; Wang, X.; Li, X. G.; Kaner, R. B. *Macromolecules* **2012**, *45*, 1570.

(30) Malinauskas, A. *J. Power Sources* **2004**, *126*, 214.

(31) Shieh, Y. T.; Jung, J. J.; Lin, R. H.; Yang, C. H.; Wang, T. L. *Electrochimica Acta* **2012**, *70*, 331.

(32) Sarauli, D.; Tanne, J.; Xu, C. G.; Schulz, B.; Trnkova, L.; Lisdat, F. *Phys. Chem. Chem. Phys.* **2010**, *12*, 14271.

(33) Beissenhirtz, M. K.; Scheller, F. W.; Stocklein, W. F. M.; Kurth, D. G.; Mohwald, H.; Lisdat, F. *Angew. Chem.-Int. Edit.* **2004**, *43*, 4357.

(34) Dronov, R.; Kurth, D. G.; Mohwald, H.; Scheller, F. W.; Lisdat, F. *Electrochimica Acta* **2007**, *53*, 1107.

(35) Dronov, R.; Kurth, D. G.; Moehwald, H.; Scheller, F. W.; Lisdat, F. *Angew. Chem.-Int. Edit.* **2008**, *47*, 3000.

(36) Wegerich, F.; Turano, P.; Allegrozzi, M.; Mohwald, H.; Lisdat, F. *Langmuir* **2011**, *27*, 4202.

(37) Spricigo, R.; Dronov, R.; Lisdat, F.; Leimkuhler, S.; Scheller, F.; Wollenberger, U. *Anal. Bioanal. Chem.* **2009**, *393*, 225.

(38) Sarauli, D.; Xu, C. G.; Dietzel, B.; Schulz, B.; Lisdat, F. *Acta Biomater.* **2013**, *9*, 8290.

(39) Hui, H. X.; Huang, D. S.; McArthur, D.; Nissen, N.; Boros, L. G.; Heaney, A. P. *Pancreas* **2009**, *38*, 706.

(40) Yamada, Y.; Aida, K.; Uemura, T. *Journal of biochemistry* **1967**, *61*, 636.

(41) Avouris, P.; Aizawa, M. In *Atomic and Nanometer-Scale Modification of Materials: Fundamentals and Applications*; Springer Netherlands: 1993; Vol. 239, p 315-316.

(42) Borrmann, T.; Dominis, A.; McFarlane, A. J.; Johnston, J. H.; Richardson, M. J.; Kane-Maguire, L. A. P.; Wallace, G. G. *J. Nanosci. Nanotechnol.* **2007**, *7*, 4303.

(43) Pornputtkul, Y.; Strounina, E. V.; Kane-Maguire, L. A. P.; Wallace, G. G. *Macromolecules* **2010**, *43*, 9982.

(44) Cho, S. I.; Lee, S. B. *Accounts Chem. Res.* **2008**, *41*, 699.

(45) Kang, E. T.; Neoh, K. G.; Tan, K. L. *Prog. Polym. Sci.* **1998**, *23*, 277.

(46) Lee, K.; Cho, S.; Park, S. H.; Heeger, A. J.; Lee, C. W.; Lee, S. H. *Nature* **2006**, *441*, 65.

(47) MacDiarmid, A. G. *Angew. Chem.-Int. Edit.* **2001**, *40*, 2581.

(48) Strounina, E. V.; Shepherd, R.; Kane-Maguire, L. A. P.; Wallace, G. G. *Synth. Met.*

2003, *135*, 289.

(49)   Amaya, T.; Saio, D.; Koga, S.; Hirao, T. *Macromolecules* **2010**, *43*, 1175.

(50)   Moulton, S. E.; Pornputtkul, Y.; Kane-Maguire, L. A. P.; Wallace, G. G. *Aust. J. Chem.* **2007**, *60*, 159.

(51)   Sanchis, C.; Ghanem, M. A.; Salavagione, H. J.; Morallon, E.; Bartlett, P. N. *Bioelectrochemistry* **2011**, *80*, 105.

(52)   Dennany, L.; O'Reilly, E. J.; Innis, P. C.; Wallace, G. G.; Forster, R. J. *Electrochimica Acta* **2008**, *53*, 4599.

(53)   Masdarolomoor, F.; Innis, P. C.; Wallace, G. G. *Electrochimica Acta* **2008**, *53*, 4146.

(54)   Schubart, I. W.; Gobel, G.; Lisdat, F. *Electrochimica Acta* **2012**, *82*, 224.

(55)   Scherbahn, V.; Putze, M. T.; Dietzel, B.; Heinlein, T.; Schneider, J. J.; Lisdat, F. *Biosens. Bioelectron.* **2014**, *61*, 631.

(56)   Gobel, G.; Schubart, I. W.; Scherbahn, V.; Lisdat, F. *Electrochem. Commun.* **2011**, *13*, 1240.

(57)   Xu, S.; Minteer, S. D. *ACS Catal.* **2014**, *4*, 2241.

(58)   Katz, E.; Lötzbeyer, T.; Schlereth, D.D.; Schuhmann, W.; Schmidt H.-L. J. Electroanal. Chem. **1994**, *373*, 189.

(59)   Sarauli, D.; Xu, C. G.; Dietzel, B.; Stiba, K.; Leimkuhler, S.; Schulz, B.; Lisdat, F. *Soft Matter* **2012**, *8*, 3848.

(60)   Liu, Y. J.; Peters, K.; Mandlmeier, B.; Müller, A.; Fominykh, K.; Rathousky, J.; Scheu, C.; Fattakhova-Rohlfing, D. *Electrochimica Acta* **2014**, *140*, 108.

INVESTIGATION OF THE PH-DEPENDENT IMPACT OF SULFONATED POLYANILINE
ON BIOELECTROCATALYTIC ACTIVITY OF XANTHINE DEHYDROGENASE

265

10. INVESTIGATION OF THE PH-DEPENDENT IMPACT OF SULFONATED POLYANILINE ON BIOELECTROCATALYTIC ACTIVITY OF XANTHINE DEHYDROGENASE

This chapter is based on the following publication:

David Sarauli, Anja Borowski, Kristina Peters, Burkhard Schulz, Dina Fattakhova-Rohlfing, Silke Leimkühler, Fred Lisdat
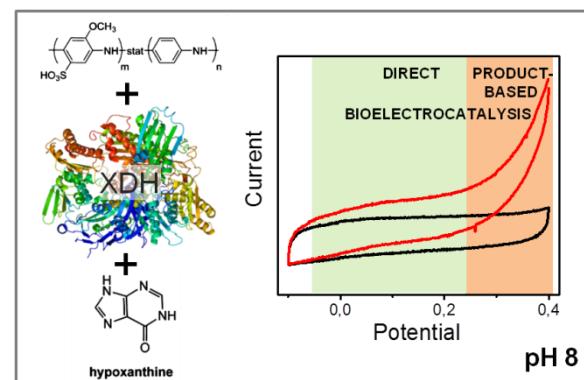
The joint project is a collaboration of different groups involving development of complex electrode architecture for efficient direct bioelectrocatalysis. Dr. D. Sarauli, A. Borowski and B. Schulz designed the bioelectrodes, which consist of xanthine dehydrogenase (XDH) entrapped in a conductive sulfonated polyaniline PMSA1. Dr. D. Sarauli studied pH-dependent bioelectrocatalytic activity of the redox enzyme. K.Peters fabricated macroporous ITO electrodes to be used as a 3D conducting host scaffold, performed conductivity measurements to characterize their conductivity and measured SEM.

We report on the pH-dependent bioelectrocatalytic activity of the redox enzyme xanthine dehydrogenase (XDH) in the presence of sulfonated polyaniline PMSA1 (poly(2-methoxyaniline-5-sulfonic acid)-*co*-aniline). Ultraviolet-visible (UV-vis) spectroscopic measurements with both components in solution reveal electron transfer from the hypoxanthine (HX)-reduced enzyme to the polymer. The enzyme shows bioelectrocatalytic activity on indium tin oxide (ITO) electrodes, when the polymer is present. Depending on solution pH, different processes can be identified. It can be demonstrated that not only product-based communication with the electrode but also efficient polymer-supported bioelectrocatalysis occur. Interestingly, substrate dependent catalytic currents can be obtained in acidic and neutral solutions, although the highest activity of XDH with natural reaction partners is in the alkaline region. Furthermore, operation of the enzyme electrode without addition of the natural cofactor of XDH is feasible. Finally, macroporous ITO electrodes have been used as an immobilization platform for the fabrication of HX-sensitive electrodes. The study shows that the efficient polymer/enzyme interaction can be advantageously combined with the open structure of an electrode material of controlled pore size, resulting in good processability, stability, and defined signal transfer in the presence of a substrate.

10.1. INTRODUCTION

The construction of bioelectrochemical platforms capable of transducing biological recognition in an electrochemical signal is essential for the development of enzyme-based analytical devices, spanning across a wide diversity of applications including healthcare, food control, or microbiology.[1] The interest to biosensors is explained by unprecedented selectivity and sensitivity of enzymes as recognition units. However, the successful operation of enzymes in such devices requires their adaptation to the constraints of artificial systems, among which the wiring of enzymes to the electrodes without the loss of biological activity is the most challenging one. One of the attractive biorecognition units for biosensor construction is the redox enzyme xanthine dehydrogenase (XDH) commonly found in bacteria and animals. XDH catalyzes the oxidation of hypoxanthine (HX) and xanthine to uric acid, which are intermediates of the purine nucleotide metabolism.[2] Since the overproduction of serum uric acid is predictive for a variety of metabolic diseases,[3] the approach of developing stable, sensitive, and selective recognition platforms for purines is of high importance. XDH is a complex molybdenum-iron-sulfur flavoprotein from the xanthine oxidoreductase class of molybdoenzymes. XDH consists of four redox active cofactors: a mononuclear, five-

INVESTIGATION OF THE PH-DEPENDENT IMPACT OF SULFONATED POLYANILINE
ON BIOELECTROCATALYTIC ACTIVITY OF XANTHINE DEHYDROGENASE

267

coordinated Mo center, two [2Fe-2S] clusters, and a flavin adenine dinucleotide (FAD).[4] The Mo site is the active, catalytic site in the protein and contains a single bidentate molybdopterin ligand, an equatorial terminal sulfido, an axial oxido, and an equatorial hydroxo ligand. This enzyme exhibits low oxidase activity and preferentially uses NAD+ as an electron acceptor.[5] This fact is beneficial for biosensor development, because of the electrochemical inertness of NAD^+. However, electrochemical NADH detection is also not trivial. Problems that are connected to the quantitative measurement are the large overvoltage required for NADH oxidation at standard electrodes, together with surface passivation due to the accumulation of reaction products.[6] Therefore, strategies have been developed to overcome these issues by novel electrode materials or modifications capable of reducing the overpotential for NADH oxidation and minimizing surface fouling effects, or the design of artificial systems able to operate without any cofactor.

Bacterial *Rhodobacter capsulatus* XDH has already been studied at pyrolythic graphite electrodes. Although the authors have reported a direct electrochemistry with the detection of all three redox centers,[7] it has been shown later that the observed signal was originated from the decomposed enzyme.[8] Further studies by the same group have demonstrated that the electron transfer between XDH and the electrode is, in fact, mediated by the products of the enzyme turnover (Scheme 10.1), namely uric acid imine, which can act as a nonphysiological electron acceptor instead of NAD^+.[7–9] Moreover, the natural substrates of XDH – hypoxanthine and xanthine – are also electrochemically active and undergo coupled two-electron–two-proton oxidations at positive potentials.[9] To gain more control over the signal transduction, phenazine methosulfate was intentionally introduced as a redox mediator.[10]
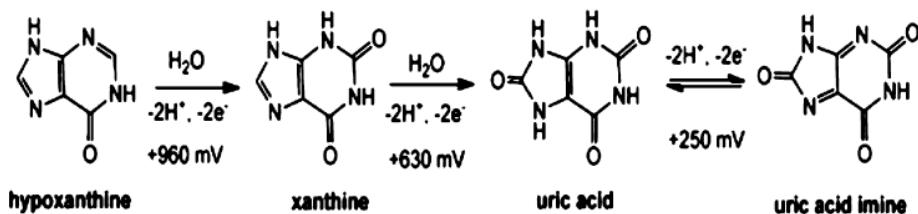
Scheme 10.1 Redox Reactions of Purines (Potentials Reported vs. Ag/AgCl, pH 8); Data taken from refs 2c and 10.

Although mediators are commonly used to wire enzymes with electrodes, the general drawback of this approach are interferences caused by chemical and electrochemical side reactions. One strategy to overcome these limitations is the immobilization/entrapment of enzymes in conducting matrices providing charge transfer pathways between enzymes and

electrodes. However, until now, no reports on the mediatorless bioelectrocatalysis of immobilized XDH have been published. Polyanilines have already been shown to provide suitable conductive matrices for the construction of bioelectrochemical platforms, since they are environmentally stable in doped and neutral states and can be easily synthesized.[11] Being able to form defined and ordered films on various surfaces, polyanilines can be used as an immobilization platform in enzyme sensors.[11b,d,12] Because of high conductivity, they have also been shown to transfer electrons in redox and enzymatic reactions.[11b,13] Polyanilines with introduced sulfonic acid groups possess improved solubility and redox activity, together with a stable electrical conductivity at pH≥4, where most biomolecules are active.[11f,13b,c,14] This is based on self-doping of the polymer by proton exchange between functional groups, instead of proton uptake from solution (which is necessary for undoped polyaniline). Here, we propose a bioelectrocatalytic system constructed from sulfonated polyaniline PMSA1 (poly(2-methoxyaniline-5-sulfonic acid) and XDH based on an efficient redox reaction between the polymer-entrapped enzyme and the substrate HX. Via entrapment of the enzyme into polymer films on both flat indium tin oxide (ITO) electrodes and three-dimensional (3D) macroporous indium tin oxide (macroITO) electrodes (Scheme 10.2), a biohybrid system can be built. This system does not require additional mediators that can cause electrochemical interferences. Moreover, the pH range of investigations can be extended to lower pH values even when, here, XDH shows limited activity (with NAD^+ as an electron acceptor). Thus, it is demonstrated that the proper design and the coassembly of building elements represent a general methodology for the creation of functional bioelectrodes.
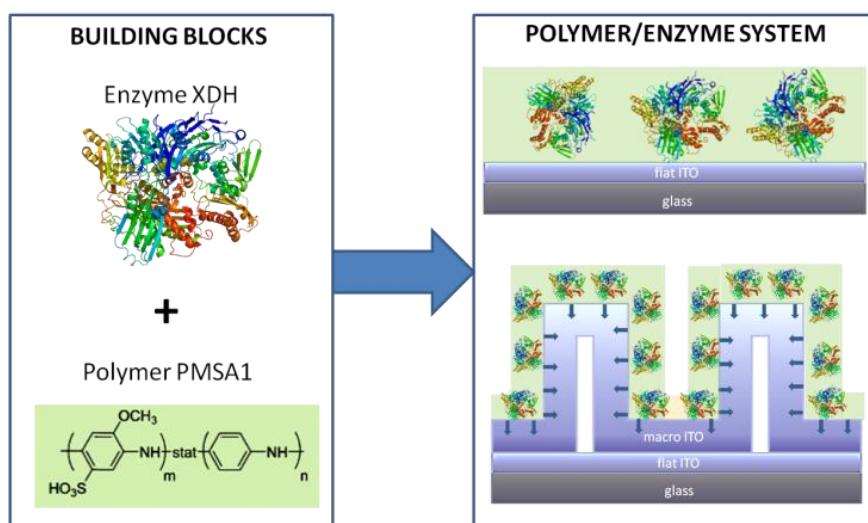
Scheme 10.2 Schematic Representation of the Constructed Polymer–Enzyme Electrode Architectures. Xanthine dehydrogenase is fixed and electrochemically connected to flat ITO or 3D macroporous ITO (macroITO) electrodes by means of the sulfonated polyaniline polymer.

INVESTIGATION OF THE PH-DEPENDENT IMPACT OF SULFONATED POLYANILINE
ON BIOELECTROCATALYTIC ACTIVITY OF XANTHINE DEHYDROGENASE

269

10.2. RESULTS AND DISCUSSION

PMSA1/XDH Interaction Studies. A precondition for the construction of a stable and functional XDH-based biohybrid electrode capable of detecting purines is an efficient electron exchange between the polymer and XDH. Therefore, this redox reaction has been first monitored in solution by means of UV-vis spectroscopy and cyclic voltammetry (CV) measurements performed at pH values from 4.5 to 9.0. The unusually broad pH range has been selected based on the different optimum conditions for the enzyme and the polymer. At pH 8, *Rhodobacter capsulatus* XDH is found to be the most active,[2c,15] while the PMSA1 polymer is found to be the most active at pH below 7, since, in this range, it can adopt the most conductive emeraldine salt (ES) state.[13b,16]
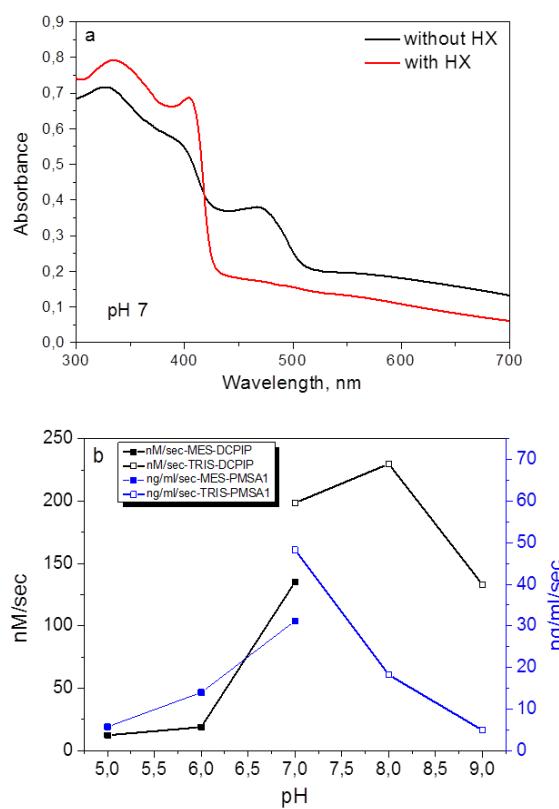
Figure 10.1   (a) Ultraviolet-visible (UV-vis) spectra of a solution with PMSA1 and XDH in the absence (black line) and in the presence (red line) of the substrate hypoxanthine at pH 7.0 (50 mM Tris + 1 mM EDTA); and (b) pH-dependent initial rates of the DCPIP (black) and polymer reduction (blue) in the presence of XDH and HX at different pH values. For the calculation of the rates from time-dependent changes in absorbance, the Lambert–Beer equation, using the extinction coefficients of DCPIP (21 700 M^{-1} cm^{-1} at 597 nm), as well as reduced PMSA1 (36.86 mg/mL M^{-1} cm^{-1} at 408 nm), has been used. Experimental conditions: [PMSA1] = 40 μg/mL, [XDH] = 1 μM, [DCPIP] = 0.1 mM, [HX] = 400 μM in 50 mM MES or 50 mM Tris buffer (+ 1 mM EDTA) at a temperature of t = 25 °C.

Figure 10.1a illustrates the spectral changes occurring after the addition of HX to the mixture of PMSA1 and XDH in solution at pH 7.0 in the absence of the natural cosubstrate NAD$^+$. The bands at 325 and 469 nm (black curve) are characteristic of π–π* transitions and a low-wavelength polaron band of PMSA1 in the ES state (half-oxidized redox state), respectively.[13b,17] The addition of HX, with its subsequent enzymatic conversion, leads to the appearance of strong bands at 330 and 408 nm (red curve), because of changes in the electronic structure of PMSA1, as a result of the enzyme reaction. No interaction between PMSA1 and HX has been measured when XDH is absent (see Figure S10.1 in the Supporting Information). These facts are strong indications of the ability of PMSA1 to act as a reaction partner for XDH. Interestingly, the reduction of PMSA1 in the presence of XDH and HX occurs in the entire pH range between 5.0 and 9.0, reaching a maximum in the polymer reduction rate at pH 7.0 (blue squares in Figure 10.1b). In order to separate the influence of the enzyme activity from that of the enzyme/polymer interaction, UV-vis measurements in the presence of 2,6-dichlorophenolindophenol (DCPIP) as a known electron acceptor of the enzyme have been performed. The results are summarized in Figure 10.1b (black curves), together with the initial reduction rates of the polymer (blue curves). The direct comparison of the reaction rates with and without polymer confirms the high activity of XDH at alkaline pH, but shows that the reaction with the polymer is more favorable at neutral pH. Even at pH 6, catalytic activity is observed in the presence of PMSA1, although, at this pH, the enzyme alone is poorly catalytically active. The results demonstrate that the reaction partner used for the enzyme can influence its activity pattern. It also means that the polymer is able to close the enzymatic cycle without the necessity of adding the natural cosubstrate. The reason for the decreased reaction rates of the polymer at alkaline pH values is most probably the partial deprotonation, which changes the polymer state from the highly conductive ES state to the less conductive emeraldine base (EB) state.[17b] The pH-induced polymer changes can also be monitored by UV-vis spectroscopy, as summarized in Figure S10.2 in the Supporting Information.

As a next step, pH-dependent CV measurements have been performed in solutions of polymer and enzyme, using ITO as working electrodes under the same experimental conditions. After the addition of HX oxidative bioelectrocatalytic currents have been observed (Figure 10.2). The observation of electrocatalytic currents is in good agreement with the spectrophotometric results, indicating that the polymer can accept electrons from the HX-reduced enzyme and transfer them to the electrode. However, note that the bioelectrocatalytic signal of the polymer/enzyme system consists of two separate processes with different onset potentials,

INVESTIGATION OF THE PH-DEPENDENT IMPACT OF SULFONATED POLYANILINE
ON BIOELECTROCATALYTIC ACTIVITY OF XANTHINE DEHYDROGENASE

271

depending on pH (for better visualization, they are indicated with different colors in Figure **10.2**).
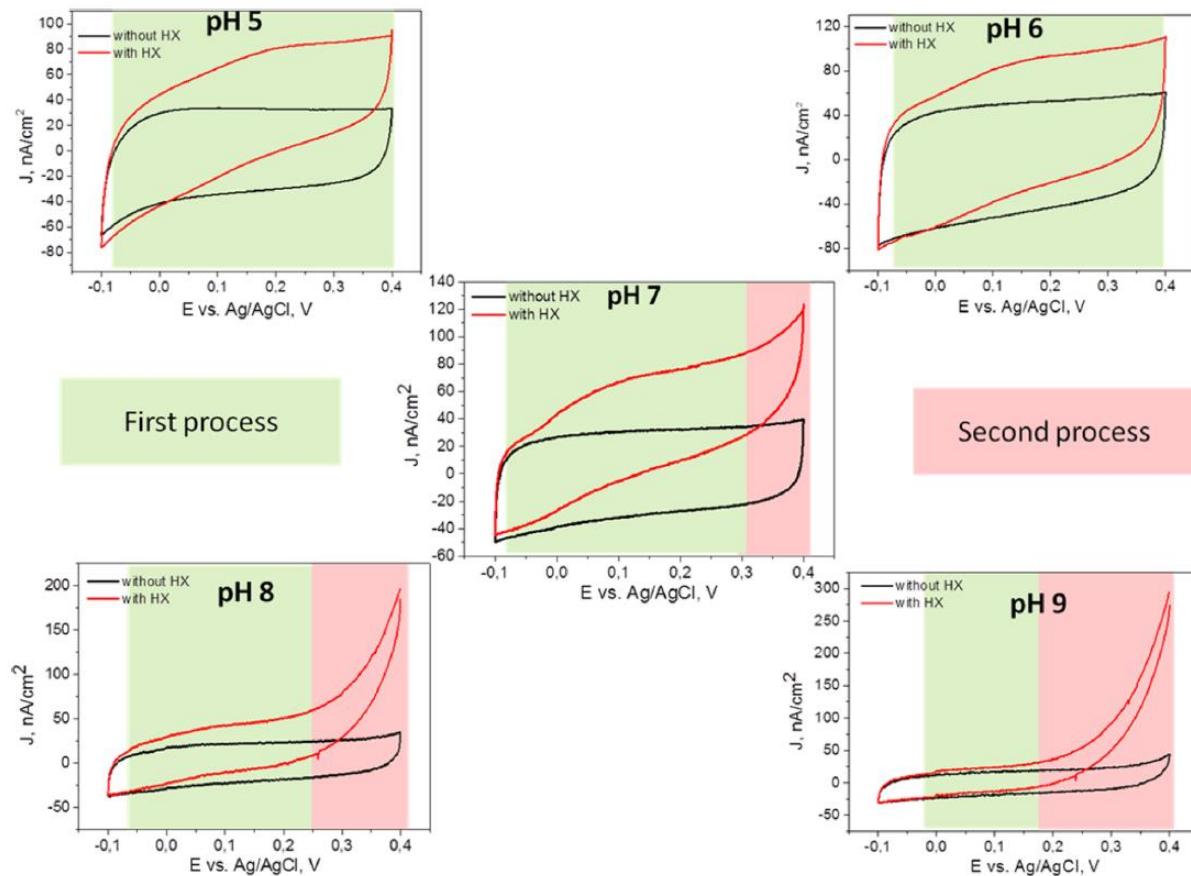
Figure 10.2 pH-dependent cyclic voltammograms of ITO electrodes in solutions of PMSA1 + XDH without HX (black lines) and after the addition of HX (red lines). The potential range in which the direct uric acid reaction governs the response (second process) is marked in red, whereas the polymer supported bioelectrocatalysis (first process) is marked with green color. Experimental conditions: [PMSA1] = 40 μg/mL, [XDH] = 1 μM, [HX] = 400 μM in 50 mM MES (pH 5) or 50 mM Tris buffer (pH 8) + 1 mM EDTA at t = 25 °C, scan rate = 5 mV/s.

At pH <7.0, the onset potential is observed between –0.1 V and –0.05 V vs. Ag/AgCl. This value is significantly lower than the formal redox potential of the polymer (E = +0.18 V vs. Ag/AgCl at pH 6);[13b] therefore, it can be concluded that the polymer does not need to be fully oxidized to ensure electron transfer. Moreover, no catalytic currents appear in the absence of PMSA1 at pH <7.0 (see Figure S10.3 in the Supporting Information), demonstrating that the presence of the polymer is essential for the electron flow to the electrode. Upon increasing pH (Figure 10.2), a second oxidative process at potentials more positive than E = +0.25 V vs. Ag/AgCl appears, in addition to the substrate-dependent catalytic current described above. The current of the second process increases drastically upon increasing the solution pH,

whereas the onset potential becomes less positive. The observed currents are unlikely to originate from HX oxidation, which occurs at much higher potentials (see Scheme 10.1).[2c,8]

To rule out possible side reactions as a reason for the observed catalytic currents, a series of reference measurements has been performed. Since XDH is able to accept oxygen as a reaction partner (although less efficient than the natural partner[2b,18]), the response of our electrode structures toward hydrogen peroxide has been tested. However, the presence of H_2O_2 (1 mM) in the enzyme/polymer solution has not induced oxidative currents (see Figure **S10.4** in the Supporting Information). Consequently, hydrogen peroxide, which might be generated during the substrate conversion, is not the reason for the two oxidation processes found at the ITO electrode.

Another possible side reaction is the oxidation of uric acid, which is produced upon enzymatic catalysis (see Scheme 10.1). The negative shift of the onset potential of the second oxidation process with increasing pH (~60 mV/pH) is an indication for a coupled two-proton–two-electron transfer process, being in accordance with the conversion of uric acid.

Therefore, uric acid has been tested alone at different pH values. The results are summarized in Figure S10.5 in the Supporting Information. They are indicating that the second oxidation process can be ascribed to the oxidation of uric acid. Therefore, the first process is assigned to the polymer-driven enzymatic conversion of XDH observed throughout the entire investigated pH range, although with different intensity, clearly decreasing with increasing pH (Figure **10.3**a). The moderate magnitude can be explained by the rather low activity for substrate conversion of the XDH in acidic solutions resulting in poor XDH–polymer interaction. A low conductivity of PMSA1 at higher pH values also plays a role. Interestingly, the maximum current has been observed not at the optimum pH value of XDH (pH 8), but rather at pH 7. A similar pH profile was detected for XDH and uric acid imine as the electron acceptor, although the reason for this dependence is not fully understood.[8]

The onset potential for the first bioelectrocatalytic process seems to be mainly correlated to the conductivity of the sulfonated polyaniline, which is highest at the mixed redox state. In order to clarify the effect of PMSA1 on the bioelectrocatalytic behavior of the system, CV measurements have been performed for a fixed enzyme/substrate concentration at pH 7, but with varying concentrations of the polymer.

The resulting curves are summarized in Figure 10.3b. It is observed that increasing the PMSA1 concentrations lead to a clear enhancement of the first bioelectrocatalytic process with an onset potential of E = –0.05 V vs. Ag/AgCl; the rather linear increase of the catalytic

current density is shown in the inset in Figure 10.3b. This demonstrates unambiguously that the enzyme/electrode interaction can be significantly improved with a higher polymer amount present in solution. Moreover, the pH region can be extended to lower values, because of the interaction between the PMSA1 and XDH.
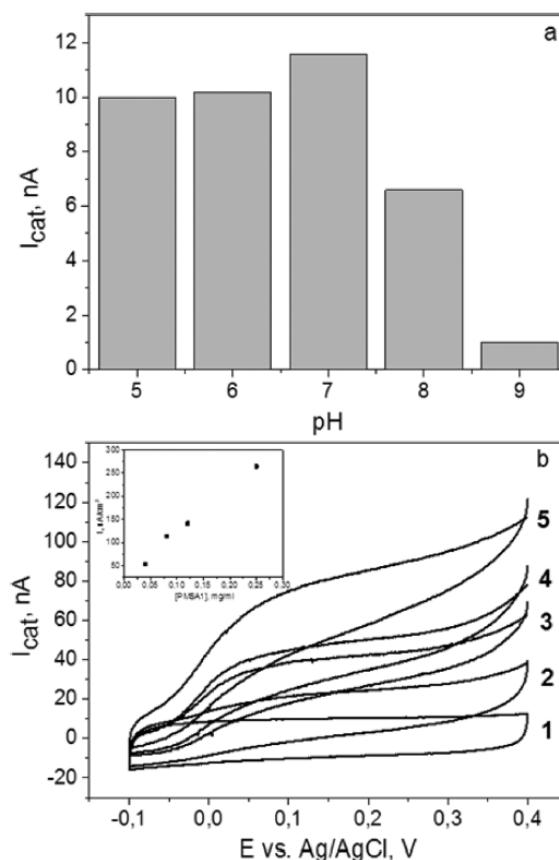
Figure 10.3 (a) Currents of the polymer-supported bioelectrocatalysis of XDH (first process, determined at +0.1 V vs. Ag/AgCl), in dependence on the solution pH. (b) Cyclic voltammetric measurements on an ITO electrode immersed in solutions of (1) XDH + HX and increasing PMSA1 concentrations ((2) 0.04, (3) 0.08, (4) 0.12, and (5) 0.25 mg/mL); inset shows the dependence of the catalytic oxidation current density at 0.35 V vs. Ag/AgCl on the PMSA1 concentration. Experimental conditions: [XDH] = 1 μM, [HX] = 400 μM in 50 mM Tris buffer + 1 mM EDTA at pH 7, t = 25 °C, scan rate = 5 mV/s.

Design of a PMSA1/XDH Biohybrid Platform. Based on the information obtained on enzyme–polymer interaction, we have constructed electrode architectures via entrapment of XDH in PMSA1 polymer films. This strategy is chosen to achieve an enhanced stability of the system. First, planar ITO electrodes are used that have been incubated in a PMSA1/XDH mixture. The electrodes are then characterized at pH 5 in order to prevent interference from the second process. It turns out that the enzyme/polymer ratio is rather important for effective

enzymatic catalysis at the electrode. Thus, the following experiments have been performed with 0.2 mg/mL PMSA1 and 5 μM XDH as solution used for electrode modification.
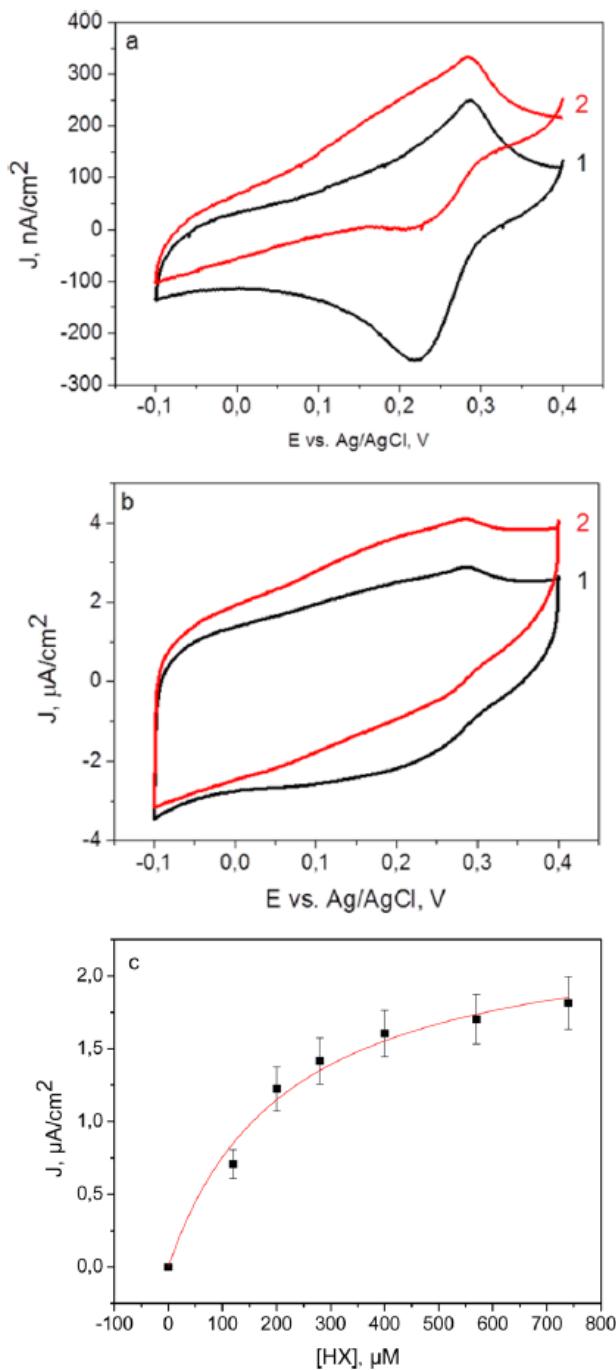
Figure 10.4 Cyclic voltammetric measurement of (a) ITO/(PMSA1:XDH) and (b) macroITO/(PMSA1:XDH) electrodes prepared in 50 mM Tris buffer pH 8 + 1 mM EDTA and measured without HX (curve 1) and with HX (curve 2) in 50 mM MES buffer pH 5 + 1 mM EDTA at pH 5.0. (c) Change in the catalytic current density on the macroITO/(PMSA1:XDH) electrode as a function of the HX concentration. Bioelectrocatalytic signals were registered from the respective cyclic voltammograms at E = +0.35 V. Experimental conditions: t = 25 °C, scan rate = 5 mV/s.

INVESTIGATION OF THE PH-DEPENDENT IMPACT OF SULFONATED POLYANILINE
ON BIOELECTROCATALYTIC ACTIVITY OF XANTHINE DEHYDROGENASE

275

Figure 10.4a exemplifies the voltammetric behavior of ITO/ (PMSA1:XDH) electrodes after an addition of the substrate. A clear bioelectrocatalytic current starting at E ≈ –0.05 V vs. Ag/AgCl appears. However, the intensity of the catalytic current significantly decreases with the number of scans within 10−20 min, which might be caused either by a loss of electrochemical communication of the enzyme with the electrode or by desorption of the XDH/polymer layer. Therefore, in order to increase the efficiency of XDH bioelectrocatalysis and improve the stability of the electrodes, 3D macroporous ITO (macro-ITO) electrodes have been used for further studies.

Three-dimensional (3D) electrode architectures attract growing attention as the promising immobilization platforms for electrocatalysis, because of their large surface area and an accessible conducting interface enabling the incorporation of large amounts of active species and their direct communication with the electrode.[16,19] For the present study, we have used porous ITO scaffolds with sufficiently large pore size able to accommodate the bulky polymer/enzyme matrix without limiting the diffusion of the substrate. The macroITO layers with a thickness of ~1.2 μm feature a uniform pore structure composed of ~300 nm interconnected spherical pores. (see Figure 10.5).

Figure 10.4b summarizes cyclic voltammograms of macroITO/(PMSA1:XDH) electrodes measured at pH 5 with and without HX. The onset potential of a clearly visible bioelectrocatalytic response upon the addition of HX is rather similar to that observed on flat ITO electrodes (see Figure 10.4a). However, the magnitude of the current response to the same HX concentration is clearly enhanced: a 5-fold increase in current density from 250 nA/cm^2 (ITO) to 1.28 μA/cm^2 (macroITO) has been measured at a potential of E = +0.35 vs. Ag/AgCl.
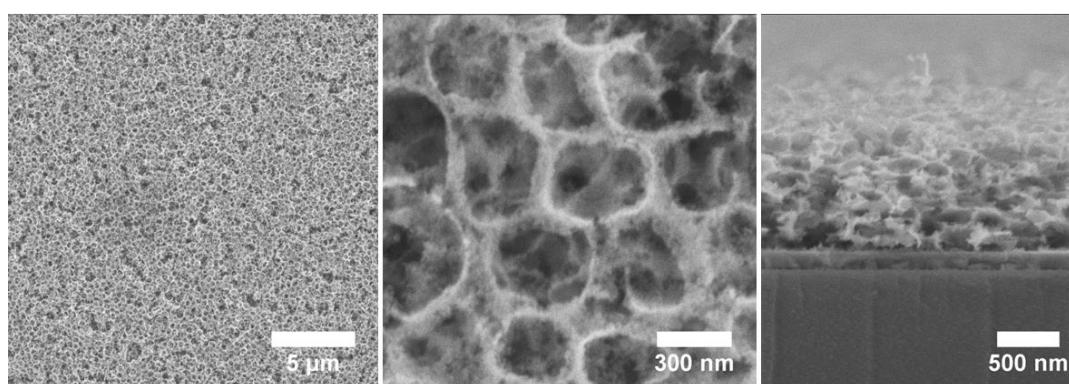
Figure 10.5 Top view (left and middle) and cross-section (right) SEM images of the macroITO electrodes.

The HX concentration dependence of the catalytic current is shown in Figure 10.4c. The current evaluated at +0.35 V vs. Ag/AgCl increases gradually with the substrate concentration within the range of 25−250 μM and has a tendency to saturate at concentrations of >400 μM, as predicted by the Michaelis−Menten kinetics ($K_{M,app}$ = 218 ± 43 μM). The apparent KM value is higher than the reported value ($K_{M, app}$ = 64.5 μM) for a XDH solution assay at pH 7.8 in 50 mM Tris buffer.[4d] This increase is most likely due to diminished mass transport of HX from the bulk solution to the reaction layer and restricted access to the enzyme active site within the polymer film on the working electrode surface. Therefore, the value is of the same order of magnitude as that reported by Kalimuthu et al. for another XDH electrode, based on edge-plane pyrolytic graphite reported (630 μM).[10]

In addition to the greatly increased bioelectrocatalytic current, the use of macroporous ITO electrodes significantly improves the long-term stability of the biohybrid platform. We have studied the stability of the constructed macroITO/(PMSA1:XDH) electrodes by testing their activity in HX solution after the electrodes have been stored at 4 °C in 50 mM Tris buffer pH 8. The catalytic current retains more than 30% of the initial value after 3 days, demonstrating that the entrapment of XDH in the polymer film within the macroporous electrode structure results in a fairly good retention of activity. It should be mentioned here that XDH is not a very stable enzyme at room temperature. In addition, the bioelectrocatalytic currents measured on flat ITO/(PMSA1:XDH) decrease within 15 min during operation. Thus, the reported pH-tunable macroporous polymer/enzyme electrode structures can be considered as a promising platform for catalytic sensing applications. A significant advantage of this system is that it functions at a very low potential and avoids undesirable interference from uric acid as the oxidation product, which has been a serious issue in previously reported xanthine oxidase-based electrochemical sensors.[20]

INVESTIGATION OF THE PH-DEPENDENT IMPACT OF SULFONATED POLYANILINE
ON BIOELECTROCATALYTIC ACTIVITY OF XANTHINE DEHYDROGENASE

277

10.3. CONCLUSIONS

We have shown that the entrapment of the redox enzyme XDH in a sulfonated polyaniline PMSA1 matrix on three-dimensional (3D) macroporous ITO enables the construction of an efficient and robust bioelectrocatalytic platform, which operates without addition of the natural cosubstrate or soluble mediators. pH variations demonstrate that, besides the polymer-supported bioelectrocatalysis of XDH, the direct conversion of the reaction product of the enzymatic conversion – uric acic – also can be observed at pH >7 and higher potentials. The direct oxidation of uric acid is enhanced at higher pH values and higher potentials, whereas the polymer-supported catalysis of XDH proceeds efficiently at pH <8 and already starts at low potentials. The macroporosity of ITO electrodes with sufficiently large pore size allows the accommodation of the polymer/XDH system without limiting the diffusion of the substrate. Moreover, it leads to an efficient bioelectrocatalytic system with enhanced stability. The direct bioelectrocatalysis, in combination with a rather wide operational pH range, are advantageous features of our electrode architecture, with respect to its applications as an enzymatic biosensor. The design of such a platform is of general importance and can be applied to other advanced fields, such as biofuel cells or biophotovoltaic devices.

10.4. EXPERIMENTAL SECTION

Chemicals. MES [2-(N-morpholino)ethanesulfonic acid] and Tris [Tris(hydroxymethyl)-aminomethane] buffers were purchased from Sigma–Aldrich (Taufkirchen, Germany). 2,6-Dichlorophenolindophenol and HX were obtained from Fluka Analytics (Taufkirchen, Germany). They were used without further purification. All measurements were performed using 18 MΩ Millipore water (Eschborn, Germany).

PMSA1 Synthesis. Poly(2-methoxyaniline-5-sulfonic acid)-co-aniline polymer (PMSA1, Scheme 10.2) was synthesized under light acidic conditions, as reported previously.[13b,c] One gram (1g) of MAS was dissolved in 30 mL of 0.5 M NH_4OH and the pH was adjusted to 4.65. The mixture was cooled to <5 °C in an ice bath. Then, 0.0011 mol of aniline was dissolved in a 2 mL mixture of acetone and H_2O (1:1). Ten (10) drops of this solution were then added to MAS before addition of the oxidant. Ammonium peroxodisulfate (1.43 g, 0.0063 mol) dissolved in 2.2 mL was added dropwise simultaneously with the rest of the aniline solution into the reaction mixture at a speed of ~1 drop per second by keeping the temperature at <5 °C. Afterward, the mixture was stirred for 5 h at temperatures of <5 °C, then overnight at room temperature. Acetone (50 mL) was added in order to precipitate the polymer. The obtained precipitate was separated by a centrifugation step, washed three times with 50 mL of acetone, and then with 2 M HCl. The product was finally washed with ethanol three times, before it was dried under dynamic vacuum for 12 h at 30 °C.

Enzyme Solution. Rhodobacter capsulatus xanthine dehydrogenase was heterologously expressed in Escherichia coli TP 1000 cells and purified, using nickel-nitrilotriacetic acid (Ni-NTA) chromatography (Q-Sepharose) and size exclusion chromatography (SEC), as described previously.[4a]

Measurements in Solution. UV-vis Spectroscopy. First, mixtures of PMSA1 and XDH were prepared in MES (50 mM + 1 mM EDTA, pH 4.5−6.5) and Tris (50 mM + 1 mM EDTA, pH 6.5−9.0) buffer after mixing and addition of the substrate HX. UV-vis spectra were collected. Since a strong absorbance band at 408 nm appears as a result of polymer reduction, the absorbance increase in time has been followed at this wavelength. Afterward, the reaction rates were calculated according to the Lambert−Beer equation,

$$A = \varepsilon dc \qquad \text{Equation 10.1}$$

INVESTIGATION OF THE PH-DEPENDENT IMPACT OF SULFONATED POLYANILINE
ON BIOELECTROCATALYTIC ACTIVITY OF XANTHINE DEHYDROGENASE

279

where A is the absorbance, ε the extinction coefficient (in M^{-1} cm^{-1}), d the pass length of the UV-vis cuvette (in cm), and c the concentration (in M). Furthermore, the same type of test was performed but with DCIP as the electron acceptor. The following concentrations were applied: [PMSA1] = 40 μg/mL, [DCPIP] = 0.1 mM, [XDH] = 1 μM, [HX] = 400 μM.

Cyclic Voltammetry. We used rectangular ITO-coated glass slides (surface resistivity = 15−25 Ω sq^{-1}, delivered by Sigma–Aldrich (Taufkirchen, Germany)) as working electrodes. For the measurements with all components in solution PMSA1 polymer, XDH and HX were added to the buffer solution (10 mM MES or Tris buffer at different pH values). After mixing, CV measurements have been performed to monitor bioelectrocatalysis. The concentrations used were: [PMSA1] = 40 μg/mL, [XDH] = 1 μM, [HX] = 400 μM.

Construction of Polymer/Enzyme Films. The polymer/enzyme films were fabricated using cleaned ITO-coated glass slides and macroporous ITO electrodes. The latter were prepared by a coassembly of poly(methyl methacrylate) beads (PMMA), together with indium tin hydroxide nanoparticles (nano-ITOH)[19c] and calcined according to a previously reported route.[19a,b] Both electrode types were then immersed in buffer solutions of the PMSA1−XDH mixture containing 0.2 mg mL^{-1} PMSA1, 1 μM XDH; 50 mM Tris buffer + 1 mM EDTA at pH 8.0 for 2 h. Prior to measurements, the (PMSA1/XDH) electrodes were dipped into 50 mM MES pH 5 + 1 mM EDTA buffer without PMSA1 and XDH to eliminate the unbound material.

Instruments. A homemade 1 mL cell containing an Ag/AgCl/1 M KCl reference (Biometra, Germany) and a platinum wire counter electrode were used for the electrochemical measurements. Voltammograms were recorded by the μAutolab Type II device (Metrohm) with a scan rate of 5 mV s^{-1}. The potential window has been set between −0.4 V and +0.4 V (vs. Ag/AgCl). GPES software (General Purpose for Electrochemical System, Eco Chemie, Utrecht, The Netherlands) was used for the analysis of CV curves. An Evolution 300 spectrophotometer (Thermo Fischer Scientific, Germany) was used for the collection of UV-vis spectra.

10.5. REFERENCES

(1)   (a) Bandodkar, A. J.; Wang, *J. Trends Biotechnol.* **2014**, *32*, 363. (b) Bhakta, S. A.; Evans, E.; Benavidez, T. E.; Garcia, C. D. *Anal.Chim. Acta* **2015**, *872*, 7. (c) Horgan, A. M.; Moore, J. D.; Noble, J. E.; Worsley, G. J. *Trends Biotechnol.* **2010**, *28*, 485–494. (d) Turner, A. *Trends Biotechnol.* **2013**, *31*, 119.

(2)   (a) Enroth, C.; Eger, B. T.; Okamoto, K.; Nishino, T.; Nishino, T.; Pai, E. F. *Proc. Natl. Acad. Sci. U. S. A.* **2000**, *97*, 10723. (b) Hille, R. *Chem. Rev.* **1996**, *96*, 2757. (c) Kalimuthu, P.; Leimkuhler, S.; Bernhardt, P. V. *J. Phys. Chem. B* **2012**, *116*, 11600.

(3)   (a) Battelli, M. G.; Bolognesi, A.; Polito, L. *Biochim. Biophys. Acta, Mol. Basis Dis.* **2014**, *1842*, 1502. (b) Nishino, T.; Okamoto, K. JBIC, *J. Biol. Inorg. Chem.* **2015**, *20*, 195. (c) Nishino, T.; Okamoto, K.; Eger, B. T.; Pai, E. F. The Xanthine Oxidoreductase Enzyme Family: Xanthine Dehydrogenase, Xanthine Oxidase, and Aldehyde Oxidase, Vol. 2; De Gruyter: Berlin, 2013. (d) Martin, A. C.; Brown, M. A. *Nat. Rev. Nephrol.* **2010**, *6*, 744. (e) Puddu, P.; Puddu, G. M.; Cravero, E.; Vizioli, L.; Muscari, A. *J. Cardiol.* **2012**, *59*, 235.

(4)   (a) Leimkuhler, S.; Hodson, R.; George, G. N.; Rajagopalan, K. V. *J. Biol. Chem.* **2003**, *278*, 20802. (b) Leimkuhler, S.; Kern, M.; Solomon, P. S.; McEwan, A. G.; Schwarz, G.; Mendel, R. R.; Klipp, W. *Mol. Microbiol.* **1998**, *27*, 853. (c) Truglio, J. J.; Theis, K.; Leimkuhler, S.; Rappa, R.; Rajagopalan, K. V.; Kisker, C. *Structure* **2002**, *10*, 115. (d) Leimkühler, S.; Stockert, A. L.; Igarashi, K.; Nishino, T.; Hille, R. *J. Biol. Chem.* **2004**, *279*, 40437. (5) Nishino, T.; Nishino, T.; Schopfer, L. M.; Massey, V. *J. Biol. Chem.* **1989**, *264*, 2518.

(6)   (a) Blaedel, W. J.; Jenkins, R. A. *Anal. Chem.* **1975**, *47*, 1337−1343. (b) Wang, J.; Angnes, L.; Martinez, T. *Bioelectrochem. Bioenerg.* **1992**, *29*, 215.

7)   Aguey-Zinsou, K. F.; Bernhardt, P. V.; Leimkuhler, S. *J. Am. Chem. Soc.* **2003**, *125*, 15352.

(8)   Kalimuthu, P.; Leimkuhler, S.; Bernhardt, P. V. *J. Phys. Chem. B* **2011**, *115*, 2655.

(9)   (a) Dryhurst, G. *Bioelectrochem. Bioenerg.* **1974**, *1*, 49.

(b)   Hansen, B. H.; Dryhurst, G. *J. Electroanal. Chem. Interfacial Electrochem.* **1971**, *30*, 417−426. (c) Hason, S.; Stepankova, S.; Kourilova, A.; Vetterl, V.; Lata, J.; Fojta, M.; Jelen, F. *Anal. Chem.* **2009**, *81*, 4302−4307.

(10)   Kalimuthu, P.; Leimkuhler, S.; Bernhardt, P. V. *Anal. Chem.* **2012**, *84*, 10359.

(11)   (a) Balint, R.; Cassidy, N. J.; Cartmell, S. H. *Acta Biomater.* **2014**, *10*, 2341. (b) Dhand, C.; Das, M.; Datta, M.; Malhotra, B. D. *Biosens. Bioelectron.* **2011**, *26*, 2811. (c) Qazi, T. H.; Rai, R.; Boccaccini, A. R. *Biomaterials* **2014**, *35*, 9068. (d) Barlett, P. N.; Cooper, J. M. *J. Electroanal. Chem.* **1993**, *362*, 1. (e) Bhadra, S.; Khastgir, D.; Singha, N. K.; Lee, J. H. *Prog. Polym. Sci.* **2009**, *34*, 783. (f) Jaymand, M. *Prog. Polym. Sci.* **2013**, *38*, 1287. (g) Kang, E. T.; Neoh, K. G.; Tan, K. L. *Prog. Polym. Sci.* **1998**, *23*, 277.

(12)   (a) Kane-Maguire, L. A. P.; Wallace, G. G. *Synth. Met.* **2001**, *119*, 39. (b) Vidal, J. C.; Garcia-Ruiz, E.; Castillo, J. R. *Microchim. Acta* **2003**, *143*, 93.

INVESTIGATION OF THE PH-DEPENDENT IMPACT OF SULFONATED POLYANILINE
ON BIOELECTROCATALYTIC ACTIVITY OF XANTHINE DEHYDROGENASE

281

(13) (a) Komathi, S.; Gopalan, A. I.; Lee, K. P. *Biosens. Bioelectron.* **2009**, *25*, 944. (b) Sarauli, D.; Xu, C. G.; Dietzel, B.; Schulz, B.; Lisdat, F. *Acta Biomater.* **2013**, *9*, 8290. (c) Sarauli, D.; Xu, C. G.; Dietzel, B.; Stiba, K.; Leimkuhler, S.; Schulz, B.; Lisdat, F. *Soft Matter* **2012**, *8*, 3848. (d) Scherbahn, V.; Putze, M. T.; Dietzel, B.; Heinlein, T.; Schneider, J. J.; Lisdat, F. *Biosens. Bioelectron.* **2014**, *61*, 631. (e) Göbel, G.; Schubart, I. W.; Scherbahn, V.; Lisdat, F. *Electrochem. Commun.* **2011**, *13*, 1240.

(14) (a) Malinauskas, A. *J. Power Sources* **2004**, *126*, 214. (b) Sanchis, C.; Ghanem, M. A.; Salavagione, H. J.; Morallon, E.; Bartlett, P. N. *Bioelectrochemistry* **2011**, *80*, 105. (c) Wei, X. L.; Wang, Y. Z.; Long, S. M.; Bobeczko, C.; Epstein, A. J. *J. Am. Chem. Soc.* **1996**, *118*, 2545.

(15) (a) Aretz, W.; Kaspari, H.; Klemme, J. H. *Z. Naturforsch., C: J. Biosci.* **1981**, *36*, 933. (b) Dietzel, U.; Kuper, J.; Doebbler, J. A.; Schulte, A.; Truglio, J. J.; Leimkühler, S.; Kisker, C. *J. Biol. Chem.* **2009**, *284*, 8768. (c) Schumann, S.; Saggu, M.; Möller, N.; Anker, S. D.; Lendzian, F.; Hildebrandt, P.; Leimkühler, S. *J. Biol. Chem.* **2008**, *283*, 16602.

(16) Sarauli, D.; Wettstein, C.; Peters, K.; Schulz, B.; Fattakhova-Rohlfing, D.; Lisdat, F. *ACS Catal.* **2015**, *5*, 2081.

(17) (a) Pornputtkul, Y.; Strounina, E. V.; Kane-Maguire, L. A. P.; Wallace, G. G. *Macromolecules* **2010**, *43*, 9982. (b) Strounina, E. V.; Shepherd, R.; Kane-Maguire, L. A. P.; Wallace, G. G. *Synth. Met.* **2003**, *135-136*, 289.

(18) Lee, M. C. I.; Velayutham, M.; Komatsu, T.; Hille, R.; Zweier, J. L. *Biochemistry* **2014**, *53*, 6615.

(19) (a) Sarauli, D.; Peters, K.; Xu, C. G.; Schulz, B.; Fattakhova-Rohlfing, D.; Lisdat, F. *ACS Appl. Mater. Interfaces* **2014**, *6*, 17887. (b) Liu, Y. J.; Peters, K.; Mandlmeier, B.; Muller, A.; Fominykh, K.; Rathousky, J.; Scheu, C.; Fattakhova-Rohlfing, D. *Electrochim. Acta* **2014**, *140*, 108. (c) Liu, Y. J.; Stefanic, G.; Rathousky, J.; Hayden, O.; Bein, T.; Fattakhova-Rohlfing, D. *Chem. Sci.* **2012**, *3*, 2367.

(20) (a) Ianniello, R. M.; Lindsay, T. J.; Yacynych, A. M. *Anal. Chem.* **1982**, *54*, 1980. (b) Shan, D.; Wang, Y.; Xue, H.; Cosnier, S. *Sens. Actuators, B* **2009**, *136*, 510. (c) Zhao, J.; O'Daly, J. P.; Henkens, R. W.; Stonehuerner, J.; Crumbliss, A. L. *Biosens. Bioelectron.* **1996**, *11*, 493.

10.6. SUPPORTING INFORMATION
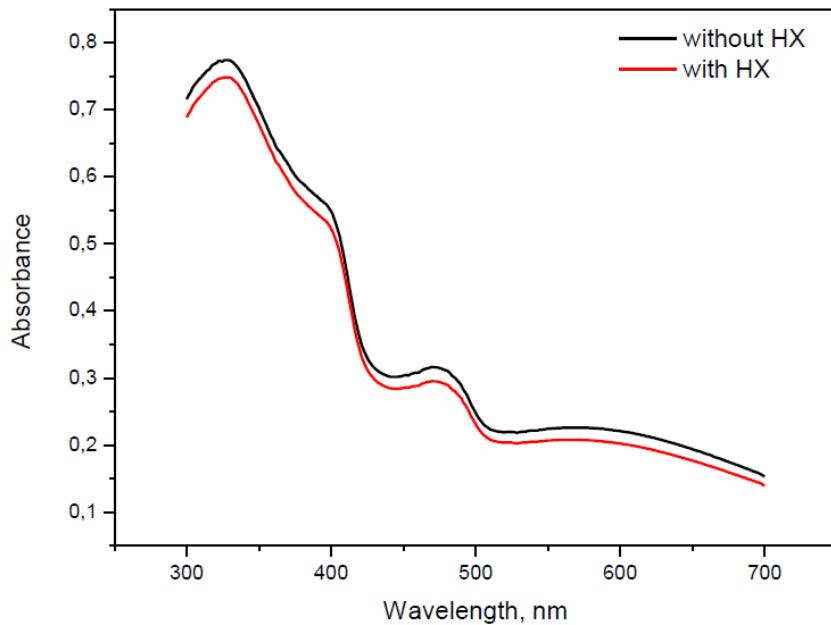
Figure S10.1 UV−vis spectra of PMSA1 in the absence (black line) and in the presence (red line) of the substrate hypoxanthine at pH 7.0 (50 mM TRIS + 1 mM EDTA).
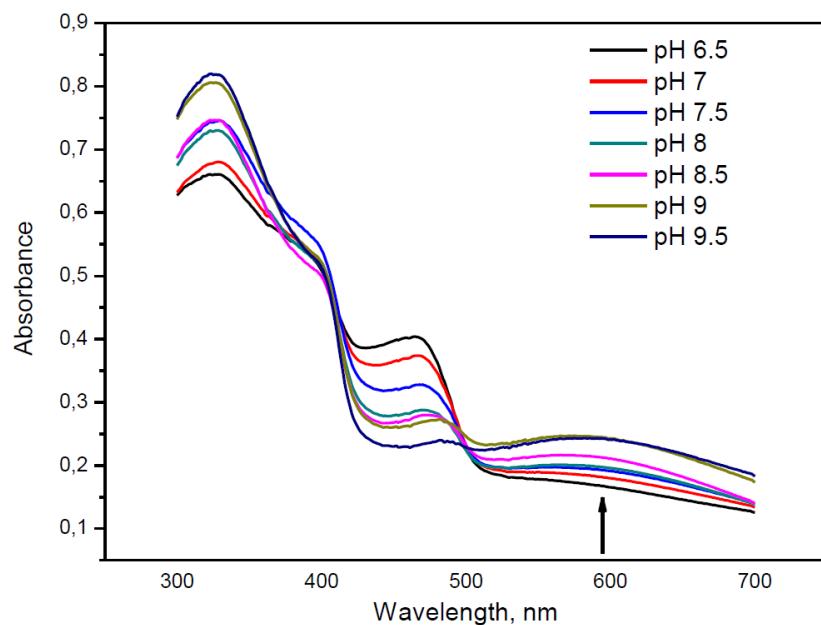
Figure S10.2 UV-vis spectraof pH-induced polymer changes. Experimental conditions: [PMSA1] = 40 µg/ml in 50 mM TRIS buffer+ 1 mM EDTA.

INVESTIGATION OF THE PH-DEPENDENT IMPACT OF SULFONATED POLYANILINE
ON BIOELECTROCATALYTIC ACTIVITY OF XANTHINE DEHYDROGENASE

283
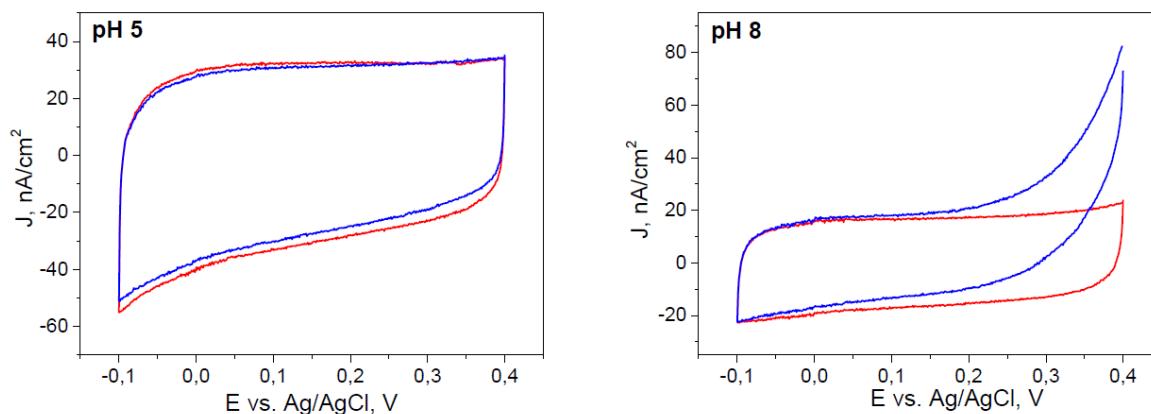
Figure S10.3 Cyclic voltammograms of ITO electrodes immersed in solutions of XDH at pH 5 and pH 8 without (red lines) and after addition of hypoxanthine (blue lines). Experimental conditions: [XDH] = 1 μM, [HX] = 400 μM in 50 mM MES (pH 5) or 50 mM Tris buffer (pH 8) + 1 mM EDTA at t = 25 °C, scan rate 5 mV/s.
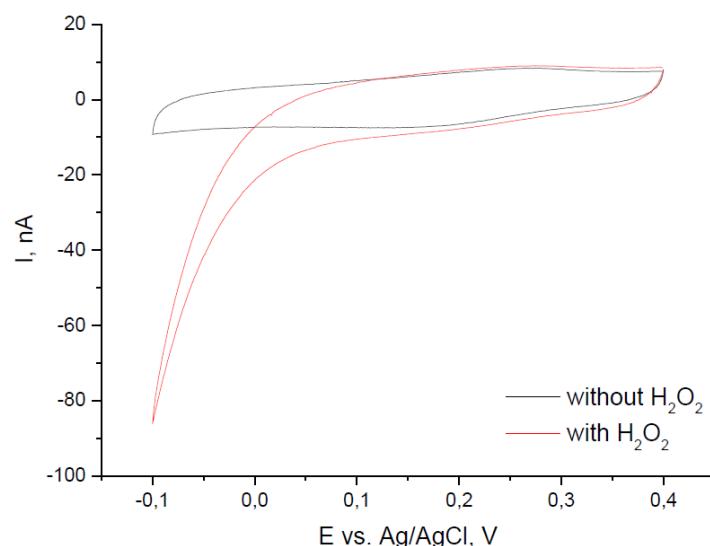
Figure S10.4 Cyclic voltammograms of ITO electrodes immersed in solutions of polymer and XDH pH 8 without (black lines) and after addition of hydrogen peroxide (red lines). Experimental conditions: [PMSA1] = 40 μg/ml, [XDH] = 1 μM, [H_2O_2] = 1 mM in 50 mM Tris buffer + 1 mM EDTA at t = 25 °C, scan rate 5 mV/s.
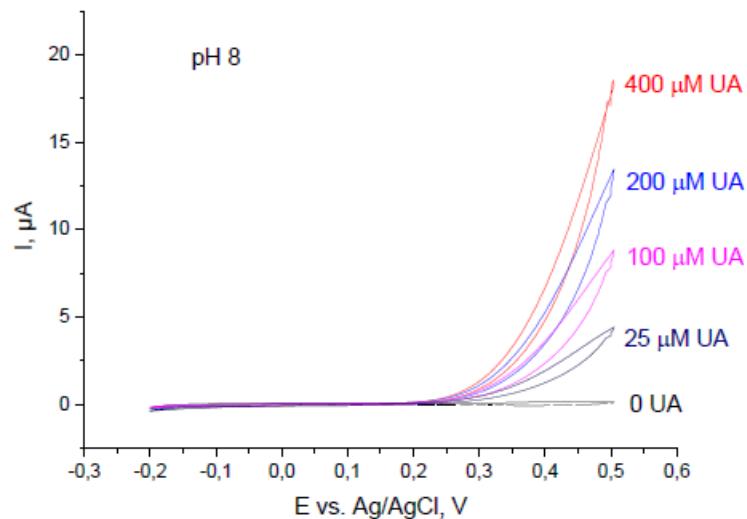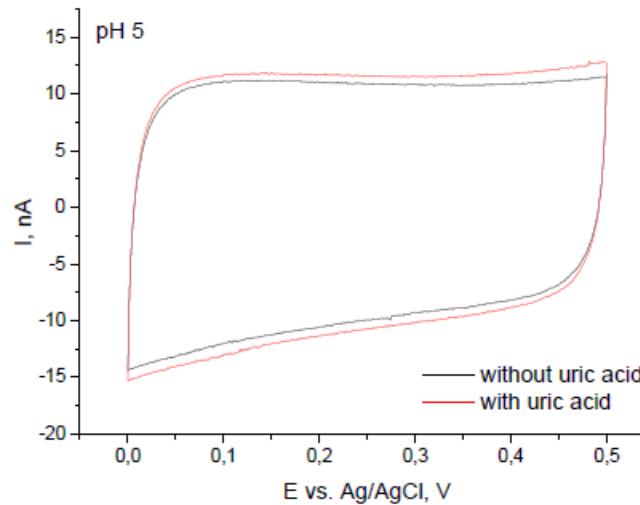
Figure S10.5 Cyclic voltammograms of ITO-PMSA1 electrodes immersed in solutions of uric acid at pH 5 and pH 8. Experimental conditions: 50 mM MES (pH 5) or 50 mM Tris buffer (pH 8) + 1 mM EDTA at t = 25 °C, scan rate 5 mV/s.

NANOSIZED ANTIMONY-DOPED TIN OXIDE/GRAPHENE COMPOSITES AS ANODE
MATERIAL IN LITHIUM-ION BATTERIES FOR FAST LITHIUM INSERTION

285

11. NANOSIZED ANTIMONY-DOPED TIN OXIDE/GRAPHENE COMPOSITES AS ANODE MATERIAL IN LITHIUM-ION BATTERIES FOR FAST LITHIUM INSERTION

Kristina Peters*, Florian Zoller*, Peter Zehetmaier, Patrick Zeller, Markus Döblinger, Zdeněk Sofer, Thomas Bein, Dina Fattakhova-Rohlfing

*Kristina Peters and Florian Zoller contributed equally

SnO_2-based materials gain increasing attention as anodes in lithium ion batteries due to their high theoretical capacity, low cost and high abundance. Especially incorporated into a carbonaceous matrix like graphene such composites are promising, as they compensate the shortcomings of the individual materials. We describe the fabrication of ATO/graphene hybrid nanocomposites with a high reversible capacity and a superior rate performance using a microwave assisted *in-situ* synthesis in *tert*-butyl alcohol. The microwave assisted solvothermal reaction enables the growth of ultra-small ATO nanoparticles with sizes below 3 nm on the surface of graphene suppressing unwanted agglomeration and restacking of the ATO nanocrystals or graphene sheets. The uniform composites feature a high gravimetric capacity of 1226 mAh g^{-1} at a current density of 1249 mA g^{-1} (equaling 1C) and a capacity retention of 71% after 100 cycles. Even at higher charging and discharging rates the capacity remains high with values of 1066 mAh g^{-1} (2C), 959 mAh g^{-1} (5C), 868 mAh g^{-1} (10C), 778 mAh g^{-1} (20C), 661 mAh g^{-1} (40C) and 577 mAh g^{-1} (60C) corresponding to 90%, 81%, 73%, 66%, 56% and 49% of the initial capacity, respectively. These ATO/graphene composites show the fastest ever-reported lithium insertion for SnO_2-based materials.

11.1. INTRODUCTION

Lithium-ion batteries (LIBs) are the most advanced energy-storage technology with energy and power densities superior to that of other rechargeable battery systems.[1-8] Still, there is an ever increasing need for Li-ion batteries with significantly higher energy densities and faster charging rates able to meet the growing demands of portable consumer devices with advanced functionalities and long-range electric vehicles.[1,9]

The state-of-the-art LIBs are based on insertion-type electrode materials such as graphite anodes and transition metal oxide cathodes.[1] The redox transformations of these compounds involve the reversible incorporation of lithium ions without major structural changes, resulting in a high cycling stability. The penalty for the structural stability is however a rather moderate specific capacity, which is limited by the amount of available lithium ion vacancies in the host structure.[1,10-13] The use of electrode materials with different charge storage chemistry, such as for example alloying/de-alloying or conversion-type materials, is a promising way to increase the storage capacity.[1,10-13] Among numerous candidates, tin oxide (SnO_2) is a very attractive anode material for replacing conventional graphite anodes due to the very high lithium insertion capacity and low working potential combined with low cost and high abundance.[11,14,15] The lithiation of SnO_2 involves its full conversion to metallic Sn followed by the alloying/dealloying of tin with lithium, with a total transfer of 8.4Li per one SnO_2 formula unit and a very high theoretical capacity of 1494 mAh g^{-1}.[1,11,16-18] The practical insertion capacity of SnO_2 is however much lower reaching only 783 mAh g^{-1} due to the irreversibility of the conversion step and the huge volume changes of 358% accompanying the structure transformation. These factors are also responsible for a very low cycling stability and a fast capacity fading of macroscopic SnO_2 materials. These shortcomings can be however successfully eliminated by using nanosized SnO_2 stabilized in a carbonaceous matrix, which is currently an established strategy to achieve high capacity and cycling stability of SnO_2 electrodes.[19] Nanoscaling of SnO_2 minimizes the strain during volume changes and results in a significantly enlarged contact area with the electrolyte providing a high lithium ion flux across the interface. Consequently, the diffusion path length is decreased enhancing the lithium ion diffusion kinetics and hence the power capability of batteries.[19] Furthermore, incorporation of nanosized SnO_2 in a carbonaceous conductive matrix buffers the volume changes and improves the electrical conductivity of the composites. Up to now, various types of carbonaceous materials including meso- and macroporous carbons[15], carbon

NANOSIZED ANTIMONY-DOPED TIN OXIDE/GRAPHENE COMPOSITES AS ANODE
MATERIAL IN LITHIUM-ION BATTERIES FOR FAST LITHIUM INSERTION

287

nanotubes[20,21], carbon hollow particles[22] and graphene[14,17,18,23-51] have been tested in SnO_2 composites. Especially graphene based nanocomposites have gained extensive attention due to the outstanding properties of graphene nanosheets (GNS) such as a high theoretical capacity (744 mAh g^{-1}), excellent conductivity, large surface area, high mechanical flexibility and chemical stability.[11] The reported strategies include hydro-/solvothermal *in-situ* synthesis of the nanoparticles on GNS[17,18,23-44], the self-assembly of preformed nanoparticles and GNS sheets,[14,45-47] mechanochemical ball milling,[48] electrostatic spray deposition (ESD)[49,50] and atomic layer deposition (ALD).[51]

A significant progress has been achieved in the last years in obtaining tin oxide-based composite electrodes with a specific capacity close to the theoretical one and a high cycling stability.[23,24,27] The high capacities could, however, only be reached at low current densities corresponding to long charging or discharging times. At higher charging/discharging rates the capacity decreases rapidly. The major reasons for the poor rate performance are significant structure changes involving several steps with a large reorganization energy, as well as resistances arising from the low conductivity of tin oxide and the contact resistances in the composite material. So far only few groups investigated the performance of SnO_2-based anodes at high current densities. Li *et al.*[26] prepared SnO_2 nanoparticles anchored on vertically aligned graphene, which maintain a specific capacity of 145 mAh g^{-1} at a current density of 20 A g^{-1}. Zhou *et al.*[52] reported on an even higher reversible capacity of 417 mAh g^{-1} for SnO_2/N-doped graphene composites at the same current density. Sun *et al.*[53] prepared SnO_2/C nanocapsules by an arc discharge method, which maintained an even higher capacity of 590 mAh g^{-1} at a current density of 20 A g^{-1}. Several groups have attempted to improve the lithiation rate of tin oxide based electrodes by increasing the electrical conductivity of SnO_2 via doping.[14,54-57] SnO_2 based anodes were doped with Sb,[14,20,21,54-61] In,[62] Zn,[63] Co,[64,65] Fe,[66] Mo,[67] Ti,[68] W,[69] and F,[64,70] however no improvement in the rate capability was observed. In- and W- doped SnO_2/graphene composites reported by Liu *et al.*[62] and Wang *et al.*[69] reach only 200 mAh g^{-1} and 300 mAh g^{-1} at a current densities of 7.8 A g^{-1} and 7 A g^{-1}, respectively. Sb doped SnO_2 (ATO)/graphene hybrid structures prepared by Zhao *et al.*[14] show a capacity of 483 mAh g^{-1} at a current density of 5 Ah g^{-1}.

In this publication we demonstrate that antimony doping of nanosized SnO_2 nanoparticles grown on the graphene sheets significantly increases the cycling stability and the rate performance of the composite anodes. The ATO/graphene nanocomposites prepared using a new *in-situ* microwave-assisted solvothermal route show a very high capacity, good cycling stability and in particular an exceptionally high rate capability.

11.2. RESULTS AND DISCUSSION

Antimony doped tin oxide/graphene oxide (ATO/GO) nanocomposites were fabricated *in-situ* using a one-step solvothermal reaction in *tert*-butyl alcohol.[56] In a typical procedure, tin(IV) and antimony(III) chlorides were dissolved in a molar ratio of 90:10 in *tert*-butyl alcohol, mixed with an aqueous graphene oxide dispersion and heated in hermetically sealed autoclaves; the formed brown nanocomposites were separated and washed by repeated redispersion and centrifugation. The SnO_2/GO composites were prepared in a similar way without addition of antimony. Furthermore, pure ATO was prepared by using the same amount of tin(IV) and antimony(III) chlorides in *tert*-butyl alcohol and adding water (the same amount as the water content in the aqueous graphene oxide dispersion, see experimental part for further details).

The reaction can be performed in a laboratory oven at temperatures from 80 to 150 °C; in this case it takes about 20 h to fully convert the precursors. The reaction time is however significantly shortened to 90 min when the reactions are performed in a microwave reactor. X-ray diffraction patterns (XRD) of washed and dried ATO/GO (Figure 11.1 and Figure **S11.1** in the supporting information) and SnO_2/GO (Figure S11.1 in the supporting information) nanocomposites demonstrate three distinct diffraction peaks corresponding to the (110), (101) and (211) reflections of tetragonal SnO_2 (cassiterite structure, space group $P4_2/mnm$, JCPDS card No.41-1445. The particle size (calculated from the line broadening of the 110 reflection) strongly depends on the synthesis temperature and the way of heating. At the same reaction temperature the particle size of microwave-heated ATO and SnO_2 nanoparticles is smaller compared to the oven heated samples. The size of ATO/SnO_2 nanoparticles within the composites increased from 3.7/3.5 nm to 4.6/4.7 nm and 6.1/5.8 nm at synthesis temperatures of 80 °C, 100 °C and 150 °C, respectively, for the oven-heated samples, and from 2.5/2.0 nm to 3.3/3.5 nm and 3.7/4.0 nm at the same temperatures for the microwave-heated samples. Only amorphous phase was observed at the temperatures below 80 °C. Formation of the ATO nanoparticles is favored by adding small amounts of water in the *tert*-butyl alcohol reaction mixture. Under synthesis conditions without water the reaction time has to be prolonged and/or the precursor concentration increased (see experimental part for further details).

The composites were pyrolyzed at 400 °C for 2 h (achieved with a ramp of 2°C min^{-1}) in nitrogen to remove organic residues and to reduce GO to reduced graphene oxide (termed as

NANOSIZED ANTIMONY-DOPED TIN OXIDE/GRAPHENE COMPOSITES AS ANODE
MATERIAL IN LITHIUM-ION BATTERIES FOR FAST LITHIUM INSERTION

289

"rGO"); the reduction process can be observed by the color change from brown to black. The results of XRD (Figure 11.1a), thermogravimetric analysis (TGA) (Figure 11.1b) and XPS (Figure 11.2) confirm that this treatment is sufficient for a reduction of GO to rGO. XRD patterns of pure GO exhibit a typical reflection (002) at 11.7° 2θ corresponding to the interlayer distance between GO sheets and a second reflection (100) around 42.2° 2θ indicating a short range order in stacked layers.[71-73] For rGO the (002) reflection is shifted to higher 2 θ values and broadened, indicating a decreased interlayer distance due to the removal of oxygen groups and a very poor ordering of the sheets along the stacking direction, respectively.[71,74] Upon pyrolysis the nanoparticles synthesized using microwave heating (80 °C) grow from 2.5 to 3.8 nm and from 2.3 to 3.5 nm for ATO/GO and SnO_2/GO nanocomposites. In contrast to the nanocomposites synthesized in an oven, weak diffraction peaks of GO or rGO could be observed in microwave synthesized composites, which is probably associated with the GO content in the composites and will be discussed in the following section.

The TGA curves of GO in air show a weight loss around 200 °C as well as between 500°C and 600°C (Figure 11.1b) associated with the decomposition of oxygen-containing groups and the gradual decomposition of the GO, respectively.[75] In contrast to that, rGO shows practically no weight loss in the range of 25 °C to 250 °C due to the absence of oxygen groups and only a small amount of adsorbed or weakly bound residues. The ATO/GO and ATO/rGO composites demonstrate similar behavior; the weight loss associated with the rGO decomposition was used for quantification of rGO in the pyrolyzed composites. For nanocomposites synthesized at temperatures of 100 °C or higher, the weight loss corresponds to the initial ratio of GO in the reaction mixture (Figure S11.2). However, for nanocomposites prepared at 80°C the mass fraction of the carbon phase is higher. The resulting ATO/rGO and SnO_2/rGO hybrids synthesized at 80°C (microwave) with an initial GO content of 10% contained 30% rGO after pyrolysis (see Figure 11.1b). One possible reason is that some fraction of the ATO precursors remains unreacted and is removed after washing and centrifugation, resulting in a higher relative GO content. These pyrolyzed composites are assigned as ATO_{70}/rGO_{30} and $SnO_{2,70}$/rGO_{30} in the following.
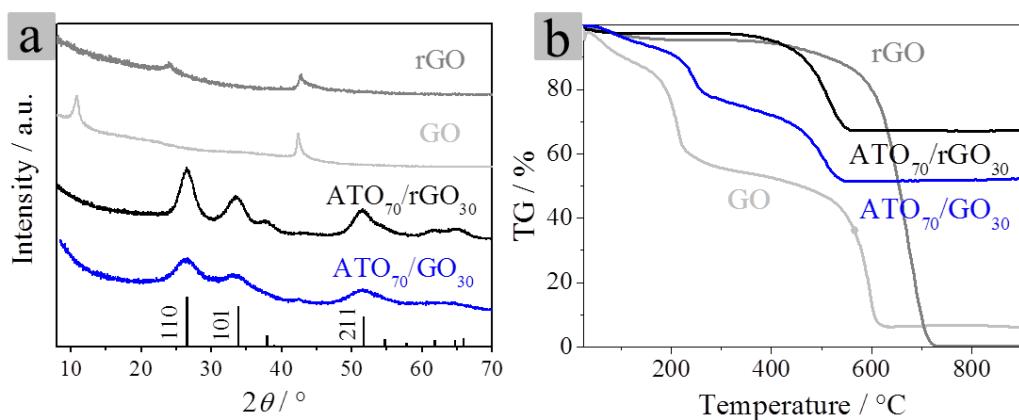
Figure 11.1 (a) XRD pattern and (b) TGA curves measured in air of a microwave synthesized ATO_{70}/GO_{30} nanocomposite and pure GO before and after pyrolysis. The bars in the bottom of the XRD pattern (a) mark the position and the intensity of the diffraction lines of SnO_2 cassiterite (space group $P4_2/mnm$, JCPDS File Card No. 41-1445). The initial weight loss between 25 °C and 150 ° in the TGA curves can be attributed to the removal of organic residues and water at the surface.

The elemental composition as well as the oxidation states of elements in the nanocomposites was studied by X-ray photoelectron spectroscopy (XPS). Figure 11.2a shows an overview spectrum of an ATO_{70}/GO_{30} composite before and after pyrolysis, which reveals the presence of carbon, oxygen, tin (IV) and antimony (III/V). The antimony content found in the nanocomposite corresponds to the initial precursor mixture of 10% Sb taken for the reaction equaling 9.8% and 10.6% for ATO_{70}/GO_{30} and ATO_{70}/rGO_{30}, respectively. The electrical conductivity of the ATO nanoparticles is generally influenced by the antimony content and its valence state in the tin oxide lattice, with Sb^{5+} ions acting as donor species beneficial for conductivity and the Sb^{3+} ions as electron traps, respectively. The ratio of Sb^{5+} species increases from 44.5 mol% to 61.1 mol% upon pyrolysis (Figure 11.2c, light grey line), pointing to an improved conductivity of the composites after the pyrolysis.[56] After pyrolysis in nitrogen the C 1s components associated with carbon-oxygen bonds significantly decrease (Figure 11.2b, light grey line) proving the successful reduction of most of the carboxyl and hydroxyl functional groups in the ATO_{70}/rGO_{30} nanocomposite.[14,23,73,74]

NANOSIZED ANTIMONY-DOPED TIN OXIDE/GRAPHENE COMPOSITES AS ANODE
MATERIAL IN LITHIUM-ION BATTERIES FOR FAST LITHIUM INSERTION

291
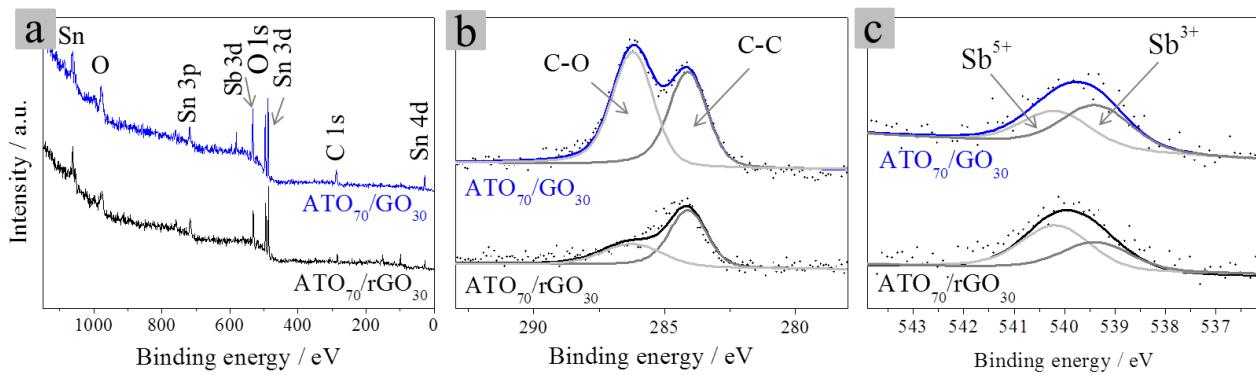
Figure 11.2 X-ray photoelectron spectra (XPS) of ATO_{70}/GO_{30} nanocomposites before (blue lines) and after reduction in nitrogen (black lines): (a) an overview, (b) the C 1s peak and (c) the Sb $3d_{3/2}$ peak. The solid black squares in (b) and (c) correspond to the experimental spectra. (b) The peak fits for C–O components (285.5–288.6 eV, light grey line) and C–C components (284.6 eV, dark grey line). The significant decrease of the peaks associated with C–O groups on the surface of GO points to a successful reduction of GO to rGO. (c) The peak fits for Sb^{5+} (540.0 eV, light grey line) and Sb^{3+} (539.2 eV, dark grey line).

The morphology of the nanocomposites as well as of individual components was studied by scanning electron microscopy (SEM). Interestingly, the ATO nanoparticles synthesized without GO form spherical agglomerates of small nanocrystals. The agglomerates are porous as follows from nitrogen sorption measurements featuring type IV isotherms typical for mesoporous materials and a BET surface area of 224 $m^2 g^{-1}$ (Figure S11.4c and Table S11.1 in the supporting information). The spherical agglomerates retain their morphology also after pyrolysis (Figure 11.3b), whereby the BET surface area decreases to 140 $m^2 g^{-1}$. The morphology of GO shows crumbled, paper-like structures with smooth edges before and after the solvothermal treatment and the pyrolysis (Figure 11.3c); also here the surface area decreased upon pyrolysis from 54 $m^2 g^{-1}$ to 26 $m^2 g^{-1}$ (Figure S11.4d and Table S11.1 in the supporting information). In contrast, the morphology of ATO_{70}/rGO_{30} composites differs significantly from that of the individual components (Figure 11.3a). The SEM images of ATO_{70}/rGO_{30} composites show the presence of laminated graphene sheets decorated with ATO nanoparticles, which seem to be uniformly distributed on the surface of the rGO separating the sheets from each other. Upon pyrolysis the agglomeration between the ATO decorated rGO sheets is reduced due to removal of organic residues between the single rGO layers of the nanocomposite, which can be seen by comparing SEM images of as-prepared and pyrolyzed samples in Figure 11.3a,d. None of the spherical ATO agglomerates was found in the composites, pointing to a homogeneous distribution of ATO nanoparticles between the rGO sheets (see low magnification SEM images in Figure S11.5 in the supporting information). The porous morphology and high specific surface area of the nanocomposites

are confirmed also by type IV nitrogen sorption isotherms with a hysteresis between the adsorption and desorption branches that is typical for mesoporous materials with relatively narrow pores (Figure S11.4a). The BET surface area of the nanocomposites remains stable around 265 $m^2\ g^{-1}$ for the as-prepared and pyrolyzed samples, respectively (see Figure S11.4 and Table S11.1 in the supporting information). The mean pore size increased from 2.6 nm for the as-prepared to 4.3 nm for the pyrolyzed ATO nanoparticles and remained stable at 6 nm for the as-prepared ATO_{70}/GO_{30} and the pyrolyzed ATO_{70}/rGO_{30} nanocomposites.
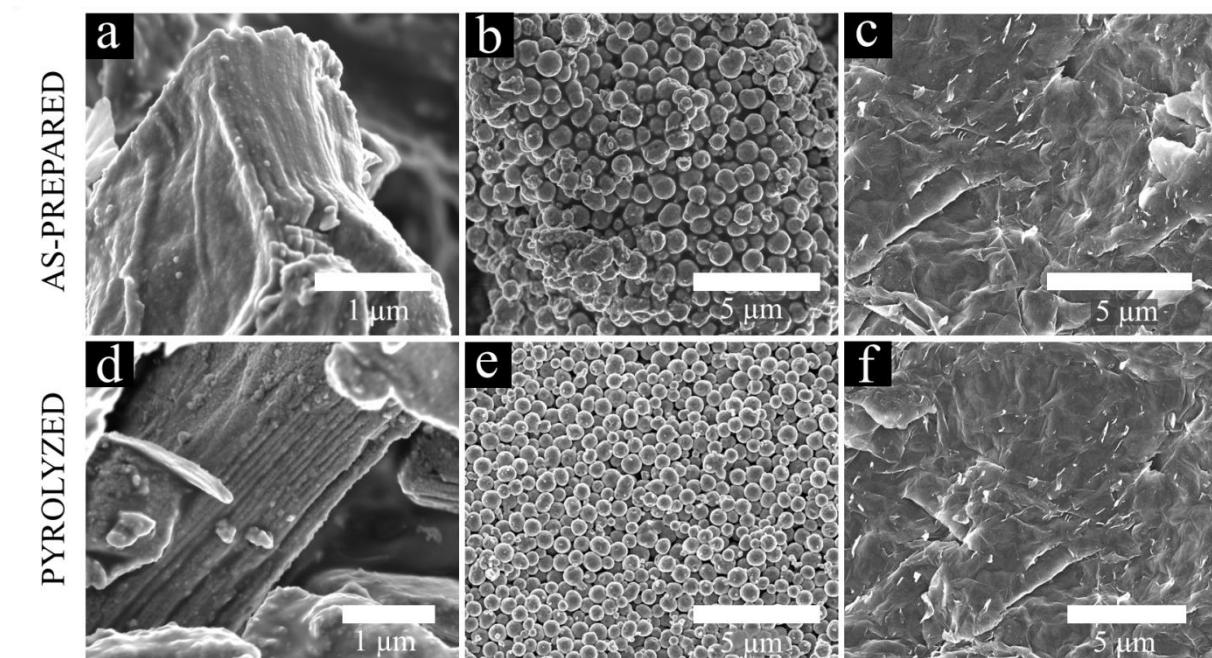
Figure 11.3   SEM images of ATO_{70}/GO_{30} forming homogeneous nanocomposites (a, d), pure ATO nanoparticles forming spherical clusters (b, e), graphene (c) and reduced graphene forming both paper-like structures (f). Top (a-c): as prepared; bottom (d-f): pyrolyzed samples (in nitrogen at 400 °C).

High-resolution transmission electron microscopy (HRTEM) analysis as well as selected area electron diffraction (SAED) patterns of the ATO_{70}/rGO_{30} nanocomposite show the presence of highly crystalline ATO nanoparticles (see Figure 11.4 and Figure S11.6 in the supporting information). The SAED pattern (Figure 11.4c) is in a good agreement with the tetragonal cassiterite structure of ATO deduced from XRD. The particle size determined from the TEM analysis (3–4 nm) is in good agreement with that calculated from the line broadening of the 110 reflection of ATO in the XRD pattern (3.8 nm) (Figure 11.1a). Due to a very low elemental contrast, graphene is not visible in the TEM. The graphene sheets were visualized only when they were aligned perpendicular to the TEM grid (as indicated by the red arrows in Figure 11.4a) or if the sheets were overlapping (see low magnification TEM images in Figure

NANOSIZED ANTIMONY-DOPED TIN OXIDE/GRAPHENE COMPOSITES AS ANODE
MATERIAL IN LITHIUM-ION BATTERIES FOR FAST LITHIUM INSERTION

293

S11.6 in the supporting information), which cause a different contrast depending on the amount of overlapping lamella. The presence of rGO can be, however, clearly identified from the sharp hexagonal diffraction spots in the SAED pattern of the nanocomposite (Figure **11.4**c), which matches the d-value of graphene (2.1 Å)[76,77]. From the SEM and TEM/SAED analyses we can conclude that the GO sheets are completely decorated with nanoparticles forming very homogeneous composites.
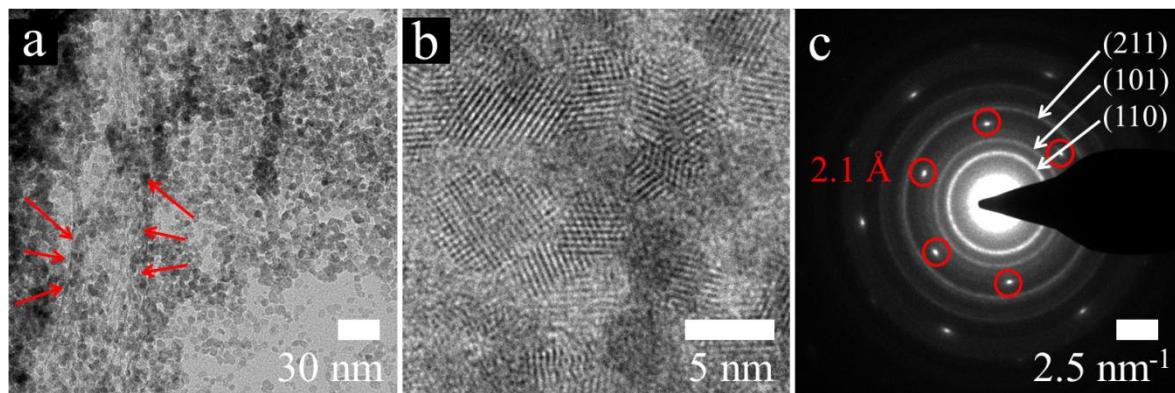
Figure 11.4 HRTEM images (a, b) and SEAD pattern (c) of an ATO_{70}/rGO_{30} nanocomposite pyrolyzed in nitrogen at 400 °C. The red arrows in (a) mark graphene sheets aligned perpendicular to the TEM grid. The HRTEM images (b) display crystalline ATO nanoparticles on the graphene surface. The SEAD pattern (c) show typical rings corresponding to ATO (d-values: 3.3 (110), 2.7 (101), and 1.8 Å (211)) and sharp hexagonal spots for rGO (d-values: 2.1 Å).[76,77]

The electrochemical performance of the ATO/GO nanocomposites was investigated using cyclic voltammetry and galvanostatic charge/discharge measurements. Generally, the electrochemical lithium insertion in SnO_2 (or $Sb_{0.1}Sn_{0.9}O_2$) proceeds via several steps according to the following reactions:[36]

(1) $Sn_{0.90}Sb_{0.10}O_2$ (ATO) $+ 4Li^+ + 4e^- \rightleftarrows 0.90\ Sn + 0.10\ Sb + 2\ Li_2O$

$SnO_2 + 2Li^+ + 2e^- \rightleftarrows SnO + Li_2O \qquad E_1 = 1.7\ V$

$SnO + 2Li^+ + 2e^- \rightleftarrows Sn + Li_2O \qquad E_2 = 0.9\ V$

⎫ Conversion

(2) $0.90\ Sn + 0.10\ Sb + 4.26Li^+ + 4.26e^- \rightleftarrows 0.90\ Li_{4.4}Sn + 0.10\ Li_3Sb$

$0.9\ Sn + 3.96\ Li^+ + 3.96\ e^- \rightleftarrows 0.90\ Li_{4.4}Sn \qquad E_3 = 0.4\ V$

$0.1\ Sb + 0.30\ Li^+ + 0.30\ e^- \rightleftarrows 0.10\ Li_3Sb \qquad E_4 = 0.4\ V$

⎫ Alloying/ dealloying
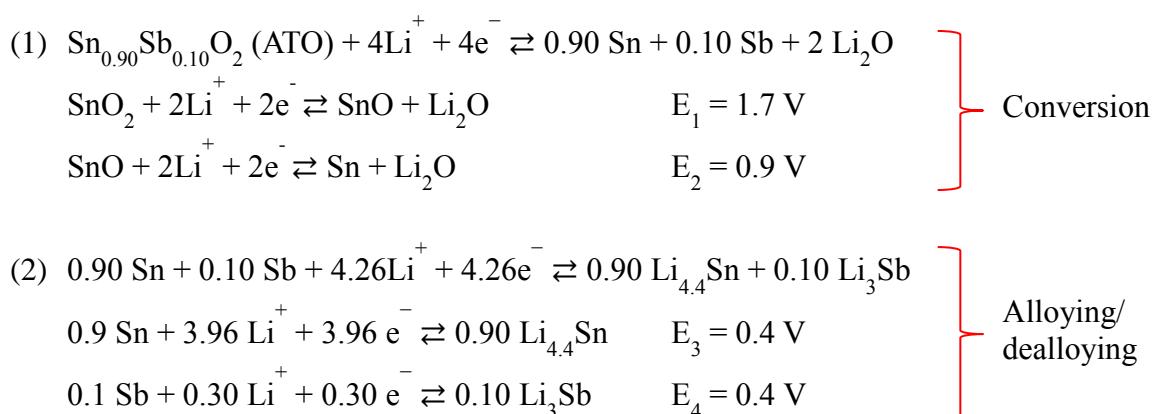
The overall electrochemical process involves the transfer of 8.4 or 8.26 Li^+ ions per one SnO_2 or ATO ($Sb_{0.1}Sn_{0.9}O_2$) formula unit with a theoretical capacity of 1494 $mAhg^{-1}$ and 1466 $mAhg^{-1}$, respectively. For bulk materials, however, the conversion reactions (1) are widely believed to be irreversible due to the huge volume changes, resulting in a lower capacity of around 783 $mAhg^{-1}$ stemming from the reversible alloying/dealloying process.[11,54] The conversion reactions become, however, reversible or at least particular reversible at the nanoscale due to a higher capability to adapt the volume changes.[36,47,78]

Cyclic voltammograms of all SnO_2 (ATO) nanoparticles and ATO/rGO nanocomposites (Figure 11.5 and Figure S11.7 in the supporting information) obtained in this work demonstrate a couple of peaks at around 0.4 V (cathodic peak: 0.2 V/ anodic peak: 0.6 V) ascribed to the reversible alloying/de-alloying process according to (2). The ATO/rGO nanocomposites show an additional pair of peaks corresponding to the intercalation of Li into graphene (see supporting information for further details).[1,3,36,79] For all investigated nanomaterials a pair of peaks at around 0.9 V and 1.7 V is observed corresponding to the conversion of ATO to Sn and Sb and the simultaneous formation of Li_2O (1). The presence of these two pairs of peaks that were so far only observed for nano-sized SnO_2 or ATO particles[36,47,78] is commonly interpreted in literature as an indication of the reversibility of the conversion reaction. This results in a higher theoretical capacity for our nano-sized ATO/SnO_2 nanoparticles (1466 mAh g^{-1}/1494 mAh g^{-1}) compared to the macroscopic ATO/SnO_2 (756 mAh g^{-1}/783 mAh g^{-1}).[1,11,16-18,36,45,80]

Although the ATO nanoparticles and the ATO/rGO_{30} and $SnO_{2,70}$/rGO_{30} nanocomposites feature similar CV fingerprint and a comparable specific capacity in the first cycles, they differ significantly in their cycling stability and in particular the rate capability. The ATO nanoparticles-only based electrodes demonstrate significant capacity fading, which is the highest among three investigated systems (Figure S11.7b in the supporting information).

NANOSIZED ANTIMONY-DOPED TIN OXIDE/GRAPHENE COMPOSITES AS ANODE
MATERIAL IN LITHIUM-ION BATTERIES FOR FAST LITHIUM INSERTION

295
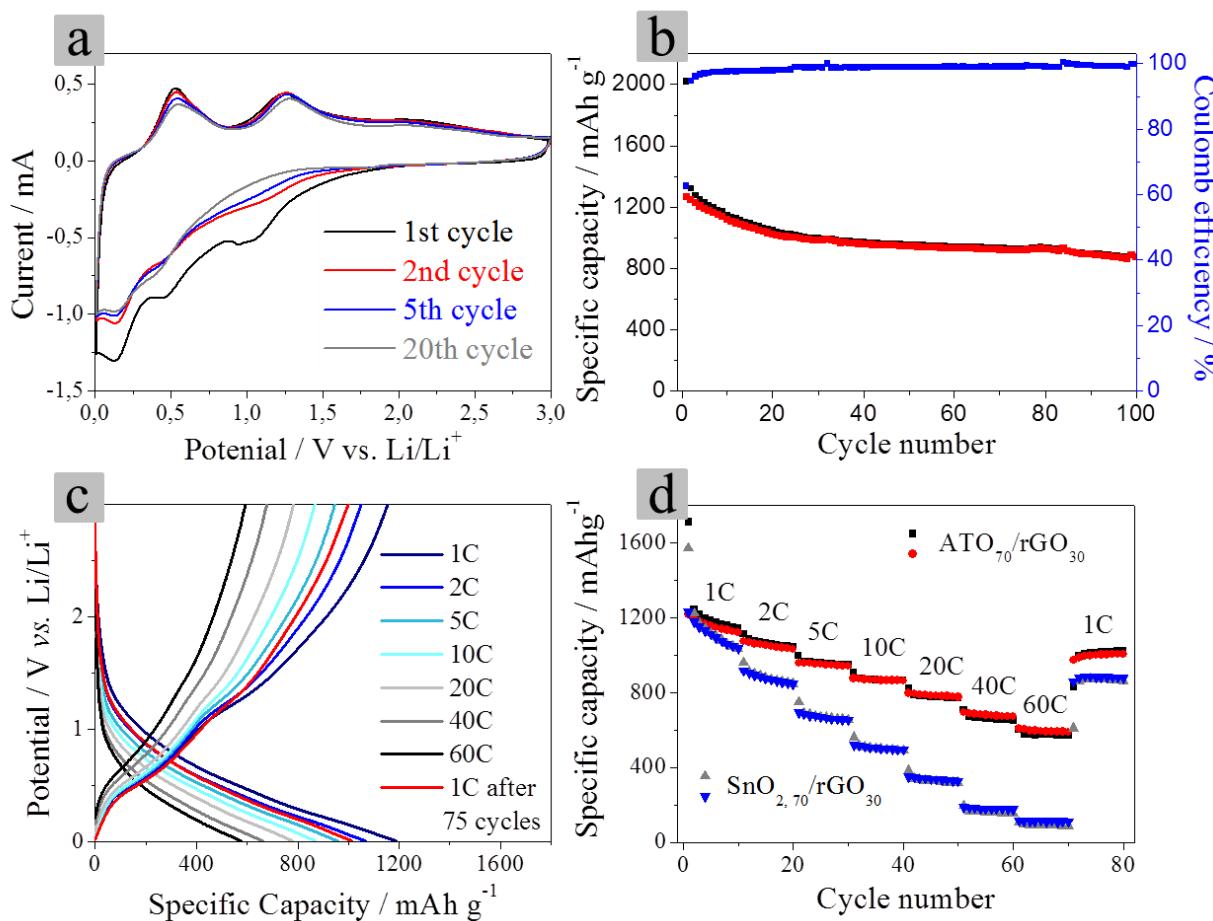
Figure 11.5   (a) Cyclic voltammogram of an ATO_{70}/rGO_{30} electrodes (loading 0.2 mg cm^{-1}) showing its cycling stability recorded with a scan rate of 0.5 mV s^{-1} and a step potential of 2.44 mV in the range 0.01 – 3 V vs. Li/Li$^+$. The first discharge curve corresponding to the lithium ion insertion process differs significantly from the subsequent cycles. It shows a dominant cathodic peak around 1.2 V, which can be attributed to the irreversible formation of a solid electrolyte interface (SEI) layer and disappears in the following scans. (b) Multicycling stability of the electrode at a rate of 1C and the corresponding coulombic efficiencies (■ blue labels). (c) Discharge/charge profiles of ATO_{70}/rGO_{30} at increasing C-rates (1–60C) each recorded in the 5th, 15th, 25th etc. cycle. (d) Rate performance of ATO_{70}/rGO_{30} and $SnO_{2,70}/rGO_{30}$ (both with a loading of 0.2 mg cm^{-1}) at different rates ranging from 1 to 60C (ten cycles at each C-rate). ATO_{70}/rGO_{30} charge and discharge capacities correspond to the red (●) and black (■) labels. $SnO_{2,70}/rGO_{30}$ charge and discharge capacities are displayed with blue (▼) and grey (▲) labels.

Galvanostatic charge/discharge measurements of the ATO_{70}/rGO_{30} nanocomposite performed at different current densities (C-rates) (Figure 11.5) show three typical plateau regions in a good agreement with the corresponding CV curves. The first discharge/charge capacities reach 2019/1264 mAh g^{-1} at a current density of 1249 mA g^{-1} (corresponding to 1C), which is higher than the theoretical capacity due to SEI formation on the electrode surface. This results in an initially low initial Coulombic efficiency of 63 %. The Coulombic efficiency however

increases to around 97% after the first three cycles (see blue line in Figure 11.5b) and remains stable above 99% after the 25th cycles. The specific capacity reaches 1226 mAh g^{-1}/1189 mAh g^{-1} (discharge/charge) in the second cycle, which is close to the theoretical lithium insertion capacity of the composite (1249 mAh g^{-1}), and remains stable reaching 875 mAh g^{-1} after 100 cycles. Notable the capacity fading of the unsupported ATO nanoparticles was more pronounced (Figure S11.10a in the supporting information) compared to the graphene supported ATO and SnO_2 (918 mAh g^{-1} after 100 cycles, see Figure S11.9 in the supporting information), reaching only 77 mAh g^{-1} after 100 cycles.

The most striking feature of the ATO/rGO composites is, however, their excellent rate capability. The charging and discharging rates of pure ATO as well as of $SnO_{2,70}$/rGO_{30} and ATO_{70}/rGO_{30} electrodes are summarized in Table 11.2 in the experimental part. Comparison between three types of electrodes with a similar thickness of 10 μm and a moderate loading of 0.2 mg cm^{-2} highlights the superior rate performance and higher cycling stability of ATO_{70}/rGO_{30} material compared to the ATO nanoparticles and the undoped $SnO_{2,70}$/rGO_{30} nanocomposite (Figure 11.5). The ATO_{70}/rGO_{30} electrodes deliver high specific discharge capacities of 1186 mAh g^{-1} (1C), 1066 mAh g^{-1} (2C), 959 mAh g^{-1} (5C), 868 mAh g^{-1} (10C), 778 mAh g^{-1} (20C), 661 mAh g^{-1} (40C) and 577 mAh g^{-1} (60C), each recorded in the 5th, 15th, 25th etc. cycle. Even at a rate of 60C (corresponding to charging and discharging within one minute) 49% of the initial capacity at 1C is (1186 mAhg^{-1}) is achieved. The capacity of the composite remains much higher than the capacity of the state-of-the-art anode material graphite (372 mAh g^{-1}). Remarkably, the capacity fading upon increasing C-rates is reversible, as the capacity recovers when the C-rate returns to 1C. The capacity retrieves to 1014 mAh g^{-1} after 80 cycles between 1C and 60C, which corresponds to 85% of the initial capacity. Also the thicker ATO_{70}/rGO_{30} electrodes with a loading of 0.6 mg cm^{-2} demonstrate a high rate capability, as shown in Figure S11.8 in the supporting information. When cycled at 60C, it still retains a capacity of 235 mAh g^{-1} and restores to a capacity of 1032 mAh g^{-1} when set back to 1C.

The electrochemical performance of $SnO_{2,70}$/rGO_{30} nanocomposites is much worse featuring a more pronounced capacity fading at higher C-rates compared to antimony doped counterparts (see Figure 11.5d). The slightly higher initial capacity of 1120 mAh g^{-1} (1C) decreases rapidly to 881 mAh g^{-1} (2C), 672 mAh g^{-1} (5C), 503 mAh g^{-1} (10C), 328 mAh g^{-1} (20C), 161 mAh g^{-1} (40C) and 93 mAh g^{-1} (60C). However also for the undoped $SnO_{2,70}$/rGO_{30} nanocomposites the capacity recovers when the C-rate is set back to 1C, but reaching only a lowered capacity of 865 mAh g^{-1} compared to the ATO_{70}/rGO_{30} composites (1021 mAh g^{-1} after 80 cycles).

NANOSIZED ANTIMONY-DOPED TIN OXIDE/GRAPHENE COMPOSITES AS ANODE
MATERIAL IN LITHIUM-ION BATTERIES FOR FAST LITHIUM INSERTION

297

This corresponds to an irreversible capacity loss of only 23%. Notable the capacity fading at higher C-rates of the unsupported ATO nanoparticles was even more pronounced (Figure **S11.10**b in the supporting information) compared to the graphene supported ATO and SnO_2 (see Figure 11.5d). Pure ATO reached only capacities of 20 mAh g^{-1} at 60C and capacity retention of only 573 mAh g^{-1} after 80 cycles, which corresponds to an irreversible capacity loss of 50% (compared to 1132 mAh g^{-1} in the 5th cycle). The lower cycling stability of pure ATO nanoparticles could be caused by the greater volume expansion of the unsupported nanoparticles causing delamination and pulverization of the active material from the electrode.

The comparison of rate performance of different electrodes is generally very ambiguous, as it strongly depends on the electrode thickness and the way of the electrode fabrication. Furthermore, the direct comparison with the literature data is complicated because of different mass loading on the electrodes ranging between 0.11 mg cm^{-2} and 10 mg cm^{-2},[52,53,81,82] or often missing information about the electrode loading. Still, to the best of our knowledge, ATO$_{70}$/rGO$_{30}$ electrodes prepared in our work show the highest ever reported capacity values at such high charging/discharging rates (60 C=75 A g^{-1}) among the reported electrodes. SnO_2/carbon composites reported previously did not reach such a high current density with a reasonably high specific capacity of 550 mAh g^{-1} at 10 A g^{-1} (Chen *et al.*, unknown loading),[81] 574 mAh g^{-1} at 10 A g^{-1} (Chen *et al.*, 1 mg cm^{-2}),[82] 428 mAh g^{-1} at 10 A g^{-1} (Sher Shah *et al.*, 1.12 mg cm^{-2}),[83] 590 mAh g^{-1} at 20 A g^{-1} (Sun *et al.*, unknown loading),[53] 417 mAh g^{-1} at 20 A g^{-1} (Zhou *et al.*, 10 mg cm^{-2}),[52] and 145 mAh g^{-1} at 20 A g^{-1} (Li *et al.*, 0.11 mg cm^{-2}).[26] Compared to low loadings of 0.11 mg cm^{-2} reported by Li *et al.*[26], our thin electrodes (0.3 mg cm^{-2}) deliver an about five time higher capacity at 10 A g^{-1} ($\approx$ 8C). Also our electrodes with a higher loading (0.6 mg cm^{-2}) have a superior rate performance 762 mAh g^{-1} at 12.5 mA g^{-1} (10C) compared to the reports of Chen *et al.*[82] (574 mAh g^{-1}, 1 mg cm^{-2}, 10 mA g^{-1}) and Sher Shah *et al.*[83] (550 mAh g^{-1}, 1.12 mg cm^{-2}, 10 mA g^{-1}). Electrodes with a very high loadings of 10 mg cm^{-2} were so far only reported by Zhou *et al.*[52] It should be however noted that the electrodes investigated in this work were not calendered, that puts limitations on the maximum loading. The attempts to manufacture thicker electrode layers without calendering were not successful, as the thick electrode layers were not mechanically stable and were delaminating from the copper foil current collector. We believe that the rate performance of our electrodes can be increased even more by electrode pressing and the optimization of electrode fabrication.

11.3. CONCLUSIONS

The one-step in-situ solvothermal reaction in *tert*-butyl alcohol enables the facile fabrication of ATO/GO nanocomposites containing ultra-small crystalline ATO nanoparticles of >3 nm in size. The particles can be synthesized in a conventional oven or microwave assisted synthesis, whereby the reaction time could be significantly reduced using microwave irradiation. The nanoparticle size could be tuned by adjusting the reaction temperature. Prior to the electrode fabrication the nanocomposites were pyrolyzed in nitrogen to improve the conductivity of the hybrid materials by reducing GO to rGO. The composites consist of laminated graphene oxide sheets decorated homogeneously with ATO nanoparticles. They show a superior Li^+ storage capacity of 1226 mAh g^{-1} at 1C, which is close to the maximum theoretical capacity of the composite. Furthermore the hybrid structures reveal an excellent cycling stability even at high current densities, reaching a capacity of 577 mAh g^{-1} at 60 C (meaning charging and discharging within one minute). By comparing ATO_{70}/rGO_{30} with undoped $SnO_{2,70}/rGO_{30}$ and pure ATO control samples, we could show the beneficial effect of antimony doping and of graphene hybrid structures on the overall battery performance. We attribute the excellent performance to the following factors: (1) the high capacity arises from the small size of the nanoparticles, which results in a high reversibility of the conversion reaction due to decreased activation energy in nano-sized ATO. (2) The higher surface area of the nanocomposites (265 m²/g) compared to pure ATO (140 m²/g) or rGO (26 m²/g) results in an enlarged effective contact area between electrode and liquid electrolyte leading to a reduced path length for Li^+ transport and therefore a better rate performance. (3) The hybrid structure formed by a direct growth of ATO on the graphene provides a strong contact of the nanoparticles on the surface of the graphene sheets and therefore increases the overall conductivity, improves the tolerance to volume changes and alleviates agglomeration/pulverization during the lithium insertion/de-insertion. (4) The use of ATO based composites is advantageous compared to SnO_2 composites, as they feature a significant reduced charge transport resistances compared to pure SnO_2 resulting in a superior cycle stability and rate capability.

NANOSIZED ANTIMONY-DOPED TIN OXIDE/GRAPHENE COMPOSITES AS ANODE
MATERIAL IN LITHIUM-ION BATTERIES FOR FAST LITHIUM INSERTION

299

11.4. EXPERIMENTAL SECTION

Materials. Tin(IV) chloride (Sigma-Aldrich), Antimony(III) chloride (abcr), *tert*-butyl alcohol (99%, Sigma-Aldrich), poly(vinylidene fluoride) (PVDF, Sigma-Aldrich), graphite microparticles (2–15 μm, 99.9995%, from Alfa Aesar), black carbon (Super C65, Timcal), 1-methyl-2-pyrrolidone (NMP, Sigma-Aldrich), PuriEL electrolyte (1.15 M $LiPF_6$ in EC/EMC/DMC = 2:2:6 v/v + 1.0%wt FEC, *soul*brain MI) and lithium metal (Rockwood) were used as received. Sulphuric acid (98%), phosphoric acid (85%), potassium permanganate (99.5%), hydrogen peroxide (30%), barium nitrate (99.5%) and N,N-dimethylformamide (DMF) were obtained from Penta, Czech Republic.

Fabrication of graphene oxide. Graphene oxide was prepared by the oxidation of graphite by potassium permanganate in sulphuric/phosphoric acid described by Marcano *et al.*[77]. For that, graphite (3.0 g) and subsequently potassium permanganate (18.0 g) were added to a cooled (under 0 °C) mixture of concentrated sulphuric acid and phosphoric acid in a volume ratio of 9:1 (360 ml : 40 ml). The reaction mixture was stirred and heated at 50 °C for 12 h. Afterwards the mixture was cooled to room temperature and poured on ice with hydrogen peroxide (3.0 ml) to remove excess permanganate ions and manganese dioxide. After the ice dissolved, 30% hydrogen peroxide was added (20 mL) to remove remaining unreacted potassium permanganate and manganese dioxide. Finally the obtained graphite oxide was purified by repeated centrifugation and redispersion in deionized water until a negative reaction on sulfate ions with $Ba(NO_3)_2$ was achieved. The graphite oxide slurry was ultrasonicated for 1 h (400 W; 20 °C) in order to exfoliate it to graphene oxide sheets. The concentration of graphene oxide was measured by gravimetry.

Fabrication of ATO/GO nanocomposites. The ATO/GO composites were prepared by a one-pot solvothermal route in *tert*-butyl alcohol. The synthesis quantities are summarized in Table **11.1**. For a ATO/GO nanocomposite with 10% GO and an antimony doping concentration of 10%, 566.0 mg (2.17 mmol) of tin(IV) chloride, 55.1 mg (0.24 mmol) of antimony(III) chloride and 1.485 ml GO (corresponding to 27.3 mg/ml in water) were dissolved in 18 ml of *tert*-butyl alcohol and heated in a hermetically sealed Teflon lined autoclave at temperatures of 80 °C, 100 °C or 150 °C for 20 h in an oven or for 90 min in microwave autoclaves with an initial heating power of 900 W (Synthos 3000, Anton Paar). The nanocomposites were

separated by centrifugation (47800 rcf for 15 min) and washed once with 20 mL of water and once 20 ml of ethanol by repeated redispersion and centrifugation.

Table 11.1   Synthesis quantities for ATO/GO and SnO_2/GO nanocomposites as well as pure ATO nanoparticles.

	Precursor		GO [27.3 mg/ml] in water		Water	*tert*-butyl alcohol
	$SnCl_4$ [ml]	$SbCl_3$ [mg]	[ml]	[mass %]	[ml]	[ml]
SnO_2/GO	630.1	-	1.485	10	-	18
ATO/GO	566.0	55.1	1.485	10	-	18
ATO	566.0	55.1	-	-	1.485	18

Fabrication of ATO nanoparticles. The antimony doped tin oxide (ATO) nanoparticles with a doping level of 10 % were prepared by a modified solvothermal route in *tert*-butyl alcohol described by some of the authors.[56] In brief, 566.0 mg (2.17 mmol) of tin(IV) chloride, 55.1 mg (0.24 mmol) of antimony(III) chloride were dissolved in a mixture of 18 ml of *tert*-butyl alcohol and 1.485 ml of water and heated in a hermetically sealed Teflon lined autoclave at different temperatures according to the graphene containing composites for 20 h or for 90 min in an oven or microwave using an initial heating power of 900 W (Synthos 3000, Anton Paar). The nanoparticles were flocculated by an addition of 20 mL of dichloromethane, separated by centrifugation (47800 rcf for 10 min), washed in 20 mL of acetone and centrifuged again at 47800 rcf for 10 min.

Battery assembly. Electrochemical measurements were carried out using ECC-PAT-Core electrochemical test cells (EL-Cell). The working electrode was prepared by coating homogeneous slurries containing the pyrolyzed active materials (ATO, ATO/rGO and SnO/rGO nanocomposites), PVDF and black carbon with a mass ratio of 80:10:10 in NMP. The slurries were stirred overnight and uniformly coated onto Cu foil (Targray Technology) with a coater (wet film thickness: 50-100 μm, corresponding to a loading of 0.2 mg cm^{-2} – 0.6 mg cm^{-2}). The electrodes were die-cut into round disks with a diameter of 18 mm (254.5 mm^2) and pyrolyzed at 400°C for 2 h in nitrogen (achieved with a ramp of 2 °C min^{-1}). The electrodes were dried at 120°C for 3 h in vacuum before being used as anodes. The cells

NANOSIZED ANTIMONY-DOPED TIN OXIDE/GRAPHENE COMPOSITES AS ANODE
MATERIAL IN LITHIUM-ION BATTERIES FOR FAST LITHIUM INSERTION

301

were assembled in an argon filled glove box using lithium metal as the counter and reference electrode and an EL-CELL ECC1-01-0011-A/L glass fiber as separator. As electrolyte we used a commercial 1.15 M $LiPF_6$ in EC/EMC/DMC in a 2:2:6 volume to volume ratio and 1.0 % wt fluoroethylene carbonate (FEC). CV curves were measured with a scan rate of 0.5 mV s^{-1} and a step potential of 2.44 mV in a potential range between 0.01 and 3.0 V vs. Li^+/Li.

The theoretical capacity of the SnO_2 and ATO was calculated assuming that all Li per formula unit participate in the electrochemical reaction using the following equation:

$$\text{Theoretical capacity:} \quad \frac{F \cdot n_{Li}}{M \cdot 3.6} \qquad \text{Equation 11.1}$$

Where F is the Faraday's constant, n_{Li} is the number of lithium ions per formula unit and M is the molecular mass of the electrode material. The overall electro-chemical process involves 8.4 and 8.33 Li^+ ions for one SnO_2 and $Sb_{0.10}Sn_{0.90}O_2$ (ATO) formula unit corresponding to a theoretical capacity of 1494 mAhg^{-1} and 1466 mAhg^{-1}, respectively. Furthermore, reversible Li intercalation/deintercalation in graphene at E = 0.1 V with an uptake of up to 2 mol Li per mol graphene should be taken into account in the composite anodes:[78]

$$6C \text{ (rGO)} + 2Li^+ + 2e^- \leftrightarrow Li_2C_6$$

The theoretical capacity of the nanocomposites was calculated from the stoichiometric amounts of SnO_2 or ATO and GO in the composition according to the following equation:[14,36]

$$C_{\text{ATO/rGO,theo.}} = C_{\text{ATO,theo}} \times \% \text{ ATO} + C_{\text{GO,theo.}} \times \% \text{ rGO} \qquad \text{Equation 11.2}$$

with a theoretical capacity of 1494 mAhg^{-1} for SnO_2, 1466 mAhg^{-1} for ATO and 744 mAh g^{-1} for rGO. The specific capacity is referred to the weight of the active material, namely the ATO nanoparticles or the ATO/rGO nanocomposites, while the mass of the additives like carbon black, PVDF and NMP are not taken into account.

Galvanostatic charge and discharge curves were recorded at various C-rates ranging from 1C–60C in a voltage window of 3.0 V to 0.01 V vs. Li^+/Li at room temperature. The corresponding current densities of the different compounds investigated in this publication are summarized in Table 11.2.

Table 11.2   Current densities of ATO_{70}/rGO_{30}, $SnO_{2,70}/rGO_{30}$ and pure ATO nanoparticles at different C-rates (1C–60C).

	Current densities [mA g^{-1}]		
C-rate	ATO_{70}/rGO_{30}	$SnO_{2,70}/rGO_{30}$	ATO
Theoretical capacity	1249 [mAh g^{-1}]	1269 [mAh g^{-1}]	1466 [mAh g^{-1}]
1C	1249	1269	1466
2C	2498	2538	2932
5C	6245	6345	7330
10C	12490	12690	14660
20C	24980	25380	29320
40C	49960	50760	58640
60C	74940	76140	87960

Characterization methods: Wide angle X-ray diffraction analysis was carried out in transmission mode using a STOE STADI P diffractometer with CuK$_{\alpha1}$-radiation ($\lambda = 1.54060$ Å) and a Ge(111) single crystal monochromator equipped with a DECTRIS solid state strip detector MYTHEN 1K. Powder XRD patterns of the samples were collected in a 2θ range from 5° to 70° with a step size of 1° and a fixed counting time of 45 seconds per step. The size of the crystalline domains was calculated from the XRD patterns for the most intensive ATO signal (110 reflection) using the Scherrer equation.

X-ray photoelectron spectroscopy (XPS) measurements of the composites on a silicon substrate were performed using a VSW TA10 X-ray source, providing non-monochromatic Al K$_{\alpha}$ radiation, and a VSW HA100 hemispherical analyzer. The samples were cleaned by Ar$^+$ sputtering (VSW AS10 ion source) for 5 min at 1 keV. The recorded elemental peaks were fitted with a Doniach-Sunjic function[84] convoluted with a Gaussian and linear background subtraction. As the O 1s and Sb 3d$_{5/2}$ peaks overlap, we used the Sb 3d$_{3/2}$ and the Sn 3d$_{3/2}$ peak (SnO_2 3d$_{3/2}$ 495.0 eV) to derive the chemical composition from the ratio of the Sb 3d$_{3/2}$ peak area to the sum of the Sb 3d$_{3/2}$ and Sn 3d$_{3/2}$ peak areas from the measured integral intensity of the peaks.[85] The composition of the valence states was evaluated by the Sb^{5+}/(Sb^{3+} + Sb^{5+}) ratio of the Sb 3d$_{3/2}$ peak following the method developed by

NANOSIZED ANTIMONY-DOPED TIN OXIDE/GRAPHENE COMPOSITES AS ANODE
MATERIAL IN LITHIUM-ION BATTERIES FOR FAST LITHIUM INSERTION

303

Terrier *et al.*[85,86] Thereby the Sb $3d_{3/2}$ peak was spitted into two Doniach-Sunjic function Gaussian lines centered at 540.04 eV[87] for Sb^{5+} and 539.24 eV[87] for Sb^{3+}. This variation of the binding energy of the Sb $3d_{3/2}$ peak is significant in XPS measurements and indicates clearly the presence of two oxidation states of antimony.

Thermogravimetric analysis (TGA) was performed on a NETZSCH STA 440 C TG/DSC using a heating rate of 10 K min^{-1} in a stream of synthetic air of about 25 mL min^{-1}.

Raman spectroscopy was carried out on a LabRAM HR UV/Vis Raman instrument from HORIBA JOBIN YVON with a OLYMPUS BX41 microscope, a SYMPHONY CCD detection system and a He-Ne laser ($\lambda = 633$ nm). In literature Raman spectroscopy is often used to verify the degree of the GO reduction by evaluating the intensity ratio of the D band and the G band, denoted as I_D/I_G. However this is not applicable to all nanocomposites, as reported by King *et al.*[88]. They reported that using the I_D/I_G ratio as a quality characteristic of graphene is problematic for both GO and rGO, as this methods rely on the analysis of the G peak, which is in fact a superposition of two peaks (G and D').[88] This is in well agreement with our results, which show almost no changes in the I_D/I_G ratio even after the thermal reduction step. All ATO/SnO_2 containing samples exhibits the typical bulk vibration modes of rutile-type SnO_2 (A_{1g} (630 cm^{-1}), B_{2g} (775 cm^{-1}) and E_g (477 cm^{-1})). Pure as-prepared ATO also exhibited the surface vibration modes (S1 (333 cm^{-1}) and S2/S3 (500 – 570 cm^{-1})), which are typical for nanosized ATO.[57] In the nanocomposites the surface vibration modes are suppressed due to particle growing and attachment to graphene (see Figure S11.3c in the supporting information).

Nitrogen sorption measurements were performed on a Quantachrome Autosorb-1 instrument at the boiling point of liquid nitrogen (approximately 77 K). Prior to the sorption experiments, the samples were degassed for 12 h at 150 ° under vacuum. The specific surface area was determined with the Brunauer-Emmett-Teller (BET) method at $p/p_0 = 0.05 - 0.2$. The pore size distribution was calculated using the DFT/Monte Carlo method and the nonlocal density functional theory (NLDFT) adsorption model with cylindrical/spherical pores.

SEM images were obtained with a FEI Helios NanoLab G3 UC scanning electron microscope equipped with a field emission gun operated at 3 kV. The powders were measured on carbon tabs glued onto a sample holder.

TEM measurements were carried out using a FEI Tecnai G2 20 S-TWIN or a Titan Themis 300 operated at 200 kV or 300 kV, respectively. For TEM sample preparation the powders

were pestle or dispersed in absolute ethanol, placed on a holey carbon coated copper grid and evaporated.

Electrochemical measurements were performed at room temperature on ECC-PAT-Core (EL-Cell) battery test cells using an Autolab potentiostat/galvanostat PGSTAT302N with a FRA32M module or a Autolab Multipotentiostat M101 with a 8AUT.M101 module operated with Nova 1.11 software. Cyclic voltammograms were recorded in a potential range of 0.01–3.0 V vs. Li/Li^+ using a scan rate of 0.5 mV s^{-1} and a step potential of 2.44 mV. The cells were charged and discharged galvanostatically at different C rates (1 C-60 C) in a voltage range of 0.01–3.0 V vs. Li/Li^+.

NANOSIZED ANTIMONY-DOPED TIN OXIDE/GRAPHENE COMPOSITES AS ANODE
MATERIAL IN LITHIUM-ION BATTERIES FOR FAST LITHIUM INSERTION

305

11.5. REFERENCES

(1)   Goriparti, S.; Miele, E.; De Angelis, F.; Di Fabrizio, E.; Proietti Zaccaria, R.; Capiglia, C. *J. Power Sources* **2014**, *257*, 421.

(2)   Pei, Z.; Li, Z.; Zheng, X. *J. Nanosci. Nanotechnol.* **2016**, *16*, 9028.

(3)   Roy, P.; Srivastava, S. K. *J. Mater. Chem. A* **2015**, *3*, 2454.

(4)   Tollefson, J. *Nature* **2008**, *456*, 436.

(5)   Etacheri, V.; Marom, R.; Elazari, R.; Salitra, G.; Aurbach, D. *Energy Environ. Sci.* **2011**, *4*, 3243.

(6)   Liu, C.; Li, F.; Ma, L. P.; Cheng, H. M. *Adv. Mater.* **2010**, *22*, E28.

(7)   Yang, Z.; Choi, D.; Kerisit, S.; Rosso, K. M.; Wang, D.; Zhang, J.; Graff, G.; Liu, J. *J. Power Sources* **2009**, *192*, 588.

(8)   Yang, Z.; Zhang, J.; Kintner-Meyer, M. C.; Lu, X.; Choi, D.; Lemmon, J. P.; Liu, J. *Chem. Rev.* **2011**, *111*, 3577.

(9)   Abraham, K. M. *J. Phys. Chem. Lett.* **2015**, *6*, 830.

(10)   Palacin, M. R. *Chem. Soc. Rev.* **2009**, *38*, 2565.

(11)   Deng, Y.; Fang, C.; Chen, G. *J. Power Sources* **2016**, *304*, 81.

(12)   Huang, X.; Boey, F.; Zhang, H. U. A. *Cosmos* **2010**, *06*, 159.

(13)   Liu, L.; Xie, F.; Lyu, J.; Zhao, T.; Li, T.; Choi, B. G. *J. Power Sources* **2016**, *321*, 11.

(14)   Zhao, X.; Zhang, J.; Zhang, J.; Gong, C.; Gu, X.; Ma, Z.; Zhou, J.; Yu, L.; Zhang, Z. *J. Power Sources* **2015**, *294*, 223.

(15)   Raju, V.; Wang, X.; Luo, W.; Ji, X. *Chemistry* **2014**, *20*, 7686.

(16)   Yin, L.; Chai, S.; Wang, F.; Huang, J.; Li, J.; Liu, C.; Kong, X. *Ceram. Int.* **2016**, *42*, 9433.

(17)   Guo, Q.; Chen, S.; Qin, X. *Mater. Lett.* **2014**, *119*, 4.

(18)   Zhu, X.; Zhu, Y.; Murali, S.; Stoller, M. D.; Ruoff, R. S. *J. Power Sources* **2011**, *196*, 6473.

(19)   Feckl, J. M.; Fominykh, K.; Döblinger, M.; Fattakhova-Rohlfing, D.; Bein, T. *Angew. Chem. Int. Ed.* **2012**, *51*, 7459.

(20)   Cevher, O.; Guler, M. O.; Tocoglu, U.; Akbulut, H. *Int. J. Energy Res.* **2014**, *38*, 499.

(21)   Cevher, O.; Tocoglu, U.; Akbulut, H. *Int. J. Hydrogen Energy* **2014**, *39*, 21429.

(22)   Liang, J.; Yu, X. Y.; Zhou, H.; Wu, H. B.; Ding, S.; Lou, X. W. *Angew. Chem. Int. Ed.* **2014**, *53*, 12803.

(23)   Liu, L.; An, M.; Yang, P.; Zhang, J. *Sci. Rep.* **2015**, *5*, 9055.

(24)   Lian, P.; Zhu, X.; Liang, S.; Li, Z.; Yang, W.; Wang, H. *Electrochim. Acta* **2011**, *56*, 4532.

(25)   Du, Z.; Yin, X.; Zhang, M.; Hao, Q.; Wang, Y.; Wang, T. *Mater. Lett.* **2010**, *64*, 2076.

(26)   Li, N.; Sonsg, H.; Cui, H.; Wang, C. *Electrochim. Acta* **2014**, *130*, 670.

(27)   Liu, X.; Zhong, X.; Yang, Z.; Pan, F.; Gu, L.; Yu, Y. *Electrochim. Acta* **2015**, *152*, 178.

(28)   Reddy, M. J.; Ryu, S. H.; Shanmugharaj, A. M. *Nanoscale* **2016**, *8*, 471.

(29)   Wang, X.; Zhou, X.; Yao, K.; Zhang, J.; Liu, Z. *Carbon* **2011**, *49*, 133.

(30)   Wu, G.; Wu, M.; Wang, D.; Yin, L.; Ye, J.; Deng, S.; Zhu, Z.; Ye, W.; Li, Z. *Appl. Surf. Sci.* **2014**, *315*, 400.

(31)   Xu, C.; Sun, J.; Gao, L. *J. Mater. Chem.* **2012**, *22*, 975.

(32)   Yang, Y.; Gao, Y.; Cheng, T.; Ma, D.; Liu, J.; Li, X. *RSC Adv.* **2016**, *6*, 67011.

(33)   Yao, J.; Shen, X.; Wang, B.; Liu, H.; Wang, G. *Electrochem. Commun.* **2009**, *11*, 1849.

(34)   Zhang, H.; Gao, L.; Yang, S. *RSC Adv.* **2015**, *5*, 43798.

(35)   Zhang, M.; Lei, D.; Du, Z.; Yin, X.; Chen, L.; Li, Q.; Wang, Y.; Wang, T. *J. Mater. Chem.* **2011**, *21*, 1673.

(36)   Zhang, M.; Sun, Z.; Zhang, T.; Sui, D.; Ma, Y.; Chen, Y. *Carbon* **2016**, *102*, 32.

(37)   Zhang, Y.; Jiang, L.; Wang, C. *Phys. Chem. Chem. Phys.* **2015**, *17*, 20061.

(38)   Zhao, B.; Zhang, G.; Song, J.; Jiang, Y.; Zhuang, H.; Liu, P.; Fang, T. *Electrochim. Acta* **2011**, *56*, 7340.

(39)   Zhao, K.; Zhang, L.; Xia, R.; Dong, Y.; Xu, W.; Niu, C.; He, L.; Yan, M.; Qu, L.; Mai, L. *Small* **2016**, *12*, 588.

(40)   Zhong, C.; Wang, J.; Chen, Z.; Liu, H. *J. Phys. Chem. C* **2011**, *115*, 25115.

(41)   Zhou, D.; Song, W.-L.; Li, X.; Fan, L.-Z. *Electrochim. Acta* **2016**, *207*, 9.

(42)   Zhou, X.; Liu, W.; Yu, X.; Liu, Y.; Fang, Y.; Klankowski, S.; Yang, Y.; Brown, J. E.; Li, J. *ACS Appl. Mater. Interfaces* **2014**, *6*, 7434.

(43)   Zhu, C.; Zhu, S.; Zhang, K.; Hui, Z.; Pan, H.; Chen, Z.; Li, Y.; Zhang, D.; Wang, D. W. *Sci. Rep.* **2016**, *6*, 25829.

(44)   Zhu, Y. G.; Wang, Y.; Xie, J.; Cao, G.-S.; Zhu, T.-J.; Zhao, X.; Yang, H. Y. *Electrochim. Acta* **2015**, *154*, 338.

(45)   Gao, T.; Huang, K.; Qi, X.; Li, H.; Yang, L.; Zhong, J. *Ceram. Int.* **2014**, *40*, 6891.

(46)   Liang, J.; Zhao, Y.; Guo, L.; Li, L. *ACS Appl. Mater. Interfaces* **2012**, *4*, 5742.

(47)   Tian, R.; Zhang, Y.; Chen, Z.; Duan, H.; Xu, B.; Guo, Y.; Kang, H.; Li, H.; Liu, H. *Sci. Rep.* **2016**, *6*, 19195.

(48)   Ye, F.; Zhao, B.; Ran, R.; Shao, Z. *Chemistry* **2014**, *20*, 4055.

(49)   Dhanabalan, A.; Li, X.; Agrawal, R.; Chen, C.; Wang, C. *Nanomaterials* **2013**, *3*, 606.

(50)   Jiang, Y.; Yuan, T.; Sun, W.; Yan, M. *ACS Appl. Mater. Interfaces* **2012**, *4*, 6216.

(51)   Li, X.; Meng, X.; Liu, J.; Geng, D.; Zhang, Y.; Banis, M. N.; Li, Y.; Yang, J.; Li, R.; Sun, X.; Cai, M.; Verbrugge, M. W. *Adv. Funct. Mater.* **2012**, *22*, 1647.

(52)   Zhou, X.; Wan, L. J.; Guo, Y. G. *Adv. Mater.* **2013**, *25*, 2152.

(53)   Sun, Y.; Zhao, C.; Shen, M.; Pan, Z.; Liu, X. *J. Alloys Compd.* **2016**, *683*, 191.

(54)   Kim, Y. S.; Kim, W. B.; Joo, Y. L. *J. Mater. Chem. A* **2014**, *2*, 8323.

(55)   Santos-Pena, J.; Brousse, T.; Sanchez, L.; Morales, J.; Scheich, D. M. *J. Power*

NANOSIZED ANTIMONY-DOPED TIN OXIDE/GRAPHENE COMPOSITES AS ANODE
MATERIAL IN LITHIUM-ION BATTERIES FOR FAST LITHIUM INSERTION

307

Sources **2001**, *97-98*, 232.

(56) Peters, K.; Zeller, P.; Stefanic, G.; Skoromets, V.; Němec, H.; Kužel, P.; Fattakhova-Rohlfing, D. *Chem. Mater.* **2015**, *27*, 1090.

(57) Müller, V.; Rasp, M.; Štefanić, G.; Ba, J.; Günther, S.; Rathousky, J.; Niederberger, M.; Fattakhova-Rohlfing, D. *Chem. Mater.* **2009** *21*, 5229.

(58) Wang, Y.; Brezesinski, T.; Antonietti, M.; Smarsly, B. *ACS Nano* **2009**, *3*, 1373.

(59) An, G. H.; Lee, D. Y.; Lee, Y. J.; Ahn, H. J. *ACS Appl. Mater. Interfaces* **2016**, *8*, 30264.

(60) Guler, M. O.; Cevher, O.; Tocoglu, U.; Cetinkaya, T.; Akbulut, H. *Acta Phys. Pol. A* **2013**, *123*, 383.

(61) Su, W.-W.; Wang, W.; Li, Y.-l.; Xu, L.; Wang, R. *Mater. Lett.* **2016**, *180*, 203.

(62) Liu, Y.; Palmieri, A.; He, J.; Meng, Y.; Beauregard, N.; Suib, S. L.; Mustain, W. E. *Sci. Rep.* **2016**, *6*, 25860.

(63) Dou, P.; Cao, Z.; Wang, C.; Zheng, J.; Xu, X. *Chem. Eng. J.* **2017**, *320*, 405.

(64) Pan, D.; Wan, N.; Ren, Y.; Zhang, W.; Lu, X.; Wang, Y.; Hu, Y. S.; Bai, Y. *ACS Appl. Mater. Interfaces* **2017**, *9*, 9747.

(65) Zhang, X.; Huang, X.; Zhang, X.; Xia, L.; Zhong, B.; Zhang, T.; Wen, G. *Electrochim. Acta* **2016**, *222*, 518.

(66) Mueller, F.; Bresser, D.; Chakravadhanula, V. S. K.; Passerini, S. *J. Power Sources* **2015**, *299*, 398.

(67) Wang, X.; Li, Z.; Zhang, Z.; Li, Q.; Guo, E.; Wang, C.; Yin, L. *Nanoscale* **2015**, *7*, 3604.

(68) Ba, C.; Shi, L.; Wang, Z.; Chen, G.; Wang, S.; Zhao, Y.; Zhang, M.; Yuan, S. *Res. Chem. Intermed.* **2017**.

(69) Wang, S.; Shi, L.; Chen, G.; Ba, C.; Wang, Z.; Zhu, J.; Zhao, Y.; Zhang, M.; Yuan, S. *ACS Appl. Mater. Interfaces* **2017**.

(70) Sun, J.; Xiao, L.; Jiang, S.; Li, G.; Huang, Y.; Geng, J. *Chem. Mater.* **2015**, *27*, 4594.

(71) Zhao, C.; Gao, H.; Chen, C.; Wu, H. *J. Mater. Chem. A* **2015**, *3*, 18360.

(72) Stobinski, L.; Lesiak, B.; Malolepszy, A.; Mazurkiewicz, M.; Mierzwa, B.; Zemek, J.; Jiricek, P.; Bieloshapka, I. *J. Electron. Spectrosc. Relat. Phenom.* **2014**, *195*, 145.

(73) Wang, Y.-X.; Chou, S.-L.; Liu, H.-K.; Dou, S.-X. *Carbon* **2013**, *57*, 202.

(74) Dubin, S.; Gilje, S.; Varshneya, R.; Wang, K.; Yang, Y.; Tung, V. C.; Kaner, R. B. *ACS Nano* **2010**, *4* 3845.

(75) Bondarenko, E. A.; Mazanik, A. V.; Streltsov, E. A.; Kulak, A. I.; Korolik, O. V. *Mater. Sci. Eng., B* **2015**, *202*, 61.

(76) Lee, W. C.; Kim, K.; Park, J.; Koo, J.; Jeong, H. Y.; Lee, H.; Weitz, D. A.; Zettl, A.; Takeuchi, S. *Nat. Nanotechnol.* **2015**, *10*, 423.

(77) Marcano, D. C.; Kosynkin, D. V.; Berlin, J. M.; Sinitskii, A.; Sun, Z.; Slesarev, A.; Alemany, L. B.; Lu, W.; Tour, J. M. *ACS Nano* **2010**, *4*, 4806.

(78) Chen, Z.; Li, H.; Tian, R.; Duan, H.; Guo, Y.; Chen, Y.; Zhou, J.; Zhang, C.; Dugnani, R.; Liu, H. *Sci. Rep.* **2016**, *6*, 27365.

(79)   Deng, D.; Kim, M. G.; Lee, J. Y.; Cho, J. *Energy Environ. Sci.* **2009**, *2*, 818.

(80)   Kim, H.; Park, G. O.; Kim, Y.; Muhammad, S.; Yoo, J.; Balasubramanian, M.; Cho, Y.-H.; Kim, M.-G.; Lee, B.; Kang, K.; Kim, H.; Kim, J. M.; Yoon, W.-S. *Chem. Mater.* **2014**, *26*, 6361.

(81)   Chen, B.; Qian, H.; Xu, J.; Qin, L.; Wu, Q.-H.; Zheng, M.; Dong, Q. *J. Mater. Chem. A* **2014**, *2*, 9345.

(82)   Chen, Y.; Song, B.; Chen, R. M.; Lu, L.; Xue, J. *J. Mater. Chem. A* **2014**, *2*, 5688.

(83)   Sher Shah, M. S. A.; Lee, J.; Park, A. R.; Choi, Y.; Kim, W.-J.; Park, J.; Chung, C.-H.; Kim, J.; Lim, B.; Yoo, P. J. *Electrochim. Acta* **2017**, *224*, 201.

(84)   Doniach, S.; Sunjic, M. *J. Phys. C: Solid State Phys.* **1970**, *3*, 285.

(85)   Terrier, C.; Chatelon, J. P.; Berjoan, R.; Roger, J. A. *Thin Solid Films* **1995**, *263*, 37.

(86)   Terrier, C.; Chatelon, J. P.; Roger, J. A. *Thin Solid Films* **1997**, *295*, 95.

(87)   Krishnakumar, T.; Jayaprakash, R.; Pinna, N.; Phani, A. R.; Passacantando, M.; Santucci, S. *J. Phys. Chem. Solids* **2009**, *70*, 993.

(88)   King, A. A.; Davies, B. R.; Noorbehesht, N.; Newman, P.; Church, T. L.; Harris, A. T.; Razal, J. M.; Minett, A. I. *Sci. Rep.* **2016**, *6*, 19491.

NANOSIZED ANTIMONY-DOPED TIN OXIDE/GRAPHENE COMPOSITES AS ANODE
MATERIAL IN LITHIUM-ION BATTERIES FOR FAST LITHIUM INSERTION

309

11.6. SUPPORTING INFORMATION
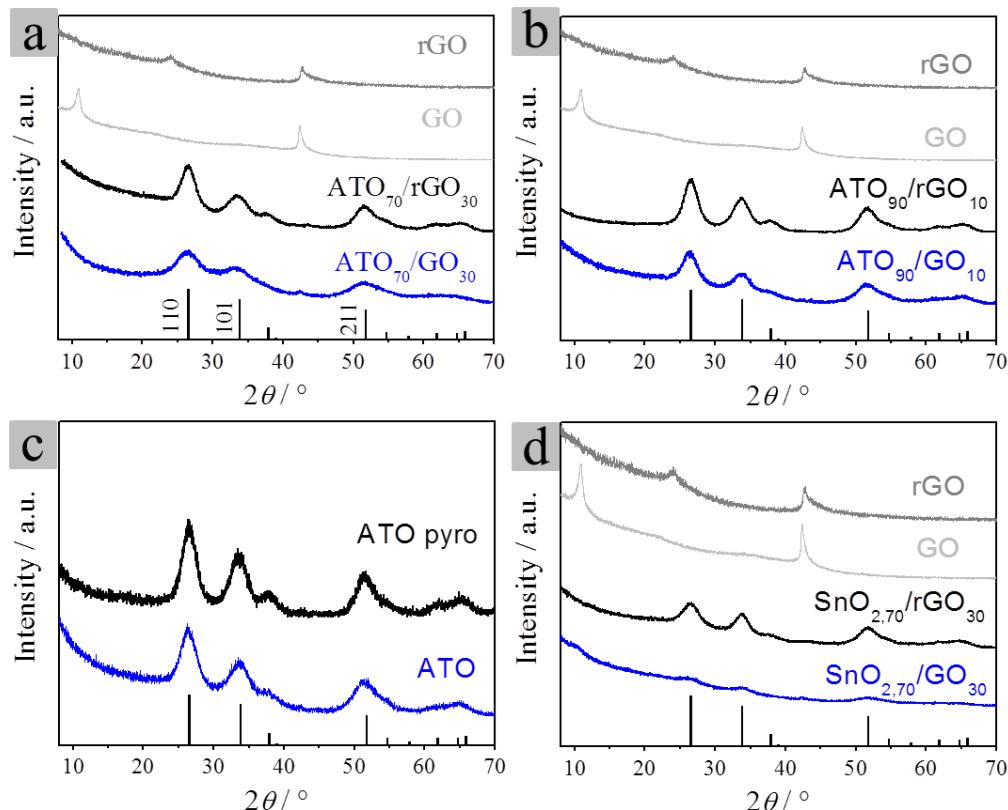
Figure S11.1 XRD pattern of microwave (a, c, d) and oven (b) synthesized ATO_{70}/GO_{30} (a), ATO_{90}/GO_{10} (b), pure ATO (c) and $SnO_{2,70}/GO_{30}$ (d) before (blue line) and after pyrolysis (black line). The bars in the bottom of the XRD pattern mark the position and the intensity of the diffraction lines of SnO_2 cassiterite (space group $P4_2/mnm$, JCPDS File Card No. 41-1445).
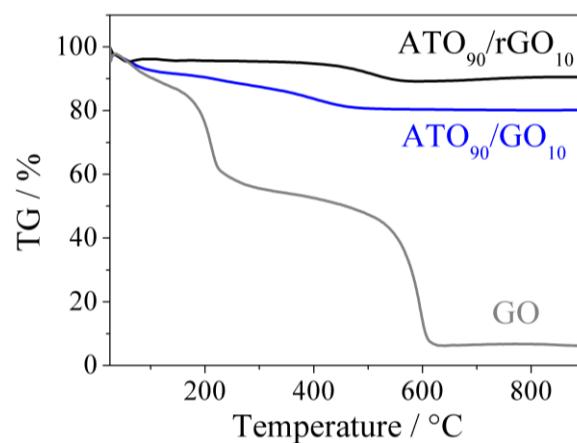
Figure S11.2 TGA curves of an oven synthesized (100°C) ATO_{90}/GO_{10} nanocomposite compared with pure GO. The weight loss associated with the rGO decomposition was used for quantification of the rGO content in the pyrolyzed composites. The weight loss corresponds to the initial ratio of GO in the reaction mixture.
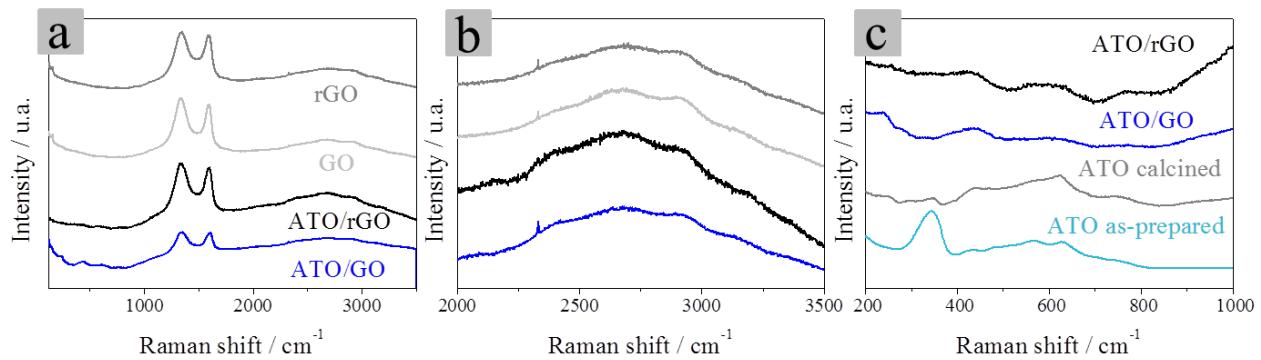
Figure S11.3 (a) Overview Raman spectra of ATO_{70}/GO_{30} nanocomposites and pure GO before and after pyrolysis. (b) Zoom-in in the high shift region of the spectra showing the 2D and D+G bands. (c) Comparison of pure ATO nanoparticles with ATO_{70}/GO_{30} nanocomposites, showing the typical bulk vibration modes corresponding to rutile-type SnO_2, namely A_{1g} (630 cm^{-1}), B_{2g} (775 cm^{-1}) and E_g (477 cm^{-1}). The surface vibrations modes typical for nano-sized SnO_2, namely S1 (333 cm^{-1}) and S2/S3 (500 – 570 cm^{-1}), are only visible for pure, as-prepared ATO nanoparticles.
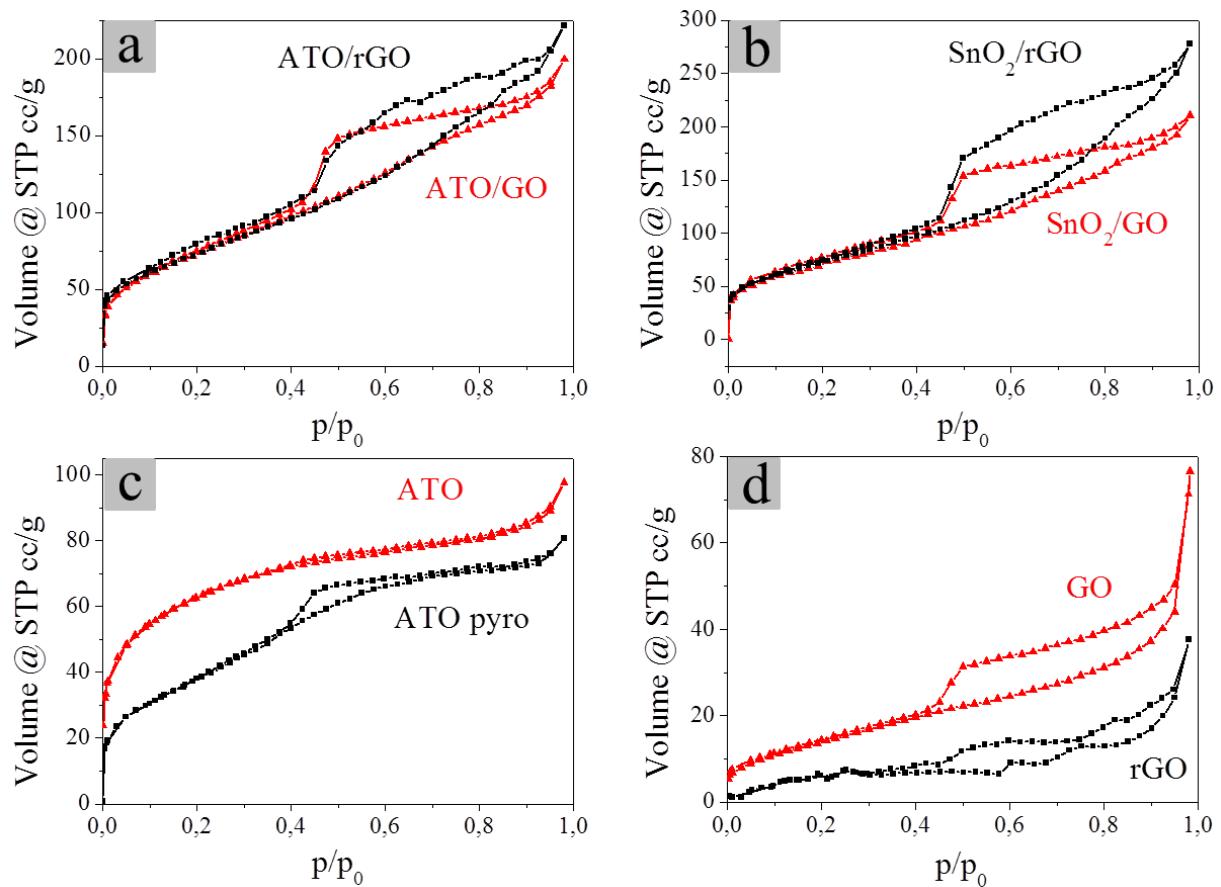
Figure S11.4 Nitrogen adsorption-desorption isotherms of ATO_{70}/GO_{30} (a), $SnO_{2,70}/GO_{30}$ (b), pure ATO nanoparticles (c) and GO (d) before (▲ red line) and after pyrolysis (■ black line). The corresponding BET surface areas and pore sizes are summarized in the following Table (Table S11.1).

Table S11.1 Textural parameters of ATO_{70}/GO_{30} (a), $SnO_{2,70}/GO_{30}$ (b), pure ATO nanoparticles (c) and GO (d) before and after pyrolysis extracted from nitrogen adsorption–desorption isotherms from Figure S11.4. The specific surface area was determined by the BET method and the pore size distribution was calculated using the nonlocal density functional theory (NLDFT) adsorption model with cylindrical/spherical pores.

Panel of Figure S11.4	Sample name	BET surface area [$m^2\ g^{-1}$]	Pore size [nm]
a (▲)	ATO_{70}/GO_{30}	270	5.8
a (■)	ATO_{70}/rGO_{30}	263	6.0
b (▲)	$SnO_{2,70}/GO_{30}$	260	6.0
b (■)	$SnO_{2,70}/rGO_{30}$	266	6.0
c (▲)	ATO	224	2.6
c (■)	ATO pyro	140	4.1
d (▲)	GO	54	3.8
d (■)	rGO	26	7.3
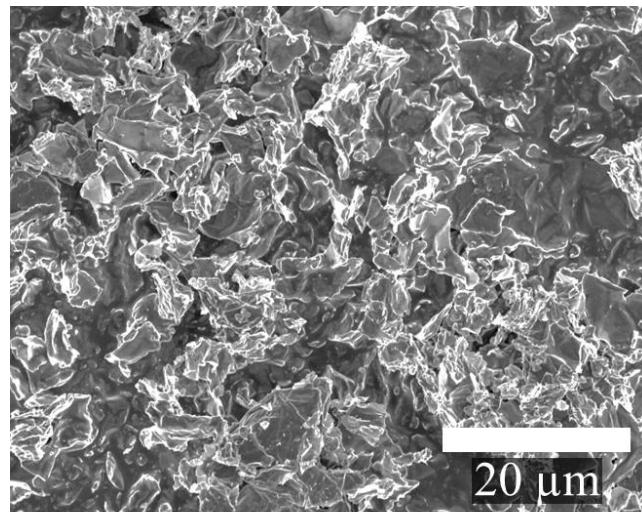
Figure S11.5 Low magnification SEM image of an pyrolyzed ATO_{70}/rGO_{30} nanocomposite proving the homogeneity of the material, as none of the spherical ATO agglomerates has been observed.
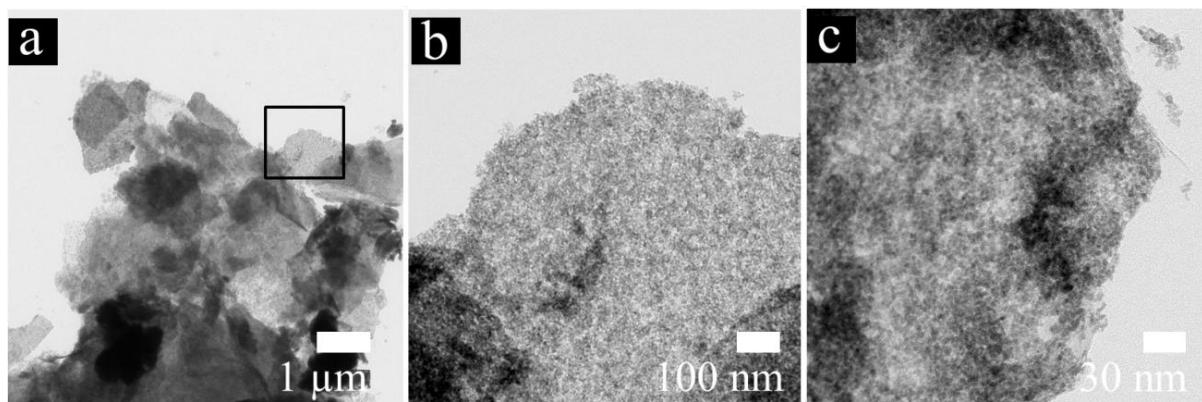
Figure S11.6 TEM images of an ATO_{70}/rGO_{30} nanocomposite pyrolyzed in nitrogen at 400 °C. (a) Low magnification TEM showing overlapping graphene flakes and (b) zoom in from the marked area in (a). (c) TEM images taken from another area showing highly crystalline, small ATO nanoparticles, which decorate the graphene nanosheets.
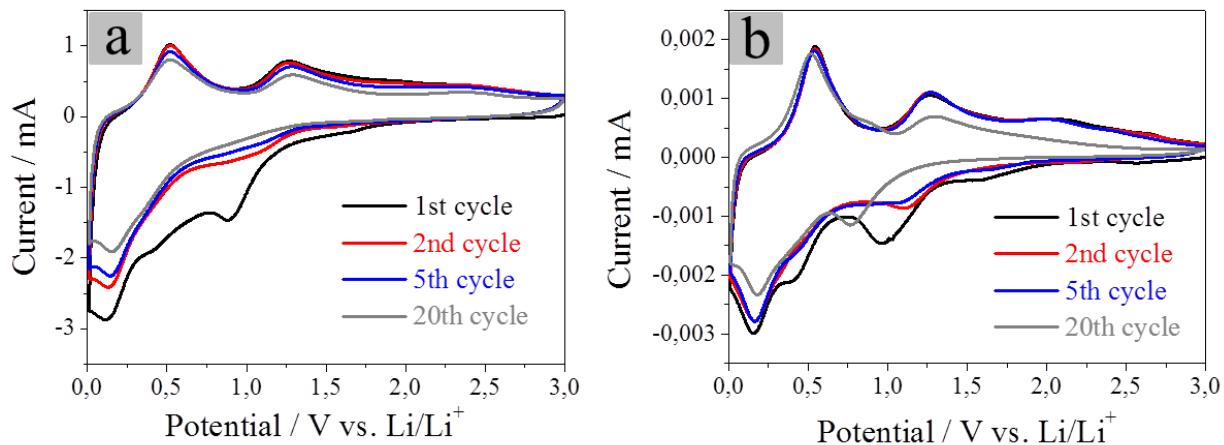
Figure S11.7 Cyclic voltammograms of $SnO_{2,70}/rGO_{30}$ nanocomposites (a) and pure ATO nanoparticle based electrodes (b) showing their cycling stability. The CVs were recorded with a scan 0.5 mV s^{-1} and a step potential of 2.44 mV in the range of 0.01 – 3 V vs. Li/Li$^+$. The first discharge curve corresponding to the lithium ion insertion process differs significantly from the subsequent cycles due to the irreversible formation of a solid electrolyte interface (SEI) layer that disappears in the following scans.

NANOSIZED ANTIMONY-DOPED TIN OXIDE/GRAPHENE COMPOSITES AS ANODE
MATERIAL IN LITHIUM-ION BATTERIES FOR FAST LITHIUM INSERTION

313
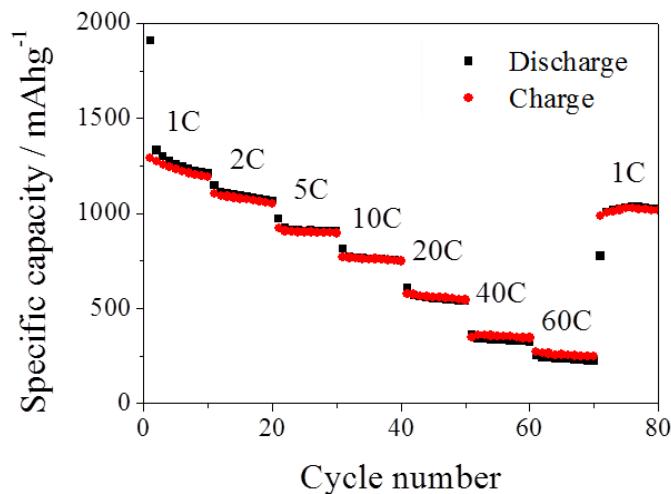
Figure S11.8 Rate performance of an ATO_{70}/rGO_{30} electrode with a loading of 0.6 mg cm^{-1} at different rates ranging from 1 to 60C (ten cycles at each C-rate). Charge and discharge capacities correspond to the red ($\bullet$) and black ($\blacksquare$) labels, respectively. The electrodes deliver specific discharge capacities of 1260 mAh g^{-1} (1C; 5th cycle),1092 mAh g^{-1} (2C; 15th cycle), 909 mAh g^{-1} (5C; 25th cycle), 762 mAh g^{-1} (10C; 35th cycle), 550 mAh g^{-1} (20C; 45th cycle), 335 mAh g^{-1} (40C; 55th cycle) and 235 mAh g^{-1} (60C; 65th cycle). These values correspond to a capacity loss of 13% (2C), 28% (5C), 40% (10C), 56% (20C), 73% (40C) and 81% (60C) compared to the initial capacity at 1C (1260 mAhg^{-1}). The capacity retrieves to 1031 mAh g^{-1} after 80 cycles between 1C and 60C, which corresponds to 82% of the initial capacity.
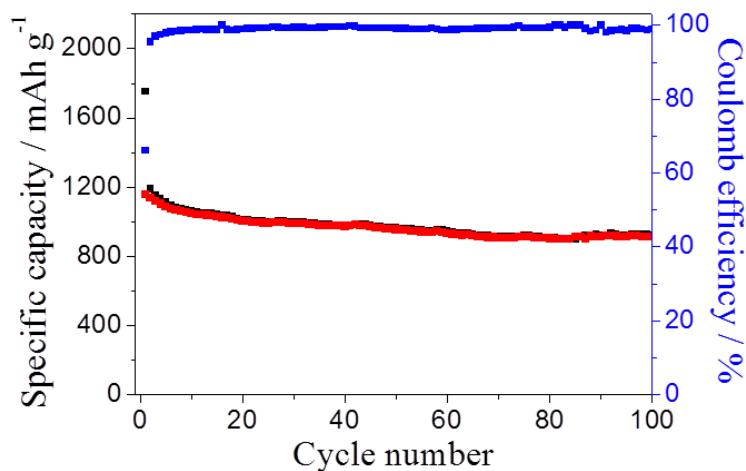
Figure S11.9 Multicycling stability of a $SnO_{2,70}/rGO_{30}$ electrode (loading 0.2 mg cm^{-1}) at a rate of 1C and the corresponding coulombic efficiencies ($\blacksquare$ blue labels). Charge and discharge capacities correspond to the red ($\bullet$) and black ($\blacksquare$) labels, respectively. The specific capacity reaches 1188 mAh g^{-1}/1135 mAh g^{-1} (discharge/charge) in the second cycle, which is close to the theoretical lithium insertion capacity of the composite (1269 mAh g^{-1}), and reaches 918 mAh g^{-1} after 100 cycles.
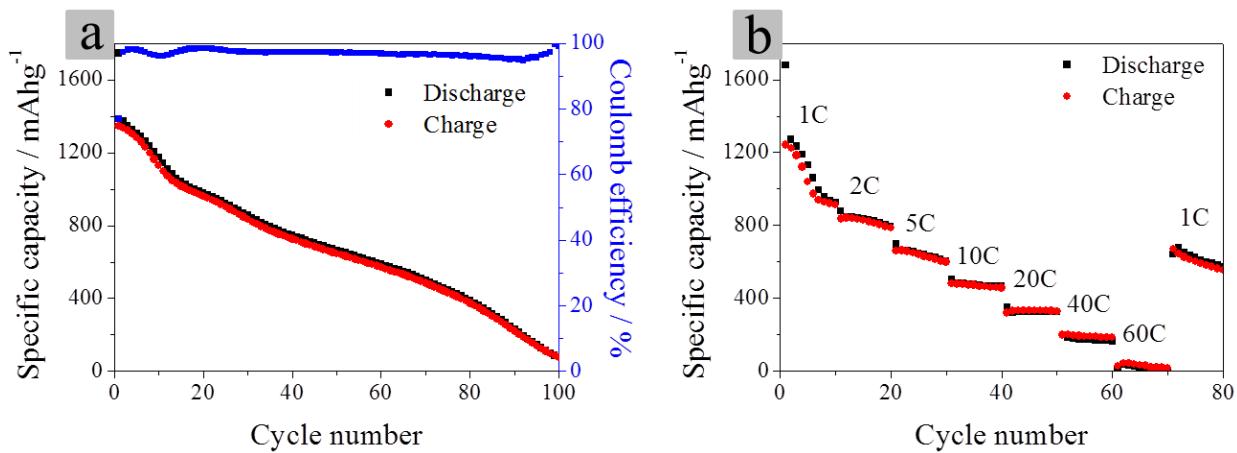
Figure S11.10(a) Multicycling stability of an ATO electrode (loading 0.2 mg cm^{-1}) at a rate of 1C and the corresponding coulombic efficiencies (■ blue labels). Charge and discharge capacities correspond to the red (●) and black (■) labels, respectively. After 100 cycles at 1C, the electrode maintains a capacity of only 77 mAh g^{-1}. (b) Rate performance of an ATO electrode at different rates ranging from 1 to 60C (ten cycles at each C-rate). The electrodes deliver specific discharge capacities of 1132 mAh g^{-1} (1C; 5th cycle), 838 mAh g^{-1} (2C; 15th cycle),647 mAh g^{-1} (5C; 25th cycle), 477 mAh g^{-1} (10C; 35th cycle), 327 mAh g^{-1} (20C; 45th cycle), 173 mAh g^{-1} (40C; 55th cycle) and 20 mAh g^{-1} (60C; 65th cycle). These values correspond to a capacity loss of 26% (2C), 43% (5C), 61% (10C), 71% (20C), 84% (40C) and 98% (60C) compared to the initial capacity at 1C (1132 mAhg^{-1}). The capacity retrieves to 573 mAh g^{-1} after 80 cycles between 1C and 60C, which corresponds to an irreversible capacity loss of 50%.

12. CONCLUSIONS AND OUTLOOK

The major objectives of this thesis were the development of procedures for the preparation of water-dispersible crystalline TCO nanoparticles and their assembly to extended electrode architectures and hybrid nanocomposite electrodes. The new high surface area electrodes and hybrid structures were successfully applied for energy conversion and storage applications, such as bioelectrocatalysis, photoelectrochemical water splitting and lithium ion batteries.

The solvothermal reaction in *tert*-butyl alcohol shown in Chapter 3 enabled the formation of ultra-small (3.1 nm ± 0.5 nm), uniform and highly crystalline ATO nanoparticles. An extraordinary high doping level of Sb (more than 50 at%) was achieved, which could be attributed to an increased element solubility on the nanoscale. The *tert*-butoxide groups offer sufficient steric control to hinder particle growth and aggregation during the synthesis resulting in the formation of uniform nanoparticles. Furthermore, the organic residues on the surface prevent the particles from agglomeration and therefore allow their redispersion in polar solvents. Due to the low boiling point of *tert*-butanol, the adsorbed surface molecules can be removed easily from the particle surface leading to an enhanced purity and conductivity of the final product. The non-calcined ATO nanoparticles prepared with 3 mol % Sb feature the highest ever reported conductivity for such small ATO nanoparticles $(6.8 \times 10^{-2}\,\text{S cm}^{-1})$. By annealing in air at 500 °C the conductivity of the doped ATO nanoparticles is increased by about three orders of magnitude up to 62 S cm^{-1}. The undoped as-prepared SnO$_2$ nanoparticles exhibited a reasonable high conductivity of $2.8 \times 10^{-3}\,\text{S cm}^{-1}$ indicating a high bulk defect concentration in the particles due to the formation of oxygen vacancies and tin interstitials. Upon calcination in air the conductivity of the undoped nanoparticles decreased due to healing of the defects.

To get insight into the charge transport mechanism of undoped and Sb-doped SnO$_2$ nanoparticles, time-domain terahertz spectroscopy was employed (Chapter 6). The measurements revealed that the conductivity increase upon doping is caused by the transition from hopping in the undoped samples to band-like conduction in the doped samples. Furthermore, it could be shown that the calcination at elevated temperatures (500°C) enhanced both intra- and inter-nanoparticle conductivity. In general, the dc conductivity did not vary substantially with doping and remained much lower than the values determined by

THz spectroscopy, supporting the conclusion that the dc conductivity is controlled mainly by interfaces rather than by the conductivity inside the nanoparticles.

Another objective of this thesis was the development of new synthesis strategies towards 3D high surface area electrodes using preformed nanocrystals (ATO or ITOH) as building blocks (Chapter 3–5). The direct co-deposition of ATO or ITOH nanoparticles with PMMA beads enabled a facile large-scale fabrication of homogeneous ATO or ITO coatings with an open interconnected macroporosity, a good adhesion to the substrate, good optical quality and tunable thickness (Chapter 3 and Chapter 5). Smaller pores could be obtained by using the evaporation induced self-assembly of ATO nanoparticles with a PEO-*b*-PHA polymer, which allowed for the fabrication of coatings with tunable pore sizes ranging from 10 nm to 80 nm by changing the solution processing conditions (Chapter 4). These strategies enabled to adjust the pore size to the specific requirements of individual applications to optimize the overall performance of the electrochemical devices.

The open interconnected porosity of the TCO scaffolds makes them suitable conducting platforms for the immobilization of redox species or for the deposition of functional electroactive layers. However, for the application as conducting electrodes it is important that the increase in surface area due to the nanostructuring fully translates into an increase in electrochemical accessible conducting interface. This was shown in Chapter 4 on an example of adsorbed molybdenum polyoxometalate anions that showed a significant increase in electrochemical response proportional to the accessible surface area. In this context we could also show the importance of a proper electrode design on the performance of Photosystem I based biophotovoltaics. A pore size of at least 80 nm was necessary to host the bulky photoactive biomolecules resulting in an 11-fold enhancement of the photocurrent compared to PSI adsorbed on flat ITO. In Chapter 5 we have demonstrated that the heme proteins cytochrome c and hemoglobin could be efficiently immobilized on macroporous ITO. The protein functionalized electrodes demonstrated a 10-times higher direct electron transfer from the heme complex to the macroporous ITO electrode compared to a flat one. A more effective strategy compared to the direct electron transfer is the entrapment of an enzyme within a conductive redox polymer network, which serves as an immobilization matrix without inhibiting the catalytic activity of the entrapped enzyme. In Chapter 8–10 we have shown that the combination of a redox polymer matrix with a high surface area ITO electrode results in a record bioelectrocatalytic performance. Using different enzymes, namely pyrroloquinoline quinone-dependent glucose dehydrogenase (Chapter 8), fructose dehydrogenase (Chapter 9) and xanthine dehydrogenase (Chapter 10) we have proven that the enzymes entrapped in a

sulfonated polyaniline matrix on macroporous ITO resulted in a 200-, 35- and 5-fold increased bioelectrocatalytic signal compared to that on flat ITO electrodes. The suitability of those conducting platforms for the immobilization of functional electroactive layers was shown for ALD deposited zinc ferrite on macroporous ATO electrodes (see Chapter 7). The photocurrent increased up to five times by using nanostructured ATO scaffolds underneath the absorber layer.

Using the *tert*-butanol route we were also able to grow ultra-small ATO nanoparticles on the graphene sheets resulting in homogeneous nanocomposites (Chapter 11). The hybrid structures showed superior electrochemical properties as anode material lithium ion batteries compared to pure ATO nanoparticles or undoped SnO_2/rGO composites. The obtained nanocomposite showed a very high initial capacity, which is close to the theoretical value and decreased only by 29% after 100 cycles. Even at higher charging and discharging rates of 60C meaning full charging or discharging in one minute, the capacity remained 49% of the initial capacity (577 mAh g^{-1}), which is the highest ever reported value at such high C-rates. Excellent electrochemical performance of the obtained nanocoposites results from the combination of several factors such as the presence of graphene buffering the volume expansion and increasing the total electrode conductivity, the increased effective contact area between electrode and liquid electrolyte, the higher conductivity brought by antimony doping and finally the small size of the nanoparticles allowing for a higher overall capacity.

In conclusion, we have developed a way to fabricate ultra small water-dispersible ATO nanocrystals that were not accessible before. Further research is needed to investigate the mechanism of nanoparticle formation in *tert*-butanol and their electrosteric stabilization in polar solvents. This knowledge could help to improve and control the nanocrystal formation as well as the surface chemistry. Furthermore, we have developed strategies to assemble the nanoparticles to porous TCO electrodes with tailored morphology using different soft and hard templates. Further research may focus on the extension of the soft-templating approach to even larger pore sizes facilitating the large scale fabrication of highly ordered macroporous TCO scaffolds. The dc conductivity of the porous scaffolds can be further improved by eliminating interfacial resistances, for example by using the brick and mortar approach. For the application as anode material in LIBs, further research is needed to investigate the stabilizing role of antimony doping in SnO_2 based materials.

13. APPENDIX

LIST OF ABBREVIATIONS

2θ	Diffraction angle
2D	Two dimensional
3D	Three dimensional
AACVD	Aerosol-assisted chemical vapor deposition
ABPE	Applied-bias power efficiency
ALD	Atomic layer deposition
AFM	Atomic force microscopy
ATO	Antimony doped tin oxide
AZO	Aluminum doped zinc oxide
BET	Brunauer-Emmett-Teller
BF	Bright field
BSE	Back scattered electron
C-AFM	Conductive atomic force microscopy
CB	Conduction band
CCT	Colloidal crystal templating
CMC	Critical micelle concentrations
CNT	Carbon nanotubes
CV	Cyclic voltammetry
CVD	Chemical vapor deposition
DCPIP	2,6-dichlorophenolindophenol
DCM	Dichloromethane
DFT	Density functional theory
DLS	Dynamic light scattering
DSC	Differential scanning calorimetry
EC	Ethylene carbonate
EDTA	Ethylenediaminetetraacetic acid
EDX	Energy dispersive X-ray spectroscopy

EELS	Electron energy loss spectroscopy
E_g	Band gap energy
EIS	Electrochemical impedance spectroscopy
EISA	Evaporation-induced self-assembly
EM	Electron microscopy
EQE	External quantum efficiency
EtOH	Ethanol
FAD	Flavin adenine dinucleotide
Fd	Ferredoxin
FDH	Fructose dehydrogenase
FTO	Fluorine doped tin oxide
FWHM	Full width at half maximum
GLAD	Glancing angle deposition
GISAXS	Grazing-incident small-angle X-ray scattering
GPC	Growth rate per cycle
HAADF-STEM	High-angle annular dark-field mode
HCl	Hydrochloric acid
HOMO	Highest occupied molecular orbital
HPC	Hydroxypropyl cellulose
HR	High resolution
HRTEM	High resolution transmission electron microscopy
HX	Hypoxanthine
ICP-MS	Inductively coupled plasma mass spectrometry
IMPS	Intensity-modulated photocurrent spectroscopy
IR	Infrared
LED	Light emitting diode
LIB	Lithium-ion battery
IPCE	Incident photon-to-current efficiency
ITO	Indium doped tin oxide
ITOH	Indium doped tin hydroxide
IUPAC	International Union of Pure and Applied Chemistry
LUMO	Lowest unoccupied molecular orbital
MAS	2-methoxyaniline-5-sulfonic acid
MWCNT	Multiwall carbon nanotube

NCC	Nano crystalline cellulose
NHE	Normal hydrogen electrode
NLDFT	Non-local density functional theory
nm	Nanometer
NP	Nanoparticle
NW	Nanowire
MMA	Methylmethacrylate
MV	Methyl viologen
Mo-POM	Molybdenum polyoxometalate anion ($PMo_{12}O_{40}^{3-}$)
OLED	Organic light-emitting diode
PEO	Poly(ethylene oxide)
PEO-*b*-PHA	poly(ethylene oxide-*b*-hexyl acrylate)
Pluronic F127	Poly((ethylene oxide)$_{106}$-(propylene oxide)$_{70}$-(ethylene oxide)106)
PMMA	Poly (methyl methacrylate)
PMSA1	Sulfonated polyaniline (poly(2-methoxyaniline-5-sulfonic acid)-*co*-aniline)
PQQ-GDH	Pyrroloquinoline quinone dependent glucose dehydrogenase
PS	Polystyrene
PSI	Photosystem I
PSII	Photosystem II
PVD	Physical vapor deposition
rpm	Rounds per minute
SAED	selected-area electron diffraction
SAXS	small angle x-ray scattering
SDA	Structure directing agent
SE	Secondary electrons
SEI	Solid electrolyte interface
SEM	Scanning electron microscopy
STEM	Scanning transmission electron microscopy
TC	Transparent conductor
TCC	Transparent conductive coating
TCO	Transparent conducting oxide
TEM	Transmission electron microscopy
THF	Tetrahydrofuran

THz	Terahertz
tert-BuOH	*tert*-Butyl alcohol
TGA	Thermal gravimetric analysis
μm	Micrometer
UHV	Ultra-high vacuum
UV-Vis	Ultraviolet-visible
VB	Valence band
VLS	Vapor–liquid–solid
wt%	Weight%
XDH	Xanthine dehydrogenase
XPS	X-ray photoelectron spectroscopy
XRD	X-ray diffraction

14. PUBLICATIONS AND PRESENTATIONS

14.1. PUBLICATIONS

FIRST AUTHOR

1. *Nanosized Antimony-doped tin oxide/ graphene composites as anode material for lithium-ion batteries for fast lithium insertion*

   Peters, K.*; Zoller, F.*; Zeller, P.; Zehetmaier, P.; Döblinger, M.; Sofer, Z.; Fattakhova-Rohlfing, D.

   Manuscript in preparation

2. *Nanostructured Antimony-Doped Tin Oxide Layers with Tunable Pore Architectures as Versatile Transparent Current Collectors for Biophotovoltaics*

   Peters, K.; Lokupitiya, H. N.; Sarauli, D.; Labs, M.; Pribil, M.; Rathouský, J.; Kuhn, A.; Leister, D.; Stefik, M.; Fattakhova-Rohlfing, D.

   Adv. Funct. Mater. **2016**, 26, 6682–6692 (front cover)

3. *Water-Dispersible Small Monodisperse Electrically Conducting Antimony Doped Tin Oxide Nanoparticles*

   Peters, K.; Zeller, P.; Stefanic, G.; Skoromets, V., Němec, H.; Kužel, P.; Fattakhova-Rohlfing, D.

   Chem. Mater. **2015**, *27*, 1090−1099

4. *Macroporous indium tin oxide electrode layers as conducting substrates for immobilization of bulky electroactive guests*

   Liu, Y.*; **Peters, K.***; Mandlmeier, B.; Müller, A.; Fominykh, K.; Rathousky, J.; Scheu, C.; Fattakhova-Rohlfing, D.

   Electrochim. Acta **2014**, *140*, 108–115

CONTRIBUTIONS

5. *Alkaline Earth Metal Salts of 5,5'-Bistetrazole – from Academical Interest to Practical Application*

    Fischer, N.; Klapötke, T. M.; **Peters, K.**; Rusan, M.; Stierstorfer, J.

    ZAAC **2011**, *637,* 1693–1701

6. *3D-Electrode Architectures for Enhanced Direct Bioelectrocatalysis of Pyrroloquinoline Quinone-Dependent Glucose Dehydrogenase*

    Sarauli, D.; **Peters, K.**; Xu, C.; Schulz, B.; Fattakhova-Rohlfing, D. and Lisdat, F.

    ACS Appl. Mater. Interfaces **2014**, *6*, 17887−17893

7. *Interaction of Fructose Dehydrogenase with a Sulfonated Polyaniline: Application for Enhanced Bioelectrocatalysis*

    Sarauli, D.; Wettstein, C.; **Peters, K.**; Schulz, B.; Fattakhova-Rohlfing, D.; Lisdat, F.

    ACS Catal. **2015**, *5,* 2081−2087

8. *Conductivity Mechanisms in Sb-Doped SnO2 Nanoparticle Assemblies: DC and Terahertz Regime*

    Skoromets V.; Němec H.; Kopeček J.; Kužel P.; **Peters K.**; Fattakhova-Rohlfing D.; Vetushka A.; Müller M.; Ganzerová K.; Fejfar A.

    J. Phys. Chem. C **2015**, *119*, 19485–19495

9. *Spray Deposition of Titania Films with Incorporated Crystalline Nanoparticles for All-Solid-State Dye-Sensitized Solar Cells Using P3HT*

    Song, L.; Wang, W.; Körstgens, V.; Moseguí González, D.; Yao, Y.; Minar, N. K.; Feckl, J. M.; **Peters, K.**; Bein, T.; Fattakhova-Rohlfing, D.; Santoro, G.; Roth, S. V.; Müller-Buschbaum, P.

    Adv. Funct. Mater. **2016,** *26*, 1498–1506 (front cover)

10. *Control of perovskite crystal growth by methylammonium lead chloride templating*

Binek, A.* Grill, I.*; Huber, N.; **Peters, K.**; Hufnagel, A. G.; Handloser, M.; Docampo, P.; Hartschuh, A.; Bein, T.

Chem. Asian J. **2016**, *11*, 1199–1204 (front cover)

11. *Zinc Ferrite Photoanode Nanomorphologies with Favorable Kinetics for Water-Splitting*

Hufnagel, A. G.; **Peters, K.**; Müller, A.; Scheu, C.;Fattakhova-Rohlfing, D.; Bein, T.

Adv. Funct. Mater. **2016**, *26*, 4435–4443 (front cover)

12. *Investigation of the pH-Dependent Impact of Sulfonated Polyaniline on Bioelectrocatalytic Activity of Xanthine Dehydrogenase*

Sarauli, D.; Borowski, A.; **Peters, K.**; Schulz, B.; Fattakhova-Rohlfing, D.; Leimkühler, S.; Lisdat, F.

ACS Catal. **2016**, *6*, 7152–7159

13. *Black Magic in Grey Titania: Noble-Metal-Free Photocatalytic H_2 Evolution from Hydrogenated Anatase*

Liu, N.; Zhou, X.; Nguyen, N. T.; **Peters, K.**; Zoller, F.; Hwang, I.; Schneider, C.; Miehlich, M. E.; Freitag, D.; Karsten, M.; Fattakhova-Rohlfing, D.; Schmuki, P

ChemSusChem **2016**, *10*, 62–67

14. *In Situ Study of Degradation in P3HT-titania Based Solidstate Dye-sensitized Solar Cells*

Song, L.; Wang, W.; Pröller, S.; Moseguí González, D.; Schlipf, J.; Schaffer, C. J.; **Peters, K.**; Herzig, E. M.; Bernstorff, S.; Bein, T.; Fattakhova-Rohlfing, D.; Müller-Buschbaum, P.

ACS Energy Lett. **2017**, *2*, 991–997

15. *In situ study of spray deposited titania photoanodes for scalable fabrication of solid-state dye-sensitized solar cells*

Song, L.; Wang, W.; Körstgens, V.; Moseguí González, D.; Löhrer, F. C.; Schaffer, C. J.; Schlipf, J.; **Peters, K.**; Bein, T.; Fattakhova-Rohlfing, D.; Roth, S. V.; Müller-Buschbaum, P.

Nano Energy **2017** *submitted*

16. *Oriented Films of Conjugated 2D Covalent Organic Frameworks as Photocathodes for Solar Water Splitting*

Sick, T.*; Hufnagel, A. G.*; Kampmann, J.*; Kondofersky, I.; Calik, M.; Rotter, J.; Evans, A.; Döblinger, M.; Herbert, S.; **Peters, K.**; Böhm, D. M.; Knochel, P.; Medina, D. D.; Fattakhova-Rohlfing, D.*; Bein, T.*

J. Am. Chem. Soc. **2017** *submitted*

17. *Conditioning Germanium for High-Columbic-Efficiency Lithium Battery Based on Macroporous Inverse Opal Structures*

Geier, S.; Jung, R.; **Peters, K.**; Gasteiger, H. A.; Fattakhova-Rohlfing, D., Fässler; T. F.

Energy Environ. Sci. **2017** *submitted*

*These authors contricuted equally

CONFERENCE PAPER

18. *Charge Transport in Sb-doped SnO$_2$ Nanoparticles Studied by THz Spectroscopy*

Skoromets, V.; Němec H.; **Peters, K.**; Fattakhova-Rohlfing, D.; Kužel, P.

40th International Conference on Infrared, Millimeter, and Terahertz waves (IRMMW-THz) **2015**, DOI: 10.1109/IRMMW-THz.2015.7327718

14.2.   ORAL PRESENTATIONS

1. *Transparent conducting electrodes with a periodic porous architecture*

   Kristina Peters, Ksenia Fominykh, Peter Zehetmaier, Thomas Bein, Dina Fattakhova-Rohlfing

   European Materials Research Society (E-MRS) spring meeting 2014, Lille, France.

2. *Porous transparent conducting electrodes assembled from nanocrystals*

   Kristina Peters, Dina Fattakhova-Rohlfing

   5. International Symposium on Transparent Conductive Materials (TCM) 2014, Crete, Greece

3. P*orous architectures of transparent conducting electrodes for bioinspired optoelectronics*

   Kristina Peters, David Sarauli, Thomas Bein, Dina Fattakhova-Rohlfing

   European Materials Research Society (E-MRS) spring meeting 2016, Lille, France.

4. *Nanostructured architectures of transparent conducting oxides for bioinspired optoelectronics*

   Kristina Peters, David Sarauli, Thomas Bein, Dina Fattakhova-Rohlfing

   International Materials Research Congress (IMRC) 2016, Cancun, Mexico.

5. *Nanostructured transparent conducting oxide layers as versatile current collectors for bioelectronics*

   Kristina Peters, David Sarauli, Thomas Bein, Dina Fattakhova-Rohlfing

   European Materials Research Society (E-MRS) spring meeting 2017, Strasbourg, France.

6. *Towards nanostructured transparent conducting oxide electrodes with tunable pore architectures*

   Kristina Peters, Morgan Stefik, Thomas Bein, Dina Fattakhova-Rohlfing

   European Materials Research Society (E-MRS) spring meeting 2017, Strasbourg, France.

14.3.   POSTER PRESENTATIONS

1. *Nanostructured transparent conducting electrodes for photoelectrochemistry*

    Kristina Peters, Ksenia Fominykh, Peter Zehetmaier, Thomas Bein, Dina Fattakhova-Rohlfing

    Soltech Workshop, 2014, Wildbad Kreuth, Germany.

2. *Porous transparent conducting electrodes assembled from nanocrystals for photoelectrochemistry*

    Kristina Peters, Peter Zehetmaier, Thomas Bein, Dina Fattakhova-Rohlfing

    Soltech Workshop, 2015, Kloster Banz, Germany.

3. *Nanostructured p-type ternary oxides for photoelectrochemical water splitting*

    Ilina Kondofersky, Kristina Peters, Halina Dunn, Goran Stefanic, Dina Fattakhova-Rohlfing, Bruce A. Parkinson, Thomas Bein

    27. Deutsche Zeolith-Tagung, 2015, Oldenburg, Germany

4. *Porous architectures of transparent conducting oxides assembled from nanocrystals*

    Kristina Peters, Ksenia Fominykh, Thomas Bein, Dina Fattakhova-Rohlfing

    MRS Spring Meeting, 2015, San Francisco, USA.

5. *Porous architectures of transparent conducting electrodes for bioinspired optolectronics*

    Kristina Peters, David Sarauli, Thomas Bein, Dina Fattakhova-Rohlfing

    Soltech Workshop, 2016, Munich, Germany.

14.4.   CONFERENCE PARTICIPATIONS

1. Nanosystems for Solar Energy Conversion, 2013, Munich, Germany

2. CeNS Workshop "Nanosciences: Great Adventures on Small Scales", 2013, Venice, Italy

15. CURRICULUM VITAE

PERSONAL INFORMATION

Name:	Kristina Peters
Address:	Perhamerstraße 33
	80687 Munich, Germany
Phone:	+ 49 (0) 176 82117192
E-Mail:	krissi_peters@web.de
Date of birth:	Novenber 22nd, 1988
Place of birth:	Schachtinsk (Kazakhstan)
Nationality:	German

EDUCATION

Since 03/2014   PhD student in the group of Prof. Dr. Dina Fattakhova-Rohlfing

- Ludwig- Maximilians-Universität (LMU), Munich

- Thesis: 'Nanostructured Current Collectors for Electrochemical Applications Based on Transparent Conducting Oxides'

RESEARCH

- Synthesis of metal oxide nanoparticles (transparent conducting oxides: ITOH, ATO, ATO/graphene composites, Nb:TiO$_2$, TiO$_2$, NiO and Fe:NiO)
- Fabrication of new three-dimensional transparent conducting oxide electrodes using hard- and soft-templating approaches for optoelectronic and photocatalytic applications
- Characterization of new materials using TEM, SEM, EDX, AFM, XRD, GISAXS, TGA, XPS, ICP, IR, Raman, UV-Vis, Sorption, Hall conductivity measurements, electrochemical measurements (cyclic voltammetry, galvanostatic analysis)
- SEM operator
- Laboratory-safety manager

TEACHING

- Organization and supervision of lab courses for undergraduates in inorganic and physical chemistry
- Group tutor for tutorials in physical chemistry
- Supervision of graduate research assistants, Bachelor, Master and (international) intern students (exchange students of the Nanosystems Initiative Munich (NIM) Summer Research Program (SRP)

10/11 – 12/13	Master of Science in chemistry, M. Sc. (**Grade: 1.1**)

- Ludwig-Maximilians-Universität (LMU), Munich
- Thesis: 'Synthesis of Antimony Doped Tin Oxide Nanocrystals and their Assembly to Macroporous Films for Applications as Nanostructured Transparent Conducting Electrodes' (**Grade: 1.0**)
- Basic subjects: physical and inorganic chemistry
- Minor subject: material sciences

10/08 – 09/11	Bachelor of Science in chemistry and biochemistry, B. Sc. (**Grade: 2.2**)

- Ludwig-Maximilians-Universität (LMU), Munich
- Thesis: 'Synthesis and Characterization of alkali and alkaline earth metal salts of 5,5'-bistetrazole' (**Grade: 1.0**)

9/99 – 5/08	Hildegardis-Gymnasium Kempten (Allgäu)
	General qualification for university entrance (**Grade: 1.9**)

RESEARCH INTERNSHIP

03/12 – 05/12	Research internship in the group of Prof. Dr. P. Brother at the University of Auckland (New Zealand)

WORK EXPERIENCE

2011 – 2016	Waitress at the Octoberfest in Munich and at the folk festival in Dachau
10/12 – 02/12	Group tutor for tutorials in physical chemistry at the LMU

2009 – 2013	Annual job in a cocktail bar at the Tollwood summer and winter festival in Munich
08/10	Holliday job in a security agency (Sida GmbH in Kempten)
07/08 – 08/08	Piece-worker (machine building industry, Swoboda GmbH Wiggensbach)

AWARDS AND SCHOLARSHIPS

- Graduate Student Award of the Materials Research Society in recognition of an outstanding paper contributed to the 2017 E-MRS Spring Meeting

- „Preis der Dr. Klaus Römer-Stiftung" for outstanding master studies 2014

- Member of the Nanosystems Initiative Munich Graduate Program (2013-2017)

- CENS travel award for the IMRC – Cancun, Mexico (2016)

- GDCh travel award for the E-MRS Spring meeting – Lille, France (2014)

- Travel award from the Lautrach foundation for the TCM – Greece (2014)

- Prosa travel award for an internship at the University of Auckland (2012)

- Bio Zukunftspreis (best high school graduate in Biology) (2008)

COMPUTER LITERACY

- MS Office, ChemDraw, Origin, ImageJ, NOVA, Diamond, SciFinder, Adobe Illustrator

LANGUAGES

- German: native speaker
- English: business fluent
- Russian: fluent (2nd native language)
- Latin: basic skills

PERSONAL INTERESTS & ACTIVITIES

- Travelling, Jogging, skiing, alpine tours, volleyball